Technical Report

TR-10-37

Counterforce applied to prevent spalling

Rune Glamheden, Golder Associates AB

Billy Fälth, Clay Technology AB

Lars Jacobsson, SP Technical Research Institute of Sweden

Johan Harrström, Geosigma AB

Johan Berglund, Vattenfall Power Consultant AB

Lars Bergkvist, Golder Associates AB

April 2010

Svensk Kärnbränslehantering AB
Swedish Nuclear Fuel
and Waste Management Co

Box 250, SE-101 24 Stockholm
Phone +46 8 459 84 00

ISSN 1404-0344
SKB TR-10-37

Counterforce applied to prevent spalling

Rune Glamheden, Golder Associates AB

Billy Fälth, Clay Technology AB

Lars Jacobsson, SP Technical Research Institute of Sweden

Johan Harrström, Geosigma AB

Johan Berglund, Vattenfall Power Consultant AB

Lars Bergkvist, Golder Associates AB

April 2010

Preface

This report describes the field experiment performed within the project termed CAPS (Counterforce Applied to Prevent Spalling). The overall aim of the project has been to demonstrate whether a small confining pressure obtained by the application of dry bentonite pellets is sufficient to suppress thermally-induced spalling in KBS-3 deposition holes.

The report is focused on the design, execution and observations made during the field experiment. The main report has been written by Rune Glamheden, while the co-authors have contributed with background memos included in the appendices. The field work was carried out at Äspö Hard Rock Laboratory in Oskarshamn, operated by SKB (Svensk Kärnbränslehantering AB).

A field experiment like the present one involves contributions from a many individuals and in addition to the project manager Rune Glamheden the following people have been taken part in the project:

Rolf Christiansson, Derek Martin and Harald Hökmark – Steering committee.

Lisa Björk – Activity leader.

Mats Lundqvist – Project coordinator and responsible for the instrumentation including calibration work and the data processing.

Richard Bäck – Responsible for design, manufacturing and installation of test equipment in the field test, as well as the design and manufacturing of the equipment for the post characterization.

Elinor Örtendahl – Project coordinator in the beginning of the project during the drilling and grouting.

Titti Falk, Birgitta Karlsson and Siren Bortelid Moen – Project administrators.

Maria Eriksson and Margareta Gerlach – Data Operators for SICADA.

Margareta Lönnqvist – Scoping calculations and set up of model for back-calculation.

Lars Jacobsson – Uniaxial compression tests of intact rock and Oedometer tests of pellets.

Torbjörn Sandén – Compression tests in pellet filled slot.

Johan Harrström – Water injection tests of the damaged zone.

Billy Fälth – Back-calculation of temperatures and stresses in the field experiment.

Sakar Koyi and Tobias Zetterberg – AutoCAD drawings within the field experiment.

Kim Forchhammer and Jonny Andersson – Reporting of temperature data.

Lars Bergkvist – Investigation of rock fragments.

Mikael Gustavsson and Roger Jonsson – Core drilling of the test holes.

Anders Larm and Björn Ekstedt – Reaming of heating holes.

Christer Gustavsson and Jaana Gustafsson – Bips-logging of core drilled holes.

Ulf Andersson, Anders Wägnerud and Oskar Sigurdsson – Mapping of core drilled holes.

Johan Berglund – Mapping of drill cores and RVS-modelling of the site geology.

Pär Kinnbom – WellCAD diagrams for geological data.

Anders Wikman –Pressure build-up tests in pilot holes.

Johan Funehag and Henrik Svensson – Design and performance of the grouting program.

Quanhong Feng – Laser scanning for documentation of initial conditions.

Rolf Berlin and David Johansson – Laser scanning for post characterization of the breakouts.

Curt-Robert Lindqvist – Photo documentation of the field experiment.

Gerry Johansson – Surveying within the field experiment.

Stefan Grandin Svärdh, Nils-Göran Myrén, Tomas Sandsten, Tony Andersson, Jan Hultgren, Åke Hultgren, Christer Jonasson, **Robert Johansson, Hampus Gustavsson and Jonas Hallberg** – Practical issues at the site and installation work in the field experiment.

The authors acknowledge Johan Andersson, Rolf Christiansson, Philip Curtis, Anders Fredriksson, John Hudson, Harald Hökmark and Derek Martin for examination of the manuscript.

Abstract

The field experiment within CAPS (Counterforce Applied to Prevent Spalling) was initiated to determine if the application of dry bentonite pellets is sufficient to suppress thermally-induced spalling in KBS-3 deposition holes. The experience gained from Äspö Pillar Stability Experiment, conducted between 2002 and 2006, indicated that spalling could be controlled by the application of a small confining pressure in the deposition holes /Andersson 2007/.

The CAPS field experiment that included four pairs of boreholes with a diameter of approximately 0.5 m, was carried out as a series of demonstration experiments in the TASQ-tunnel. The first and second heating tests were performed in open holes, without any confining pressure on the borehole wall and the third and fourth heating tests with a confining pressure created by expanded clay pellets (LECA). The first heating test was initiated at the end of August 2008 and the final test was finished at the end of May 2009.

The trials suggest that the small confining pressure offered by the LECA pellets was adequate to control spalling and prevent the formation of a highly conductive zone of fractured rock in the 500-mm-diameter holes. It is recommended that a full-scale test be carried out to assess if the findings are applicable to 1,750-mm-diameter deposition holes. Should the full scale tests support the findings from these initial trials, filling the gap between the bentonite blocks and rock wall with dry bentonite pellets will provide a viable engineered solution for controlling the effects of thermally-induced spalling in the KBS-3 deposition holes.

Sammanfattning

Fältförsöken inom CAPS (Counterforce Applied to Prevent Spalling) initierades för att fastställa om applicering av torr bentonitpellets är tillräckligt för att förhindra uppkomsten av termisk inducerad spjälkning i KBS-3 deponeringshål. Erhållen erfarenheten från pelarförsöket vid Äspölaboratoriet (APSE), som utfördes mellan åren 2002 och 2006, indikerade att spjälkning kan förhindras genom applicering av ett litet mothållande tryck i deponeringshålen /Andersson 2007/.

Fältförsöket CAPS, som inkluderade fyra par borrhål med en diameter av ungefär 0,5 m, utfördes som en serie demonstrationsförsök i TASQ tunnel. Det första och det andra uppvärmningsförsöket utfördes i öppna hål, utan något tryck mot borrhålsväggen, medan det tredje och fjärde försöket utfördes med ett mothållande tryck som skapades av lecakulor. Det första uppvärmningsförsöket påbörjades i slutet av augusti 2008 och det sista försöket avslutades i slutet av maj 2009.

Försöken tyder på att det lilla mothållande tryck som lecakulorna ger upphov till är tillräckligt för att begränsa spjälkningen och förhindra uppkomsten av en starkt genomsläpplig zon av uppsprucket berg i de aktuella 500 mm hålen. Det rekommenderas att ett fullskaligt försök utförs för att bestämma om forskningsresultaten är applicerbara på hål med 1 750 mm diameter. Skulle fullskaleförsöken bekräfta resultaten från dessa inledande försök, kan utfyllnad av spalten mellan bentonitblocken och berget med torr bentonitpellets utgöra en praktisk ingenjörsmässig lösning för att begränsa inverkan av termisk inducerad spjälkning i KBS-3 deponeringshål.

Abbreviations and definitions

The most important abbreviations and symbols utilized in the report are compiled in this section, along with the definitions of important rock mechanics terms.

Geological, rock mechanical and thermo-mechanical abbreviations

σ_1, σ_2, σ_3	Major, Intermediate and Minor principal stress, (MPa)
E, E_m	Intact rock, rock mass Young's modulus, (GPa)
ν, ν_m	Intact rock, rock mass Poisson's ratio
α	Coefficient of linear thermal expansion, (10^{-6}/K)
λ	Thermal conductivity, (W/mK)
κ	Thermal diffusivity, (10^{-6} m^2/s)
C	Heat capacity, (MJ/m^3K)
CI	Crack initiation threshold, (MPa)
BTS	Brazilian tensile strength of intact rock, (MPa)
UCS	Uniaxial compressive strength of intact rock, (MPa)
UCS_m	Uniaxial compressive strength of the rock mass, (MPa)

Other abbreviations

APSE	Äspö Pillar Stability Experiment
CAPS	Counterforce Applied to Prevent spalling
EDZ	Excavation Damaged Zone
LECA	Light Expanded Clay Aggregates
TASQ	The Q-tunnel at Äspö HRL

Definitions

Spalling	Rock fracturing that form thin slabs on the boundary of the deposition holes in the position of the maximum tangential stress. The spalling strength is normally estimated as a fraction of the determined UCS or by the determined CI value.
Breakouts	Breakouts are zones of enlargement of the heating holes due to failure of the rock in the spalling process.
UCS	Uniaxial compressive strength of a cylindrical sample of rock, 45–55 mm in diameter and 125–150 mm in length. The value should be view as a standard index.
BTS	Brazilian (indirect) tensile strength as a measure of true (direct) tensile strength (T). The ratio of UCS to T is an indicator of spalling potential.
CI	Crack initiation threshold for the rock sample. This threshold is marked by the onset of systemically increasing damage (cracks) with increasing applied stress. This threshold can be determined by acoustic emission monitoring or by lateral strain measurements. This threshold marks the lower bound for in situ rock strength.

Contents

1 Introduction

1.1 Background

The KBS-3 disposal concept consist of copper canisters with cast iron inserts containing spent nuclear fuel, which are surrounded by bentonite clay and deposited at approximately 500 m depth in saturated granitic rock, see Figure 1-1 /SKB 2006/. Not indicated in the figure, is that the reference design includes a small slot between the buffer and the rock, which will be filled with bentonite pellets.

For a repository at the proposed depth of 500 m, the site description of Forsmark indicates high in situ stresses in relation to the compressive strength of the intact rock and spalling of the deposition holes is expected to occur during the drilling /SKB 2008/. The process of spalling is defined as fracturing of rock that forms thin slabs on the boundary of the deposition holes in the position of the maximum tangential stress. The spalling strength is normally estimated as a fraction of the determined uniaxial compressive strength of intact rock.

Spalling before deposition of spent nuclear fuel is possibly only a concern for practical engineering; whereas the process of thermally-induced spalling in deposition holes may impact the safety of a repository if a continuous damaged zone is developed along the hole. A hydraulic conductive spalled zone intersected by conductive fractures, will enhance the risk for mass transfer from the deposition hole /SKB 2006/.

To obtain a better understanding of the spalling process and examine the possibilities of reducing its impact on the safety of a repository, Swedish Nuclear Fuel and Waste Management Company (SKB) has carried out two large field experiments at Äspö HRL. The first experiment called the Äspö Pillar Stability Experiment (APSE), conducted between 2002 and 2006, indicated that spalling could be controlled by application of a small confining pressure (≈150 kPa) in the deposition holes /Andersson 2007/.

The promising results from the APSE experiment lead to the initiation of a subsequent field experiment termed CAPS (Counterforce Applied to Prevent Spalling), which is reported here. The object being to determine if the small counterforce obtained by application of dry bentonite pellets in the slot between the buffer and the rock, could be sufficient to suppress or at least reduce thermally-induced spalling.

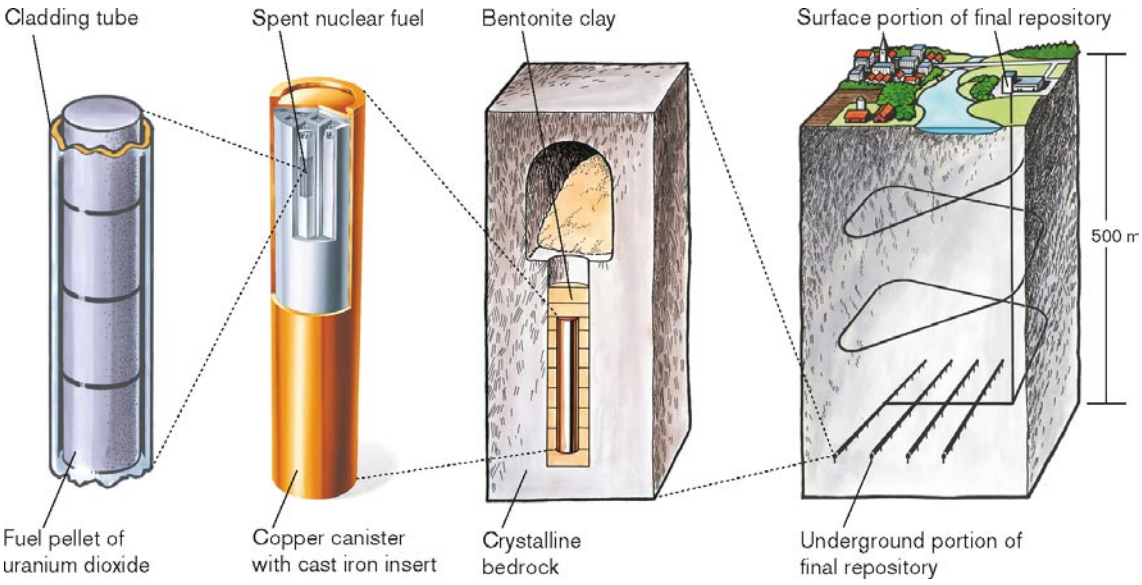

Figure 1-1. *The KBS-3 concept for disposal of spent nuclear fuel /SKB 2006/.*

The CAPS field experiment included a total of eight boreholes that were heated up in a series of demonstration experiments in the TASQ-tunnel. Each test consisted of two heating holes with a diameter of approximately 0.5 m and a depth of 4 m, separated by a 0.7 m thick pillar, which were surrounded by a number of boreholes equipped with temperature gauges. The boreholes included in the field experiment are presented with labels in Figure 1-2. The first and the second heating tests were performed in open holes without any confining pressure on the borehole wall. The third and the fourth heating tests were carried out in holes with loosely placed LECA pellets (expanded clay), in a 50 mm gap created between an inner tube and the borehole wall, to observe any difference in the occurrence of spalling compared to the previous tests. The first heating test was initiated at the end of August 2008 and the final test was finished by the end of May 2009.

After the final heating test, post characterization of the spalled damaged zone in the heating holes was carried out. The post characterization included examination of the hydraulic transmissivity of the spalled zone in one heating hole in the final test, and documentation of the geometry of the spalled zone in the other heating holes. The post characterization of the spalled zone was completed by mid-September 2009.

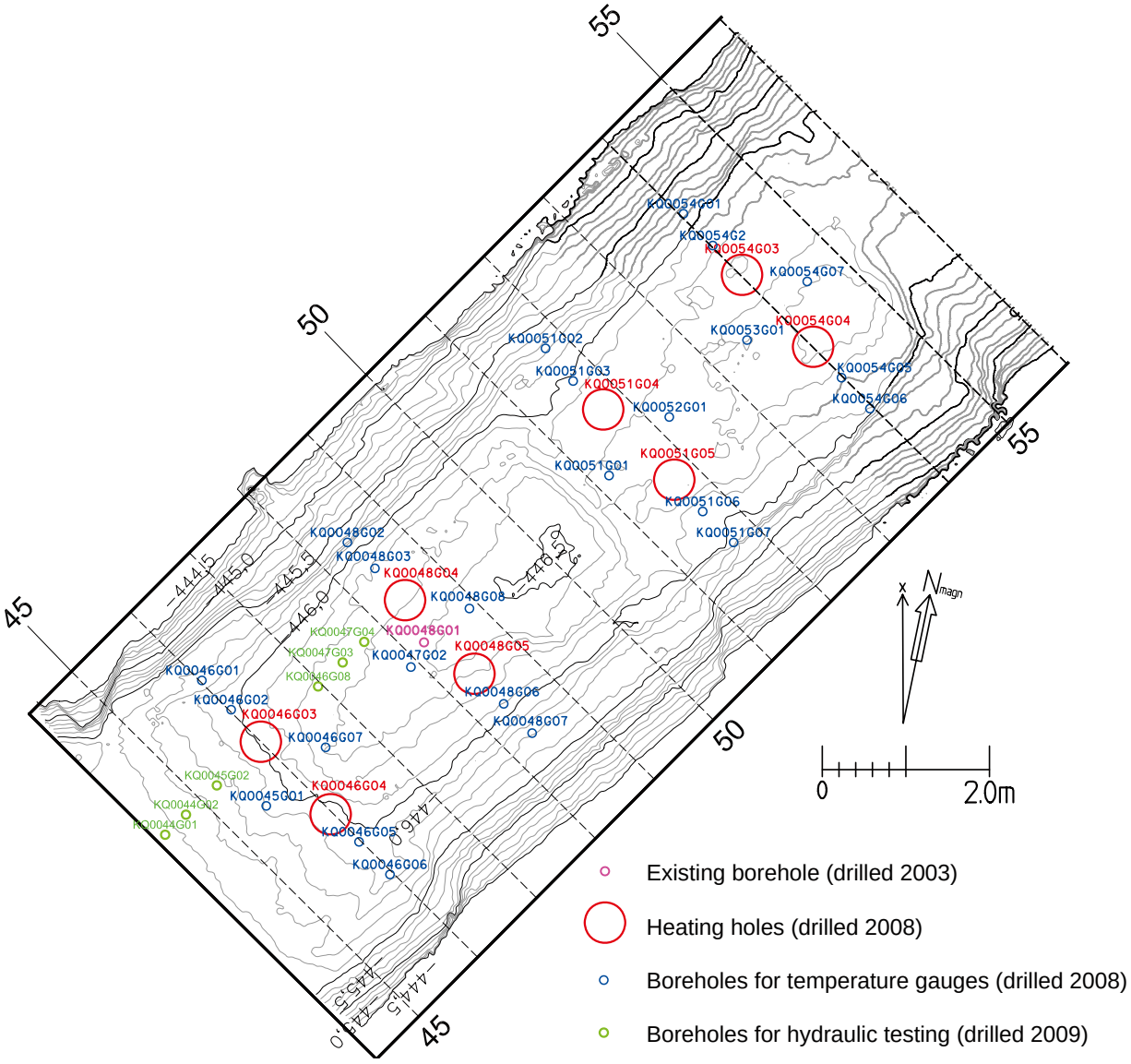

Figure 1-2. *Drawing showing the configuration and the labels of the boreholes included in the field experiment. ÄSPÖ96 coordinates system. The difference in elevation between the iso-lines is 0.1 m.*

1.2 Experience from APSE field experiment

In this section a short account of the experience from Äspö Pillar Stability Experiment (APSE) is given. The APSE field experiment was conducted between 2002 and 2006 to examine the spalling process in a heterogeneous slightly fractured rock mass (approx. 1–2 fracture/m) subjected to excavation and thermal induced stresses /Andersson 2007/. The field experiment was carried out on the 450 m level at ÄSPÖ HRL in the TASQ tunnel, in a part of the tunnel (Section 62–68) beyond that used for CAPS field experiment (Section 45–55), see Figure 1-3.

The APSE field experiment consisted of two large boreholes with a diameter of 1.75 m and a depth of 6.5 m separated by an approximately 1 m thick pillar. To prevent excavation induced spalling occurring in the first borehole a confining pressure of about 700 kPa was applied on the borehole wall by a large rubber bladder before excavation of the second hole commenced. The rock in the second hole spalled from a depth of approximately 0.5 m down to 2 m when excavated.

To induce thermal stresses in the pillar, it was heated by electrical elements in two pair of core drilled holes located on each side of the pillar. The temperature on the pillar wall reached approximately 30 degrees before the heater was turned off. The superimposed thermal stresses caused spalling along the pillar wall in the unconfined hole, which propagated down to approximately 5 m depth close to the bottom of the hole before the heater was turned off /Andersson 2007/.

When the temperature increase in the pillar had stopped and steady state was reached, the confinement pressure in the protected hole was reduced gradually in 50 kPa steps from 700 kPa to zero pressure under a period of 1.5 days. Large acoustic activity on the confining side of the pillar was not observed until the confining pressure was reduced to about 150 kPa. The results indicated that spalling could be controlled by application of a small confining (100–200 kPa) pressure in the deposition holes and this was the key finding for the planning of the follow up CAPS field experiment /Andersson 2007/.

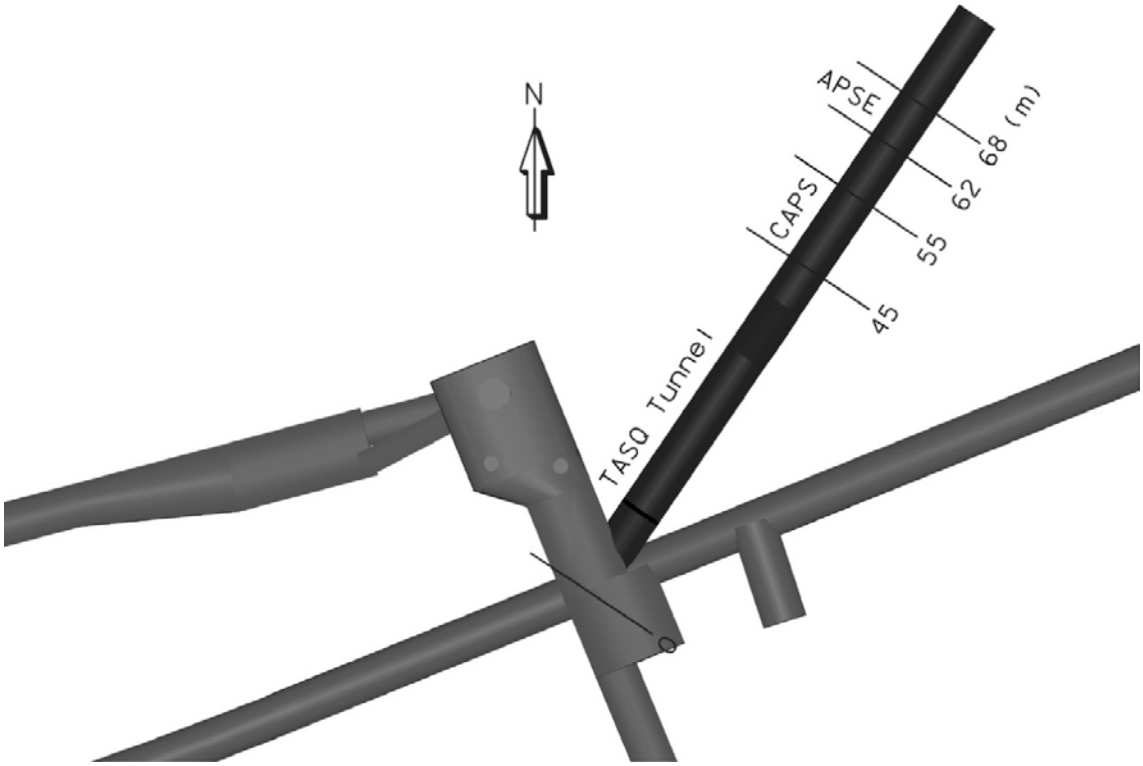

Figure 1-3. *Location of APSE field experiment in relation to CAPS field experiment.*

1.3 Objective and scope of work of the study

The CAPS field experiment has had the following twofold objective:

1. Establish that thermally-induced spalling will occur at a tangential stress corresponding to about 60% of the uniaxial compressive strength in open boreholes of 0.5 m diameter and 4 m depth, i.e. as for the open full scale APSE hole.
2. Establish if dry bentonite pellets are sufficient to suppress or significantly reduce thermally-induced spalling.

The overall aim of the project is to provide the Safety Assessment work groups with experimental results that support a viable engineered solution for controlling the effects of thermally –induced spalling.

The scope of work of the field experiment has included the following main activities:

- Scoping calculation to determine the optimal hole configuration for the field experiment and the positioning of instruments. These calculations also involved estimation of the thermal energy and temperature required to achieve the spalling along the borehole wall and estimation of the stress magnitudes that would develop on the wall of the boreholes.
- Development of proper equipment for central heating of the test holes and a frame that produces a 50 mm gap for filling of pellets against the borehole wall.
- Development of a fixture for attachment of temperature gauges on the wall at several levels in the heating holes and development of monitoring cameras for observation of spalling in the heating holes.
- Selection of a suitable pellet substitute for bentonite pellets based on odometer tests and compression tests of a pellet-filled slot.
- Core drilling, water loss measurements and grouting of test holes. Reaming of pilot holes to the desired diameter for the heating holes.
- Uniaxial compression tests of rock samples from the test holes.
- Documentation of the conditions of the heating holes by photographs and laser scanning before heating.
- Realization of Tests 1–4, which comprise installation of test equipment, heating and cooling of the test holes and documentation of the occurrence of spalling before scaling of the borehole wall by photographs and video recording.
- Post characterization of the notch geometry after scaling of the borehole wall by photographs, thin lighted slots, laser scanning and video recording.
- Post characterization of the hydraulic transmissivity of the spalled damaged zone by water injection tests of one heating hole in the final test (KQ0046G03) after sealing of the pellet filled slot.
- Evaluation and reporting of the results.

The field work at Äspö HRL was initiated by the core drilling in March 2008 and completed in September 2009 by the final post characterization.

The work presented in the report is divided into sections, including site conditions (Chapter 2), design of the experiment (Chapter 3), preparation of the test site (Chapter 4), execution of the field experiment (Chapter 5), spalling observations (Chapter 6), post characterization (Chapter 7), analysis of test results (Chapter 8) and finally summary of the results, conclusions and recommendations (Chapter 9–11). 22 appendices are also incorporated into the report (Appendix A–V).

2 Site conditions

2.1 Overview of the geology

A map of the tunnel floor showing rock types and structures is shown in Figure 2-1, and an isometric view of the test area with borehole sections logged with oxidation and the boundaries of a shear zone running through the site, is presented in Figure 2-2.

The dominating rock type around TASQ tunnel is quartz monzodiorite to granodiorite (Äspö diorite, 501037). The grain size is medium to coarse and the rock has a faint to weak foliation. Mapped drill cores taken from the tunnel floor in general show weak to medium oxidization in the uppermost 1–1.5 m of the rock, see Figure 2-2. The oxidation, which is a result of alteration of the rock over geological time, might be accompanied by a slight weakening of the rock /Staub et al. 2004/.

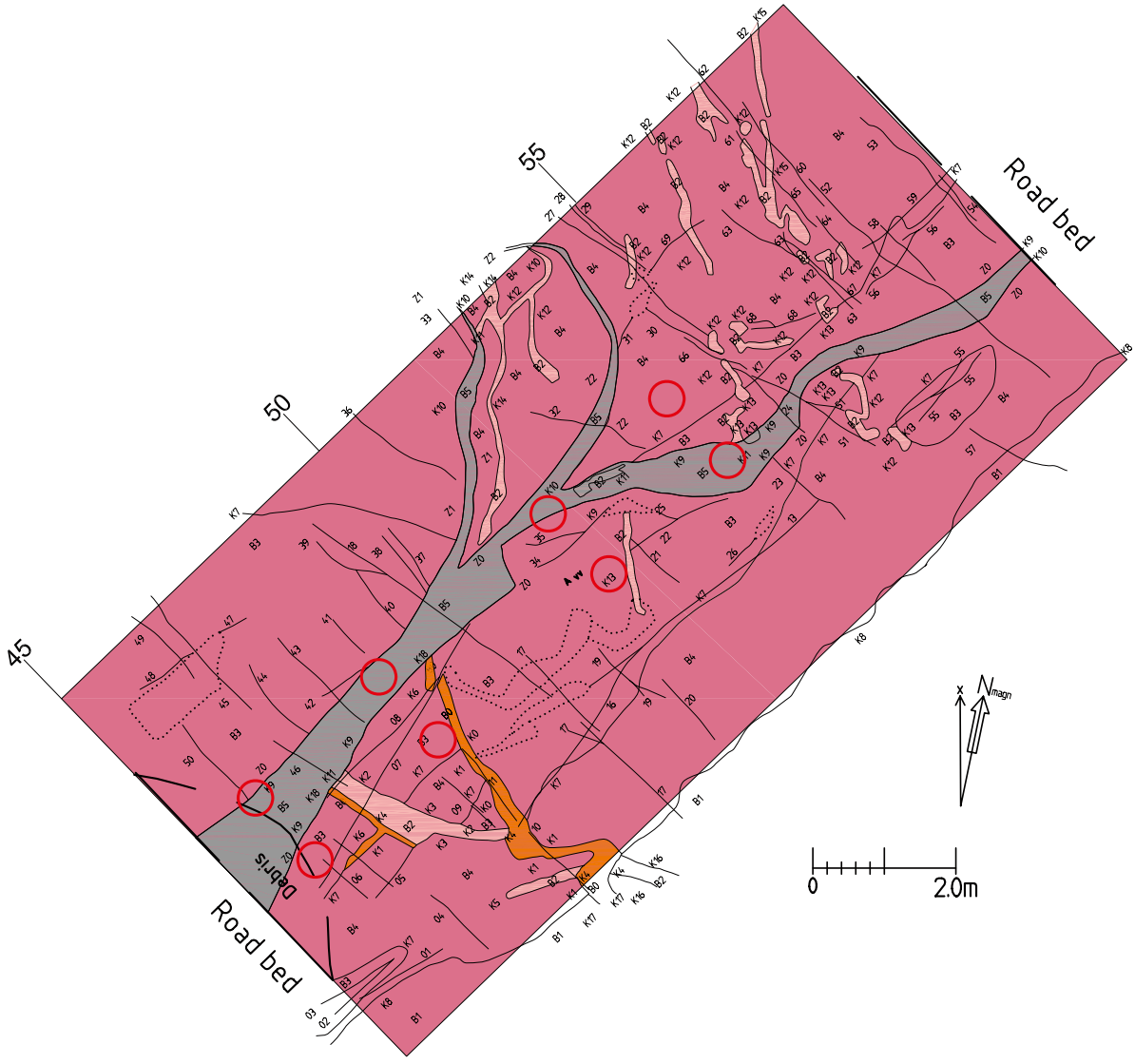

Figure 2-1. *Map of rock types and the ductile shear zone (mylonite) occurring in the tunnel floor in the part of the tunnel utilized for the CAPS experiment. The positions of the heating holes are also indicated in the figure. Fine grained granite – light pink; Äspö diorite – dark pink; Pegmatite – brown; Mylonite – grey.*

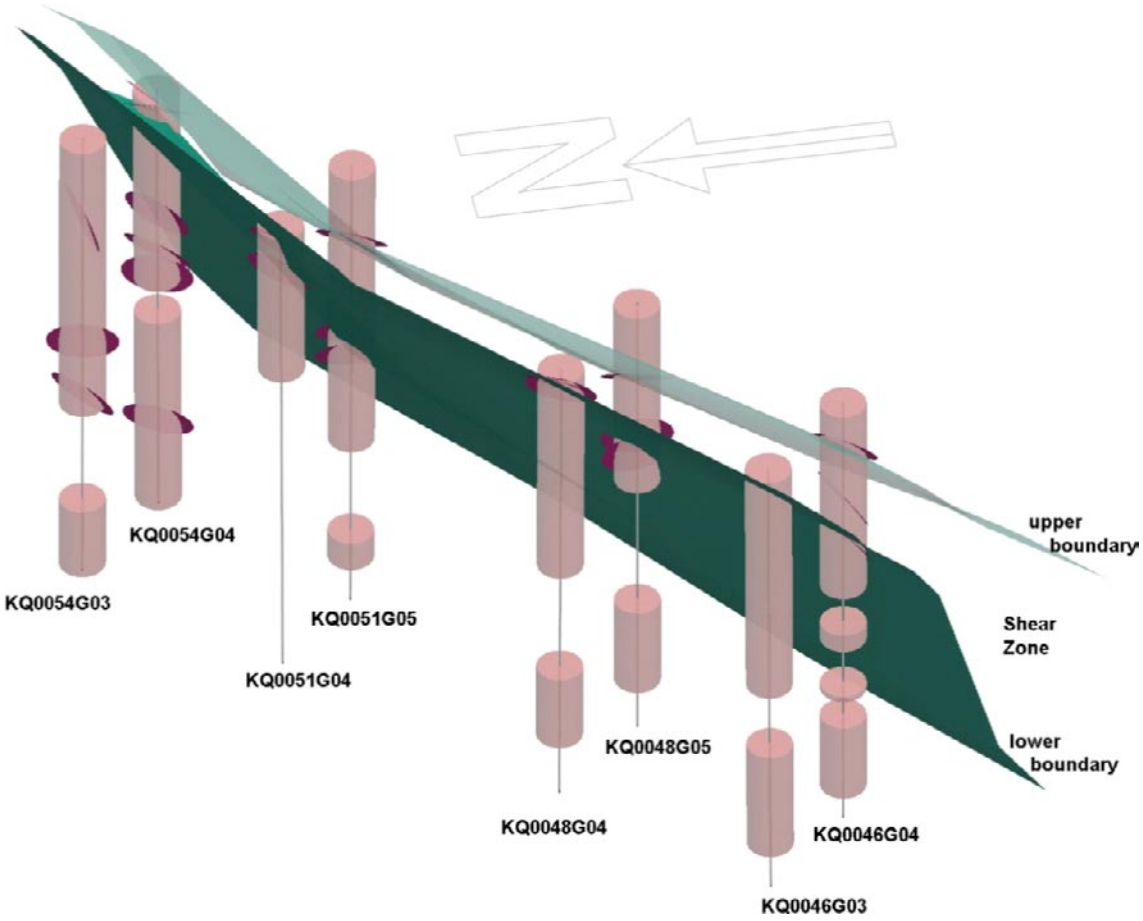

Figure 2-2. *Isometric view of the test area showing borehole sections logged with oxidation and the boundaries of a shear zone running through the site. The pink cylinder sections indicate oxidized rock and the purple disks indicate mapped shear zone boundaries.*

Other rock types in the area are medium to coarse, red pegmatite (501061) and fine- to medium-grained red granite (511058) occurring as veins normally less than 0.5 m wide. Another structure observed in the tunnel floor is a complex brittle-ductile shear zone (mylonite) with several branches. The width of the branches is normally between 0.1–1 m and the dip is typically 50–60 degrees to the southeast, see Figure 2-2. Although composed mainly of sealed fractures, there was a desire to avoid intersection between the heating holes and the shear zone, in order to obtain as far as possible homogeneous rock conditions for the experiment. However, at the assigned site intersection was unavoidable, since the zone's strike is parallel with the tunnel.

The fractures observed in the tunnel can be generalized as belonging to three characteristic fracture sets. The dominating fracture set is orientated approximately in a steep northwest-southeast direction, the other two being a sub-horizontal one and a steep set, sub-parallel to the tunnel direction. Most of the fractures observed around the tunnel are sealed and include mineral fillings. Fracture coatings or fillings of calcite, chlorite and epidote are the most common. The sealed fractures are judged to have only a minor influence on the mechanical properties of the rock and these fractures are normally non-transmissive. The open water bearing fractures in the current Section 45–55 of TASQ tunnel are actually very few.

The estimation of the quality of the rock mass in the part of the tunnel used for CAPS was based on a rock mass classification performed for the APSE project using the Q-index /Barton 2003/. The Q-index estimated for the rock in tunnel sections 25 to 60 vary between 8 and 2,130 with a mean value of 110. The estimated Q-value corresponds to "good to excellent" rock quality.

2.2 Properties of intact rock

2.2.1 Mineralogy

The dominating rock type around the TASQ tunnel, Äspö Diorite (501037), is in a fresh condition with the following mineral composition: 46% plagioclase, 15% quartz, 15% biotite, 12%, K-feldspars, 6% epidote, 2% amphibole, 1% chlorite and 4% accessories. In general, the largest grains are of K-feldspar, with a size of 1–5 mm. The grains of plagioclase and quartz are normally 0.5–2 mm /Andersson 2007/.

Alteration of the rock has occurred by oxidation or mylonization with alteration of plagioclase and K-feldspar to quartz and calcite, and of biotite to chlorite. A minor study on thin sections reported by /Andersson 2007/, indicate that the oxidized rock found in TASQ tunnel has an increased content of epidote and calcite, while the mylonitic rock has an increased content of quartz, epidote and calcite compared to unaltered rock. The observed exchange of the minerals in the alteration process suggests reduced strength in the oxidized rock and increased strength in the mylonitic rock. Laboratory tests on oxidized rock or rock containing sealed fracture networks, confirm a lower compressive strength relative to fresh Äspö Diorite. The ratio is approximately 0.5–0.6 compared to fresh rock /Staub et al. 2004/.

2.2.2 Density and porosity

Density and porosity of intact rock samples were previously measured in the laboratory /Staub et al. 2004/. Wet and dry bulk densities, as well as effective porosity, were conducted on a total of 5 samples collected in two boreholes in the TASQ tunnel in the section used for APSE. The results, which show normal values for this type of rock, are listed in Table 2-1.

2.2.3 Mechanical properties

The deformation and strength properties of intact rock were previously measured in uniaxial tests /Andersson 2007/. The tests included eighteen samples collected in four boreholes in the TASQ tunnel in the tunnel section used for APSE /Staub et al. 2004/. The results are presented in Table 2-2.

In the current field experiment another ten samples were collected for measurements of deformation and strength properties of intact rock from the CAPS tunnel section, see Appendix C. The results from these additional tests are summarized in Table 2-3. The latest laboratory results are close to those earlier reported.

Table 2-1. Dry and wet density as well as effective porosity of intact rock evaluated from five samples collected in the tunnel section used for APSE /Staub et al. 2004/.

Parameter	Mean	Range	Unit
Dry bulk density	2,746	2,740–2,750	kg/m^3
Wet bulk density	2,754	2,750–2,760	kg/m^3
Effective porosity	0.3	0.15–0.40	%

Table 2-2. Deformation and strength properties of intact rock evaluated from eighteen samples collected in the tunnel section used for APSE /Andersson 2007/.

Parameter	Mean	Range	Unit
E	76	69–79	GPa
ν	0.25	0.21–0.28	–
CI	121	80–160	MPa
UCS	211	187–244	MPa
BTS	15	13–16	MPa

Note: The crack initiation stress is evaluated from acoustic emission.

Table 2-3. Deformation and strength properties of intact rock evaluated from ten samples collected in the tunnel section used for CAPS, see Appendix C.

Parameter	Mean	Range	Unit
E	74	71–78	GPa
ν	0.29	0.22–0.32	–
CI	116	85–152	MPa
UCS	227	170–294	MPa

Note: The Crack initiation stress is evaluated from uniaxial tests using the strain method.

Although the last results indicate a somewhat higher uniaxial compressive strength compared to in earlier tests, the difference is judged to be within the accuracy of the applied testing method. It should also be noted that the two sets of testing were performed by different laboratories (SP Technical Research Institute and Helsinki University of Technology, respectively).

Since the number of samples included in both sets of laboratory test was relatively small, it is only the evaluated mean values that are judged to be representative for the rock. The given ranges are mainly a result of having small number of samples and probably do not indicate real differences in the rock properties. However, the evaluated deformation and strength properties of the intact rock are likely to be influenced by local variations in the geology. Alteration by oxidation and epidotization are examples of conditions in the rock that might influence the strength. The more foliated parts of the rock might also show a certain directional dependence of the strength properties. It should be noted that the core sections used for the specimens have been selected with the aim avoiding sections with sealed fractures that have an acute angle to the direction of the axial load.

The crack initiation threshold is evaluated based on two different methods, acoustic emission monitoring in the earlier tests and strain based monitoring in the present tests. More confidence is given to the results evaluated from the monitoring of the acoustic emission, since this method is judged to be more exact.

The tensile strength was not determined during the present field test, since the uncertainty in the results of the previous laboratory tests was judged to be small. Furthermore, in the present study the parameter is used mainly to predict the spalling potential of the rock via the ratio of the compressive strength to tensile strength. In the current experiment the ratio of UCS/BTS is about 15, which indicates that the spalling potential of the rock is high.

Although composed mainly of sealed fractures, the observations in the APSE field experiment indicate that the mylonitized shear zone has a slightly different spalling strength compared to the surrounding Äspö diorite /Andersson 2007/. The risk that the shear zone would influence the outcome of the field test was consequently assessed. However, the selected location was considered to be the most suitable found in the TASQ-tunnel.

2.2.4 Thermal properties

The thermo-physical properties of intact rock in TASQ tunnel were determined previously for the APSE field test /Andersson 2007, Staub et al. 2004/. These results are presented in Table 2-4. Additional testing of the thermo-physical properties for CAPS field experiment was considered unnecessary, since the results for the APSE test were rather homogenous.

Table 2-4. Coefficient of thermal expansion and thermal properties of intact rock evaluated from samples collected in the tunnel section used for APSE /Andersson 2007, Staub et al. 2004/.

Parameter	Mean	Range	Unit
α	7.0	6.2–8.3	10^{-6}/K
λ	2.6	2.4–2.8	W/mK
C	2.1	2.0–2.5	MJ/m^{3}K
κ	1.1	1.0–1.3	10^{-6} m^2/s

2.3 In situ state of stress

In situ stress measurements in the body of rock, where the TASQ tunnel is located, have been performed by three different methods in two orthogonal boreholes /Christiansson and Janson 2002/. The in situ stress around the TASQ tunnel has also been evaluated based on a back calculation of convergence measurements made in the tunnel /Andersson 2007/. The resulting best fit stress tensor from the back calculation is presented in Table 2-5. The major difference between the stress tensor evaluated from borehole measurements and the tensor evaluated from convergence measurements in the tunnel, is related to the plunge and the trend. The major principal stress is assumed to be perpendicular to the direction of the TASQ tunnel.

Table 2-5. Evaluated in situ stress field in the rock mass at TASQ tunnel, based on back calculation from convergence measurements taken in the tunnel during excavation /Andersson 2007/.

	σ_1	σ_2	σ_3
Magnitude (MPa)	30	15	10
Trend (Äspö 96)	310	0	220
Plunge	0	90	0

Note: The values correspond to the best fit stress tensor derived by numerical modelling using a Young's modulus E_m = 55 GPa.

2.4 Damaged and disturbed rock mass zone

The rock around a blasted opening is normally damaged and disturbed to some distance from the rock face. The Excavation Damage Zone (EDZ) may be defined as a zone where existing macro-cracks are opened or extended, or where new macro-cracks are induced by blasting. Furthermore there is a disturbed zone that is wider than the damaged zone. In this zone, rock mass properties of importance for the construction, or in this case the experiment, are affected by factors like blasting, stress redistribution and weathering. Obviously, the degree of damage and disturbance is strongly dependent on the blasting technique employed.

A theoretical section of the TASQ tunnel is shown in Figure 2-3. The tunnel, which has a total height of 7.5 m and width of 5 m, was excavated by a 5.5 m high pilot drift followed by a 2 m high bench. This excavation method was used to minimize the damaged and disturbed zone in the tunnel floor. There was also stringent control of the borehole precision to minimize the EDZ /Olsson et al. 2004/.

Investigation of the resulting EDZ in the tunnel floor of TASQ indicates that the zone has an extent of 100–200 mm /Olsson et al. 2004/. There is, however, no evidence of any continuous damage zone in the tunnel floor.

2.5 Water flow into heater holes

The hydraulic conductivity of the rock in the tunnel section used for the CAPS field experiment was examined by pressure build-up tests and water loss measurements. A criterion for acceptable inflow to the heating holes was established at 0.05 l/min to limit the heat transport by water movements during the field tests. The results from the water loss measurements indicated that this criterion might be exceeded in a couple of the holes and limited grouting was performed with silica sol prior to the reaming of these holes, see Section 4.4.

After completion of the reaming, the actual inflow of water to the heating holes was measured based on the change in water level in the holes during a period of 20 hours. The results from these measurements, which were performed in July 2007, are presented in Figure 2-4. The measurements indicate a slightly larger inflow into the holes located on the NW-side of the tunnel axis compared to those located on the SE-side. The measured inflow exceeded the established criterion in only one of the heating holes.

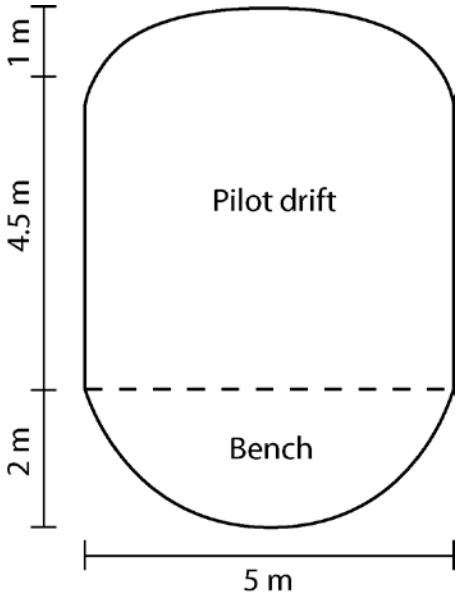

Figure 2-3. *Theoretical section of the TASQ tunnel. The tunnel was blast as a pilot drift and a separate bench /Andersson 2007/.*

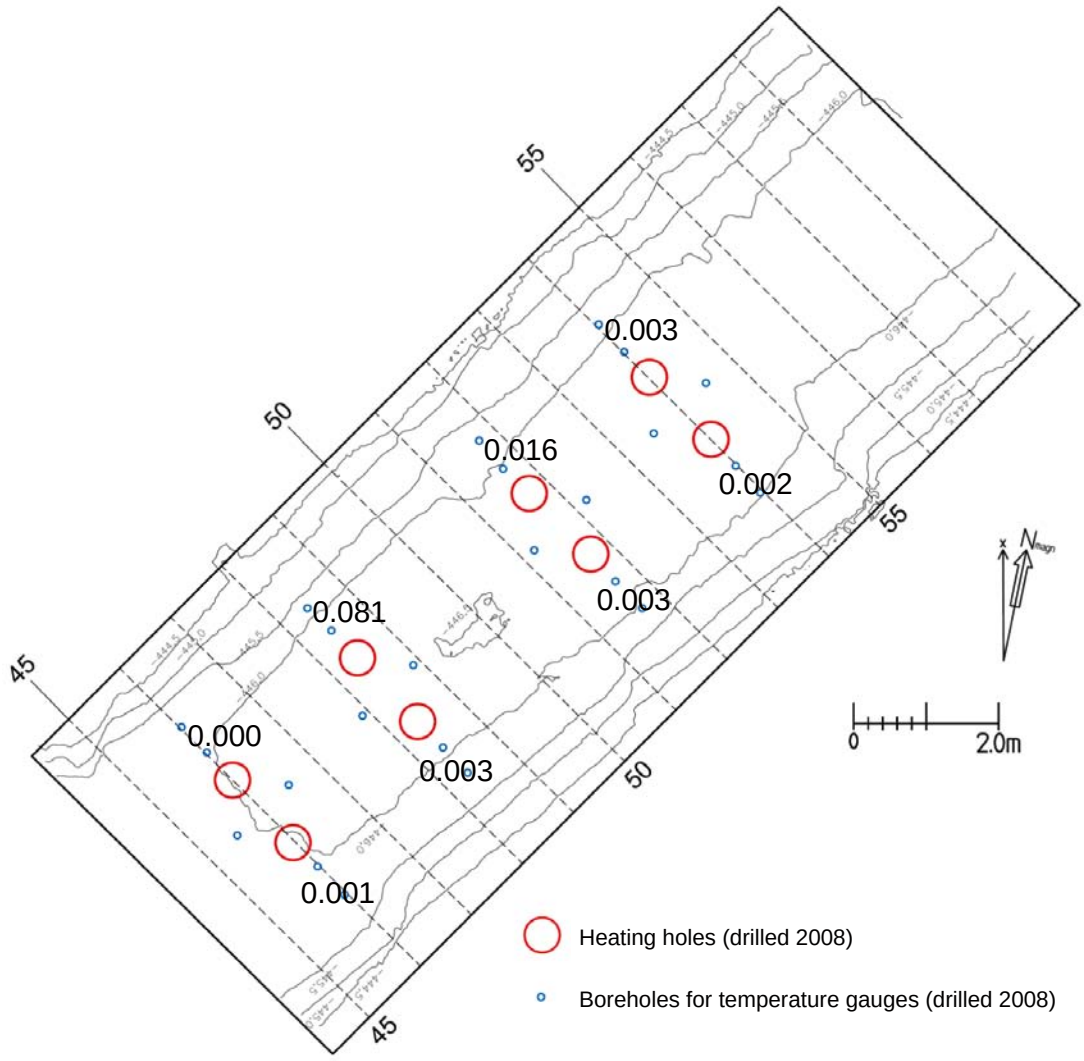

Figure 2-4. *Recorded inflow of water to the heating holes in July 2007 after reaming before heating (l/min).*

3 Design of the field experiment

3.1 Layout of the experiment

The field experiment has been carried out on the 450 m level at Äspö HRL in Section 45 to 55 of the TASQ tunnel. A photograph of the test site is presented in Figure 3-1. The configuration of the holes and the position of the instruments were settle based on scoping calculations /Lönnqvist et al. 2008/. Drawings showing the layout for each separate test are presented in Appendix G.

The test site consists of four pairs of heating holes, each surrounded by six instrumentation holes. The heating holes have a diameter of approximately 485 mm and a length of 4 m in rock. The centre to centre distance between the heating holes is 1.2 m giving a pillar width of 0.7 m. The diameter of the instrumentation holes is 56 mm.

The bottom of the heating holes has a telescopic shape over the last 1 m length, since they were reamed from a core-drilled hole in four steps (76 – 162 – 242 – 354 – 486 mm). To seal the heating holes from water on the tunnel floor, each hole had a cast 0.1–0.5 m thick concrete collar. The total length of each heating hole is consequently around 5.4 m with the collar of all holes at level –446.0 m.

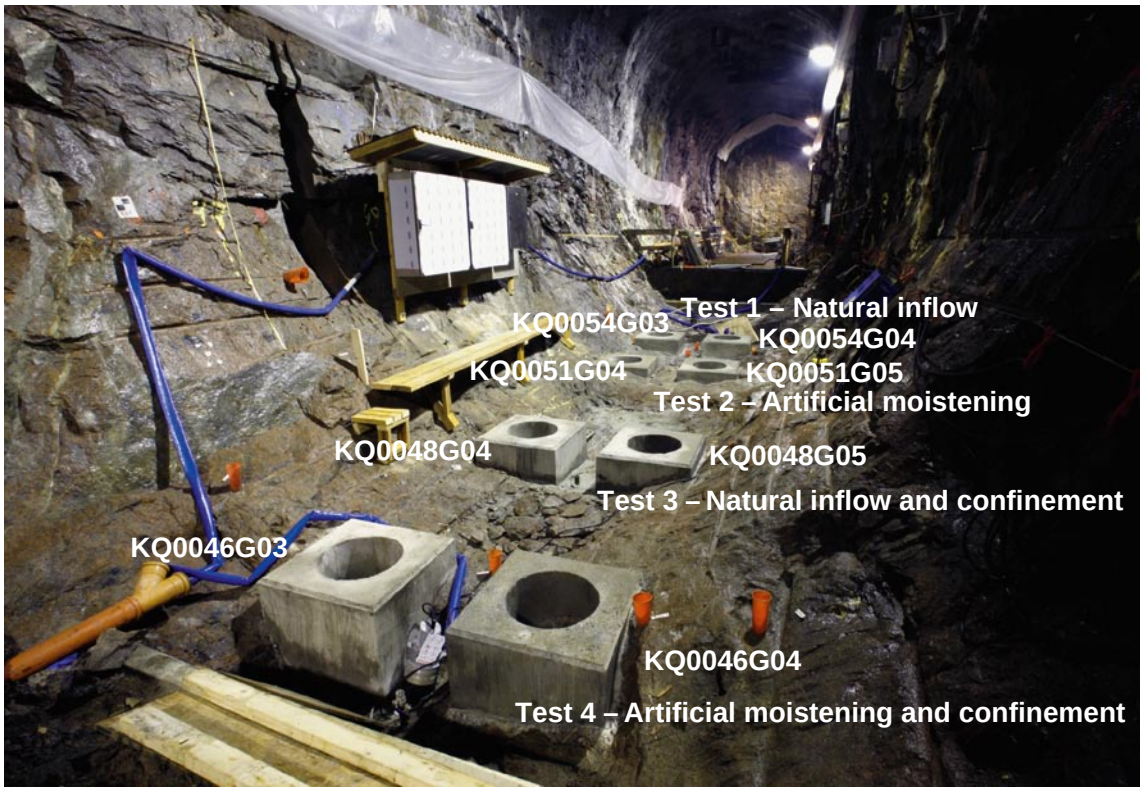

Figure 3-1. *Photograph of the test site of CAPS in TASQ tunnel Äspö HRL. The photograph was taken before all of the instrumentation holes had been drilled. The test sequence of the field experiment as well as labels of the heating holes, are indicated in the figure (Photo C-R Lindqvist).*

3.2 Test sequence

The test sequence of the field experiment and labels of the heating holes, are indicated in Figure 3-1**.** The first test in the sequence included the heating of one pair of holes without any counterforce applied on the borehole wall. This test was performed to ensure that spalling occurred and could be observed in the holes. The heating period in the first test was initiated at the end of August 2008. Compared to the original plan, the heating period was prolonged from two to four weeks, due to a larger heat loss and slower temperature increase than expected in the test.

The second test was performed in November 2008 with a heating period of little more than two weeks. It was performed as a repetition of the first test with improved sealing of the heater holes and with a system for moistening the holes by generation of steam from heater tubes. The observations during the first test indicated that the inflow of water and the humidity in the holes had a significant influence on the results and that it was important to control this parameter during the tests.

The third test was performed in December 2008, promptly after the second test had been completed. This test was the first that included pellets of LECA (Light Expanded Clay Aggregates) loosely placed in a 50 mm gap created between a large inner tube of stainless steel and the borehole wall. The test was designed to observe any difference in the occurrence of spalling compared to the previous tests.

The final heating test was initiated in mid-February 2009 and the heating continued for two months. The test was performed as a repetition of the third test, but compared to the previous test, with artificial wetting of the heating holes to preserve the moisture content of the borehole wall. Another distinction from the third test was that the heating power was applied in a stepwise manner in this test to reduce the temperature gradient in the surrounding rock. The cooling period was also increased to ensure the return to ambient temperature before emptying the pellet filled gap.

3.3 Substitute for bentonite pellet

The confining pressure in the field test on the borehole wall was accomplished with the use of LECA pellets (Light Expanded Clay Aggregates) instead of bentonite pellets. The use of bentonite pellets was impractical due to the inflow of water into the boreholes and the fact that the counterforce of dry pellets, without the effect of the swelling component, was to be investigated.

Pellets of LECA were judged to be a suitable substitute for dry bentonite based on oedometer tests, which demonstrated similar stiffness of both pellet materials, see Appendix E. In addition to the oedometer tests, calibration of the confining pressure was also carried out in compression tests using a pellet filled slot with the same dimensions as in the field experiment, see Appendix F. These latter tests indicated that the static horizontal confinement pressure from the pellet filling, i.e. the counter pressure without any wall movements, is very low (approximately 1 kPa) for both bentonite and LECA filling. The results are depending mainly on the silo effect of the slot and the static confinement pressure does not vary much with the filling height. The results from the pellets filled slot as well demonstrated that the LECA filling is slightly stiffer than the bentonite filling when compressed. The difference between the two laboratory tests is probably caused by differences in the degree of compaction.

When the rock wall fragments move in response to the progressing failure, the compressibility becomes important. The results from the oedometer tests indicate that loosely placed LECA pellets generate a confinement pressure on the borehole wall in the range of 10–20 kPa for 0.5% deformation, see Appendix E. The compression tests performed in the pellet filled slot give confining pressures of approximately 30 kPa for 0.5% deformation, see Appendix F.

A photograph of the pellet filled slot during preparation for Field Test 4 is presented in Figure 3-2. Typical properties of the selected LECA pellet are shown in Table 3-1.

Figure 3-2. *Photograph of the pellet filled slot during preparation of Field Test 4 (Photo R Glamheden).*

Table 3-1. Typical properties of the selected LECA pellet.

Parameter	Value	Unit
Fraction	8–14	mm
Bulk density	~270	kg/m^3
Water ratio on delivery	5–10	%
Young's modulus	10–20	MPa
Compressive strength	≥ 0.85	MPa
Heat conductivity	0.12–0.17	W/mK

3.4 Test equipment and instrumentation

The instrumentation in the field experiment included temperature gauges, relative humidity gauges and monitoring cameras. A photograph of the test equipment and instrumentation installed in the heating holes in Test 1 is presented in Figure 3-3 and of Test 3 in Figure 3-4. Drawings of the test equipment and instrumentation with dimensions are presented for each separate test in Appendix G and additional photographs of the instrumentation are presented in Appendix U.

The installation of the test equipment is report in Section 4.6 and the operational experience of the test equipment is reported in Section 5.1.

Except for a number of modifications to improve the test equipment, the equipment used in Tests 2 and 4 was similar to the one used in Tests 1 and 3, respectively. Most changes were carried out between the first and the second test. The most important modifications to the test equipment between Test 1 and 2 are listed below:

- Improved sealing of the hole cover to keep the moisture in the heating holes.
- Location of temperature gauges on the outside of the heater tube to improve the temperature control of the field test.
- Increased gap between temperature gauge and the guide bushing to ensure good thermal contact between the temperature gauge and the borehole wall.
- Changed space material from polyurethane to clinker since the flushing point was too low.
- Monitoring cameras removed to limit the heat loss and drying up of the heating holes.
- Continuous monitoring of relative humidity in the heating holes since signs were observed that the humidity of the holes had an impact on the spalling occurrence.
- Artificial wetting of the heating holes to prevent drying up of the borehole wall.
- Level control of the drainage pump to limit the ventilation of the holes.
- Modification of the bottom disc to be able to unscrew when lifting the holder.

The modifications are further discussed in Section 5.1, which documents the operational experience of the test equipment. The changes of the equipment are also illustrated by a number of photographs in Appendix U.

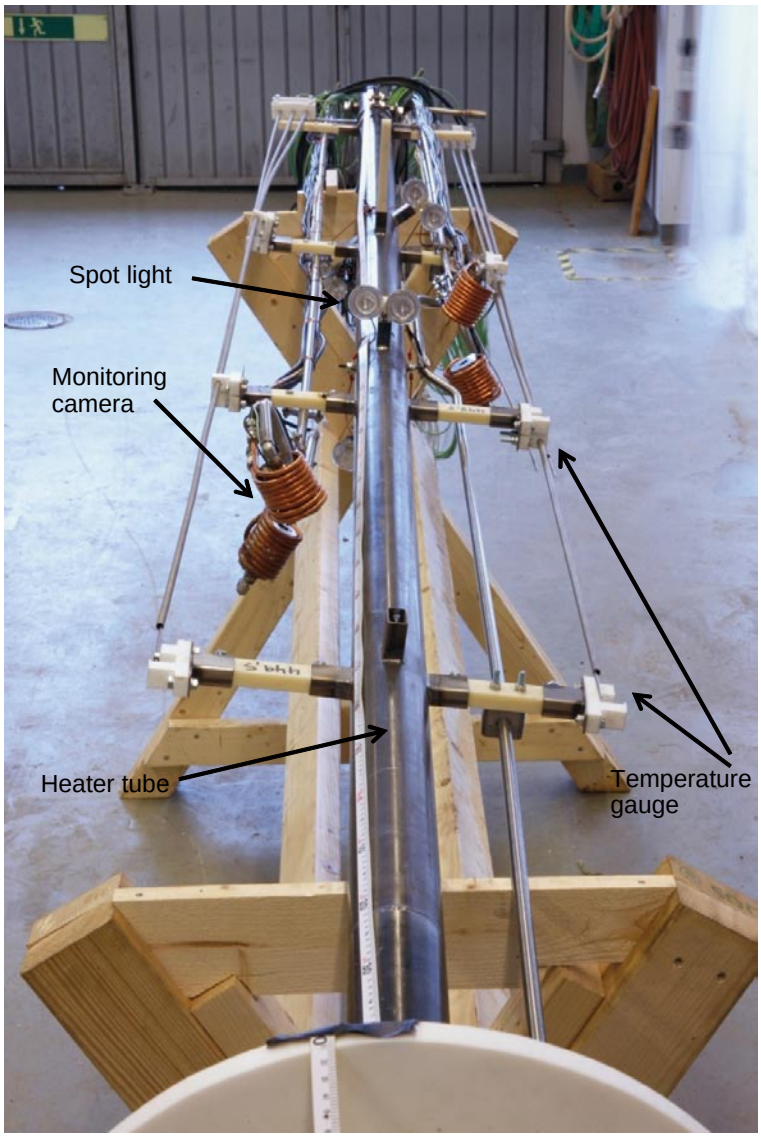

Figure 3-3. *Photographs of the test equipment and the instrumentation installed in the heating holes in Test 1 (Photo C-R Lindqvist).*

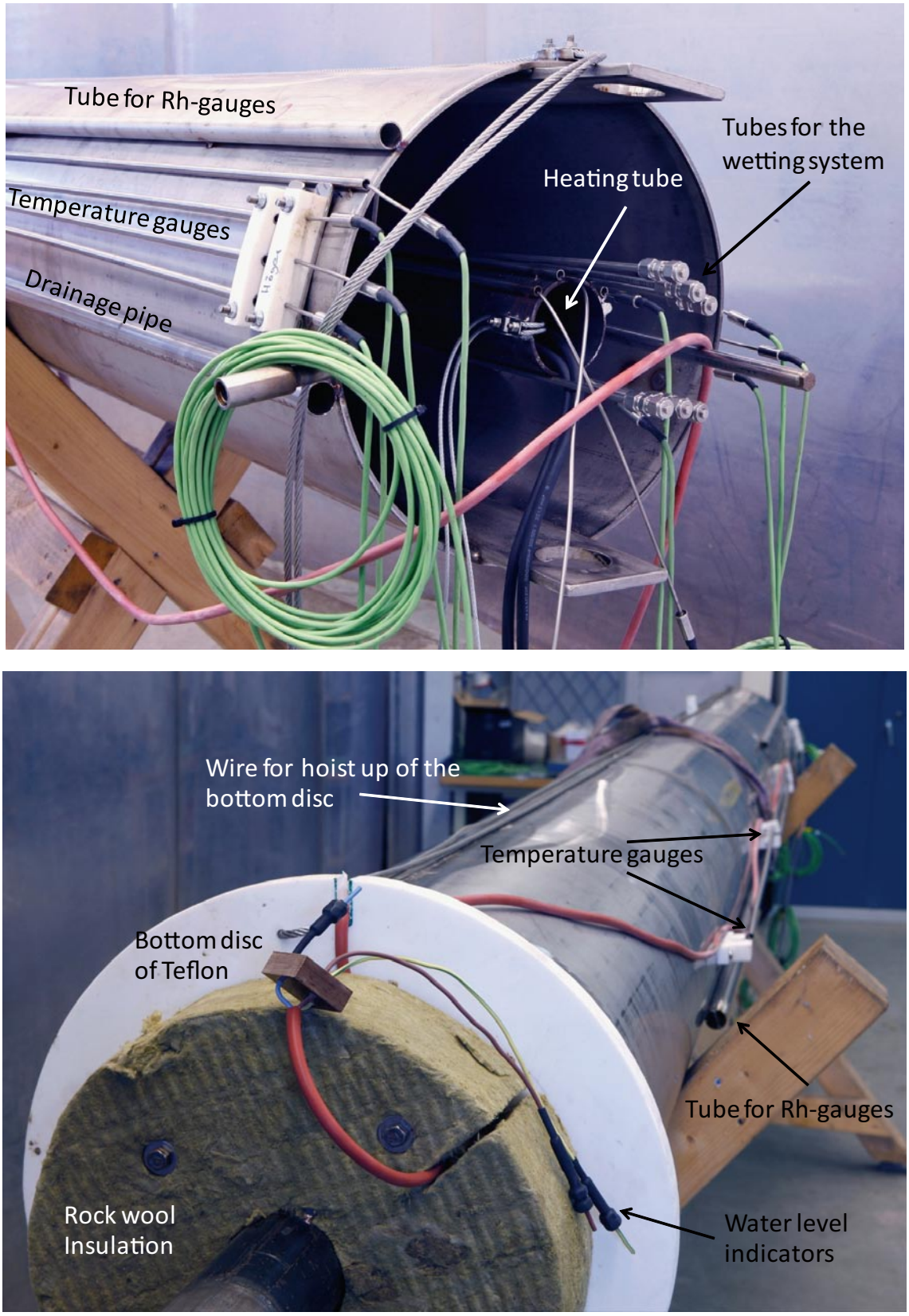

Figure 3-4. *Photographs of the test equipment and the instrumentation installed in the heating holes in Test 3 (Photo C-R Lindqvist).*

3.4.1 Instrument holder

The test equipment and instrumentation used in the heating holes were mounted on a holder for installation as one unit into the hole. In Tests 1 and 2 the equipment installed consisted of a centre tube in carbon steel (Ø76 mm) that included the heater, and three pairs of adjustable spacers (195 mm length) for centring of the tube. The instruments were in this case mounted on the spacers, see Figure 3-3. In Tests 3 and 4, the holder was complemented with a larger tube in stainless steel (Ø385 mm and 5 mm thickness) that created a 50 mm slot towards the borehole wall. In this case the main part of the instrumentation was mounted directly on the surface of the larger tube, see Figure 3-4.

After installation of the holder into the heating holes, the spring loaded temperature gauges were released to come in contact with the borehole wall. Then the centre tube and the larger tube were filled with sand to prevent thermal convection in the tube and to improve the thermal conductivity towards the surface of the tube. Photographs of the test equipment in place are shown in Appendix V. The operational experience with the holder is reported in Section 5.1.1.

3.4.2 Drainage system

The heating holes were drained by two suction pumps, one per hole, that were installed via a pipe located on the holder running from the top to the bottom of the hole, see Appendix G. In the first test the suction pumps were running continuously without any interruption, while in the subsequent tests the pumps were controlled by a level guard or by a timer. A number of drainage pumps were also installed in the tunnel to keep it free from water and prevent the heating holes from being flooded. The operational experience from the drainage work is discussed in Section 5.1.2.

3.4.3 Heating system

The temperature in the experiment was controlled by Backer electrical heater elements located in the sand filled tube in the centre of the heating hole, see Figure 3-3 and Figure 3-4. The length of the heater elements was 4.2 m, while the active length of the elements that generated heat was 4 m. The elements were installed with the active part between level –446.4 and –450.4 m in the boreholes. The dimensional output of the heater elements was limited to 2,300 W and the maximum allowable temperature of the elements was limited to 700°C. To reduce the power output of the heaters and to achieve redundancy in the system, each heating hole was equipped with two parallel heating elements that were used simultaneously. Furthermore, the last field test was equipped with an additional heating element as a reserve, since the heating period was considerably longer in this test compared to the previous.

The heater power control was managed by *Jumo* thyristors, one for each heater, which were possible to operate via the internet. The heater output was also supplemented with alarm levels and supplied by back-up power in case of power supply failure. Additional technical specifications of the heater system are to be found in Appendix H. The operational experience of the system is discussed in Section 5.1.3 and the heating procedure in Section 5.3.

3.4.4 Wetting system

The second and the fourth heating tests were performed with artificial wetting of the heating holes to preserve the moisture content of the borehole wall. In the second test the wetting was achieved using a system that generated steam in the heating holes. A small flux of water was conducted through six small pipes to drip plates located in pairs on three levels on the heating tube where it vaporized, see Figure 3-5. Drawings of the system are presented in Appendix G.

The instrument holder used in the fourth test was equipped with a wetting system similar to the one used in the second test. However, the system was replaced by another system during the installation and the original one was never used. The system used instead was based on a loop that circulated water in the pellet filled slot and by re-pumping the water from the bottom to an elevated tank shown in Figure 3-6. Both the tank and the pipes were well insulated to minimize the heat loss from the system. The operational experience of the wetting system is discussed in Section 5.1.4.

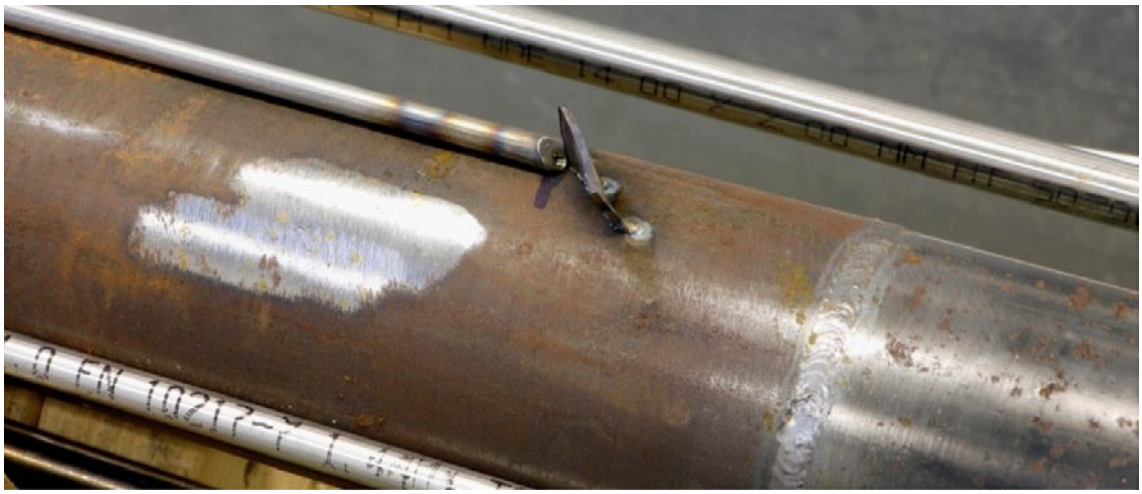

Figure 3-5. *Close-up view of the pipe and the drip plate included in the wetting system used in the second heating test (Photo C-R Lindqvist).*

Figure 3-6. *Shows the tank and part of the pipe work of the wetting system installed in the last field test. Both the tank and the pipes were well insulated to minimize heat loss from the system (Photo C-R Lindqvist).*

3.4.5 Measurement of relative humidity

In the beginning of the field experiment the relative humidity was monitored mainly for observation of ambient conditions and possible seasonal variation by manual readings. However, as signs were observed that the humidity of the heating holes had a direct impact on the occurrence of spalling, measurements of the relative humidity by installed gauges was introduced in the later part of the initial field test. The reading frequency was every 10 min except for in the last field test where it was increased to every 20 min.

Relative humidity gauges were installed on two levels in the heating holes in the second and the third test (–447.6 and –449.6 m) and on one level in the last heating test (–447.9 m), see Appendix G. In Tests 3 and 4 the gauges were located in tubes in the pellet filled slot, which were perforated in the bottom part in the position of the gauge, see Figure 3-4.

The RH-gauges used were from three different manufactures, Test 2 – *Rotronics*, Test 3 – *Comet* and Test 4 – *Kimo*. Different types of gauges were utilized since it was difficult to find a gauge that was really suitable for the conditions in the field experiment. A photograph of the gauge used in the late part of the initial field test and in the second field test is shown in Figure 3-7. The technical description of the RH-gauges and the calibration procedure are to be found in Appendix H. The operational experience of the gauges is discussed in Section 5.1.5 and the monitoring results are presented in Section 5.4.

3.4.6 Monitoring of temperatures

The temperature in and around the heating holes was monitored to control the experiment and for estimation of the thermal induced stresses in the surrounding rock mass. Temperature measurements were also performed as a basis for comparison of the heat flow applied in simulations of the field tests and the one actually recorded in the field experiment. The temperature was recorded every 10 min except for the last field test where it was recorded every 20 min.

Figure 3-7. *Close-up view of the type of RH-gauges (Rotronic) used temporarily in the late part of initial field test and for continuous readings in the second field test (Photo C-R Lindqvist).*

Temperature gauges were installed inside the heating holes on one level to measure the air temperature and on three levels to measure the borehole wall temperature. The gauges that measured the borehole wall temperature were spring loaded to ensure good contact with the borehole wall. The mechanism that pressed the gauge towards the borehole wall is shown in a close-up view in Figure 3-8.

Temperature gauges were also installed on several levels in six boreholes surrounding each pair of heating holes, see Appendix G. To achieve good thermal contact between the gauge and the borehole wall and to minimize the potential for thermal convection in the borehole, the boreholes were filled with sand.

The temperature gauges used in the field test were thermocouple Type K element supplied by *Pentronic AB*. The technical description of the gauge and the calibration procedure are given in Appendix H. The operational experience of the gauges is given in Section 5.1.6 and the monitoring results are presented in Section 5.5.

3.4.7 Monitoring cameras

In the two initial tests, in heating holes without pellet filling, spalling observations were performed regularly during the heating phase. In the first test the observations were carried out with monitoring cameras and visual inspection while in the second test only by visual inspections. Spalling observations during the heating phase was used to observe the initiation of spalling and for assessment of the development the thermal stresses around the heating holes.

The first field test included in total eight monitoring cameras installed in pairs on two levels in the heating holes, –448.0 (–447.9) m and –449.0 (–448.9 m), viewing both the NE- and SW-side of the heating holes. The monitoring camera used in the first field test is presented in a close-up view in Figure 3-9.

The system digital video camera and digital recorder were supplied by Eneo, while the fixture and protection housing of the video camera were developed by the staff at Äspö HRL. The camera was cooled by circulating water and the camera lens was kept free from mist by compressed air that swept out in a slit between the housing and the lens. Spotlights on two levels illuminated the heating holes. The function of the system was verified in a pre-test over a period of two week performed in a heated concrete tube. The technical specification of the digital video camera is to be found in Appendix H. The operational experience is discussed in Section 5.1.7 and the spalling observations obtained by the monitoring system are described 6.2.

In the second test the spalling was observed by regular visual inspections and the use of a mobile video camera. The mobile video camera was also based on a digital video camera supplied by Eneo, see Appendix H.

3.4.8 Data acquisition system

The instrument analogue output signals were converted to digital signals and transmitted to a monitoring computer by *Compact FieldPoint* modules supplied by *National Instruments*. The programming of the monitoring computer was carried out by the *LabView* software supplied by *National Instruments* as well.

The monitoring data was logged continuously during the field experiment and saved to the computer hard drive every 10 min in Test 1–3 and every 20 min in Test 4. A back up of the monitoring data was taken every 10 min. In case of power supply failure, the monitoring system was supplied with a UPS and a diesel generator for continuous operation.

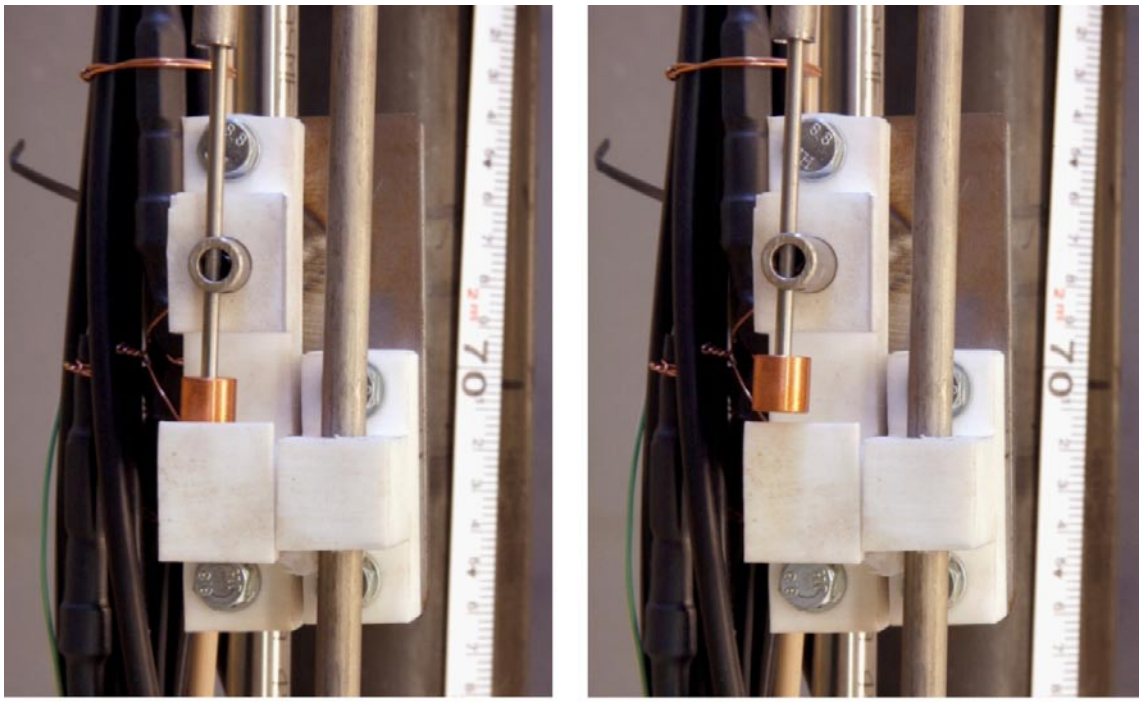

a) Mechanism in locked position b) Mechanism in unlocked position

Figure 3-8. *Close-up view of temperature gauge installed inside the heating holes. a) Shows the spring loaded mechanism in the locked position and b) the mechanism in the unlocked position (Photo C-R Lindqvist).*

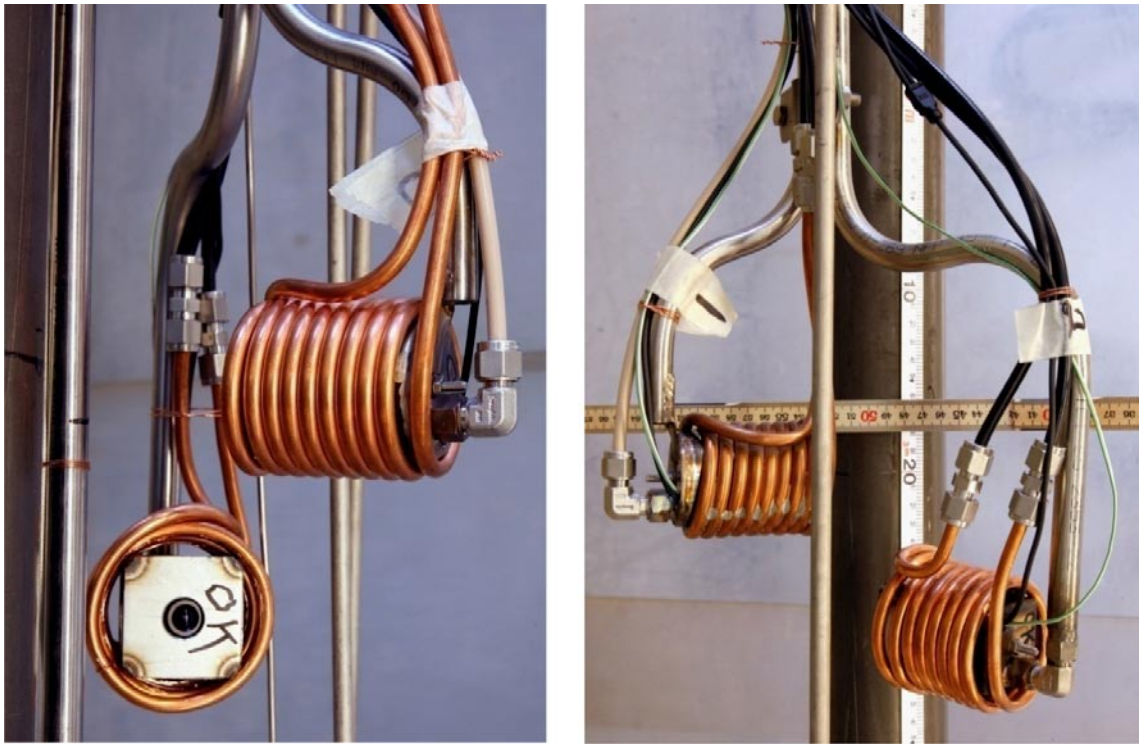

Figure 3-9. *Close-up view of the monitoring camera installed inside the heating holes in Test 1 (Photo C-R Lindqvist).*

4 Preparation of the test site

4.1 Drilling of the test holes

The heating holes were reamed up from a core drilled pilot hole of 76 mm to a final dimension by percussion drilling in four steps: 76 – 162 – 242 – 354 – 486 mm. The drilling bits utilized for the reaming were equipped with a guide of about 5–20 cm length to minimize the borehole deviation. The drilling technique used produced a telescopic shape to the bottom of the heating holes over approximately 1 m length. The instrumentation holes were all core drilled with a 56 mm diameter. In Figure 4-1 and Figure 4-2 photographs of the drilling equipment are shown with close-up views of some of the drilling bits utilized for reaming of the heating holes.

The contractor for the core drilling was MiRo Diamantborrning AB and the contractor for the reaming was Sven Andersson AB. The core drilling was carried out in two campaigns, one that was completed in April 2008, which included eight pilot holes and 12 instrumentation holes, and second campaign that was completed in July 2008 which included 12 instrumentation holes. The boreholes included in the first campaign of the core drilling are indicated in Figure 4-3.

The reaming of the heating holes was carried out approximately within a month, started in May and finished in June 2008. The dates of complete for respective heating holes are shown in Figure 4-4.

The deviation of the core drilled holes was checked by surveying on a centralised rod located in the collar of the boreholes. The results from these measurements are presented in a Table 4-1. According to the compilation the error in the positioning is within 38 mm and the deviation of the boreholes from the vertical line is within 0.3 degrees.

Figure 4-1. *A photograph of the equipment used for the core drilling (Photo R Glamheden).*

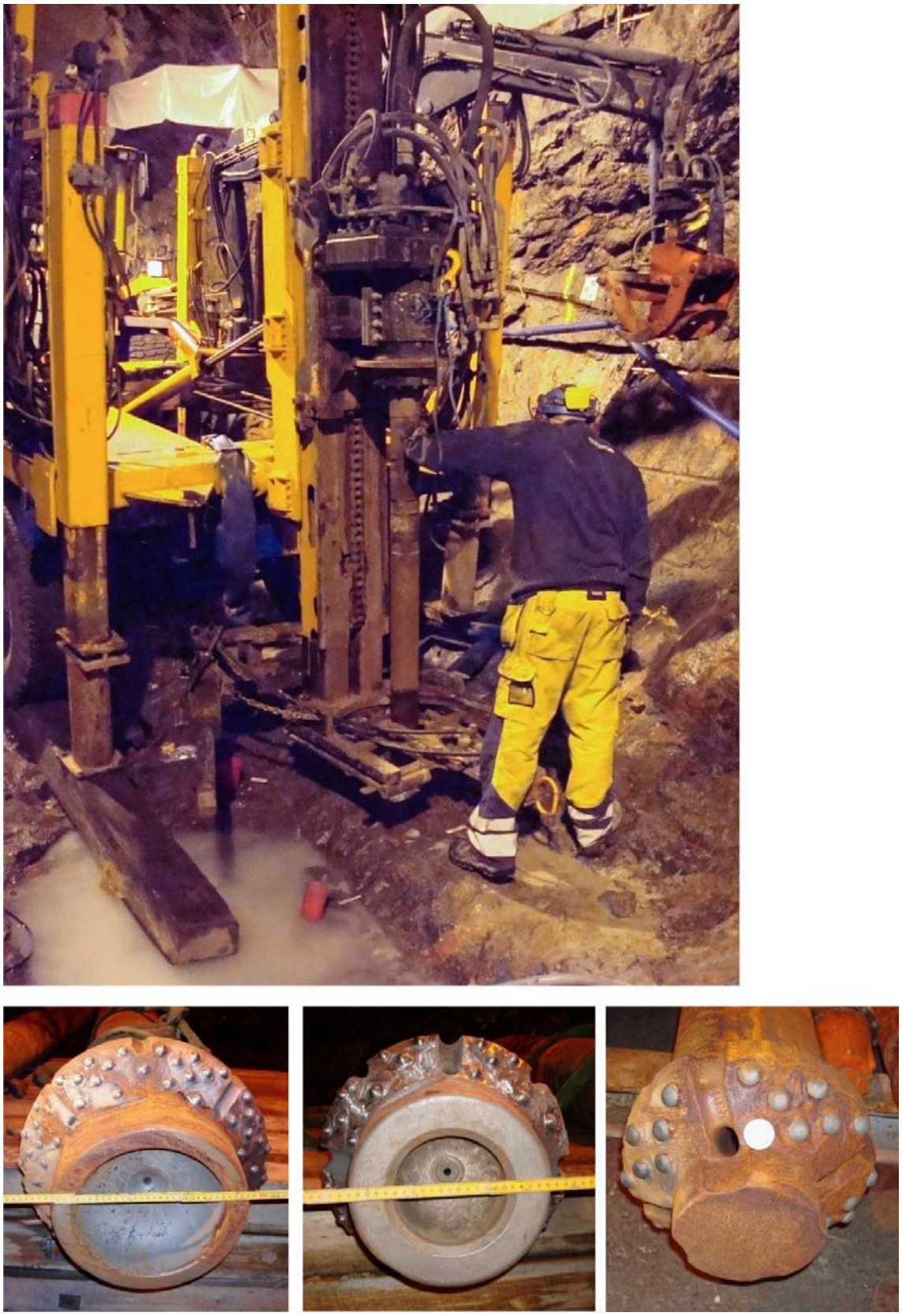

Figure 4-2. *A photograph of the equipment used for reaming the heating holes with close-up views of some of the drill bits that were utilized (Photo R Glamheden).*

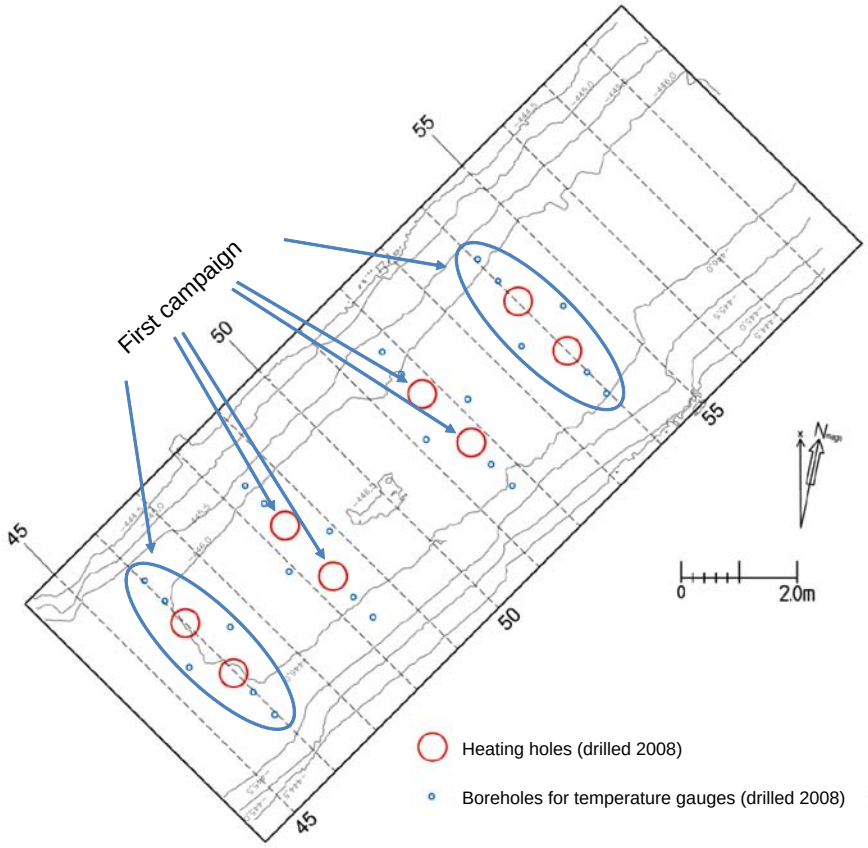

Figure 4-3. *Boreholes included in the first campaign of the core drilling completed in April 2008.*

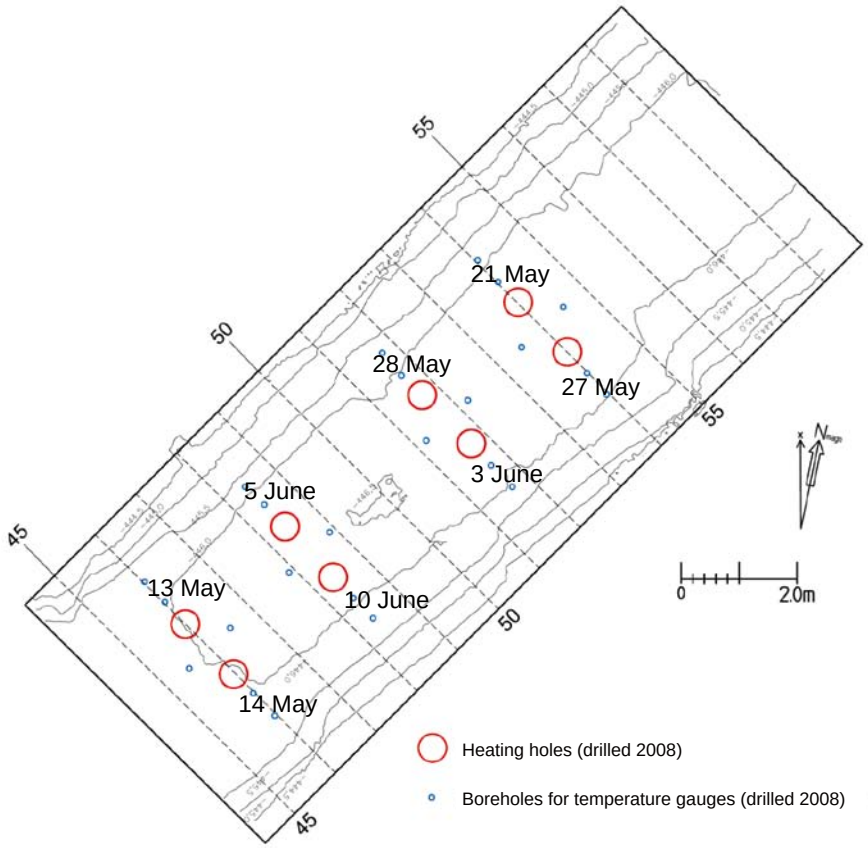

Figure 4-4. *Completion dates for individual heating holes.*

Table 4-1. Determined borehole deviation in core drilled pilot holes and fully reamed heating holes.

Borehole	Core drilling[1]		Deviation at reaming[2]	
	Positioning (mm)	Inclination (deg)	Top/Mid-height (mm)	Top/Bottom (mm)
KQ0046G03[3]	18	89.9	–	–
KQ0046G04	38	89.9	13	6
KQ0048G04	20	89.7	6	6
KQ0048G05	19	89.8	8	7
KQ0051G04	9	89.7	13	5
KQ0051G05	10	89.8	5	20
KQ0054G03	23	89.7	9	16
KQ0054G04	16	89.8	1	18

1) The values are based on surveying of a centralised rod located in the collar of the boreholes.

2) The values correspond to the centre coordinate and are based on lasers scanning during the post characterization (Top –446.5 m, Mid –448.2 m, Bottom –450.0 m)

3) The deviation of KQ0046G03 was not measured since the hole had been grouted.

The deviation of the heating holes was checked after the first and the last reaming step. The check after the first reaming step was carried out in the same manner as for the core drilled pilot holes. The control after completion of the holes was based on laser scanning and plumbing along the borehole wall of the boreholes. The procedure employed in the laser scanning is described in Section 7.1.3. The plumbing of the borehole wall was carried out in the depth interval with a large diameter (–446.5 to –450.4 m) using a laser beam located in four positions, two parallel with the tunnel axis and two normal to the tunnel axis. The results from the laser scanning are shown in Table 4-1, while the results from the plumbing are presented in Appendix N. The laser scanning shows a deviation of centre coordinate of up to 20 mm and the plumbing a deviation of the borehole wall of up to approximately 40 mm. In some instances the results from the laser scanning show larger deviations between the top and the mid-height position than between the top and the bottom positions. The recorded borehole deviation was within the specified limit, which corresponds to 1% of the borehole length (40 mm). However, the current deviation effected the monitoring of the wall temperature slightly and resulted in a variation in the width of the pellet filled slot, see Section 5.1.6 and 5.2. It also made the post characterization of the spalled notch more complicated, see for example Section 7.1.3.

In addition to the borehole deviation, the variation of the borehole diameter and the roughness of the borehole wall surface were also determined for the heating holes. The diameter of the heating holes was checked by ultrasonic measurements and as well by laser scanning. The procedure for the measurements is described in Sections 7.1.2 and 7.1.3 respectively. The results from the laser scanning show similar results to the ultrasonic measurements and only the latter are reported here.

The variation of the diameter, compiled in two perpendicular directions based on the ultrasonic measurements, is presented in Table 4-2 and by graphs in Appendix N. The determined mean values for the heating holes show a variation that ranges from 486 mm to 494 mm. The variation in diameter along the individual heating holes in general is between 10–15 mm. The smallest diameter that was recorded along the heating holes was 483 mm and the largest 502 mm. The diameter of the heating holes consequently differed between 3–16 mm from the specified diameter after complete reaming. The variation in borehole diameter influenced the field test in a similar way as described above regarding the borehole deviation.

The roughness of the borehole wall surface was determined in a vertical direction at 0.75 m depth in two boreholes (KQ0046G03 and KQ0048G04) using a 150 mm long profile form. The recorded profiles, which are presented in Figure 4-5 indicate an asperity height between 0.5–1 mm of the borehole wall surface.

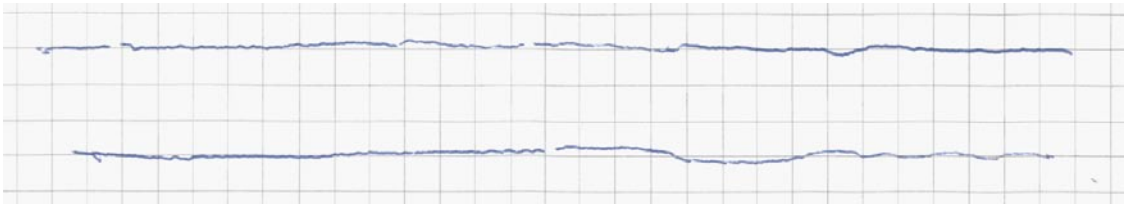

a) Heating hole KQ0046G03

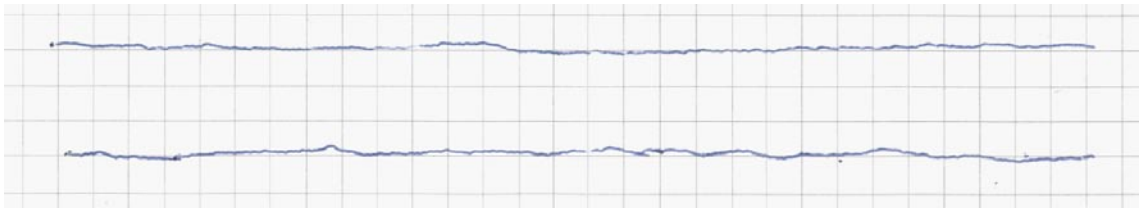

b) Heating hole KQ0048G04

Figure 4-5. *Determined roughness of the borehole wall in two profiles in borehole a) KQ0046G03 respective b) KQ0048G04 and at 0.75 m depth. The distance between the gridlines corresponds to 5 mm.*

Table 4-2. Determined variations in borehole diameter based on ultra sonic measurements in two directions across the heating holes.

Borehole	Section in N-S direction Mean, *Min–max* (mm)	Section in E-W direction Mean, *Min –Max* (mm)
KQ0046G03[1]	–	–
KQ0046G04	494 *(487–502)*	490 *(483–499)*
KQ0048G04	486 *(484–493)*	486 *(484–493)*
KQ0048G05	486 *(484–490)*	486 *(483–491)*
KQ0051G04	487 *(485–491)*	486 *(483–492)*
KQ0051G05	488 *(486–492)*	487 *(484–493)*
KQ0054G03	488 *(486–496)*	487 *(485–493)*
KQ0054G04	489 *(484–493)*	488 *(485–497)*

Note: The diameter of KQ0046G03 was not measured since the hole was grouted.

4.2 Mapping of the core drilled holes

The core drilled pilot holes in the centre of the heating holes and the surrounding instrumentation holes, as well as the water injection holes drilled for post characterization, were all mapped according to the SKB Boremap system (MD 146.003 version 2.0).

The mapping was performed on three occasions by different geologists. A preliminary mapping of the pilot holes were carried out in April 2008 by Oskar Sigurdsson. The instrumentation holes, mapped in September 2008, and the water injections holes mapped in June 2009, were carried out by geologists from Vattenfall Power Consultants.

The Bips-logging, which provided basic data for the mapping, was performed by Malå GeoScience AB at the following dates: 2008-04-24, 2008-08-05 and 2009-05-28.

WellCad diagrams for the geological data of the pilot holes are presented in Appendix A and pictures from RVS-modelling of the site geology are shown in Appendix B. The RVS-modelling was carried out by Johan Berglund Vattenfall Power Consultants.

4.3 Pressure build-up tests

The hydraulic conductivity of the rock in the tunnel section used for the CAPS field experiment was examined preliminary by pressure build-up tests in the pilot holes and later on by water loss measurements in both pilot and instrumentations holes.

The pressure build-up tests were carried out by Anders Wikman SKB, according to the methodology reported in /Almén and Stenberg 2005/. The tests included only the eight pilot holes in the centre of the heating holes. The flow out of the holes was checked during approximately 45 min before the holes were closed. Borehole packers were installed in all holes during the tests, both pilot and instrumentation holes. To avoid leakage through shallow fractures in the tunnel bottom, the packers were located at approximately 0.6 m depth in the boreholes. The duration of the pressure build-up tests went from 4 hours in the case of non flowing holes to up to 2.5 days in one of the holes with very small inflow (KQ0054G03).

Inflow and pressure response were only observed in two pilot holes, KQ0048G04 and KQ0054G03. The evaluated results for these holes are presented in Table 4-3. The results indicated that the established inflow criteria 0.05 ml/min for a complete heating hole, might be exceeded at least in the position of KQ0048G04, and it was decided that grouting should be performed.

4.4 Performed grouting program

Before the heating holes were reamed grouting was performed in six of the pilot holes and four of the instrumentation holes located in tunnel Section 46. The pilot holes of KQ0046G03 and KQ0046G04 and one of the instrumentation holes in Section 46 was not grouted, since all packers became broken and the reaming had to start before the replacing ones could be delivered. The work was accomplished in the mid of May 2008 during two days just before the reaming started. At the present date were in total 20 holes completed, 8 pilot holes and 12 instrumentation holes.

The grouting program was designed by Johan Funehag at *Chalmers* and a team consisting of staff from Golder Associates, NCC and Chalmers carried out the work. The equipment used was a Unigrout E22H, developed for the project at Äspö HRL concerning sealing of tunnels at great depth.

The grout was based on Silica sol, Meyco MP320 with 10% NaCl as accelerator. Two ratios of a mixture between Silica sol and the brine solution were used, 5.0:1 for the Ø56 mm holes to get a gel time of approximately 25 min and 5.5:1 for the Ø76 mm holes to get a gel time of approximately 40 min. The grouting pressure was 37 bar.

The supplementary water loss measurements performed to control the grouting indicated water loss in only KQ048G04 and KQ0054G03. The grout take of the boreholes varied between 2.4 and 8.7 litres (Min KQ0054G04 and Max KQ0051G05).

Table 4-3. Evaluated results from the pressure build-up tests in the two boreholes that showed a response.

Borehole	Inflow (ml/min)	Pressure (bar)	Transmissivity (10^{-8} m^2/s)
KQ0048G04	27.5	4.2	6.7
KQ0054G03	0.5	19.8	0.2

4.5 Establishment of initial conditions in the heating holes

The initial conditions in the heating holes, regarding the geometry and the breakouts, were documented by photographing and laser scanning of the holes. Breakouts are zones of enlargement of the heating holes developed due to failure of the rock by spalling. Photographs were taken in a top view of the heating holes before initiating the field experiment. The direction of the tunnel axis is marked by a measuring tape on the SW-side of the borehole wall and by a red string on the NE-side. Any breakouts in the holes were also documented by a fish-eye photo perpendicular to the wall. The initial conditions of the heating holes are described in Section 6.1 and relevant photographs are presented in Appendix T. Included in the appendix are also two additional series of photographs taken after the heating phase, one before the scaling of the wall and another after the scaling. All photographs of the heating holes included in the report were taken by Curt-Robert Lindqvist.

It became apparent the laser scanning carried out for establishment of the initial conditions had insufficient accuracy. The measurements indicated an apparent deviation of the holes (up to 175 mm) and the point cloud from the measurement was too thick (5–7 mm). The reasons for the problem are reported in Section 7.1.3. The preliminary scanning is therefore to be considered mainly as trial runs to develop a proper procedure for the scanning. The results from the initial scanning have not been included in the report with the exception of an orthophoto from KQ0048G04. The results included here are instead from the post characterization, which is described in Section 7.1.3.

4.6 Installation of the test equipment

The test equipment and instrumentation used in the heating holes were mounted on the holder described in Section 3.4.1 and installed as one unit by a loading crane. Photographs from the installation of the holder in Tests 1 and 3 are shown in Figure 4-6. Suction pumps were connected to the holder drainage pipe directly after installation of the holder to protect the instruments from inflow of water into the heating holes. A number of drainage pumps were also installed in the tunnel.

Figure 4-6. *The installation of the holder in a) Field Test 1 and b) Field Test 3 (Photo C-R Lindqvist).*

The function of all the instrumentation was checked before transport into the tunnel, as well as after installation and connection. With the instruments in place the function and position of the gauges were spot check by a heating pulse.

After finishing the function check-up, the spring loaded temperature gauges were released to come in contact with the borehole wall. The installation was checked by use of a moveable video camera to ensure that the gauges were in good thermal contact with the borehole wall.

Subsequently the heater elements were connected and the temperature gauges in the surrounding instrumentation holes were installed. After function checks on these instruments, the centre tube, the larger tube in Test 3 and 4 and the surrounding instrumentation holes were filled with sand. The tubes and the surrounding instrumentation holes were sand filled to prevent thermal convection and to improve the thermal conductivity between the surface of the tube and the borehole wall.

In Field Tests 3 and 4 the slot between the larger tube and the borehole wall was filled by pellets of LECA. The pellets were simply poured down into the slot. The filling process was checked by a moveable video camera that was lowered down into the slot.

Subsequently the heating holes were closed and covered by insulation. The final step of preparation for the field test, involved the tunnel bottom in the vicinity of the heating holes being covered by blankets of insulation. A photograph of the test site just before starting the second field test is shown in Figure 4-7. Additional photographs from the installation and of the test equipment in place in the various field tests are included in Appendix V.

Figure 4-7. *The test site just before starting the second field test (Photo R Glamheden).*

5 Execution of the field experiment

5.1 Operational experience with the test equipment

The present section outlines the operational experience with the test equipment during the field experiment. Focus has been placed on conditions that are of importance for the evaluation of the monitoring results, however certain experience of a more general nature has also been included.

5.1.1 Instrument holder

The spacer material of the holder was changed from polyurethane in the first test to clinker in the second test, since the fusing-point of the polyurethane (ca 80°C) was too low. A photograph of one of the spacers used in the first test after removal of the equipment is shown in Figure 5-1. The melting of the spacers might have caused a re-deflection of some spring loaded gauges and an apparent increase of the temperature in the final part of the heating period. However, the recorded temperatures do not show any obvious signs of this, which indicates that the gauges could have lost the contact with the borehole wall, see Appendix K and R. The tolerance of the spring loaded mechanics (approximately 20 mm) possibly was able to bridge the change in distance of the spacers.

A drawback with the clinker material used as spacer material in the second test was its brittleness. A couple of spacers broke during the installation of the equipment in the heating holes and had to be exchanged.

In spite of the fact that the large tube and the minor pipes for the RH-gauges and the wetting system were manufactured in stainless steel, considerable corrosion occurred during the heating tests. An illustration of this is shown in Figure 5-2, which shows the large tube and the pipe for the upper RH-gauge after removal of the holder used from KQ0048G04 in Test 3. The corrosion caused clogging of the perforated part of the tube for the lower RH-gauge in Test 3, see Section 5.1.5. But besides this, the corrosion does not seem to have had any obvious influence on the experiment. The saline water at the site in combination with the elevated temperature of the field experiment, is most likely the reason for the corrosion.

Figure 5-1. *Photograph of one of the spacers used in the first heating test. The spacer of polyurethane became too hot and started to melt (Photo R Glamheden).*

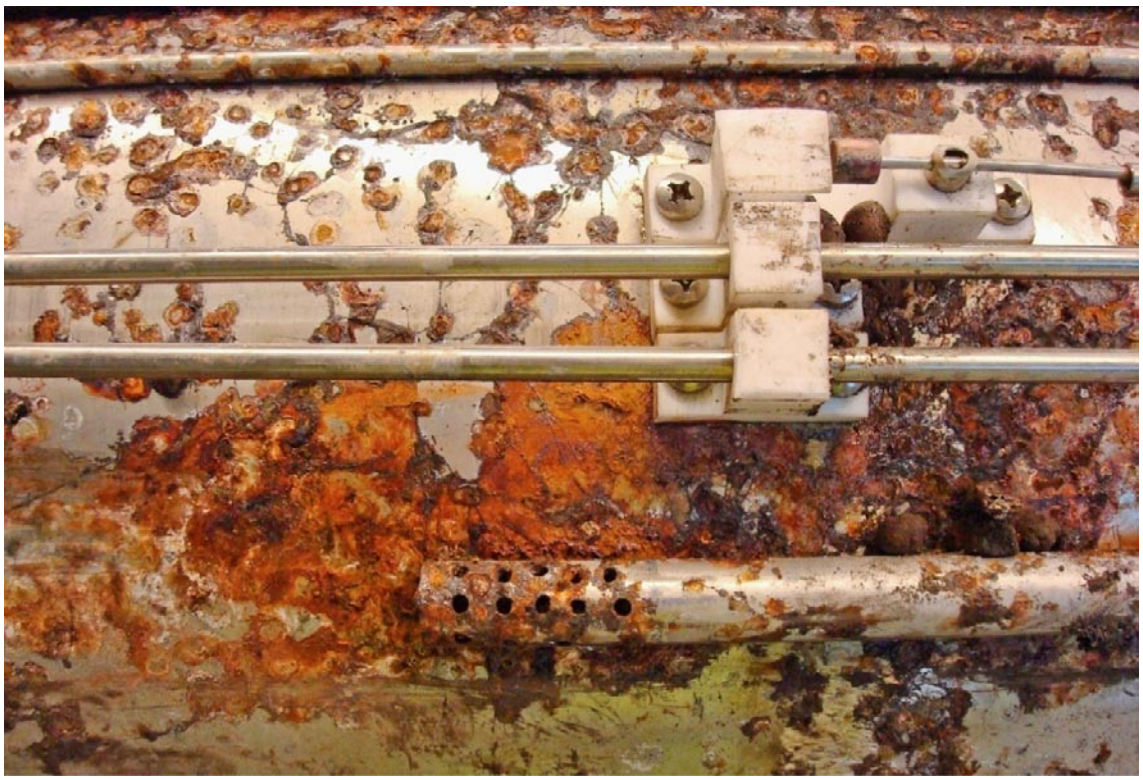

Figure 5-2. *Illustrates the corrosive degradation process the test equipment was exposed to during the heating tests. The photograph shows part of the large tube and the minor tube for the upper RH-gauge from hole KQ0048G04 in Test 3 (Photo R Glamheden).*

5.1.2 Drainage system

In the first test suction pumps were running continuously without interruption even when the pump pit was being emptied of water. This procedure resulted in the undesired circulation of air in the heating holes and associated extra heat loss. To overcome this problem, the pumps in the subsequent tests were controlled by a level guard or by a timer. The timer was used as a complement to the level guard, since the level control failed on occasion. A problem with the level guard in the second field test was probably due to the high electrical conductivity of the drainage water. In the third field test problems were caused by a broken cable in KQ0048G05 and in last test the level guard in KQ0046G03 was adjusted incorrectly.

The suction pumps on the whole were reliable, but a couple of pumps had to be replaced during the field experiment. Moreover, in the last heating test both pumps stopped functioning completely at the end of the heating phase. The suction capability of the pumps ceased when the temperature of the drainage water approached boiling point. The stop of the suctions pumps resulted in a shutdown of the wetting system and also meant that the temperature in the heating holes was higher than intended in the latter part of the final test, see Section 5.1.4 and 5.5 for additional details.

5.1.3 Heating system

The incorporated redundancy of installed heaters in the last field test was insufficient. Altogether three heaters stopped working at different times in KQ0046G04 due to short-circuits or interruption in the element. The broken heaters were replaced by installing additional elements in separate pipes located in the sand ca 10 mm outside the central heating tube, see Figure 5-3. The active length of these heating elements was moved approximately 0.1 m up the hole and at the same time the sand filling had to be lowered between 0.2–0.3 m depth.

The heaters that stopped functioning caused short periods with reduced heating capacity, see Section 5.3. However, since it was possible to replace the heaters relatively quickly the disturbance to the experiment was limited.

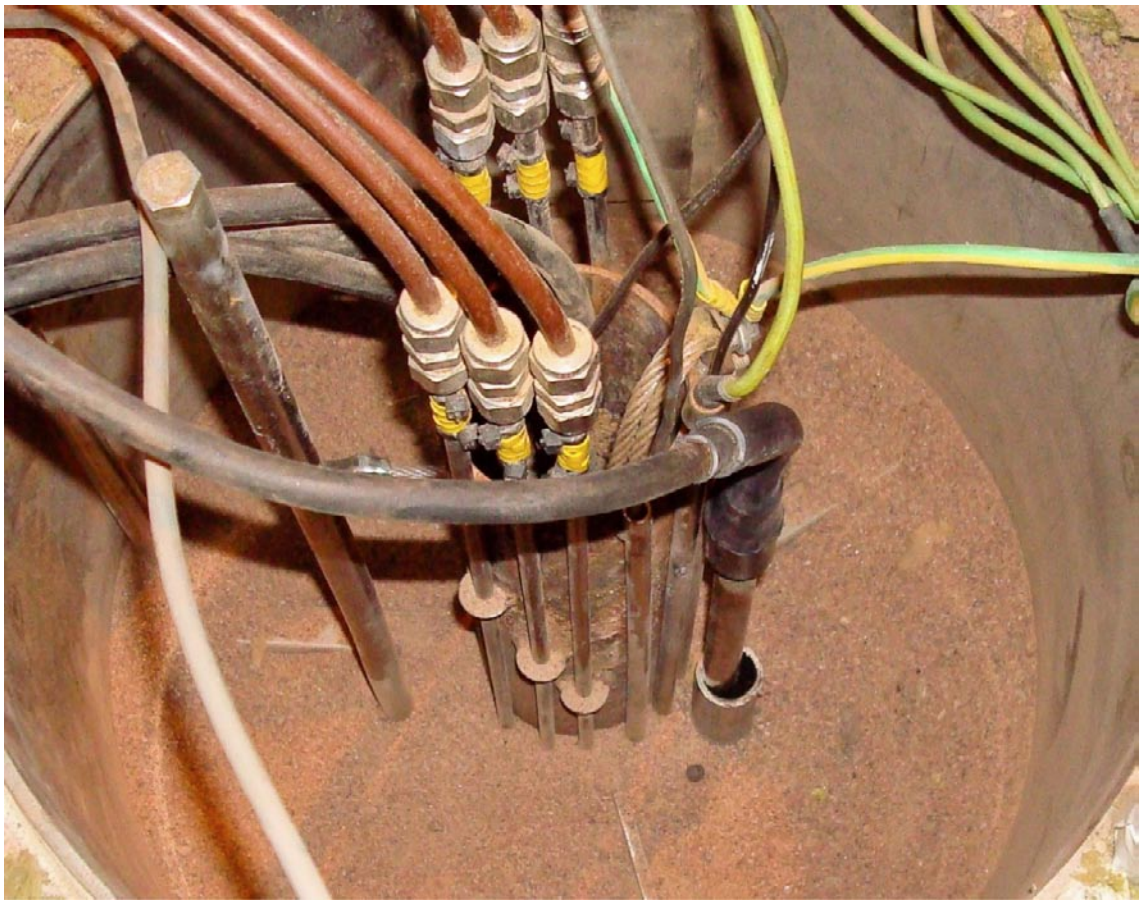

Figure 5-3. *Shows an example from KQ0046G04 in Test 4, where a replacement heater element was installed in the sand in separate pipes outside the heating tube (Photo R Glamheden).*

5.1.4 Wetting system

The wetting system utilized during the second field test aimed to maintain the desired moisture of the borehole wall in the heating holes, but the system proved to be difficult to operate. The system was very sensitive to small changes in the influx of water and the influx was not stable with time due to variation of the pressure in the tunnel water-supply system. At a slightly raised influx, the temperature on the heating tube declined considerably, sometimes temporarily below 100°C, which prevented the water from vaporizing. The difficulties in operating the wetting system diminished to a certain extent after installing a pressure reducing valve on the water supply system, but problems with the wetting system operation are still clearly reflected in the monitored temperatures of the heating tube, see Appendix K.

After removal of the equipment the occurrence of lime deposits in the drip holes was noted, see Appendix U. Thus, the water used also had a tendency to clog the system even for the short period of the second test, which only lasted for a little more than two weeks.

The wetting system utilized in the final field test was easier to operate than the former one and it also reduced earlier heat losses, since the same water was circulated in a closed system. However, the system might have had the effect of equalizing the temperature on different levels in the slot, see Appendix K. Moreover, the wetting system shut down when the pumps stopped operating at a water temperature close to boiling point, see Section 5.1.2.

5.1.5 Measurement of relative humidity

The gauge from *Rotronics* in general worked well during the heating phase and did not stop functioning until the filter became wet during the cooling phase. However, the size of the gauge was too large to be installed in the pellet filled slot in the subsequent tests.

The gauge from *Comet* had appropriate dimensions, but the gauge cover was of plastic and the upper temperature limit of the instrument was not sufficient (+125°C).

The gauge from *Kimo* was a robust one of stainless steel with an upper temperature limit of +180°C. However, like the gauges utilized in the previous tests, this gauge was only able to withstand the conditions during part of the field experiment. The RH-gauges seem to be sensitive to hot water vapour produced during the heating period. They also seem to be sensitive to the rapid variation in temperature that occurred when the gauges were hoisted up and down in the heating holes for drying and cleaning of the gauge filter.

In Tests 3 and 4, where the gauges were installed in tubes located in the pellet filled slot, additional factors that influenced the measurements appeared. The perforated part of the tube of the lower RH-gauge was for example clogged due to substantial corrosion during Test 3, see Figure 5-4. Moreover, in the last heating test it was observed that the RH-tubes caused air circulation in the slot. Air was entering in the shorter tube and vapour went out in the longer tube. The problem was solved by simply sealing the opening of the tubes by tape after the test had been ongoing for some days. The conditions were most likely similar in Test 3 although not observed. Thus, it is likely that the recorded values in Test 3 and during a part of Test 4 have been slightly lower than the true values.

5.1.6 Monitoring temperatures

The mechanism, which is shown in a close-up view in Figure 3-8, was modified slightly after the first test to improve the thermal contact between the gauge and the borehole wall and to manage a larger gap between the fixture and the borehole wall due to deviation of the boreholes, see Appendix U. Nevertheless, the deviations of the boreholes have caused some differences in the thermal contact between the gauges and the borehole wall and in a couple of positions in Test 3 and 4 the gauges were not in firm contact with the borehole wall (PXU485T08, PXU463T02 and PXU464T04).

In some of the boreholes with temperature gauges installed in sand, the settlement of the sand during the field test resulted in the upper part of the borehole becoming water-filled. This seems to have caused a reduction in the temperatures recorded by the gauges located on the upper level in the surrounding holes.

Figure 5-4. *Photograph of the perforated part of the tube of the lower RH-gauge after removal of the test equipment in Test 3. The perforation was clogged due to substantial corrosion during the test (Photo R Glamheden).*

5.1.7 Monitoring cameras

The system with observation cameras worked relatively well but the system was excluded from Test 2 due to large energy losses and disturbance of the moisture content of the borehole wall in the heating holes. The cooling system of the cameras began to work as heat exchangers and the system of compressed air to keep the camera lenses free from mist reduced the humidity of the heating holes.

Besides the problem of increased energy losses in the field test, there were also problems that affected the function of the cameras. For example, already before the field test had started leakage of water occurred in the circuit of CAM5. This meant the camera was only being cooled during the test by compressed air, though it functioned during a large part of the test until the temperature reached 95°C. Most likely, a further two cameras stopped working due to overheating after about 20 days of operation (CAM1 and CAM6).

Interruption of the video signal occurred in two cameras just some days after the test start (CAM7 and CAM8) and during the cooling phase the signal from another two cameras was interrupted (CAM2 and CAM3). The latter pair most likely stopped working due to moisture causing a short-circuit. The problem of mist on the lens was experienced by CAM4 after about 20 days and temporarily by CAM6 when the air tube became loose. The function of CAM6 restored after the tube was reconnected.

5.2 The pellet filled slot

The LECA pellets were easy to handle and filled up the slot smoothly without forming bridges. The total volume of LECA pellets used for filling the heating hole slots was in the range of 300–307 litres, see Table 5-1. This value corresponds well with theoretical volume of the slot. The variation in pellet volume between the holes reflects the variation in borehole diameter between the heating holes, see Section 4.1. Besides this, the deviation of the boreholes resulted in a variation of the slot width that ranged between 40–60 mm.

The weight of the pellet filling poured down into the slot before the test was started varied between 92–95 kg in the various field tests, see Table 5-1. The determined weight and volume corresponds to a density of the pellet filling of approximately 308 kg/m^3, which was somewhat higher than the specified bulk density given in Table 3-1.

In order to examine to what extent water was absorbed by the pellet filling during the test, the weight and corresponding bulk density was determined, as well as the water ratio after finishing Field Test 3, see Table 5-1. The results indicate that a considerably amount of water was absorbed by the filling in heating hole KQ0048G04, while the amount of water was more modest in KQ0048G05. The variation in water ratio of the pellet filling in Test 3 most likely has influenced the thermal conductivity of the material.

Table 5-1. Determined volume, weight, bulk density and water ratio of the pellet filling used in Test 3.

	Volume (litre)	Weight[1] (kg)		Bulk density[2] (kg/m^3)		Water ratio[3] (%)
		Start	End	Start	End	
Test 3						
KQ0048G04	300	92	164	306	546	76–80
KQ0048G05	300	93	101	308	336	8–20
Test 4[4]						
KQ0046G03	307	95	–	311	–	–
KQ0046G04	305	94	–	309		–

1) Weight of the pellets filling determined before and after the field test.

2) Bulk density for the pellet filling determined before and after finishing of the field test. The results are based on the change in weight.

3) Laboratory determined water ratio of the pellet filling after finishing field test. The water ratio on delivery was approximately 4%.

4) The values after finishing field test were not determined for the last field test.

Displacements in the pellet filled slot were measured during the field experiment to check possible movements due to saturation or thermal volume expansion of the pellets. Movements in the pellet filling are an indication of possible changes in the confining pressure of the rock wall. The check for movements in the third test was carried out by manual readings with a jointed rule located on the top of the pellet filling with the hole cover as reference. It became clear that this method was too coarse since the upper surface of the pellet filling was uneven and the hole cover flexed somewhat during the heating phase. The precision of these measurements was estimated to be about ±20 mm.

In the final heating test the measurement method was improved by installing a level gauge on top of the pellet filling with a scale fixed on the concrete edge, see Figure 5-5. However, the accuracy in these measurements suffered somewhat due to high friction between the measure rod and the entry point through the hole cover. The precision was estimated to be within ±2 mm.

The measurements show approximately 20 mm settlement in the pellet filling in KQ0046G04. In the other holes the observed movements in the pellet filled slot were within the precision of the measurements. No heave was noticed in the pellet filling in any of the heating holes.

After finishing the field test the pellet filled slot was emptied easily by a suction-cleaner. The emptying process was carried out in steps of about 0.5–1 m to determine the approximate borehole depth of slabs included in the pellet filling. To be able to pick-up the slabs the pellet filling was removed by simple screening.

Figure 5-5. *Photograph of the level gauge installed in the final heating test for checking movements in the pellet filled slot (Photo R Glamheden).*

5.3 Heating procedure

The recorded heating power per hole in each test is complied in a joint graph in Figure 5-6 . A corresponding table and the recorded heating power per element and test are presented by graphs in Appendix I. The values given in the figure are based on mean values of the recorded power for each heating step. The variation in recorded power during a heating step was usually in the range of ±10 W.

The highest heating power was applied in the first field test, where it reached 3,785 W in the final stage. The reason for applying such a high heating power in first test was the large heat losses caused by the camera cooling system. The heating power in Field Tests 2 and 4 are enhanced compared to Field Test 3 due to additional heat losses in the wetting system applied in these tests, see Section 3.4.4. The necessity to increase the heating power a couple of times to follow the desired temperature development in the rock gave a stepwise increase of the heating power in Tests 1 and 2. Similarly the heating power in the last test was applied in a stepwise manner to reduce the temperature gradient in the surrounding rock.

The heating power applied in the respective field tests was varied somewhat between the heating holes with the intention of balancing the temperature between the holes. The divergence in the applied heating power was largest in Field Test 3. The difference in applied heating power is a reflection of the relative humidity of the heating holes, which was largest in the heating hole where the highest heating power was applied, see 5.4.

In Test 3 a change of power may be noticed in KQ0048G04 during a short interval of 0.5–1.5 days. This change was caused by an incorrect adjustment of the power of the heating elements. The short periods of reduced power during Test 4 correspond to the replacement of the faulty elements, see 5.1.3.

The temperature on the heaters reached close to the maximum allowable temperature of the element (700°C) in Field Test 3 and 4 performed with the pellet filling. The maximum temperature in Field Test 1 and 2 on the heaters ranged between 300–600°C, see Appendix K.

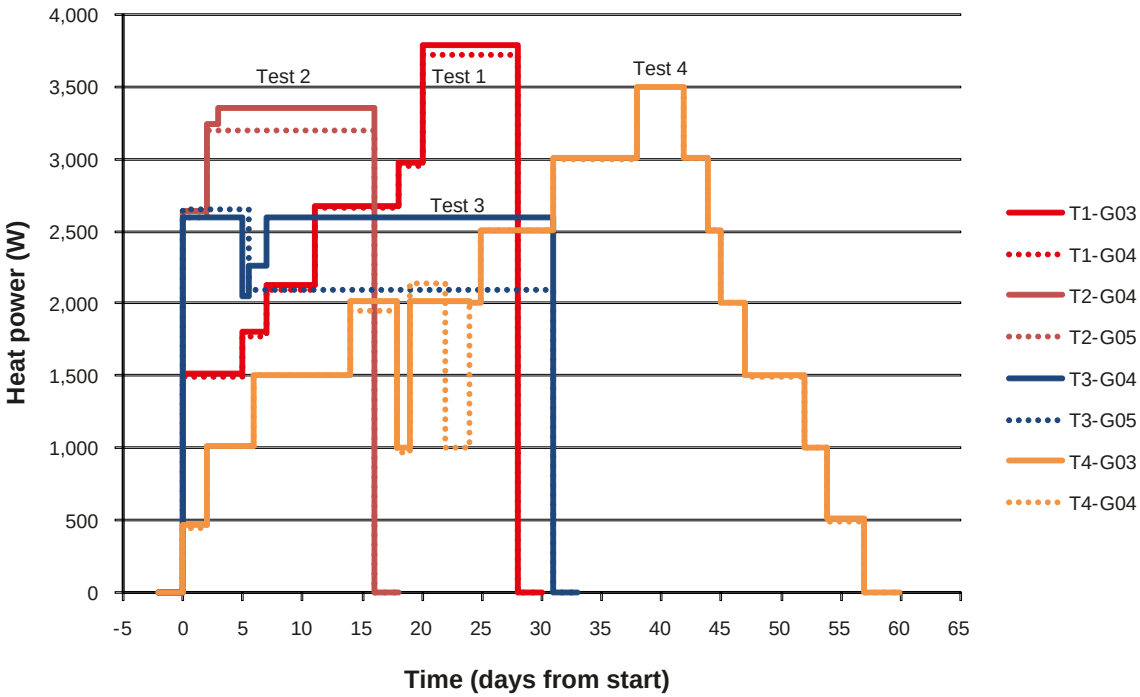

Figure 5-6. *Applied heating power in each hole during the field tests. Recorded mean values for respective heating step. The borehole label is shortened in the figure. The complete label included "KQ00" and borehole number. The time has been round off to the closest day. Test 1: 080829 11:08–080926 (G03) 18:28, (G04) 20:58; Test 2: 081106 14:51–081122 (G04) 16:19, (G05) 18:09; Test 3: 081128 13:06–091229 (G04) 12:33, (G05) 14:13; Test 4: 090213 10:51–090411 19:31.*

5.4 Relative humidity

A compilation of the relative humidity recorded in the field tests is presented in a Table 5-2 and Table 5-3, and by graphs in Appendix J.

The tables show recorded humidity in the tunnel and the heating holes before and during the heating period as well as during the cooling period. Since several RH-gauges failed early in the heating period the recorded numbers during the cooling phase are limited. The faulty gauges have also brought about reduced accuracy in the measurements.

The measurements in the tunnel display stable humidity with only minor variations due to the heating in the field tests or probably due to seasonal variation. The recorded relative humidity before starting the heating period in all heating holes, with the exception of KQ0048G05, was in the range of 95–100%.

In Field Tests 1 and 3, which were performed without artificial moistening, a difference in relative humidity of approximately 75% and 85% were observed between the recorded mean values of the heating holes. The lowest relative humidity in both tests was recorded in the SE-hole, where it reached a value of around 5%. The atmosphere in the heating holes in the first test became so dry that salt was deposited on the borehole wall.

The artificial moistening in Field Tests 2 and 4 was not able to maintain the relative humidity at the initial value in the heating holes but the humidity of the holes were similar and the reduction of the humidity during the heating period was limited.

Table 5-2. Compilation of relative humidity recorded during the Field Tests 1 and 2.

Test/Borehole	Initial value[2]		Heating		Cooling[3]	
	T (°C) Mean Min–Max	RH (%) Mean Min–Max	T (°C) Mean Min–Max	RH (%) Mean Min–Max	T (°C) Mean Min–Max	RH (%) Mean Min–Max
Test 1						
Tunnel[1]	17	95	18	86	–	–
KQ0054G03[1]	17	96	100	20	40	85
KQ0054G04[1]	17	96	100	5	–	82
Test 2						
Tunnel	–	–	16 15–18	80 68–92	–	–
KQ0051G04-1[3]	–	–	91 90–92	88 57–93	52 49–56	94 86–97
KQ0051G04-2[4]	15 15–16	98 96–99	96 85–100	74 57–98	51 48–55	100 98–100
KQ0051G05-1[3]	–	–	94 91–96	100 Eq.	58 54–63	100 Eq.
KQ0051G05-2[4]	16 15–17	94 89–97	92 86–100	87 59–97	57 53–62	92 91–94

Note: Borehole level 1 equal to –449.6 m and borehole level 2 equal to –447.6 m.

1) Based on separate manual readings during the test.

2) Based on readings during one day before the test start.

3) Based on readings during the final day of heating and cooling.

4) Based on readings during the heating period 10–15 days after test start.

Table 5-3. Compilation of relative humidity recorded during the Field Tests 3 and 4.

Test/Borehole	Initial value		Heating		Cooling	
	T (°C) Mean Min–Max	RH (%) Mean Min–Max	T (°C) Mean Min–Max	RH (%) Mean Min–Max	T (°C) Mean Min–Max	RH (%) Mean Min–Max
Test 3						
Tunnel[1, 2]	– –	– –	12 12–13	66 62–74	12 11–12	63 55–71
KQ0048G04-1[3]	19 Eq.	100 Eq.	88 83–91	78 73–87	–	–
KQ0048G04-2[3]	17 Eq.	100 Eq.	100 Eq.–	52 29–66	–	–
KQ0048G05-1[4]	18 17–19	100 Eq.	107 77–143	16 10–21	–	–
KQ0048G05-2[4]	17 Eq.	89 86–94	94 89–100	8 5–12	–	–
Test 4						
Tunnel	12 12–13	59 56–63	12 Eq.	70 66–75	–	–
KQ0046G03-2[5]	15 Eq.	100 Eq.	70 60–78	45 24–77	–	–
KQ0046G04-2[5]	16 15–16	100 Eq.	71 61–82	18 8–36	80 77–84	66 54–90

Note: Borehole level 1 equal to –449.6 m and borehole level 2 equal to –447.6 m.

1) Based on readings during the heating period 25–30 days after test start.

2) Based on readings during the cooling period 30–35 days after test start.

3) Based on readings during the heating period 5–10 days after test start.

4) Based on readings during the heating period 1–4 days after test start.

5) Based on readings during the heating period 30–35 days after test start.

5.5 Temperatures

The temperature development during the field tests is synthesized in Table 5-4, where the recorded rock temperature is presented at three moments during the field tests for the points indicated in Figure 5-7. The initial value corresponds to the temperature before the heating power was turned on, the maximum value corresponds to the temperature before the cooling phase was initiated and the final value is the temperature recorded before the gauges were disconnected.

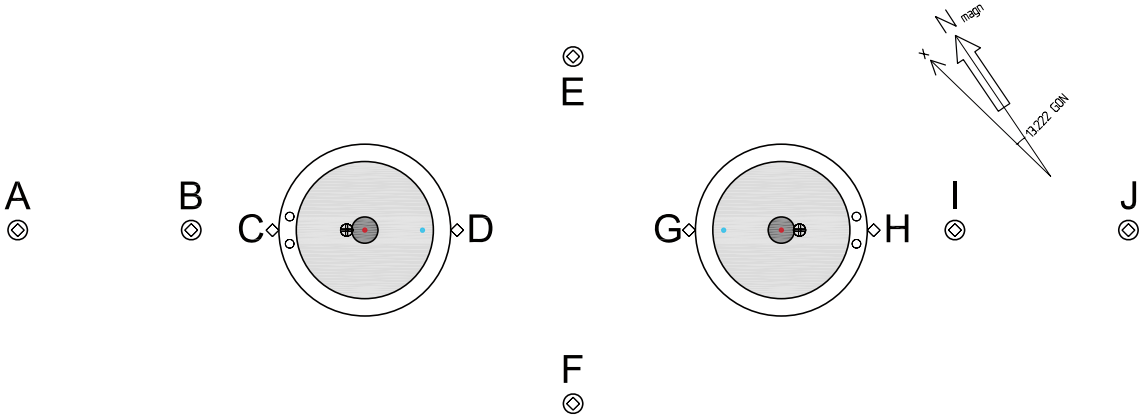

Figure 5-7. *Drawing indicating the location of the points of recorded temperature in Table 5-4.*

Table 5-4. Temperature in the field tests at three moments for the points indicated in Figure 5-7 located at the hole mid height (level –448.5 m).

	A	B	C	D	E	F	G	H	I	J
Test 1										
Initial value	15.2	16.1	18.2	18.6	16.2	16.2	17.6	18.2	16.0	15.2
Max value	39.0	60.4	83.1	77.5	64.6	65.7	100.0	99.5	69.8	44.7
Final value	35.0	40.2	39.4	42.2	47.6	49.0	43.3	43.8	44.3	39.4
Test 2										
Initial value	16.4	15.8	16.0	16.2	16.2	16.3	16.3	16.5	16.1	16.3
Max value	42.2	65.6	93.3	89.0	69.6	66.9	92.3	94.4	63.7	41.0
Final value	39.9	47.5	53.2	48.3	57.5	56.8	51.3	56.3	49.0	39.5
Test 3										
Initial value	17.9	18.1	18.5	18.6	20.9	17.0	18.4	18.1	17.9	17.5
Max value	46.4	66.6	96.9	93.1	72.9	72.5	101.8	120.0	61.8	43.9
Final value	27.6	28.4	28.2	28.3	29.6	30.0	27.0	27.8	28.5	27.6
Test 4										
Initial value	17.2	16.5	15.6	15.7	16.3	16.8	15.7	16.0	16.2	15.8
Max value	51.3	73.4	134.0	140.2	82.2	78.3	146.6	137.5	81.6	50.7
Final value	21.7	21.7	21.7	21.6	21.3	21.1	21.3	21.3	18.7	18.5

Note: The time limits given below correspond to the first and the last recorded values in the different tests.
Test 1: 080823 15:52–080929 11:08.
Test 2: 081105 15:19–081124 13:09.
Test 3: 081127 13:06–090112 14:03.
Test 4: 090212 14:48–090511 10:12, Point I–J 090528 08:27.

In addition to the table, recorded temperatures versus time are presented by graphs in Appendix K. The recorded temperature of the rock mass, in a vertical section through the heating holes, when the cooling phase was initiated and the temperature starts to decline, is also included in Appendix K. The position of the gauges is marked with blue squares in the latter pictures shown in the current appendix.

The initial temperature of the rock mass before starting the first field was around 15°C. In the following tests, the initial temperature increased slightly due to the disturbance from the nearby previous heating test. The initial temperature was highest in Field Test 3, with a value of approximately 18°C when starting the field test.

The maximum temperature on the wall in the heating holes, reached just before the cooling phase was initiated, ranged from approximately 80°C in the first test to 140°C in the last one. The temperature in the last test exceeded the target value, which was set to approximately 115°C. This was due to the installed wetting system which stopped operating, see Section 5.1.4. The shutdown of the wetting system also meant that the temperature gradient in the surrounding rock was not reduced as intended compared to the previous tests. In fact the temperature gradient around the heating holes, at the time of initiating the cooling phase, became steepest in the final test, see Figure R-29 in Appendix R.

With the exception of Tests 2 and 4, the temperature development in the field tests was somewhat uneven between the heating holes, see Figure 5-8. The temperature development in Test 3 showed the largest differences between the heating holes. The difference in temperature is a reflection of the relative humidity of the heating holes, which was largest in the heating hole with least temperature change, see Section 5.4.

In all heating holes the temperature on the borehole wall reached the calculated temperature necessary to induce thermal spalling along the main part of the wall, see Appendix R. The major principal stress on the borehole wall was estimated to exceed the crack initiation stress of the rock (120 MPa) down to a depth of at least 3.5 m at a wall temperature of approximately 70–80°C. To guarantee that spalling would occur in Tests 3 and 4, where the borehole wall of the heating holes was supported by pellets of LECA, the temperature was increased above the recorded temperatures in Tests 1 and 2.

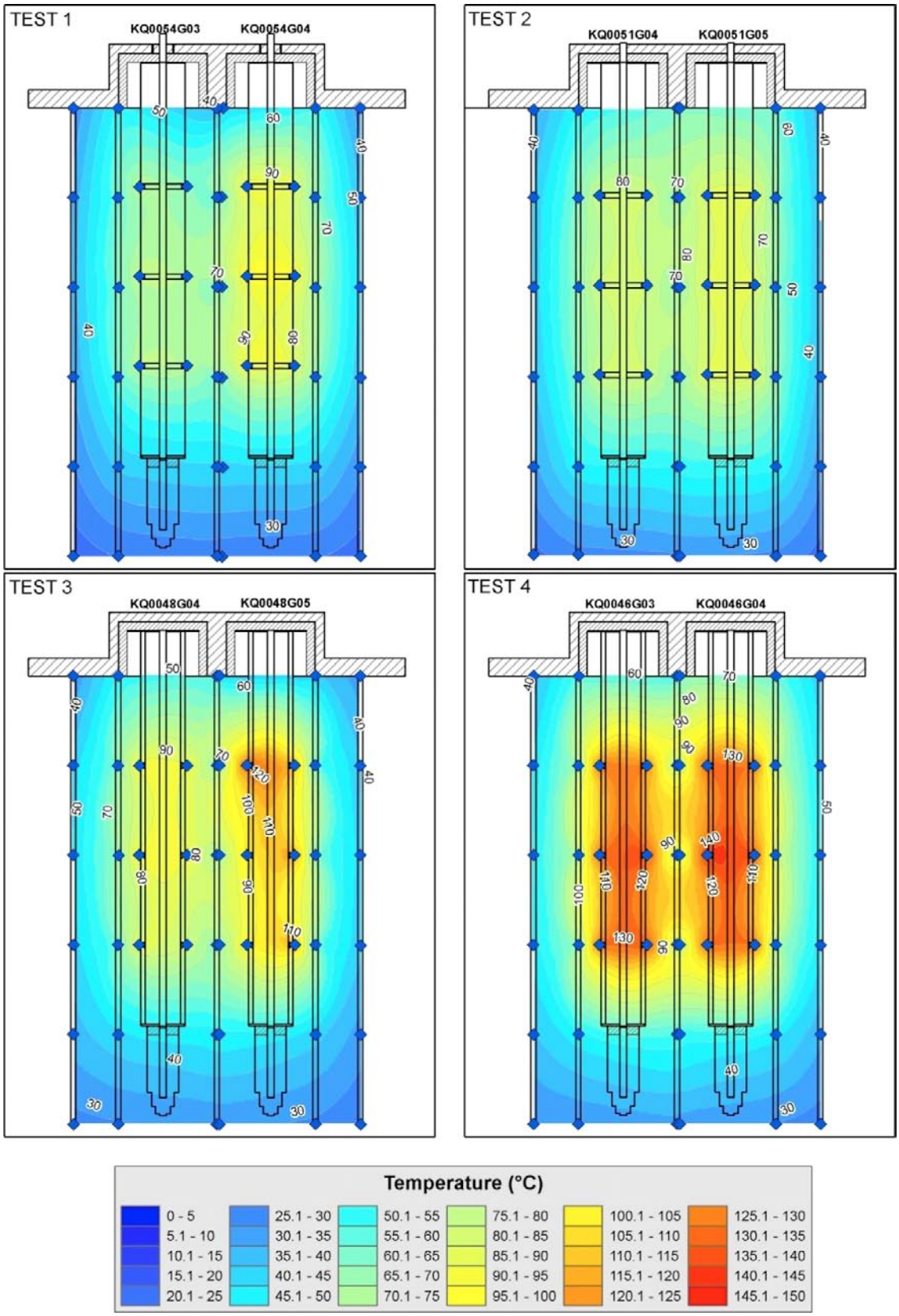

Figure 5-8. *Recorded temperatures of rock mass in Test 1–4 when the cooling phase was initiated. The squares in blue indicate the position of the temperature gauges that were included in the natural neighbour interpolation of the recorded values.*

6 Spalling observations

6.1 Initial observations

The spalling that occurred as a result of stress concentration during the drilling of the heating holes was checked visually after each reaming step and documented by photographs and laser scanning after the reaming had been completed. A compilation of the observed spalling in the completed holes is shown in Table 6-1. Any occurrences of spalling were noticed in former reaming steps.

Spalling related to the drilling of the boreholes was only observed in three of the heating holes. In two of these holes, KQ0054G03 and KQ0054G04, the observed spalling was minor and included only a couple of tiny rock slabs, whereas the size and number of spalled rock slabs in KQ0048G04 were more substantial and comprised an estimated volume of 1.0 litre. The breakout in KQ0048G04 is presented at two occasions by a fish-eye photo and an ortho-photo from the laser scanning in Figure 6-1. The breakout seems to have increased slightly between the two dates of observation. The rock slabs that dropped down in this heating hole during drilling did not have the sharp shape typical for thermal spalling, but were instead spherical and probably formed by existing fractures. According to the core mapping of the pilot holes the current section of breakout in KQ0048G04 corresponds to a section with a high frequency of open or partly open fractures, which most likely is the explanation of the larger breakout, see Appendix A.

The small amount of spalling related to the drilling process might be a result of the reaming of the heating holes to full size in several steps from a core drilled pilot hole, see Section 4.1. The progressive development of the spalled damaged zone due to the reaming process is considered to reduce the extent of the zone compared to if full size drilling was performed directly. According to the estimated stresses, the drilling should have caused a stress concentration sufficient to create spalling down to at least 1 m depth in the holes, see Appendix R.

Except for the heating holes used in the final field test (KQ0046G03 and KQ0046G04) the borehole walls were not scaled from loose fragments before the heating phase. This means there is a possibility for the occurrence of some loose slabs outside of the wedge area documented by the photographs and the laser scanning.

Table 6-1. Compilation of the observed spalling in the heating holes after the drilling was finished.

Test /Borehole	Observations on NE Wall				Observation on SW Wall			
	Exist	Depth[1] (m)	Volume (litre)	Type[2]	Exist	Depth (m)	Volume (litre)	Type
Test 1								
KQ0054G03	Yes	0.60–0.80	0.1	R	No	–		–
KQ0054G04	No	–	–	–	Yes	1.25–1.30	0.1	S
Test 2								
KQ0051G04	No	–		–	No	–		–
KQ0051G05	No	–		–	No	–		–
Test 3								
KQ0048G04	Yes	0.70–1.30	1.0	R, S	Yes	0.65–0.80	0.1	R
KQ0048G05	No	–	–		No			
Test 4								
KQ0046G03[3]	No	–	–	–	No	–	–	–
KQ0046G04[4]	No	–	–	–	No	–	–	–

1) The borehole depth and the volume are estimated based on photographs exposed before test start.

2) The observations are divided into spalling in intact rock (R) and spalling along structures (S).

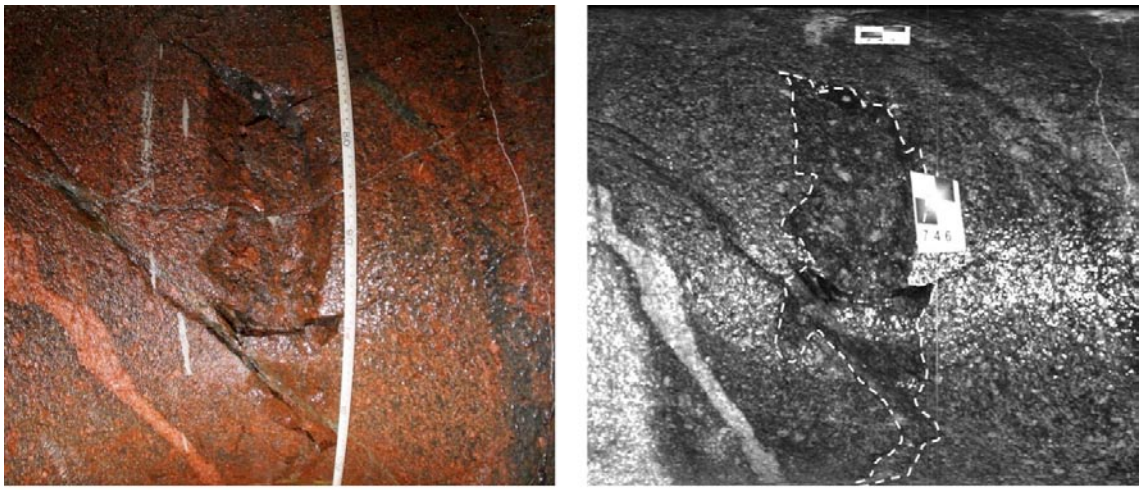

a) Fish-eye photo, 2008-07-07 b) Ortho photo, 2008-11-18

Figure 6-1. *Shows the observed breakout in KQ0048G04 of the NE-side of the borehole wall after the reaming was finished (Photo C-R Lindqvist).*

6.2 Observations during the heating

Spalling observations during the heating phase were possible to perform in the first and the second field test without the filling of LECA pellets. In the first test the observations during the heating phase were carried out by a number of stationary monitoring cameras in combination with a couple of visual inspections. In the second test the observations were based on regular visual inspection in combination with a mobile monitoring camera, see Section 3.4.7.

In the first field test the initiation of spalling was picked up by monitoring cameras in three positions; two positions on two levels in heating hole KQ0054G03 and in one position in KQ0054G04. The reason for not monitoring spalling by further cameras was that spalling only occurred in isolated points in KQ0054G04 and that a couple of cameras stopped working, see Section 5.1.7. An overview of the development of spalling during the heating phase, based on the monitoring cameras, is presented in Table 6-2 and based on the visible inspection in Table 6-3. Included in the tables is also the mean temperature on the borehole wall at the time of observation as well as an estimation of the tangential stress on the borehole wall based on the calculated results presented in Figure 8-7.

The initiation of spalling was most distinct in the borehole monitored by camera CAM1 located in hole KQ0054G03. Pictures from this position on three occasions, 1.5, 4.5 and 14.5 days after the heating was initiated, are presented in Figure 6-2. The first sign of spalling in this part of the borehole wall was observed already after 1–2 days of heating, when a tiny slab, approximately 20×30 mm, loosened, see Picture A. The temperature of the borehole wall when this occurred was approximately 37°C corresponding to a tangential stress of about 118 MPa. During the next two days the size of the slab was essentially unchanged, however, there was an abrupt growth to approximately 50×60 mm after 4–5 days of heating, when the temperature reached approximately 42°C. Subsequently the slab grew continuously to reach an ultimate size of approximately 50×200 mm after 14–15 days of heating, when the temperature on the borehole wall was about 60°C, see Picture C.

The first signs of spalling at the deeper level in hole KQ0054G03 occurred after 15–16 days of heating at a temperature of 61°C on the borehole wall corresponding to a tangential stress of about 117 MPa. Signs of spalling in hole KQ0054G04 were picked up by CAM6 on the upper level after 8–9 days at a wall temperature of 54°C, which corresponds to a tangential stress of about 122 MPa. The latter observation agrees quite well with the temperature (stress magnitude) that was numerically calculated for initiation of spalling, see Figure 8-7, whereas the observations by CAM1 display an initiation of spalling at a somewhat lower temperature, see Table 6-2.

The observed progress of the spalling along the borehole wall with increasing depth, in the heating holes in Tests 1 and 2, are presented in Table 6-3 and agree relatively well with the estimated development based on numerical simulations, see Figure 8-8. The variation that exists between the heating holes in the development of spalling is most likely a reflection of local variation in the rock strength depending of the geology or the humidity of the holes. The effect of these conditions is further discussed in Section 8.2.

Table 6-2. Time, temperature and estimated tangential stress when the first signs of spalling were picked up by the monitoring cameras installed in Field Test 1.

Borehole No	Camera Label	Level (m)	View Direction	Depth[1] (m)	Time[2] (days)	Temperature[3] (°C)	Stress[4] (MPa)
KQ0054G03	CAM1	–447.9	NE	1.75–2.05	1.5	37	118
KQ0054G03	CAM4	–449.0	SW	2.80–3.20	15.5	61	117
KQ0054G04	CAM6	–448.0	SW	1.75–2.20	8.5	54	122

1) Borehole depth with the concrete upper edge as reference, level –446.0 m.

2) Time after test start when spalling was observed.

3) Mean of temperature on the borehole wall when spalling was observed.

4) Estimated tangential stress on the borehole wall for the recorded temperature at the borehole depth of observation based on the calculated results presented in Figure 8-7.

Table 6-3. Visual observations of the development of spalling in Test 1 and 2.

Test/Borehole	Time[1] (days)	Temp[2] (°C)	Stress[3] (MPa)	Observations on NE Wall		Observation on SW Wall	
				Depth[4] (m)	Type[5]	Depth (m)	Type
Test 1							
KQ0054G03	12	57	120	0.5–1.5	C	–	–
	19	64	124	0.5–1.8, 2.4	C, S	0.5–2.0	C, S
KQ0054G04	12	60	122	0.5–1.0	S	–	–
	19	75	130	0.5–1.0, 2.4	S	0.5–1.0, 1.8	S
Test 2							
KQ0051G04	5	68	126	0.5–2.1, 3.6	C; S	0.5–1.7	C, S
	12	86	138	0.5–2.6, 3.6	C, S	0.5–2.6, 3.8	C, S
KQ0051G05	5	68	126	1.2, 2.1	S	0.8, 1.2, 3.8	S
	12	87	139	0.5–2.5	S	0.5–1.2, 2.6, 3.8	S

1) Days since test start. The first occasion of inspection in Test 1 is 11 days after test start.

2) Mean temperature on the borehole wall.

3) Estimated tangential stress on the borehole wall for the mean temperature at 2.5 m borehole depth based on the calculated results presented in Figure 8-7.

4) Borehole depth with the concrete upper edge as reference, level –446.0 m.

5) The observations are divided into continuous spalling (C) and spots of spalling (S).

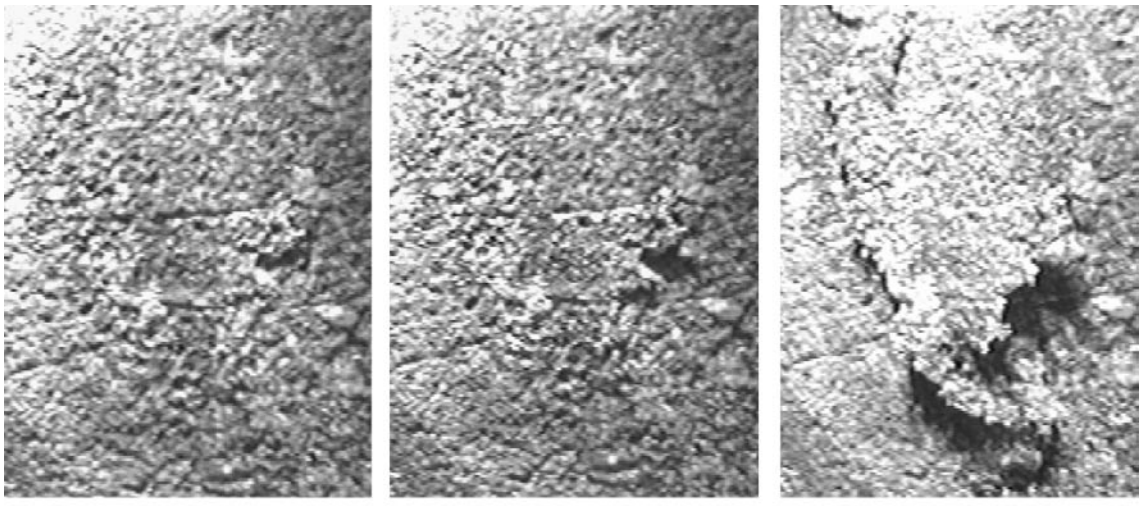

a) 1.5 day 080830, 23.59 b) 4.5 days 080902, 23.59 c) 14.5 days 080912, 23.59

Figure 6-2. *Pictures from monitoring camera CAM1 at three occasions in Field Test 1. The view is from 1.75–2.05 m depth in hole KQ0054G03.*

6.3 Observations after cooling

The observations of spalling in the heating holes, after the cooling phase and before scaling of the rock wall, are presented in this section. The observations are described regarding extension and width along the holes and differences in the proportions of the spalling between the heating holes. The account is based on visual observation in the holes documented by notes, photographs and video records.

In the first field test the design of the instrument holder restricted the possibility of observation, since it had to be carried out with the test equipment in place. After the first test the bottom disc was modified to be able to unscrew it before lifting the holder, which made it possible to inspect the holes after removal of all the installed equipment in the subsequent tests, see Section 3.4. In Tests 3 and 4 this also included the larger tube that created the slot with LECA pellets.

A general view of the spalling observations in each test is given in Table 6-4. The table presents the interval between the upper and lowest spalling observation and an estimation of width of the spalled zone. The spalling observations are also classified as continuous spalling or spots of spalling.

The uppermost spalling observation in the heating holes is encountered around 0.5 m below the concrete upper edge and the lowest observation around 3.5 m below the same reference level. The width of the damaged zone ranges between 100–250 mm in Tests 1 and 2, performed without the confinement provided by LECA pellets, and between 50–200 mm in Tests 3 and 4 that included confinement provided by LECA pellets.

Field Tests 1 and 2, which were carried out without the confinement provided by LECA pellets, showed large heterogeneity in the proportion of observed spalling between the heating holes, as well as between the opposite sides of individual heating holes. This fact is clearly illustrated in Figure 6-3, which shows two photographs from the boreholes that were heated up in Test 2. In general, the occurrence of spalling was smallest in the heating holes located on the SE-side of the tunnel axis. In those holes the spalling occurred mainly as separate spots, while in the holes located on the NW-side of the tunnel axis, at least in the upper part of the holes, the spalling was continuous along the borehole wall.

The reason for the large difference in the amount of spalling between the holes placed to the NW-side compared to the ones placed to SE-side of the tunnel axis is most likely caused by the shear zone striking parallel with the tunnel axis, see Section 2.1. There are also indications that the amount of spalling correlates to the water inflow and the relative humidity of the heating holes, see Section 2.5 and 5.4. Additional analysis regarding this are presented in Section 8.2.

Table 6-4. Observation of spalling in the heating holes after the cooling phase. Tests 1 and 2 were performed without confinement and tests 3 and 4 with confinement.

Test/borehole	Observations on NE Wall			Observation on SW Wall		
	Interval[1] (m)	Width[2] (mm)	Type[3]	Interval (m)	Width (mm)	Type
Test 1						
KQ0054G03	0.5–2.0	250	C	0.5–3.0	150	C
KQ0054G04	0.5–2.6	150	S	0.5–1.8	100	S
Test 2						
KQ0051G04	0.5–3.8	200	C	0.5–3.6	250	C
KQ0051G05	0.5–2.5	150	S	0.5–3.8	100	S
Test 3						
KQ0048G04	0.7–3.4	200	C	0.6–3.9	150	S
KQ0048G05	0.5–2.9	150	S	0.4–3.2	100	S
Test 4[4]						
KQ0046G04	0.5–0.8	50	S			

1) Interval between the upper and lowest observation with the concrete upper edge as reference, level –446.0 m. The test equipment restricted the possibility to observation in Test 1.

2) Maximum width of the damaged zone.

3) The damaged zone is classified as continuous spalling (C) or spots of spalling (S).

4) Inspection of the damage zone in KQ0046G03 has not been carried out since the hole was grouted.

Figure 6-3. *Photographs of the borehole wall in heating hole KQ0051G04 (A) and KQ0051G05 (B) in Test 2 after the cooling phase and before scaling of the wall. Field Test 2 was performed without confinement provided by LECA pellets. The photographs illustrate the heterogeneity in the proportions of observed spalling (Photo C-R Lindqvist).*

Field Tests 3 and 4, performed with the confinement provided by LECA pellets, like the previous tests, show large heterogeneity in the proportion of spalling between the heating holes. Among the present heating holes, the damage was largest on the NE-side of the wall in borehole KQ0048G04. Two photographs of the borehole wall in KQ0048G04, before scaling, are shown in Figure 6-4. A photograph of the SW-side in borehole KQ0048G05 is also included in the figure to demonstrate the heterogeneity in the results.

Borehole KQ0048G04 was the hole that displayed most breakouts after the drilling, see Section 6.1. It is considered that it was in this hole that it was most difficult to prevent thermal induced spalling. It should also be pointed out that some of the damage observed after the cooling phase could be a result of the actual drilling, since the wall was not scaled before heating. Another circumstance that might have caused additional damage to the wall, down to a borehole depth of 1.5 m, is the fact that the slot was emptied of pellets when the temperature in the surrounding rock mass was still approximately 15°C above the initial rock mass temperature. The elevated temperature generating thermal

stresses on the borehole boundary, which corresponds to approximately 125 MPa, see Figure 8-7 in Section 8.1.3.

In spite of the relatively large breakout observed in KQ0048G04, the overall conclusion based on the results from all holes, is that the confinement provided by LECA pellets has reduced the thermal spalling, whereas it could not fully prevent the borehole wall from cracking up when heated. When comparing the photographs in Figure 6-4 from Test 3 with the photographs in Figure 6-3 from Test 2, it is apparent that the confinement provided by the LECA pellets has the capability to keep rock slabs with larger dimension than the pellet fraction in place in the borehole wall. Based on this observation it is also reasonable to assume that the counter pressure from LECA pellets has the capacity to reduce the hydraulic transmissivity of the damaged zone by supporting the slabs and keeping the thermally induced cracks in the borehole wall closed. Additional results that support the current assumption are presented in Section 7.4.

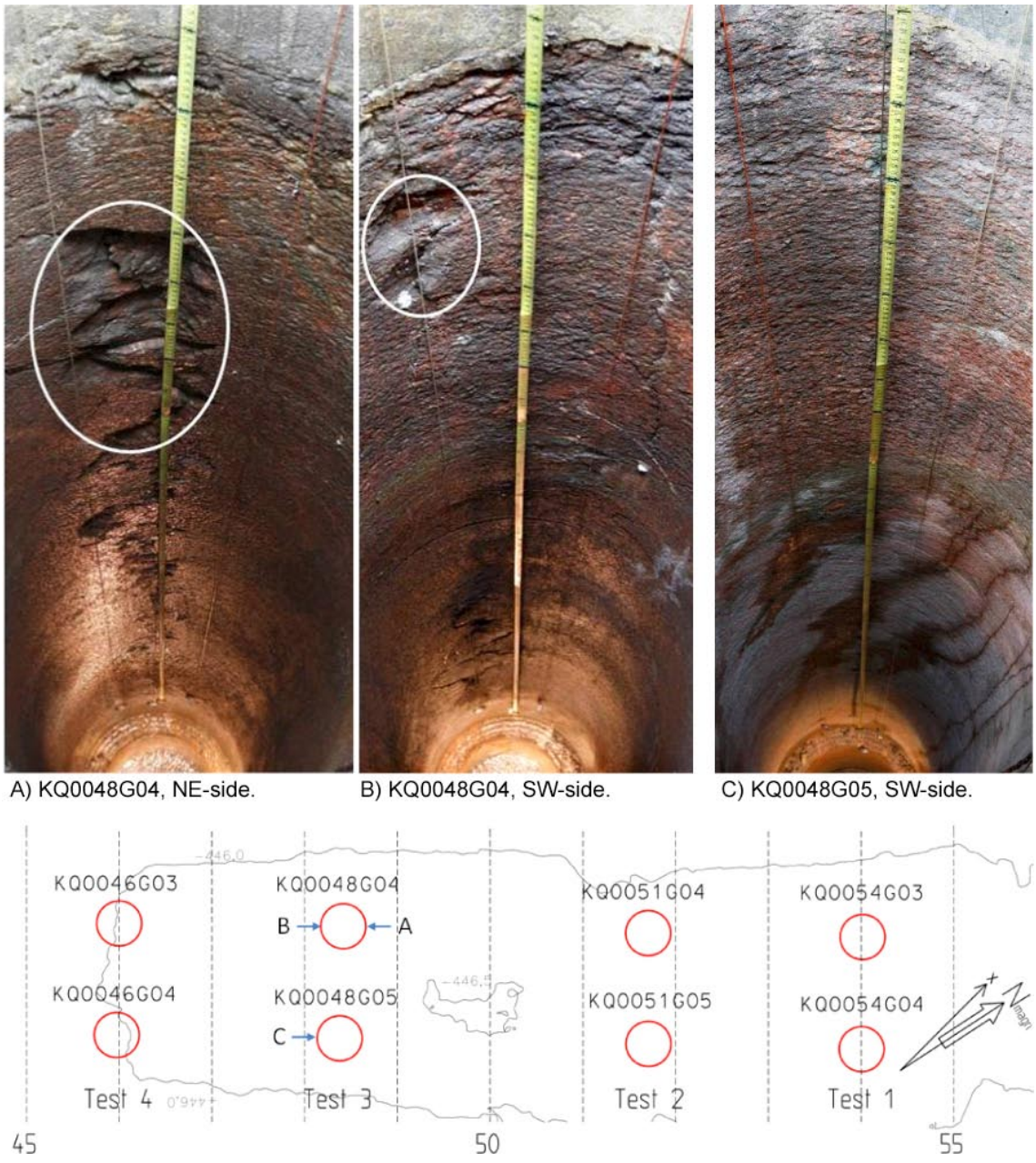

Figure 6-4. *Photographs of the borehole wall in heating hole KQ0048G04 (A and B) and KQ0048G05 (C) in Test 3 after finished cooling phase, before scaling of the wall. Field Test 3 was performed with confinement provided by LECA pellets. The photographs illustrate the heterogeneity in the proportions of observed spalling. The breakouts in the areas marked by a white ellipse occurred mainly before the heating (Photo C-R Lindqvist).*

7 Post characterization

7.1 Procedure for the post characterization

After completion of the final heating test, post characterization of the spalled damaged zone was carried out. The post characterization included measurements of the borehole diameter and documentation of the geometry of the notch induced by the thermal spalling by a number of monitoring methods, namely ultrasonic measurements, laser scanning, photographing with thin lighted slot, video recording and ordinary photographs of the holes. Furthermore, the hydraulic transmissivity of the spalled zone was examined by water injection tests in a number of cored drill holes penetrating the damaged zone in one of the heating holes in the final test (KQ0046G03) after sealing of the pellet filled slot. The purpose of the measurements, the test equipment and the procedure used for each separate measurement included in the post characterization are further described in separate sections below.

7.1.1 Lifting device for documentation of the notch

The monitoring methods used to measure the hole diameter and to characterize the notch geometry, (ultrasonic measurements, laser scanning, photographing with thin lighted slot, and video recording), all used the same lifting device for hoisting up and down of the monitoring equipment in the heating holes. The lifting device, which was developed at Äspö HRL is shown in Figure 7-1.

The lifting device was screwed tightly onto the concrete collar before the measurements to ensure stability. The profile that went up and down had roller bearings and was adjusted in the vertical line by a laser plummet. The borehole depth of the equipment was recorded continuously by a digital gauge. The gauge was calibrated by staff at Äspö HRL towards a graduated rule located in a concrete tube (Ø0.5 m and depth 2 m) and in place in the heating holes. The resolution in the depth positioning along the holes was approximately ±5 mm and the accuracy in depth position was estimated to be within ±10 mm.

Figure 7-1. *Lifting device for documentation of the spalled notch in the heating holes.*

7.1.2 Ultrasonic measurements

The ultrasonic measurements were carried out to determine the variation of the diameter along the heating holes and the depth of the spalled notch. The results were used for scaling the photographs produced with a thin lighted slot and for verification of the results from the laser scanning by an independent method, see Section 7.1.3 and 7.1.4. The results from the ultrasonic measurements are presented in Appendix N.

The measurements were performed by four gauges manufactured by *Sick*, which were installed in a horizontal direction on a cross formed fixture of bars with perpendicular angles. The positions of the gauges were 0, 90, 180 and 270 degrees in a local system directed with the 0–180 gauges in the N-S-direction, respectively. The distance between the gauges was 365 mm in the 0–180 direction and 367 mm in the 90–270, except for in the measurements that were performed in KQ0046G04, where the distance was 373 mm in both directions. For the current distance 55–60 mm between the gauges and the borehole wall the results corresponded to a mean value for a measuring point with approximately 40 mm in diameter. A sketch of the set-up for the ultrasonic measurements along with a photograph of the equipment is shown in Figure 7-2.

The gauge was calibrated by staff at Äspö HRL in a concrete tube (Ø0.5 m and depth 2 m) and in place in the heating holes. The resolution of the measurements was approximately ±0.5 mm and the accuracy was estimated to ± 2 mm. What reduced the accuracy were mainly the borehole curvature and the surface roughness of the borehole wall. The measurements were carried out jointly by staff at Äspö HRL and Golder Associates AB.

7.1.3 Laser scanning

Of all the measuring methods used in the post characterization, the one that supplied the most complete and important results, was the laser scanning. However, this measuring method was also the most difficult to accomplish and a couple of trial runs had to be performed before a proper procedure for the measurements had been developed. The trial runs, which were carried out prior to the heating tests for documentation of the initial conditions, were performed by ÅF infrastructure AB, while the scanning for the purpose of post characterization was done by ATS AB. The results included in this section are based solely on the scanning performed by ATS. However, the results from the preliminary laser scans performed by ÅF are available in SICADA.

What caused problems in the outset were the deviation of the heating holes and the large difference in the measuring distance in the radial direction, compared to the axial direction of the holes. The short measuring distance in the radial direction also entailed that the scanning equipment had to be recalibrated, since the distance was outside the certified measuring range. The solution to the described problem was installation of reference targets in four directions with 0.5 m interval along the holes and sectioning of the laser scanning in the intervals with the same distance. The scanner equipment was hoisted up and down in the heating holes with the lifting devices described in Section 7.1.1. A photograph of the scanner equipment in place in one of the heating holes is shown in Figure 7-3.

The scanning equipment used by ATS AB was supplied by *FARO*. The scanning was performed on two occasions by two different instrument models, LS 880 in the first campaign and Photon 80 in the second campaign. The two instrument models have almost equivalent specifications. The resolution is 0.6 mm and the accuracy ±2–3 mm for a measuring range of 0.6–76 m.

The results from the laser scanning have been used for evaluation of the occurrence and position of breakouts in the heating holes, as well as determination of the dimensions of the breakouts (depth, width, length and volume). The scanning results have also been used for the evaluation of a possibly correlation between the spalling occurrence and the geology based on orthophotos of the borehole wall. Furthermore, the scanning results were used for a general evaluation of the deviation of the heating holes. The scanning results, which are accounted for in Section 7.3, are compiled in Appendix M.

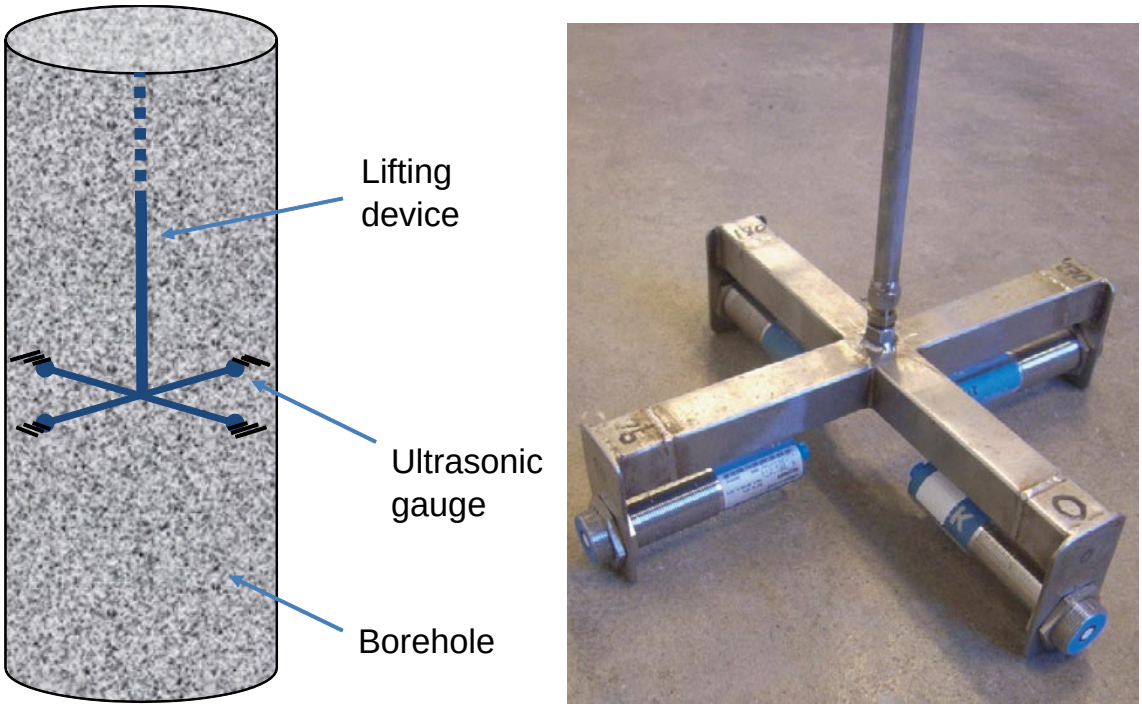

Figure 7-2. *Sketch of the set-up for the ultrasonic measurements along with a photograph of the measurement equipment. (Photo M Lundqvist).*

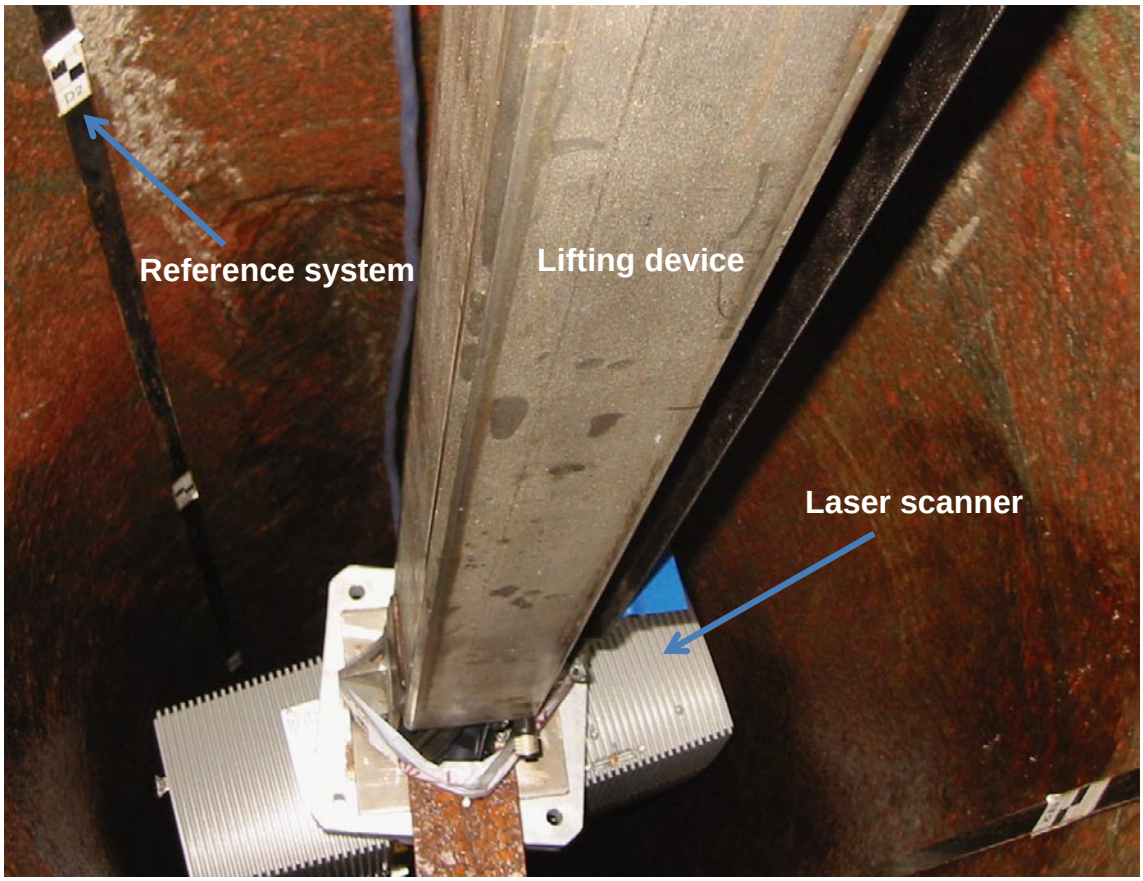

Figure 7-3. *The laser scanning equipment in place in one of the heating holes. (Photo R Berlin).*

7.1.4 Photographing with thin lighted slot

Photographing with a thin lighted slot was performed as a complement to the laser scanning to determine the position and geometry of breakouts along the heating holes. The slot photographs of the borehole wall, which were taken with an interval of 0.1 m, were used to produce horizontal cross-sections of the holes after processing in AutoCAD. The results are presented in Section 7.3 and in Appendix O.

A sketch of the set-up for photographing with a thin lightened slot along with an example of a photograph by the slot is shown in Figure 7-4. The thin lighted slot was created by a halogen lamp mounted between two discs with a 40 mm gap in between. The upper disc, which was dark to attain a sharp contrast to the lighted slot, was located 560 mm below the camera lens. The package, consisting of the camera and the two discs, were mounted on the lifting device described above, see Section 7.1.1.

The lighted slot on the rock wall was 55 mm thick and the distance between the upper edge of the upper disc and the lighted slot was 25 mm. The centre point in the picture and two scale lengths of 50 mm were marked by small lighted holes in the upper disc, see Figure 7-4. However, the final adjustment of the scale in the picture was based on the borehole diameter determined by the ultrasonic measurements in the current cross-section, see Section 7.1.2.

The orientation of the photographs was achieved by installing plumb lines in the heating holes, three on the NE-side and two on the SW-side. The interval between the lines was 100 mm, with the centre on a line parallel with the tunnel axis.

The accuracy in the determined notch dimension using this method was estimated to be within ±5 mm. The accuracy in the borehole depth positioning was estimated to be within ±10 mm, see Section 7.1.1.

7.1.5 Video recording

Video recording of the heating holes was carried out to get detailed visual observations of the occurrence of breakout along the borehole wall. The documentation has been used to confirm the breakouts determined by the laser scanning and for evaluation of possible correlations between spalling and geology. The video recording includes both the NE-side and the SW-side of the borehole wall.

Video recording of the heating holes has been carried out on two occasions with different equipment. The first occasion was directly after the heating holes had been emptied of the testing equipment and includes records both before and after scaling of the borehole wall. The recording at this time was performed with an observation camera mounted on a rod that was hoisted up and down using a simple tripod. These films are sometimes of poor picture quality due camera shake.

Later video recording was performed to improve the quality of the films. The equipment used by this time was a digital video camera provided with a wide angle lens. To avoid camera shake the video camera was mounted on the lifting device described in Section 7.1.1. These films are of higher quality and only show the spalled notch after scaling of the borehole wall. Pictures from the video recording are not included in this report, but are available from SICADA.

The borehole depth in the heating holes was indicated by a measuring-tape suspended along the borehole wall in the position of a line parallel to the tunnel axis. The concrete upper edge worked as a reference level (–446.0 m equal to distance 4.3 m). The width of the breakouts was indicated by two plumb lines located 100 mm on each side of the measuring-tape.

7.1.6 Photographs

Photographs of a top view of the heating holes were taken for all the heating holes before initiation of the field tests, see Section 4.5. These photographs were complemented by a new series of photographs, one on the NE-side and another of the SE-side of the holes, after the field tests, before and after scaling of the borehole wall, see Appendix T. Borehole depth, orientation and width of the breakouts in the photographs, are indicated in the same manner as used for the video recording, see Section 7.1.5.

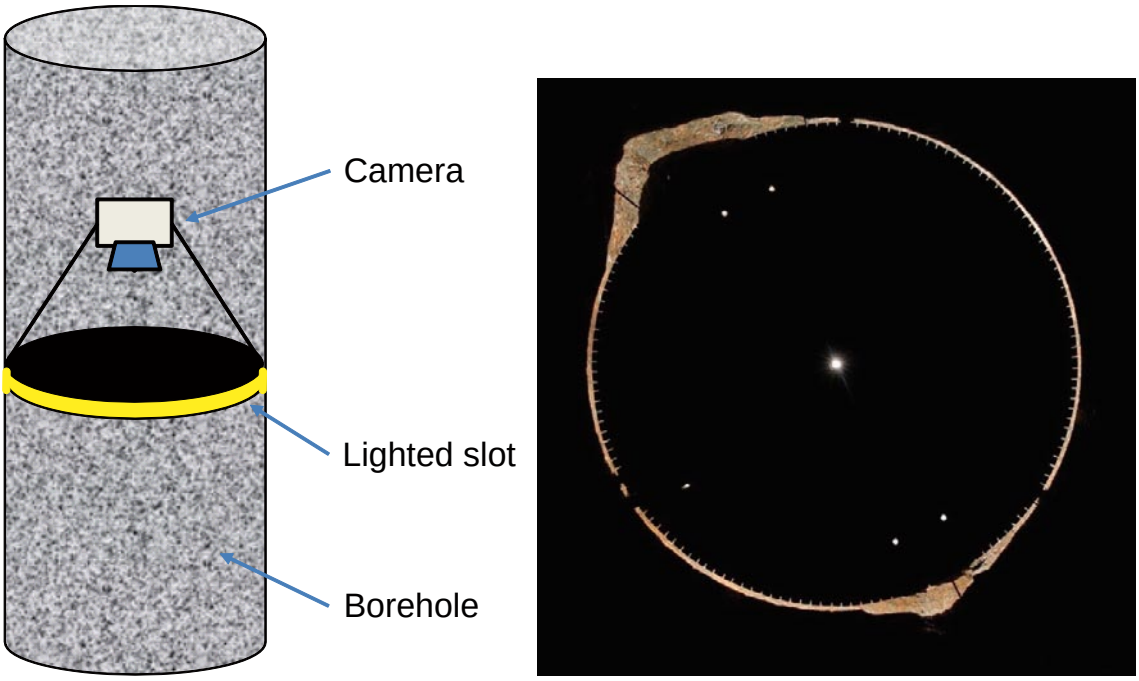

Figure 7-4. *Sketch of the set-up for the photographing with thin lighter slot along with a photograph with thin lighted slot showing a section in KQ0051G04. (Photo C-R Lindqvist).*

7.1.7 Water injection tests after sealing of the pellet filled slot

In one of the heating holes in the final test (KQ0046G03) the hydraulic transmissivity of the spalled damaged zone was examined by water injection tests in a number of cored drill holes penetrating the damaged zone as shown in the drawing in Figure 7-5. Dykes and fractures, mapped in the pilot hole of the KQ0046G03 and the surrounding instruments holes, are also included in the figure. A three dimensional image of geological structures close to KQ0046G03, that also takes into account the mapped injection holes, is found in Appendix B.

The hydraulic transmissivity of the damaged zone was examined in situ by drill holes of the configuration presented, since it was expected to keep the disturbance of the hydraulic properties to a minimum. Drilling water injection holes for example along the damage zone or to use overcoring techniques and examine the hydraulic properties in laboratory, were also considered, however, it was judge that this would affect the hydraulic properties of the zone too much. The change of the tangential stresses around the heating hole, by applying any of the other methods considered, would have induced additional damage to the zone.

Before the drilling of the water injection holes, the pump pit of the heating hole and the pellet-filled slot were sealed by a grout of ordinary Portland cement (d_{95}~ 65 µm). The grout had the following mix: 100 kg cement, 26 l water, 0.2 l Sika EVO 26 and 1.5 Sika Control 40. The cement grout was tested by sealing tests in pellet filled steel pipes and in a pellet filled 50 mm slot, created between an outer concrete tube and an inner steel tube. The set-up of these tests is shown by a sketch in Figure 7-6.

The steel pipes were used for tightness tests by applying a water pressure through a side hole penetrating the sealed LECA filling, see Figure 7-6. The pellet filled slot was used for pumping and penetration tests. No water leakage was observed in the tightness test that went on for two days at 15 bar overpressure. The grouting tests in the pellet filled slot showed excellent filling of the voids and a tight contact surface. A photograph of the sealed pellet filling is shown in Figure 7-7. Additional photographs from the sealing tests are shown in Appendix V.

The grout was pumped under low pressure (5–10 bars) into the pump pit and thereafter into the pellet-filled slot through four pipes located in the slot. A top view of the pellet filled slot before starting the grouting is shown in Figure 7-9. Additional photographs from the sealing process are found in Appendix V.

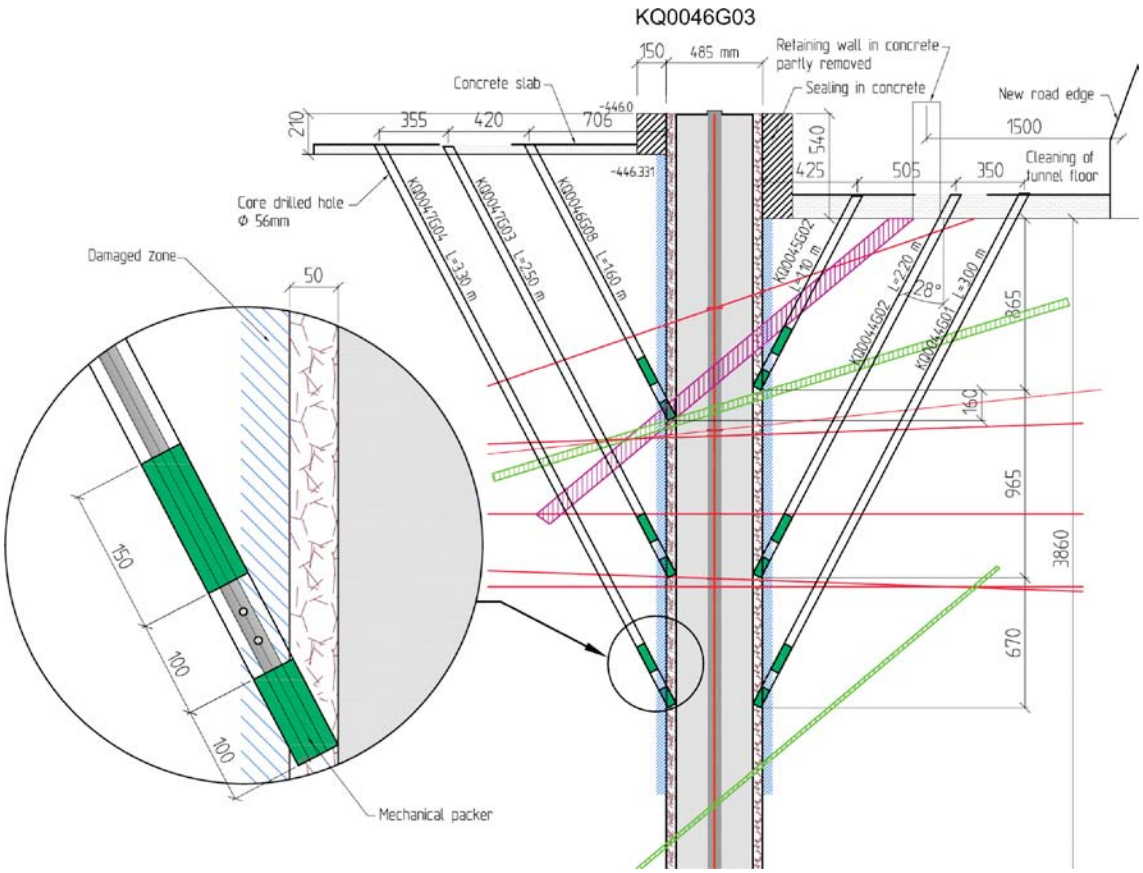

Figure 7-5. *Drawing of the set-up for the water injection tests of the damaged zone in heater hole KQ0046G03. Included in the drawing are also dykes and fractures mapped in the previous core drilled holes. Red structure – Pegmatite, Green structure – Cataclasis Äspödiorite, Unbroken line – broken fracture with specified strike and dip, Dashed line – broken fracture with unspecified strike and dip.*

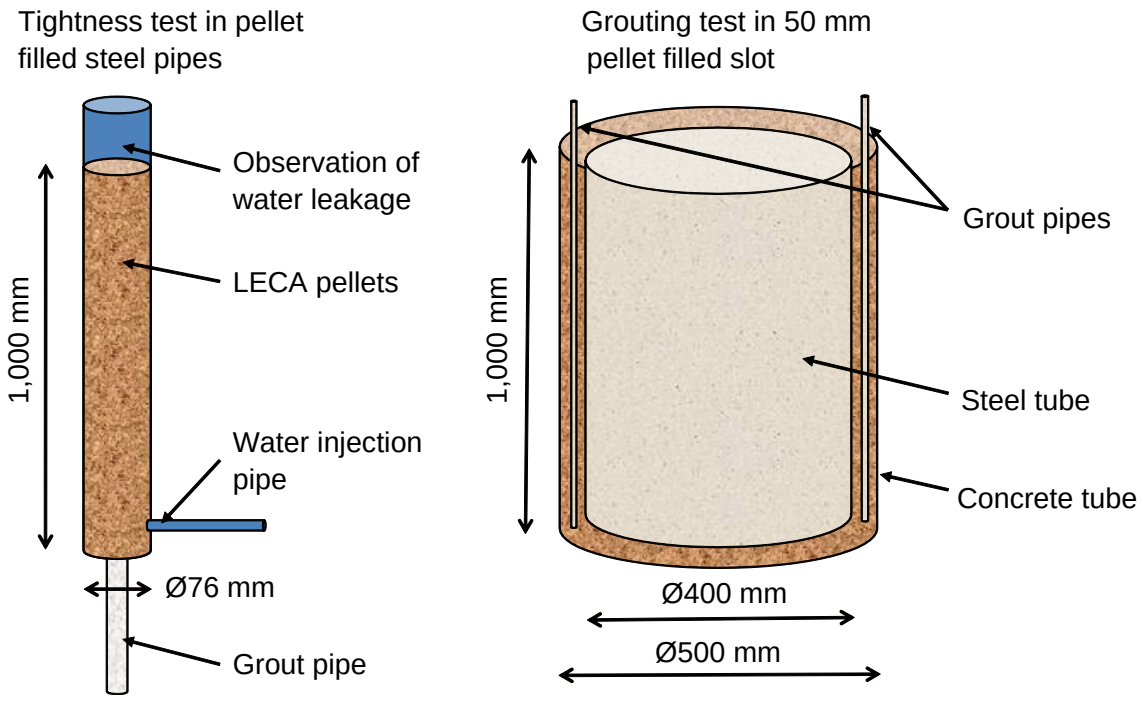

Figure 7-6. *Sketch of the set-up for sealing tests in steel pipes and grouting tests in a 50 mm pellet filled slot.*

Figure 7-7. *Photograph from sealing test in 50 mm pellet filled slot. The voids are completely filled and the contact surface is tight (Photo R Glamheden).*

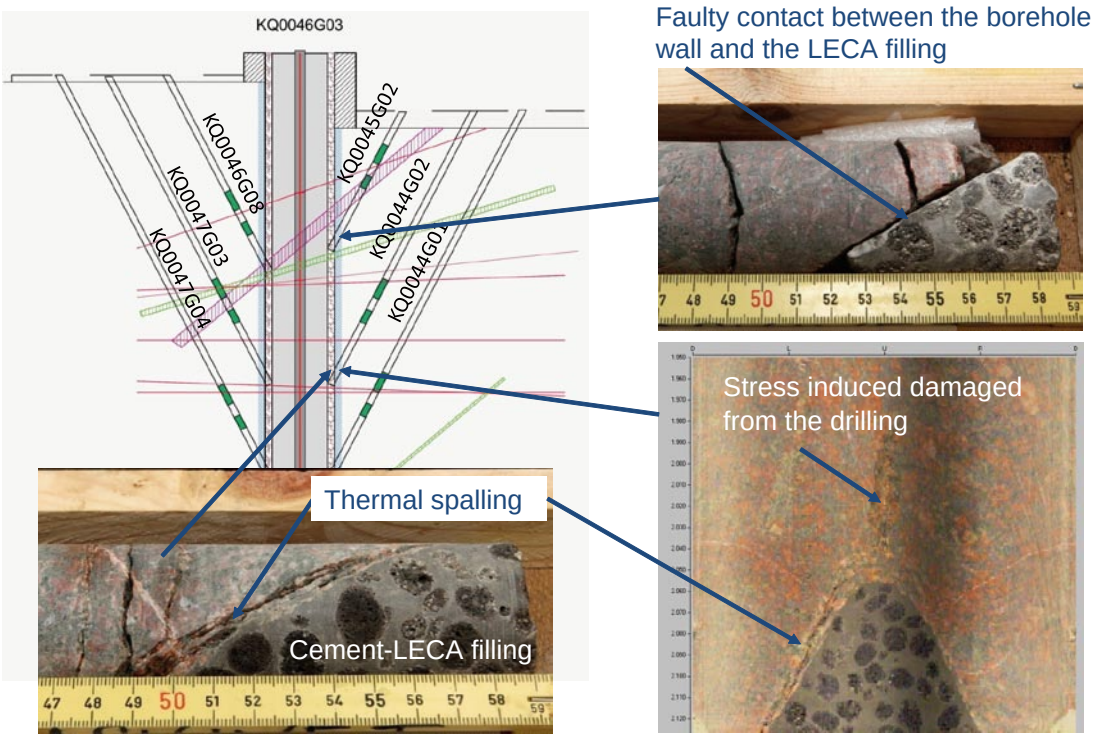

Figure 7-8. *Shows the quality of the contact between the borehole wall and the LECA filling in the boreholes indicated on the drawing. Fractures induced by thermal spalling were observed in the examined position in KQ0044G02 (Photo C-R Lindqvist).*

Figure 7-9. *A top view of the pellet filled slot before the start of grouting (Photo R Glamheden).*

After filling up to about the slot mid-height, the pumping pressure started to increase and two rubber tubes failed. At which time the grout height had reached about 2.8 m above the bottom. The casting process was preceded by lifting the pumping pipes in steps right up to the top. In total, approximately 500 kg cement was used to fill both the borehole pump pit and the pellet-filled slot. The quality of the sealing was examined through drill cores and Bips images of the boreholes and was found to be of excellent quality except for in borehole KQ0045G02, see Figure 7-8. In this borehole the sealed pellet filling showed signs of faulty contact between the borehole wall and the sealing. Fractures induced by thermal spalling were observed in the examined contact position in KQ0044G02. The quality of the contact in the other holes is presented in Appendix Q.

The grout was assumed not to penetrate the damaged zone, since the pellet-filled slot was grouted without any counter-pressure and the particle size distribution of the cement most likely exceeded the aperture of most of the cracks in the spalled damaged zone.

The injection test was carried out by Geosigma AB with assistance from staff of Golder Associates AB. The hydraulic testing was performed with equipment designed by Geosigma, termed WIC (Water Injection Controller), which allows for monitoring of time, pressure and water flow. The resolution in the flow measurements is specified to 2 ml/min. A photograph of the utilized equipment is presented in Figure 7-10.

The injection tests were performed as constant pressure tests with a pressure build-up of approximately 2 bars for 30 minutes. The observation boreholes were sealed off with packers about 0.2 m from the bottom and continuously monitored with pressure transducers. Pressure gauges for manual reading were installed in 12 surrounding boreholes used as instrumentation holes in Field Tests 3 and 4. Additional information on the testing procedure is to be found in Appendix Q. The results are presented in Section 7.4 and an analysis of the confinement effect on the transmissivity is presented in Section 8.2.4.

Figure 7-10. *Shows the equipment utilized for the water injection tests (Photo R Glamheden).*

7.2 Investigation of rock fragments

The rock slabs formed during the spalling process were removed from the heating holes by scaling. Using a scaling rod the borehole wall was cleaned from loose pieces until sound rock was exposed from the top to the bottom of the hole. Most fragments were hoisted up on a wooden plate during the scaling. Fragments that had dropped down to the borehole bottom were brought up with a suction pipe. The fragments collected in this way were at first used to estimate the total volume of the spalled notches along the heating holes. Later on the fragments were also examined in a more extensive way regarding weight, dimensions and failure surfaces. The purpose of this latter study was to investigate the possible difference in geometry and size distribution of the fragments related to variations in counter pressure, moisture content of the rock and other geological conditions. The study is also an indirect way to obtain information of the structure of the damaged zone, i.e. the size distribution of the developed fractures and the frequency of coated fractures.

A photograph of the fragments collected in KQ0054G03 is shown in Figure 7-11 in order to give a general indication of the size and character of typical spalled fragments. Photographs of the fragments collected in the other heating holes, along with further details are presented in Appendix L.

The total amount of all collected fragments in the heating holes, as well as the weight and estimated volume of the largest individual fragments, is presented in Table 7-1. It should be noted that no slabs were collected in KQ0046G03, since the pellet filled slot was grouted in this hole. Furthermore, in KQ0046G04 only one side of the borehole wall was scaled to allow for future independent observation of the conditions that occurred by the removal of the pellets.

The total weight of the rock fragments that dropped down due to thermal spalling in the heating holes amounts approximately 80 kg. The total weight of rock fragments that were collected from the holes heated without the confinement provided by the pellets varies between 4–33 kg (1.4–12.0 litres). The corresponding total weight for the holes heated with the confinement provided by the pellets, varies between 1–19 kg (0.3–7 litres). The amount of fragments that were included in the pellet filling when it was removed from the confined holes was negligible. This indicates that the fragments size before scaling of the holes was mainly above the fraction of the LECA filling 8–14 mm.

Figure 7-11. *Shows the rock fragments collected in KQ0054G03 in Test 1 (Photo C-R Lindqvist).*

Table 7-1. Estimated volume of scaled rock fragments based on the weight of the fragments. Tests 1 and 2 were performed without confinement provided by LECA pellets and Tests 3 and 4 with confinement provided by LECA pellets.

Test/Borehole	Sum of all fragments		Largest fragment	
	Weight (kg)	Volume[1] (litre)	Weight (kg)	Volume[1] (litre)
Test 1				
KQ0054G03 (NW)	13.50	4.91	0.50	0.18
KQ0054G04 (SE)	3.95	1.44	0.55	0.20
Test 2				
KQ0051G04 (NW)	32.85	11.95	0.90	0.33
KQ0051G05 (SE)	4.75	1.73	0.30	0.11
Test 3				
KQ0048G04 (NW)	18.70[2]	6.80	1.55	0.56
KQ0048G05 (SE)	6.45	2.35	0.11	0.04
Test 4				
KQ0046G03[3] (NW)	–	–	–	
KQ0046G04[4] (SE)	0.91	0.33	0.07	0.03

1) The volume is estimated based on the density of intact rock 2.75 g/cm^3, /Andersson 2007/.

2) The weight is reduced with 2.9 kg to correct for fragments spalled during drilling.

3) The borehole walls have not been inspected after the heating period since the slot was grouted.

4) Only one side of the borehole was scaled after the heating period.

The rock slabs range in weight from small fragments of less than one gram up to large discs of more than 1 kg. The weight of the largest fragments collected in the heating holes without the confinement varies between 0.3–0.9 kg and between 0.1–1.5 kg for fragments collected in heating holes with the confinement provided by the pellets. (The largest fragment in the APSE field experiment had a weight of 4.2 kg /Neretnieks and Andersson 2009/.)

In relation to the volume of the heating holes, the total volume of fragments ranges between 0.20–1.55% in the tests without confinement and 0.05–1.05% in the tests with the confinement provided by the pellets. Although not unambiguous, the results indicate that application of LECA pellets generates a pressure on the borehole wall that is capable of reducing the spalling in the heating holes. However, the most obvious fact from the table above is that the amount of fragments collected in the SE-holes is consistently much smaller than the amount collected in the NW-holes, as was also remarked in the previous Section 6.3.

The reason for the large difference in the amount of fragments is most likely due to the shear zone striking parallel with the tunnel axis, see Section 8.2.2. The large amount of fragments in KQ0048G04 in Test 3 is probably due to a section with a high frequency of open or partly open fractures in the upper part of the hole, see Appendix A.

The fragments that were examined in more detail were limited to those with a length larger than 50 mm. The distribution of the length of the investigated fragments is presented per borehole in Figure 7-12. The length varies from 50–290 mm with the majority between 50–100 mm in length. Thus, the results indicate that the damage zone is composed of large quantity of short fractures.

The length distribution of the fragments in KQ0051G04 diverges somewhat from the distribution of the fragments seen in the other holes, but generally the length distributions of the fragments in the different holes are quite similar.

The maximum width of the collected fragments was 180 mm. The distribution of width/length ratio indicates that most fragments have a width that corresponds to half the length, see Figure 7-13. It should be noted that this distribution might be disturbed by the handling of the fragments, breaking the fragments into smaller pieces. However, the results are similar to the observations in the APSE field experiment /Neretnieks and Andersson 2009/.

In Figure 7-14 the ratio between thickness and length is presented. The thickness of the fragments is typically 0.1 of the length, which again is close to the observations in the APSE field experiment /Neretnieks and Andersson 2009/. The graphs show a larger amount of thinner fragments in the holes of Field Test 1 and 2 compared to the fragments collected in Field Test 3, which seems to indicate that the confinement resulted in slightly thicker fragments. The thickest fragment was 78 mm thick and was collected in heating hole KQ0048G04. The thinnest fragments were collected in the heating holes of Field Test 2.

The minerals found on the failure surfaces and in sealed fractures in the fragments were mainly calcite, chlorite, epidote and small amounts of quartz, k-feldspars (adularia), biotite and iron oxide coatings. The occurrence of the mineral prehnite was not investigated, since it was judged to be difficult to reliably identify by visual inspection.

The thickness of the mineral coating in general ranged from very thin coatings of 0.2–0.4 mm, which covered only a part of the surface, up to a thickness of 3–4 mm. The frequency of fragment failure surfaces that contain the various mineral coatings of the investigated fragments is presented in Figure 7-15. The frequency ranges from 8 to 16% between the fragments collected in the different heating holes. The amount of coated failure surfaces is largest in KQ0051G04 and KQ0048G04, which are also the holes that had the largest volume of fragments, see Table 7-1.

The proportions of different types of minerals on the failure surfaces of the investigated fragments are presented in Figure 7-16. The diagram may be used to evaluate possible correlation between fracture filling and the amount of collected fragments in the separate heating holes. The investigation indicates larger proportions of calcite on fragments collected in the holes located on the NW-side in the tunnel compared to those collected in the holes on the SE-side. The dominating mineral coating on the fragments collected in the holes on the SE-side of the tunnel, was chlorite in KQ0051G05 and KQ0054G04 and epidote in KQ0048G05. This distribution may possibly reflect the borehole length penetrating the shear zone that strikes parallel to the tunnel axis, see Figure 2-2. The divergence in dominating mineral coating between KQ0051G05 and KQ0054G04 compared to KQ0048G05 might give an explanation to the larger amount of breakouts encountered in KQ0048G05 in spite of applied confinement pressure.

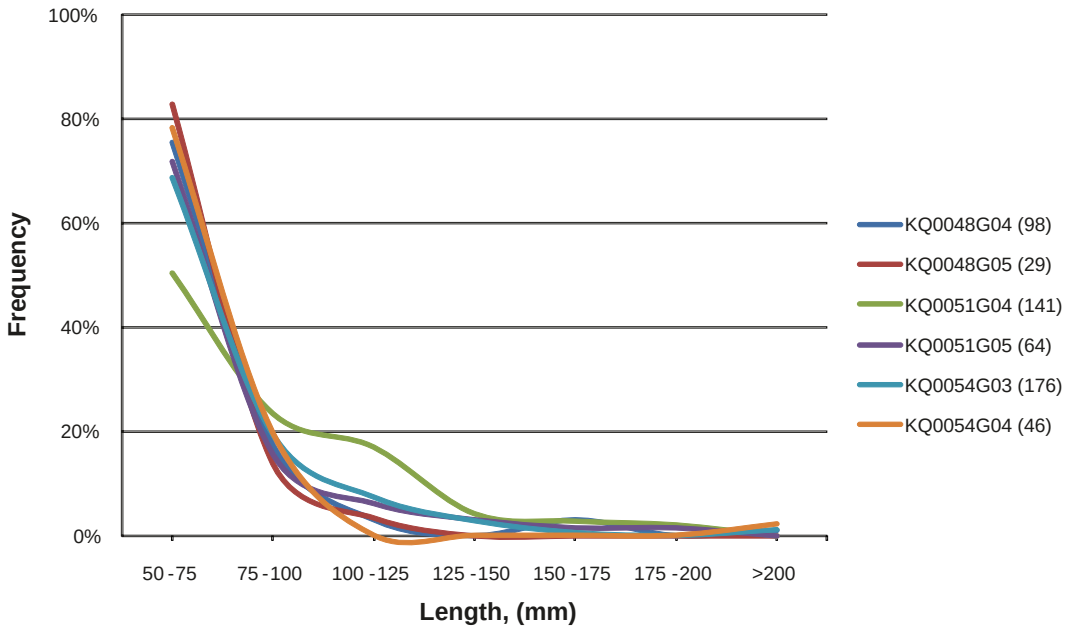

Figure 7-12. *Length distribution of investigated fragments. The minimum length was limited to 50 mm. The number of fragments included in the investigation is indicated in the legend.*

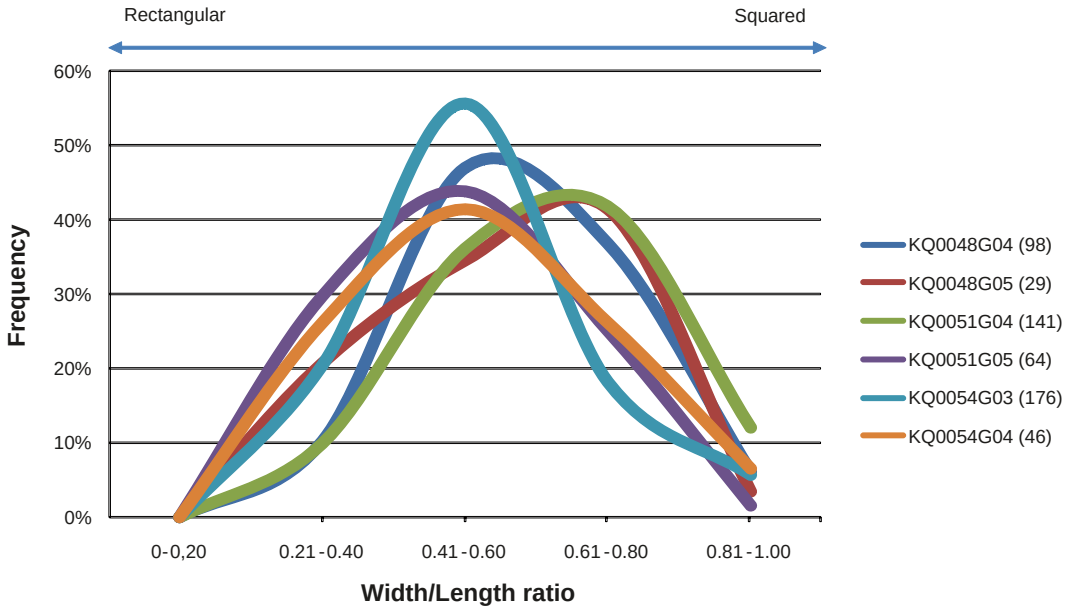

Figure 7-13. *Width to length ratios of the investigated fragments. The number of fragments included in the investigation is indicated in the legend.*

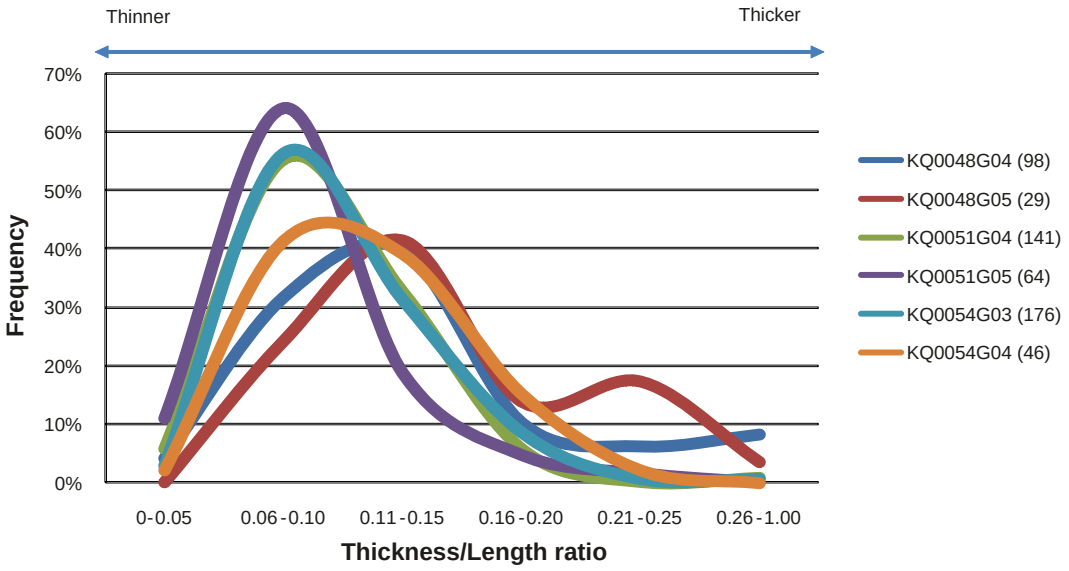

Figure 7-14. *Thickness to length ratios of the investigated fragments. The number of fragments included in the investigation is indicated in the legend.*

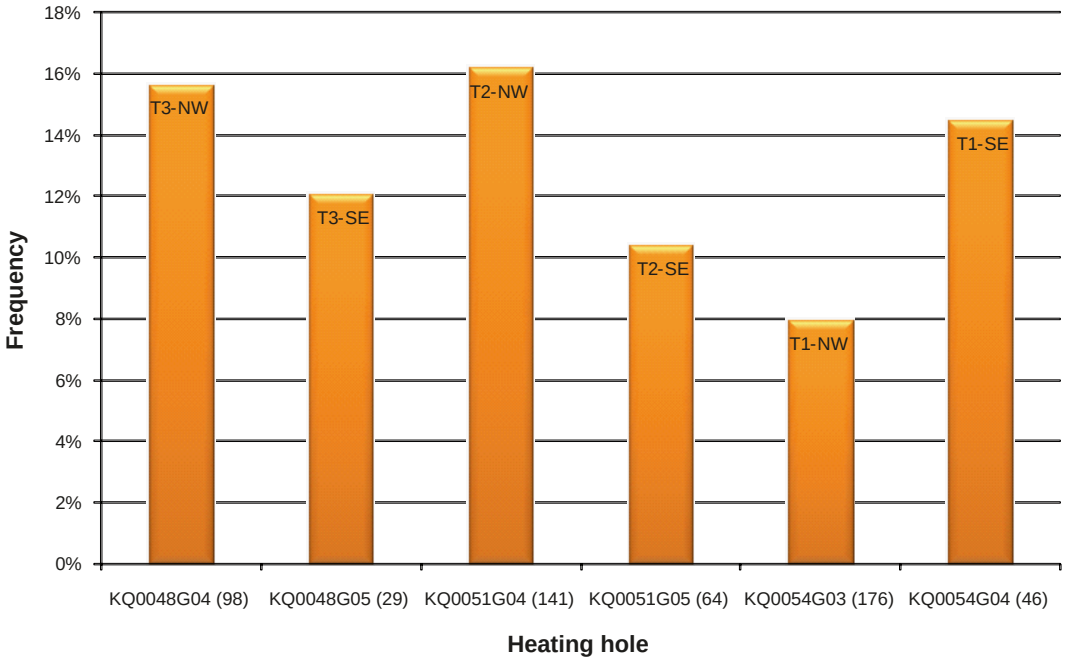

Figure 7-15. *Frequency of fragment failure surfaces that contain any mineral coating calculated on the basis that each fragment has six surfaces.*

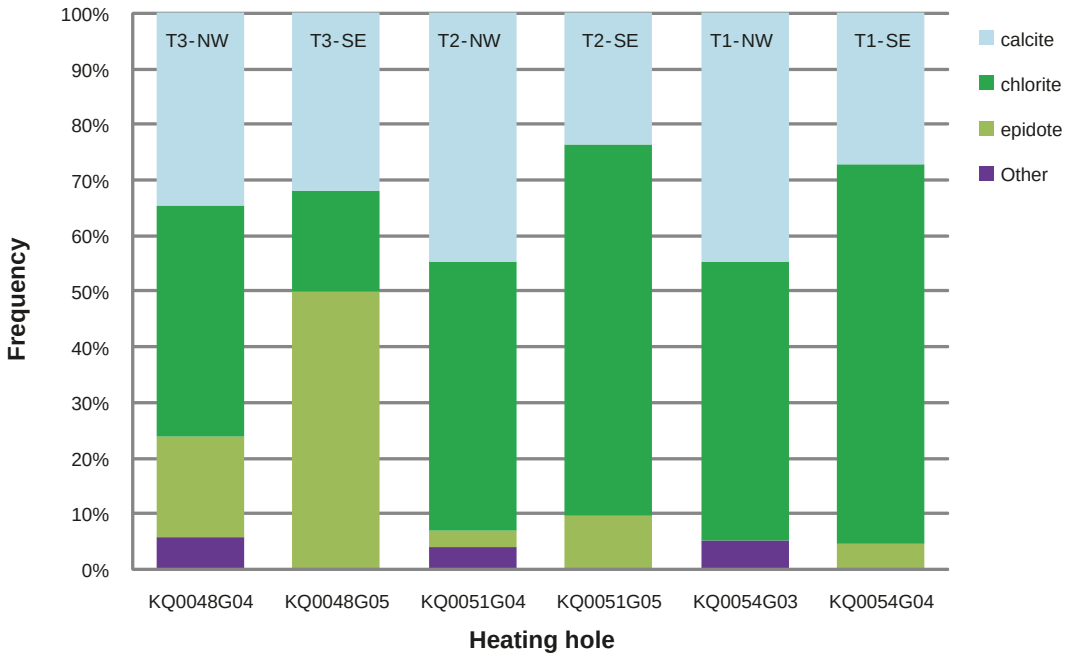

Figure 7-16. *Proportions of different type of minerals on the failure surfaces of the investigated fragments.*

7.3 Geometry of the spalled notch

The geometry of the notch created by the spalling has been characterized with a number of monitoring methods: laser scanning, ultrasonic measurements, photographing with a thin lighted slot, video recording and ordinary photographs. The procedures of the measurements are presented in Section 7.1. The measurements were finished by mid-September 2009.

The determination of the notch geometry has been carried out after removal of the rock slabs that formed during the spalling process. Using a scaling rod the borehole walls were cleaned from loose pieces until sound rock was reached from the top to the bottom of the holes.

In Figure 7-17 the geometry of the notches created in heating hole KQ0051G04 is illustrated by two photographs, one of the NE-side and another of the SW-side of the borehole wall. The notches in this heating hole were the most developed with the largest dimensions of all notches created in the heating holes. A projection of the current notches from the borehole based on the laser scanning is presented in Figure 7-18. A cross-section based on the photographing with a thin lighted slot is shown in Figure 7-19. Projections for all the heating holes based on the laser scanning are shown in Figure 7-20 and Figure 7-21. Cross-sections showing the maximum dimension of the notches developed in all the heating holes are presented in Figure 7-22 and Figure 7-23. Additional drawings and photographs of the notches created in all heating holes are to be found in Appendix M, O and T.

The maximum dimensions of the developed notches in all heating holes are presented in Table 7-2. A compilation of the breakout angle, opening angle and trend of the developed notches, as defined in Figure 7-19 is shown in Table 7-3. The determined volume of the notches in 0.5 m interval along the holes is presented in Table 7-4.

The uppermost observation of breakouts in the heating holes was encountered in the interval 0.4–0.8 m below the concrete upper edge and the lowest observation in the interval 3.1–4.1 m below the same reference level. The observations are in close agreement with the expected interval of the damaged zone based on the results from the numerical modelling, which corresponds to a depth interval of approximately 1.2–4.2 m below the used reference level, see Figure 8-8.

The length of the breakouts varies from less than 0.1 m up to approximately 2.6 m. It is mainly in the upper part of the heating holes that the breakouts form a continuous notch. The breakouts in the lower part of the heating holes consist of separate sectors of a length that normally is less than 0.1–0.2 m, see Appendix M. The notch was least developed in KQ0046G04 in Test 4, performed with confinement provided by LECA pellets.

The compilation in Table 7-2 gives the width and depth of the notches that reach approximately 270 mm and 70 mm, respectively. When normalised to the initial hole radius, the depth of the notches reaches up to about 0.3 of the hole radius. The maximum width and depth of the notches are approximately half the size of the dimensions observed in APSE project (width ≤500 mm, depth ≤135 mm) /Andersson 2007/.

The determined breakout angle ranged from approximately 5 degrees for the tiny breakouts to up to 60 degrees for the fully developed ones, with a mean around 30 degrees for all observations. The corresponding values of the opening angles were 90 degrees for deep asymmetric breakouts and up to 160 degrees for shallow symmetric ones, with a mean of around 130 degrees for all observations, see Table 7-3. The opening angle is comparable with the observation in APSE, while the breakout angle is approximately half the mean value /Andersson 2007/.

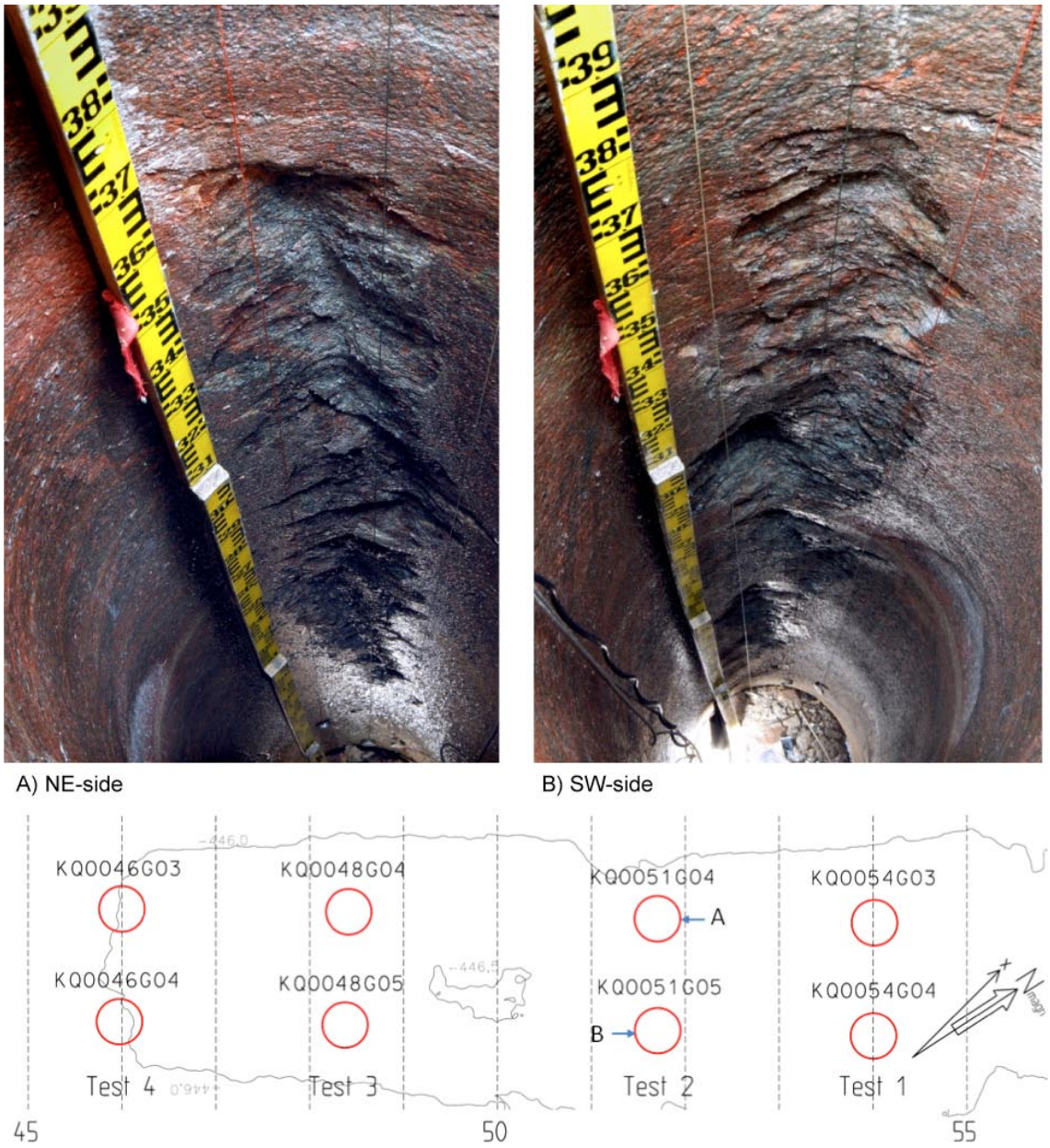

Figure 7-17. *Photographs of the borehole wall in heating hole KQ0051G04 after scaling the wall from loose rock fragments (Photo C-R Lindqvist).*

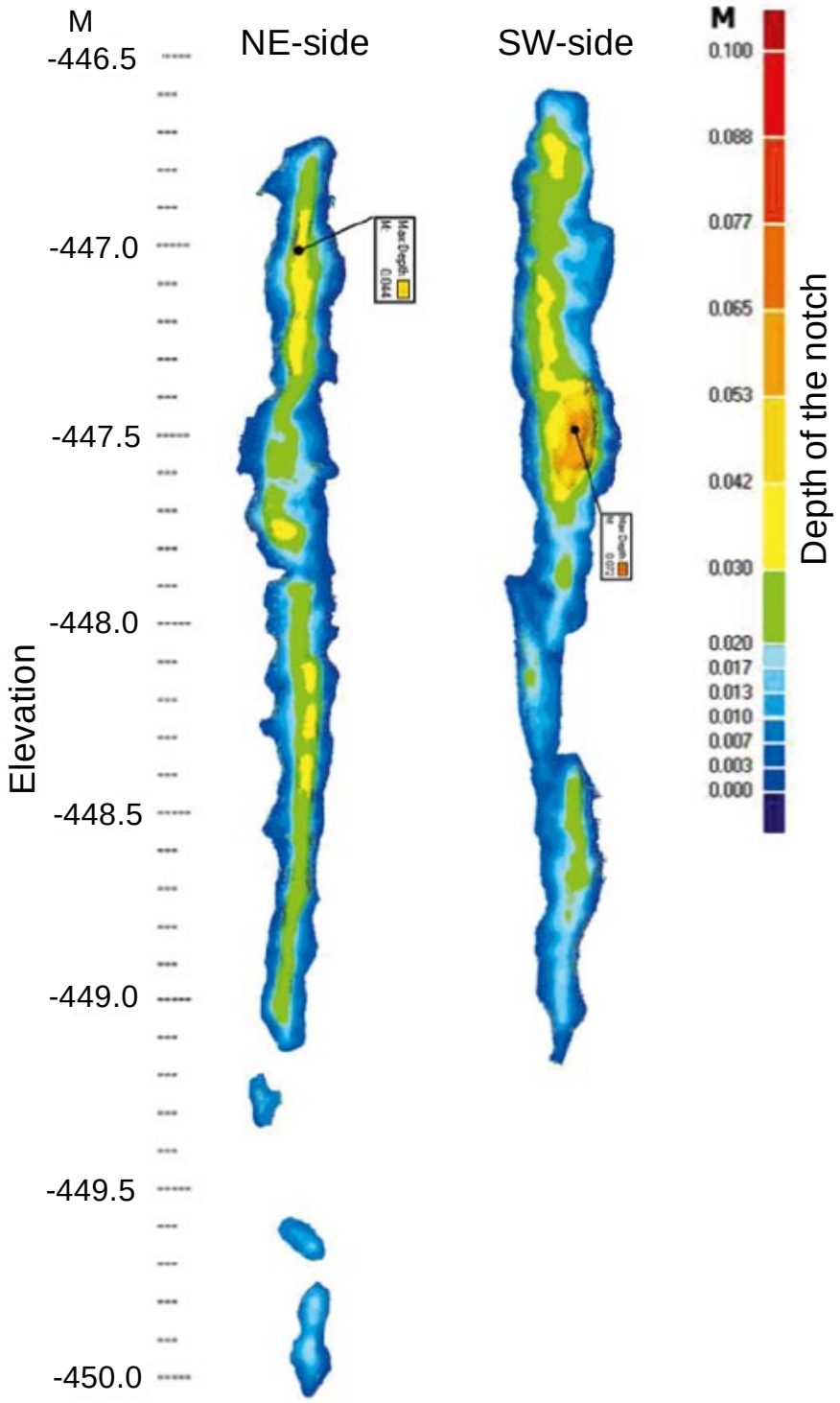

Figure 7-18. *Projection from the outside of the notches developed in KQ0051G04 based on laser scanning. The notches developed in this heating hole had the largest dimensions of all notches created in the heating holes. The notch depth is indicated by the colour.*

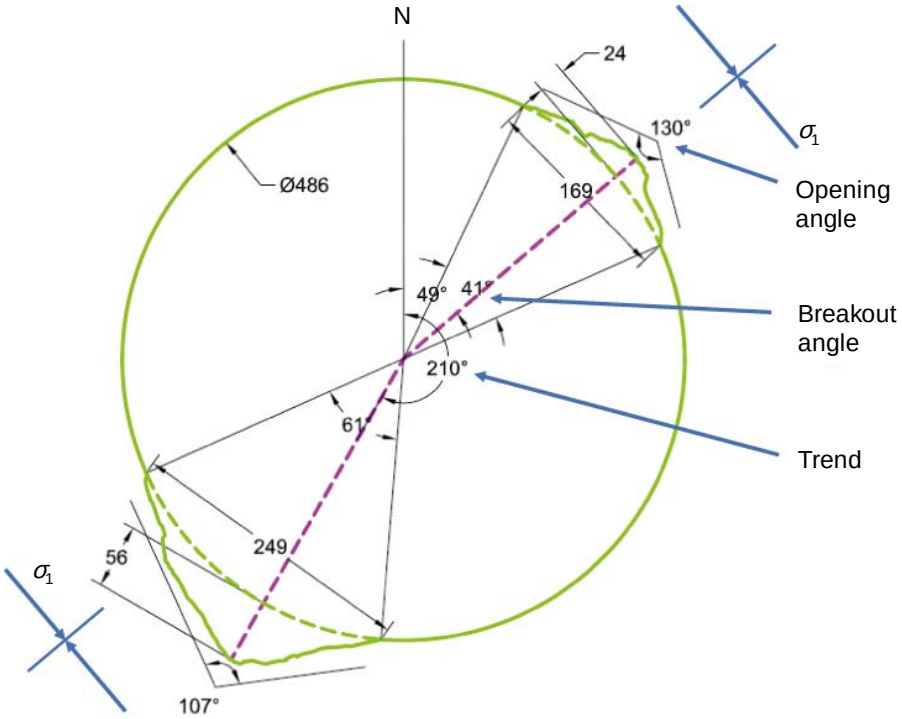

Figure 7-19. *Cross-section on level –447.5 m where the largest dimension of the SW-notch was determined in KQ0051G04 based on the photographing with a thin lighted slot. The figure also defines the evaluated breakout angle, opening angle and trend of the notches compiled in Table 7-4, as well as the trend of the major principal stress.*

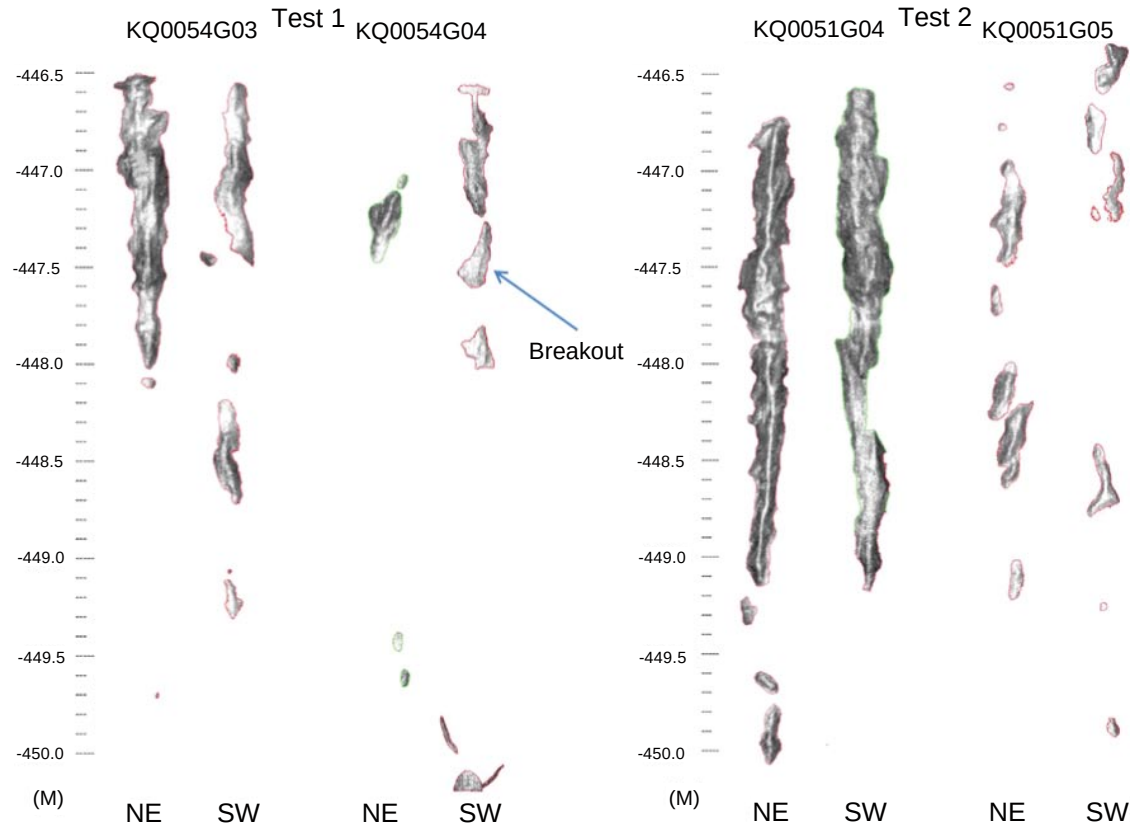

Figure 7-20. *Sections of observed breakouts in Tests 1 and 2 performed without confinement by LECA pellets. The projections of the breakouts are from the outside.*

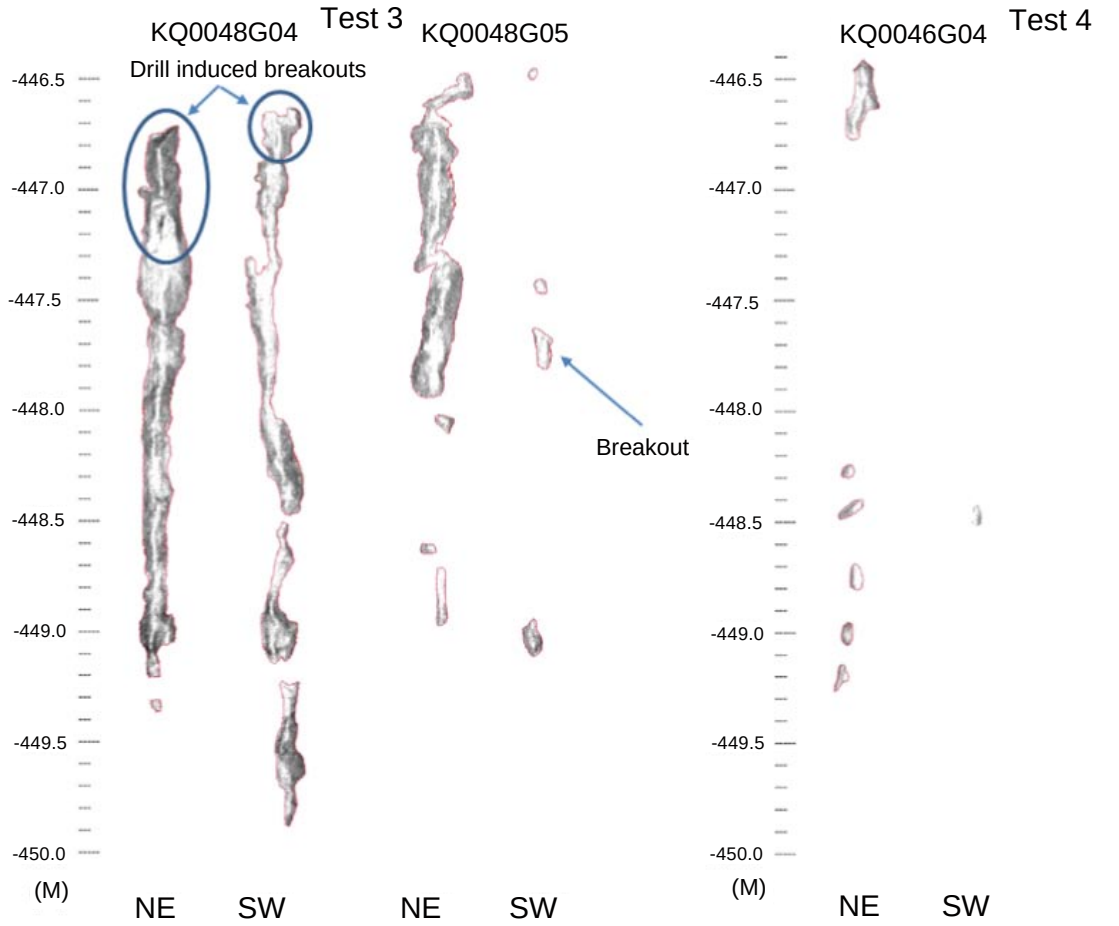

Figure 7-21. *Sections of observed breakouts in Tests 3 and 4 performed with confinement by LECA pellets. The projections of the breakouts are from the outside.*

The trend of the damaged zone, which was evaluated separately for each side of the borehole wall, varies between N20–53E degrees (mean N38E deg) and N193–263E degrees (mean N212E deg), respectively. The results should be compared with a direction normal to the trend of major principal stress, which according to the evaluations in APSE corresponds to N40E or N220E degrees /Andersson 2007/, see Figure 7-19. The observed position of the damaged zone consequently agrees relatively well with the theoretical position in the holes. The observed variations seem to be caused mainly by the foliation and by the shear zone and minor dykes that intersect the heating holes, see Appendix S.

The compilation of the notch volumes in Table 7-3 clearly shows that the breakouts in most cases were largest in the holes located on the NW-side of the tunnel axis. Moreover, the breakouts in general were larger on the NE-side of the borehole wall and the main part of the breakouts occurred in an interval between 0.5 to 2.5 m depth in the boreholes (Sector 2-5 in Table 7-4). However, the largest notch volume, which amounted to approximately 7 litres, occurred on the SW-side in KQ0051G04.

When comparing the geometry of the notches that formed in Tests 1 and 2, without confinement, and Tests 3 and 4, with the confinement provided by LECA pellets, there is no clear reduction of the notch dimensions in Test 3 but definitely in Test 4. Factors that might have caused the observed difference in the results between Test 3 and Test 4 are described in Section 8.2.2.

The difference in the total breakout volume determined by laser scanning and the volume estimated from scaled fragments is within ±10–15%. The discrepancy most likely corresponds to the accuracy in determined volume. When verifying the indicated breakouts by the laser scanning by comparison with the ones that are visible on the video records, it is apparent that the laser scanning was not able to pick-up all the shallow and tiny breakouts in the lower part of the holes.

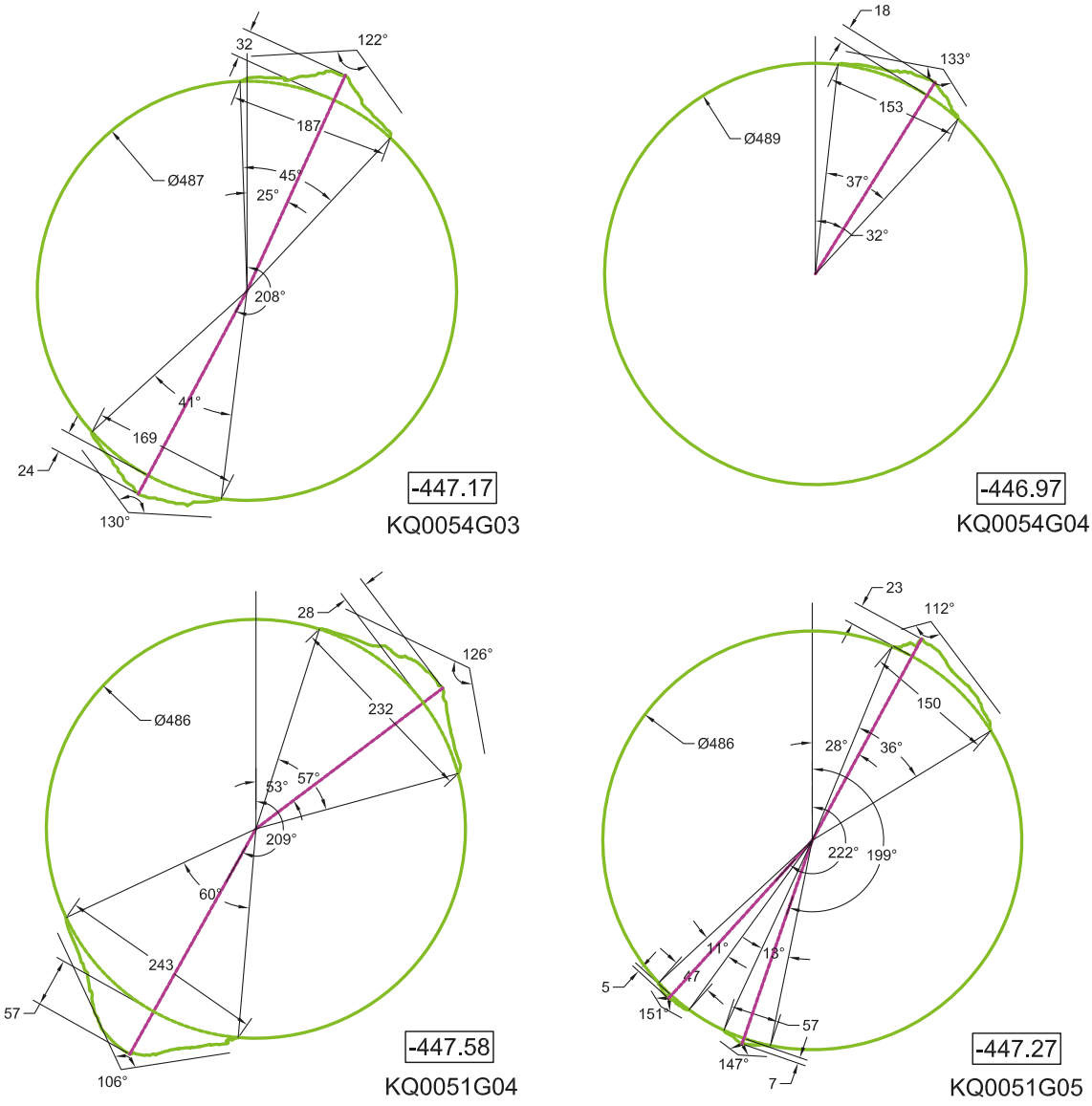

Figure 7-22. *Cross-sections where the largest dimension of the notch was determined in heating holes in Tests 1 and 2 performed without confinement. The drawings are based on the photographing with a thin lighted slot.*

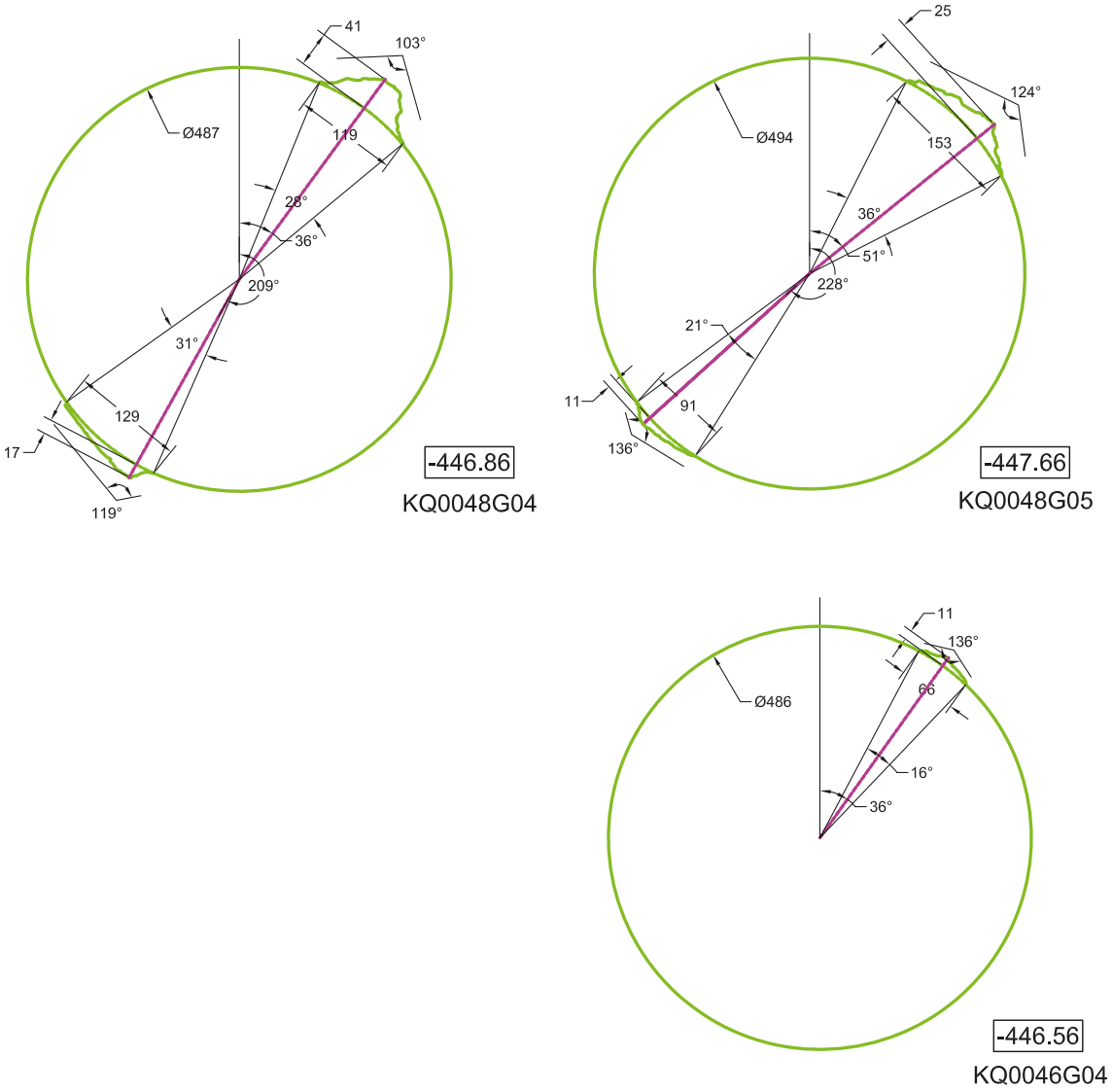

Figure 7-23. *Cross-sections where the largest dimension of the notch was determined in heating holes in Tests 3 and 4 performed with confinement. The drawings are based on the photographing with a thin lighted slot.*

Table 7-2. Max dimensions of the notches developed in the heating holes based on the results from laser scanning, photographs with thin lighted slot and video recording.

Test/Borehole	Observations on NE-side				Observation on SW-side			
	I[1] (m)	L[2] (m)	W[3] (mm)	D[4] (mm)	I (m)	L (m)	W (mm)	D (mm)
Test 1								
KQ0054G03	0.5–3.8	1.5	262	37	0.6–3.3	0.9	179	23
KQ0054G04	0.9–3.9	0.4	164	26	0.5–4.1	0.7	163	19
Test 2								
KQ0051G04	0.7–4.1	2.4	268	44	0.7–4.0	2.6	270	72
KQ0051G05	0.4–3.3	0.6	164	27	0.4–4.0	0.4	146	31
Test 3								
KQ0048G04	0.8–3.8	2.5	244	52	0.6–3.9	1.9	181	32
KQ0048G05	0.6–3.1	1.5	206	31	0.5–3.2	0.2	82	14
Test 4[5]								
KQ0046G04[6]	0.4–3.5	0.4	113	17	2.4–2.5	0.1	42	8

1) Interval between the upper and lowest breakout with the concrete upper edge as reference, level –446.0 m. The evaluation is based primarily on the video recording.

2) Maximum continuous length of the notch.

3) Maximum width of the notch.

4) Maximum depth of the notch.

5) Inspection of the damage zone in KQ0046G03 has not been carried since it was grouted with cement.

6) Only the NE-side of borehole KQ0046G04 was scaled of loose pieces.

Table 7-3. Breakout and opening angle along with evaluated trend of the deepest part of the notch based on results from photographs with thin lighted slot. The evaluated angles are defined in Figure 7-19.

Test/Borehole	Observations on NE-side			Observation on SW-side		
	Breakout[1] Mean *Min–Max* (deg)	Opening[2] Mean *Min–Max* (deg)	Trend[3] Mean *Min–Max* (deg)	Breakout Mean *Min–Max* (deg)	Opening Mean *Min–Max* (deg)	Trend Mean *Min–Max* (deg)
Test 1						
KQ0054G03	40 *25–59*	127 *116–142*	37 *22–49*	31 *21–41*	136 *127–147*	210 *187–263*
KQ0054G04	30 *18–41*	136 *128–145*	31 *21–43*	22 *17–27*	137 *129–149*	212 *203–230*
Test 2						
KQ0051G04	42 *22–57*	121 *111–130*	43 *34–53*	46 *31–61*	123 *106–139*	220 *205–235*
KQ0051G05	22 *9–36*	135 *112–148*	37 *23–52*	19 *5–28*	137 *94–151*	212 *199–228*
Test 3						
KQ0048G04	29 *17–44*	123 *90–145*	32 *20–46*	26 *10–40*	137 *119–160*	211 *193–229*
KQ0048G05	36 *28–50*	130 *124–137*	43 *38–52*	19 *17–20*	133 *126–139*	223 *220–226*
Test 4[4]						
KQ0046G04[5]	16 *13–20*	139 *125–147*	40 *35–46*	*4*	*145*	*195*

1) Variation in breakout angle.

2) Variation in opening angle.

3) Variation in trend of the deepest part of the notch.

4) Inspection of the damage zone in KQ0046G03 has not been carried since grouted with cement.

5) Only the NE-side of borehole KQ0046G04 was scaled of loose pieces.

Table 7-4. Notch volume on each side of the borehole wall determined in 0.5 m intervals based on results from laser scanning.

Section	Test 1 KQ0054 G03 (litre)		G04 (litre)		Test 2 KQ0051 G04 (litre)		G05 (litre)		Test 3 KQ0048 G04 (litre)		G05 (litre)		Test 4 KQ0046 G04 (litre)	
	NE	SW	NE	SW	NE	SW	NE	SW	NE	SW	NE	SW	NE	SW
1	–	–	–	0.01	–	–	–	0.18	–	–	–	**0.08**	0.05	–
2	**1.51**	0.46	0.05	**0.36**	0.50	1.35	0.05	**0.22**	0.80	**0.35**	0.55	0.00	**0.20**	–
3	1.49	**0.61**	**0.07**	0.17	**1.37**	**2.48**	**0.51**	0.04	**1.89**	0.18	0.88	0.01	–	–
4	0.63	0.01	–	0.10	1.29	1.81	0.06	–	0.70	0.21	**1.04**	0.03	–	–
5	0.02	0.18	–	–	1.18	0.64	0.32	0.01	0.43	0.58	0.03	–	0.04	**0.02**
6	–	0.14	–	–	0.75	0.81	0.07	0.13	0.40	0.20	0.13	0.01	0.04	–
7	–	0.04	0.04	–	0.24	0.10	0.05	–	0.10	0.33	–	0.05	0.03	–
8	–	–	–	0.07	0.28	–	–	0.01	–	0.19	–	–	–	–
9	–	–	–	–	0.02	–	–	–	–	–	–	–	–	–
Sum	**3.64**	**1.43**	**0.56**	**0.70**	**5.63**	**7.19**	**1.06**	**0.58**	**4.31**	**2.04**	**2.63**	**0.11**	**0.36**	**0.02**
Total	**5.07**		**1.26**		**12.82**		**1.64**		**6.35**		**2.74**		**0.38**	

Note: The empty boxes in the table correspond to section without any breakouts.

7.4 Hydraulic transmissivity of the damaged zone

The results from the third test, being the first test with confinement provided by the LECA pellets, indicated that confinement provided by the pellets cannot prevent the borehole wall from cracking, whereas the LECA pellets has the capability to keep rock slabs with larger dimension than the pellet fraction in place on the borehole wall. The results generated a focus on the hydraulic transmissivity of the spalled damaged zone in the final field test and this parameter was examined by water injection tests in boreholes intersecting heating hole KQ0046G03. The procedure in these tests is described in Section 7.1.7, while the results are summarized here. Additional details from the test are to be found in Appendix Q.

The results from the water injection tests are presented in Figure 7-24. The stationary transmissivity evaluated for the borehole sections indicated in the figure are marked on the water injection holes. In all measurements presented in the figure the water was injected below the double packer.

Accept for one hole, KQ0045G02, the evaluated hydraulic transmissivity corresponds to the measurement limit of the equipment used (2 ml/min). The lower transmissivity for the test sections in hole KQ0044G02 and KQ0047G03 is determined from measurements with a doubled injection pressure.

In KQ0045G02 where a detectible flow occurred, six additional injection tests with the packer in different positions were performed. The evaluated transmissivity in the subsequent tests were all below the value of the initial test and ranged from $3 \cdot 10^{-7}$ to $3 \cdot 10^{-9}$ m^2/s in the five measurements with detectible flow. The drop in flow after the initial test may be an indication that the water injection caused some kind of movement in the flow path connected to KQ0045G02. Another condition that should be noted regarding the tests in KQ0045G02, is that during the injection tests below the double packer, water was flowing out of heating hole KQ0046G03. This suggests that the higher transmissivity determined in this injection hole might be a result of faulty sealing in the pellet filled slot intersected by this part of the heating hole.

No interference was detected between the water injection holes penetrating heating hole KQ0046G03. This indicates that the thermal spalling has not induced a continuous hydraulic zone along the heating hole. The results also demonstrate that the injection holes were not connected by a single water bearing fracture.

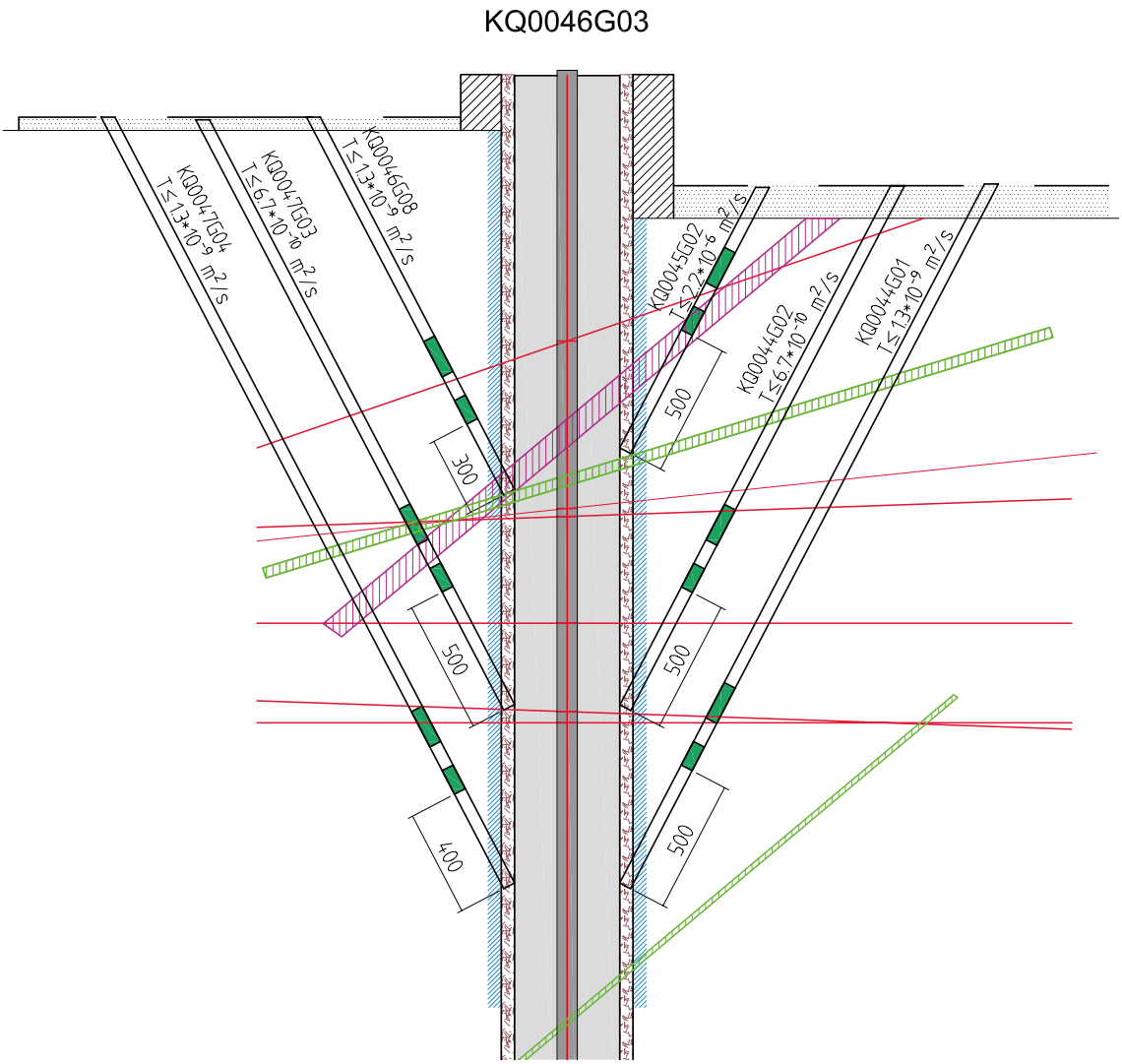

Figure 7-24. *Stationary transmissivity evaluated for the borehole sections indicated on the drawing.*

8 Analysis of the test results

8.1 Comparison of recorded and back-calculated values

In this section the applied heating power and resulting temperature distribution in the field experiment are compared with back-calculated values based on numerical simulations performed by Clay Technology AB. Moreover, estimated tangential stresses on the wall of the heater holes based on numerical simulation are presented. In the simulations the rock mass was assumed to be an elastic isotropic medium with linear heat conduction. The account here summarises the results presented in Appendix R, where further details of the numerical modelling are included.

8.1.1 Evaluation of heat losses

The heating power applied in the field experiment was in general larger than the value obtained in the numerical calculations by fitting the recorded temperatures, see Figure 8-1 and Figure 8-2. The main reasons for discrepancy between the applied and back-calculated heating power are additional sources of heat loss not included in the calculations. The cooling of the monitoring cameras is for instance one extra source of heat loss during the first field test. The application of an artificial wetting system is another factor that caused additional heat loss during the second and fourth field tests. The necessity to increase the heating power a couple of times to follow the desired temperature development in the rock gave a stepwise increase to the heating power in Tests 1 and 2. However, in the last test the heating power was applied in a stepwise manner to reduce the temperature gradient in the surrounding rock.

The results from the numerical simulation indicate that the heating power that enters the rock mass is about 20–40% lower than the applied power in the field tests. The calculated and recorded heating power show best agreement in the third field test, see Figure 8-2. The third field test was carried out without the wetting system, which limited the heat losses.

8.1.2 Temperature distribution

The temperature development of the numerical models was calibrated primarily towards the temperatures recorded in the outer heating holes at some depth below the tunnel floor. What are relevant to compare with the modelling results are thus mainly the recorded temperatures in other parts of the rock volume. The applied rock mass thermal conductivity and thermal diffusivity in the model was larger than the values determined on laboratory samples, see Section 2.2.4 (λ_{model} = 3.2 W/mK, κ_{model} = 1.5·10^{-6} m^2/s).

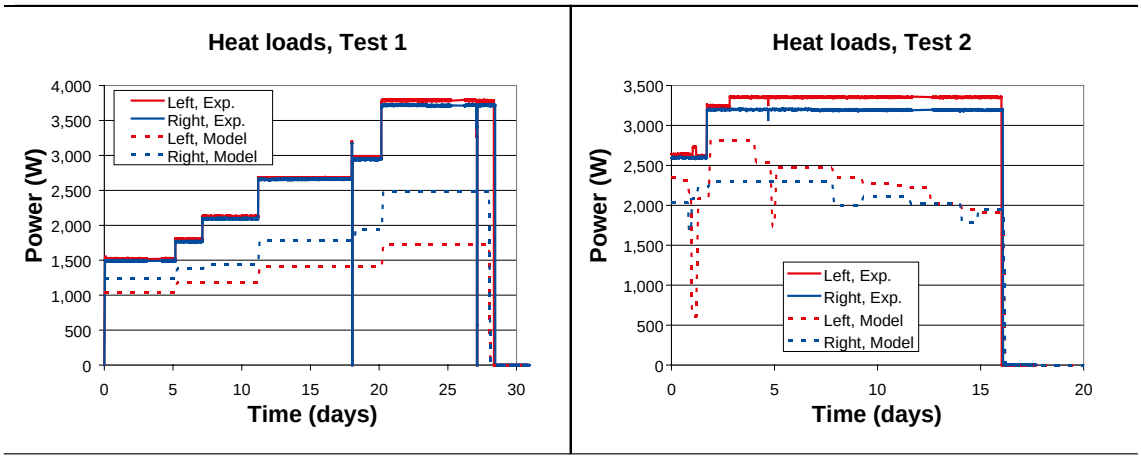

Figure 8-1. *The diagrams show the temporal development of heat loads applied in the models plotted together with the heat loads in the corresponding Field Tests 1 and 2.*

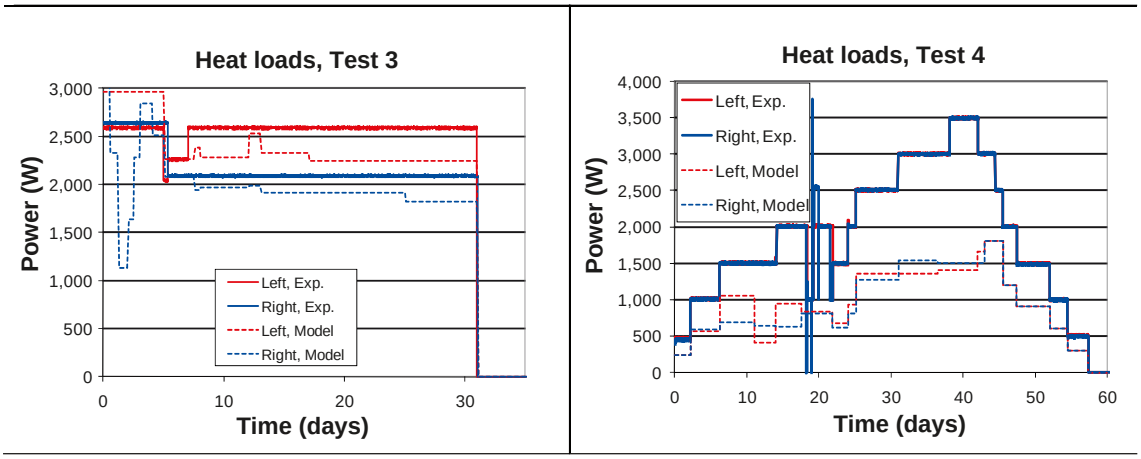

Figure 8-2. *The diagrams show the temporal development of heat loads applied in the models plotted together with the heat loads in the corresponding Field Tests 3 and 4.*

The calculated and recorded temperature distribution of the field tests demonstrates reasonable agreement in Tests 1 and 2, while a more modest agreement was achieved in Tests 3 and 4, see Appendix R. What proved to be difficult to achieve was the fitting between calculated and recorded temperatures on the wall of the heating holes, especially in Tests 3 and 4, see Figure 8-3 to Figure 8-6.

A possible reason for the discrepancy in Field Tests 1 and 2 is that recorded temperature on the borehole wall to a certain extent represents a mean value of the wall temperature and the air temperature in the hole. The monitored temperature may also vary somewhat depending on the thermal contact between the gauge and the borehole wall. In Field Tests 3 and 4 it is possible that the pellet filling is one of the factors causing a major discrepancy between the calculated and recorded results. Contact losses between the gauges and the pellets might have resulted in the recorded temperature being close to the temperature of the filling instead of the temperature on the borehole wall. The assumed and real moisture content (thermal conductivity) of the pellet filling during the field test is another factor that might have caused divergence between the calculated and recorded results, see Section 5.2.

In addition to the discrepancy in temperature of the heating holes, at several locations the fit between calculated and recorded temperature for gauges close to the tunnel floor was poor. In this case the divergence may be a result of differences in assumed and real conditions of the thermal insulation on the tunnel bottom. Convection in partly water filled instrumentation holes is another possible factor for the observed discrepancy.

8.1.3 Thermal stress evolution

The calculated tangential stresses versus recorded temperature on the borehole wall in the heating holes are presented for the different field tests in Figure 8-7. The applied thermo-mechanical properties of the rock mass were: E_m = 55 GPa, ν_m = 0.25 and $\alpha = 7 \cdot 10^{-6}$/K. The properties of other materials included in the model are presented in Appendix R. It should be noted that the recorded temperature and the calculated stresses are at different positions on the borehole wall, as indicated by the figure bottom inset.

The simulation indicates that the major principal stress on the borehole wall exceeds the determined spalling threshold of 120 MPa at a wall temperature of 20°C at 1.5 m depth and at a wall temperature of 80°C at 3.5 m depth. Additional results presented in Figure 8-8 indicate that spalling is to be expected in a depth interval between 1.2 m and 4.2 m below the concrete upper edge in the various field tests. As already pointed in Section 6, the simulated results correspond well with the actual observations of breakouts, see Figure 8-8.

The maximum tangential stress in the model (190–200 MPa) occurs just below the tunnel floor. However, the presence of an excavated damage zone, as accounted for in Section 2.4, most likely reduces the stresses close to the tunnel floor /Olsson et al. 2004, Staub et al. 2004/. The maximum tangential stress and the corresponding max dimension of the breakout in the heating holes are consequently expected to be located slightly lower down in the holes. The observations in the heating holes indicate a maximum of the breakout dimensions in the interval 0.75–1.5 m depth below the concrete upper edge, see Figure 8-8.

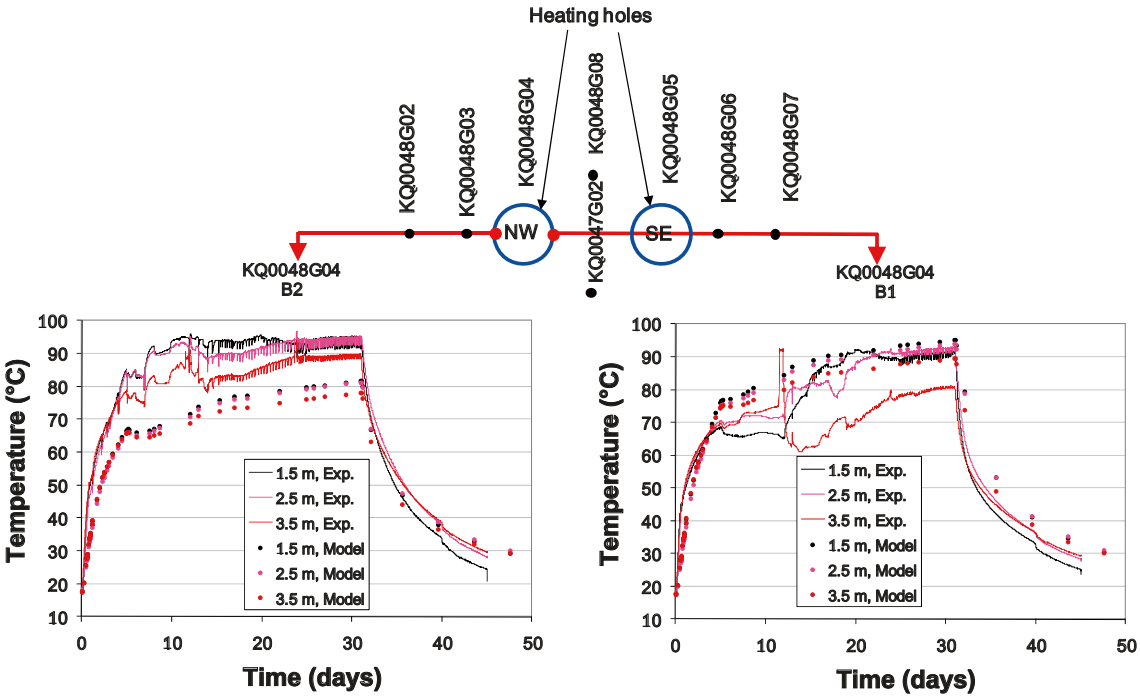

Figure 8-3. *Comparison between temperatures recorded at the borehole wall in KQ0048G04 during Test 3 and corresponding calculated temperatures.*

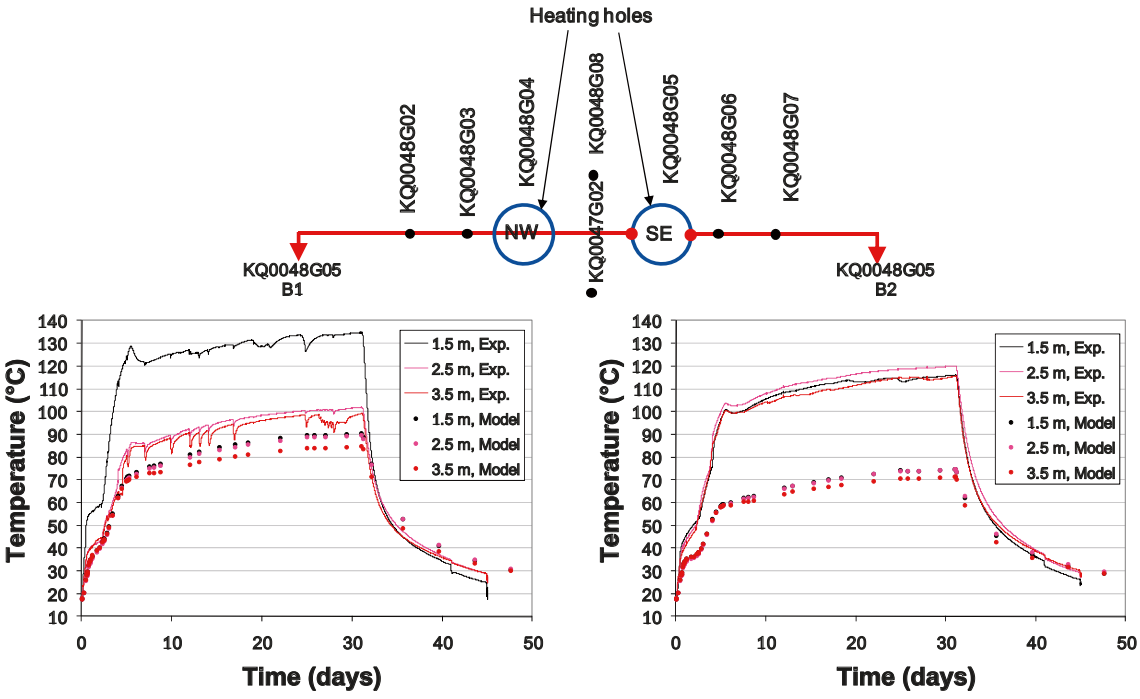

Figure 8-4. *Comparison between temperatures recorded at the borehole wall in KQ0048G05 during Test 3 and corresponding calculated temperatures.*

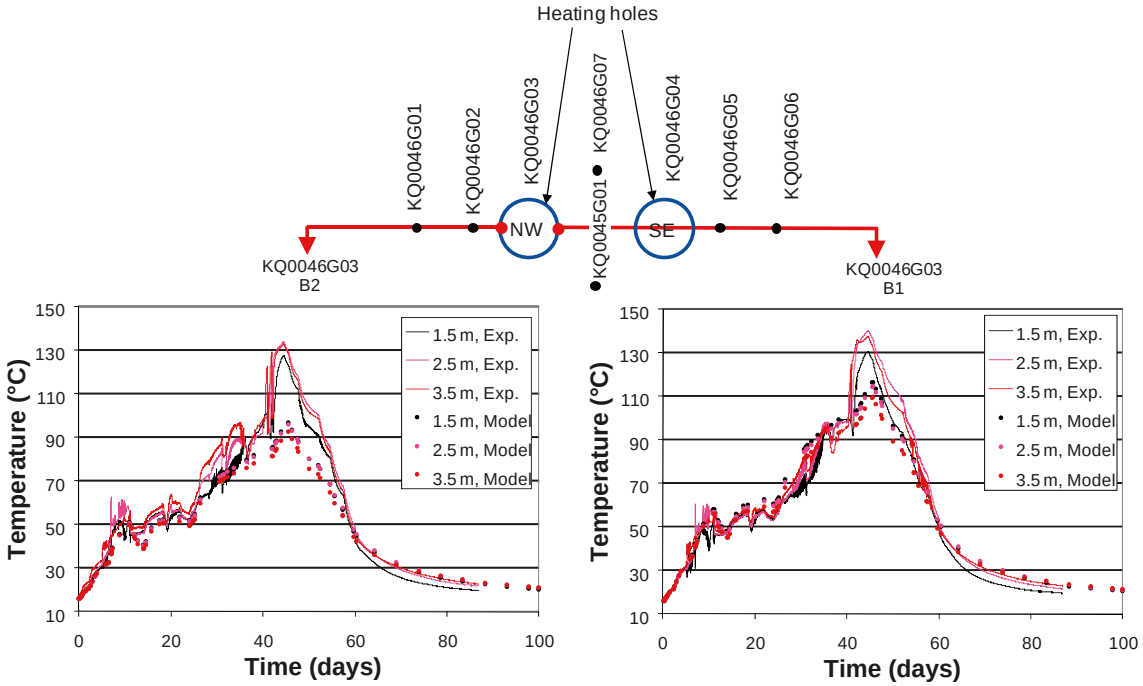

Figure 8-5. *Comparison between temperatures recorded at the borehole wall in KQ0046G03 during Test 4 and corresponding calculated temperatures.*

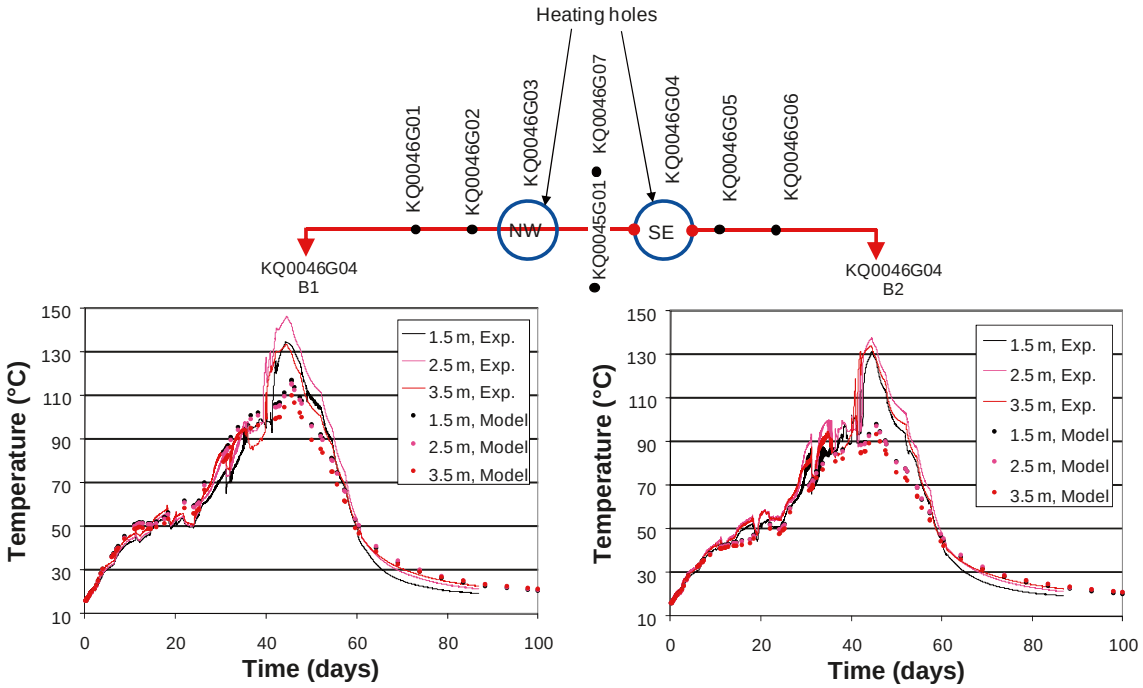

Figure 8-6. *Comparison between temperatures recorded at the borehole wall in KQ0046G04 during Test 4 and corresponding calculated temperatures.*

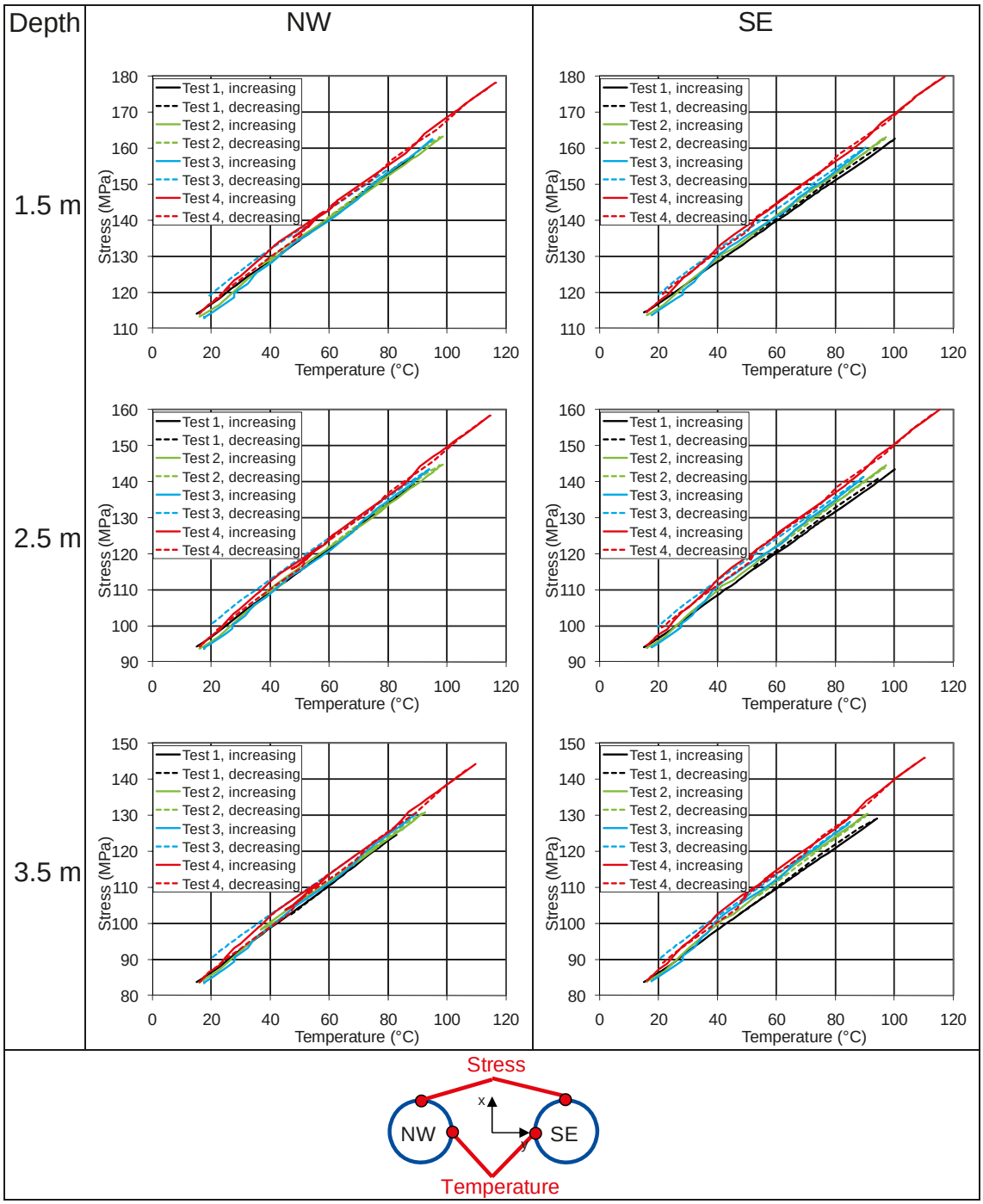

Figure 8-7. *Calculated tangential stress on the heating hole wall versus temperature for three depths in the different field tests. Note that the recorded temperature and the calculated stresses are at different positions on the borehole wall, as indicated by the bottom inset.*

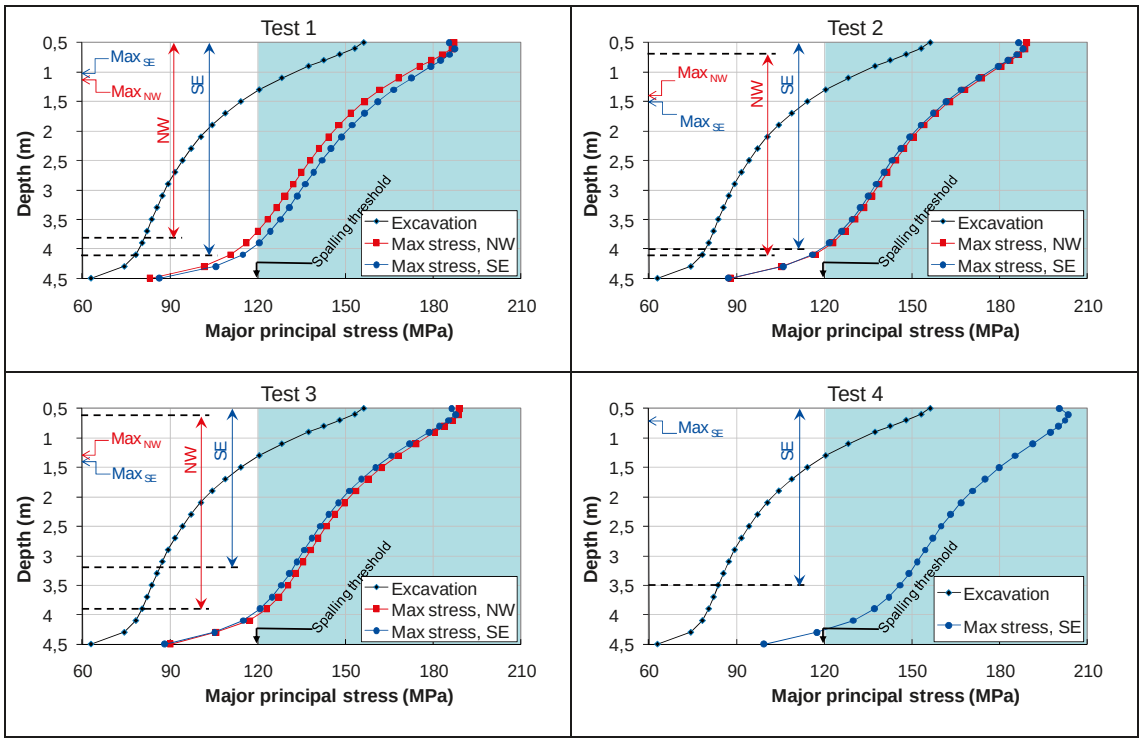

Figure 8-8. *Comparison between calculated tangential stresses and the occurrence of breakouts along the heating holes. The calculated results correspond to the conditions after the excavation and when the cooling phase was initiated. The intervals of observed breakouts are indicated by the dimension lines. The position of the observed maximum breakout in respective hole is also indicated in the diagrams.*

In spite of a somewhat uneven temperature development between the heating holes, the modelling results show an induced stress that is rather similar in both of the heating holes of any individual field test, see Figure 8-7. This indicates that the observed differences in spalling between the heating holes located on the NW-side and those on the SE-side of the tunnel axis are not caused by variations in the induced stresses.

The calculated tangential stresses versus distance from the borehole wall are presented on two occasions at 1.5 m depth in the NW heating hole in Figure 8-9. The simulated results show that the induced stress gradient in the various field tests was flattest in Test 4 at the beginning of the heating period and steepest in the same field test when the cooling phase was initiated. The reason for this is the fast temperature increase in the last field test, when the drainage pumps stopped and the wetting system shut down, see Section 5.1.2 and 5.1.4.

According to the results presented in Figure 8-9 the nominal spalling strength was exceeded up to a distance of 50–90 mm from the borehole wall in the different field tests. The shallowest value was estimated for Test 1 and the deepest value for Test 4. Despite the fact that the numerical simulation was performed by a linear elastic model that does not predict the post failure stresses, a comparison of the results with the field observations gives an indication of the beneficial confinement effect of the pellet filling. In the field experiment the maximum notch depth was observed in Field Test 2 rather than Test 4.

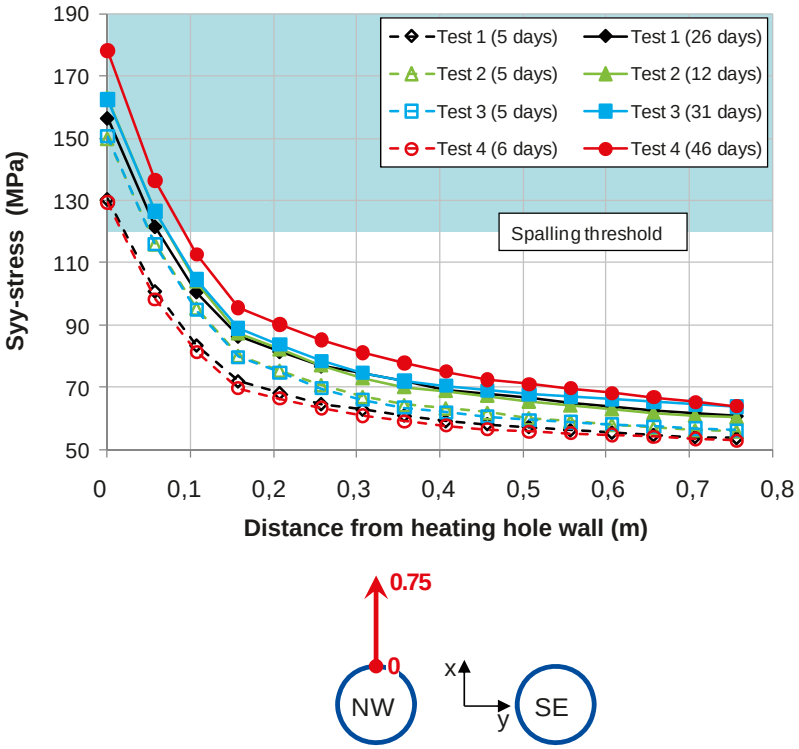

Figure 8-9. *Calculated tangential stress versus distance from the borehole wall on two occasions in a position located 1.5 m down into the NW heating hole.*

8.2 The occurrence of breakouts

The occurrence of breakouts in the heating holes is a function of the induced stresses and the rock strength. The estimated stress described in Section 8.1.3, suggests that one should expect an even distribution of breakouts in the heating holes if the strength of the rock was the same throughout the volume employed by the field experiment. Moreover, if the rock strength was equal, the distribution of breakouts along the borehole wall should be expected to form a continuous notch along both sides of the borehole wall. However, the observed outcome of the field experiment clearly illustrated that this is not the case.

As indicated in the previous sections, the results suggest a correlation between the natural humidity in the heating holes and the volume of breakouts in the individual tests. Possible reasons for this are discussed in Section 8.2.1 below. A possible explanation to the observed breakout distribution may also be associated with the geology, which causes local variation in the rock strength or the in situ stresses. Possible geological factors are described in Section 8.2.2.

8.2.1 Influence of humidity

The results from the field experiment appear to indicate that the volume of breakout in the heating holes can be correlated with the water inflow and the natural humidity of the heating holes, see Table 8-1. After the completion of the first field test, the large difference in proportion of breakouts between the heating holes was interpreted as a result of disturbance to the natural humidity in the holes. The heating and the system of compressed air to keep the camera lenses free from mist resulted in a reduced humidity in the heating holes during the first test. The least amount of breakout was observed in the heating hole with lowest relative humidity. The drying-up of the boreholes was initially assumed to have caused a slight apparent confinement of the borehole wall due to suction within the borehole boundary.

The observations resulted in the decision to perform the next test as a repetition of the first, however, with controlled humidity in the holes. In the second test the sealing of the heating holes was improved and a system to maintain the humidity in the holes, by the generation of steam via the heating tubes was

employed, see Section 3.4.4. Furthermore, the observation cameras were not included in the second test to exclude the disturbance caused by the compressed air. However, these actions to prevent the rock from drying up during the second test did not result in the expected more uniform breakout distribution in the heater holes, see Table 8-1.

Another possible explanation of the observations is that the dry and the wet parts of the borehole wall have different rock strength. Laboratory results on dry and water saturated samples of Äspö diorite confirm a difference in both the crack initiation stress and the uniaxial compressive strength of the rock, see Appendix C. However, the difference is only about 10%, which probably is too small to explain the observed results. Moreover, the variation in strength within the dry and saturated sample group is much larger than between the groups. Consequently the heterogeneity in the breakout occurrence is assumed to be caused by other factors than just the humidity in the heater holes. Other geological conditions that possibly correlate with the humidity of the heater holes are discussed in the section below.

8.2.2 Correlation between breakouts and geology

Possible correlations between the occurrence of breakouts and aspects of the geology were evaluated based on photographs, video recording, laser scanning and RVS modelling of the geology. The geological factors that were considered of interest to examine were the shear zone that intersects the area, rock mass foliation and alteration such as oxidation and epidotization, along with the distribution of sealed fracture networks. A number of pictures produced to evaluate possible correlation between the occurrence of breakouts and the geology are included in Appendix B. A separate study by Vattenfall Power Consultant regarding this subject is presented in Appendix S. The account here summarizes the findings in the current study.

The boundary of the shear zone is shown in Figure 8-10. All heating holes penetrated the shear zone, but the holes on the SE-side of the tunnel axis are drilled through the full width of the zone, while boreholes on the NW-side only penetrate the zone partly and mainly are excavated below the zone. The occurrence of breakouts is more extensive in the latter holes, which mainly runs below the shear zone, Figure 8-11 and Figure 8-12.

Another condition related to the shear zone that is illustrated by the figures, is that the occurrence of breakouts is reduced in areas of more pronounced foliation, i.e. the volume between the upper and lower boundary of the shear zone that has previously been exposed to high levels of strain. In foliated rock where breakouts do occur, the foliation to a certain degree influencing the boundary of the breakout, both affecting its position slightly and generating a stepped contour, see Figure 8-13.

Alteration by oxidation, which is more pronounced in the upper part of the heating holes, does not seem to influence the occurrence of breakouts in any systematic way, see Appendix B. This lack of any identifiable systematic pattern is also seen in the case of the epidotization and distribution of sealed fracture networks, which are commonly associated with the more foliated parts of the rock. However, it appears that the dimension of breakouts is larger in sections of more pronounced oxidation, see Appendix B. Moreover, the sealed fracture networks in some cases, for example in upper part of the KQ0048G04, appear to have controlled the shape of the breakouts.

The above described observations related to the shear zone and the oxidation are in accordance with the findings in Section 2.2.1, which indicate that parts of the strong foliated rock in the shear zone are expected to have higher strength, while parts of oxidized rock possibly has lower strength. A variation in the intensity in the foliation or the oxidation might be the cause of differences in the amount of breakouts observed on the different sides of the wall in a heating hole. However, the mapping that the RVS modelling was based have not sufficient resolution to confirm that assumption, since mapping was carried out on cores of the pilot holes in the centre of the heating holes.

Table 8-1. Compilation of breakout volumes, water inflow and relative humidity in the heating holes.

Borehole/Test	Breakouts[1] (litre)	Inflow[2] (litre)	Relative humidity[3]	
			Temp (°C)	RH (%)
Test 1				
KQ0054G03	5.1	0.003	100	20
KQ0054G04	1.3	0.002	100	5
Test 2[5]				
KQ0051G04	12.8	0.016	94	81
KQ0051G05	1.6	0.003	93	94
Test 3				
KQ0048G04	6.4[4]	0.081	94	65
KQ0048G05	2.7	0.003	100	12
Test 4[5]				
KQ0046G04	0.4	0.001	71	18

1) Breakouts volume in the heating holes based on results from the laser scanning.
2) Inflow of water into the heater holes based on the changed in water level during a period of 20 hours.
3) Estimated mean value of temperature and relative humidity during the heating period.
4) The value has been corrected for breakouts that occurred during the drilling.
5) The field test was performed with artificial wetting of the heating holes.

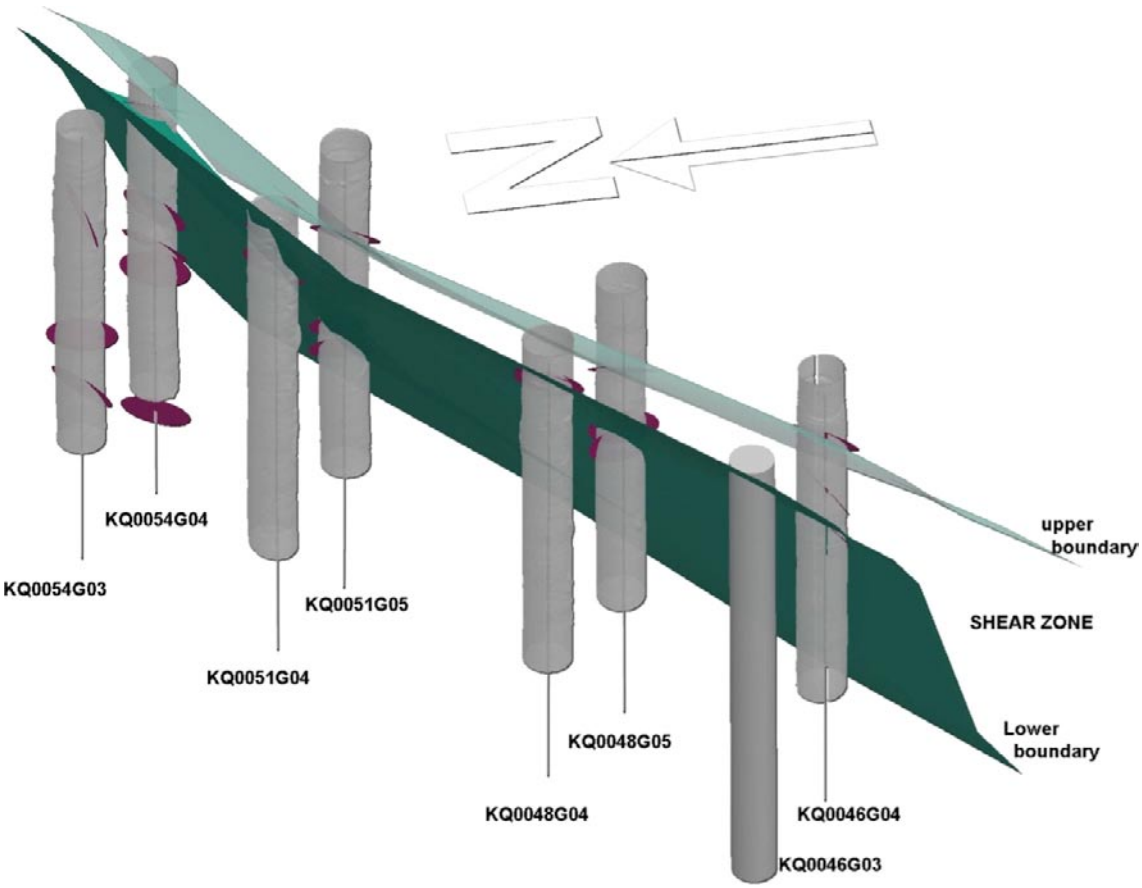

Figure 8-10. *Isometric view of the test area showing the heating boreholes and the boundaries of the shear zone running through the site. The geometry of the boreholes is based on the laser scanning except for KQ0046G03 for which no mesh has been produced. The purple disks in the northeastern part indicate splays of the shear zone.*

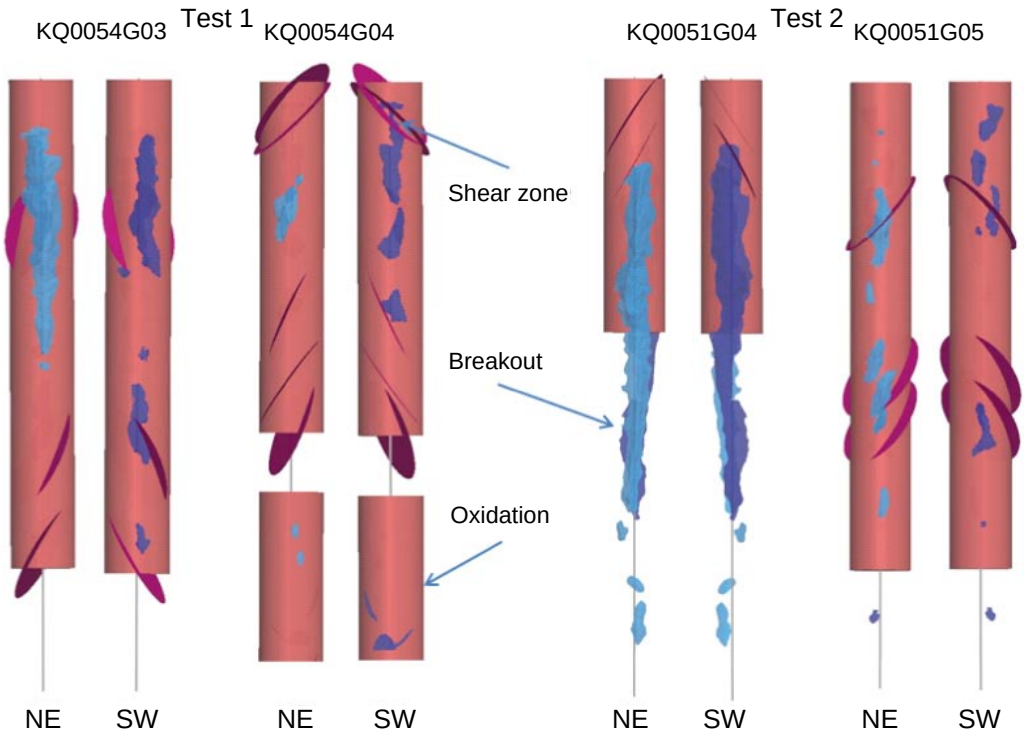

Figure 8-11. *Visualization of mapped boundaries of the shear zone and sections of oxidations together with sections of observed breakouts in Tests 1 and 2 performed without confinement by LECA pellets. The projections of the breakouts are from the outside.*

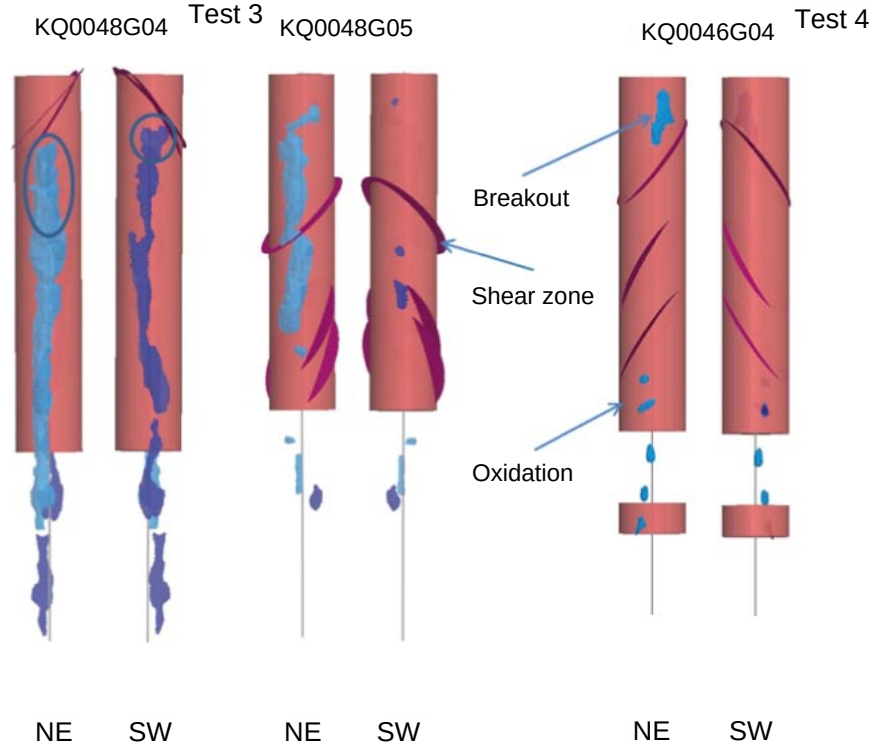

Figure 8-12. *Visualization of mapped boundaries of the shear zone and sections of oxidations together with sections of observed breakouts in Tests 3 and 4 performed with confinement by LECA pellets. The projections of the breakouts are from the outside. The breakouts in the areas marked by a blue ellipse and a circle occurred mainly before the heating.*

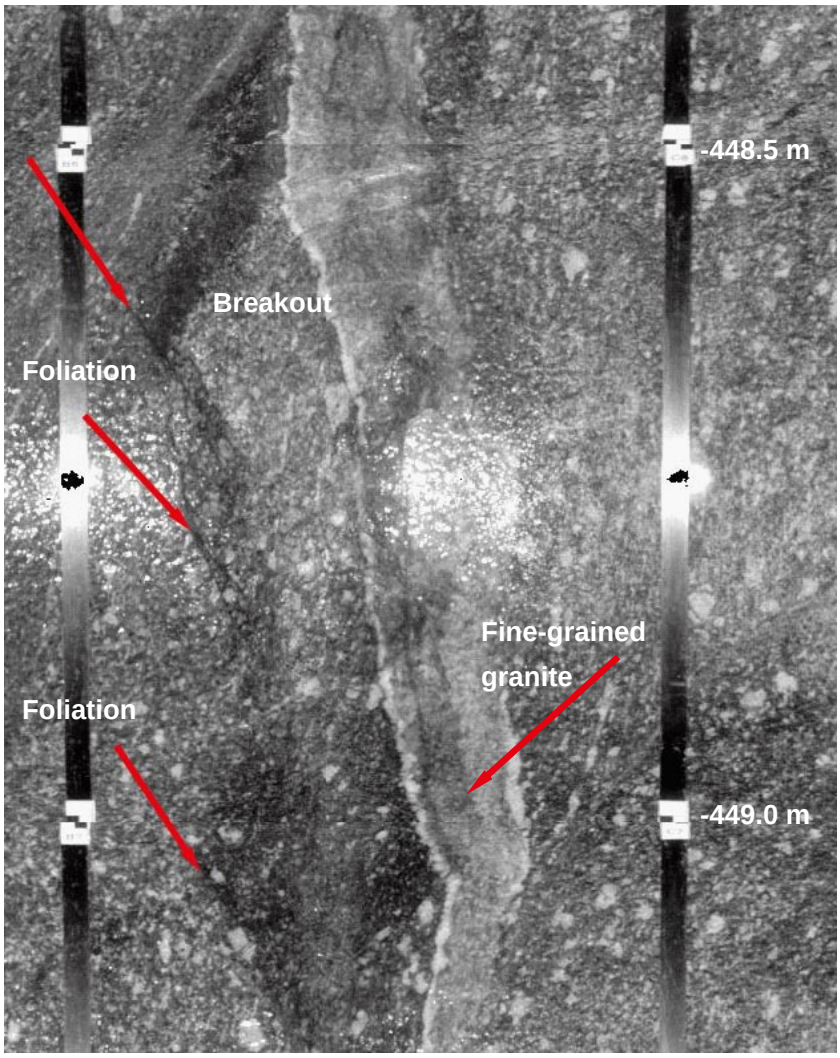

Figure 8-13. *The picture shows an example where the foliation affects the left boundary of the breakout, whereas the narrow fine-grained granite does not appear to have any impact on the breakout border.*

8.2.3 Confinement effect on spalling

The evaluation of the confinement effect on spalling is not unequivocal due to the heterogeneity in the spalling results between heating holes from the same group, i.e. Tests 1 and 2 without confinement compared to Tests 3 and 4 with confinement. The heterogeneity in the results, which most likely is caused by the shear zone striking parallel with the tunnel, means that evaluation of the holes on the NW-side of the tunnel axis must be made separately from those on the SE-side. Moreover, the differences in temperature development and resulting thermal stresses in the various field tests must be considered. Based on the numerical calculations, the largest dimensions of the breakout are expected in Field Test 4 followed in declining sequence by Field Test 3, 2 and 1.

When evaluating the results from Test 3, it should be noted that the boreholes were not scaled before the heating period and that breakouts already existed in the upper part of the NW-hole (KQ0048G04). It should also be observed that the removal of pellets in Test 3 was carried out when the temperature in the surrounding rock was to a certain degree still elevated.

The NW-hole from Field Test 4 is not included in the comparison since it was grouted. In the hole presented from Test 4, only the NE-side of the borehole wall was scaled.

The parameters that have been included in the evaluation of the confinement effect on spalling are the maximum length, width and depth of the created notch as well as the volume of breakouts in the holes, see Figure 8-14 to Figure 8-17. It should be noted that the volume in KQ0048G04 in Test 3 (NW-hole) has been corrected for the initial breakout during drilling, see Section 6.1.

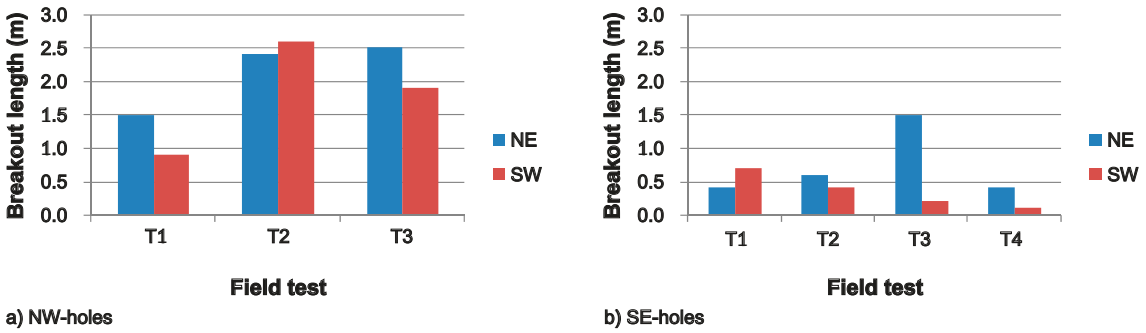

Figure 8-14. *Comparison of max breakout length in the heating holes, a) holes on NW-side and b) holes on SE-side. Field Test 3 and 4 were performed with confinement. The NW-hole from Field Test 4 is omitted since it was grouted. The breakout length in Field Test 3 includes the part that spalled during the drilling.*

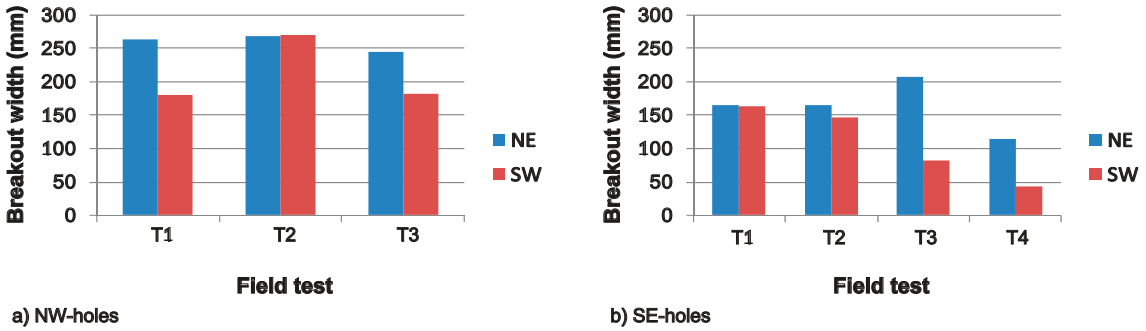

Figure 8-15. *Comparison of maximum breakout width in the heating holes, a) holes on NW-side and b) holes on SE-side. Field Test 3 and 4 were performed with confinement. The NW-hole from Field Test 4 is omitted since it was grouted. The maximum breakout width on the NE-side in Field Test 3 is located in the part that spalled during the drilling.*

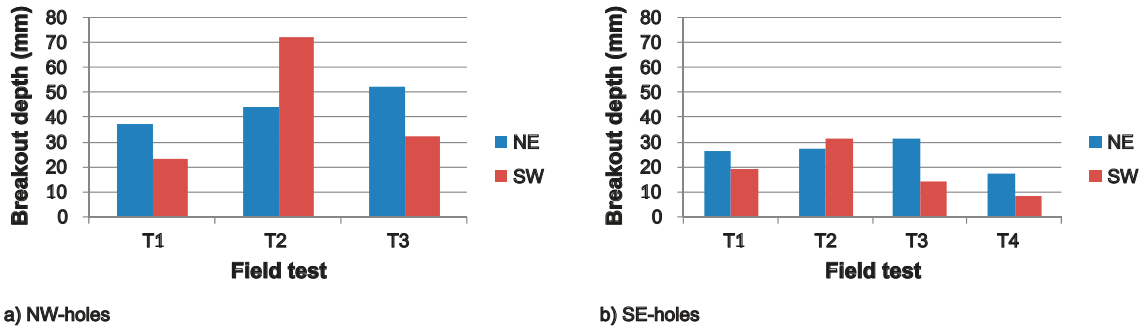

Figure 8-16. *Comparison of max breakout depth in the heating holes, a) holes on NW-side and b) holes on SE-side. Field Test 3 and 4 were performed with confinement. The NW-hole from Field Test 4 is omitted since it was grouted. The maximum breakout depth on the NE-side in Field Test 3 is located in the part that spalled during the drilling.*

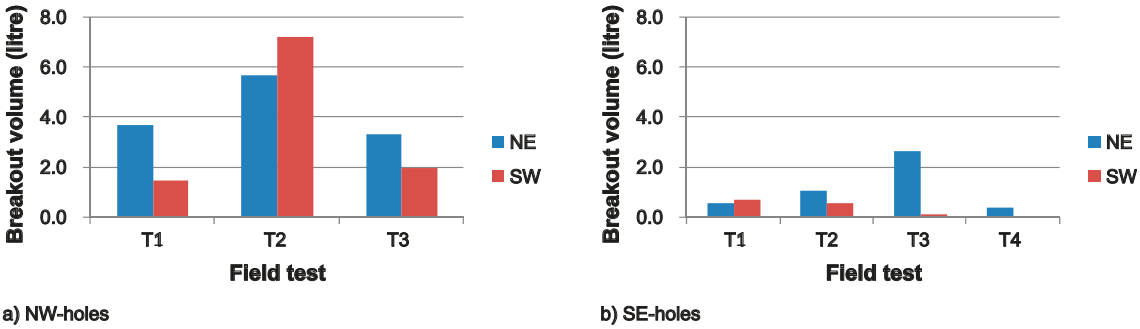

Figure 8-17. *Comparison of breakout volume in the heating holes, a) holes on NW-side and b) holes on SE-side. Field Test 3 and 4 were performed with confinement. The NW-hole from Field Test 4 is omitted since it was grouted. The volume in KQ0048G04 has been corrected for the initial breakout during drilling (NW-holes, T3).*

When comparing the dimensions of the notches in the various heating holes, the results indicate equal or smaller dimensions of the notches created in holes performed with confinement compared to those carried out without confinement. The trend is similar when comparing the breakout volume in the holes, the volume is equal or smaller in the holes performed with confinement compared to those carried out without confinement. The only exception to this trend is the result on the NE-side in KQ0048G05, where the maximum volume occurred in the upper part of the hole and which might be a consequence of the removal of pellets when the temperature was still elevated.

Considering that the numerical calculations indicate that the nominal spalling strength is exceeded further into the borehole wall in Tests 3 and 4 compared to Tests 1 and 2, the overall conclusion from the present evaluation, is that the confinement provided by LECA pellets has reduced the thermal-induced spalling. Besides this, as already pointed out in Section 6.3, the confinement provided by the LECA pellets has the capability to keep rock slabs with larger dimensions than the pellet fraction in place on the borehole wall.

8.2.4 Confinement effect on the hydraulic conductivity

The results from the water injection tests demonstrate that the transmissivity of the damaged zone with confinement by LECA pellets is typically below $5 \cdot 10^{-9}$ m^2/s, see Section 7.4. The corresponding hydraulic conductivity for an assumed thickness of the damage zone between 10–50 mm is estimated to be less than $5 \cdot 10^{-7}$ m/s. This conductivity is much larger than the hydraulic conductivity of undisturbed matrix rock at Äspö, which according to determinations by the GeoMod project is approximately $1 \cdot 10^{-12}$ m/s /Vidstrand 2003/. However, the resolution of the measurements performed in the current experiment is unfortunately insufficient to determine how close the hydraulic conductivity of the investigated damaged zone is to the matrix background hydraulic conductivity.

In order to assess the benefit from the confinement effect of the hydraulic conductivity of the damage zone, the results reported here were compared with the results from a study by /Neretnieks and Andersson 2009/. In the study the hydraulic conductivity was estimated for a spalled damage zone, consisting of a zone of increased porosity but with the fragments in place. The results are based on data obtained from the rock fragments collected in the APSE field experiment. The results from this study indicate that the damage zone had a hydraulic conductivity above approximately $1 \cdot 10^{-4}$ m/s, see Figure 8-18.

Although the results generated by data from APSE are based on a methodology quite different from the one used in CAPS, a comparison of the results indicates that the confinement provided by LECA pellets has noticeably reduced the hydraulic conductivity of the damage zone. The inferred reason for this is not only that the cracks of the damage zone are kept closed by the confinement, but that the net of flow paths becomes more complex, by keeping the slab in place on the borehole wall.

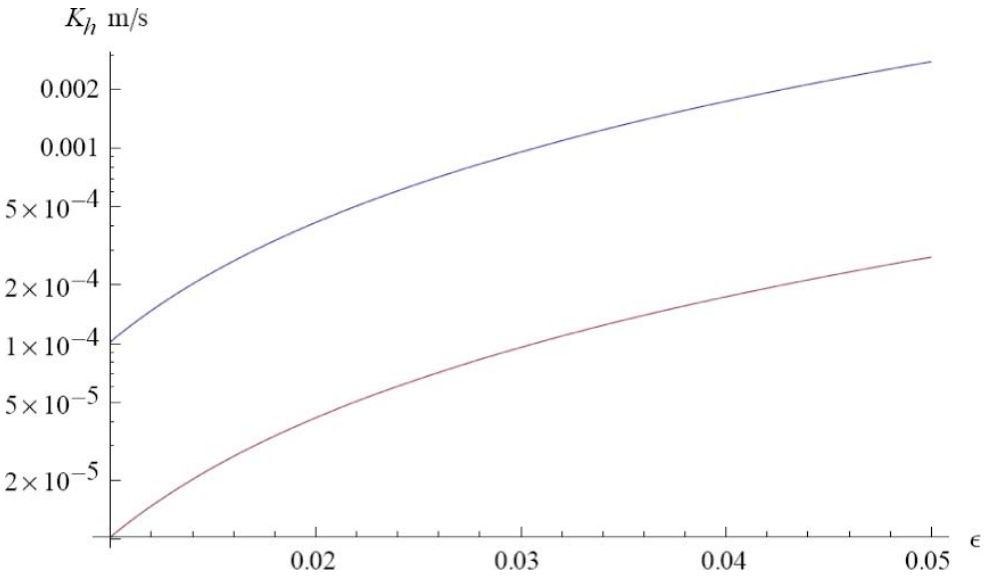

Figure 8-18. *Estimated hydraulic conductivity versus porosity of a spalled damaged zone. The upper curve corresponds to flow parallel to the spalled fragment and the lower curve to flow across the fragment. After /Neretnieks and Andersson 2009/.*

9 Summary of the results

9.1 Heat losses

The heating power applied in the field experiment was in general larger than the value obtained in the numerical calculations by fitting the recorded temperatures. The main reasons for discrepancy between the applied and back-calculated heating power are additional sources of heat loss not included in the calculations.

The results from the numerical simulation indicate that the heating power that enters the rock mass is about 20–40% lower than the applied power in the field tests. The calculated and recorded heating power showed best agreement in the third field test, which was carried out without artificial wetting.

9.2 Relative humidity

The measurements in the tunnel displayed stable humidity with only minor variations. The recorded relative humidity before starting the heating period in all heating holes was in the range of 90–100%.

In Field Tests 1 and 3, which were performed without artificial moistening, the lowest relative humidity in both tests was recorded in the SE-hole, where it reached a value of around 5%. The artificial moistening in Field Tests 2 and 4 was not able to maintain the relative humidity at the initial value in the heating holes but the humidity of the holes were balanced and the reduction of the humidity during the heating period was limited.

9.3 Temperature distribution

The initial temperature of the rock mass before starting the first field experiment was around 15°C. In the following tests, the initial temperature increased slightly and reached a maximum of 18°C in Field Test 3 due to the disturbance from the nearby previous heating test.

The maximum temperature on the wall in the heating holes, reached just before the cooling phase was initiated, ranged from approximately 80°C in the first test to 140°C in the final test. In all heating holes the temperature on the borehole wall reached the calculated temperature necessary to induce thermal spalling along the main part of the wall.

With the exception of Tests 2 and 4, the temperature development in the field tests was somewhat uneven between the heating holes. The difference in temperature is a reflection of the relative humidity of the heating holes, which was largest in the heating hole with least temperature change.

The calculated and recorded temperature distribution of the field tests demonstrates reasonable agreement in Tests 1 and 2, while a more modest agreement was achieved in Tests 3 and 4. What proved to be difficult to achieve was the fitting between calculated and recorded temperatures on the wall of the heating holes, especially in Tests 3 and 4.

9.4 Thermal stress evolution

The numerical simulation indicates that the spalling stress threshold for Äspö diorite (120 MPa) is exceeded down to a depth of about 1.2 m below the edge of the concrete collar after excavation and to a depth of 4.2 m in the various field tests during the heating phase.

According to the simulations the highest stresses are expected to occur close to the tunnel floor in the heating holes. In Tests 1–3 the calculated tangential stress amounts to 185–190 MPa, while in the last test it exceeds 200 MPa in the model. However, no EDZ was accounted for in the simulations and it is thus likely that in the model the stresses in the upper part of the tunnel floor, within approximately 0.3 m distance, are overestimated.

The stress gradients close to the heating holes in the numerical model are correlated to the calculated stress levels. The highest stress gradients are consequently estimated in the last test where the temperatures and the stress levels were highest.

There is a linear relationship between the calculated stress changes and the temperature changes. The dependence seems to be similar both during temperature increase and temperature decrease and for all borehole depths.

In spite of a somewhat uneven temperature development between the heating holes, the modelling results demonstrate induced stresses that are rather similar in both of the heating holes of any individual field test.

According to the numerical simulations, the nominal spalling strength was exceeded up to a distance of 50–90 mm from the borehole wall in the different field tests. The shallowest value was estimated for Test 1 and the deepest value for Test 4.

9.5 Spalling observations

Spalling related to the drilling of the boreholes was only observed in three of the heating holes and was in general minor involving only few rock slabs in the depth interval of 0.6–1.3 m. According to the estimated stresses, the drilling should have caused a stress concentration sufficient to create spalling down to at least 1.2 m depth in all the holes. The small amount of spalling related to the drilling process might be a result of reaming the heating holes to full size in several steps from a core drilled pilot hole, which is supposed to reduce the extent of the damage zone.

The uppermost observation of breakouts in the holes after the heating phase was encountered in the interval 0.4–0.8 m below upper edge of the concrete collar and the lowest observation in the interval 3.1–4.1 m below the same reference level. The observations are in close agreement with the expected interval of the damaged zone based on the results from the numerical modelling.

The results show large heterogeneity in the proportion of observed spalling between the heating holes as well as between opposite sides of any individual heating hole. The largest amount of spalling was observed in the heating holes with the largest inflows of water, even though the temperature increase was smallest in these holes. The moisture content of the borehole wall appears to influence the results. However, the overall pattern is most likely dominated by the effect of the shear zone that strikes parallel to the tunnel axis, causing local variations in the strength of the rock.

The length of the breakouts varies from less than 0.1 m up to approximately 2.6 m. It is mainly in the upper part of the heating holes that the breakouts form a continuous notch. The breakouts in the lower part of the heating holes consist of separate sectors of a length that normally is less than 0.1–0.2 m. The notch was least developed in Test 4, performed with confinement provided by LECA pellets.

The width and depth of the notches reach approximately 270 mm and 70 mm, respectively. When normalised to the initial hole radius, the depth of the notches reaches up to about 0.3 of the hole radius. The maximum width and depth of the notches are approximately half the size of the dimensions observed in the APSE project (width≤500 mm, depth ≤ 135 mm) /Andersson 2007/.

The determined breakout angle ranged from approximately 5 degrees for the tiny breakouts to up to 60 degrees for the fully developed ones, with a mean around 30 degrees for all observations. The corresponding values of the opening angles were 90 degrees for deep asymmetric breakouts and up to 160 degrees for shallow symmetric ones, with a mean of around 130 degrees for all observations. The opening angle is comparable with the observation in APSE, while the breakout angle is approximately half the mean value /Andersson 2007/.

The trend of the damaged zone, which was evaluated separately for each side of the borehole wall, varies between N20–53E degrees (mean N38E degrees) and N193–263E degrees (mean N212E degrees), respectively. The observed position of the damaged zone agrees relatively well with a direction normal to the trend of the major principal stress, which according to the evaluations in APSE corresponds to N40E or N220E degrees /Andersson 2007/. The observed variations seem to be caused mainly by the foliation, by the shear zone and minor dykes that intersect the heating holes.

9.6 Investigation of rock fragments

The total weight of the rock fragments due to thermal spalling that dropped down in the heating holes amounts approximately 80 kg. The total weight of rock fragments that were collected from the holes heated without the confinement provided by the pellets varies between 4–33 kg (1.4–12.0 litres). The corresponding total weight for the holes heated with the confinement provided by the pellets, varies between 1–19 kg (0.3–7.0 litres).

The rock fragments range in weight from less than 1 gram up to discs with a weight of 1.6 kg. The maximum recorded length of the collected rock fragments was 290 mm, while the maximum width was 180 mm. The distribution of the width/length ratios indicates that most fragments have a width that corresponds to half their length, which corresponds well with the observations in the APSE field experiment /Neretnieks and Andersson 2009/.

The thickness of the collected fragments is typically 0.1 of the length, which likewise is close to the observations in the APSE field experiment /Neretnieks and Andersson 2009/.The investigation shows a larger amount of thinner fragments in the holes of Field Tests 1 and 2 compared to the fragments collected in Field Test 3, which seems to indicate that the confinement resulted in slightly thicker fragments.

9.7 Hydraulic test

The results from the water injection tests, in a heating hole with confinement provided by LECA filling, demonstrate that the transmissivity of the damaged zone is typically below $5 \cdot 10^{-9}$ m^2/s. The corresponding hydraulic conductivity for an assumed thickness of the damage zone between 10–50 mm is estimated to be less than $5 \cdot 10^{-7}$ m/s. The measured conductivity is much lower than the expected hydraulic conductivity of a damage zone with incomplete confinement, which is estimated to be approximately $1 \cdot 10^{-4}$ m/s by /Neretnieks and Andersson 2009/. The hydraulic conductivity of undisturbed matrix rock at Äspö is approximately $1 \cdot 10^{-12}$ m/s /Vidstrand 2003/.

The lack of interference between the water injection holes during the hydraulic tests indicates that the thermal spalling has not produced a continuous damage zone along the heating holes where confinement is provided by LECA filling.

10 Conclusions

Thermally-induced spalling occurred in the unsupported holes at approximately the magnitudes of tangential stress that were predicted, i.e. at a tangential stress corresponding to about 60% of the uniaxial compressive strength.

The largest amount of spalling was observed in the heating holes with the largest inflows of water, even though the temperature increase was smallest in these holes. The moisture content of the borehole wall seems to influence the results. However, the overall pattern is most likely dominated by the effect of the shear zone that strikes parallel to the tunnel axis.

The uppermost and lowest observation of breakouts in the holes after the heating phase is in close agreement with the expected interval of the damaged zone based on the results from the numerical modelling. However, it is mainly in the upper part of the heating holes that the breakouts form continuous notches. The breakouts in the lower part of the heating holes consisted mainly of isolated spots of spalling.

The nonuniform development of thermally-induced spalling is probably associated with local variation in the rock strength caused by a variable geology. The deflection of the strength variation in the breakout occurrence is probably enhanced for the current hole size compared to full size deposition holes. The results simply indicate that the current scale was too small to be fully representative for the present rock conditions. In a full scale-hole, the nominal spalling strength would be exceeded in a significantly larger volume, meaning that the probability for local high-strength parts on the borehole wall to block the formation of a continuous spalled zone would be smaller. In full size deposition holes, without confinement, it is expected the breakouts would be more likely to form continuous notches along the holes.

The results indicate that dry pellets cannot prevent the borehole wall from cracking, whereas they will keep slabs in place with larger dimensions than the pellet fraction. These slabs represent a sufficiently large proportion of the spalled volume to obtain a reduced hydraulic transmissivity of the damage zone compared to the unsupported case where all fragments are free to detach.

When comparing the breakout dimensions and breakout volumes in the various heating holes, the results indicate equal or smaller breakouts in the holes performed with confinement compared to those carried out without confinement. Considering that the numerical calculations indicate that the nominal spalling strength is exceeded further into the borehole wall in the confined holes compared to the unconfined ones, the conclusion is that the confinement provided by LECA pellets has reduced the thermal-induced spalling.

11 Recommendations

Since the results indicate that the current scale was too small to be fully representative for the encountered rock conditions, it is recommended that a full-scale test be carried out to assess whether the findings are applicable to 1,750-mm-diameter deposition holes. Such a test should involve regular dry bentonite pellets instead of LECA pellets, since the laboratory results indicate that a LECA filling might be stiffer than a bentonite filling. Moreover, the time dependent temperature change with the corresponding stress path for the full scale tests should be close to the expected conditions in a repository located in Forsmark. Should the full scale tests support the findings from these initial trials, filling the gap between the bentonite blocks and rock wall with dry bentonite pellets may provide a viable engineered solution for controlling the effects of thermally-induced spalling in the KBS-3 deposition holes.

In a future field experiment attempts should also be made to obtain a site with less heterogeneity in the geology, and also to achieve a similar temperature gradient around all heating holes included in the experiment. Implementation of monitoring by acoustic emission for observation of possible spalling activity during the heating period and when the confinement pressure is released should also be considered.

12 References

Almén K-E, Stenberg L, 2005. Äspö Hard Rock Laboratory. Characterisation methods and instruments. Experiences from the construction phase. SKB TR-05-11, Svensk Kärnbränslehantering AB.

Andersson J C, 2007. Äspö Hard Rock Laboratory. Äspö Pillar Stability Experiment, Final report. Rock mass response to coupled mechanical thermal loading. SKB TR-07-01, Svensk Kärnbränslehantering AB.

Barton N, 2003. Äspö Hard Rock Laboratory. Äspö Pillar Stability Experiment. Q-logging of the TASQ tunnel at Äspö. For rock qulity assessment and for development of preliminary model parameters. SKB IPR-04-07, Svensk Kärnbränslehantering AB.

Christiansson R, Janson T, 2002. Test with three different stress measurement methods in two orthogonal boreholes. In the proceedings of NARMS-TAC 2002. The 5th North American Rock Mechanics Symposium, Toronto, Canada July 7–11, 202, p. 1429–1436.

Lönnqvist M, Kristensson O, Hökmark H, 2008. Äspö Hard Rock Laboratory. CAPS – Confining Application to Prevent Spalling. Scoping calculations – Field test at Äspö HRL. SKB IPR-08-08, Svensk Kärnbränslehantering AB.

Neretnieks I, Andersson J C, 2009. Characterization of spalling fragments to obtain data for flow and solute transport in damaged zones. In the proceedings for the SINOROCK 2009 International Symposium on Rock Mechanics. University of Hong Kong, May 19–22.

Olsson M, Niklasson B, Wilson L, Andersson J C, Christiansson R, 2004. Äspö HRL, Experiences of blasting of the TASQ tunnel. SKB R-04-73, Svensk Kärnbränslehantering AB.

SKB, 2006. Long-term safety for KBS-3 repositories at Forsmark and Laxemar – a first evaluation. Main Report of the SR-Can project. SKB TR-06-09, Svensk Kärnbränslehantering AB.

SKB, 2008. Site description of Forsmark at completion of the site investigation phase. SKB TR-08-05, Svensk Kärnbränslehantering AB.

Staub I, Andersson J C, Magnor B, 2004. Äspö Pillar Stability Experiment, Geology and mechanical properties of the rock in TASQ. SKB R-04-01, Svensk Kärnbränslehantering AB.

Vidstrand P, 2003. Äspö Hard Rock Laboratory. Update of the hydrogeological model 2002. SKB IPR-03-35, Svensk Kärnbränslehantering AB.

Appendices

Appendix A

WellCad diagrams for geological data of the pilot holes

The diagrams present geological data for the core drilled pilot holes located in the centre position of the later reamed heating holes

Title **LEGEND FOR ÄSPÖ**

Site ÄSPÖ

Title GEOLOGY IN KQ0046G03

Site	ÄSPÖ	**Coordinate System**	ÄSPÖ96
Borehole	KQ0046G03	**Northing [m]**	7307.43
Diameter [mm]	76	**Easting [m]**	2113.30
Length [m]	5.190	**Elevation [m.a.s.l.]**	-446.35
Bearing [°]	187.75	**Drilling Start Date**	2008-04-02 15:15:00
Inclination [°]	-89.85	**Drilling Stop Date**	2008-04-03 14:30:00
Date of coremapping	2008-06-12 16:17:00	**Plot Date**	2010-02-08 23:01:11
Rocktype data from	p_rock	**Signed data**	2010-02-09

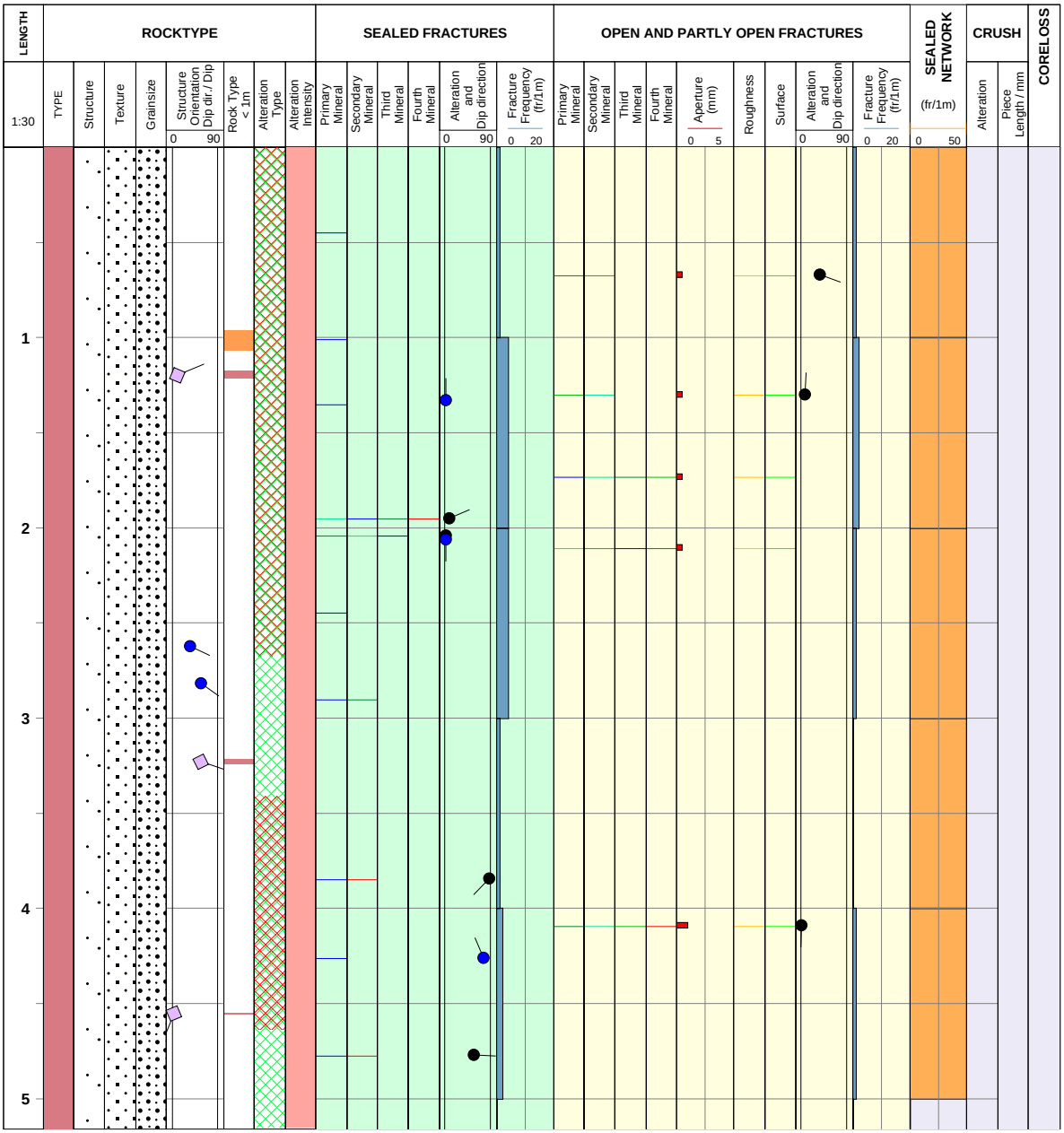

Title GEOLOGY IN KQ0046G04

Site	ÄSPÖ	**Coordinate System**	ÄSPÖ96
Borehole	KQ0046G04	**Northing [m]**	7306.56
Diameter [mm]	76	**Easting [m]**	2114.13
Length [m]	5.140	**Elevation [m.a.s.l.]**	-446.35
Bearing [°]	255.62	**Drilling Start Date**	2008-03-28 11:30:00
Inclination [°]	-89.90	**Drilling Stop Date**	2008-04-02 13:00:00
Date of coremapping	2008-06-05 15:41:00	**Plot Date**	2010-02-08 23:01:11
Rocktype data from	p_rock	**Signed data**	2010-02-09

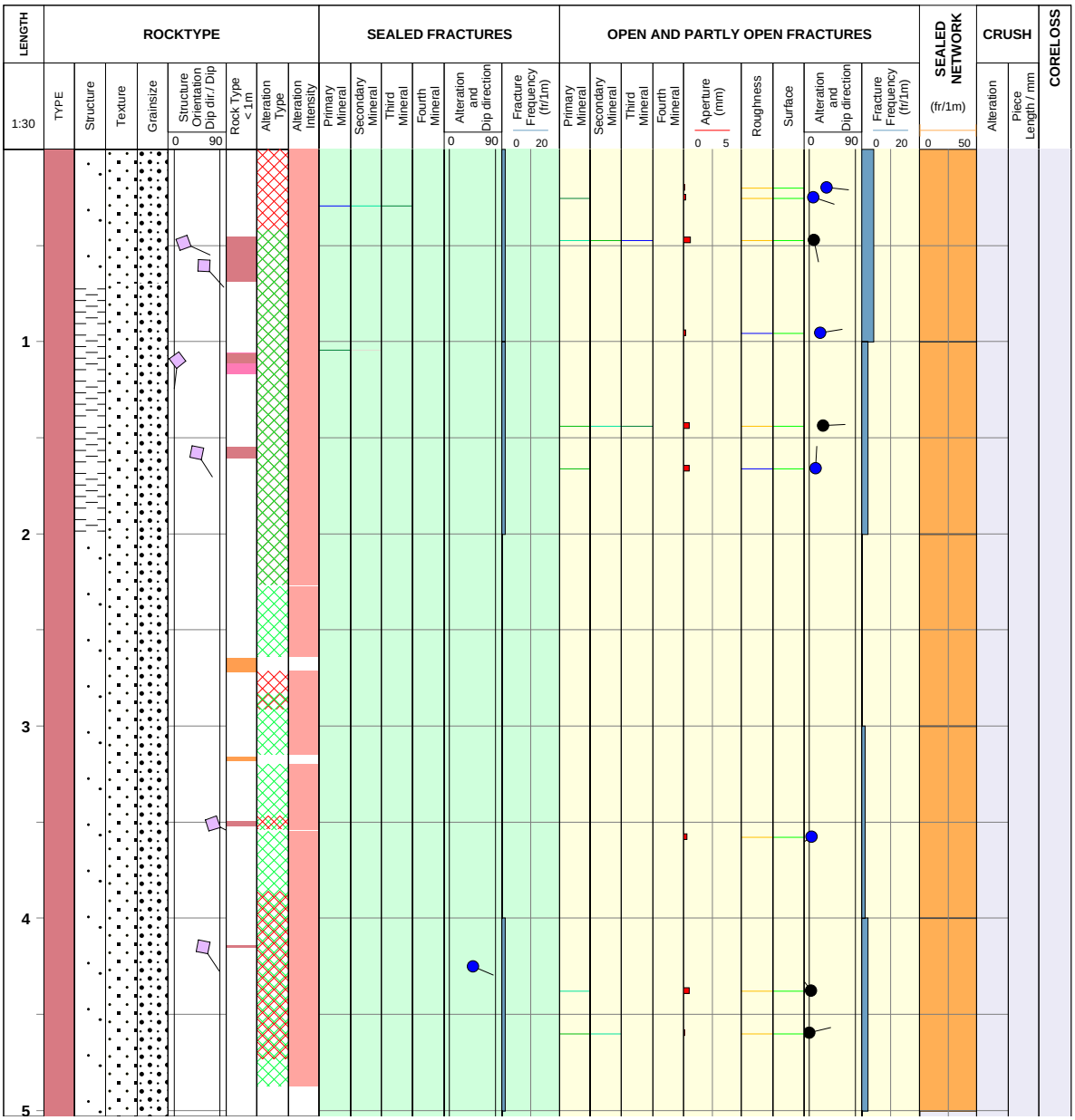

Title GEOLOGY IN KQ0048G04

Site	ÄSPÖ	**Coordinate System**	ÄSPÖ96
Borehole	KQ0048G04	**Northing [m]**	7309.12
Diameter [mm]	161	**Easting [m]**	2115.02
Length [m]	5.240	**Elevation [m.a.s.l.]**	-446.29
Bearing [°]	346.41	**Drilling Start Date**	2008-04-03 17:00:00
Inclination [°]	-89.70	**Drilling Stop Date**	2008-04-04 15:00:00
Date of coremapping	2008-06-18 14:08:00	**Plot Date**	2010-02-08 23:01:11
Rocktype data from	p_rock	**Signed data**	2010-02-09

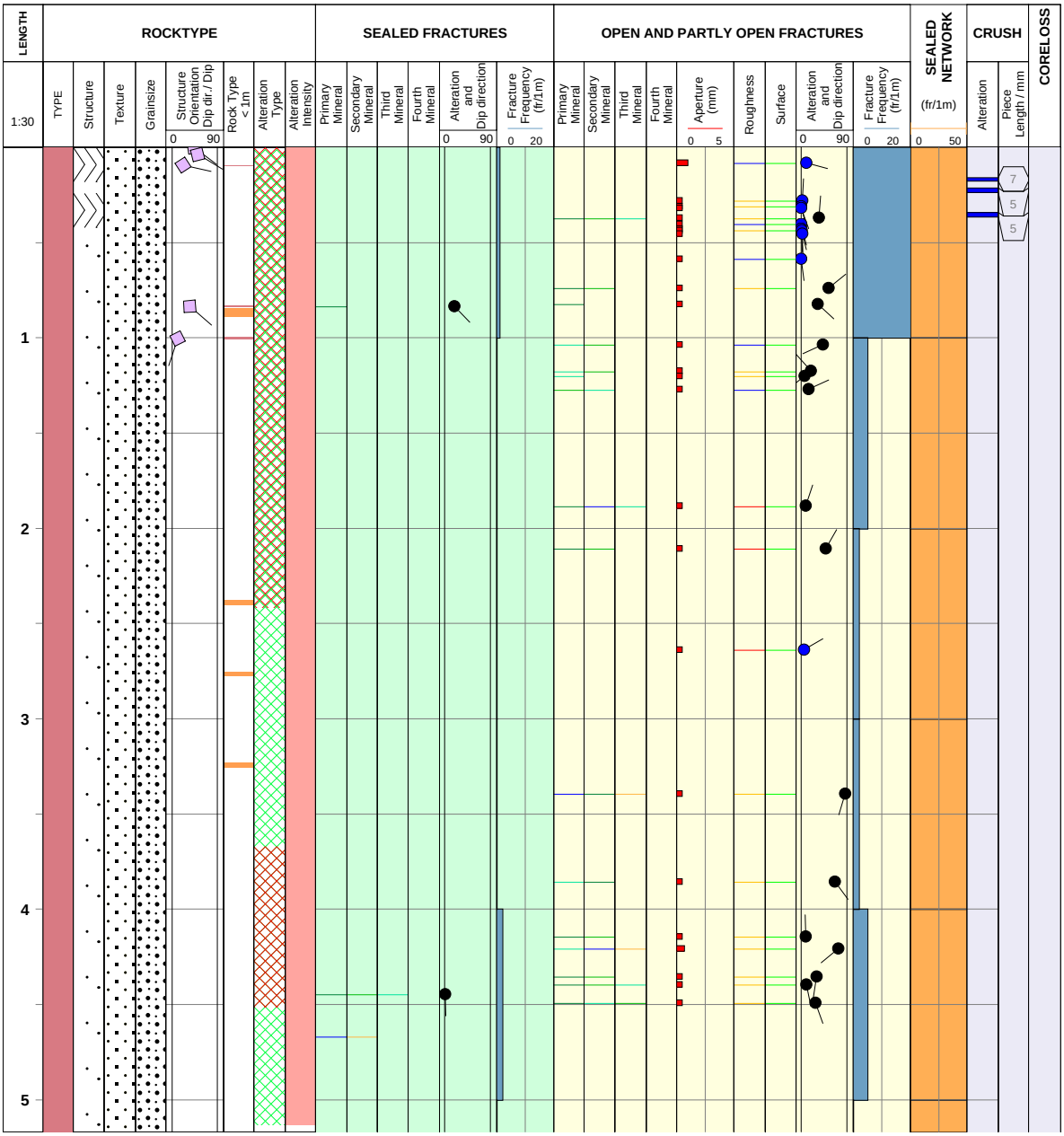

Title GEOLOGY IN KQ0048G05

Site	ÄSPÖ	**Coordinate System**	ÄSPÖ96
Borehole	KQ0048G05	**Northing [m]**	7308.24
Diameter [mm]	161	**Easting [m]**	2115.85
Length [m]	5.240	**Elevation [m.a.s.l.]**	-446.29
Bearing [°]	254.55	**Drilling Start Date**	2008-04-07 13:00:00
Inclination [°]	-89.83	**Drilling Stop Date**	2008-04-07 19:30:00
Date of coremapping	2008-06-19 14:55:00	**Plot Date**	2010-02-08 23:01:11
Rocktype data from	p_rock	**Signed data**	2010-02-09

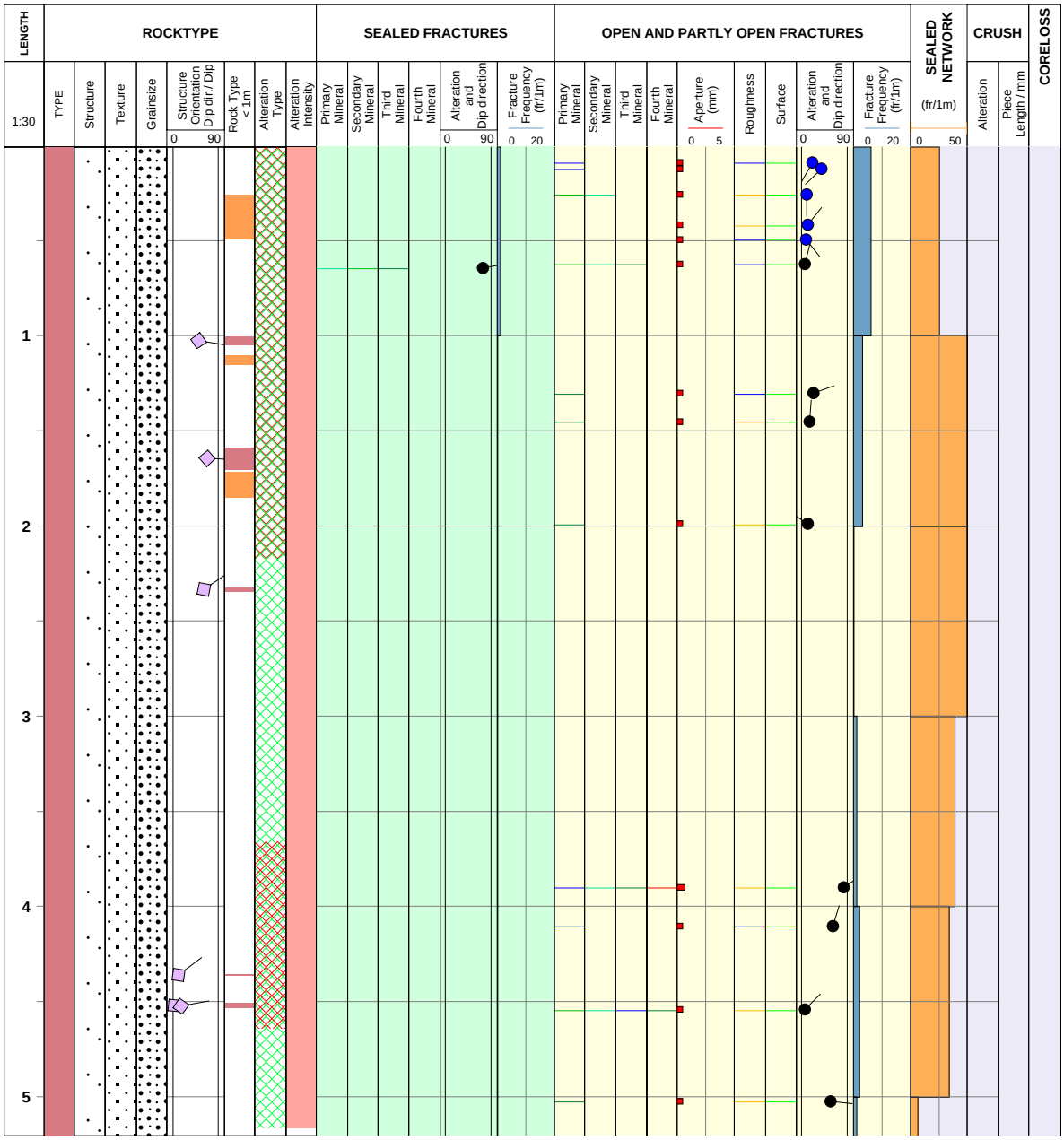

Title GEOLOGY IN KQ0051G04

Site	ÄSPÖ	**Coordinate System**	ÄSPÖ96
Borehole	KQ0051G04	**Northing [m]**	7311.40
Diameter [mm]	161	**Easting [m]**	2117.39
Length [m]	5.430	**Elevation [m.a.s.l.]**	-446.13
Bearing [°]	195.49	**Drilling Start Date**	2008-04-08 11:30:00
Inclination [°]	-89.69	**Drilling Stop Date**	2008-04-08 19:30:00
Date of coremapping	2008-06-18 08:50:00	**Plot Date**	2010-02-09 23:01:19
Rocktype data from	p_rock	**Signed data**	2010-02-09

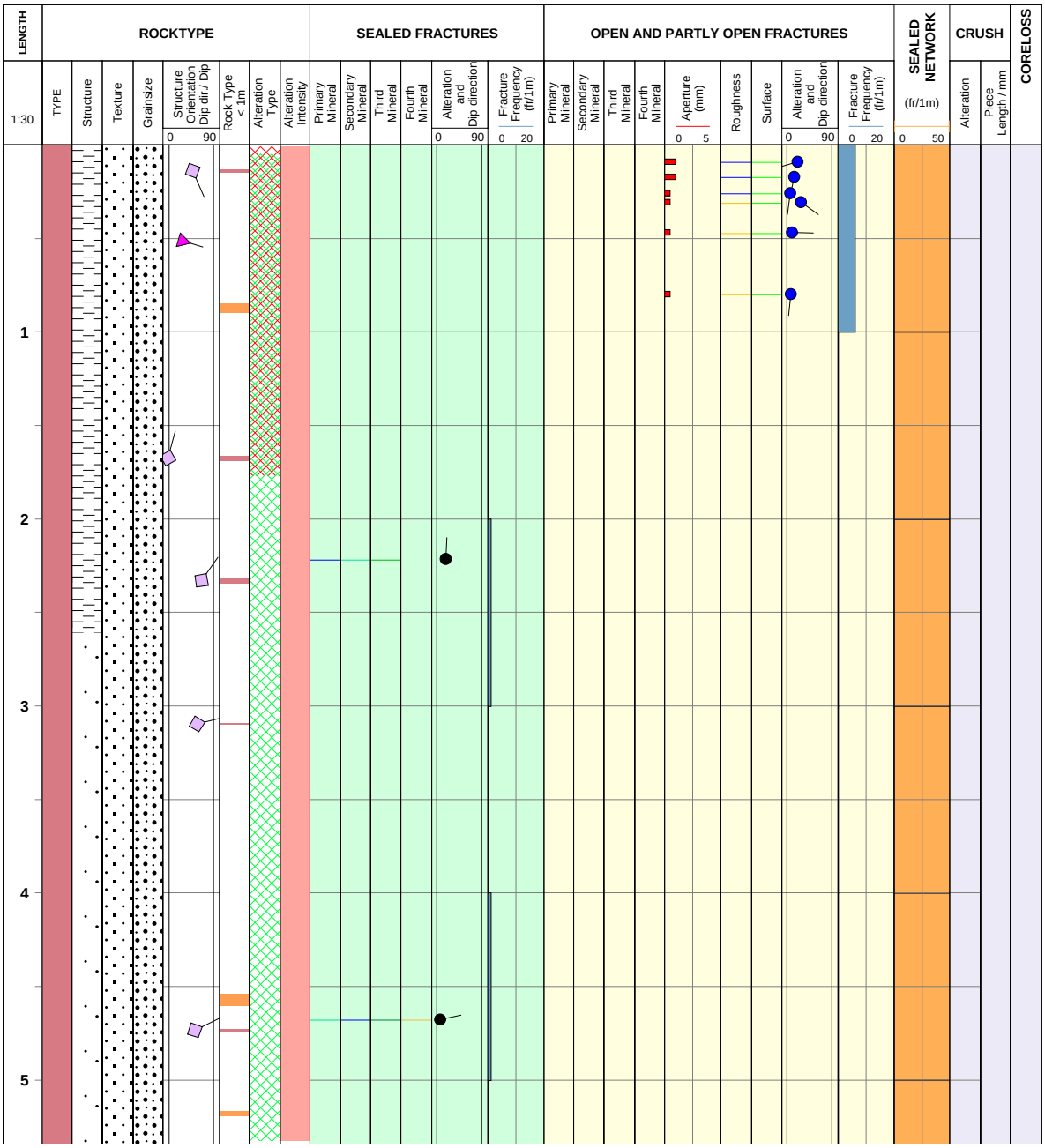

Title GEOLOGY IN KQ0051G05

Site	ÄSPÖ	**Coordinate System**	ÄSPÖ96
Borehole	KQ0051G05	**Northing [m]**	7310.56
Diameter [mm]	161	**Easting [m]**	2118.25
Length [m]	5.400	**Elevation [m.a.s.l.]**	-446.22
Bearing [°]	43.66	**Drilling Start Date**	2008-04-09 11:30:00
Inclination [°]	-89.82	**Drilling Stop Date**	2008-04-09 18:30:00
Date of coremapping	2008-06-04 15:01:00	**Plot Date**	2010-02-09 23:01:19
Rocktype data from	p_rock	**Signed data**	2010-02-09

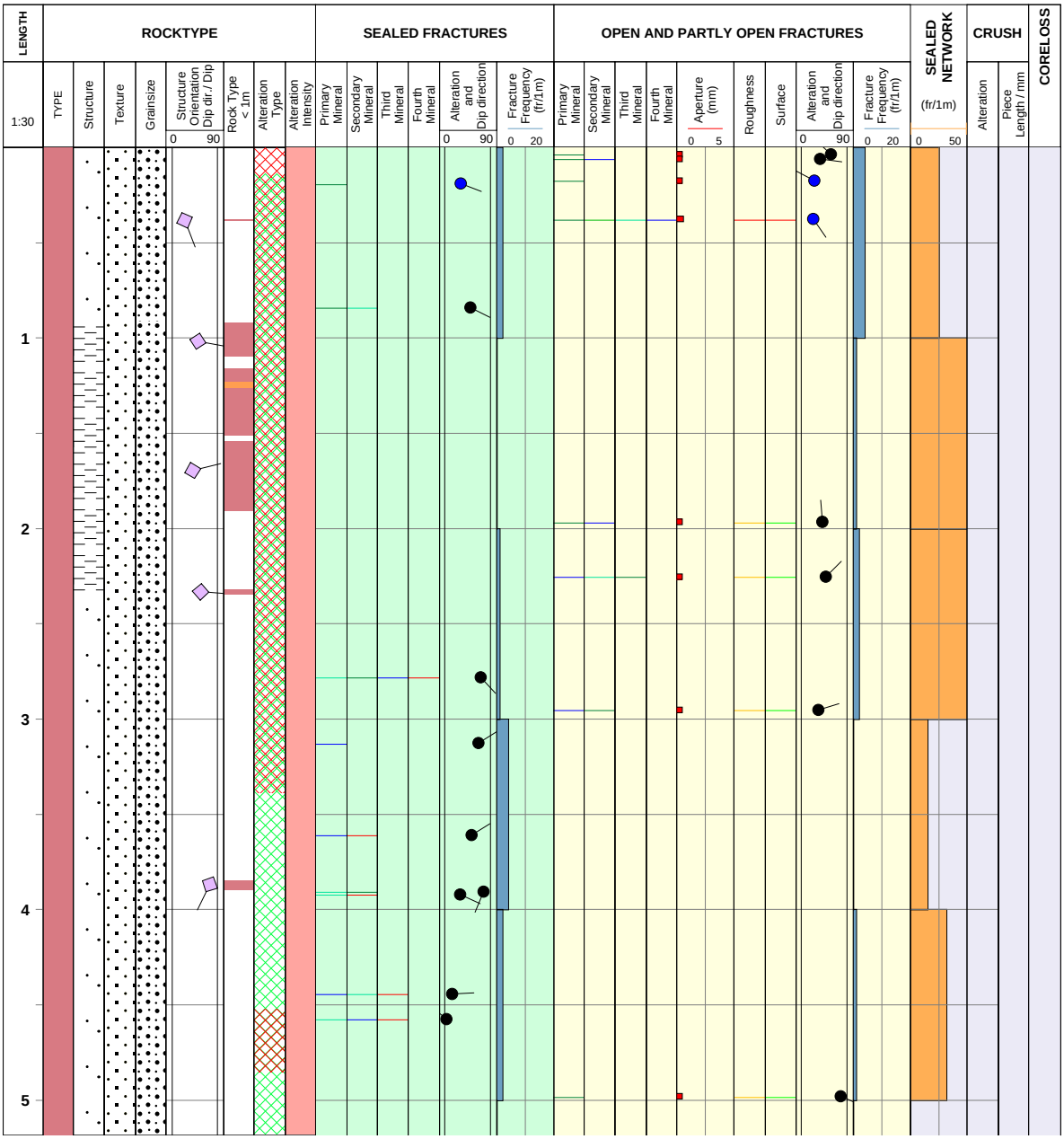

Title GEOLOGY IN KQ0054G03

Site	ÄSPÖ	**Coordinate System**	ÄSPÖ96
Borehole	KQ0054G03	**Northing [m]**	7313.01
Diameter [mm]	162	**Easting [m]**	2119.05
Length [m]	5.330	**Elevation [m.a.s.l.]**	-446.20
Bearing [°]	282.90	**Drilling Start Date**	2008-03-19 10:00:00
Inclination [°]	-89.73	**Drilling Stop Date**	2008-03-20 08:30:00
Date of coremapping	2008-06-23 12:40:00	**Plot Date**	2010-02-08 23:01:11
Rocktype data from	p_rock	**Signed data**	2010-02-09

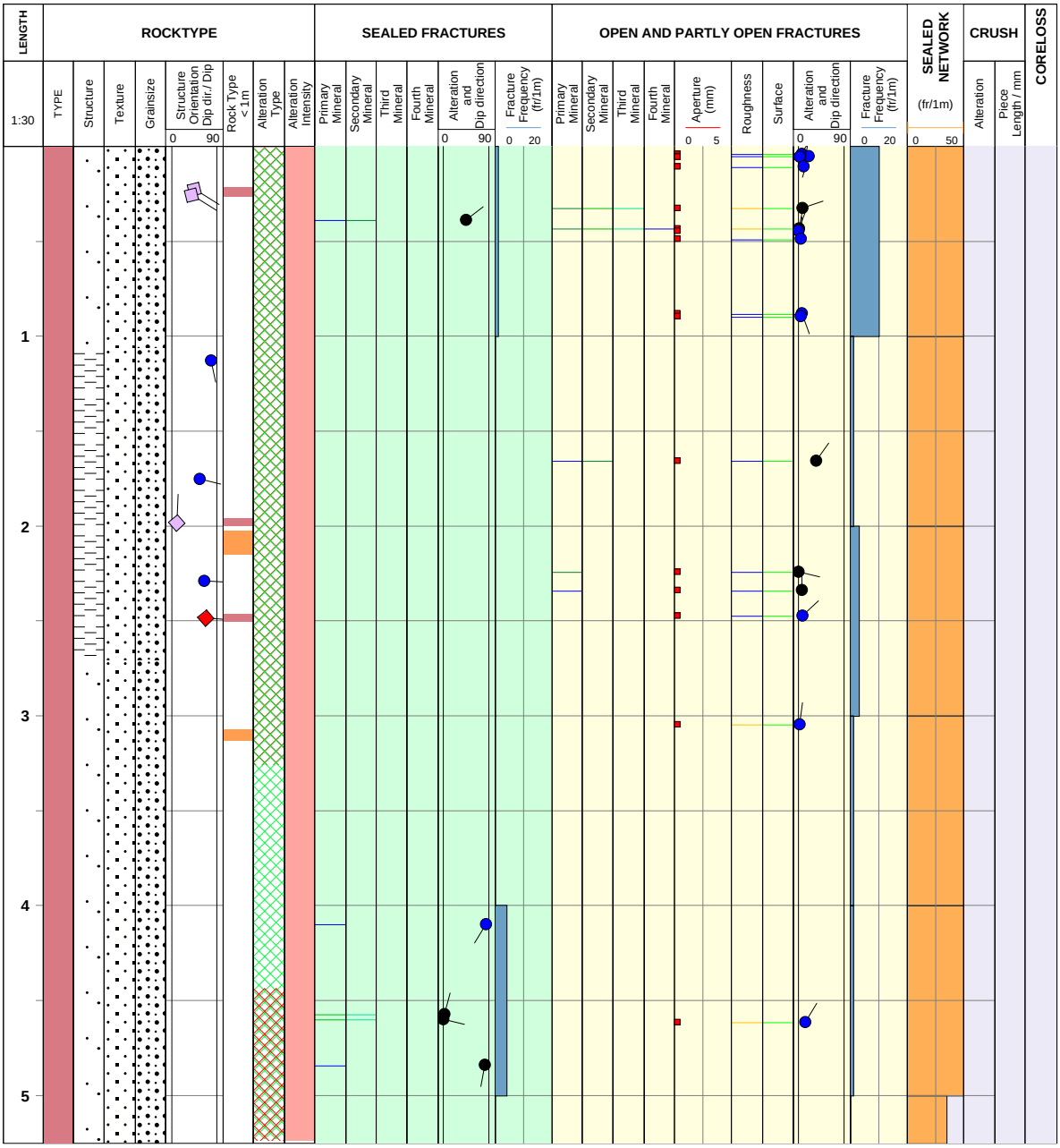

Title GEOLOGY IN KQ0054G04

Site	ÄSPÖ	**Coordinate System**	ÄSPÖ96
Borehole	KQ0054G04	**Northing [m]**	7312.15
Diameter [mm]	162	**Easting [m]**	2119.90
Length [m]	5.140	**Elevation [m.a.s.l.]**	-446.41
Bearing [°]	176.71	**Drilling Start Date**	2008-03-12 11:30:00
Inclination [°]	-89.81	**Drilling Stop Date**	2008-03-13 11:30:00
Date of coremapping	2008-06-23 16:19:00	**Plot Date**	2010-02-08 23:01:11
Rocktype data from	p_rock	**Signed data**	2010-02-09

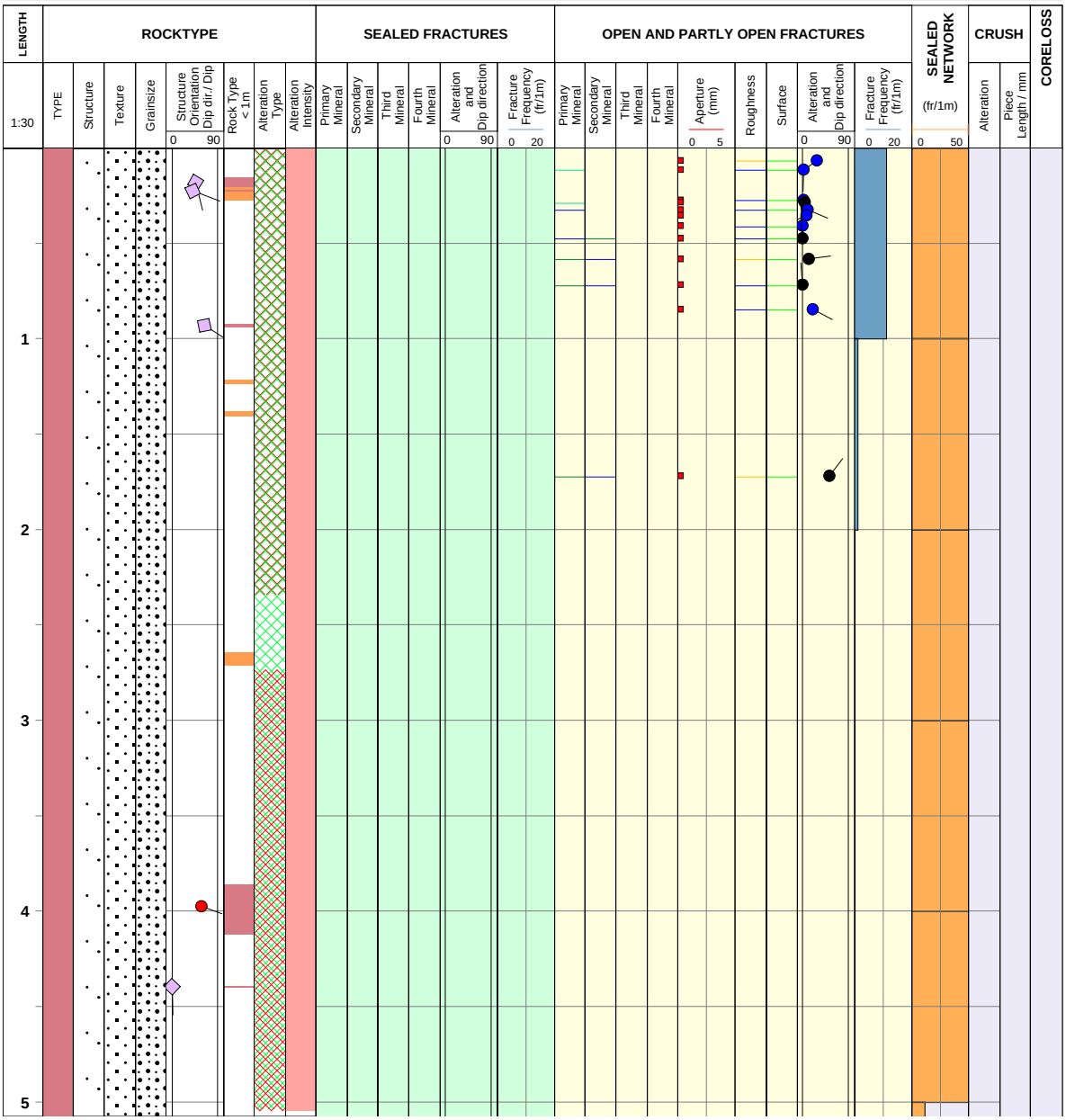

Appendix B

Visualisation of the geological data

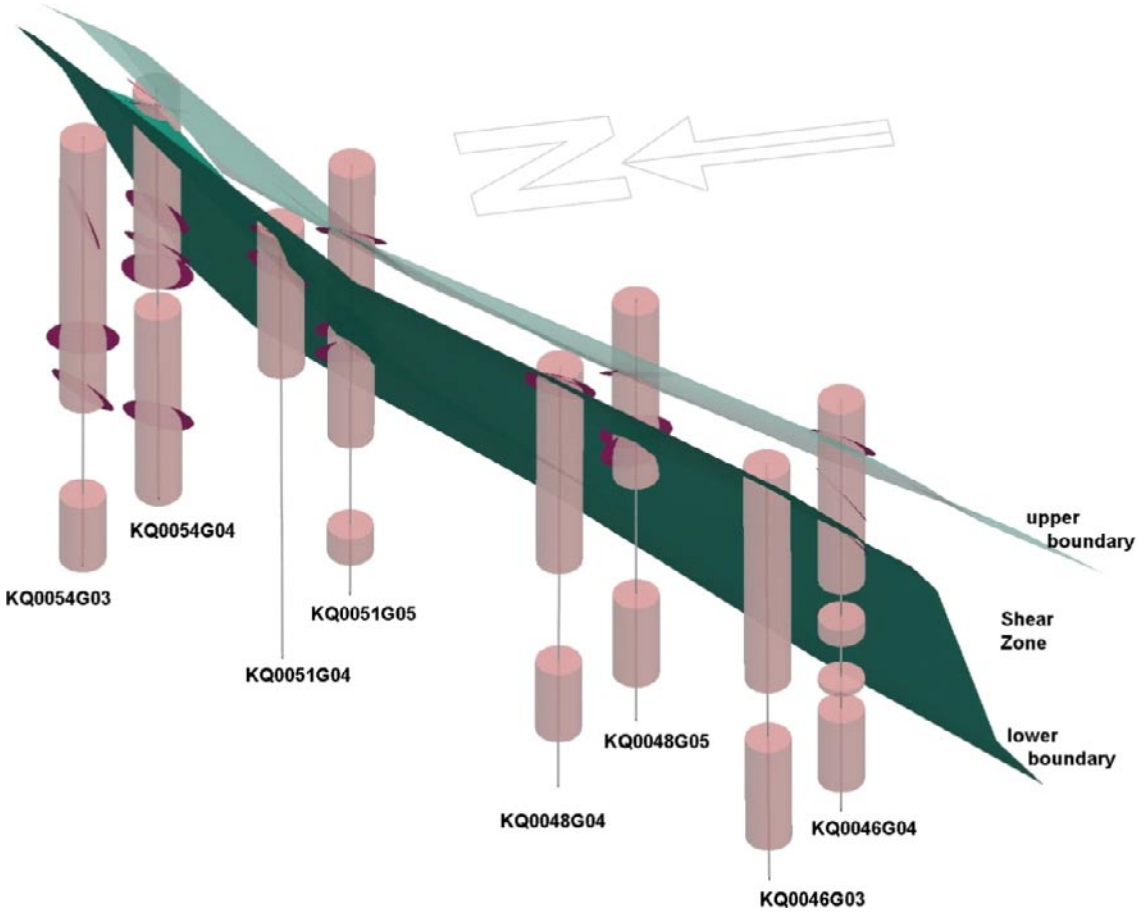

Figure B-1. *Isometric view, looking down to the east, of the heating holes. Sections logged with oxidation in pink and the outline of the shear zone running through the investigation area. In the northeastern part the shear zone splay downwards.*

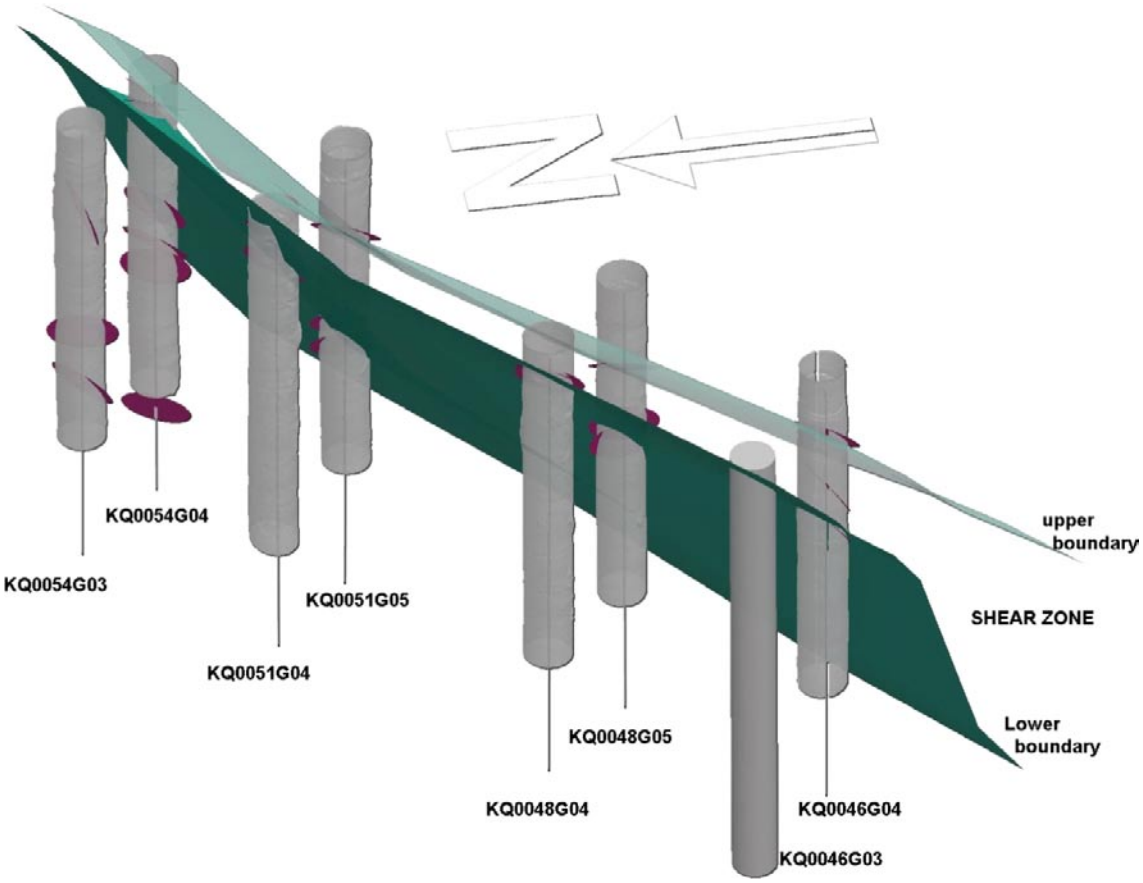

Figure B-2. *Isometric view, looking down to the east, of the heating holes. Laser scanned mesh is visualized as grey mesh in the boreholes (no mesh has been produced for KQ0046G03) and also the outline of the shear zone running through the investigation area. In the northeastern part the shear zone splay downwards.*

In the following images the breakouts are visualized on both sides of the heating holes; darker blue color on the southwest side and lighter blue on the northeast side. NE and SW denote view towards the northeast and southwest, respectively.

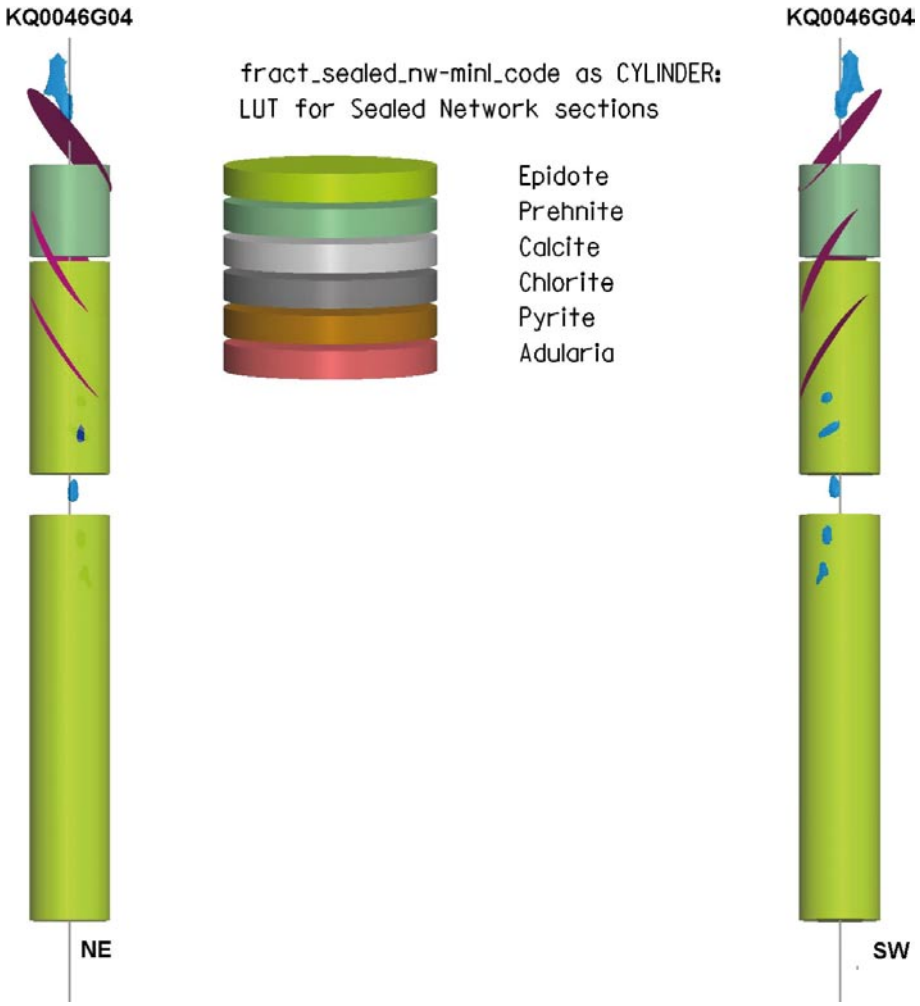

Figure B-3. *Visualization of breakouts (light bluish) together with sections of Sealed Networks in KQ0046G04, visualized as the primary mineral sealing of the fractures in the network. Also visualized is the upper and lower boundary of the shear zone and its internal foliation (reddish disks). NE and SW denote view direction towards the northeast and the southwest, respectively.*

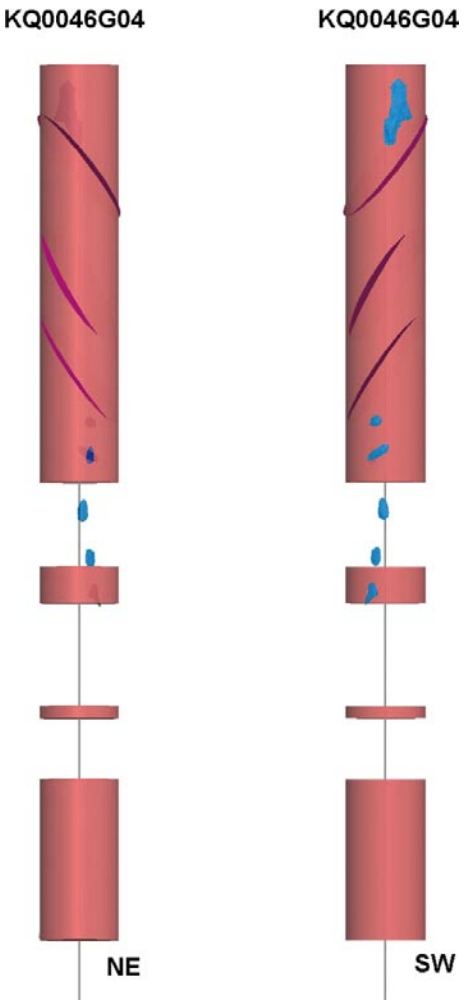

Figure B-4. *Visualization of breakouts (light bluish) together with sections of oxidation in KQ0046G04. Also visualized is the upper and lower boundary of the shear zone and its internal foliation (reddish disks). NE and SW denote view direction towards the northeast and the southwest, respectively.*

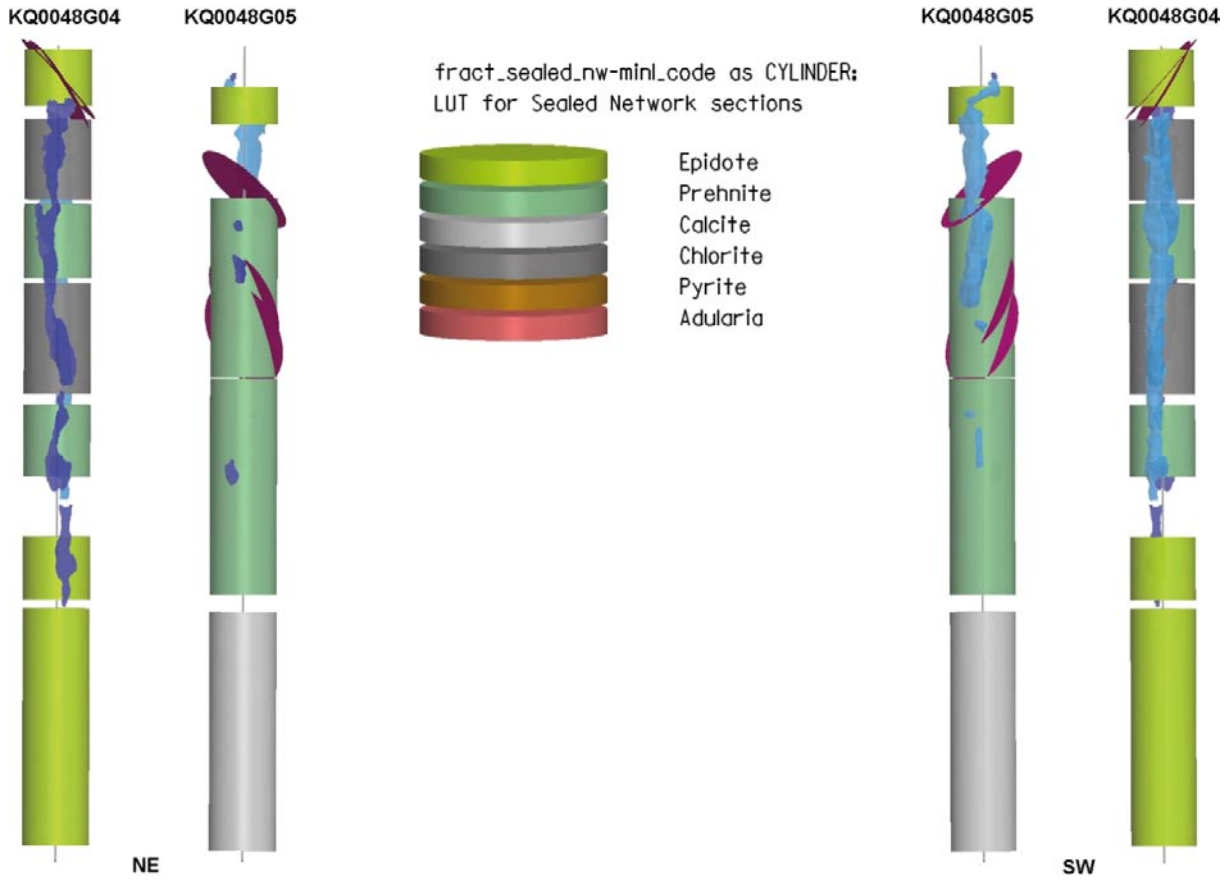

Figure B-5. *Visualization of breakouts (light bluish) together with sections of Sealed Networks in KQ0048G04 and -G05, visualized as the primary mineral sealing of the fractures in the network. Also visualized is the upper and lower boundary of the shear zone and its internal foliation (reddish disks). NE and SW denote view direction towards the northeast and the southwest, respectively.*

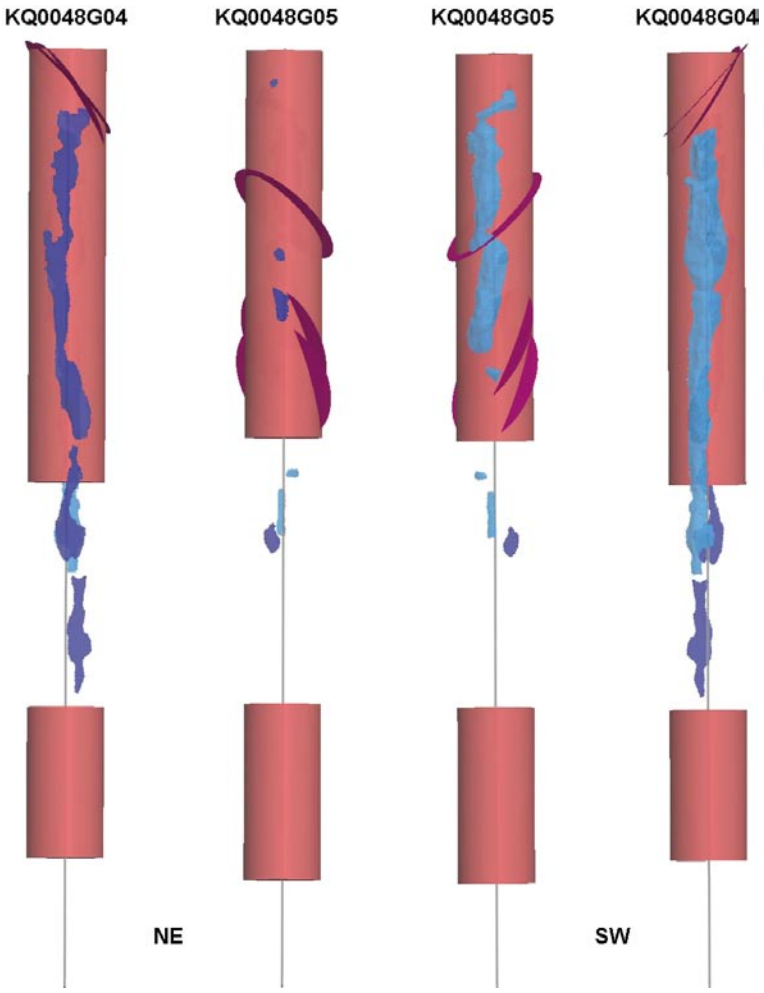

Figure B-6. *Visualization of breakouts (light bluish) together with sections of oxidation in KQ0048G04 and -G05. Also visualized is the upper and lower boundary of the shear zone and its internal foliation (reddish disks). NE and SW denote view direction towards the northeast and the southwest, respectively.*

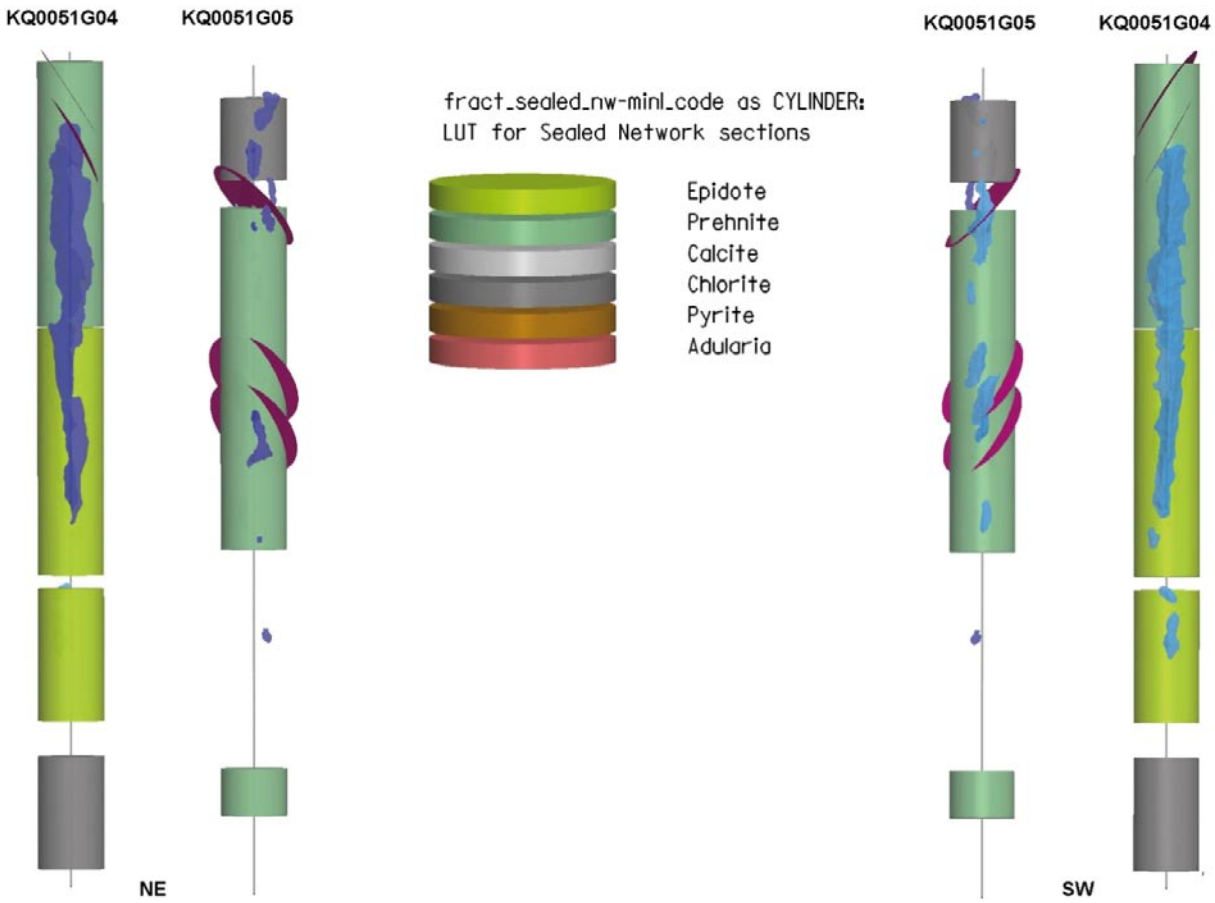

Figure B-7. *Visualization of breakouts (light bluish) together with sections of Sealed Networks in KQ0051G04 and -G05, visualized as the primary mineral sealing of the fractures in the network. Also visualized is the upper and lower boundary of the shear zone and its internal foliation (reddish disks). NE and SW denote view direction towards the northeast and the southwest, respectively.*

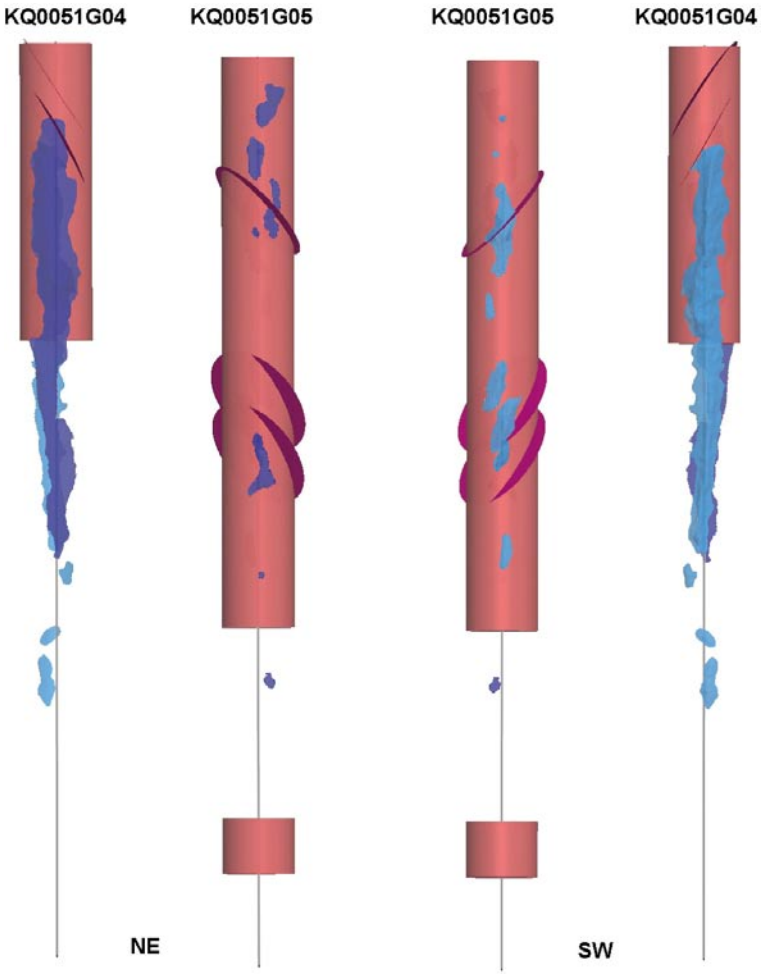

Figure B-8. *Visualization of breakouts (light bluish) together with sections of oxidation in KQ0051G04 and -G05. Also visualized is the upper and lower boundary of the shear zone and its internal foliation (reddish disks). NE and SW denote view direction towards the northeast and the southwest, respectively.*

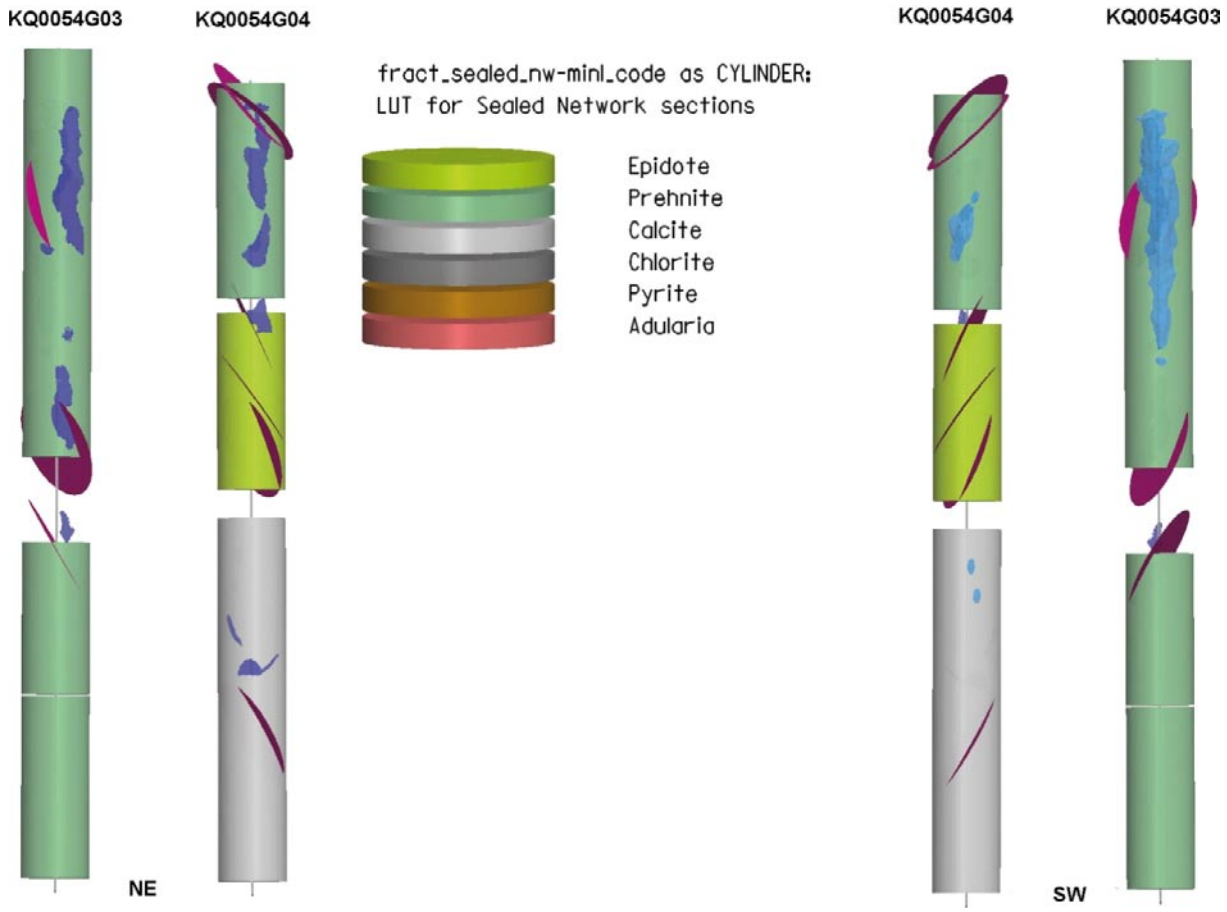

Figure B-9. *Visualization of breakouts (light bluish) together with sections of Sealed Networks in KQ0054G03 and -G04, visualized as the primary mineral sealing of the fractures in the network. Also visualized is the upper and lower boundary of the shear zone and its internal foliation (reddish disks).The zone here only affect the upper part of KQ0054G04, but in this part of the tunnel several less extensive offsets of the zone exists (not visualized) below the major zone. NE and SW denote view direction towards the northeast and the southwest, respectively.*

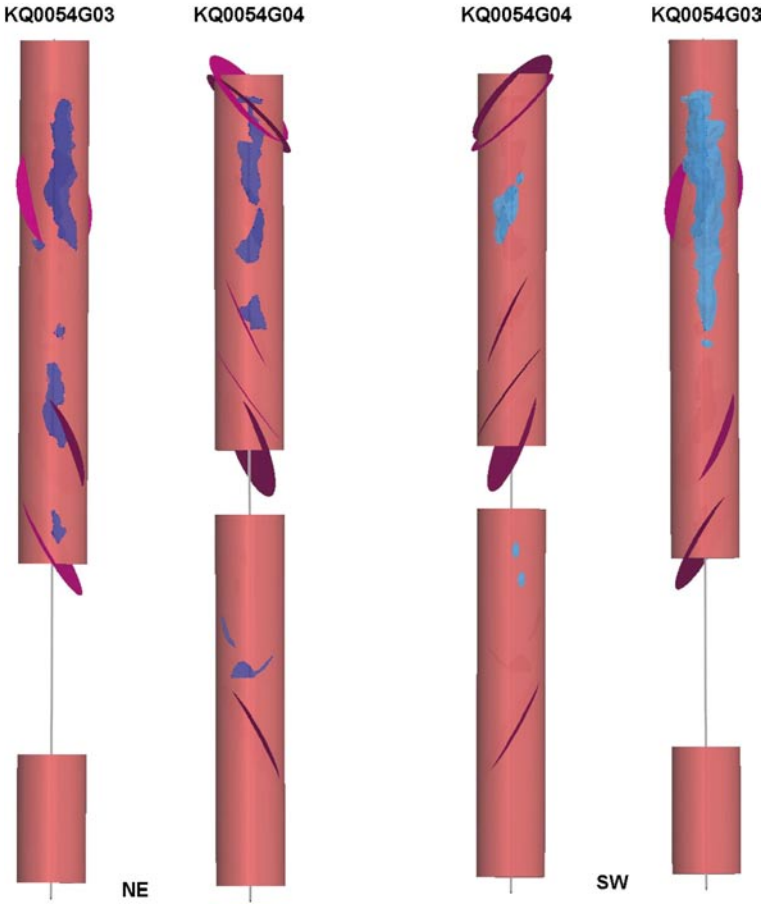

Figure B-10. *Visualization of breakouts (light bluish) together with sections of oxidation in KQ0051G03 and -G04. Also visualized is the upper and lower boundary of the shear zone and its internal foliation (reddish disks). NE and SW denote view direction towards the northeast and the southwest, respectively.*

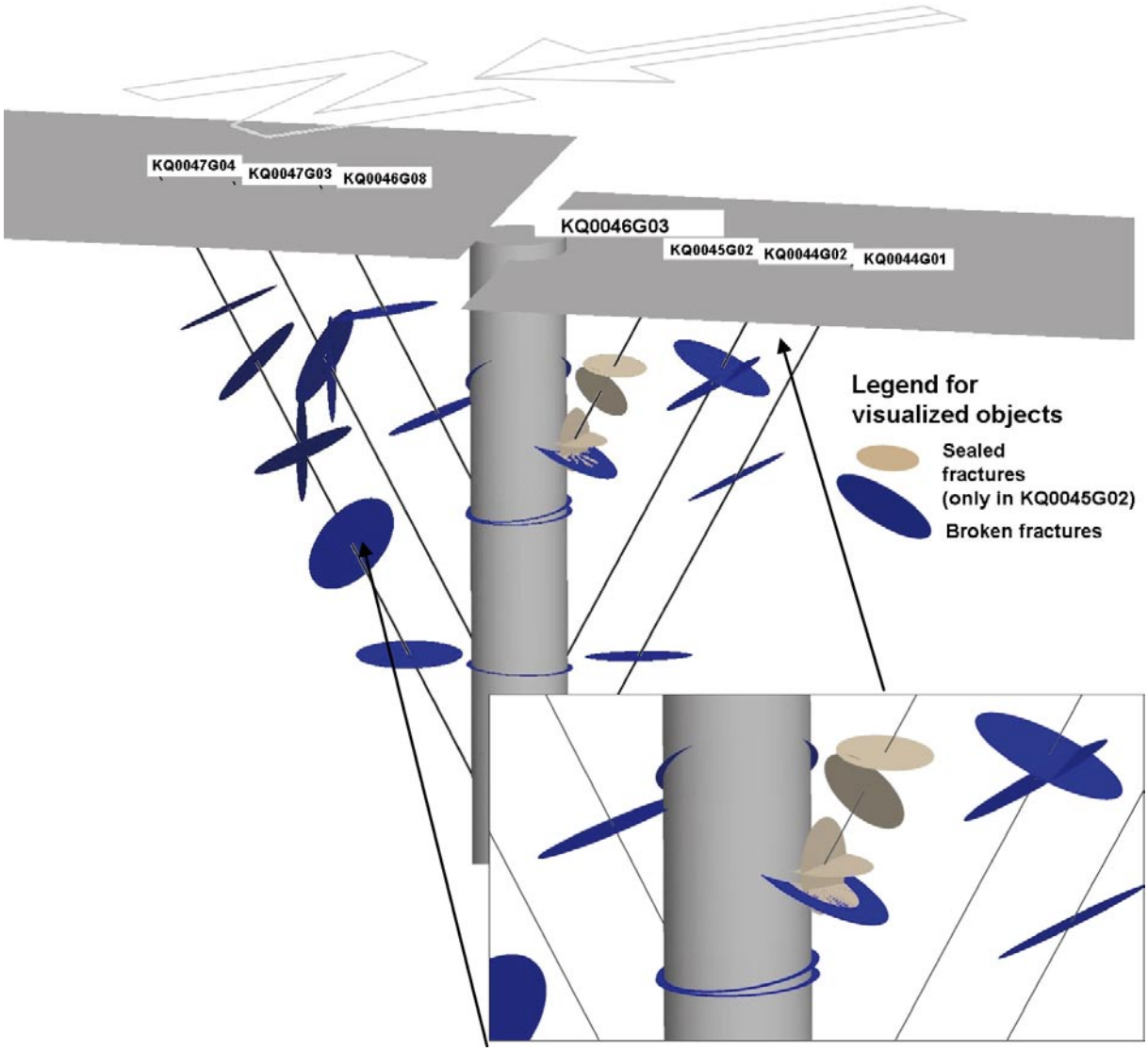

Figure B-11. *Visualization of broken fractures in the boreholes intersecting heating hole KQ0046G03, which were used in the water injection tests.*

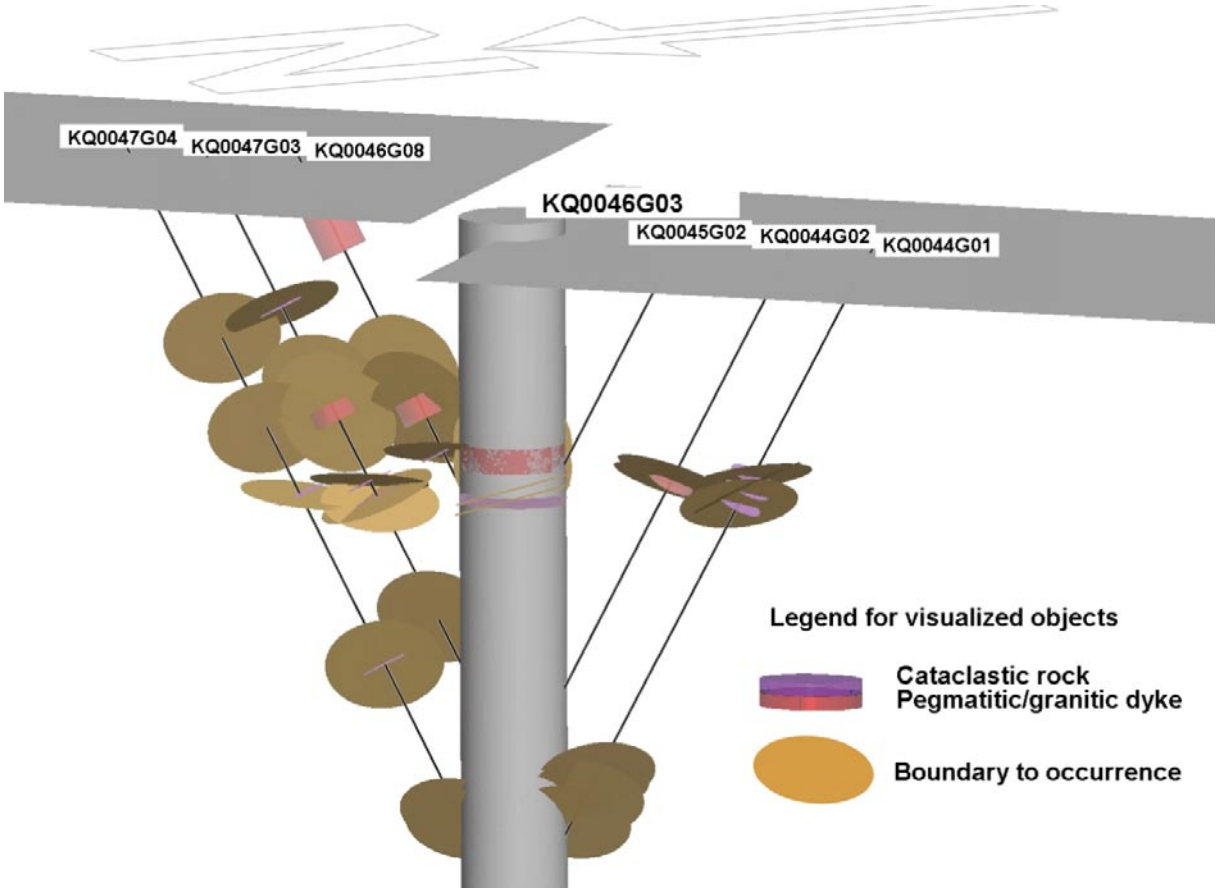

Figure B-12. *Visualization of dykes in boreholes intersecting heating hole KQ0046G03, which were used in the water injection tests.*

Results from uniaxial compression tests on intact rock

Lars Jacobsson, SP Technical Research Institute of Sweden

March 2010

CAPS project

TASQ Tunnel

Uniaxial compression test of intact rock

Lars Jacobsson, SP Technical Research Institute of Sweden, Borås, Sweden

March 2010

Keywords: Rock mechanics, Uniaxial compression test, Elasticity parameters, Stress-strain curve, Crack initiation stress, PM Doc ID 1181445.

Abstract

Uniaxial compression tests with loading up to and just passing compressive failure were carried out on 10 water saturated specimens of intact rock from the TASQ-tunnel at the Äspö HRL. The sampled rock type was Äspö diorite. The cylindrical specimens were taken from drill cores ranging between 0.2–5.8 m borehole length. The elastic properties, represented by Young's modulus and the Poisson ratio, the crack initiation stress and the uniaxial compressive strength were deduced from these tests. The wet density of the specimens was determined before the mechanical tests. The specimens were photographed before as well as after the mechanical testing.

The measured densities for the water saturated specimens were in the range 2,710–2,780 kg/m^3 yielding a mean value of 2,742 kg/m^3. The crack initiation stresses were in the range 84.9–152.5 MPa and the peak values of the axial compressive stress were in the range 170.5–293.6 MPa. The elastic parameters were determined at a load corresponding to 50% of the failure load, and it was found that Young's modulus was in the range 70.8–77.9 GPa and that the Poisson ratio was in the range of 0.22–0.32.

Sammanfattning

Enaxiella kompressionsprov med belastning upp till brott och strax efter brott har genomförts på 10 stycken vattenmättade cylindriska provobjekt av intakt berg från TASQ-tunneln i Äspö HRL. Bergarten hos proverna var Äspö diorit. Proverna har tagits vid en borrhålslängd som låg mellan 0,2–5,8 m. De elastiska egenskaperna, representerade av elasticitetsmodulen och Poissons tal, har bestämts ur försöken. Bergmaterialets densitet i vått tillstånd hos proverna mättes upp före de mekaniska proven. Provobjekten fotograferades såväl före som efter de mekaniska proven.

Den uppmätta densiteten hos de vattenmättade proven uppgick till mellan 2 710–2 780 kg/m^3 med ett medelvärde på 2 742 kg/m^3. De uppmätta sprickinitieringsspänningarna var mellan 84,9–152,5 MPa och toppvärdena för den kompressiva axiella spänningen låg mellan 170,5–293,6 MPa. De elastiska parametrarna bestämdes vid en last motsvarande 50 % av högsta värdet på lasten, vilket gav en elasticitetsmodul mellan 70,8–77,9 GPa och Poissons tal mellan 0,22–0,32.

Contents

C1 Introduction

This document reports performance and results of uniaxial compression tests, with loading just beyond the failure point, on water-saturated drill core specimens sampled from the boreholes KQ0046G02, KQ0048G02, KQ0051G01, KQ0054G01, KQ0054G02, KQ0054G05 and KQ0054G06 at the TASQ tunnel at Äspö HRL. The tests were carried out in the material and rock mechanics laboratories at the Department of Building Technology and Mechanics at the Technical Research Institute of Sweden (SP). The activity is part of the investigation of the TASQ tunnel at Äspö HRL managed by SKB (The Swedish Nuclear Fuel and Waste Management Company).

The controlling documents for the activity are listed in Table C-1. Both PM and Method Descriptions are SKB's internal controlling documents, whereas the Quality Plan referred to in the table is an SP internal controlling document.

The rock type in the cores was Äspö diorite. (Rock type code 501037.)

SKB supplied SP with rock cores which arrived at SP in October 2008 and were tested during November 2008. Cylindrical specimens were cut from the cores and selected based on the preliminary core logging with the strategy to investigate the deformation properties of the sealed fracture network in the transition area of the deformation zones in the rock mass. The method description SKB MD 190.001 was followed both for sampling and for the uniaxial compression tests, whereas the density determinations were performed in compliance with method description SKB MD 160.002.

As to the specimen preparation, the end surfaces of the specimens were grinded in order to comply with the required shape tolerances. The specimens were put in water and kept stored in water for a minimum of 7 days, up to density determination and uniaxial testing. This yields a water saturation, which is intended to resemble the in situ moisture condition. The density was determined on each specimen and the uniaxial compression tests were carried out at this moisture condition. The specimens were photographed before and after the mechanical testing.

The uniaxial compression tests were carried out using radial strain as the feed-back signal as described in the method description SKB MD 190.001 and in the ISRM suggested method /1/. The axial ε_a and radial strain ε_r together with the axial stress σ_a were recorded during the test. The crack initiation stress σ_{ci} and the peak value of the axial compressive stress σ_c were determined at each test. Furthermore, two elasticity parameters, Young's modulus E and Poisson ratio ν, were deduced from the tangent properties at 50% of the peak load. Diagrams with the volumetric and crack volumetric strain versus axial stress are reported.

Table C-1. Controlling documents for performance of the activity.

PM	**Number**	**Version**
CAPS Provtagning av borrkärnor	1181445	1.0
Method Description	**Number**	**Version**
Uniaxial compression test for intact rock	SKB MD 190.001	3.0
Determining density and porosity of intact rock	SKB MD 160.002	2.0
Quality Plan		
SP-QD 13.1		

C2 Objective

The purpose of the testing is to obtain a good knowledge of the deformation and strength properties of the Äspö diorite at the tunnel location where the CAPS field experimens were carried out as earlier investigations have shown that the strength properties of Äspö diorite has a large scatter in general. The results in this investigation can be viewed as a complement to the other experiments conducted in another part of the tunnel before the APSE field experiments.

The elastic properties, represented by Young's modulus and the Poisson ratio as well as the crack initiation stress and the uniaxial compressive strength were determined on cylindrical specimens sampled from drill cores. Moreover, the specimens had a water content corresponding to the in situ conditions.

C3 Equipment

C3.1 Specimen preparation and density measurement

A circular saw with a diamond blade was used to cut the specimens to their final lengths. The surfaces were then grinded after cutting in a grinding machine in order to achieve a high-quality surface for the axial loading that complies with the required tolerances. The measurements of the specimen dimensions were made with a sliding calliper. Furthermore, the tolerances were checked by means of a dial indicator and a stone face plate. The specimen preparation is carried out in accordance with ASTM 4543-01 /2/.

The specimens and the water were weighed using a scale for weight measurements. A thermometer was used for the water temperature measurement. The calculated wet density was determined with an uncertainty of ± 4 kg/m^3.

C3.2 Mechanical testing

The mechanical tests were carried out in a servo controlled testing machine specially designed for rock tests, see Figure C-1. The system consists of a load frame, a hydraulic pump unit, a controller unit and various sensors. The communication with the controller unit is accomplished by means of special testing software run on a PC connected to the controller. The load frame is characterized by a high stiffness and is supplied with a fast responding actuator, cf the ISRM suggested method /1/.

The stiffness of the various components of the loading chain in the load frame has been optimized in order to obtain a high total stiffness. This includes the load frame, load cell, load platens and piston, as well as having a minimum amount of hydraulic oil in the cylinder. Furthermore, the sensors, the controller and the servo valve are rapidly responding components. The axial load is determined using a load cell, which has a maximum capacity of 1.5 MN. The uncertainty of the load measurement is less than 1%.

The axial and circumferential (radial) deformations of the rock specimens were measured. The rock deformation measurement systems are based on miniature LVDTs with a measurement range of +/– 2.5 mm. The relative error for the LVDTs is less than 0.6% within a 1 mm range for the axial deformation measurements and less than 1.3% within a 3 mm range for the circumferential deformation measurement. The LVDTs have been calibrated by means of a micrometer.

Two independent systems were used for the axial deformation measurement in order to obtain two comparative results. The first system (S1), see Figure C-2, comprises two aluminium rings attached on the specimen, placed at ¼ and ¾ of the specimen height. Two LVDTs mounted on the rings are used to measure the distance change between the rings on opposite sides of the specimen. As to the attachment, two rubber bands made of a thin rubber hose with 0.5 mm thickness are first mounted on the specimen right under where the two rings are to be positioned. The rings are supplied with three adjustable spring-loaded screws, each with a rounded tip pointing on the specimen with 120 degrees division. The screw tips are thus pressing on the rubber band, when the rings are mounted. The second system (S2), see Figure C-3, consists of two aluminium plates clamped around the circular loading platens of steel on top and on bottom of the specimen. Two LVDTs, mounted on the plates, measure the distance change between these plates at opposite sides of the specimen at corresponding positions as for the first measurement system (S1).

Figure C-1. *Rock testing system. From left: Digital controller unit, pressure cabinet (used for triaxial tests) and load frame. The PC with the test software (not shown in the picture) is placed on the left hand side of the controller unit.*

The radial deformation was obtained by using a chain mounted around the specimen at mid-height, see Figures C-2 and C-3. The change of the chain-opening gap was measured by means of one LVDT and the circumferential, and thereby also the radial deformation could be obtained. See Appendix AC1.

The specimens were photographed with a 4.0 Mega pixel digital camera at highest resolution and the photographs were stored in a jpeg-format.

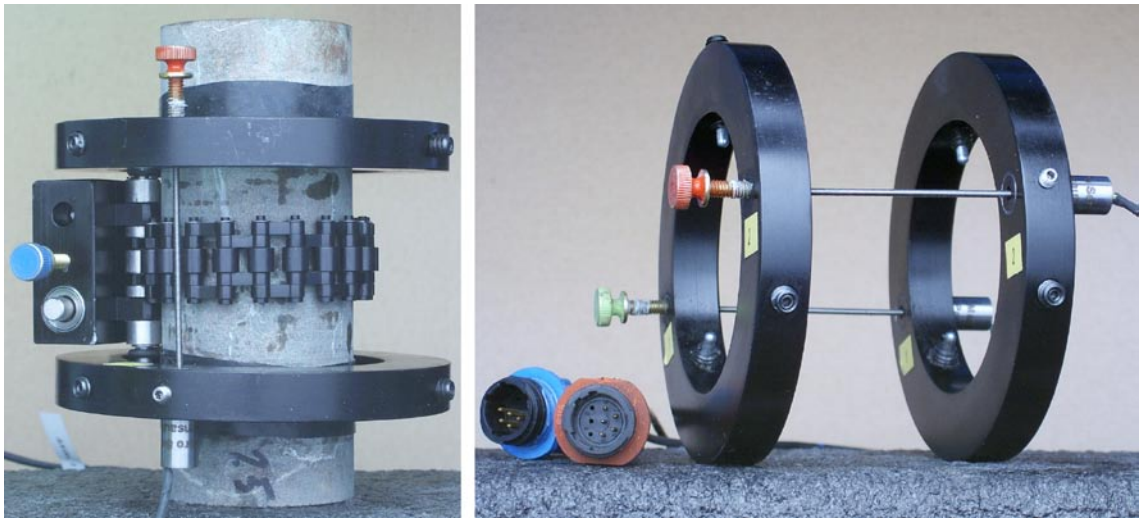

Figure C-2. *Left: Specimen with two rubber bands. Devices for local axial and circumferential deformation measurements attached on the specimen. Right: Rings and LVDTs for local axial deformation measurement.*

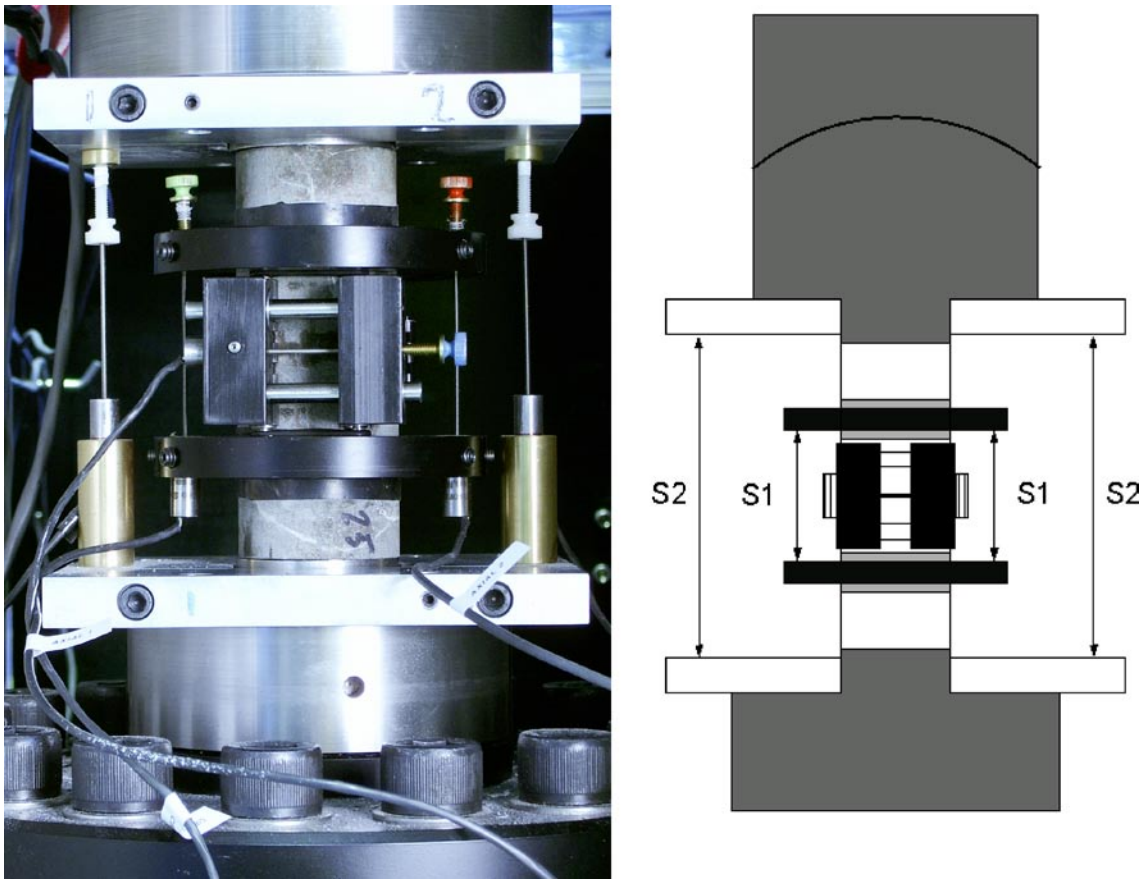

Figure C-3. *Left: Specimen inserted between the loading platens. The two separate axial deformation measurement devices can be seen: system (S1) that measures the local axial deformation (rings), and system (S2) that measures the deformation between the aluminium plates (total deformation). Right: Principal sketch showing the two systems used for the axial deformation measurements.*

C4 Execution

The water saturation and determination of the density of the wet specimens were made in accordance with the method description SKB MD 160.002 (SKB internal controlling document). This includes determination of density in accordance to ISRM /3/ and water saturation by SS EN 13755 /4/.
The uniaxial compression tests were carried out in compliance with the method description SKB MD 190.001 (SKB internal controlling document). The test method is based on ISRM suggested method /1/.

C4.1 Description of the specimens

The rock type characterization was made according to Stråhle /5/ using the SKB mapping system (Boremap). The identification marks, upper and lower sampling depth (Secup and Seclow) and the rock type are shown in Table C-2.

C4.2 Specimen preparation and density measurement

The temperature of the water was 16.1°C, which equals to a water density of 998.9 kg/m^3, when the determination of the wet density of the rock specimens was carried out. Further, the specimens had been stored during 7 days in water when the density was determined.

An overview of the activities during the specimen preparation is shown in the step-by step description in Table C-3.

Table C-2. Specimen identification, sampling level (borehole length) and rock type for all specimens (based on the Boremap).

Identification	Adj Secup (m)	Adj Seclow (m)	Rock type
KQ0046G02-113-02	5.07	5.22	Äspö diorite
KQ0046G02-113-03	5.22	5.37	Äspö diorite
KQ0046G02-113-04	5.37	5.52	Äspö diorite
KQ0046G05-113-01	5.50	5.65	Äspö diorite
KQ0048G02-113-01	3.345	3.495	Äspö diorite
KQ0048G02-113-02	3.495	3.645	Äspö diorite
KQ0051G01-113-01	4.27	4.42	Äspö diorite
KQ0054G01-113-02	5.75	5.89	Äspö diorite
KQ0054G02-113-01	4.09	4.24	Äspö diorite
KQ0054G06-113-01	0.08	0.23	Äspö diorite

Table C-3. Activities during the specimen preparation.

Step	Activity
1	The drill cores were marked where the specimens are to be taken.
2	The specimens were cut to the specified length according to markings and the cutting surfaces were grinded.
3	The tolerances were checked: parallel and perpendicular end surfaces, smooth and straight circumferential surface.
4	The diameter and height were measured three times each. The respective mean value determines the dimensions that are reported.
5	The specimens were then water saturated according to the method described in SKB MD 160.002 and were stored for minimum 7 days in water, whereupon the wet density was determined.

C4.3 Mechanical testing

The specimens had been stored 21–24 days in water when the uniaxial compression tests were carried out. The functionality of the testing system was checked before starting the tests. A check-list was filled in successively during the work in order to confirm that the different specified steps had been carried out. Moreover, comments were made upon observations made during the mechanical testing that are relevant for interpretation of the results. The check-list form is an SP internal quality document.

An overview of the activities during the mechanical testing is shown in the step-by step description in Table C-4.

Table C-4. Activities during the mechanical testing.

Step	Activity
1	Digital photos were taken on each specimen before the mechanical testing.
2	Devices for measuring axial and circumferential deformations were attached to the specimen.
3	The specimen was put in place and centred between the frame loading platens.
4	The core on each LVDT was adjusted by means of a set screw to the right initial position. This was done so that the optimal range of the LVDTs can be used for the deformation measurement.
5	The frame piston was brought down into contact with the specimen with a force corresponding to 1.0 MPa axial stress.
6	A load cycle with loading up to 5 MPa and unloading to 1.0 MPa was conducted in order to settle possible contact gaps in the spherical seat in the piston and between the rock specimen and the loading platens.
7	The centring was checked again.
8	The deformation measurement channels were zeroed in the test software.
9	The loading was started and the loading rate was set to a radial strain rate of –0.025%/min.
10	The test was manually stopped shortly after the peak load had been reached.
11	Digital photos were taken on each specimen after the mechanical testing.

C4.4 Data handling

The test results were exported as text files from the test software and stored in a file server on the SP computer network after each completed test. The main data processing, in which the elastic moduli were computed and the crack initiation and peak stresses were determined, has been carried out using the program MATLAB /6/. Moreover, MATLAB was used to produce the diagrams shown in Section C5.1 and in Appendix AC2. The summary of results in Section C5.2 with tables containing mean value and standard deviation of the different parameters and diagrams were provided using MS Excel. MS Excel was also used for reporting data to the Sicada database.

C4.5 Analyses and interpretation

As to the definition of the different results parameters we begin with the axial stress σ_a, which is defined as

$$\sigma_a = \frac{F_a}{A}$$

where F_a is the axial force acting on the specimen, and A is the specimen cross section area. The peak value of the axial stress during a test is representing the uniaxial compressive strength σ_c in the results presentation.

The average value of the two axial displacement measurements on opposite sides of the specimen is used for the axial strain calculation, cf Figure C-3. In the first measurement system (S1), the recorded deformation represents a local axial deformation δ_{local} between the points at ¼ and ¾ height. A local axial strain is defined as

$$\varepsilon_{a,local} = \delta_{local}/L_{local}$$

where L_{local} is the distance between the rings before loading.

In the second measurement system (S2), the recorded displacement corresponds to a total deformation that, in addition to total rock deformation, also contains the local deformations that occur in the contact between the rock and the loading platens, and further it also contains the deformation of the steel loading platens at each side of the specimen ends. The average value of the two total deformation measurements on opposite sides of the specimen is defined as the total deformation δ_{total}. An axial strain based on the total of the deformation is defined as

$$\varepsilon_{a,total} = \delta_{total}/L_{total}$$

where L_{total} is the height of the rock specimen.

The radial deformation is measured by means of a chain mounted around the specimen at mid-height, cf Figures C-2 and C-3. The change of chain opening gap is measured by means of one LVDT. This measurement is used to compute the radial strain ε_r, see Appendix AC1. Moreover, the volumetric strain ε_{vol} is defined as

$$\varepsilon_{vol} = \varepsilon_a + 2\varepsilon_r$$

The stresses and the strains are defined as positive in compressive loading and deformation. The elasticity parameters are defined by the tangent Young's modulus E and tangent Poisson ratio ν as

$$E = \frac{\sigma_a(0.60\sigma_c) - \sigma_a(0.40\sigma_c)}{\varepsilon_a(0.60\sigma_c) - \varepsilon_a(0.40\sigma_c)}$$

$$\nu = -\frac{\varepsilon_r(0.60\sigma_c) - \varepsilon_r(0.40\sigma_c)}{\varepsilon_a(0.60\sigma_c) - \varepsilon_a(0.40\sigma_c)}$$

The tangents were evaluated with values corresponding to an axial load between 40% and 60% of the axial peak stress σ_c.

Two important observations can be made from the results:

(i) The results based on the total axial deformation measurement (S2) display a lower axial stiffness, i.e. a lower value on Young's modulus, than in the case when the results are based on the local axial deformation measurement (S1). This is due to the additional deformations from the contact interface between the rock specimen and the steel loading platens and also due to the deformation of the loading platens themselves.

(ii) It can be seen that the response differs qualitatively between the results obtained with the local axial deformation measurement system (S1) and the system that measures total axial deformation (S2). In some cases the post-peak response obtained with the local deformation measurement system seems not to be physically correct. This can be due to a number of reasons, e.g. that a crack caused a localized deformation, see Figure C-4. Another explanation could be that the rings attached to the specimens have slightly slipped or moved, for example if a crack was formed nearby one of the attachment points.

It is reasonable to assume that results based on the local axial deformation measurement (S1) are fairly accurate up to the formation of the first macro-cracks or up to the peak load, but not thereafter. However, the results obtained with the total axial deformation measurement (S2) seem to be qualitatively correct after failure. We will therefore report the results based on the total axial deformation measurement, but carry out a correction of those results as described below in order to obtain overall good results.

The total axial deformation δ_{total} measured by (S2) is a summation of several deformations

$$\delta_{total} = \delta_{rock} + \delta_{system} \tag{C-1}$$

where

$$\delta_{system} = \delta_{interface} + \delta_{loading\ platens}$$

and δ_{rock} is the axial deformation of the whole rock specimen. Assume that the system deformation is proportional to the applied axial force F_a in the loading chain, i.e.

$$\delta_{system} = F_a/K_{system} \tag{C-2}$$

where K_{system} is the axial stiffness in the system (containing the interface between the rock and loading platens and the deformation of the loading platens). Combining C-1 and C-2 leads to

$$\delta_{rock} = \delta_{total} - F_a/K_{system} \tag{C-3}$$

where an expression of the axial deformation in the whole specimen is obtained. This can be viewed as a correction of the measurements made by system (S2). By using δ_{rock} to represent the axial deformation of the specimen that is based on a correction of the results of the total axial deformation will yield good results both in the loading range up to failure and at loading after failure. However, it is noticed that K_{system} is not known and has to be determined.

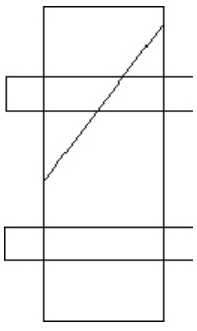

Figure C-4. *Example of cracking that may cause results that are difficult to interpret with a local deformation measurement.*

It was previously suggested that the local axial deformation measurement (S1) represents the real rock deformation well up to the load where the macro-cracks form. Further, it is fair to assume that the axial deformation is homogenous at this part of the loading. Hence, we get

$$\delta_{rock} = \delta_{local} \cdot L_{total}/L_{local} \quad \text{(C-4)}$$

This yields representative values of the total rock deformation for the first part of the loading up to the point where macro-cracking is taking place. It is now possible to determine δ_{system} up to the threshold of macro-cracking by combining C-1 and C-4 which yields

$$\delta_{system} = \delta_{total} - \delta_{local} \cdot L_{total}/L_{local} \quad \text{(C-5)}$$

Finally, we need to compute K_{system}. By rewriting C-2 we get

$$K_{system} = \frac{F_a}{\delta_{system}}$$

We will compute the system stiffness based on the results between 40% and 60% of the axial peak stress σ_c. This means that the Young's modulus and the Poisson ratio will take the same values both when the data from the local axial deformation measurement (S1) and when the data from corrected total axial deformation are used. Thus, we have

$$K_{system} = \frac{F_a(0.60\sigma_c) - F_a(0.40\sigma_c)}{\delta_{system}(0.60\sigma_c) - \delta_{system}(0.40\sigma_c)} \quad \text{(C-6)}$$

The results based on the correction according to C-3 and C-6 are presented in Section C5.1, whereas the original measured unprocessed data are reported in Appendix AC2.

Results on volumetric strain and crack volume strain are reported. By subtracting the elastic volumetric strain ε_{vol}^{e} from the total volumetric strain, a volumetric strain corresponding to the crack volume ε_{vol}^{cr} is obtained. We thus have

$$\varepsilon_{vol}^{cr} = \varepsilon_{vol} - \varepsilon_{vol}^{e}$$

Assuming linear elasticity leads to

$$\varepsilon_{vol}^{cr} = \varepsilon_{vol} - \frac{1-2\nu}{E}\sigma_a$$

where $\sigma_r = 0$ was used. The axial stresses on which the onset of an increased crack volume strain and total volumetric strain during uniaxial compression of intact rock core specimens without sealed joints occur, have commonly been related to the crack initiation stress σ_i and the crack damage stress σ_d respectively, cf /7, 8/. The crack initiation stress σ_i was determined as the stress value when the crack volume strain turned into dilation.

C4.6 Nonconformities

The testing was conducted according to the method description with some deviations. The circumferential strains have been determined within a relative error of 1.5%, which is larger than what is specified in the ISRM-standard /1/. Further, double systems for measuring the axial deformation have been used, which is beyond the specifications in the method description. This was conducted as development of the test method specially aimed for high-strength brittle rock.

Specimen KQ0054G01-113-3 was replaced by specimen KQ0046G05-113-1. Besides this, the activity plan was followed with no departures.

C5 Results

The results of the individual specimens are presented in Section C5.1 and a summary of the results is given in Section C5.2. The reported parameters are based both on unprocessed raw data obtained from the testing and processed data and were reported to the Sicada database, where they are traceable by the activity plan number. These data together with the digital photographs of the individual specimens were handed over to SKB. The handling of the results follows SDP-508 (SKB internal controlling document) in general.

C5.1 Results for each individual specimen

The cracking is shown in photos of the specimens, and comments on observations made during the testing are reported. The elasticity parameters have been evaluated by using the results from the local axial deformation measurements. The data from the adjusted total axial deformation measurements, cf Section C4.4, are shown in this section. Red rings are superposed on the graphs indicating every five minutes of the progress of testing.

Diagrams showing the data from both the local and the total axial deformation measurements, system (S1) and (S2) in Figure C-3, and the computed individual values of K_{system} used at the data corrections are shown in Appendix AC2. Diagrams displaying actual radial strain rates versus the test time are also presented in Appendix AC2. The results for the individual specimens are as follows:

Specimen ID: KQ0046G02-113-2

Before mechanical test

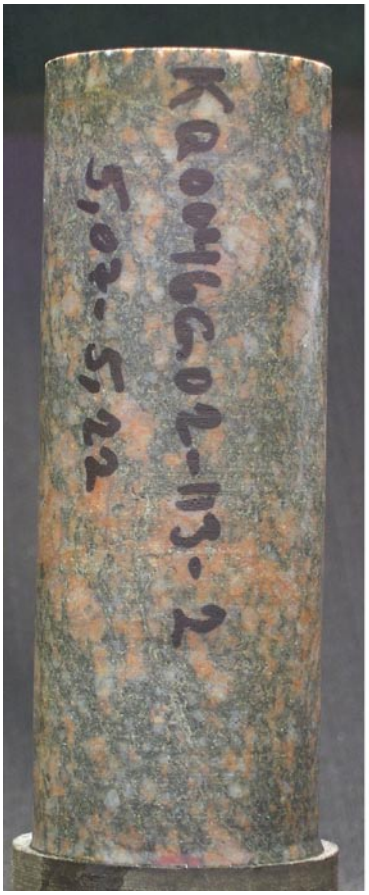

After mechanical test

Diameter (mm)	Height (mm)	Density (kg/m³)
45.2	123.0	2,740
Comments:	A vertical fracture has developed along the specimen.	

Specimen ID: KQ0046G02-113-02

Youngs Modulus (E):	77.9	[GPa]
Poisson Ratio (ν):	0.221	[-]
Axial peak stress (σ_c):	170.5	[MPa]
Crack initiation stress (σ_{ci}):	84.9	[MPa]

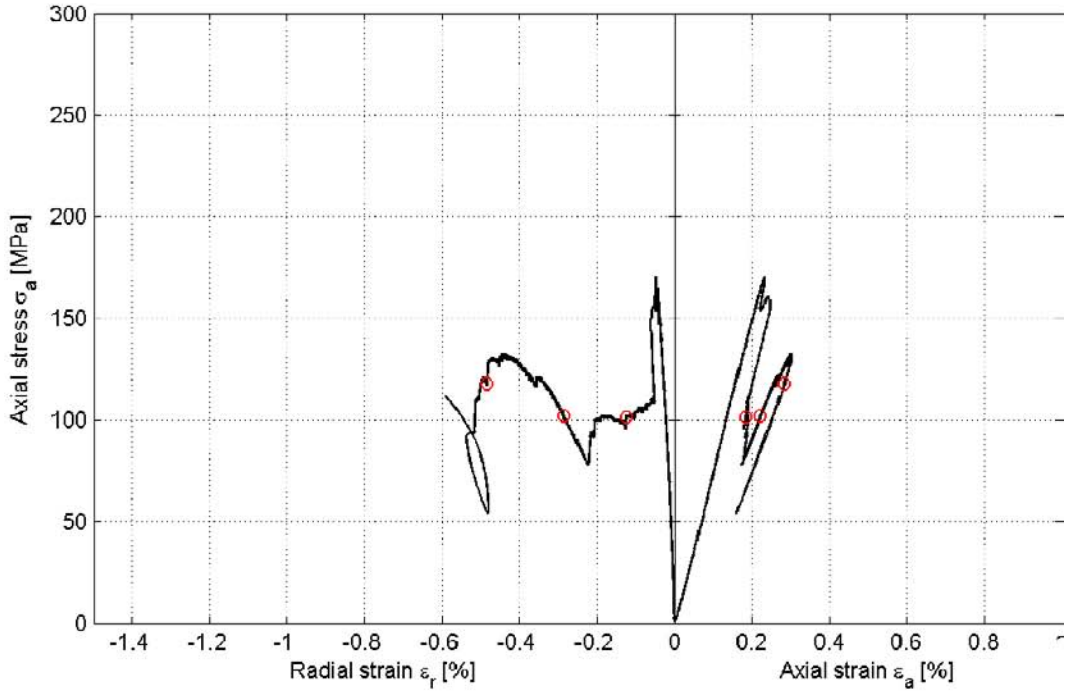

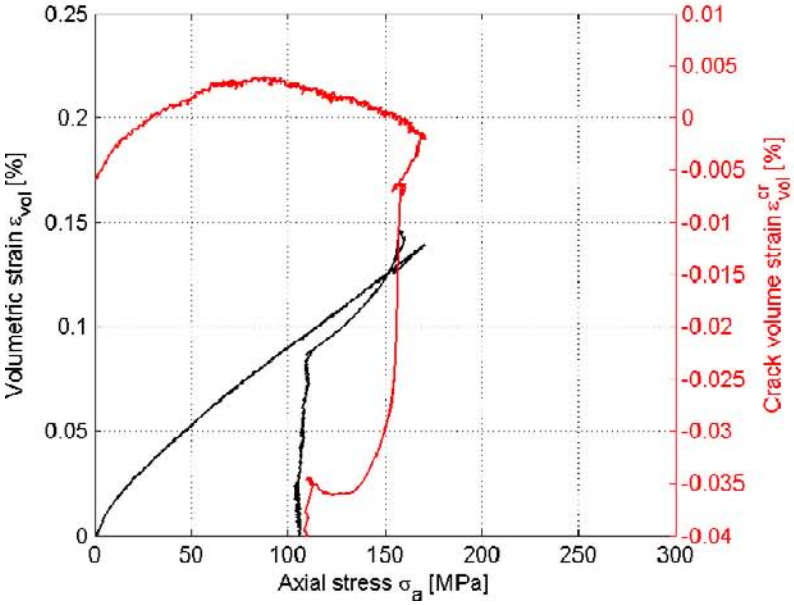

Specimen ID: KQ0046G02-113-3

Before mechanical test

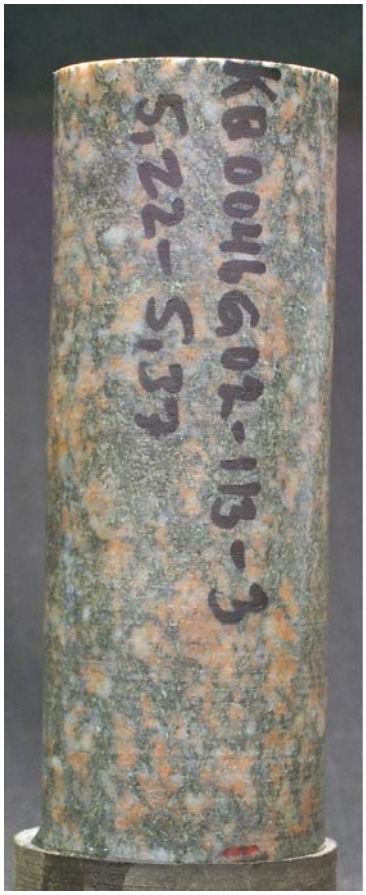

After mechanical test

Diameter (mm)	Height (mm)	Density (kg/m³)
45.2	122.0	2,740
Comments:	Deep spalling is observed along one side of the specimen.	

Specimen ID: KQ0046G02-113-03

Youngs Modulus (E):	76.8	[GPa]
Poisson Ratio (ν):	0.278	[-]
Axial peak stress (σ_c):	238	[MPa]
Crack initiation stress (σ_{ci}):	132.7	[MPa]

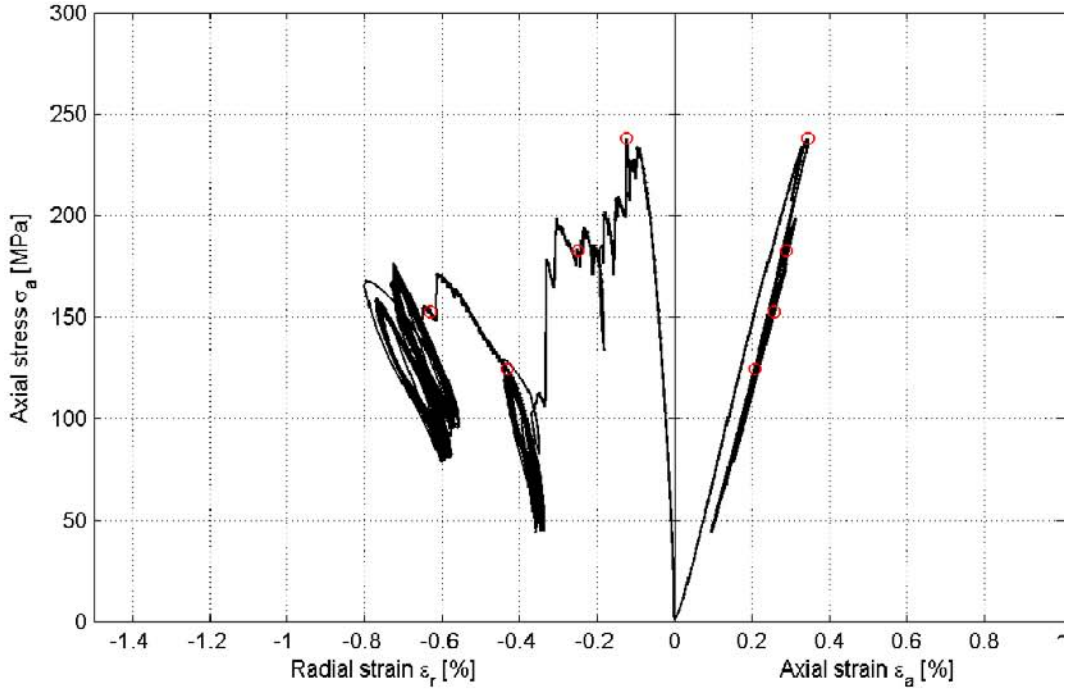

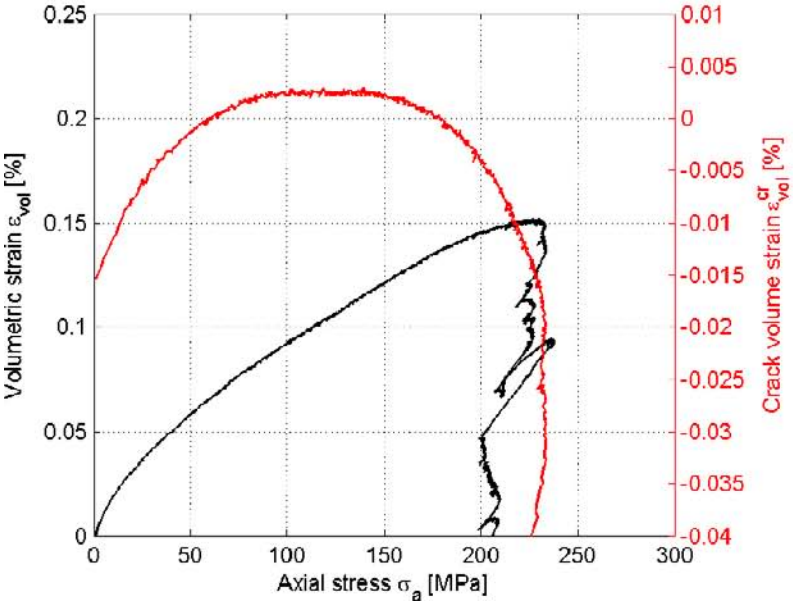

Specimen ID: KQ0046G02-113-4

Before mechanical test

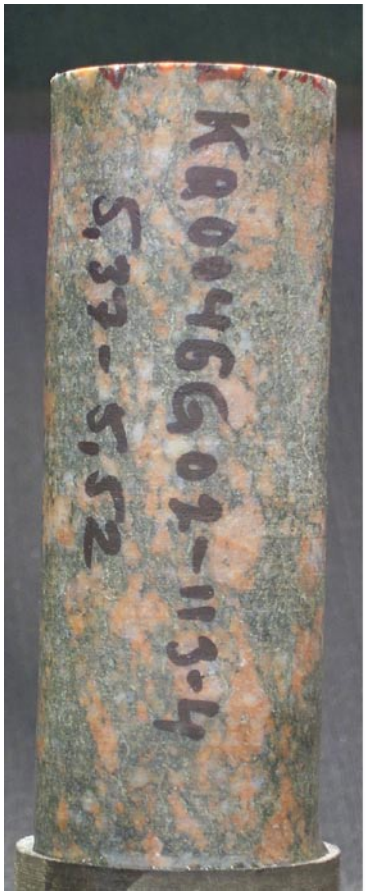

After mechanical test

Diameter (mm)	Height (mm)	Density (kg/m³)
45.3	121.5	2,740
Comments:	Spalling is observed along one side of the specimen.	

Specimen ID: KQ0046G02-113-04

Youngs Modulus (E):	74	[GPa]
Poisson Ratio (ν):	0.293	[-]
Axial peak stress (σ_c):	242.1	[MPa]
Crack initiation stress (σ_{ci}):	122.6	[MPa]

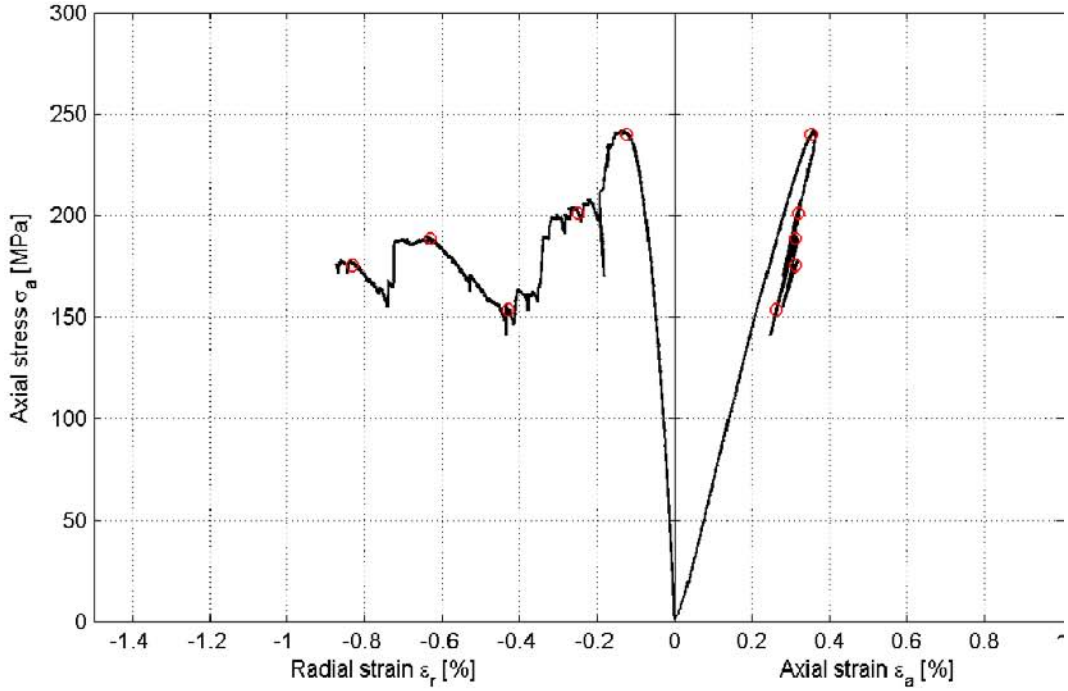

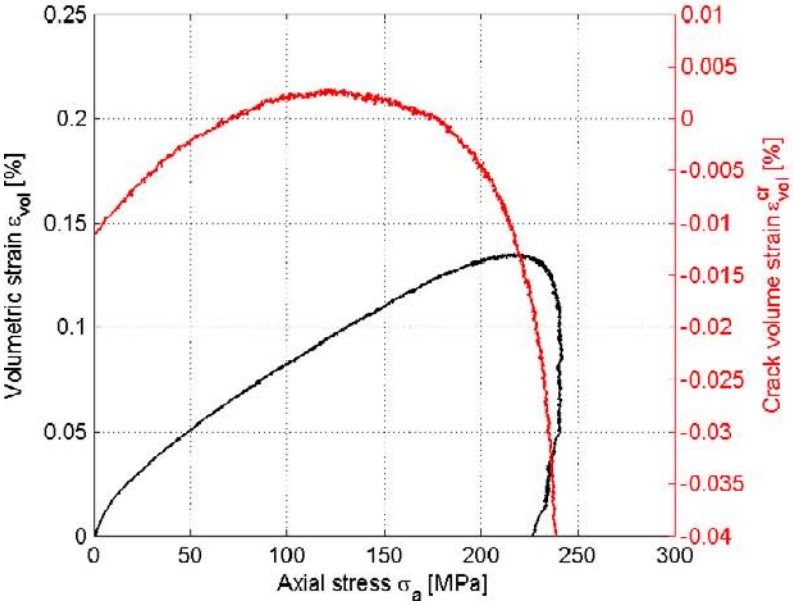

Specimen ID: KQ0046G05-113-1

Before mechanical test

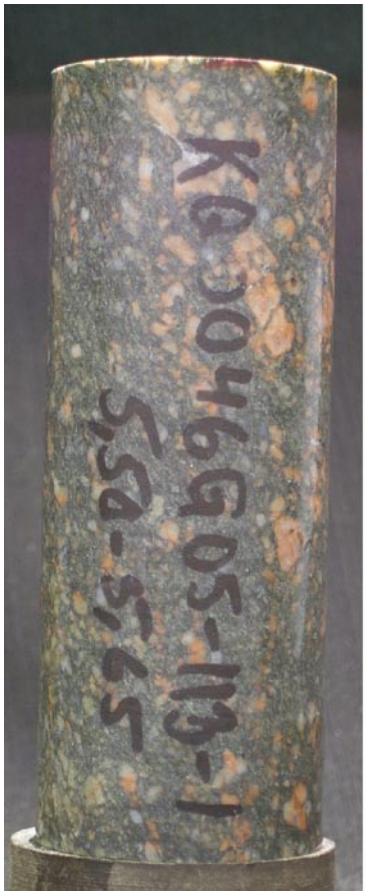

After mechanical test

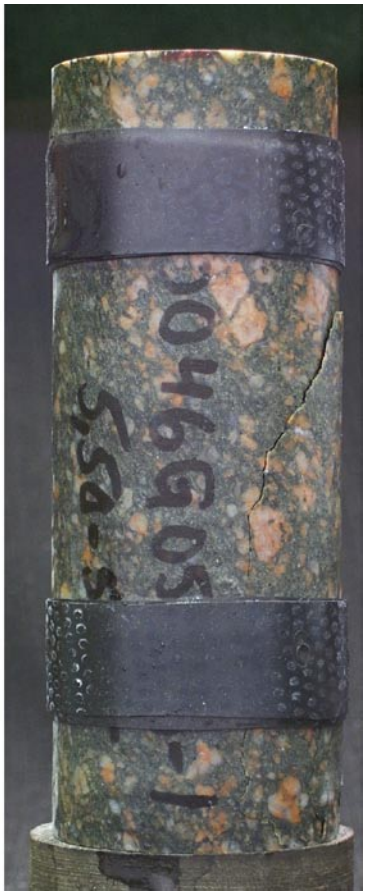

Diameter (mm)	Height (mm)	Density (kg/m³)
45.3	121.4	2,780
Comments:	A V-shaped fracture was developed through the specimen.	

Specimen ID: KQ0046G05-113-01

Youngs Modulus (E):	72.6	[GPa]
Poisson Ratio (ν):	0.298	[-]
Axial peak stress (σ_c):	203.3	[MPa]
Crack initiation stress (σ_{ci}):	101	[MPa]

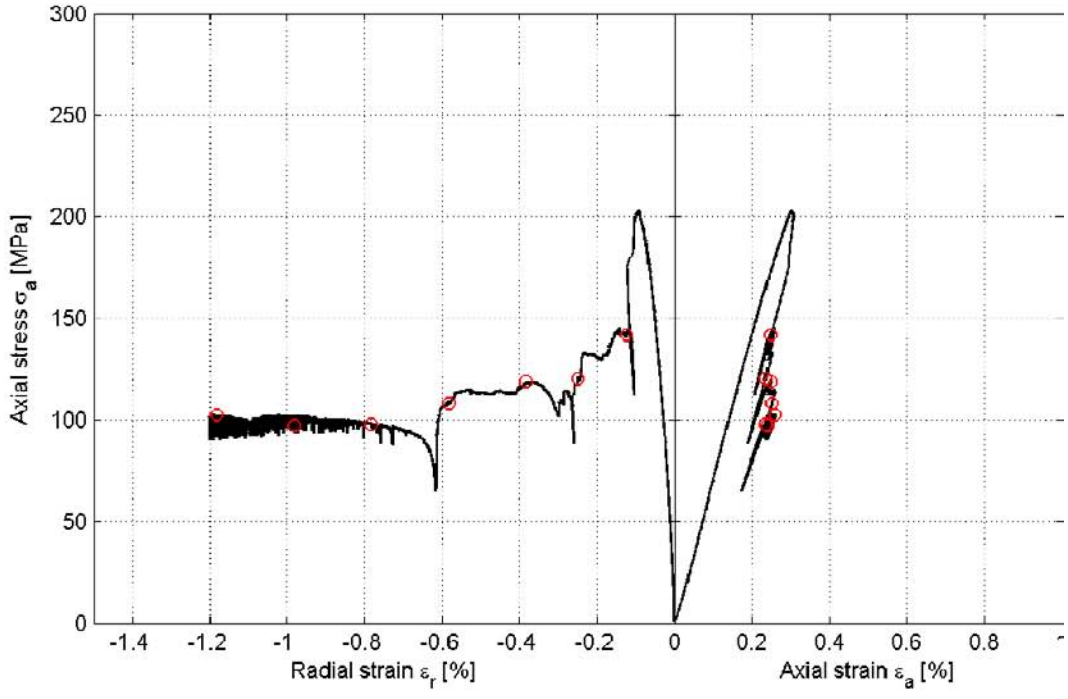

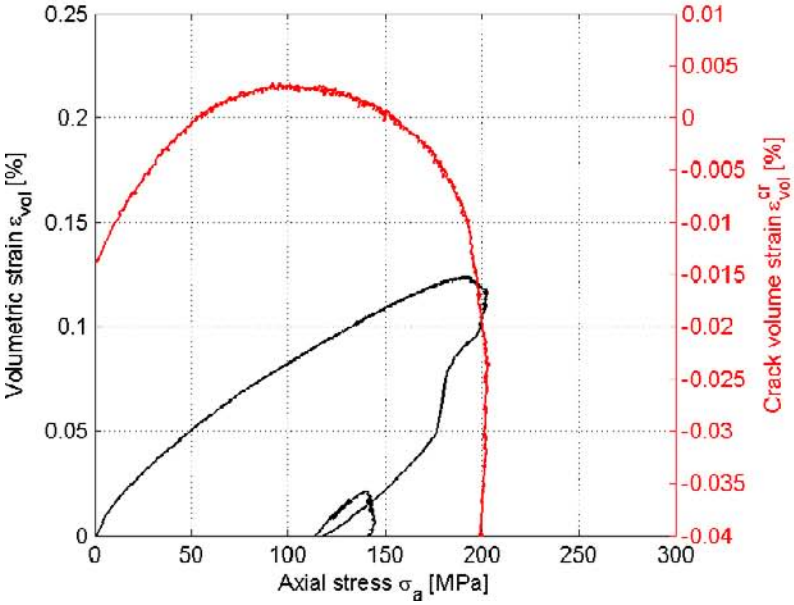

Specimen ID: KQ0048G02-113-1

Before mechanical test

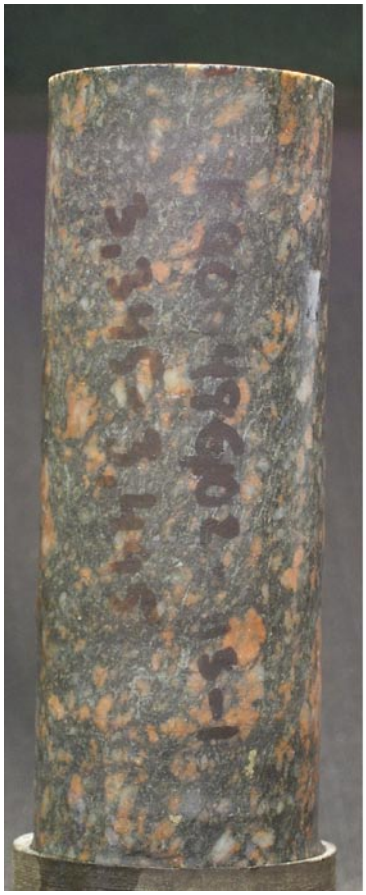

After mechanical test

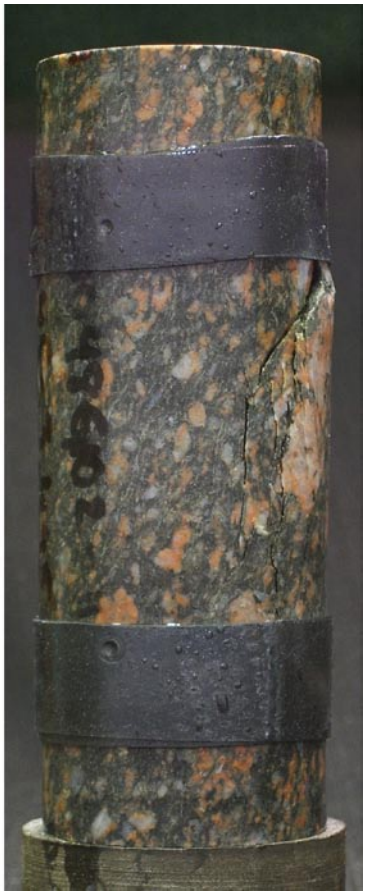

Diameter (mm)	Height (mm)	Density (kg/m³)
45.2	121.6	2,750
Comments:	Spalling is observed along one side of the specimen.	

Specimen ID: KQ0048G02-113-01

Youngs Modulus (E):	74.9	[GPa]
Poisson Ratio (ν):	0.318	[-]
Axial peak stress (σ_c):	223.8	[MPa]
Crack initiation stress (σ_{ci}):	109.2	[MPa]

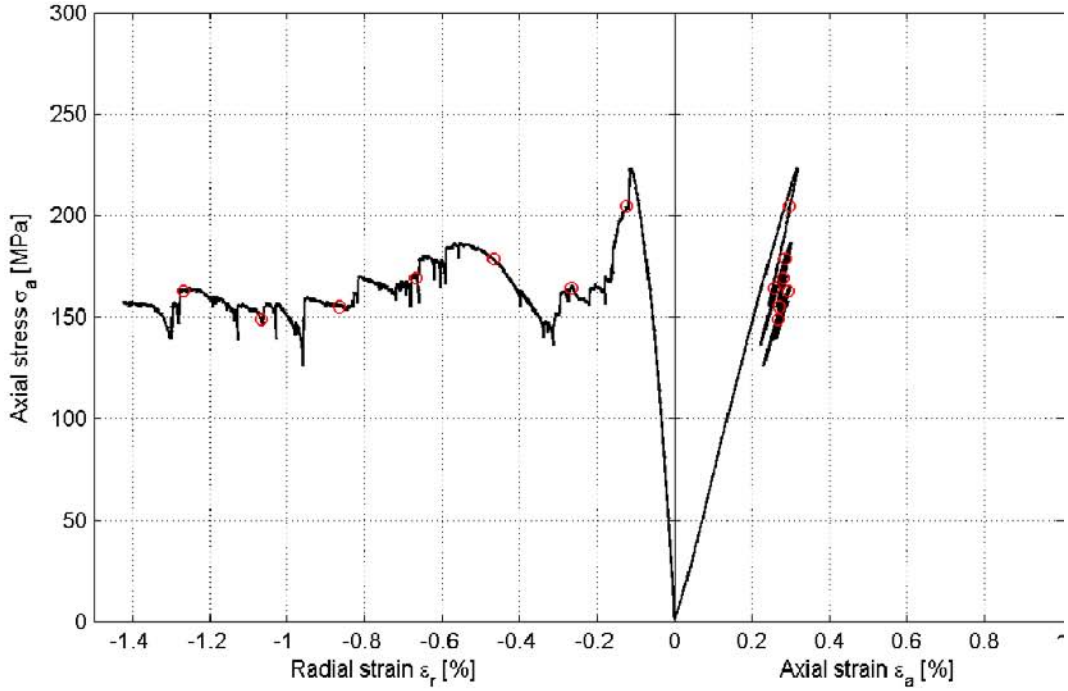

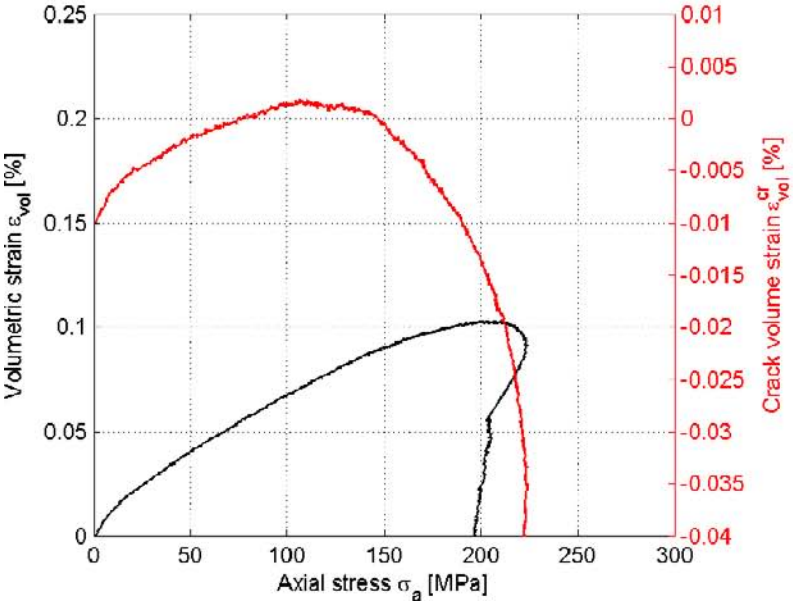

Specimen ID: KQ0048G02-113-2

Before mechanical test

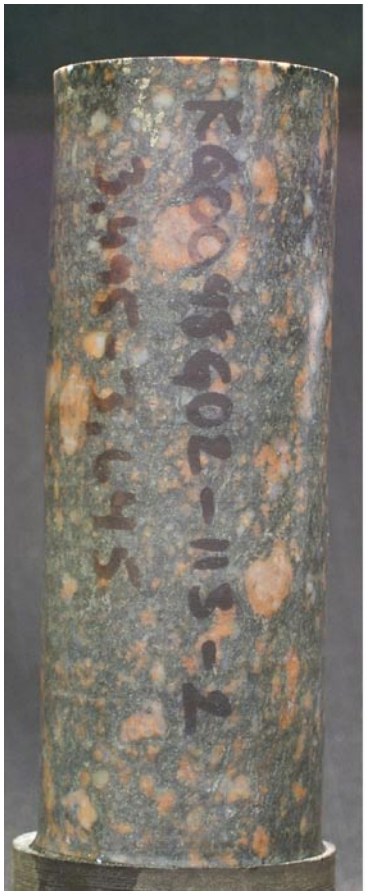

After mechanical test

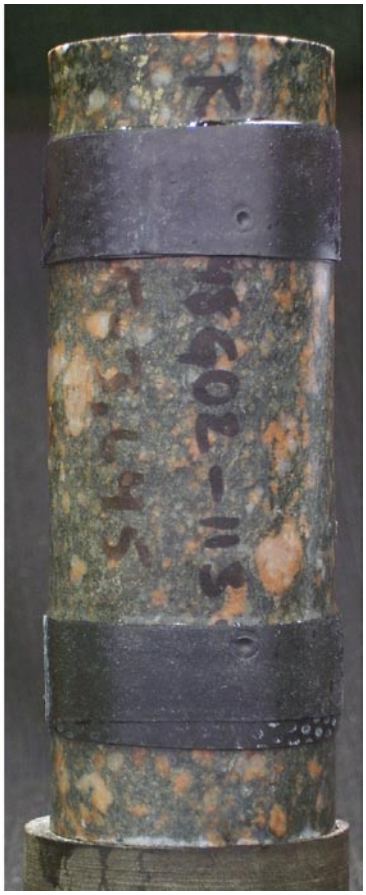

Diameter (mm)	Height (mm)	Density (kg/m^3)
45.3	122.6	2,740
Comments:	Spalling is observed along one side of the specimen.	

Specimen ID: KQ0048G02-113-02

Youngs Modulus (E):	73.3	[GPa]
Poisson Ratio (ν):	0.317	[-]
Axial peak stress (σ_c):	223.6	[MPa]
Crack initiation stress (σ_{ci}):	112.5	[MPa]

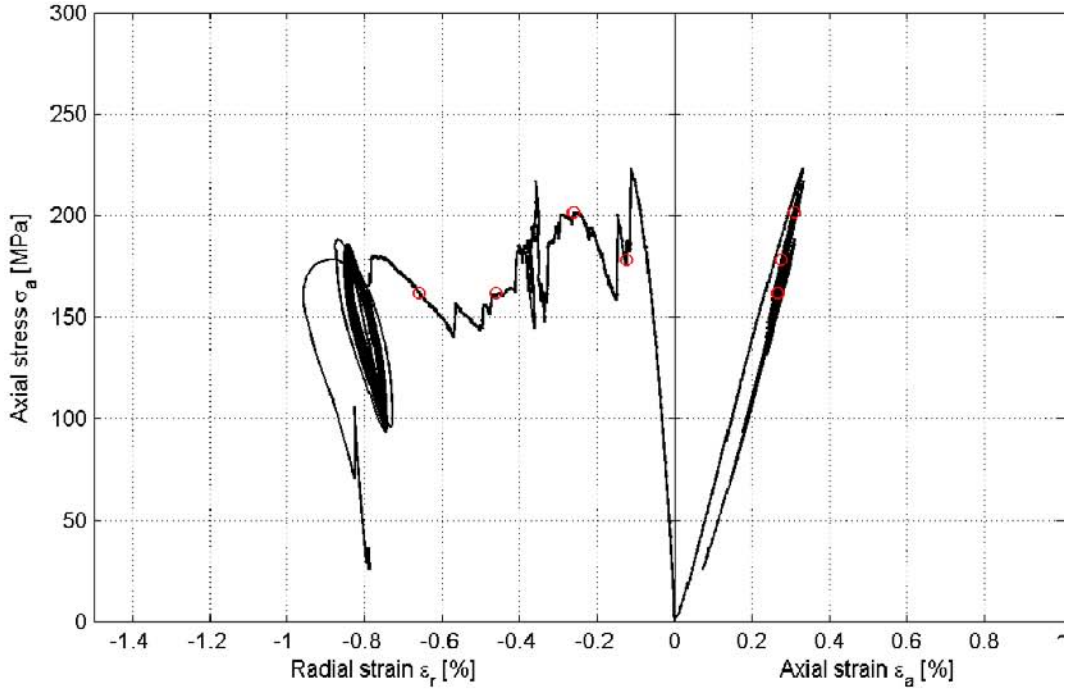

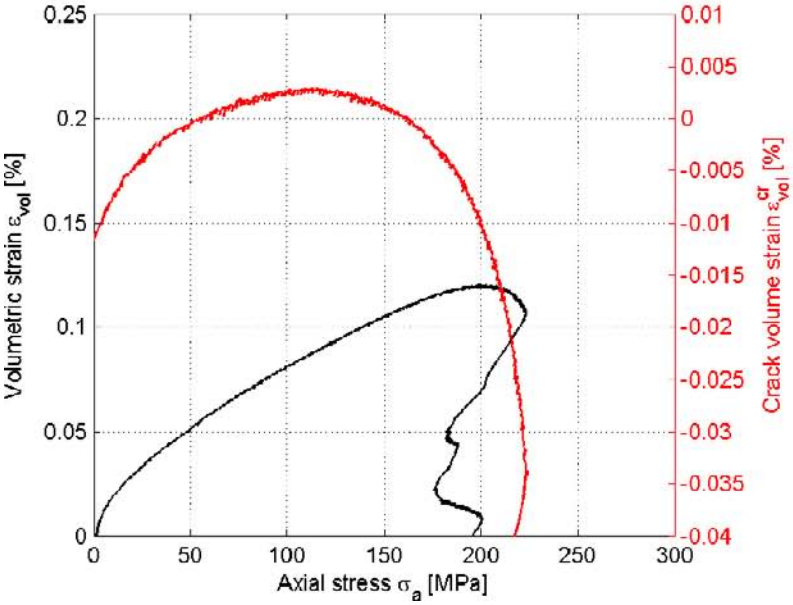

Specimen ID: KQ0051G01-113-1

Before mechanical test

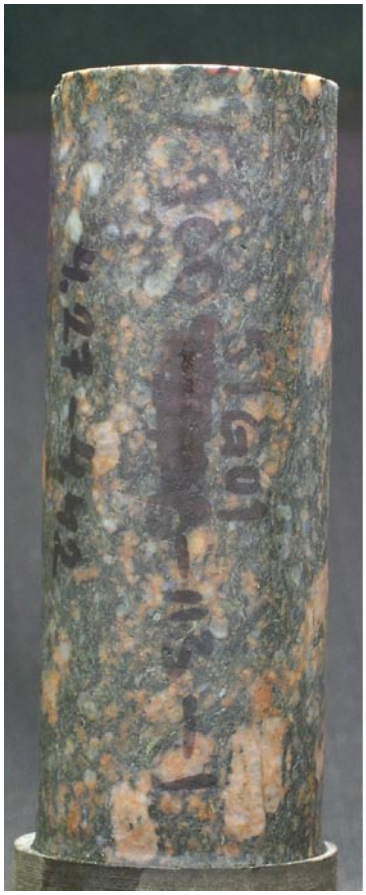

After mechanical test

Diameter (mm)	Height (mm)	Density (kg/m^3)
45.6	121.5	2,750
Comments:	Vertical fractures have been developed along the specimen.	

Specimen ID: KQ0051G01-113-01

Youngs Modulus (E):	70.9	[GPa]
Poisson Ratio (ν):	0.289	[-]
Axial peak stress (σ_c):	217.7	[MPa]
Crack initiation stress (σ_{ci}):	110.9	[MPa]

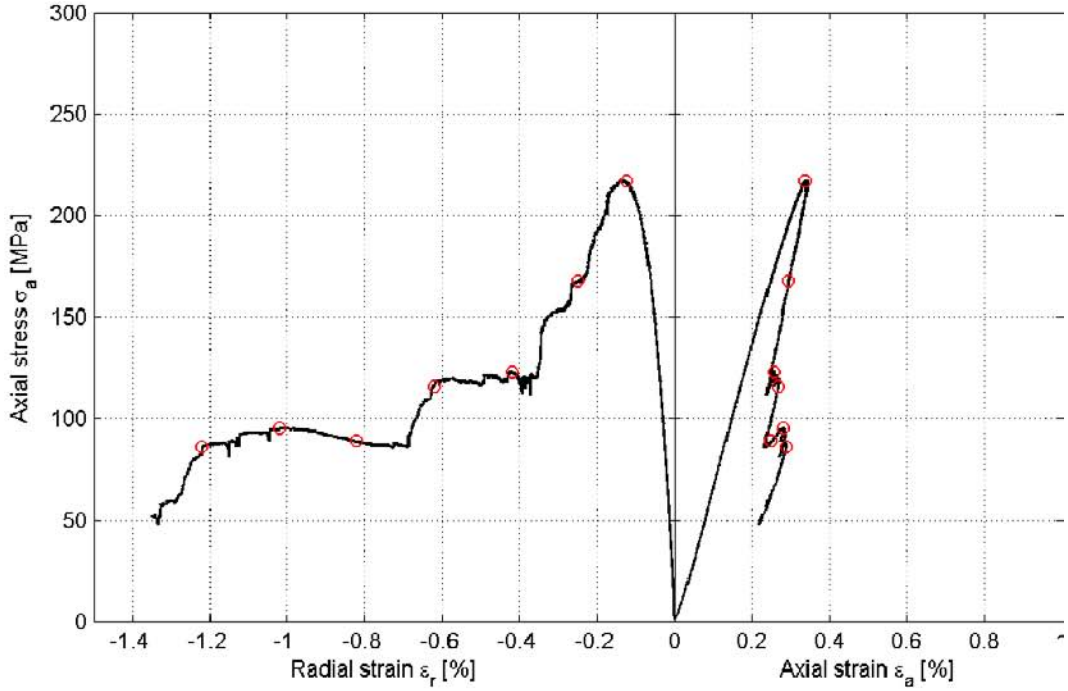

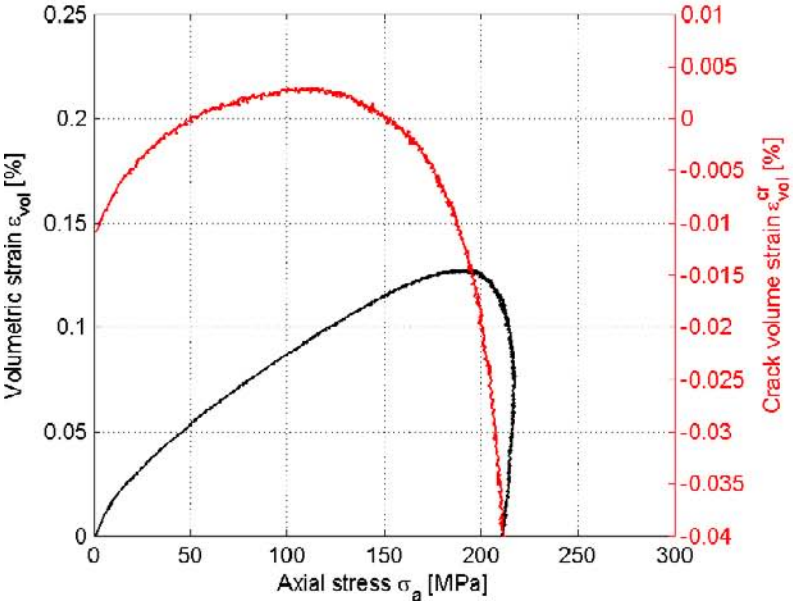

Specimen ID: KQ0054G01-113-2

Before mechanical test

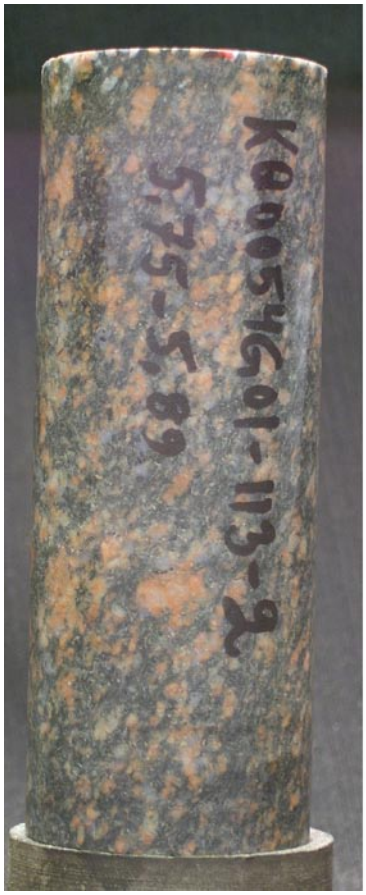

After mechanical test

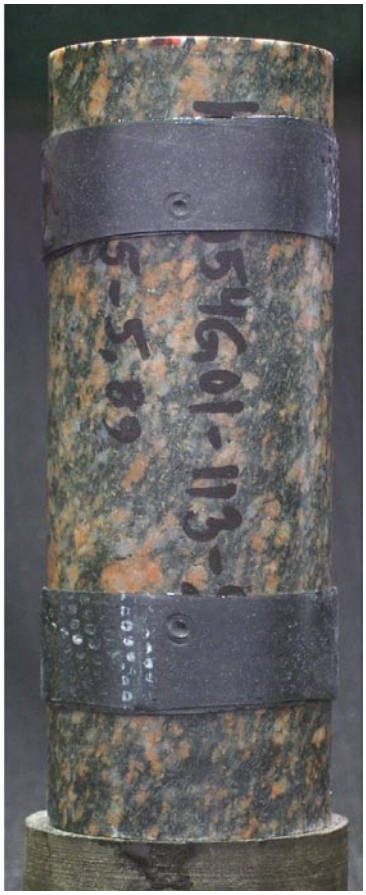

Diameter (mm)	Height (mm)	Density (kg/m³)
45.4	122.0	2,720
Comments:	Spalling is observed along one side of the specimen.	

Specimen ID: KQ0054G01-113-02

Youngs Modulus (E):	71.9	[GPa]
Poisson Ratio (ν):	0.306	[-]
Axial peak stress (σ_c):	293.6	[MPa]
Crack initiation stress (σ_{ci}):	152.5	[MPa]

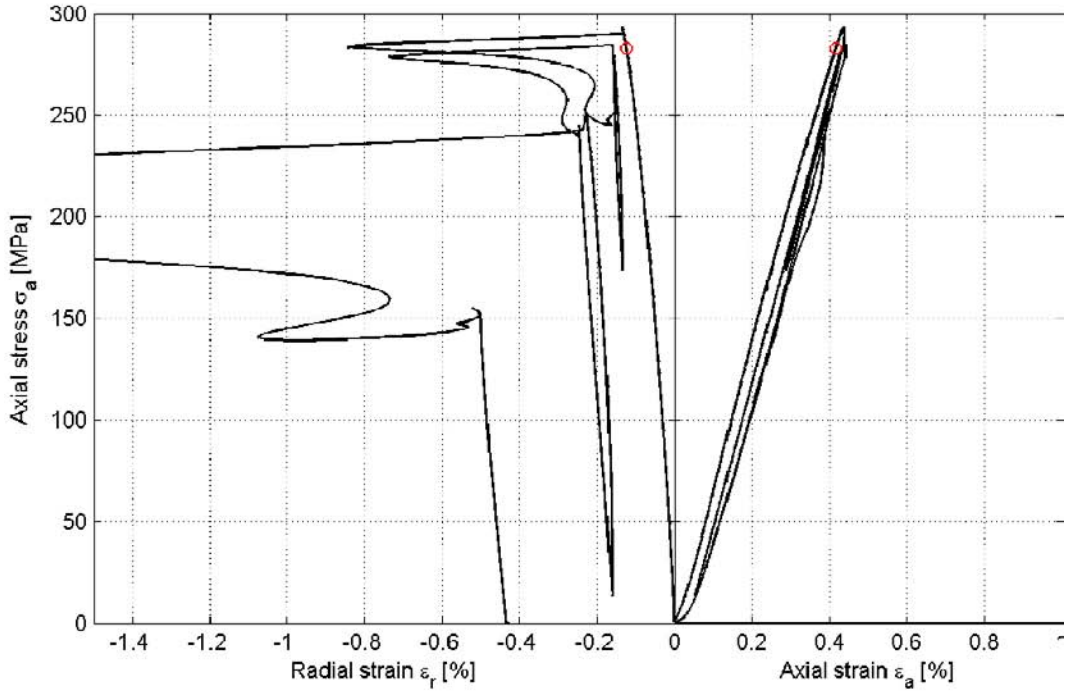

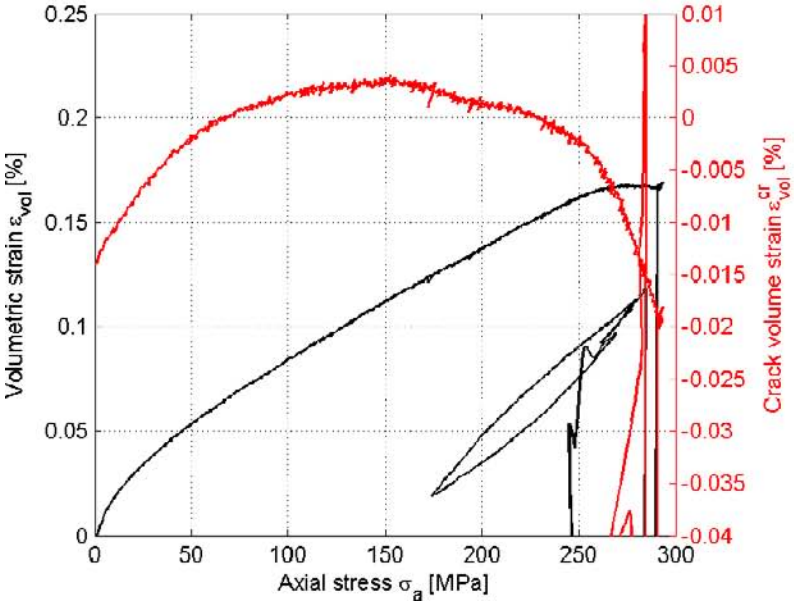

Specimen ID: KQ0054G02-113-1

Before mechanical test

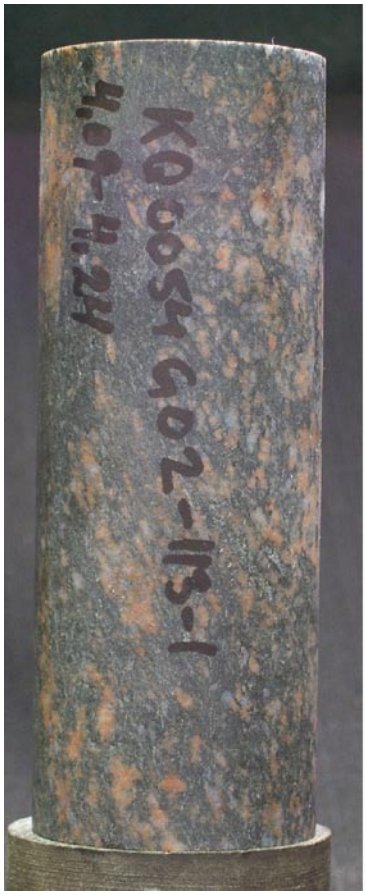

After mechanical test

Diameter (mm)	Height (mm)	Density (kg/m³)
45.2	123.0	2,710
Comments:	Spalling is observed along one side of the specimen.	

Specimen ID: KQ0054G02-113-01

Youngs Modulus (E):	77	[GPa]
Poisson Ratio (ν):	0.275	[-]
Axial peak stress (σ_c):	236.8	[MPa]
Crack initiation stress (σ_{ci}):	120	[MPa]

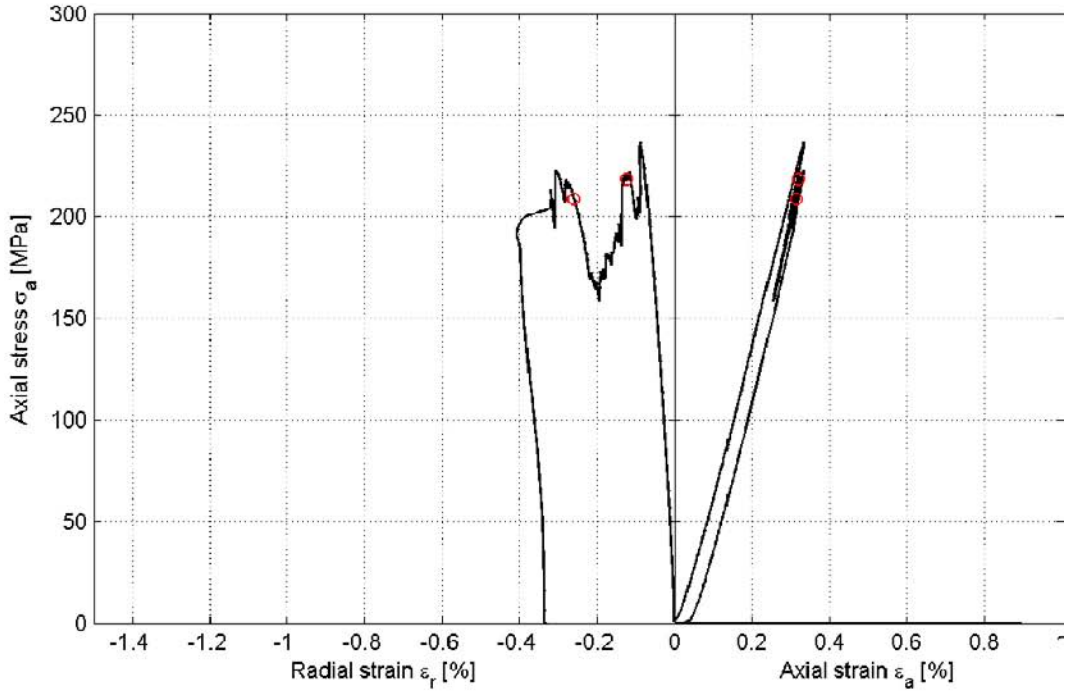

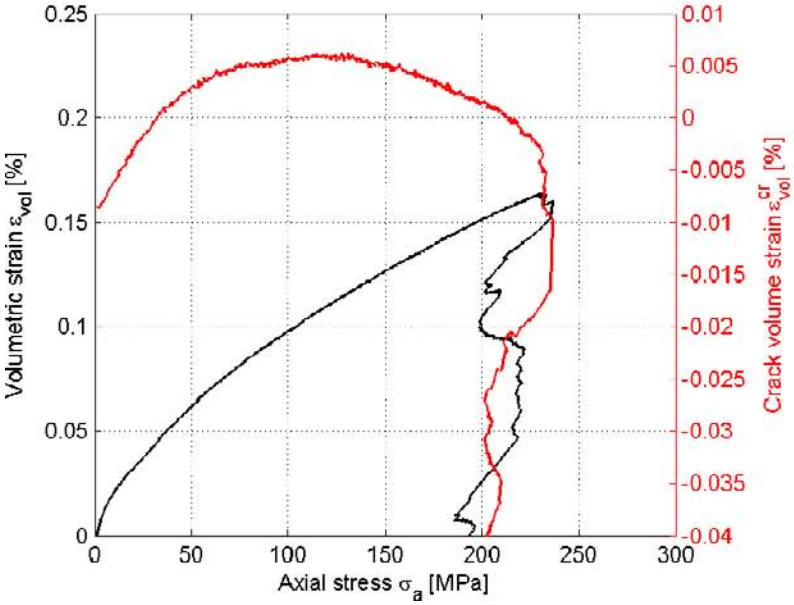

Specimen ID: KQ0054G06-113-1

Before mechanical test

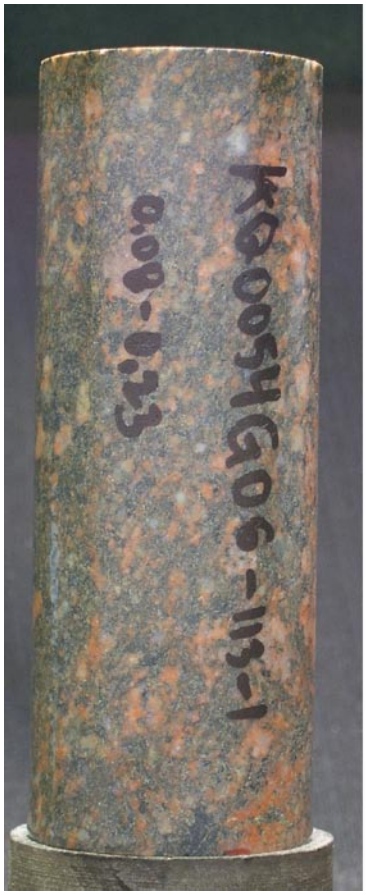

After mechanical test

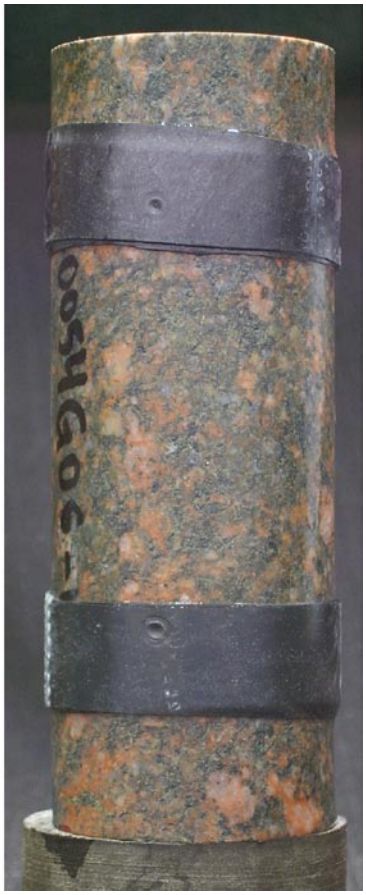

Diameter (mm)	Height (mm)	Density (kg/m³)
45.2	122.6	2,750
Comments:	Spalling is observed along one side of the specimen.	

Specimen ID: KQ0054G06-113-01

Youngs Modulus (E):	70.8	[GPa]
Poisson Ratio (ν):	0.285	[-]
Axial peak stress (σ_c):	217.6	[MPa]
Crack initiation stress (σ_{ci}):	112.4	[MPa]

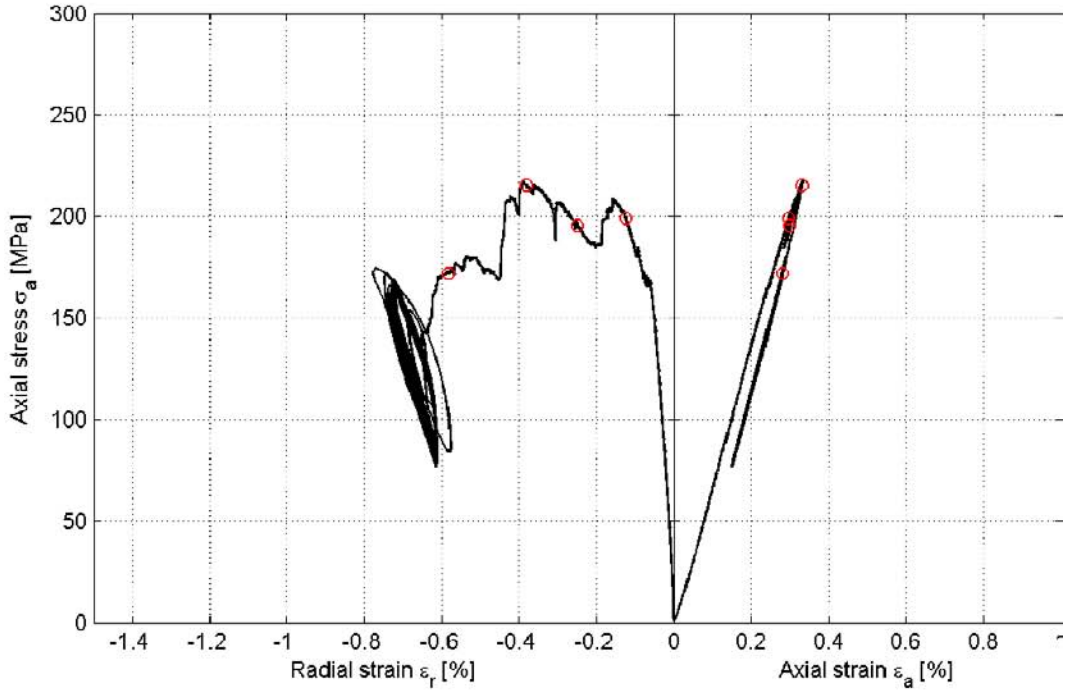

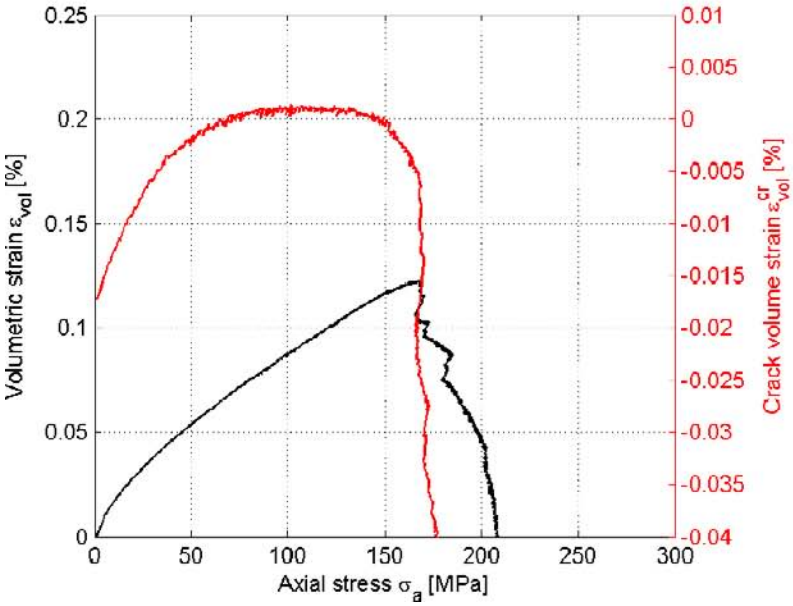

C5.2 Results for the entire test series

A summary of the test results is shown in Tables C-5 and C-6. Other results on Äspö diorite from /9/ and /10/ are shown in Table C-7. It is seen that the measured crack initiation stress is in the range of values that was previously determined. Moreover, it seems that the crack initiation stress is slightly dependent on the moisture condition, cf Borehole KF in Table C-7.

Table C-5. Summary of results.

Identification	Density (kg/m³)	Crack initiation stress (MPa)	Compressive strength (MPa)	Young's modulus (GPa)	Poisson ratio (–)	σ_{ci} / σ_c (–)
KQ0046G02-113-02	2,740	84.9	170.5	77.9	0.22	0.50
KQ0046G02-113-03	2,740	132.7	238.0	76.8	0.28	0.56
KQ0046G02-113-04	2,740	122.6	242.1	74.0	0.29	0.51
KQ0046G05-113-01	2,780	101.0	203.3	72.6	0.30	0.50
KQ0048G02-113-01	2,750	109.2	223.8	74.9	0.32	0.49
KQ0048G02-113-02	2,740	112.5	223.6	73.3	0.32	0.50
KQ0051G01-113-01	2,750	110.9	217.7	70.9	0.29	0.51
KQ0054G01-113-02	2,720	152.5	293.6	71.9	0.31	0.52
KQ0054G02-113-01	2,710	120.0	236.8	77.0	0.28	0.51
KQ0054G06-113-01	2,750	112.4	217.6	70.8	0.29	0.52

Table C-6. Calculated mean values and standard deviation for all specimens.

	Density (kg/m³)	Crack initiation stress (MPa)	Compressive strength (MPa)	Young's modulus (GPa)	Poisson ratio (–)	σ_{ci} / σ_c (–)
Mean value	2,742	115.9	226.7	74.0	0.29	0.51
Standard deviation	19	18.1	31.3	2.6	0.03	0.02

Table C-7. Other results carried out on Äspö diorite where the crac initiation stress was evaluated using the strain method (SM) and by means of acoustic emission (AE).

Borehole	Density (kg/m³)	Crack initiation stress (MPa)	Compressive strength (MPa)	Young's modulus (GPa)	Poisson ratio (–)	σ_{ci} / σ_c (–)
KA3376B01 (SM)*	2,730	87.1	199	68	0.28	0.44
KQ (SM) **	2,755	96.3	216	76	0.27	0.48
KQ (AE) **	2,755	121	216	76	0.27	0.61
KF (SM) ***	2,678	149.9	302.3	71.6	0.29	0.50
KF (SM) ****	2,684	137.5	278.3	70.3	0.30	0.50

* From /9/. Dry specimens. Mean value of two specimens.

** From /9/. Dry specimens. Mean value of five specimens from boreholes KQ0064G01, KQ0064G07 and KQ0065G01.

*** From /10/. Dry specimens. Mean value of five specimens from boreholes KF0066A01 and KF0069A01.

**** From /10/. Saturation by formation water. Mean value of five specimens from boreholes KF0066A01 and KF0069A01.

References

/1/ **ISRM, 1999.** Draft ISRM suggested method for the complete stress-strain curve for intact rock in uniaxial compression. Int. J. Rock. Mech. Min. Sci. 36(3), pp. 279–289.

/2/ **ASTM 4543-01, 2001.** Standard practice for preparing rock core specimens and determining dimensional and shape tolerance.

/3/ **ISRM, 1979.** Suggested Method for Determining Water Content, Porosity, Density, Absorption and Related Properties and Swelling and Slake-durability Index Properties. Int. J. Rock. Mech. Min. Sci. & Geomech. Abstr. 16(2), pp. 141–156.

/4/ **SS-EN 13755.** Natural stone test methods – Determination of water absorption at atmospheric pressure.

/5/ **Stråhle A, 2001.** Definition och beskrivning av parametrar för geologisk, geofysisk och bergmekanisk kartering av berg. SKB R-01-19, Svensk Kärnbränslehantering AB. In Swedish.

/6/ **MATLAB, 2007.** The Language of Technical computing. Version 7.5. MathWorks Inc.

/7/ **Martin C D, Chandler N A, 1994.** The progressive fracture of Lac du Bonnet granite. Int. J. Rock. Mech. Min. Sci. & Geomech. Abstr. 31(6), pp. 643–659.

/8/ **Eberhardt E, Stead D, Stimpson B, Read R S, 1998.** Identifying crack initiation and propagation thresholds in brittle rock. Can. Geotech. J. 35, pp. 222–233.

/9/ **Staub I, Andersson J C, Magnor B, 2004.** Äspö pillar stability experiment. Geology and mechanical properties of the rock in TASQ. SKB R-04-01, Svensk Kärnbränslehantering AB.

/10/ **Jacobsson L, Bäckström A, 2005.** Äspö Hard Rock Laboratory. DECOVALEX. Uniaxial compression test of intact rock at dry condition and at saturation by three different liquids: distilled, saline and formation water. SKB IPR-05-33, Svensk Kärnbränslehantering AB.

Appendix AC1

The following equations describe the calculation of radial strains when using a circumferential deformation device, see Figure AC1-1.

$$\varepsilon_r = \frac{\Delta C}{C_i}$$

where

$C_i = 2\,\pi\,R_i$ = initial specimen circumference

ΔC = change in specimen circumference = $\dfrac{\pi \cdot \Delta X}{\sin\left(\dfrac{\theta_i}{2}\right) + \left(\pi - \dfrac{\theta_i}{2}\right)\cos\left(\dfrac{\theta_i}{2}\right)}$

and

ΔX = change in LVDT reading = $X_i - X_f$

(X_i = initial chain gap; X_f = current chain gap)

θ_i = initial chord angle = $2\pi - \dfrac{L_c}{R_i + r}$

L_c = chain length (measured from center of one end roller to center of the other end roller)

r = roller radius

R_i = initial specimen radius

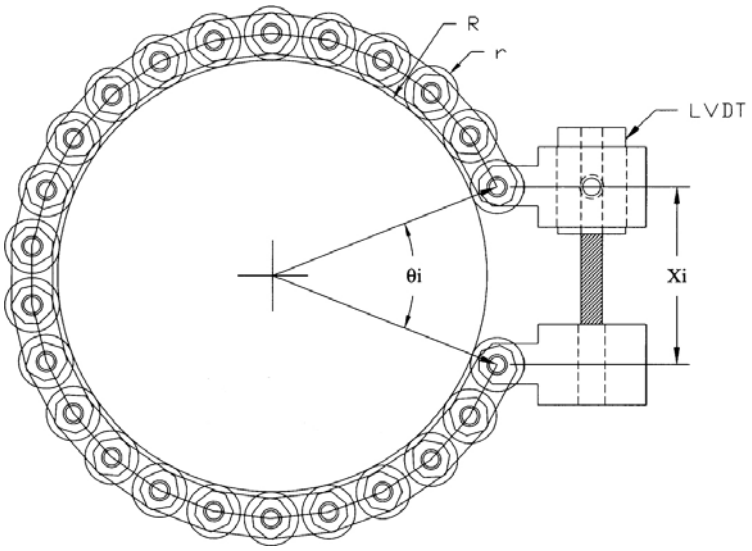

Figure AC1-1. *Chain for radial deformation measurement.*

Appendix AC2

This Appendix contains results showing the unprocessed data and values on the computed system stiffness K_{system} that was used for the data processing, cf Section C4.4. In addition graphs showing the volumetric strain ε_{vol} versus the axial strain ε_a and the actual radial strain rate $d\varepsilon_r$ /dt versus time are also displayed.

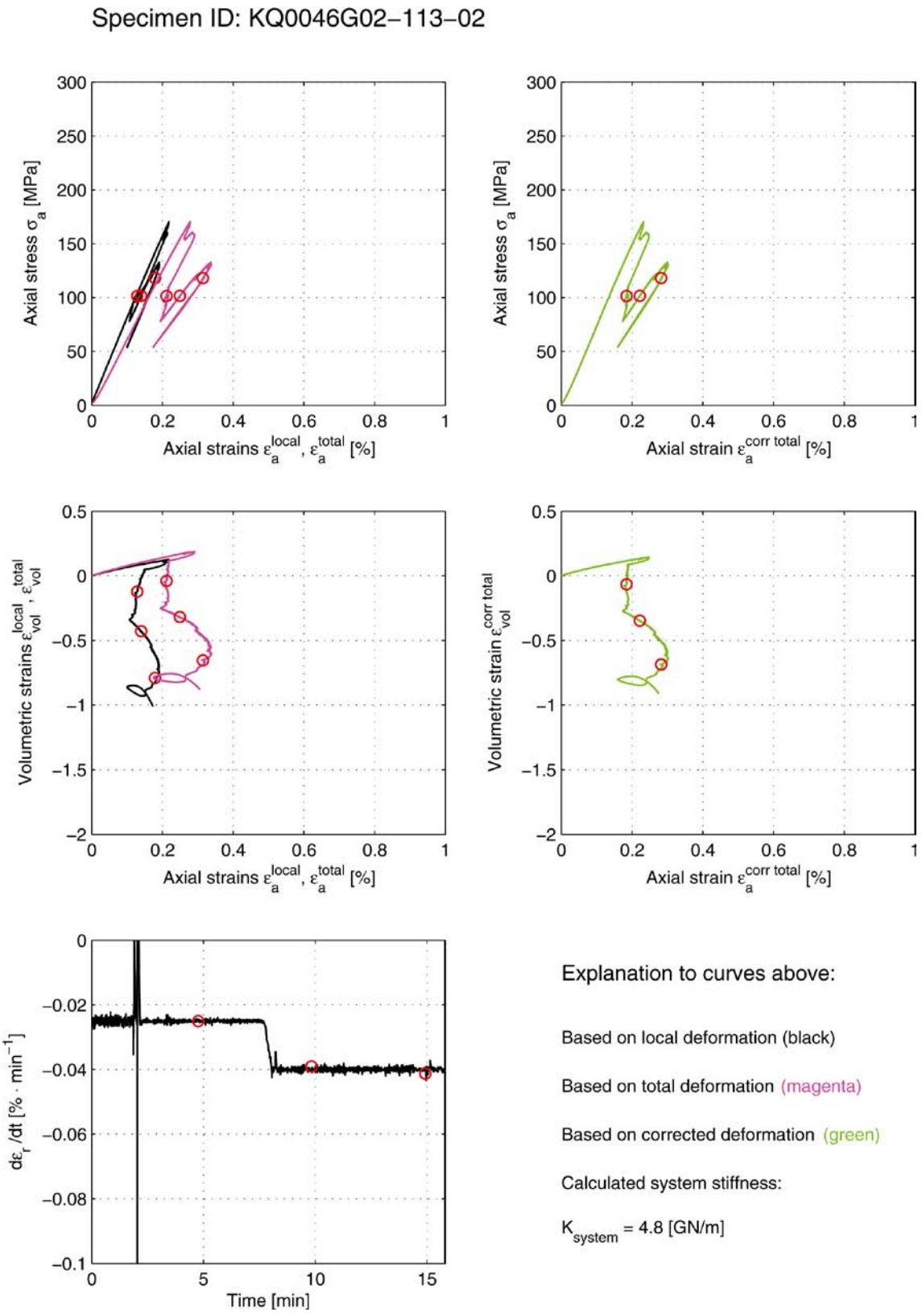

Specimen ID: KQ0046G02–113–03

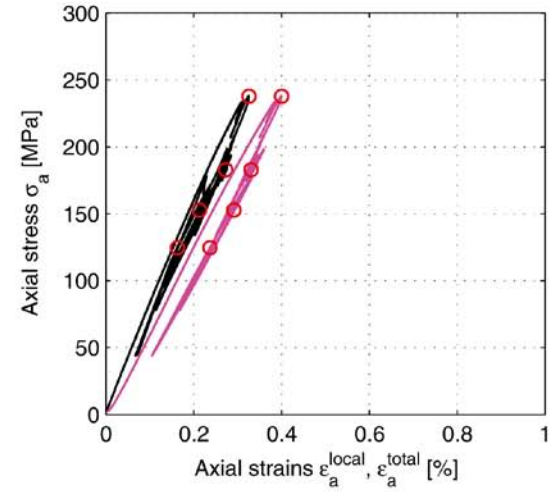

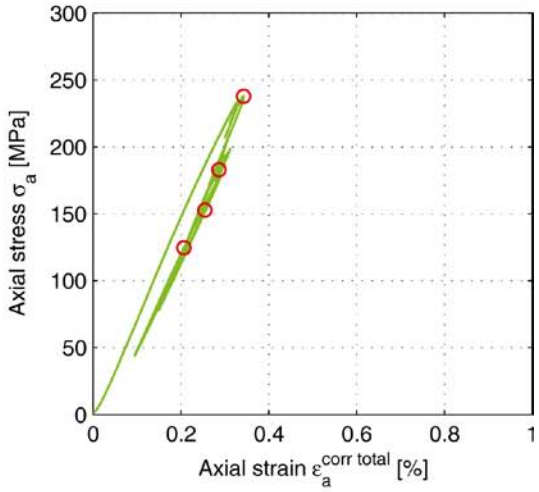

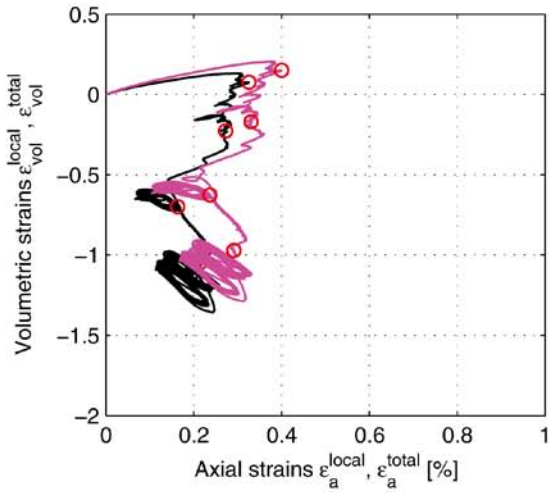

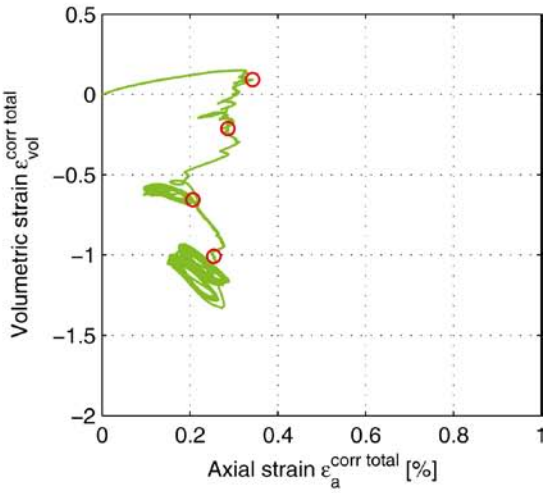

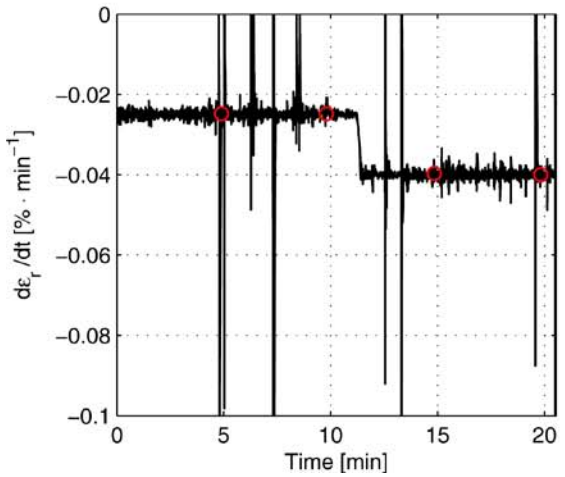

Explanation to curves above:

Based on local deformation (black)

Based on total deformation (magenta)

Based on corrected deformation (green)

Calculated system stiffness:

K_{system} = 5.5 [GN/m]

Specimen ID: KQ0046G02-113-04

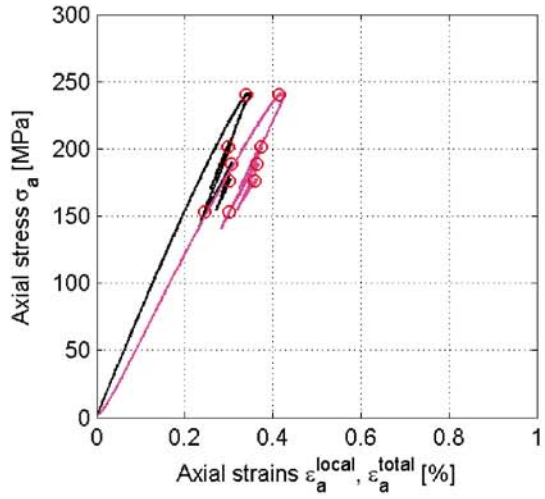

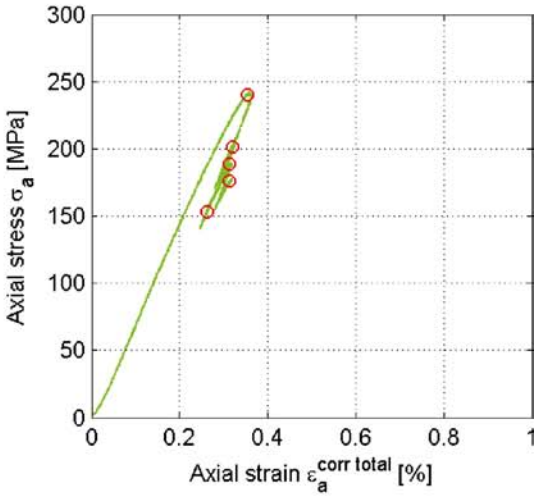

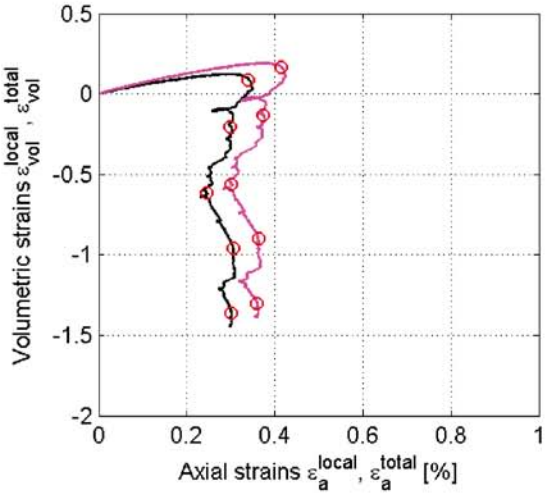

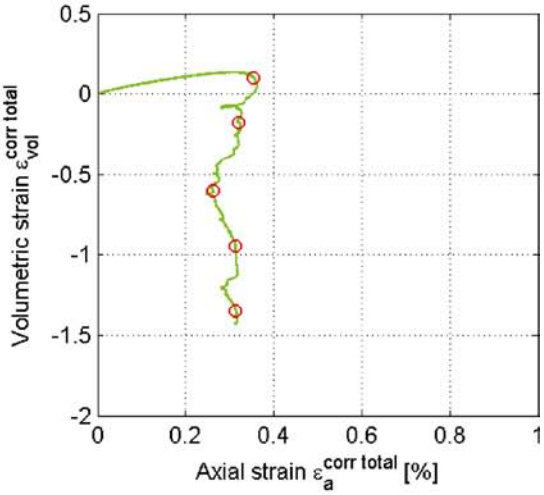

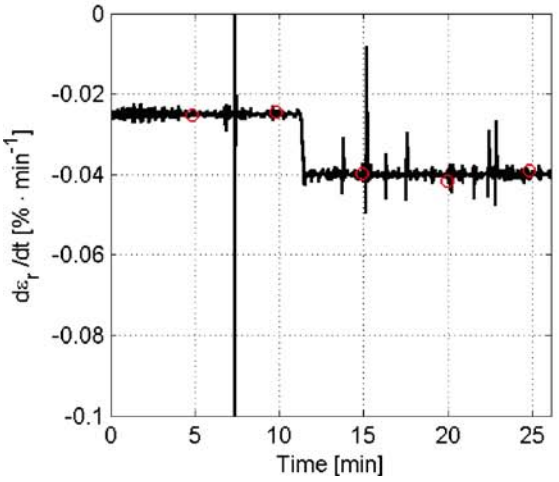

Explanation to curves above:

Based on local deformation (black)

Based on total deformation (magenta)

Based on corrected deformation (green)

Calculated system stiffness:

K_{system} = 5.2 [GN/m]

Specimen ID: KQ0046G05-113-01

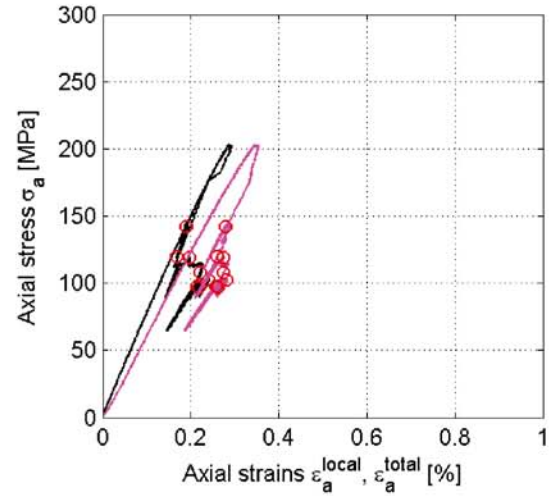

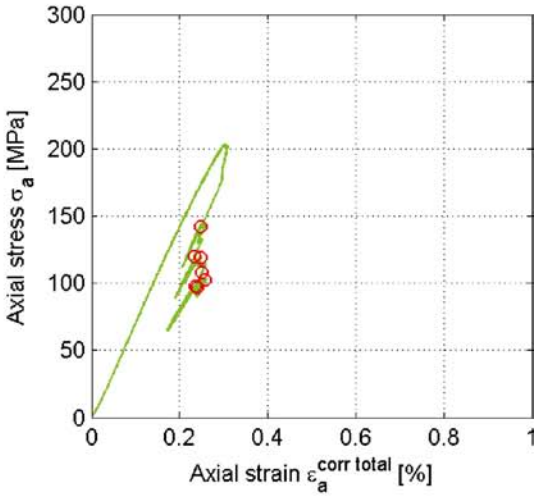

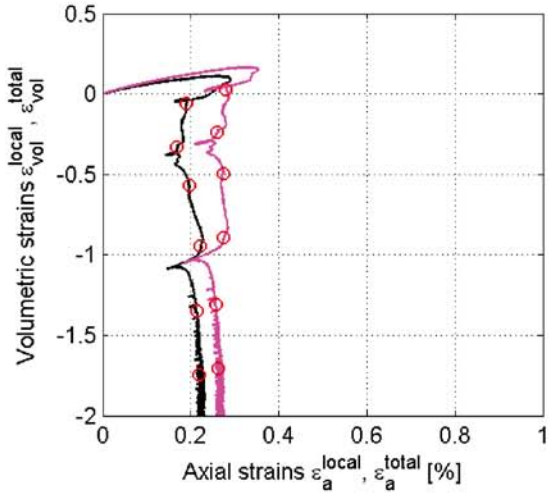

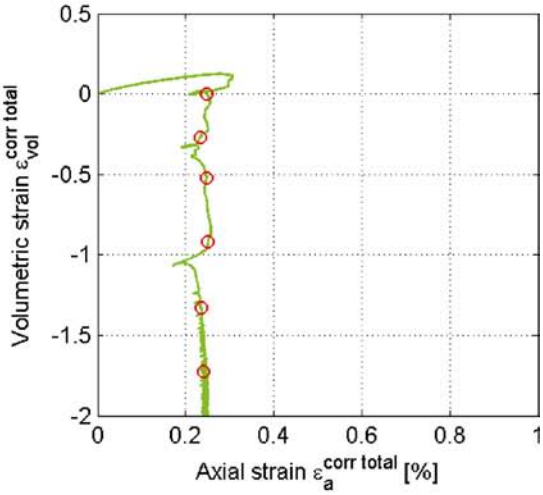

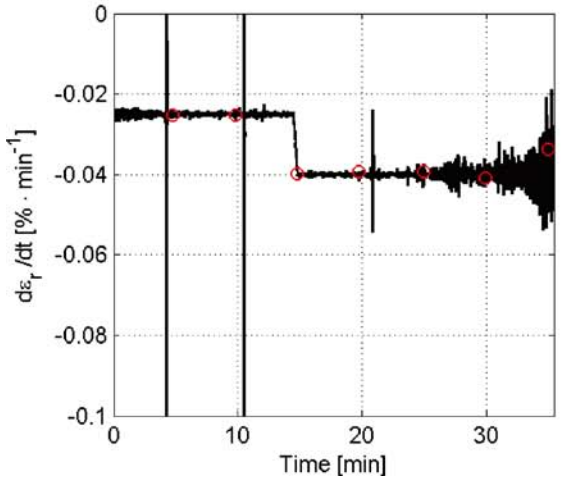

Explanation to curves above:

Based on local deformation (black)

Based on total deformation (magenta)

Based on corrected deformation (green)

Calculated system stiffness:

K_{system} = 5.9 [GN/m]

Specimen ID: KQ0048G02-113-01

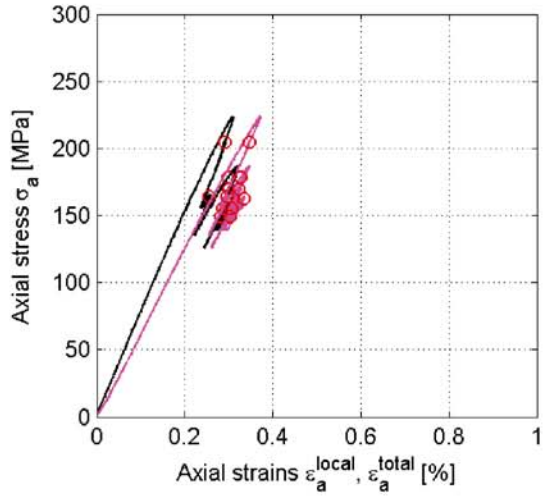

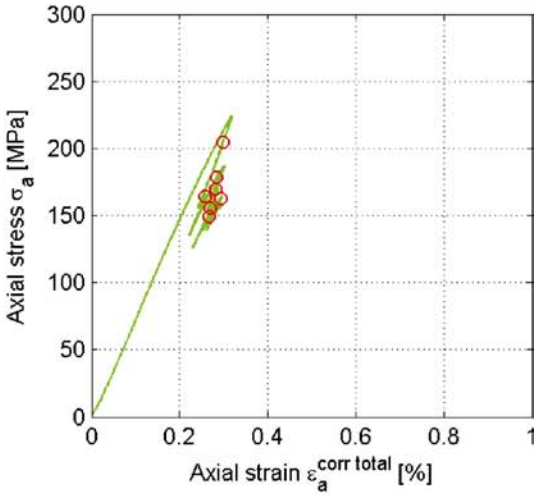

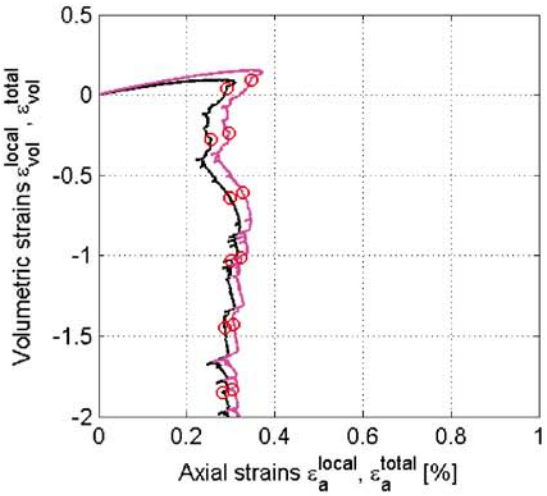

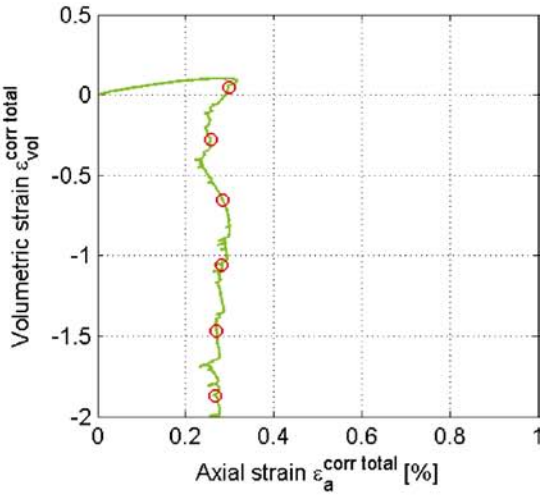

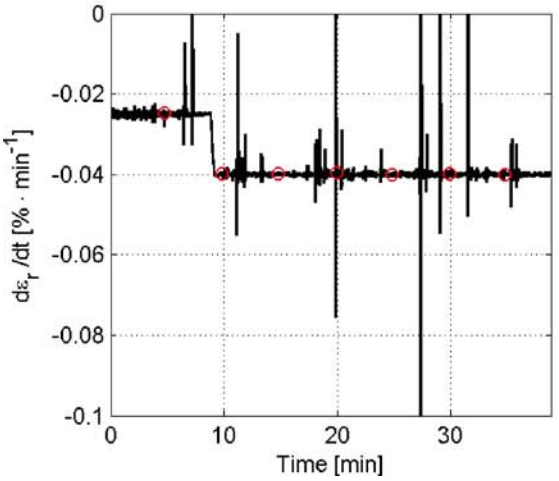

Explanation to curves above:

Based on local deformation (black)

Based on total deformation (magenta)

Based on corrected deformation (green)

Calculated system stiffness:

K_{system} = 5.5 [GN/m]

Specimen ID: KQ0048G02–113–02

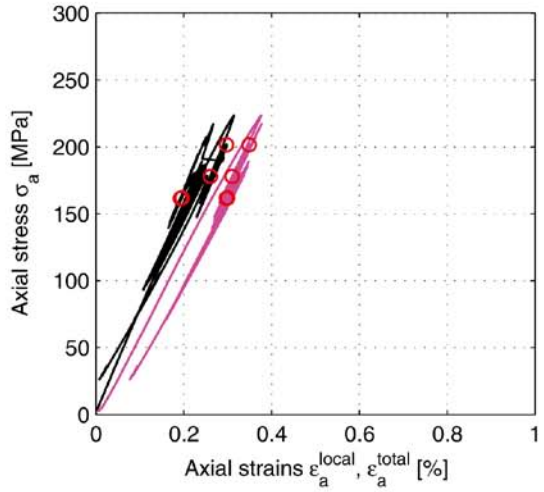

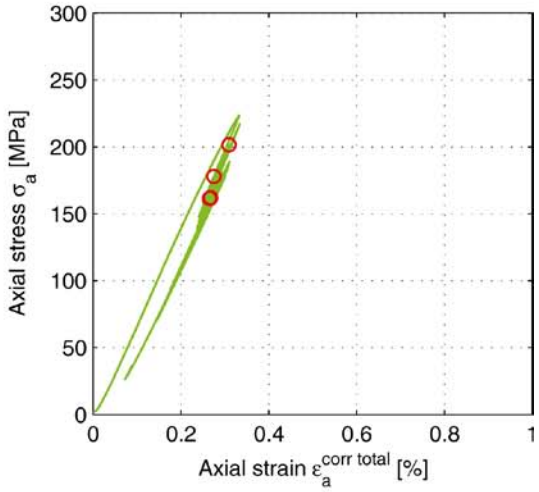

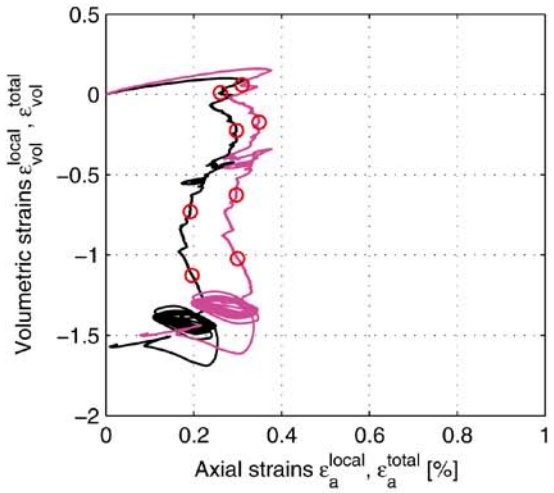

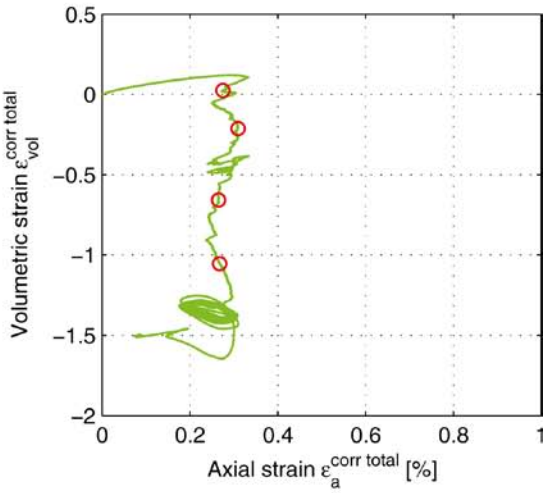

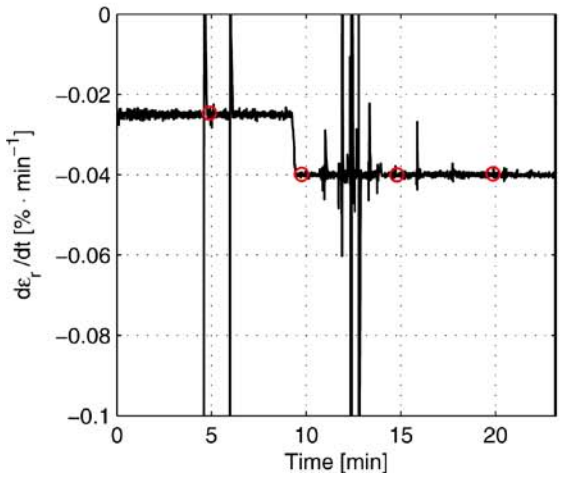

Explanation to curves above:

Based on local deformation (black)

Based on total deformation (magenta)

Based on corrected deformation (green)

Calculated system stiffness:

K_{system} = 6.7 [GN/m]

Specimen ID: KQ0051G01−113−01

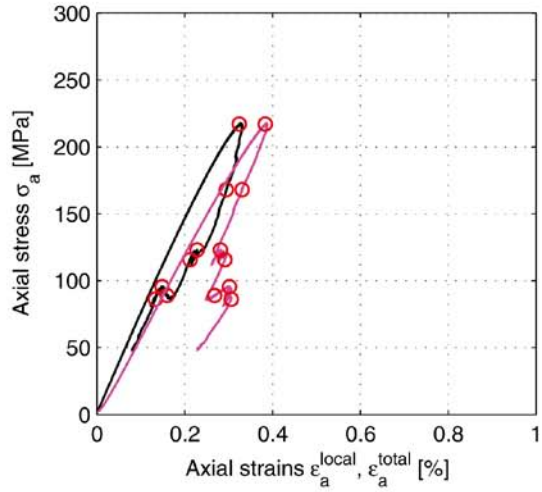

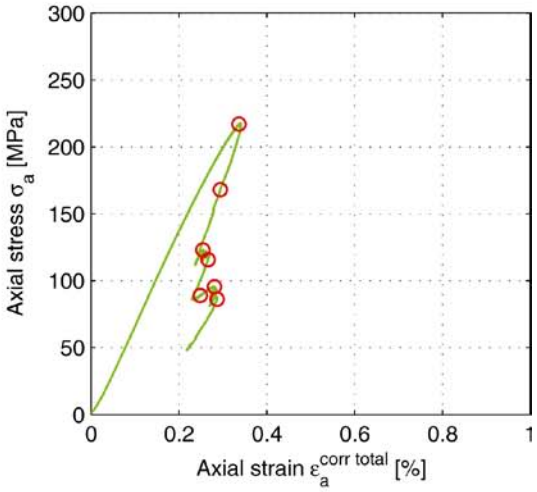

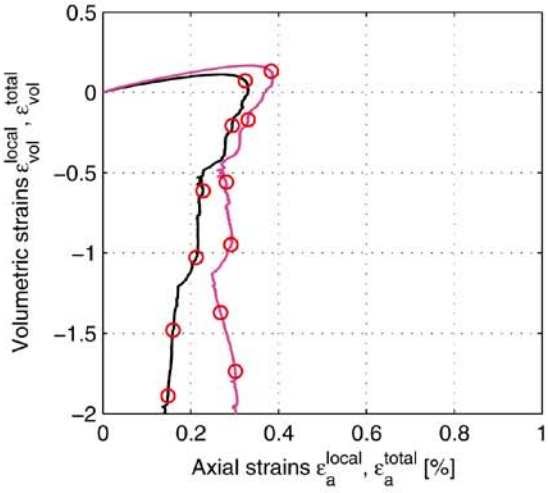

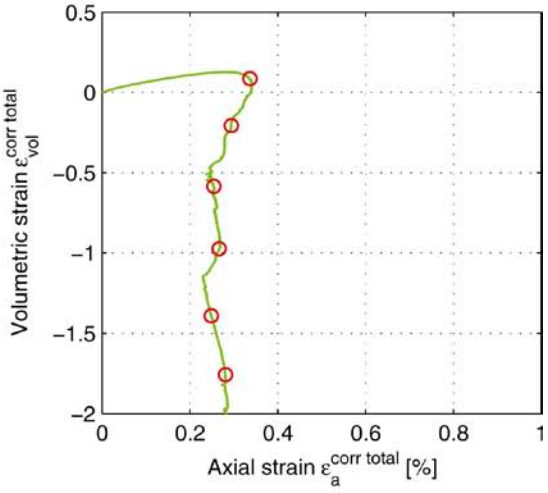

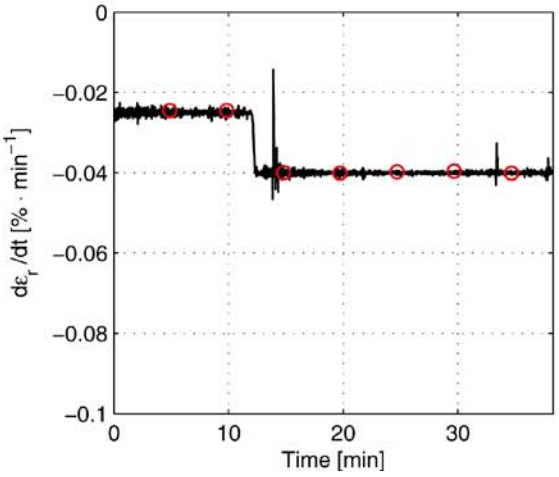

Explanation to curves above:

Based on local deformation (black)

Based on total deformation (magenta)

Based on corrected deformation (green)

Calculated system stiffness:

K_{system} = 6.3 [GN/m]

Specimen ID: KQ0054G01–113–02

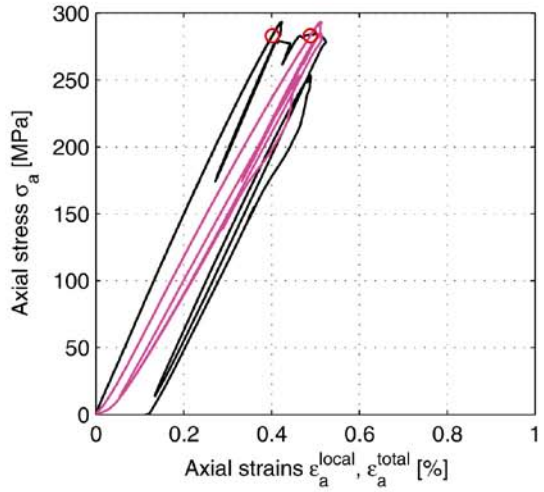

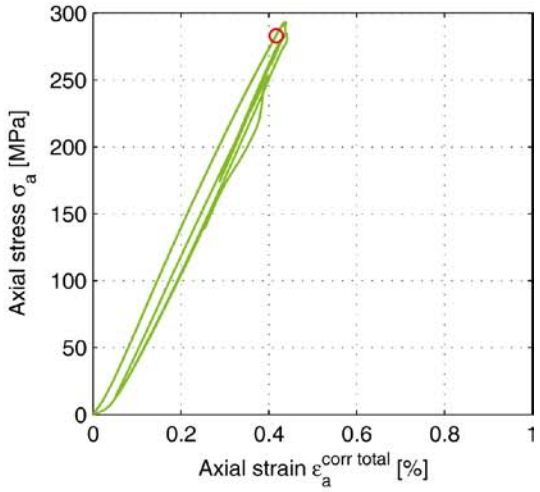

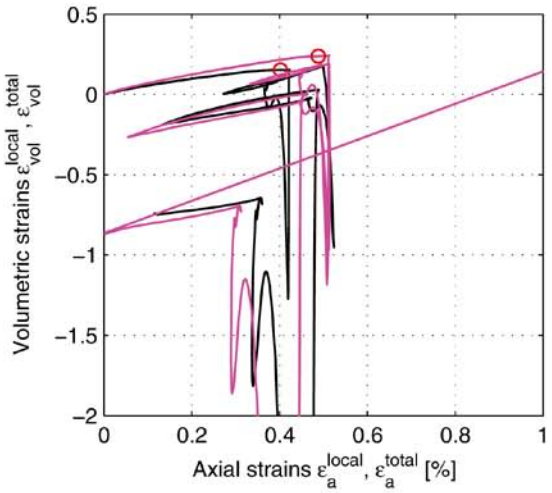

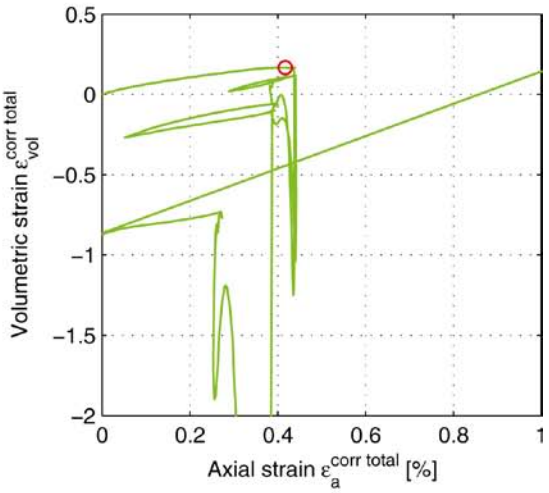

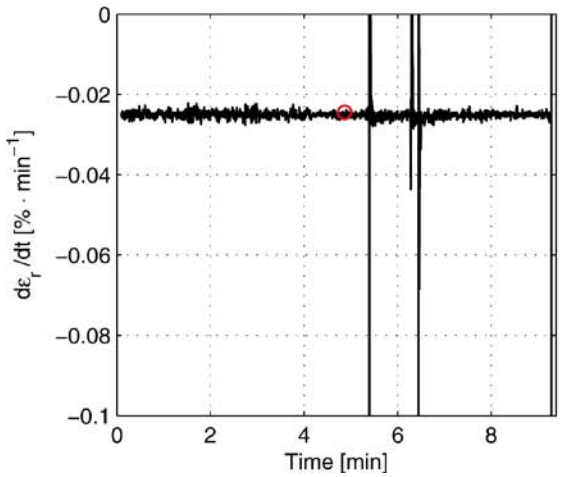

Explanation to curves above:

Based on local deformation (black)

Based on total deformation (magenta)

Based on corrected deformation (green)

Calculated system stiffness:

K_{system} = 5.2 [GN/m]

Specimen ID: KQ0054G02–113–01

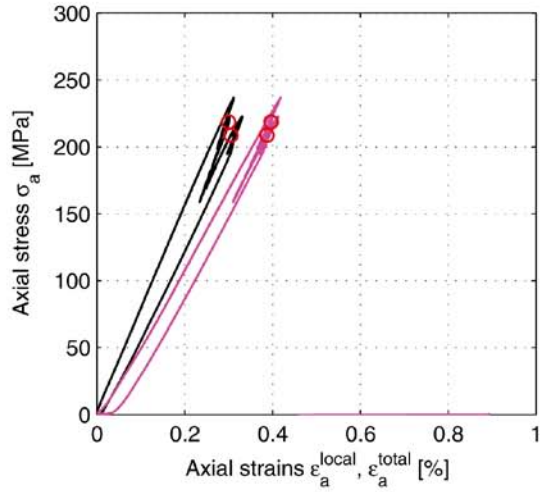

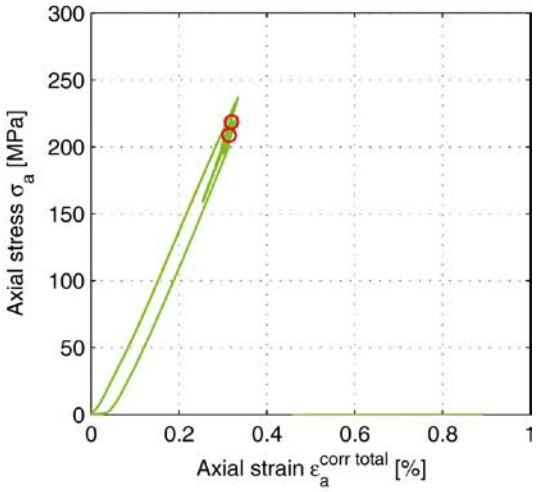

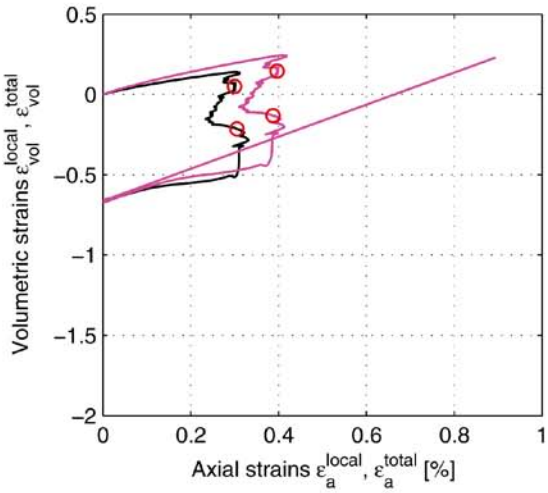

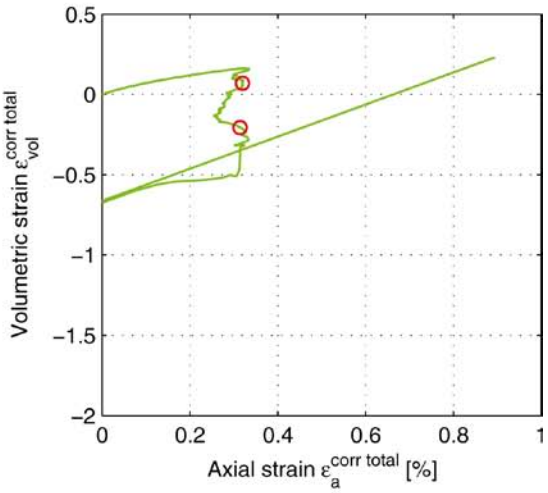

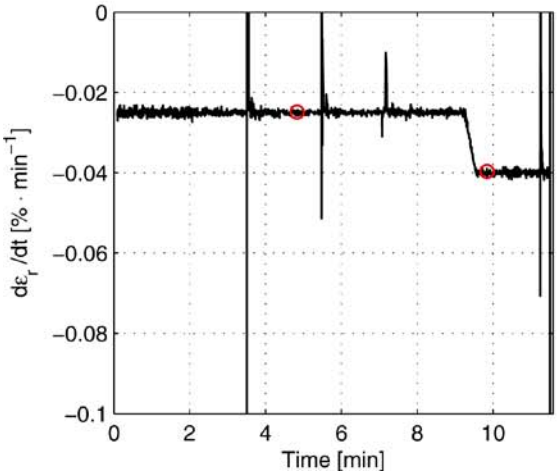

Explanation to curves above:

Based on local deformation (black)

Based on total deformation (magenta)

Based on corrected deformation (green)

Calculated system stiffness:

K_{system} = 3.7 [GN/m]

Specimen ID: KQ0054G06–113–01

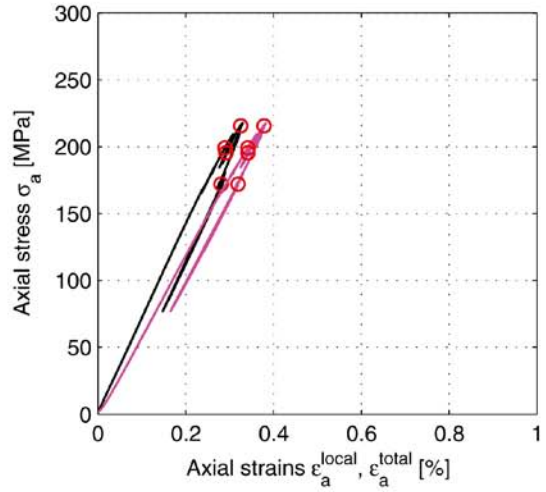

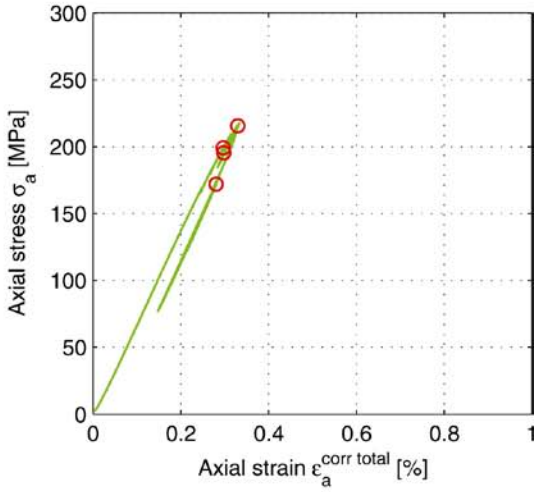

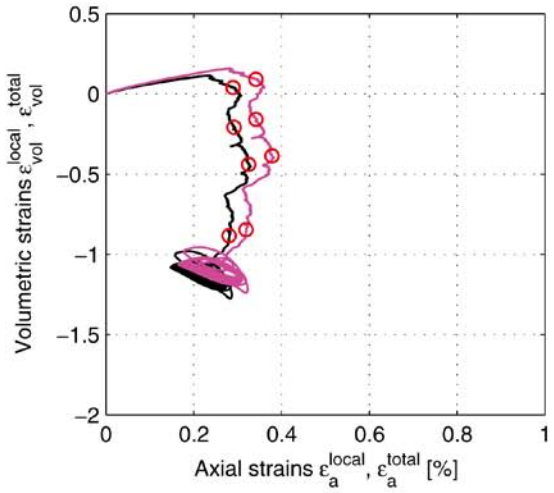

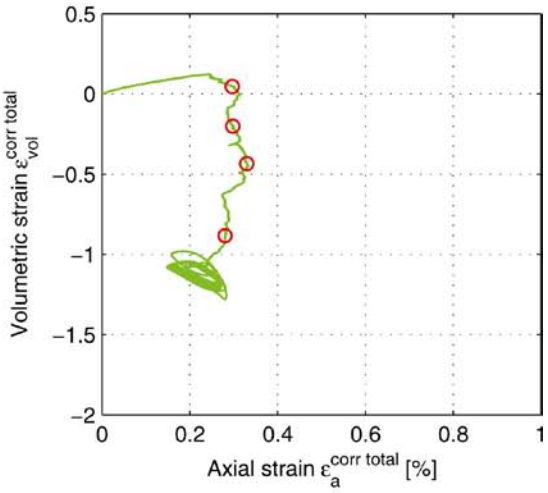

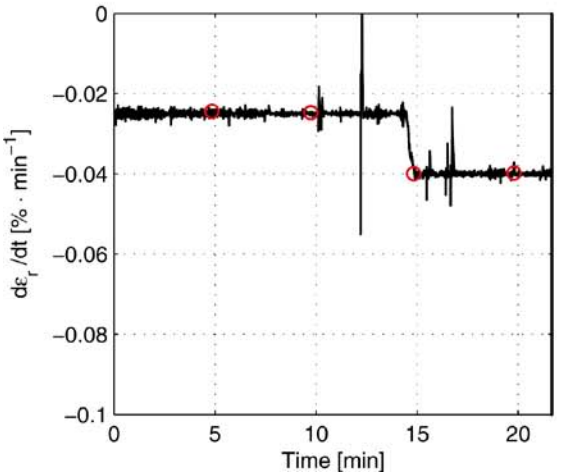

Explanation to curves above:

Based on local deformation (black)

Based on total deformation (magenta)

Based on corrected deformation (green)

Calculated system stiffness:

K_{system} = 5.8 [GN/m]

Appendix D

Drawings of borehole positions

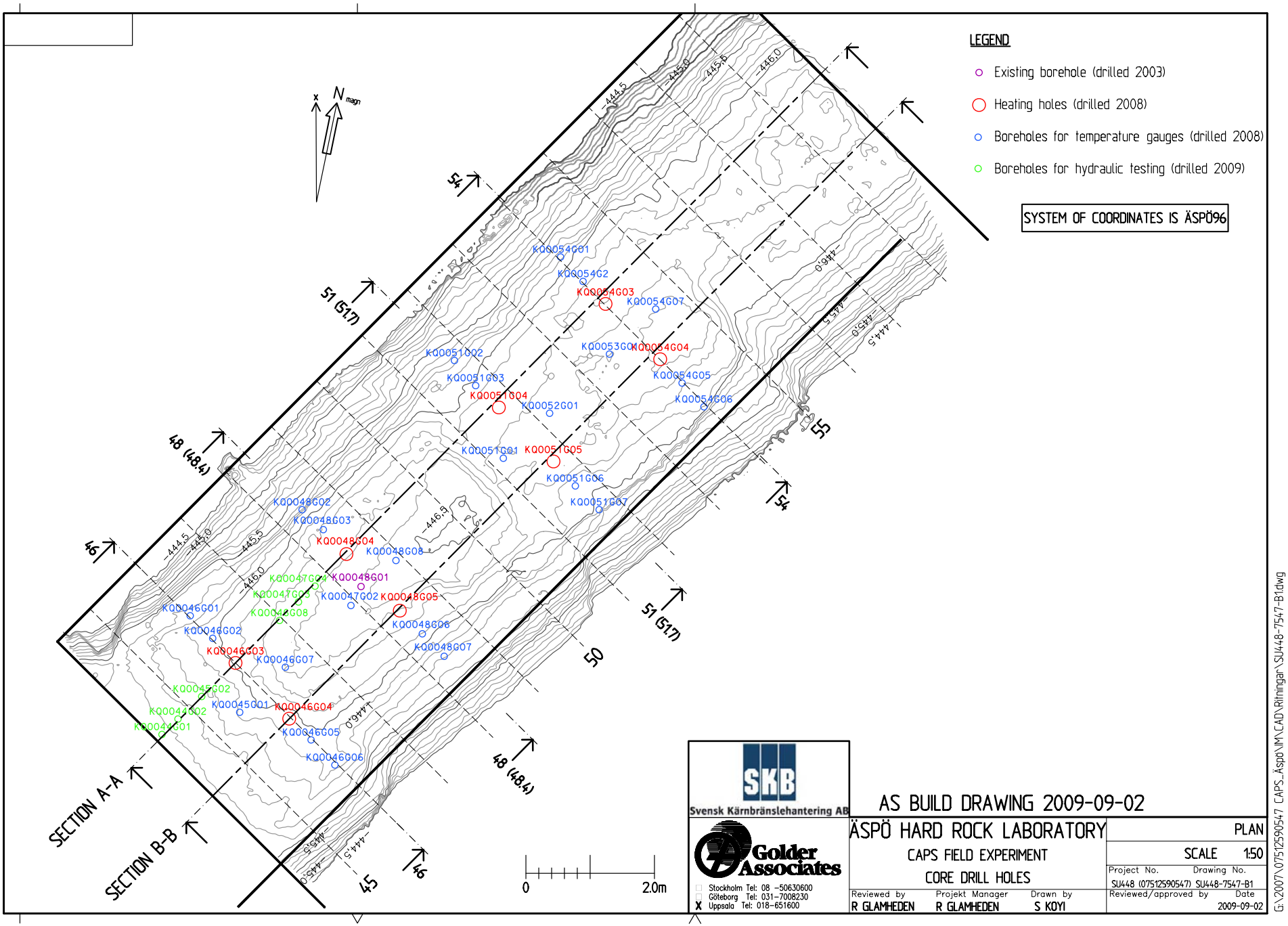
LEGEND
Existing borehole (drilled 2003)
Heating holes (drilled 2008)
Boreholes for temperature gauges (drilled 2008)
Boreholes for hydraulic testing (drilled 2009)
SYSTEM OF COORDINATES IS ÄSPÖ96
N magn
KQ0054G01
KQ0054G02
KQ0054G03
KQ0054G07
KQ0051G02
KQ0053G01
KQ0054G04
KQ0051G03
KQ0054G05
KQ0051G04
KQ0052G01
KQ0054G06
KQ0051G01
KQ0051G05
KQ0051G06
KQ0051G07
KQ0048G02
KQ0048G03
KQ0048G04
KQ0048G08
KQ0047G01
KQ0048G01
KQ0047G03
KQ0047G02
KQ0048G05
KQ0048G08
KQ0046G01
KQ0048G06
KQ0046G02
KQ0046G03
KQ0048G07
KQ0046G07
KQ0045G02
KQ0045G01
KQ0046G04
KQ0044G02
KQ0044G01
KQ0046G05
KQ0046G06
SECTION A-A
SECTION B-B
0
2.0m
Svensk Kärnbränslehantering AB
Golder Associates
Stockholm Tel: 08 -50630600
Göteborg Tel: 031-7008230
Uppsala Tel: 018-651600
AS BUILD DRAWING 2009-09-02
ÄSPÖ HARD ROCK LABORATORY
CAPS FIELD EXPERIMENT
CORE DRILL HOLES
PLAN
SCALE 1:50
Project No. SU448 (07512590547)
Drawing No. SU448-7547-B1
Reviewed by R GLAMHEDEN
Projekt Manager R GLAMHEDEN
Drawn by S KOYI
Reviewed/approved by
Date 2009-09-02
G:\2007\07512590547 CAPS_Äspö\IM\CAD\Ritningar\SU448-7547-B1.dwg

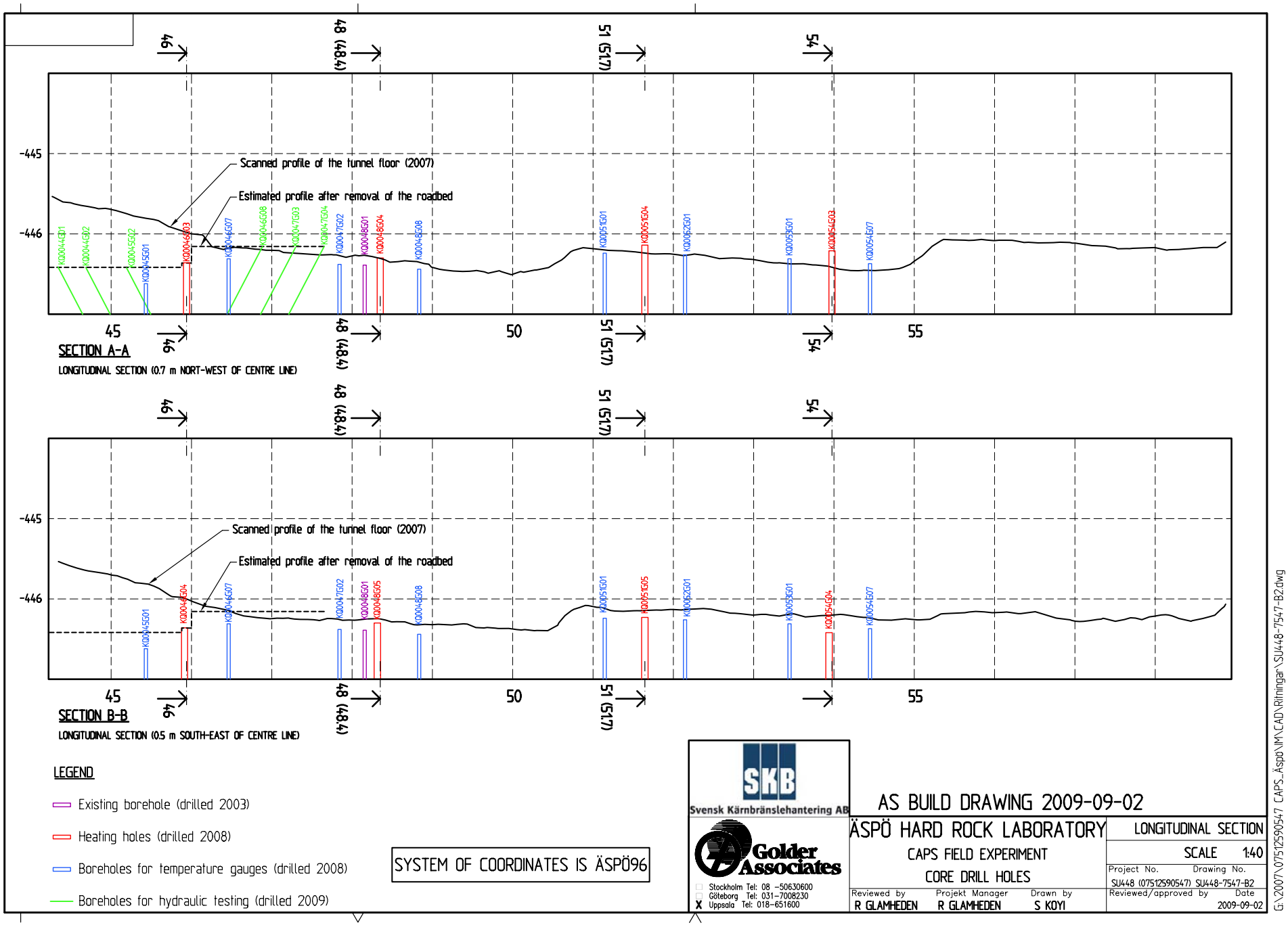

LEGEND

- Existing borehole (drilled 2003)
- Heating holes (drilled 2008)
- Boreholes for temperature gauges (drilled 2008)
- Boreholes for hydraulic testing (drilled 2009)

SYSTEM OF COORDINATES IS ÄSPÖ96

SKB
Svensk Kärnbränslehantering AB
Golder Associates
Stockholm Tel: 08 -50630600
Göteborg Tel: 031-7008230
X Uppsala Tel: 018-651600

AS BUILD DRAWING 2009-09-02

ÄSPÖ HARD ROCK LABORATORY
CAPS FIELD EXPERIMENT
CORE DRILL HOLES

LONGITUDINAL SECTION
SCALE 1:40
Project No. Drawing No.
SU448 (07512590547) SU448-7547-B2

Reviewed by	Projekt Manager	Drawn by	Reviewed/approved by	Date
R GLAMHEDEN	R GLAMHEDEN	S KOYI		2009-09-02

G:\2007\07512590547 CAPS_Äspö\IM\CAD\Ritningar\SU448-7547-B2.dwg

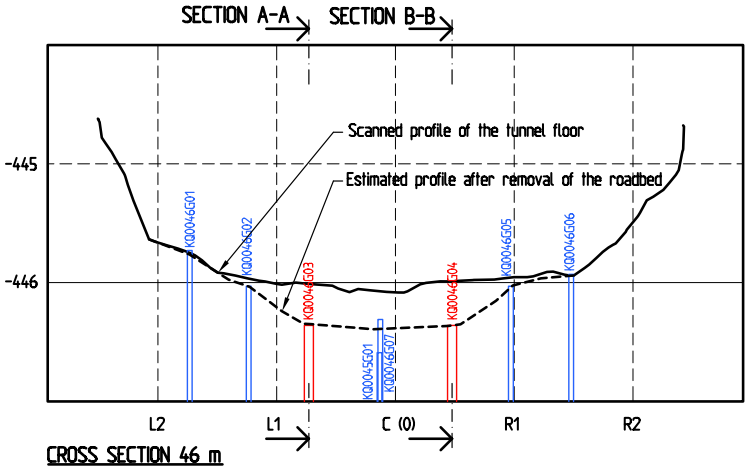

CROSS SECTION 46 m

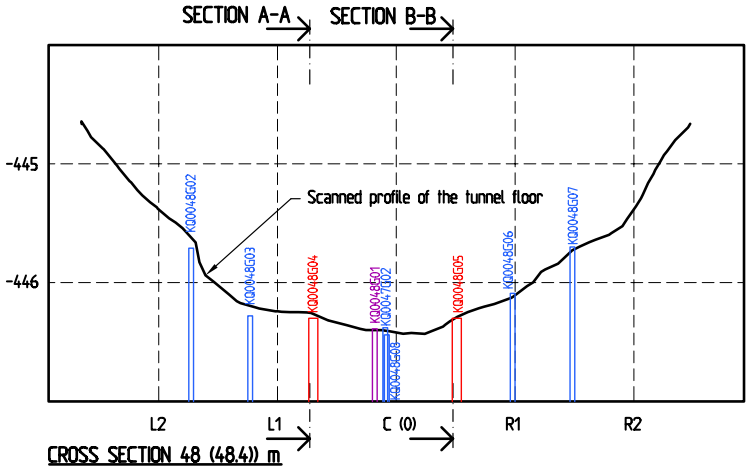

CROSS SECTION 48 (48.4) m

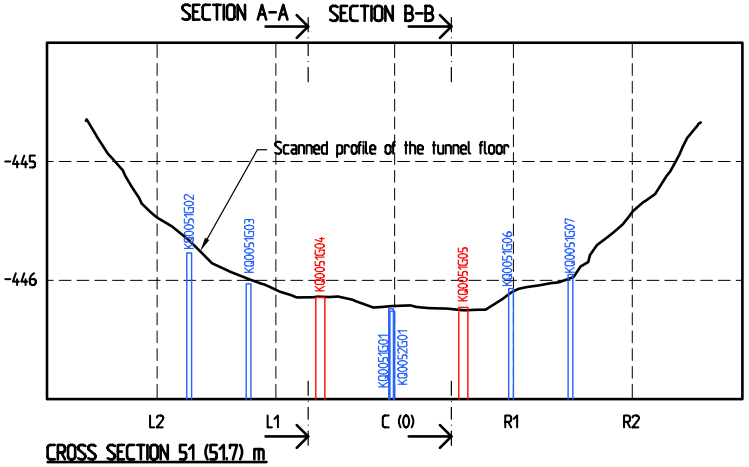

CROSS SECTION 51 (51.7) m

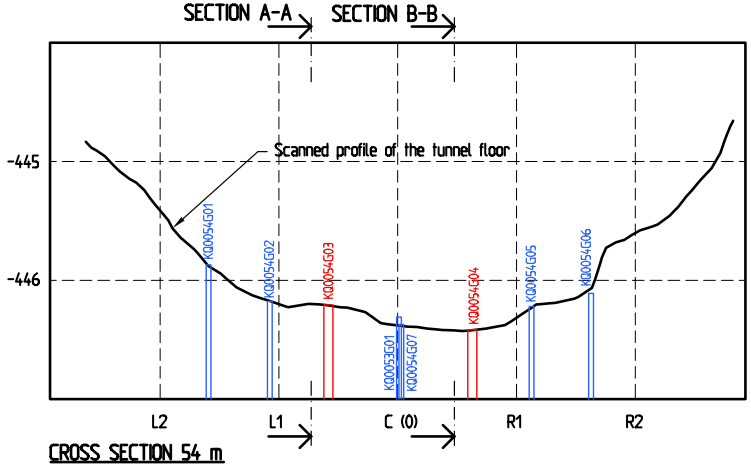

CROSS SECTION 54 m

LEGEND

- Existing borehole (drilled 2003)
- Heating holes (drilled 2008)
- Boreholes for temperature gauges (drilled 2008)

SYSTEM OF COORDINATES IS ÄSPÖ96

Svensk Kärnbränslehantering AB

Golder Associates
Stockholm Tel: 08 -50630600
Göteborg Tel: 031-7008230
X Uppsala Tel: 018-651600

AS BUILD DRAWING 2009-09-02

ÄSPÖ HARD ROCK LABORATORY
CAPS FIELD EXPERIMENT
CORE DRILL HOLES

CROSS SECTION
SCALE 1:40

Reviewed by	Projekt Manager	Drawn by
R GLAMHEDEN	R GLAMHEDEN	S KOYI

Project No. SU448 (07512590547)
Drawing No. SU448-7547-B3
Reviewed/approved by R GLAMHEDEN
Date 2009-09-02

G:\2007\07512590547 CAPS_Äspö\IM\CAD\Ritningar\SU448-7547-B3.dwg

Appendix E

Results from oedometer test on pellets

Lars Jacobsson, SP Technical Research Institute of Sweden

March 2010

Oedometer tests on bentonite, expanded clay and natural gravel

Summary

Uniaxial compression tests (oedometer tests 0–250 kPa) of bentonite clay, expanded clay and natural gravel at two compaction states have been carried out in order to determine the compressibility. A customized oedometer cell was used yielding a specimen size with 200 mm diameter and 50 mm height. The specimen height was chosen to be the same as the slot between the borehole wall and the inner tube in the heating holes of CAPS field experiment. It was found that the bentonite and the expanded clay had similar compressibility, whereas the natural gravel was significantly stiffer. In addition, the grain size distributions of the expanded clay and the natural gravel were determined. Two complementary studies were carried out in a smaller stress range (0–15 kPa) in order to investigate the low stress range more closely. It was found that the bentonite and the expanded clay had similar compressibility in this stress range for uncompacted material. The bentonite clay seem to have about twice as high stiffness as the expanded clay after moderate compaction. An overall observation is that there is a large scatter between the results with in the various test series. This is probably related to the rather low ratio between the specimen height and the particle sizes.

Contents

E1 Introduction

This investigation was conducted in three steps during July 2008 (I) and March and May 2009 (II), respectively September 2009 (III) as a part in the CAPS-project conducted by the Swedish Nuclear Fuel and Waste Management Co (SKB). The initial study (July 2008) comprised uniaxial compression tests, so called oedometer tests, which were carried out in laboratory on "pillow-shaped" pieces of bentonite clay (MX80), expanded clay (Leca) and natural gravel. The tests were carried out in order to compare the compressibility of these materials, within a loading range of 0–250 kPa, under such compaction state that will occur in the 50 mm slot between the borehole wall and the inner tube in the heating holes of CAPS field experiment. The dimensions of the holes are approximately 4.5 m in height and 0.5 m in diameter.

It is well known that the compressibility of granular material is dependent on the compaction state. However, the actual amount of compaction that will take place when the material is poured into the deposition holes is unknown. It was then decided that compression tests would be carried out on the different materials at two compaction states, loose compaction and moderate compaction, which should set the upper and lower bound of the compaction that will take place in the field tests.

Two complementary investigations were carried out during March and May 2009 respectively September 2009 in order to conduct the uniaxial compression tests on bentonite clay and expanded clay (Leca) and at a significantly smaller loading range 0–15 kPa as the expected confinement in-field is expected to be in this stress range. The initial tests carried out during July 2008 revealed that the natural gravel was not a representative substitute material for bentonite clay and was therefore omitted during the complementary investigations. An overview of the mechanical tests are shown in Table E-1.

Table E-1. Type of tests carried out for the various test occasions.

	0–250 kPa Loosely compacted Steel cover	**0–250 kPa Moderately compacted Steel cover**	**0–15 kPa Loosely compacted Aluminium cover**	**0–15 kPa Moderately compacted Aluminium cover**
Bentonite	I	I	II	III
Expanded clay	I	I	II	III
Natural gravel	I	I	–	–

E2 Test material

Three types of materials were tested: "pillow-shaped" bentonite pellets (width 16 mm and thickness 8 mm), expanded clay (8–14 mm) and natural gravel. The material was sent to SP in plastic buckets with a total amount of approximately 15 litres per material type. Respective material was split up in a number of portions for the sieving, compaction tests and the compression tests following SS-EN 932-2, section 7, by means of a rotatary sample divider.

The grain-size distribution was determined for the expanded clay and the natural stone gravel according to SS-EN 933-1, where the natural gravel was washed and screened and the expanded clay was dry-screened. The grain-size distribution was not determined for the bentonite as it was judged that it would be too much damaged during the screening operation. The results from the screening are shown in Appendix AE1 (material for the initial investigation) and Appendix AE2 (material for the complementary investigation). The density of the LECA clay and expanded clay was determined according to SS-EN 1097-3 on the material used for the complementary investigation, Appendix AE3.

E3 Equipment and test procedure

E3.1 I. Initial tests (July 2008)

A customized oedometer cell with a diameter of 200 mm and a height of 50 mm were manufactured. The height of the cell represents the slot width in the CAPS field experiment. The cover of the cell is a steel plate with a weight of 13.2 kg.

The material kept in a plastic bag was carefully poured into the cell as shown in Figure E-1 in order to obtain a loose packing. A ruler was used to carefully levelling the material and scraping off excess material. Some grains were manually picked and replaced. The cover was placed on the cell and the initial height was measured, see Figure E-2 (bentonite clay). A picture showing the natural gravel placed in the cell is shown in Appendix AE4.

The compaction ability of the materials was investigated by a separate vibration test. The material was poured into the cell and the cover was placed on the cell as previously described, yielding an initial state with a loose compaction. The cell was placed on a vibrating table and the initial specimen height was recorded corresponding to zero time compaction. The vibrating table was turned on

Figure E-1. *Bentonite is poured into the cell. (The label on the plastic bag is not correct.)*

Figure E-2. *The bentonite material placed in cell.*

for some seconds and switched off and the new specimen height was recorded. This was repeated a number of times yielding a sequence with the amount of compaction at certain total vibration times. The compaction was recorded at 0 (reference), 3, 6, 12, 18, 30 and 60 seconds. The vibration test was repeated two times for each material, see Figure E-3.

The oedometer cell was placed in a load frame during the compression tests. The force was measured using a electrical load cell. The deformation was measured using two linear displacement transducers, see Figure E-4. Tests on loose compacted material (no vibration) and on moderately compacted material (three seconds vibration) were carried out three times per material and compaction state. One extra test was carried out in one case.

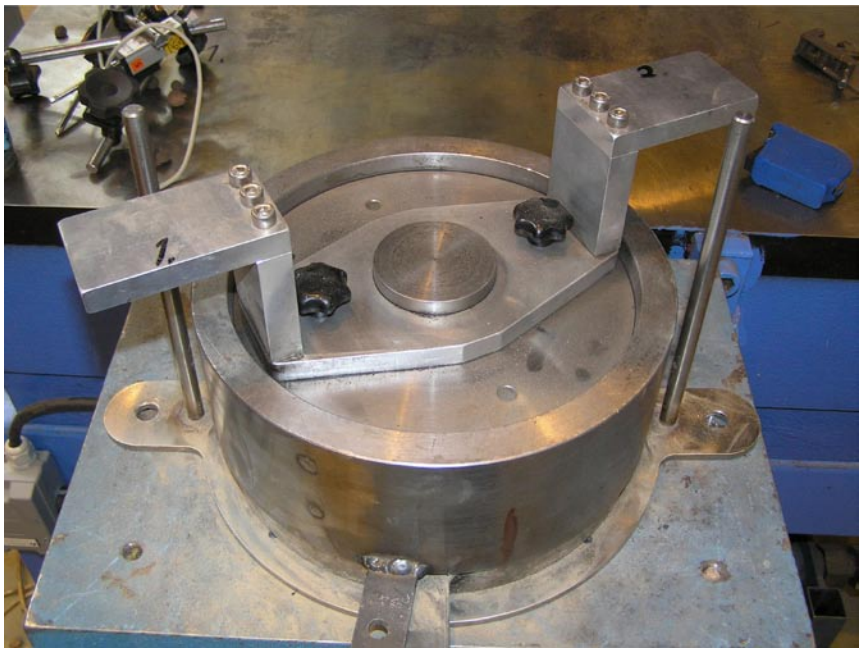

Figure E-3. *The cover is placed on the cell and is standing on the vibration table.*

Figure E-4. *The oedometer cell is placed in the load frame. The piston is pressing on the cell cover via a spherical joint. The two linear displacement transducers are installed.*

E3.2 II. Complementary tests (March and May 2009)

The same oedometer cell was used during the complementary tests. A lighter aluminium cover with a weight of 1.62 kg was manufactured for the complementary tests, in addition to the original cover made of steel. The weight of the cover of the oedometer cell made a contribution to the confinement that could not be neglected as the loading range was decreased. The steel cover yields an initial confinement of 4.1 kPa and the aluminium cover yields an initial confinement of 0.52 kPa.

Moreover, the smaller loading range implied that deformation gauges with smaller deformation range were used in order to get sufficient resolution of the deformation measurements.

All tests were carried out on a loosely compacted material and prepared in the same way as during the initial investigation, see Section E3.1. Tests using a steel cover and aluminium cover were conducted for comparison. The tests where a steel cover is used are conduced in the same way as for the initial tests described in Section E3.1, which means that they are an exact repetition of the tests, but with higher resolution deformation measurement gauges and a smaller loading range.

E3.3 III. Complementary tests (September 2009)

Additional tests were carried out almost in the same manner as the tests described in Section E3.2. The difference is that the materials was first compacted by vibration the material for three seconds using the steel cover during the vibration as described in Section E3.1. Then the cover was carefully replaced to the aluminium cover and the compression test was subsequently carried out.

E4 Results

E4.1 I. Vibration tests (initial tests July 2008)

The results from the vibration tests are shown in Figures E-5 to E-7. It is seen that the expanded clay is compacted about 10–20% more than the other two materials at any time. Moreover, the bentonite clay and the natural gravel seem to reach dense state quicker as the compaction vs vibration time level-out earlier for those materials.

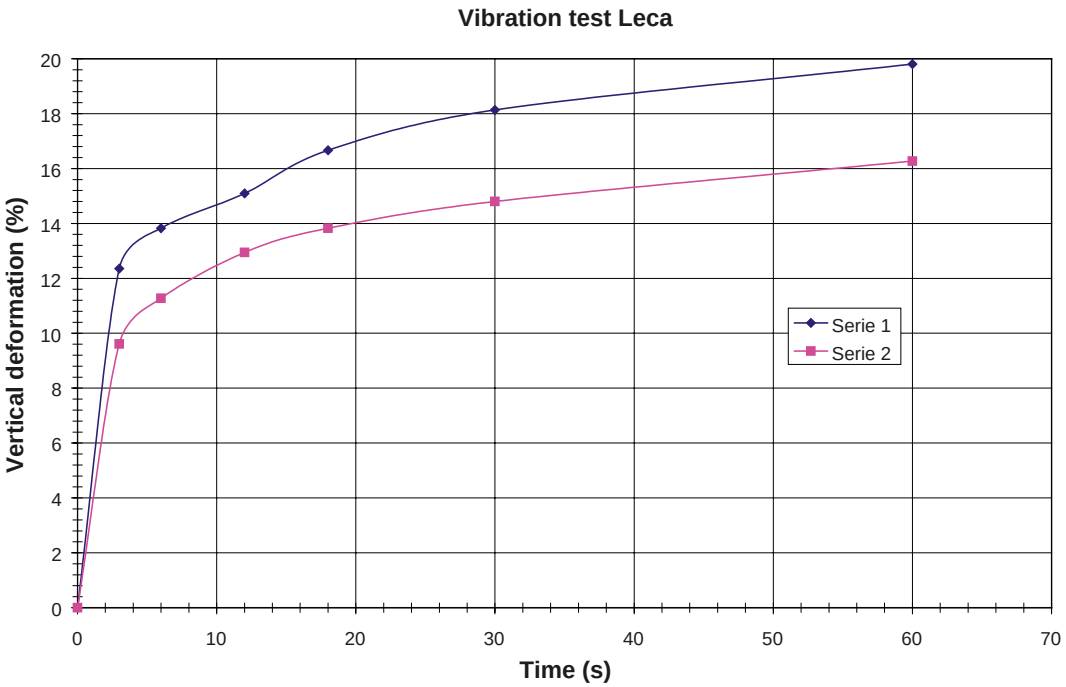

Figure E-5. *Results of the vibration test for the expanded clay.*

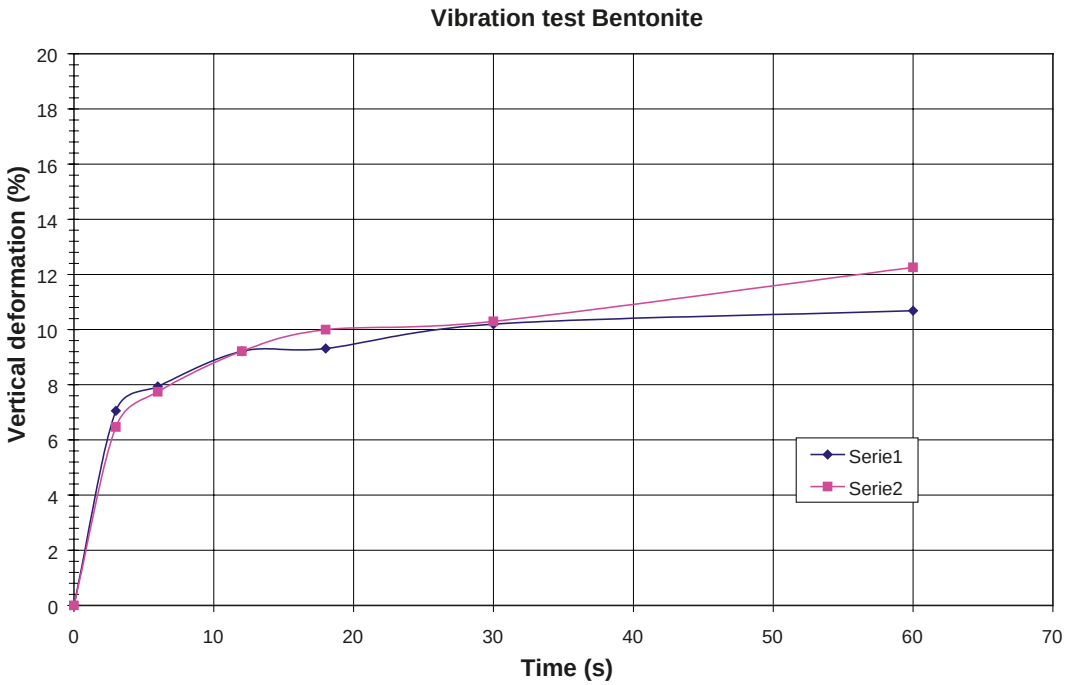

Figure E-6. *Results of the vibration test for the bentonite.*

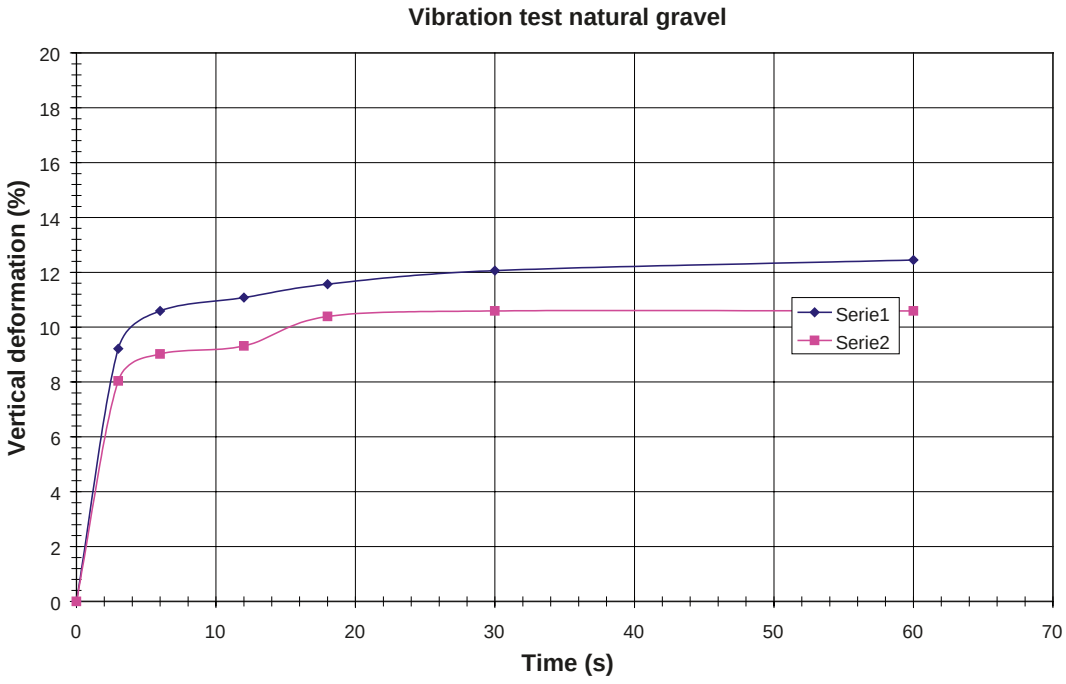

Figure E-7. *Results of the vibration test for the natural gravel.*

E4.2 I. Compression tests (initial tests July 2008)

The results from the initial compression tests are shown in Figures E-8 to E-9. The weight of the cell cover yields a confinement of 4.1 kPa (0.0041 MPa) which has been omitted in the stress calculations. The stiffness of the bentonite and the expanded clay is close to each other, whereas the stiffness of the natural gravel is significantly higher. Two results from the tests on vibrated expanded

clay (Leca 8-14, specimens 1 and 2) display a low initial and progressively increasing stiffness, see Figure E-9a and E-9b. The results from the third specimen (Leca 8-14, specimen 3), Figure E-9a and E-9b, displays an expected behaviour. One extra specimen was tested (Leca 8-14, specimen 4) which yielded results close to Leca 8-14, specimen 3.

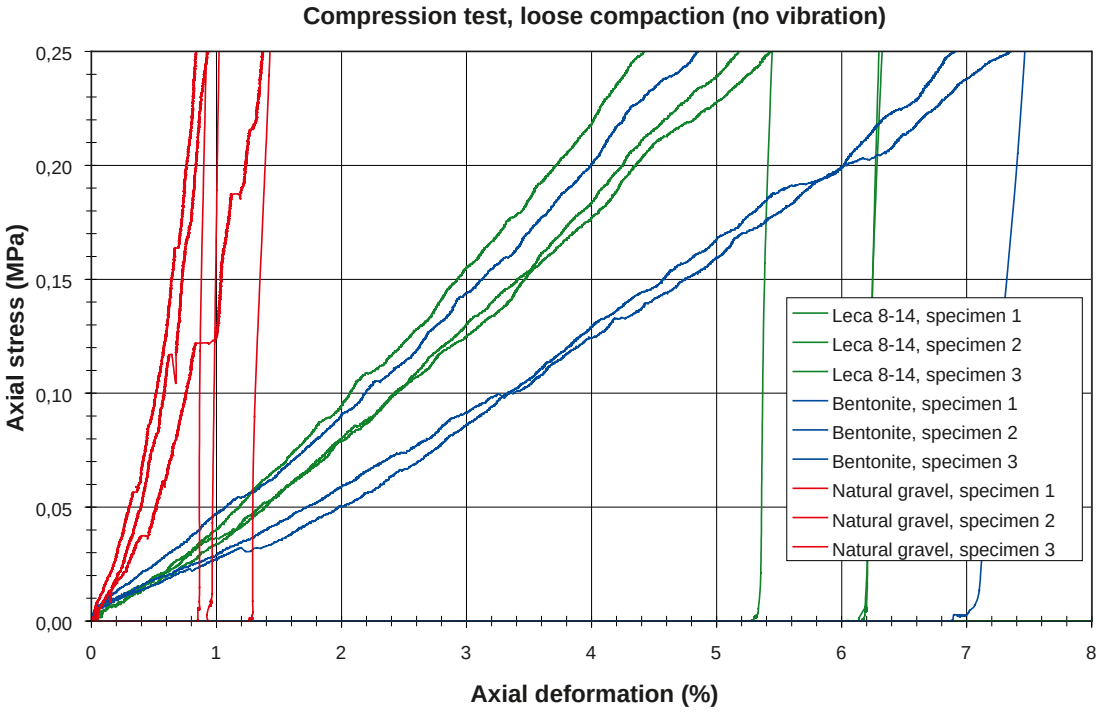

Figure E-8a. *Results from compression tests. The material has not been compacted.*

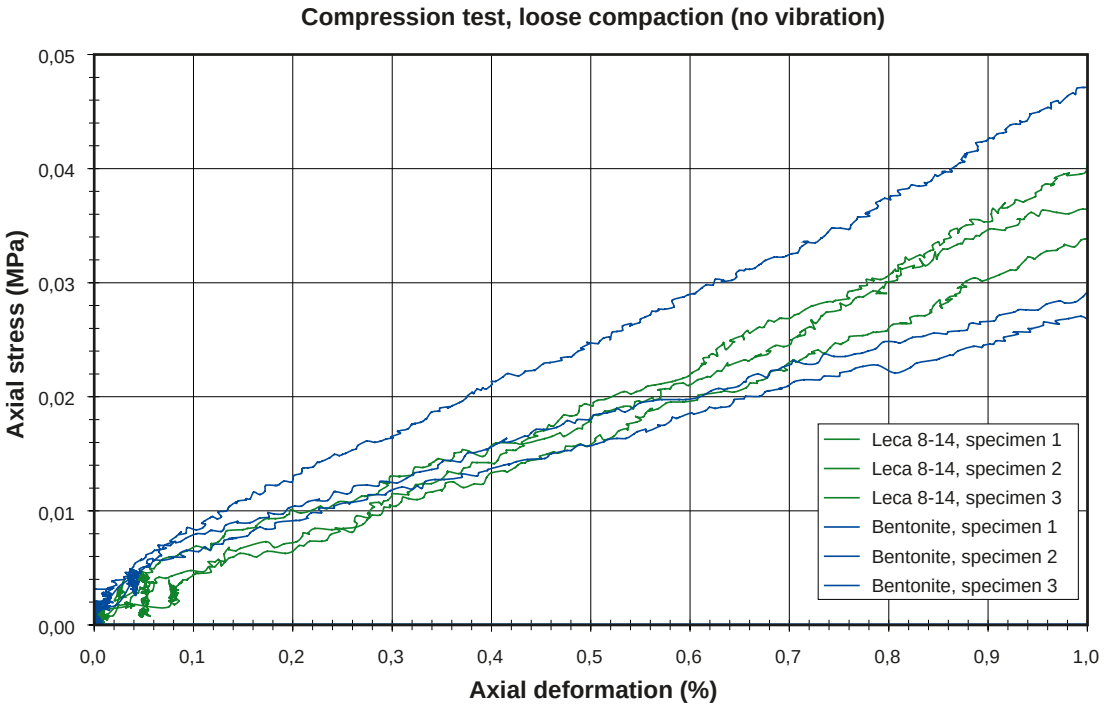

Figure E-8b. *Close-up of the results from compression tests shown in Figure E-8a (0–50 kPa).The material has not been compacted.*

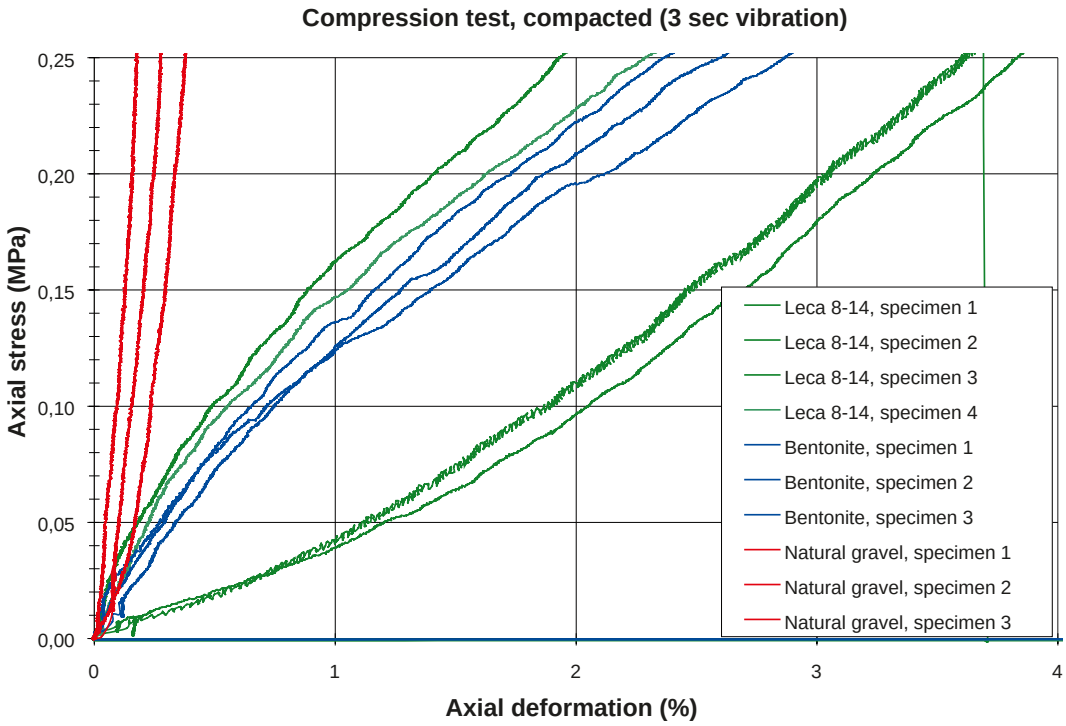

Figure E-9a. *Results from compression tests. The material has been compacted by vibration during three seconds.*

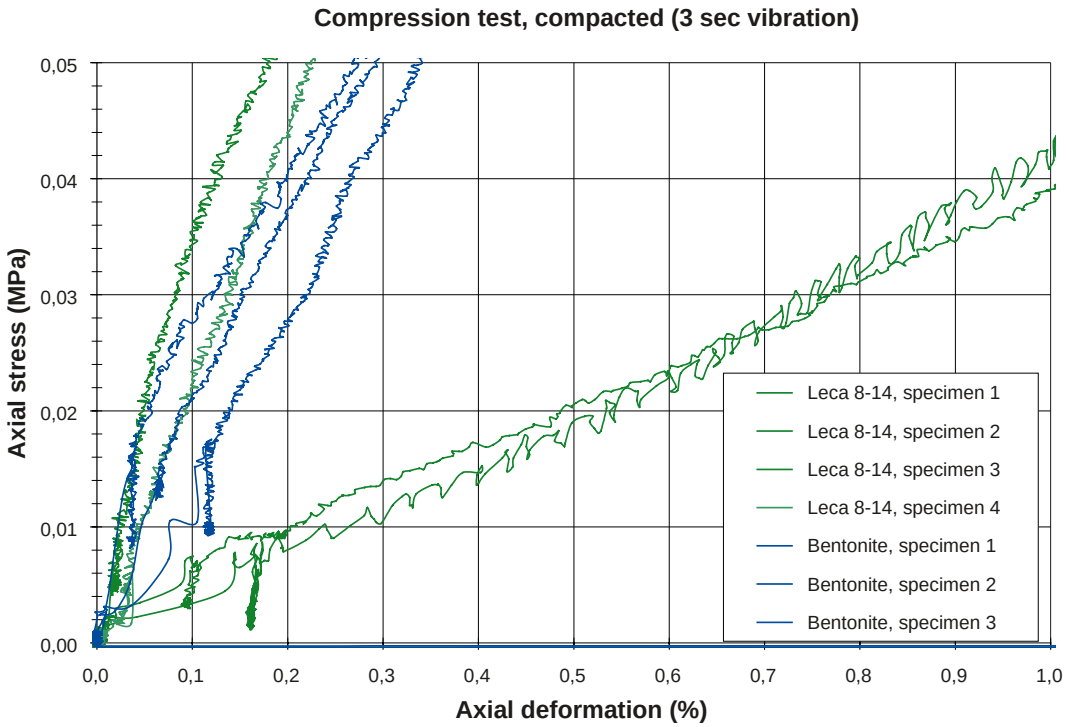

Figure E-9b. *Close-up of the results from compression tests shown in Figure E-9a (0–50 kPa). The material has been compacted by vibration during three seconds.*

E4.3 II. Compression tests (complementary tests March and May 2009)

The results from the complementary compression tests are shown in Figures E-10 to E-13. The weight of the cell covers yield a confinement of 4.1 kPa (steel) and 0.52 kPa (aluminium), respectively, which has been omitted in the stress calculations. It was seen once again that the stiffness of the bentonite and the expanded clay is close to each other. Moreover, it is seen that the axial stiffness is much lower when the initial confinement is lower, i.e. when the aluminium cover was used. The results in Figures E-12 and E-13 are fully comparable with those in Figure E-8a.

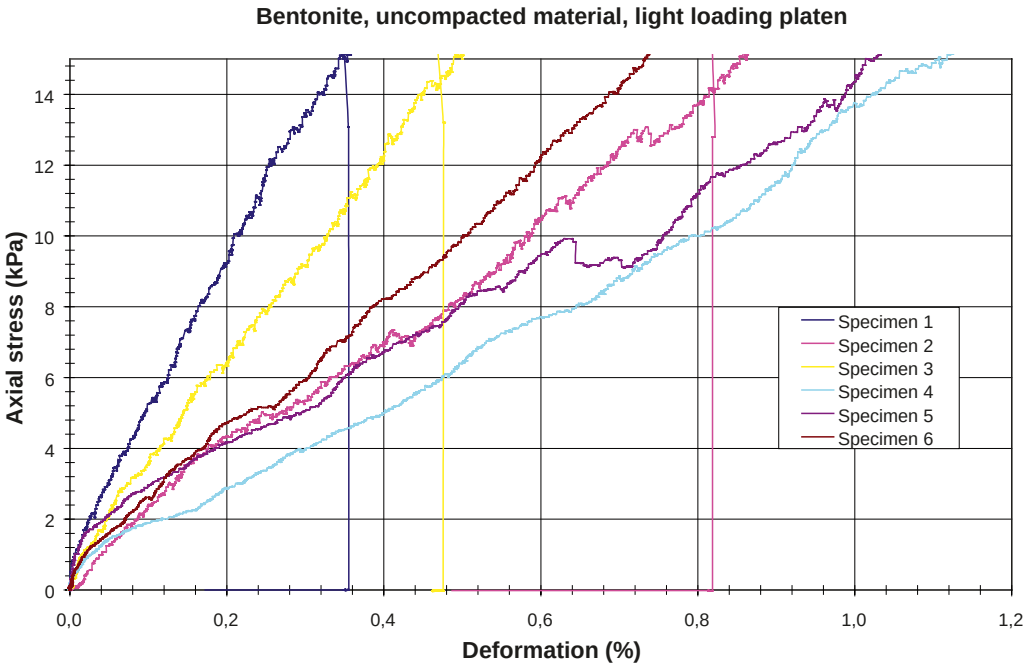

Figure E-10. *Results from compression tests on bentonite clay using an aluminium cover on the oedometer cell. The material has not been compacted.*

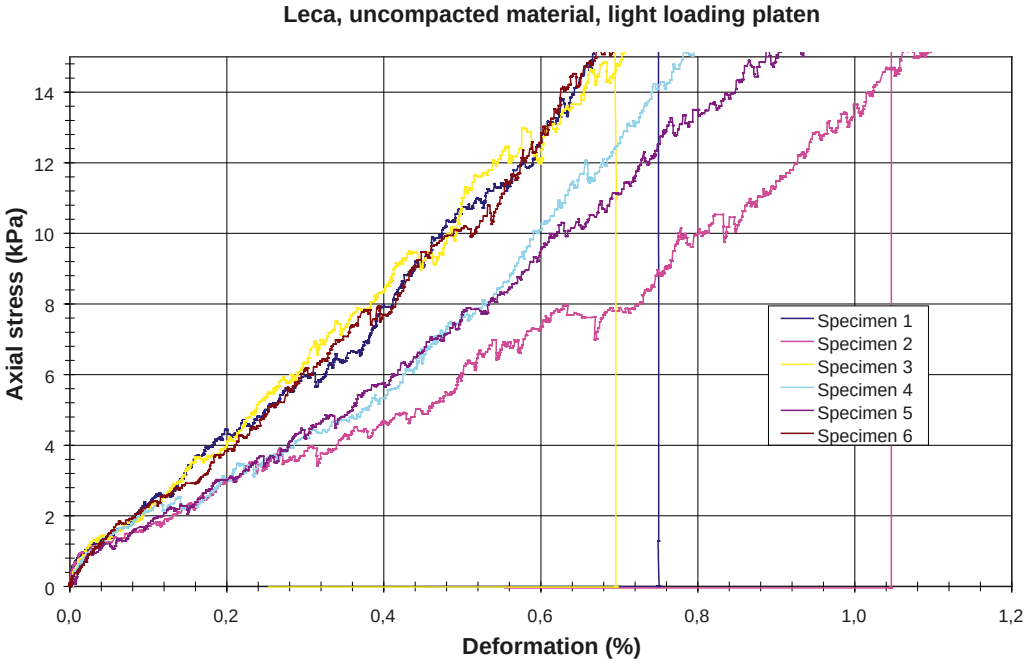

Figure E-11. *Results from compression tests on expanded clay using an aluminium cover on the oedometer cell. The material has not been compacted.*

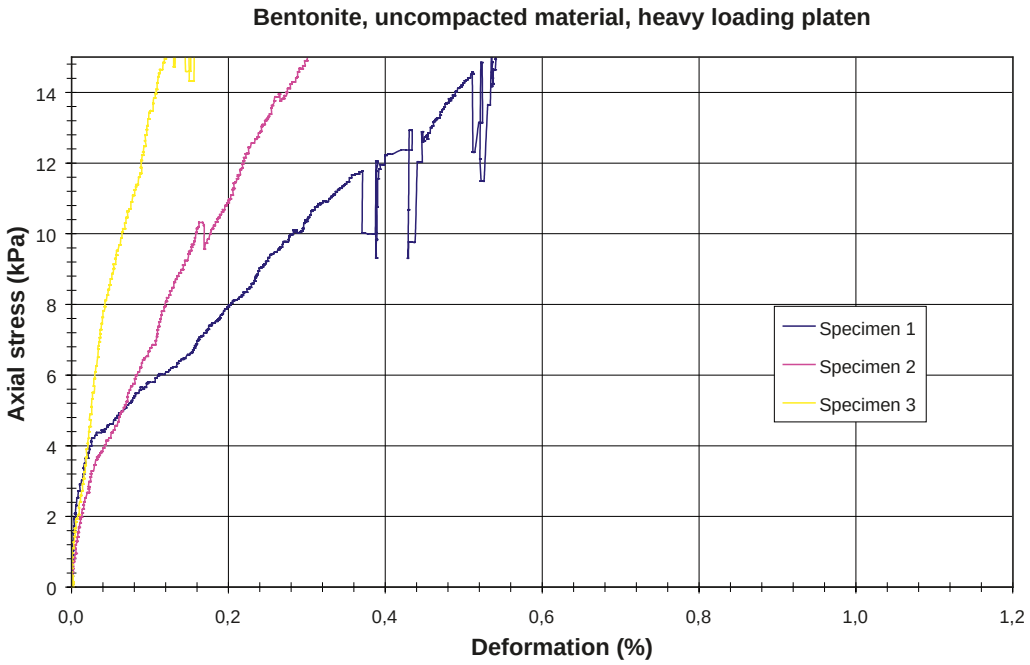

Figure E-12. *Results from compression tests on bentonite clay using an steel cover on the oedometer cell. The material has not been compacted.*

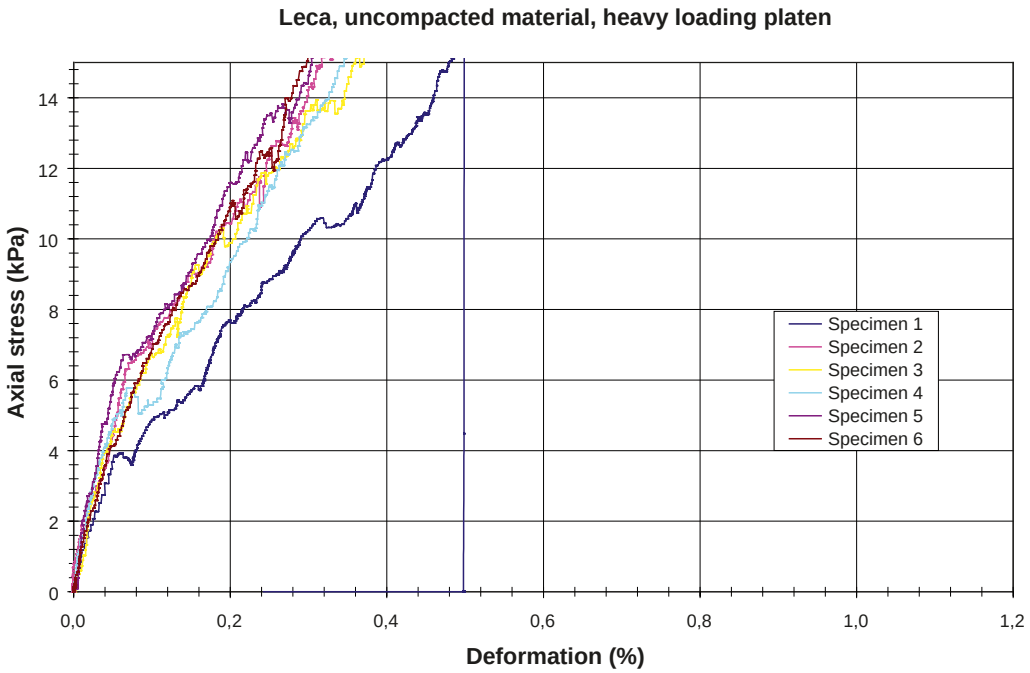

Figure E-13. *Results from compression tests on expanded clay using an steel cover on the oedometer cell. The material has not been compacted.*

E4.4 III. Compression tests (complementary tests September 2009)

The results from the complementary compression tests are shown in Figures E-14 and E-15. The weight of the cell cover (aluminium) yield a confinement of 0.52 kPa, which has been omitted in the stress calculations. It is seen that the stiffness of the bentonite is twice as high as for the expanded clay. Moreover, it is seen that the axial stiffness is much lower when the initial confinement is lower, i.e. when the aluminium cover was used.

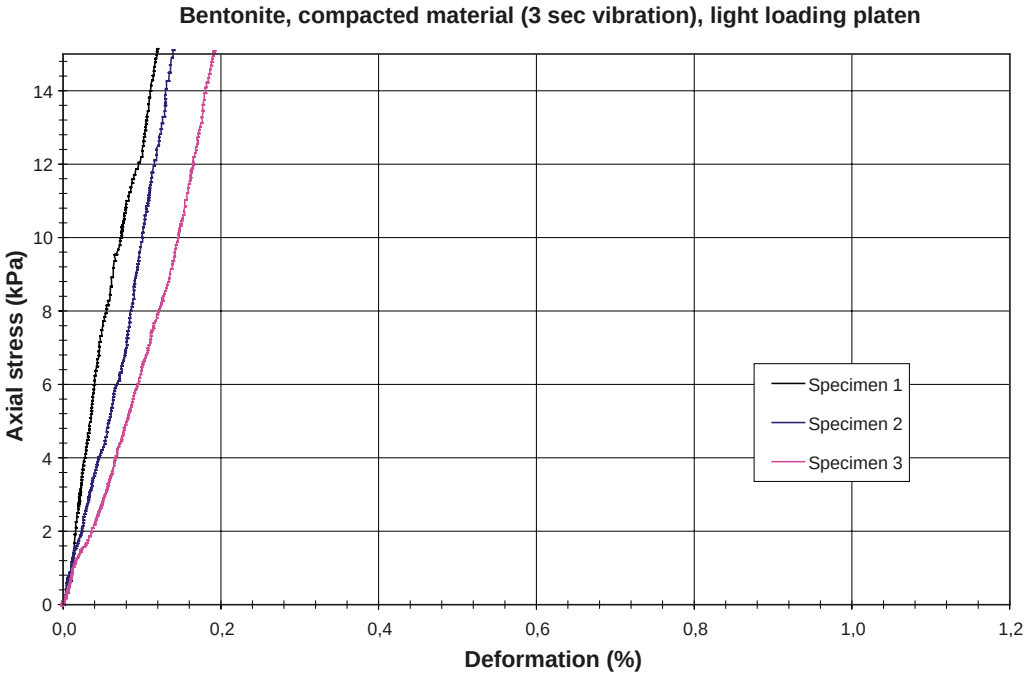

Figure E-14. *Results from compression tests on bentonite clay using an aluminium cover on the oedometer cell. The material has been compacted by vibration during three seconds.*

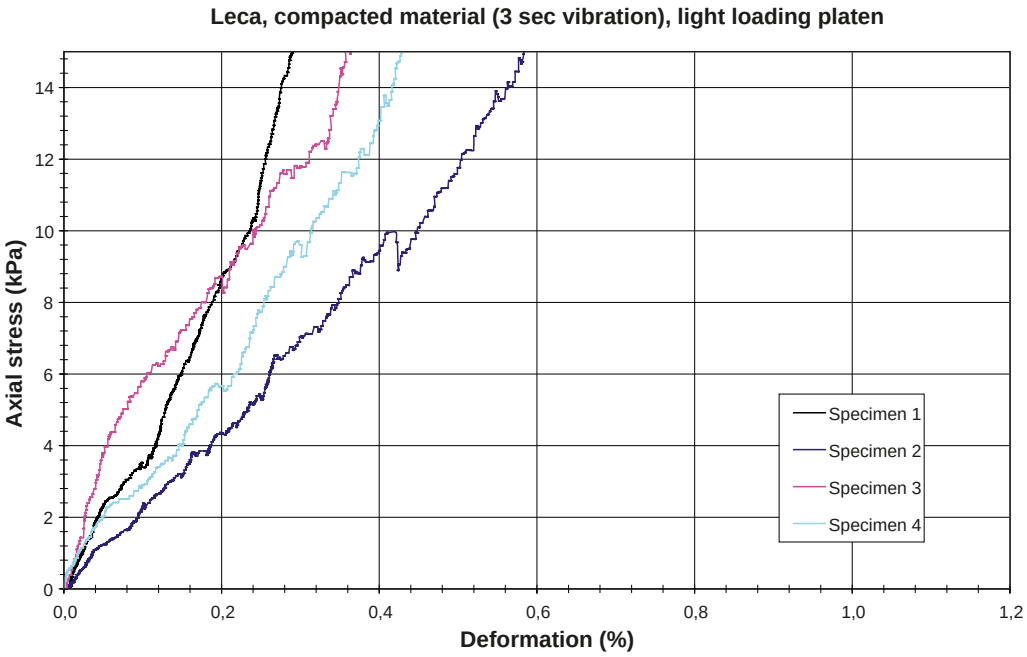

Figure E-15. *Results from compression tests on expanded clay using an aluminium cover on the oedometer cell. The material has been compacted by vibration during three seconds.*

E5 Concluding remarks

E5.1 Initial tests (July 2008)

The results from the vibration tests display that more than 50% of the compaction takes place during the first three seconds of vibration. This holds for all three materials. It was judged that the compaction in the field tests would not exceed the compaction that is obtained after three seconds of vibration. The compression tests were therefore conducted on material which had not been vibrated and on material that was vibrated three seconds. The compression tests of the bentonite and the expanded clay show that the compressibility of the two materials are similar. The compression tests on the natural gravel display that the stiffness is significantly larger than for the bentonite and the expanded clay.

E5.2 Complementary tests (March and May 2009)

Complementary tests was carried out on uncompacted bentonite clay and expanded clay in a smaller loading range 0–15 kPa instead of 0–250 kPa. The smaller loading range made the initial confinement caused by weight of the original cover of the oedomenter cell rather significant (4.1 kPa). A lighter cover was manufactured in order to be able to examine the behaviour at low stress. The lighter cover yields an initial confinement of 0.52 kPa. It was seen that the initial confinement was an important factor, yielding much higher axial stiffness when the confinement was higher. The compression tests of the bentonite and the expanded clay show that the compressibility of the two materials are similar as was found during the initial compression tests.

E5.3 Complementary tests (September 2009)

Tests of moderately compacted bentonite clay and expanded clay was carried out in a loading range of 0–15 kPa. It is seen that the stiffness of the bentonite clay is twice as high compared to the expanded clay.

E5.4 Overall conclusions

The mechanical response of all three tested materials is strongly dependent on the initial compaction state and the initial confinement. Moreover, the variation between the individual specimens in a test series can be significant. This is most likely related to the rather small specimen volume in comparison with the particle sizes. Especially the small specimen height (50 mm) as compared with the particle sizes yielded ratio of the specimen height to particle size of down to 3.1–3.5. The specimen height was set to be equal to the slot between the borehole wall and the inner tube in the heating holes of CAPS field experiment. It is seen that the recorded deformation in the complementary tests for the bentonite clay specimens at 15 kPa axial stress without initial vibration were 0.12–0.55% (Figure E-12) and with three seconds of initial vibration 0.12–0.19% (Figure E-14). The corresponding results for the expanded clay were 0.28–0.48% (Figure E-13) without initial vibration and 0.28–0.58% (Figure E-15) with three seconds of initial vibration. This indicates the bentonite clay easier reduces the stiffness variation between the specimens as compared with the expanded clay. It indicates that the bentonite clay attains a given compaction state easier than the expanded clay.

Beteckning: F80028
Märkning: P803046 Leca 8/14

Kornstorleksfördelning

Maskvidd (mm)	Mängd (g) Delprov 1	2	Vikt (%) Delprov 1	2	Ack vikt% passerande Delprov 1	2	Medelvärde
22,4	0,00	0,00	0,00	0,00	100,00	100,00	100,0
16	0,00	1,00	0,00	0,33	100,00	99,67	99,8
14	11,70	8,70	3,98	2,88	96,02	96,79	96,4
12,5	52,80	55,00	17,98	18,22	78,04	78,57	78,3
11,2	93,70	88,30	31,90	29,25	46,14	49,32	47,7
8	122,40	135,50	41,68	44,88	4,46	4,44	4,4
5,6	7,40	7,20	2,52	2,38	1,94	2,05	2,0
4	1,40	1,10	0,48	0,36	1,46	1,69	1,6
2	0,40	0,50	0,14	0,17	1,33	1,52	1,4
0,063	2,30	2,60	0,78	0,86	0,54	0,66	0,6
Botten	1,60	2,00	0,54	0,66			
Summa :	293,70	301,90	100,00	100,00			
Invägt :	294,10	302,50					
Förlust :	0,40	0,60					

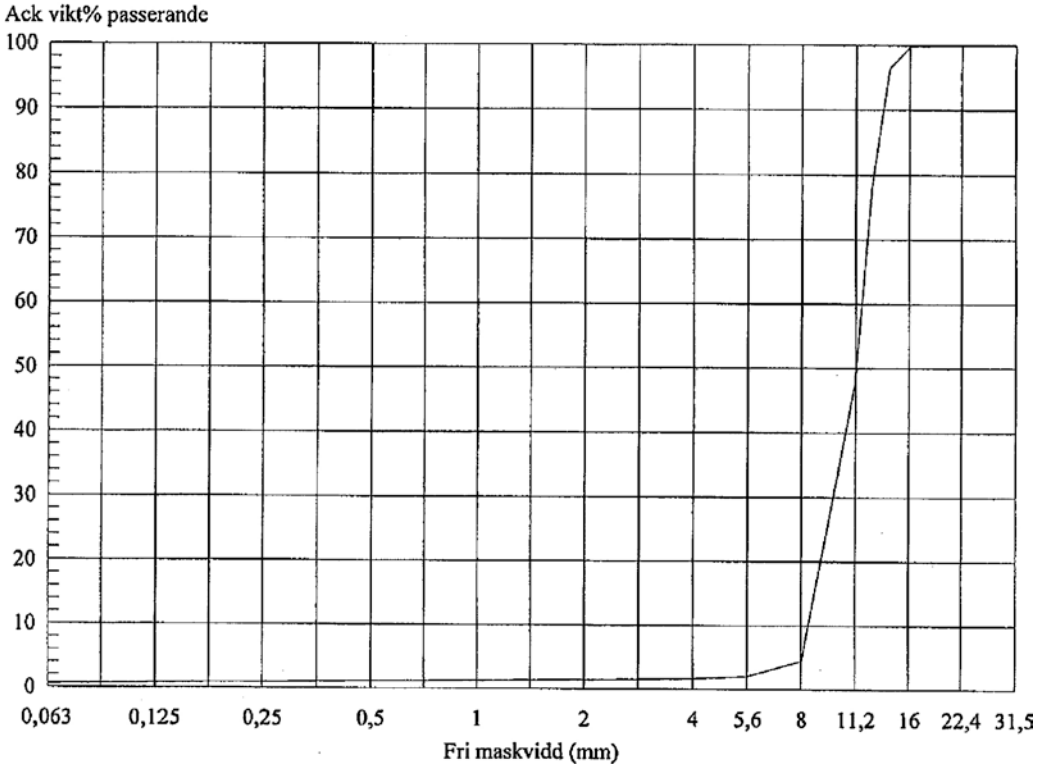

Figure AE-1. *Grain-size distribution of the expanded clay.*

Beteckning: F80028
Märkning: P803046 Natur ballast 8/16

Kornstorleksfördelning

Maskvidd (mm)	Mängd (g) Delprov 1	2	Vikt (%) Delprov 1	2	Ack vikt% passerande Delprov 1	2	Medelvärde
22,4	0,00	0,00	0,00	0,00	100,00	100,00	100,0
16	6,40	0,00	0,44	0,00	99,56	100,00	99,8
14	100,20	62,60	6,88	4,08	92,68	95,92	94,3
12,5	203,50	189,90	13,98	12,37	78,69	83,56	81,1
11,2	279,30	373,00	19,19	24,29	59,50	59,27	59,4
8	737,40	779,20	50,67	50,74	8,84	8,53	8,7
5,6	109,30	110,60	7,51	7,20	1,33	1,33	1,3
4	0,90	1,20	0,06	0,08	1,26	1,25	1,3
2	0,50	0,70	0,03	0,05	1,23	1,20	1,2
0,063	8,80	9,70	0,60	0,63	0,63	0,57	0,6
Botten	9,10	8,80	0,63	0,57			
Summa :	1455,40	1535,70	100,00	100,00			
Invägt :	1455,40	1534,90					
Förlust :	0,00	-0,80					

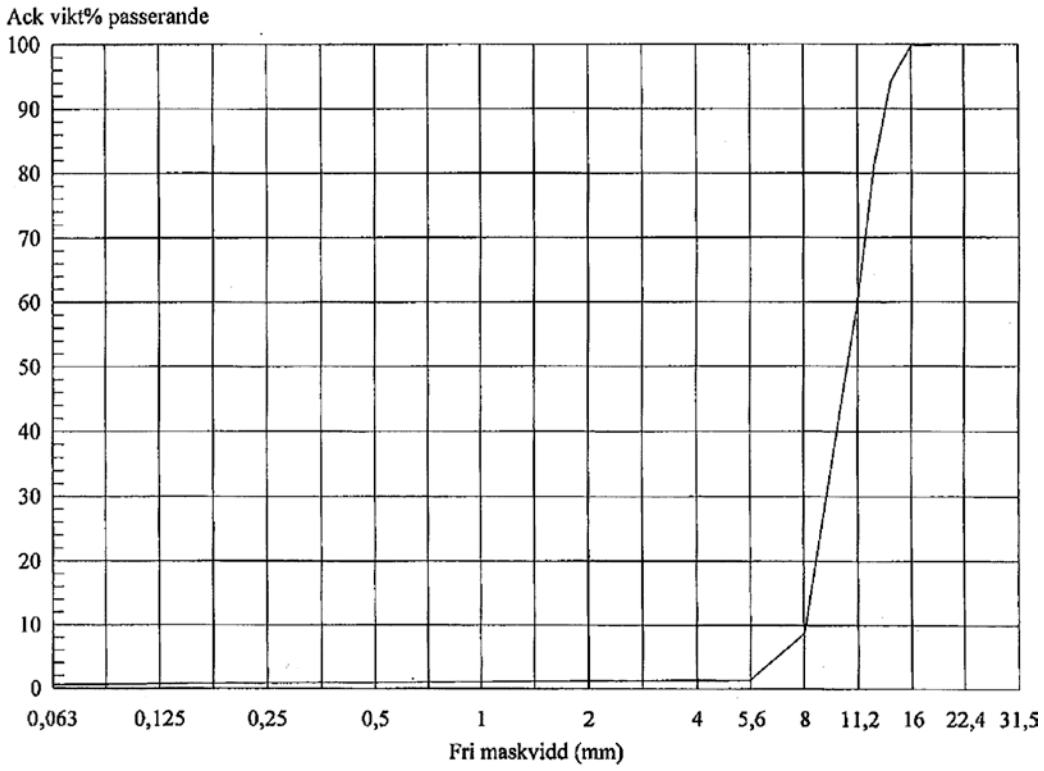

Figure AE-2. *Grain-size distribution of the natural gravel.*

F80616
SPs märkning: P803046, Leca 8/14

Metod: SS-EN 933-1 Datum: 2008-12-16

Maskvidd (mm):	Mängd (g)		Vikt %		Ack. Vikt % passerande		
	Delprov 1	Delprov 2	Delprov 1	Delprov 2	Delprov 1	Delprov 2	Medelvärde
22,4	0	0	0,0	0,0	100,0	100	100
16	0	1	0,0	0,6	100,0	99,4	100
14	7,2	10,9	4,2	6,3	95,8	93,1	94
12,5	31,6	34,1	18,3	19,8	77,6	73,3	75
11,2	52,6	48,1	30,4	27,9	47,2	45,4	46
9,5	67,3	62,9	38,9	36,5	8,3	8,8	9
8	8,2	8,4	4,7	4,9	3,6	3,9	4
5,6	2,5	3,3	1,4	1,9	2,1	2,0	2
4	0,5	0,7	0,3	0,4	1,8	1,6	2
2	0,4	0,2	0,2	0,1	1,6	1,5	2
1	0,5	0,3	0,3	0,2	1,3	1,3	1
0,5	0,2	0,2	0,1	0,1	1,2	1,2	1
0,25	0,2	0,4	0,1	0,2	1,1	1,0	1
0,125	0,5	0,5	0,3	0,3	0,8	0,7	1
0,063	0,5	0,4	0,3	0,2	0,5	0,5	0,5
0	0,9	0,8	0,5	0,5	0,0	0,0	0
Summa (g)	173,1	172,2					
Invägt (g):	173,7	171,4					

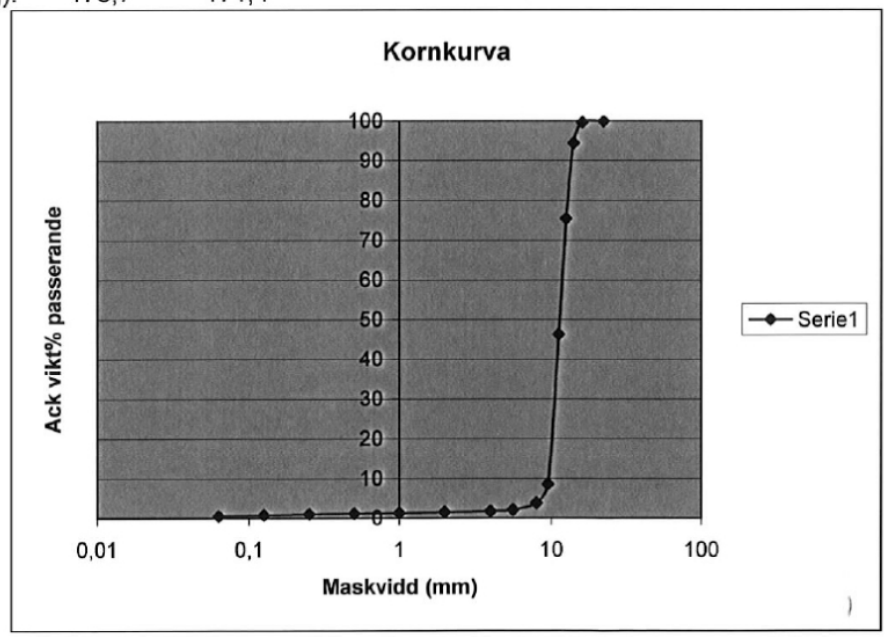

Provningsprotokoll: Skrymdensitet enligt SS-EN 1097-3

Provningsmetod: SS-EN 1097-3
Provningsdatum: se resp sort
Provat av: MHS

Uppdrag: F80616

Märkning: P803046 (sp)

Sortering (mm)		**8/14**	**2008-12-13**		
Delprov	(nr)	**1**	**2**	**3**	**Medel**
Kärl	(nr)	5A	5A	5A	3A
Volym kärl	(dm3)	5,43	5,43	5,43	5,43
Tara kärl	(g)	1224,9	1224,9	1224,9	1224,9
Tara + torrt prov	(g)	2749,7	2733,2	2751,7	2744,9
Torrt prov	(g)	1524,8	1508,3	1526,8	1520
Skrymdensitet, torr. Medelv.	**(kg/m3)**	**281**	**278**	**281**	280
Skrymdensitet, torr. Std avv.	**(kg/m3)**				**2**
Skrymdensitet, torr. Avr. värde	***(kg/m3)***				***280***

Sortering (mm)		**Bentonit**	**2008-12-13**		
Delprov	(nr)	**1**	**2**	**3**	**Medel**
Kärl	(nr)	5A	5A	5A	3A
Volym kärl	(dm3)	5,43	5,43	5,43	5,43
Tara kärl	(g)	1224,9	1224,9	1224,9	1224,9
Tara + torrt prov	(g)	7368,2	7258,3	7345,7	7324,1
Torrt prov	(g)	6143,3	6033,4	6120,8	6099
Skrymdensitet, torr. Medelv.	**(kg/m3)**	**1131**	**1111**	**1127**	1123
Skrymdensitet, torr. Std avv.	**(kg/m3)**				**11**
Skrymdensitet, torr. Avr. värde	***(kg/m3)***				***1125***

OBS! Bentonit ej torkad i 110oC, provats naturfuktig

Figure AE-3. *The natural gravel is placed in cell.*

Appendix F

Compression test of pellet filled slot

Torbjörn Sandén, Lennart Börgesson
Clay Technology AB

February 2010

Full scale laboratory tests for investigating the lateral pressure on the rock in a pellets filled slot

Laboratory tests in large scale

Torbjörn Sandén, Lennart Börgesson
Clay Technology AB

February 2010

Keywords: Spalling, Bentonite, Pellets.

Abstract

After deposition of canister and buffer in a deposition hole, it is possible that the emitted heat from the canister could cause a thermally-induced spalling (brittle failure induced by thermally-induced tangential stresses occurring in the walls of the deposition hole). This process can result in rock fragments falling out creating a zone with high hydraulic conductivity close to the buffer.

Earlier investigations have shown that spalling of the rock surface can be prevented with a rather low confining pressure. According to the present reference design, the slot between bentonite blocks and rock (width about 6 cm) will be filled with bentonite pellets. A possible effect is that the horizontal pressure from the pellets against the rock surface prevents spalling. In order to determine the magnitude of the pressure from pellets in the outer slot between bentonite blocks and the rock wall in a deposition hole, a number of laboratory tests in different scales have been performed and are described in this report together with a theoretical calculation.

The following activities are described:

1. A pilot study in order to determine the angle of internal friction of the pellets material, the angle of friction between the pellets and the rock wall in a deposition hole and between the pellets and the surface of the bentonite blocks. In order to achieve walls (in the artificial test slot that was to be constructed) with friction properties similar to the real ones, the angle of friction between bentonite pellets and a number of different building materials was also tested.
2. A theoretical study of the expected pressures in a pellets-filled slot.
3. Design and construction of an artificial slot in large scale (height 3.6 m and width 2 m) with ability to measure the horizontal pressure in four points.
4. After finishing the construction the following tests were performed:
   - Measurement of the static horizontal pressure from the pellets filling.
   - Same as above but the filling was vibrated in order to increase the bulk density.
   - The artificial slot was re-built and the compression properties of pellets filling installed in the artificial slot were measured.

The tests in the large slot were performed both with bentonite pellets and with spheres made of light weight expanded clay aggregate (LECA). The reason for this was that this material was used in the field test at Äspö HRL instead of bentonite pellets. The LECA balls have about the same size and the mechanical properties are not greatly affected by water. The main reasons for choosing LECA balls as substitute for the bentonite pellets are given in the main text.

The results show that the performed laboratory tests verify the theoretical calculations very well. The counter pressure from a pellets filling will be low, around 1 kPa.

Sammanfattning

Efter installation av kapsel och buffert i ett deponeringshål är det möjligt att den värme som avges från kapseln kan orsaka en termiskt inducerad spjälkning (sprödbrott som orsakas av termiskt inducerade tangentiella spänningar som uppstår i deponeringhålets vägg). Denna process kan resultera i att en zon med hög hydraulisk konduktivitet uppstår nära bufferten.

Tidigare undersökningar har emellertid visat att spjälkning kan förhindras med ett förhållandevis lågt mottryck. Med den nuvarande designen kommer spalten mellan bentonitblock och berg (spaltvidd ca 6 cm) att fyllas med bentonitpellets. Ett möjligt scenario skulle kunna vara att det horisontella trycket från pelletsfyllningen mot bergytan skulle kunna förhindra spjälkning. För att bestämma storleken på trycket från pelletsen har ett antal laboratorieförsök i olika skala genomförts. Dessa är beskrivna i denna rapport tillsammans med en teoretisk beräkning.

Följande aktiviteter finns redovisade i denna rapport:

1. En förstudie gjordes för att bestämma den inre friktionsvinkeln hos pellets samt friktionsvinkeln mellan pellets–berg och mellan pellets–bentonitblock. För att senare kunna bygga en storskalig spalt med väggar som har rätt friktionsegenskaper bestämdes också friktionsvinkeln mellan pellets och ett antal olika byggnadsmaterial.
2. En teoretisk studie för att beräkna de förväntade trycken i en pelletsfylld spalt.
3. En spalt i stor skala (höjd 3.6 m och bredd 2 m) byggdes. I spalten kan det horisontella trycket från pelletsen mätas i fyra olika punkter.
4. Efter att ha färdigställt den konstgjorda spalten gjordes ett antal olika försök:
   - Bestämning av det statiska horisontella trycket från en pelletsfyllning
   - Samma som ovan men under installationen vibrerades pelletsen för att få en tätare fyllning.
   - Efter en ombyggnad av spalten gjordes också en bestämning av kompressionsegenskaperna hos en pelletsfyllning.

Testerna i spalten gjordes både med bentonitpellets och med lecakulor. Lecakulorna testades eftersom dessa har använts istället för bentonitpellets i fältförsök som har genomförts på Äspö HRL. Lecakulorna har ungefär samma storlek och de mekaniska egenskaperna påverkas inte särskilt av vatten. Huvudskälen för att välja lecakulor som ersättning för bentonitpelletsen ges i huvudtexten.

Resultaten från laboratorieförsöken har verifierat de teoretiska beräkningarna. Mottrycket från en pelletsfyllning kommer att vara lågt, omkring 1 kPa.

Contents

F1 Introduction

After deposition of canister and buffer in a deposition hole, it is possible that the emitted heat from the canister could cause a thermally-induced spalling (brittle failure induced by thermally-induced tangential stresses occurring in the walls of the deposition hole). This process can result in rock fragments falling out creating a zone with high hydraulic conductivity close to the buffer.

Earlier investigations have shown that spalling of the rock surface can be prevented with a rather low confining pressure. According to the present design, the slot between buffer and rock (width about 6 cm) will be filled with bentonite pellets /SKB 2010/. A possible effect is that the horizontal pressure from the pellets against the rock surface prevents spalling.

In order to determine the magnitude of the pressure from pellets in the outer slot between bentonite blocks and the rock wall in a deposition hole, a number of laboratory tests in different scales have been performed and are described in this report together with a theoretical calculation.

F2 Performed tests

F2.1 General

This report describes the following activities:

1. A pilot study in order to determine the angle of internal friction of the pellets material, the angle of friction between the pellets and the rock wall in a deposition hole and between the pellets and the buffer surface. In order to achieve walls (in the artificial slot that was to be constructed) with friction properties similar to the real ones, the angle of friction between bentonite pellets and a number of different building materials was also tested.
2. A theoretical study of the expected pressures in a pellets filled slot.
3. Design and construction of an artificial slot in large scale (height 3.6 m and width 2 m) with ability to measure the horizontal pressure in four points.
4. After finishing the construction the following tests were performed:

Five tests have been performed in the artificial pellets slot:

- **Test 1**. The slot was filled with pellets in steps. During the filling the horizontal pressure was measured (MX-80 pellets).
- **Test 2**. Same as above but during the filling the pellets were vibrated in order to increase the density of the filling, possible influence on silo effects, and study how this would influence the achieved horizontal pressure (MX-80 pellets).
- **Test 3**. Same test type as number 1 above but instead of bentonite pellets, a filling of LECA balls was tested. The reason for this was that this material was planned to be used in a field test at Äspö HRL.
- **Test 4 and 5.** One of the pressure cells (see Chapter F5.2) was rebuilt (equipped with a hydraulic piston) and instead of measuring the achieved static pressure from the pellets filling, the piston was moved against the pellets filling at a constant rate and the achieved pressure was measured together with the displacement (MX-80 pellets and LECA).

F3 Pilot study in order to determine the internal angle of friction for the pellets material and the angle of friction between pellets and other materials

F3.1 General

Two pellets material were investigated in the pilot study, MX-80 /Karnland et al. 2006/ and Cebogel QSE (Data sheet is provided in Appendix AF). In the large scale tests performed after the pilot study only the MX-80 pellets was used.

- **MX-80 pellets**. Specially made pellets consisting of MX-80 Wyoming bentonite with a smectite content of about 75–80%. The pellets are "pillow" shaped with the approximate dimensions 18×18×8 mm.
- **Cebogel QSE pellets**. Pellets made of a commercial bentonite with a montmorillonite content of about 80%. Extruded cylindrical rods with a diameter of 6.5 mm and a length of 5–20 mm. The origin of the material is Milos, Greece. The pellets are delivered by Cebo Holland BV.

F3.2 Measurement of the internal angle of friction

The internal angle of friction was determined by pouring pellets on the ground and then measure the angle of the slope, see Figure F-1. The results from the measurements showed that the internal angle of friction was about the same for the two tested materials:

MX-80 pellets: ca 36.3°

Cebogel QSE: ca 37.9°

Figure F-1. *Picture showing a heap of MX-80 pellets. The red angle shows how the angle of friction was determined.*

F3.3 Measurement of the angle of friction between bentonite pellets and a number of different materials

F3.3.1 Method

The determination of the friction angle between pellets and different surfaces was done according to the following:

1. A cylinder, diameter 80 mm and height 50 mm, was placed on the test surface.
2. The cylinder was filled with pellets and a plastic piston was positioned on the pellets surface. The outer cylinder was then pulled upwards a few mm in order to avoid contact with the rock surface.
3. A dynamometer was connected to the cylinder, see Figure F-2. The dynamometer was pulled by hand and the force needed in order to start a movement and continue a certain length was registered.
4. Measurements were done with the weight of the pellets but also with increasing load by piling weight on the top of the pellets surface.

F3.3.2 Results

The investigation was done in two steps:

1. The friction angle between bentonite pellets and a rock surface (TBM-drilled) and between bentonite pellets and compacted bentonite, i.e. the two types of surfaces that can be present in a deposition hole, was determined, see Figure F-3.
2. The friction angle between bentonite pellets and a number of different materials such as plywood, wood particle board, Plexiglas, concrete and LECA (light weight expanded clay aggregate) was then determined in order to find suitable materials for use when building a large scale slot, see Figure F-4 and F-5.

The friction angle was determined as the inclination of the lines (see diagrams in Figure F-3, F-4 and F-5) between the maximum value and the origin of coordinates.

Figure F-2. *Principle of the measurements. The picture shows a test where the friction between pellets and a TBM drilled rock surface is tested. The cylinder is filled with MX-80 pellets and a normal force of about 20 N is applied on the top.*

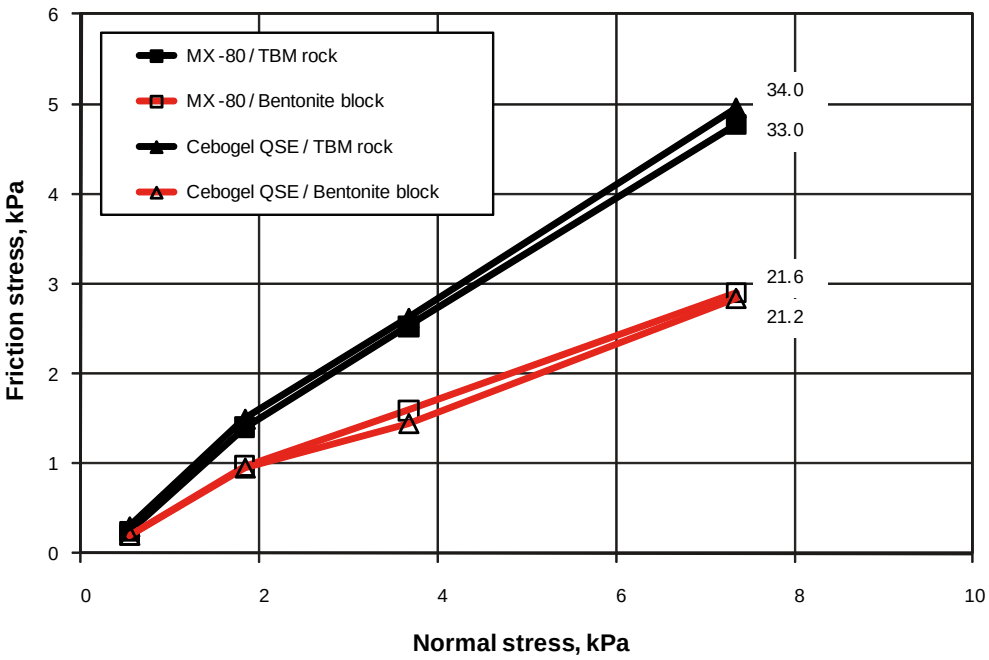

Figure F-3. *Friction stress plotted vs. normal stress in the tests where the shear stress between the two pellets materials and the rock surface or the bentonite block was measured.*

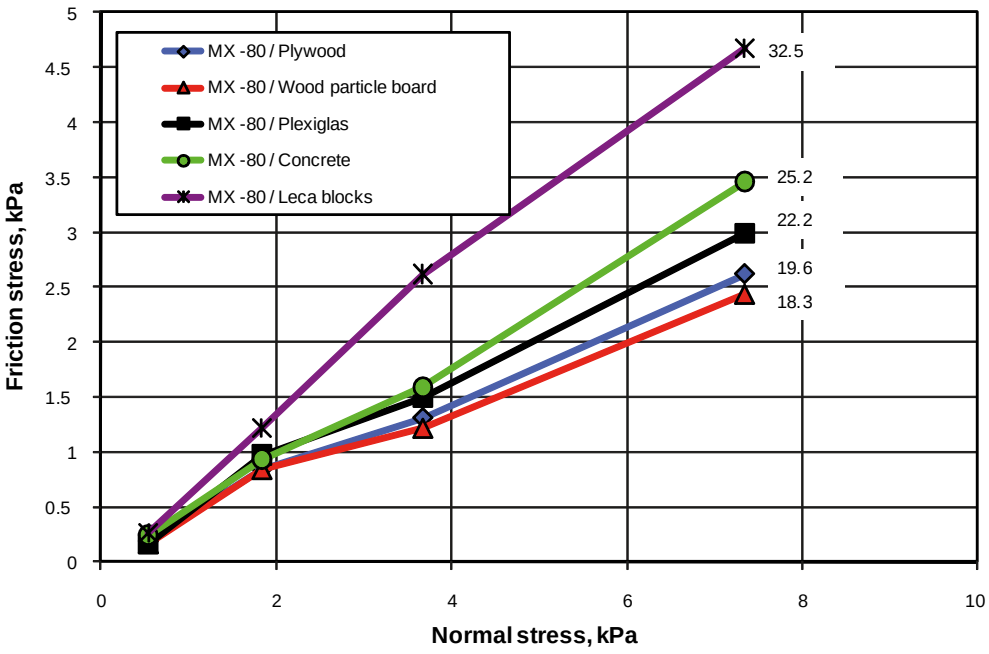

Figure F-4. *Friction stress plotted vs. normal stress in the tests where the shear stress between the MX-80 pellets and a number of different materials was measured.*

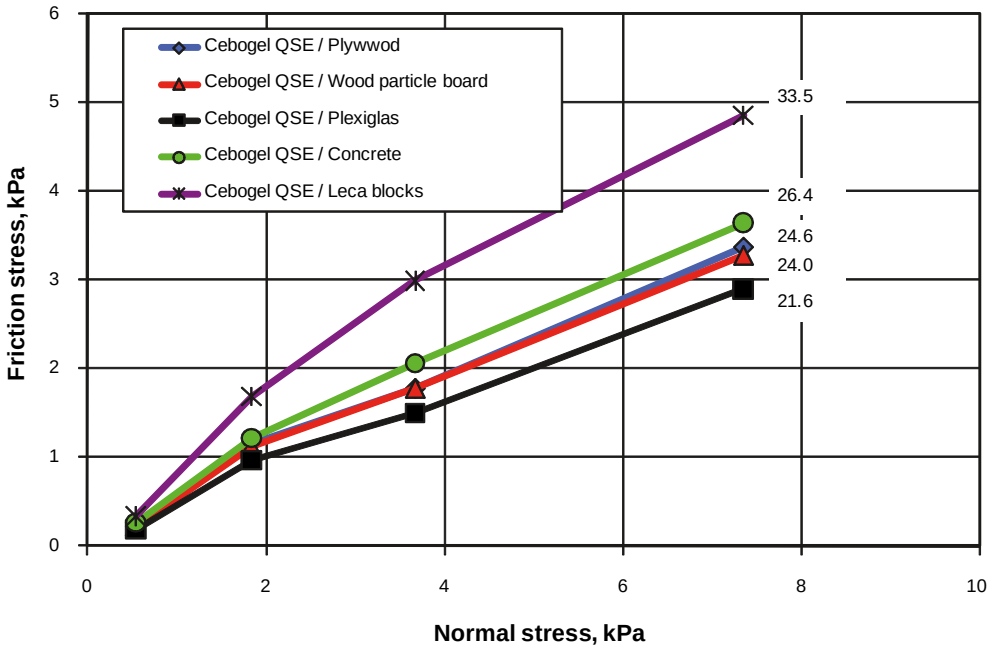

Figure F-5. *Friction stress plotted vs. normal stress in the tests where the shear stress between Cebogel pellets and a number of different materials was measured.*

F3.4 Conclusions

The performed tests showed the following:

- The internal friction angle was almost similar for the two tested materials, 36.3° (MX-80) and 37.9° (Cebogel).
- The friction angle between pellets and TBM rock and compacted bentonite was also almost similar for the two pellets materials, 33.0°–34.0° against rock and 21.2°–21.6° against bentonite block.
- The tests showed that the material that best could simulate a TBM-drilled rock surface was blocks made of LECA (32.5°–33.5°). The bentonite block surface was best simulated by using Plexiglas (21.2°–21.7°).

F4 Theoretical calculation of the lateral wall pressure in a pellets filled slot

F4.1 General

The theoretical lateral pressure, generated by a pellets filling in a slot has been calculated in two different ways:

1. As earth pressure at rest.
2. As silo pressure.

In the following calculations the theoretical lateral pressure has been evaluated according to /Handboken Bygg-Geoteknik 1983/.

F4.2 Results

If the friction against the side walls is neglected the horizontal pressure can be evaluated according to Equation F-1.

Earth pressure at rest

$P_0 = K_0\sigma_v$ (F-1)

where

P_0 = earth pressure at rest

K_0 = pressure coefficient ≈ 1–sin ϕ (ϕ = internal angle of friction for the material)

$\sigma_v = \rho g z$

where

g = constant of gravitation

ρ = density (ca 1,100 kg/m^3)

z = depth

This gives for different depths:

$P_0(z = 1m) \approx 5$ kPa

$P_0(z = 4m) \approx 18$ kPa

$P_0(z = 4m) \approx 36$ kPa

Earth pressure at rest with respect to the silo pressure

Since the vertical pressure is strongly reduced by the friction against the walls a better estimation is to use the silo pressure according to Equation F-2.

$$P_0 = \frac{A\rho g}{O\mu}(1 - \exp(-O\mu\lambda z / A)) \quad \text{(F-2)}$$

where

A = area of the cross section (calculation is made as if the silo has the shape of a long narrow rectangle (5×0.05 meter).

O = (the inner circumference)

μ = coefficient of friction between pellets and silo walls (=tan φ)

λ = 1–sinϕ (coefficient of pressure)

This gives:

$P_0(z = 1) \approx P_0(z = 8) \approx 0.4$–$0.7$ *kPa* (depending if using the angle of friction between pellets/rock or the one between pellets/bentonite block.

F4.3 Conclusions

The calculations show that the horizontal pressure in a slot in a deposition hole generated by the pellets filling is very low, probably below 1 kPa. This depends mainly on the silo effect, i.e. the rather high friction between pellets and walls will make the material “hang on the walls”.

F5 Large slot tests in laboratory

F5.1 General

A theoretical calculation of the horizontal pressure achieved from a pellets filling in the slot between rock and bentonite blocks in a deposition hole was done in Chapter F4. In order to check the results, also large scale laboratory tests in the artificial slot have been done.

Five tests have been performed in the artificial pellets slot:

- **Test 1**. The slot was filled with pellets in steps. During the filling the horizontal pressure was measured (MX-80 pellets).
- **Test 2**. Same as above but during the filling the pellets were vibrated in order to increase the density of the filling and study how this would influence the achieved horizontal pressure (MX-80 pellets).
- **Test 3**. Same test type as number 1 above but instead of bentonite pellets, a filling of LECA balls was tested. The reason for this was that this material was used in the field test at Äspö HRL instead of bentonite pellets. The LECA balls have about the same size and the mechanical properties are not greatly affected by water. The main reasons for choosing LECA balls as substitute for the bentonite pellets are given in the main text.
- **Test 4 and 5.** One of the pressure cells (see Chapter F5.2) was rebuilt (equipped with a hydraulic piston) and instead of measuring the achieved static pressure from the pellets filling, the piston was moved against the pellets filling at a constant rate and the achieved pressure was measured together with the displacement (MX-80 pellets and LECA).

F5.2 Test equipment

In order to simulate the slot between the rock wall and the installed bentonite blocks in a deposition hole, a wall consisting of blocks made of light weight expanded clay (LECA) was built in the laboratory, see Figure F-6. This material has almost the same friction characteristic as the rock surface in a TBM drilled deposition hole according to the investigation in Chapter F3. The surface of compacted bentonite blocks was, according to the same investigation, best simulated with Plexiglas. The Plexiglas sheets were mounted at a distance of between 55 and 60 mm from the LECA wall, in accordance with the present design, i.e. 60 mm between bentonite blocks and rock wall /SKB 2010/. In order to stabilize the Plexiglas sheets they were supported by wooden beams.

The artificial slot is equipped with four pressure cells, two on the “rock” side and two on the “bentonite” side. The cells consists of pistons (d=150 mm) and cylinders made of PE (poly ethane). The pressure from the pellets filling is transferred by the piston to a load-cell mounted on the outside where the achieved load can be registered, see Figure F-7.

The pressure cells on the “rock” side are mounted 0.25 and 1.25 m from the bottom of the slot, respectively, and the pressure cells on the “bentonite” side are mounted 0.75 and 1.75 m from the bottom of the slot, respectively.

F5.3 Results

In the first test, pellets were poured into the slot in three steps, up to 1 m, 2 m and 3.6 m above the floor. The results from this test can be seen in Figure F-8. In the diagram, the measured pressure at the different measuring points is plotted versus the pellets height. In the diagram also the theoretical pressure is plotted (see Chapter F4). The achieved pressures are very low in all positions, less than 1 kPa, and the influence of the pellets height seems to be negligible.

Test number two was performed with the same material and in the same filling steps as in test number one, but in addition the filling was vibrated after each step. The vibrating was performed in order to increase the bulk density of the filling. Possibly, this would increase the achieved horizontal pressure. The vibration was made with a concrete vibrator (ANBONI, AX 38). The vibrating staff was placed in the slot before pouring in the pellets and then pulled up in steps, see Figure F-9. During the vibrating, it was observed that the filling was compacted but this seemed to occur rather locally, i.e.

Figure F-6. *An artificial slot was built in the laboratory (width=2 m and height 3.6 m). The rock wall is simulated with LECA blocks and the bentonite blocks with Plexiglas. The horizontal pressure can be measured at four points, two on the rock wall and two on the bentonite side.*

Figure F-7. *Left: Pressure cell mounted on the "bentonite" side. Right: Pressure cell mounted on the "rock" wall.*

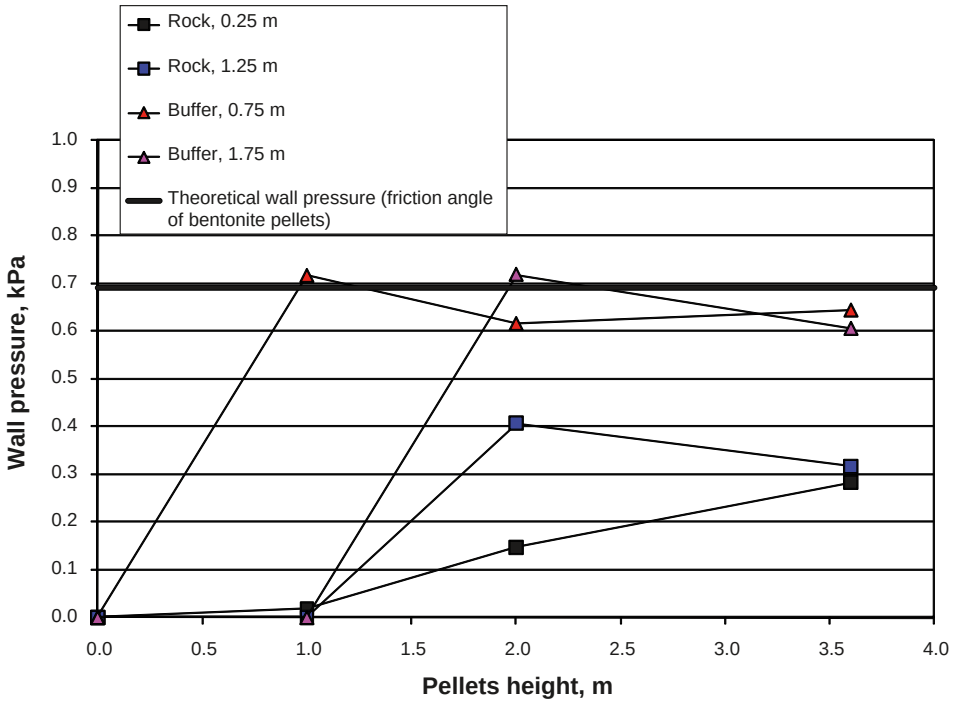

Figure F-8. *The measured horizontal pressures plotted versus the height of the pellets filling. In the diagram is also the theoretical wall pressure plotted.*

Figure F-9. *Photo showing the pellets filling and the tube that holds the vibrating staff inside the pellets filling.*

only the volume closest to the vibrator was influenced. The results from the measurements are shown in Figure F-10. In the diagram also the theoretical pressure is plotted (see Chapter F4). The diagram shows that there seems to be an influence from the vibrating but the horizontal pressures measured are still at a very low level.

Test number three was similar to test one but instead of bentonite pellets, spheres made of lightweight expanded clay aggregate (LECA) was tested (this material was not tested in the earlier performed laboratory tests on internal friction, see Chapter F3). The reason for also testing this material was that in the field tests performed at Äspö HRL where the spalling issue is studied, this material will be used in the slots. The results from the measurements are shown in Figure F-11. The achieved pressures are in the same range as for the bentonite pellets.

F5.4 Compression tests

In addition to the three earlier tests where the horizontal pressure was measured at static conditions, two compression tests, one with each of the materials, (MX-80 pellets and balls of LECA) have been performed. In order to perform these tests, one of the pressure cells on the "rock" side was rebuilt and equipped with a hydraulic piston which made it possible to move the piston forward at a constant rate (6–7 mm/hour), see Figure F-12. During the movement the displacement and the achieved pressure were measured and registered.

The results from the two tests are shown in Figure F-13. The diagram shows that the LECA spheres give significantly higher counter pressure than the bentonite pellets does. At a compression of 2 mm (4% strain) the LECA gives about 6.8 times higher pressure than the bentonite pellets.

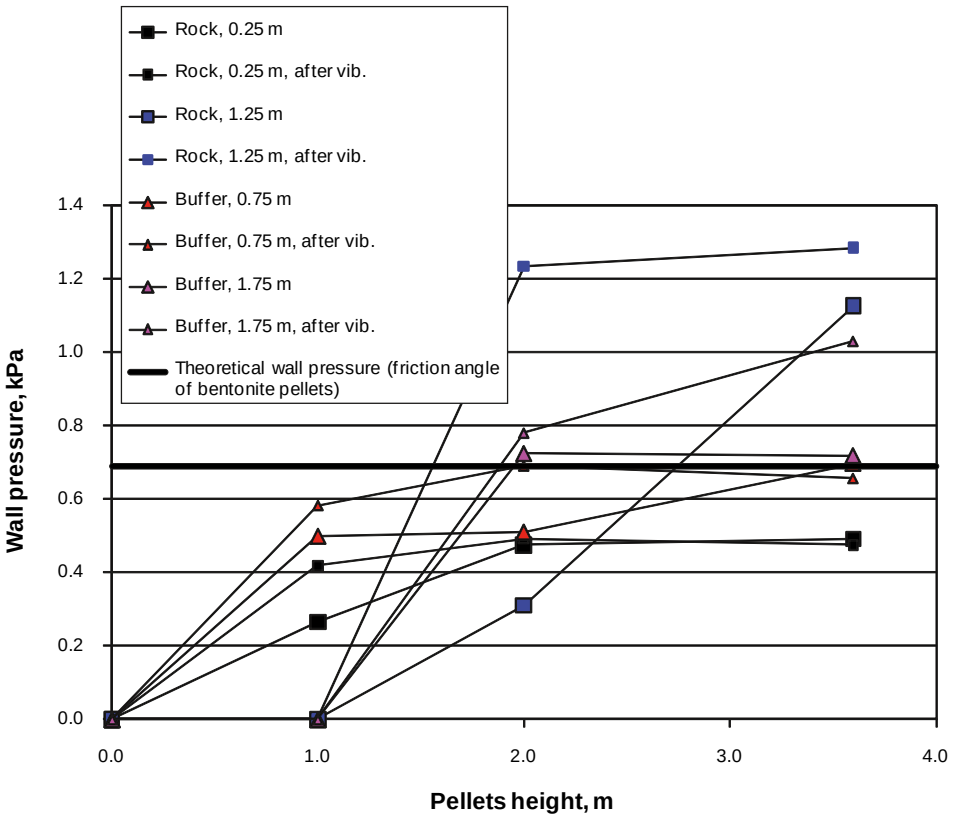

Figure F-10. *The measured horizontal pressures plotted versus the height of the pellets filling. The smaller dots show the pressure after vibrating. In the diagram is also the theoretical wall pressure plotted.*

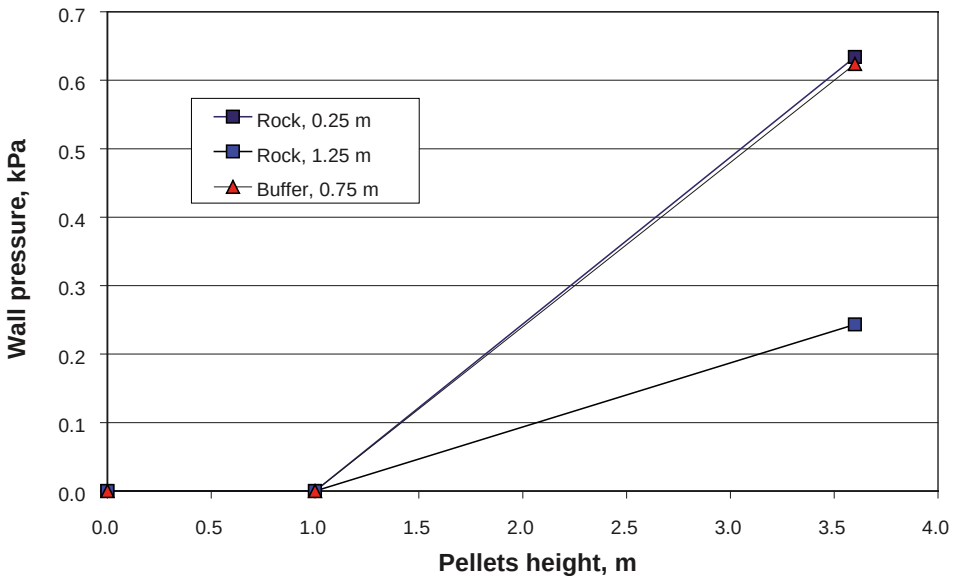

Figure F-11. *The measured horizontal pressures plotted versus the height of the LECA filling.*

Figure F-12. *One of the pressure cells on the "rock" side was rebuilt and equipped with a hydraulic piston which was controlled by a GDS (microprocessor controlled pump). This made it possible to move the piston with a constant rate forward and measure the displacement and the achieved pressure.*

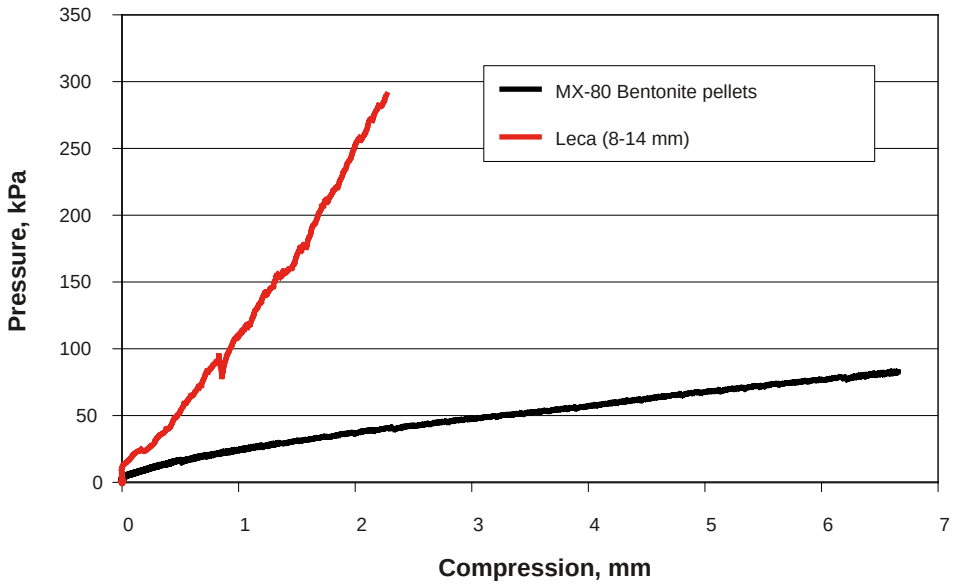

Figure F-13. *The achieved pressure plotted versus the compression.*

F6 Conclusions

F6.1 General

The performed laboratory tests verify the theoretical calculations very well. The static horizontal counter pressure from pellets filling established after the pellets have been emplaced in a deposition hole will be very low, around 1 kPa.

The compression tests shows that the 60 mm bentonite pellets filling must be compressed at least 3 mm in order to give a lateral pressure of 50 kPa. For the LECA filling, a significantly smaller compression, about 0.5 mm, is required

References

Handboken Bygg-Geoteknik, 1983.

Karnland O, Olsson S, Nilsson U, 2006. Mineralogy and sealing properties of various bentonites and smectite-rich clay materials. SKB TR-06-30, Svensk Kärnbränslehantering AB.

SKB, 2010. Design, production and initial state of the buffer for the safety assessment SR-Site. SKB TR-10-15, Svensk Kärnbränslehantering AB.

Data sheet Cebogel pellets

PRODUCT DATA

Cebo Holland

CEBOGEL QSE

Use
The large swelling capacity makes CEBOGEL QSE suitable for:
The complete repair of drilled-through or damaged clay layers
Securing spring-loaded charges in the ground for seismological study
Making dams, dykes and water barriers non-water-permeable
Rapidly sealing damaged wells, etc..

Careful and even dosing are required for an optimal result.
Bridge formation can occur in the event of dosing too rapidly.

Description
Cylindrical bentonite rods (granules)made from 100 % activated sodium bentonite. A characteristic of CEBOGEL QSE is its considerable water absorption capacity, as a result of which it swells up considerably when in contact with water. The QSE quality is KIWA certified in the field of toxicological aspects.

Advantages
- The assurance of a strong, virtually watertight layer which can only be achieved using a pure sodium bentonite
- Has extra swelling capacity for sealing irregularities in the borehole wall or difficult to reach cavities
- Certified according to KIWA-ATA, therefore absolutely safe for use in drinking water areas
- Easy to apply
- Absolutely environmentally-friendly

Specification
Complies with the requirements set in BRL-K20236/01 for borehole clay for sealing boreholes in bottom layers with poor water permeability
Supplied with KIWA certificate for Toxicological Aspects (ATA), which guarantees an environmentally-friendly product

Parameter	Method	Requirement	Typical Value
Water absorption capacity after 24 hours	ASTM E946-92	≥ 600 % (BRL-265/01)	800 %

Cebo Holland BV
Westerduinweg 1
NL-1976 BV IJMUIDEN
P.O. Box 70
NL-1970 AB IJMUIDEN

Tel.: +31 255546262
Fax: +31 255546202
e-mail : sales@cebuf ulland.com
www.ceboholland.com

PRODUCT DATA

Cebo Holland

Typical values

Montmorillonite level	X-ray diffraction	80 %
Moisture content	DIN 18121	16 %

Chemical and physical properties

Composition	High-quality activated sodium bentonite
Colour	Grey green
Form	Cylindrical rods
Dimensions	Diameter 6.5 mm Length 5 – 20 mm
Density	2100 kg/m^3
Bulk density	1100 kg/m^3

Packaging

- 1000 kg packed in 25 kg polyethylene bags on a pallet with shrink film
- 1000 kg big bags

Cebo Holland BV
Weiterduinweg 1
NL-1976 BV IJMUIDEN
P.O. Box 70
NL-1970 AB IJMUIDEN

Tel.: +31 255546262
Fax: +31 255546202
e-mail : sales@cebohol land.com
www.cebohol land.com

Revision date : 10-07-2003
Document no : CQ03IP

Drawings of the instrumentation

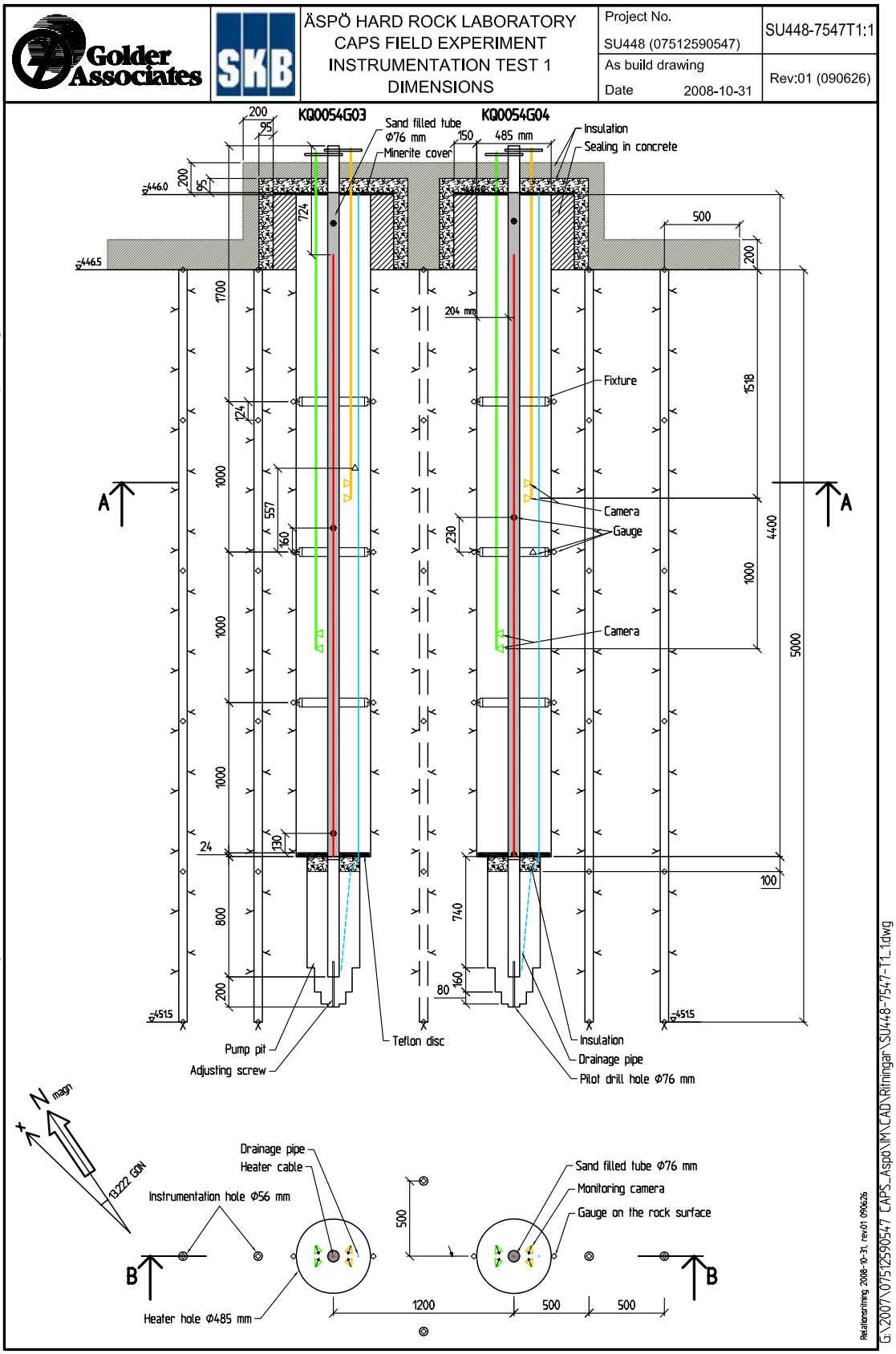

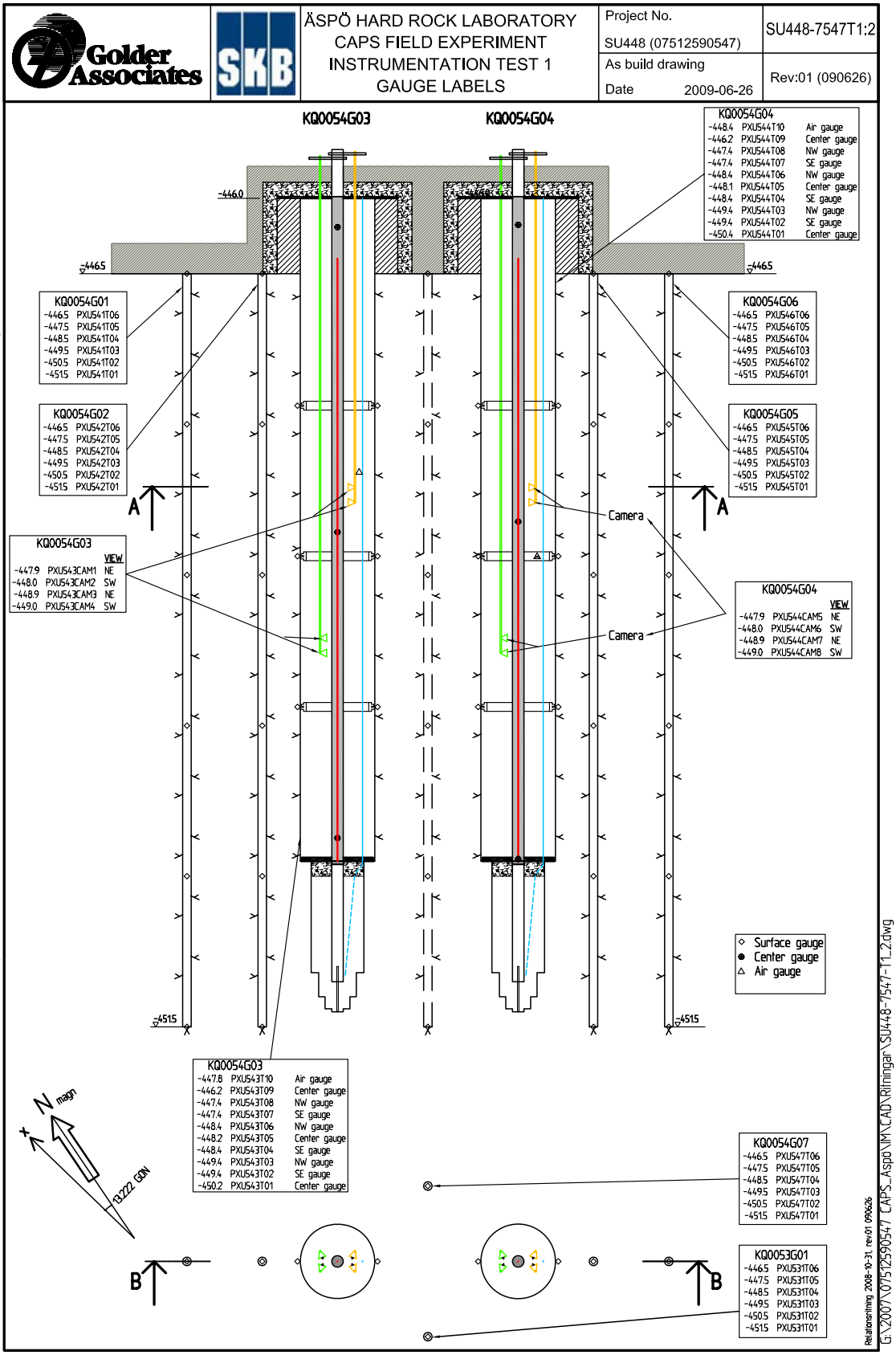
Golder Associates
SKB
ÄSPÖ HARD ROCK LABORATORY
CAPS FIELD EXPERIMENT
INSTRUMENTATION TEST 1
GAUGE LABELS
Project No.
SU448 (07512590547)
As build drawing
Date 2009-06-26
SU448-7547T1:2
Rev:01 (090626)
Project Manager: R GLAMHEDEN
Person responsible: R GLAMHEDEN
Drawn by: S KOYI
Source:
KQ0054G03
KQ0054G04
KQ0054G01
KQ0054G02
KQ0054G06
KQ0054G05
KQ0053G01
KQ0054G07
Camera
Camera
A
A
B
B
N magn
13.222 GON
Surface gauge
Center gauge
Air gauge
Relationsritning 2008-10-31 rev:01 090626
G:\2007\07512590547 CAPS_Aspo\IM\CAD\Ritningar\SU448-7547-T1.2.dwg

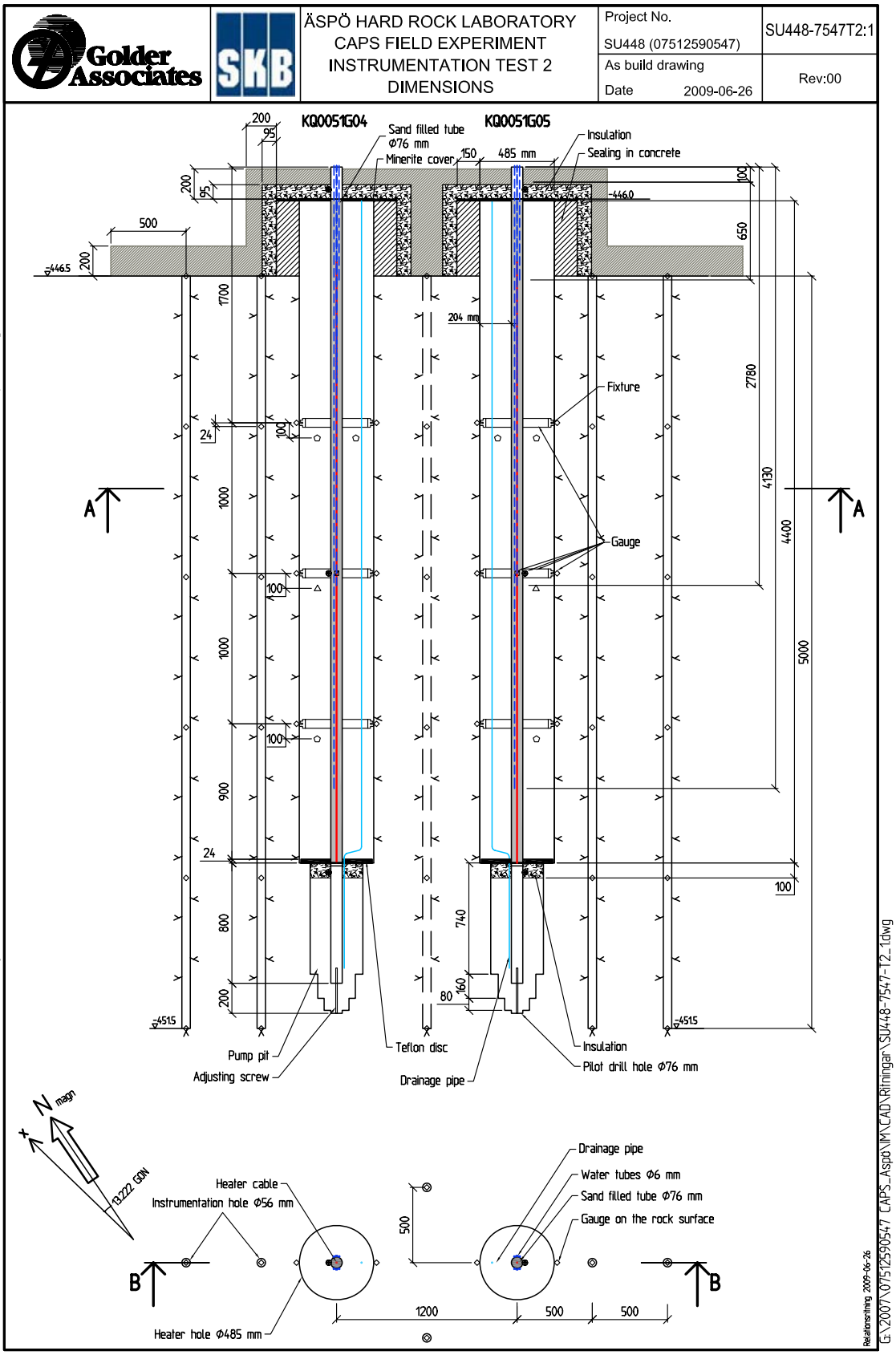
Golder Associates
SKB
ÄSPÖ HARD ROCK LABORATORY
CAPS FIELD EXPERIMENT
INSTRUMENTATION TEST 2
DIMENSIONS
Project No.
SU448 (07512590547)
As build drawing
Date 2009-06-26
SU448-7547T2:1
Rev:00
Project Manager: R GLAMHEDEN
Person responsible: R GLAMHEDEN
Drawn by: S KOYI
Source:
KQ0051G04
KQ0051G05
Sand filled tube Φ76 mm
Minerite cover
Insulation
Sealing in concrete
485 mm
150
Fixture
Gauge
204 mm
Pump pit
Adjusting screw
Teflon disc
Drainage pipe
Insulation
Pilot drill hole Φ76 mm
N magn
13.222 GON
Heater cable
Instrumentation hole Φ56 mm
Heater hole Φ485 mm
Drainage pipe
Water tubes Φ6 mm
Sand filled tube Φ76 mm
Gauge on the rock surface
1200
500
500
A
B
Relationsmitning 2009-06-26
G:\2007\07512590547 CAPS_Aspö\VM\CAD\Ritningar\SU448-7547-T2_1.dwg

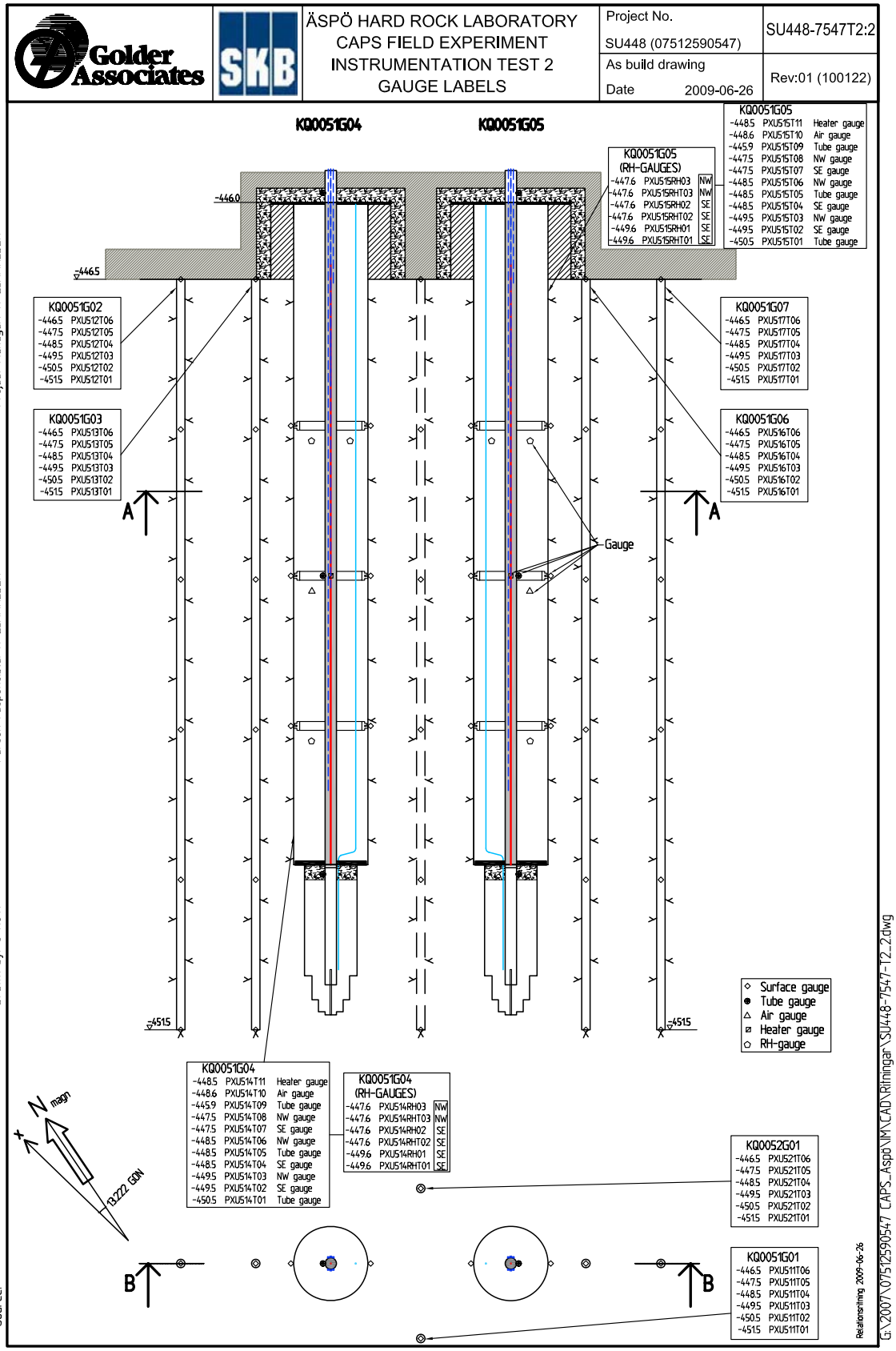
Golder Associates
SKB
ÄSPÖ HARD ROCK LABORATORY
CAPS FIELD EXPERIMENT
INSTRUMENTATION TEST 2
GAUGE LABELS
Project No.
SU448 (07512590547)
As build drawing
Date 2009-06-26
SU448-7547T2:2
Rev:01 (100122)
Project Manager: R GLAMHEDEN
Person responsible: R GLAMHEDEN
Drawn by: S KOYI
Source:
KQ0051G04
KQ0051G05
KQ0051G05
-448.5 PXU515T11 Heater gauge
-448.6 PXU515T10 Air gauge
-445.9 PXU515T09 Tube gauge
-447.5 PXU515T08 NW gauge
-447.5 PXU515T07 SE gauge
-448.5 PXU515T06 NW gauge
-448.5 PXU515T05 Tube gauge
-448.5 PXU515T04 SE gauge
-449.5 PXU515T03 NW gauge
-449.5 PXU515T02 SE gauge
-450.5 PXU515T01 Tube gauge
KQ0051G05
(RH-GAUGES)
-447.6 PXU515RH03 NW
-447.6 PXU515RHT03 NW
-447.6 PXU515RH02 SE
-447.6 PXU515RHT02 SE
-449.6 PXU515RH01 SE
-449.6 PXU515RHT01 SE
-446.0
-446.5
KQ0051G02
-446.5 PXU512T06
-447.5 PXU512T05
-448.5 PXU512T04
-449.5 PXU512T03
-450.5 PXU512T02
-451.5 PXU512T01
KQ0051G03
-446.5 PXU513T06
-447.5 PXU513T05
-448.5 PXU513T04
-449.5 PXU513T03
-450.5 PXU513T02
-451.5 PXU513T01
KQ0051G07
-446.5 PXU517T06
-447.5 PXU517T05
-448.5 PXU517T04
-449.5 PXU517T03
-450.5 PXU517T02
-451.5 PXU517T01
KQ0051G06
-446.5 PXU516T06
-447.5 PXU516T05
-448.5 PXU516T04
-449.5 PXU516T03
-450.5 PXU516T02
-451.5 PXU516T01
A
A
Gauge
-451.5
-451.5
Surface gauge
Tube gauge
Air gauge
Heater gauge
RH-gauge
KQ0051G04
-448.5 PXU514T11 Heater gauge
-448.6 PXU514T10 Air gauge
-445.9 PXU514T09 Tube gauge
-447.5 PXU514T08 NW gauge
-447.5 PXU514T07 SE gauge
-448.5 PXU514T06 NW gauge
-448.5 PXU514T05 Tube gauge
-448.5 PXU514T04 SE gauge
-449.5 PXU514T03 NW gauge
-449.5 PXU514T02 SE gauge
-450.5 PXU514T01 Tube gauge
KQ0051G04
(RH-GAUGES)
-447.6 PXU514RH03 NW
-447.6 PXU514RHT03 NW
-447.6 PXU514RH02 SE
-447.6 PXU514RHT02 SE
-449.6 PXU514RH01 SE
-449.6 PXU514RHT01 SE
N magn
13.22 GON
KQ0052G01
-446.5 PXU521T06
-447.5 PXU521T05
-448.5 PXU521T04
-449.5 PXU521T03
-450.5 PXU521T02
-451.5 PXU521T01
KQ0051G01
-446.5 PXU511T06
-447.5 PXU511T05
-448.5 PXU511T04
-449.5 PXU511T03
-450.5 PXU511T02
-451.5 PXU511T01
B
B
Relationshring 2009-06-26
G:\2007\07512590547 CAPS_Aspö\VM\CAD\Riningar\SU448-7547-T2_2.dwg

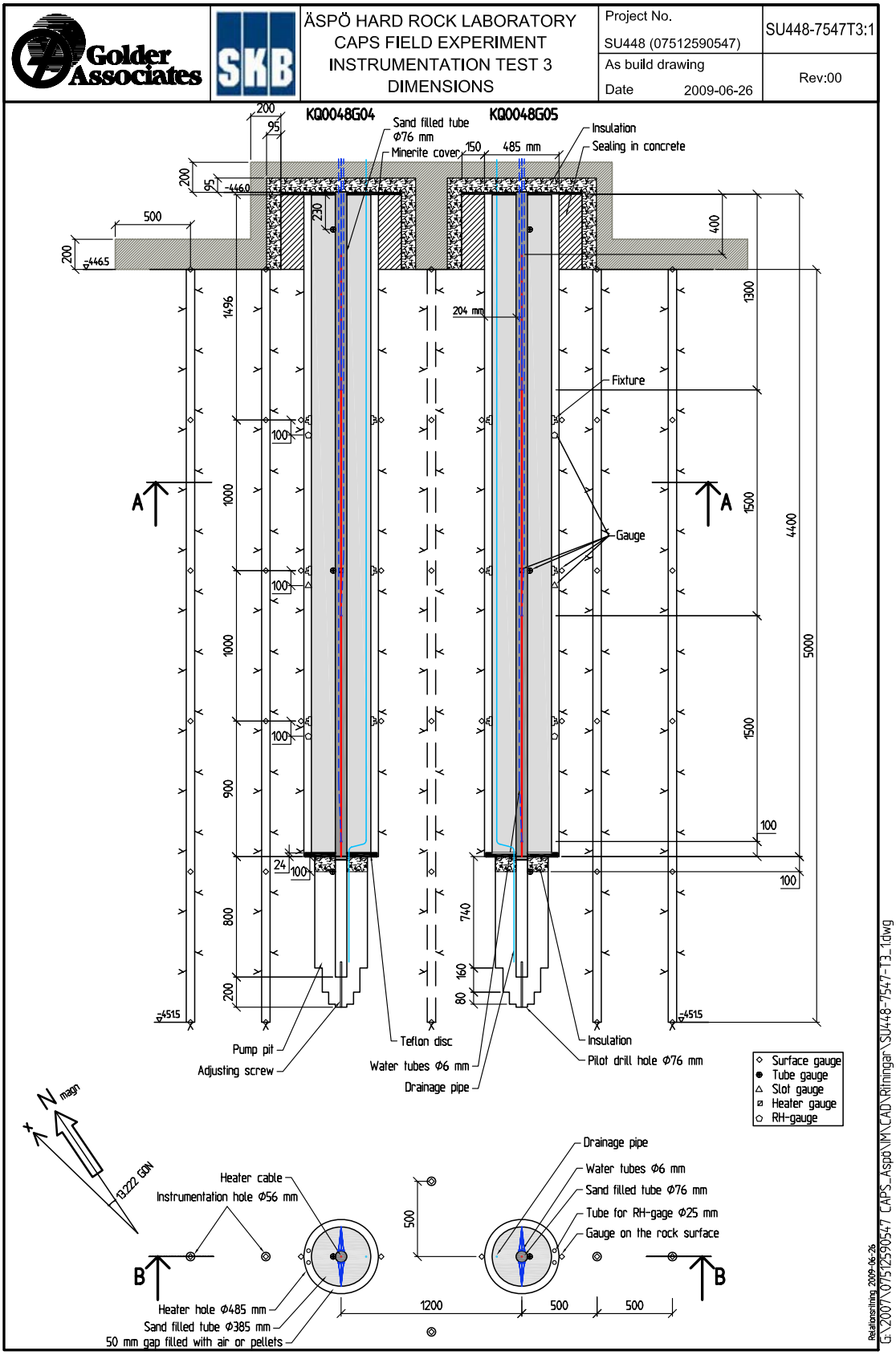
Golder Associates
SKB
ÄSPÖ HARD ROCK LABORATORY
CAPS FIELD EXPERIMENT
INSTRUMENTATION TEST 3
DIMENSIONS
Project No.
SU448 (07512590547)
SU448-7547T3:1
As build drawing
Date 2009-06-26
Rev:00
Project Manager: R GLAMHEDEN
Person responsible: R GLAMHEDEN
Drawn by: S KOYI
Source:
KQ0048G04
KQ0048G05
Sand filled tube Φ76 mm
Minerite cover
Insulation
Sealing in concrete
485 mm
150
Fixture
Gauge
204 mm
Pump pit
Adjusting screw
Teflon disc
Water tubes Φ6 mm
Drainage pipe
Insulation
Pilot drill hole Φ76 mm
Surface gauge
Tube gauge
Slot gauge
Heater gauge
RH-gauge
N magn
13.22° GON
Heater cable
Instrumentation hole Φ56 mm
Heater hole Φ485 mm
Sand filled tube Φ385 mm
50 mm gap filled with air or pellets
Drainage pipe
Water tubes Φ6 mm
Sand filled tube Φ76 mm
Tube for RH-gage Φ25 mm
Gauge on the rock surface
1200
500
500
Relationsritning 2009-06-26
G:\2007\07512590547 CAPS_Aspo\VM\CAD\Ritningar\SU448-7547-T3_1.dwg

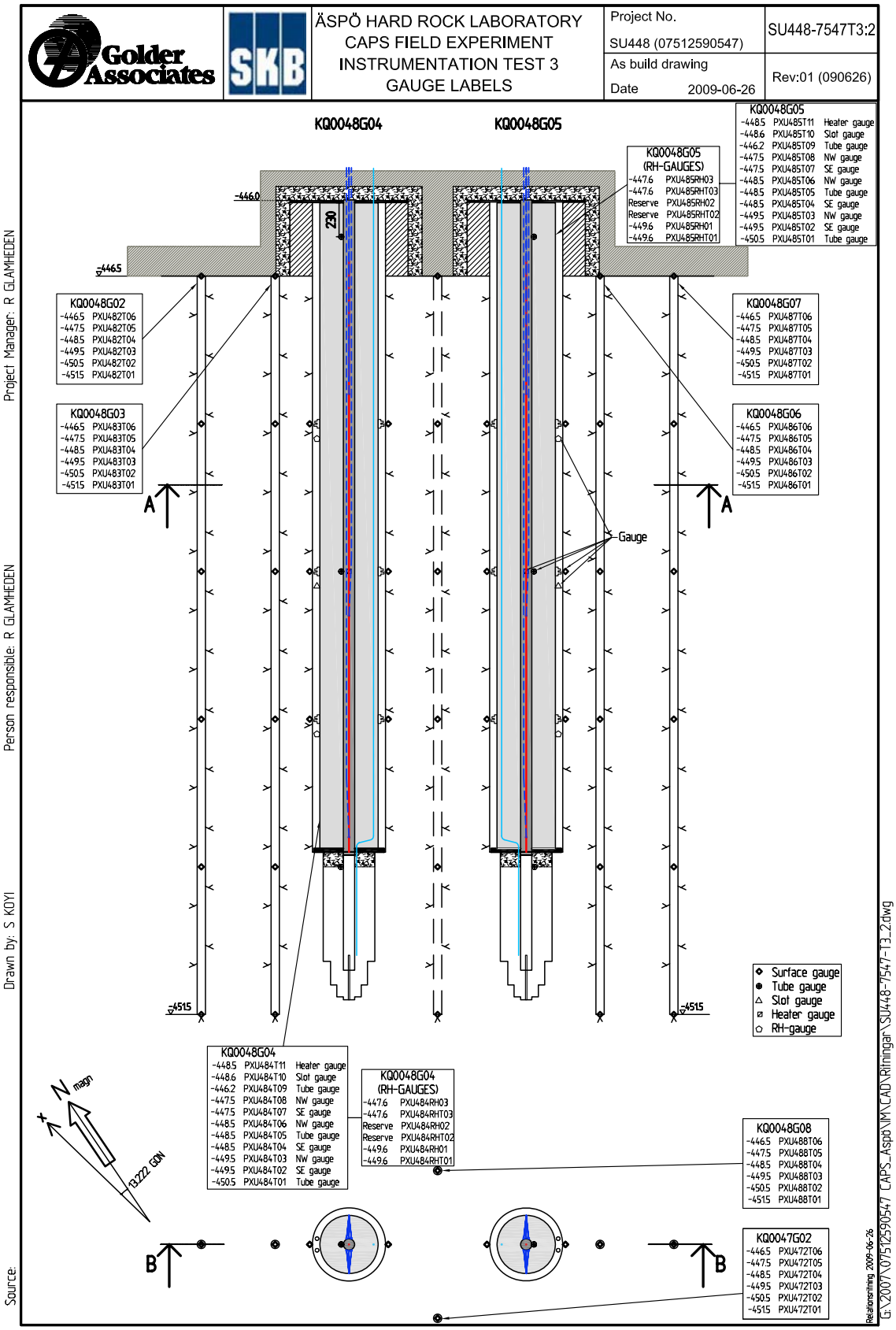
ÄSPÖ HARD ROCK LABORATORY
CAPS FIELD EXPERIMENT
INSTRUMENTATION TEST 3
GAUGE LABELS
Project No.
SU448 (07512590547)
SU448-7547T3:2
As build drawing
Date 2009-06-26
Rev:01 (090626)
Golder Associates
SKB
KQ0048G04
KQ0048G05
KQ0048G05 (RH-GAUGES)
-447.6 PXU485RH03
-447.6 PXU485RHT03
Reserve PXU485RH02
Reserve PXU485RHT02
-449.6 PXU485RH01
-449.6 PXU485RHT01
KQ0048G05
-448.5 PXU485T11 Heater gauge
-448.6 PXU485T10 Slot gauge
-446.2 PXU485T09 Tube gauge
-447.5 PXU485T08 NW gauge
-447.5 PXU485T07 SE gauge
-448.5 PXU485T06 NW gauge
-448.5 PXU485T05 Tube gauge
-448.5 PXU485T04 SE gauge
-449.5 PXU485T03 NW gauge
-449.5 PXU485T02 SE gauge
-450.5 PXU485T01 Tube gauge
-446.0
230
-4465
KQ0048G02
-446.5 PXU482T06
-447.5 PXU482T05
-448.5 PXU482T04
-449.5 PXU482T03
-450.5 PXU482T02
-451.5 PXU482T01
KQ0048G03
-446.5 PXU483T06
-447.5 PXU483T05
-448.5 PXU483T04
-449.5 PXU483T03
-450.5 PXU483T02
-451.5 PXU483T01
KQ0048G07
-446.5 PXU487T06
-447.5 PXU487T05
-448.5 PXU487T04
-449.5 PXU487T03
-450.5 PXU487T02
-451.5 PXU487T01
KQ0048G06
-446.5 PXU486T06
-447.5 PXU486T05
-448.5 PXU486T04
-449.5 PXU486T03
-450.5 PXU486T02
-451.5 PXU486T01
A
A
Gauge
-4515
-4515
Surface gauge
Tube gauge
Slot gauge
Heater gauge
RH-gauge
KQ0048G04
-448.5 PXU484T11 Heater gauge
-448.6 PXU484T10 Slot gauge
-446.2 PXU484T09 Tube gauge
-447.5 PXU484T08 NW gauge
-447.5 PXU484T07 SE gauge
-448.5 PXU484T06 NW gauge
-448.5 PXU484T05 Tube gauge
-448.5 PXU484T04 SE gauge
-449.5 PXU484T03 NW gauge
-449.5 PXU484T02 SE gauge
-450.5 PXU484T01 Tube gauge
KQ0048G04 (RH-GAUGES)
-447.6 PXU484RH03
-447.6 PXU484RHT03
Reserve PXU484RH02
Reserve PXU484RHT02
-449.6 PXU484RH01
-449.6 PXU484RHT01
N magn
13.222 GON
KQ0048G08
-446.5 PXU488T06
-447.5 PXU488T05
-448.5 PXU488T04
-449.5 PXU488T03
-450.5 PXU488T02
-451.5 PXU488T01
B
B
KQ0047G02
-446.5 PXU472T06
-447.5 PXU472T05
-448.5 PXU472T04
-449.5 PXU472T03
-450.5 PXU472T02
-451.5 PXU472T01
Project Manager: R GLAMHEDEN
Person responsible: R GLAMHEDEN
Drawn by: S KOYI
Source:
Relationsritning 2009-06-26
G:\2007\07512590547 CAPS_Aspö\MK\CAD\Ritningar\SU448-7547-T3_2.dwg

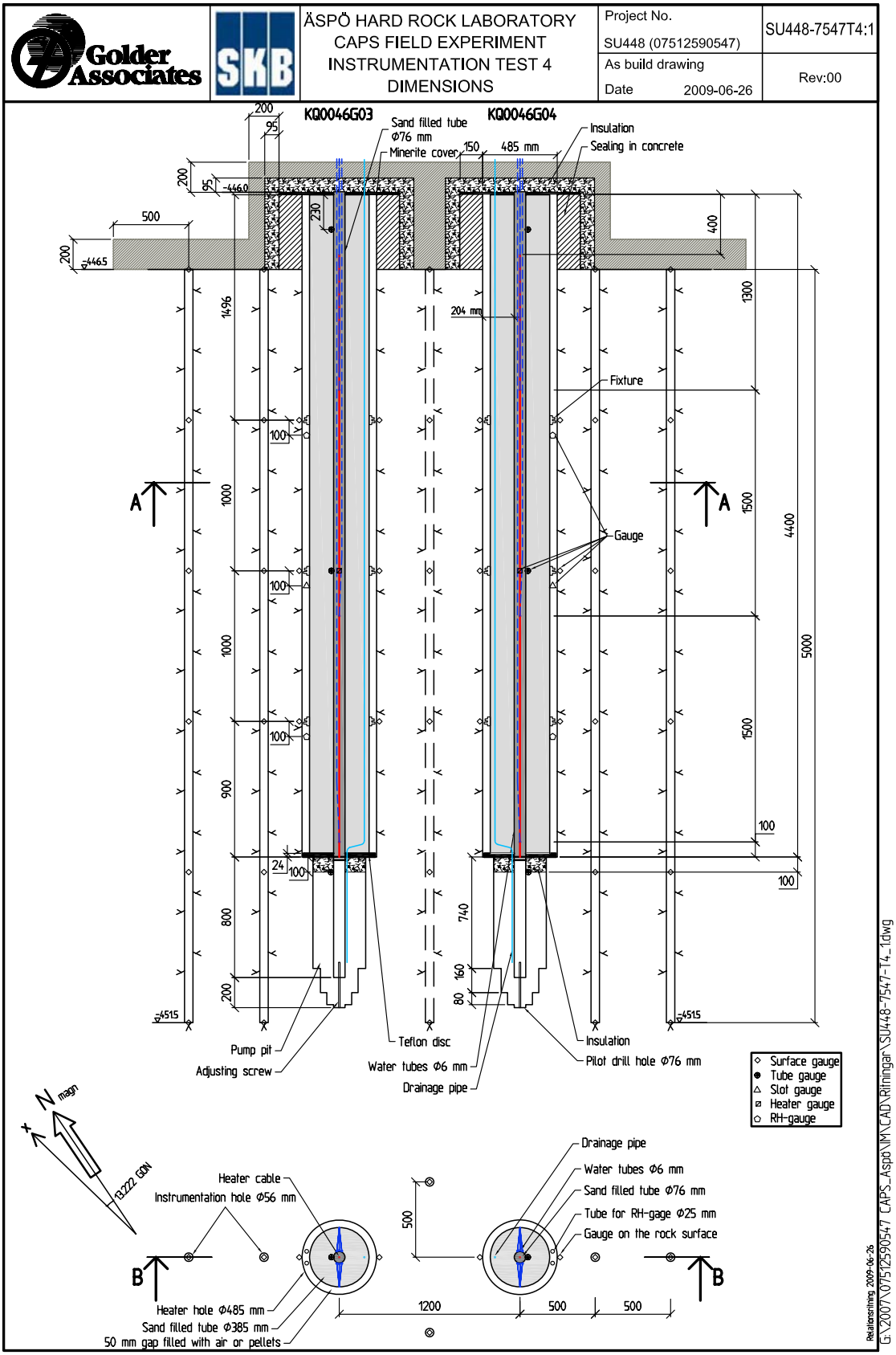
Golder Associates
SKB
ÄSPÖ HARD ROCK LABORATORY
CAPS FIELD EXPERIMENT
INSTRUMENTATION TEST 4
DIMENSIONS
Project No.
SU448 (07512590547)
SU448-7547T4:1
As build drawing
Date 2009-06-26
Rev:00
Project Manager: R GLAMHEDEN
Person responsible: R GLAMHEDEN
Drawn by: S KOYI
Source:
KQ0046G03
KQ0046G04
Sand filled tube Φ76 mm
Minerite cover
Insulation
Sealing in concrete
485 mm
150
Fixture
Gauge
204 mm
Pump pit
Adjusting screw
Teflon disc
Water tubes Φ6 mm
Drainage pipe
Insulation
Pilot drill hole Φ76 mm
Surface gauge
Tube gauge
Slot gauge
Heater gauge
RH-gauge
N magn
13.22° GON
Heater cable
Instrumentation hole Φ56 mm
Heater hole Φ485 mm
Sand filled tube Φ385 mm
50 mm gap filled with air or pellets
Drainage pipe
Water tubes Φ6 mm
Sand filled tube Φ76 mm
Tube for RH-gage Φ25 mm
Gauge on the rock surface
1200
500
500
Relationsritning 2009-06-26
G:\2007\07512590547 CAPS_Aspo\MK\CAD\Ritningar\SU448-7547-T4_1.dwg

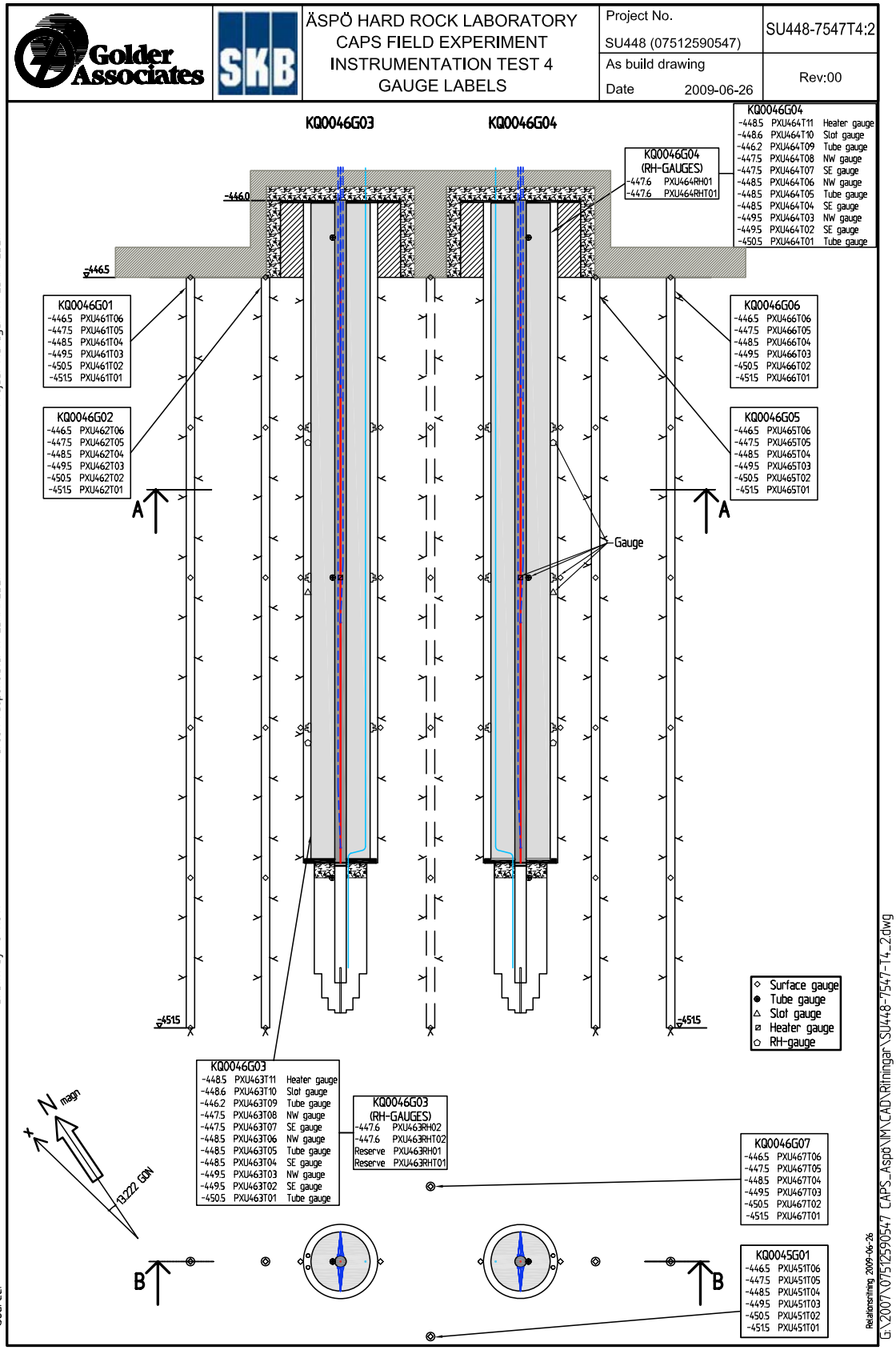
ÄSPÖ HARD ROCK LABORATORY
CAPS FIELD EXPERIMENT
INSTRUMENTATION TEST 4
GAUGE LABELS
Project No.
SU448 (07512590547)
SU448-7547T4:2
As build drawing
Date 2009-06-26
Rev:00
KQ0046G03
KQ0046G04
KQ0046G04 (RH-GAUGES)
KQ0046G01
KQ0046G02
KQ0046G06
KQ0046G05
Gauge
KQ0046G03 (RH-GAUGES)
KQ0046G07
KQ0045G01
Surface gauge
Tube gauge
Slot gauge
Heater gauge
RH-gauge
N magn
13.222 GON
Project Manager: R GLAMHEDEN
Person responsible: R GLAMHEDEN
Drawn by: S KOYI
Source:
G:\2007\07512590547 CAPS_Aspö\MX\CAD\Ritningar\SU448-7547-T4_2.dwg
Relationsritning 2009-06-26

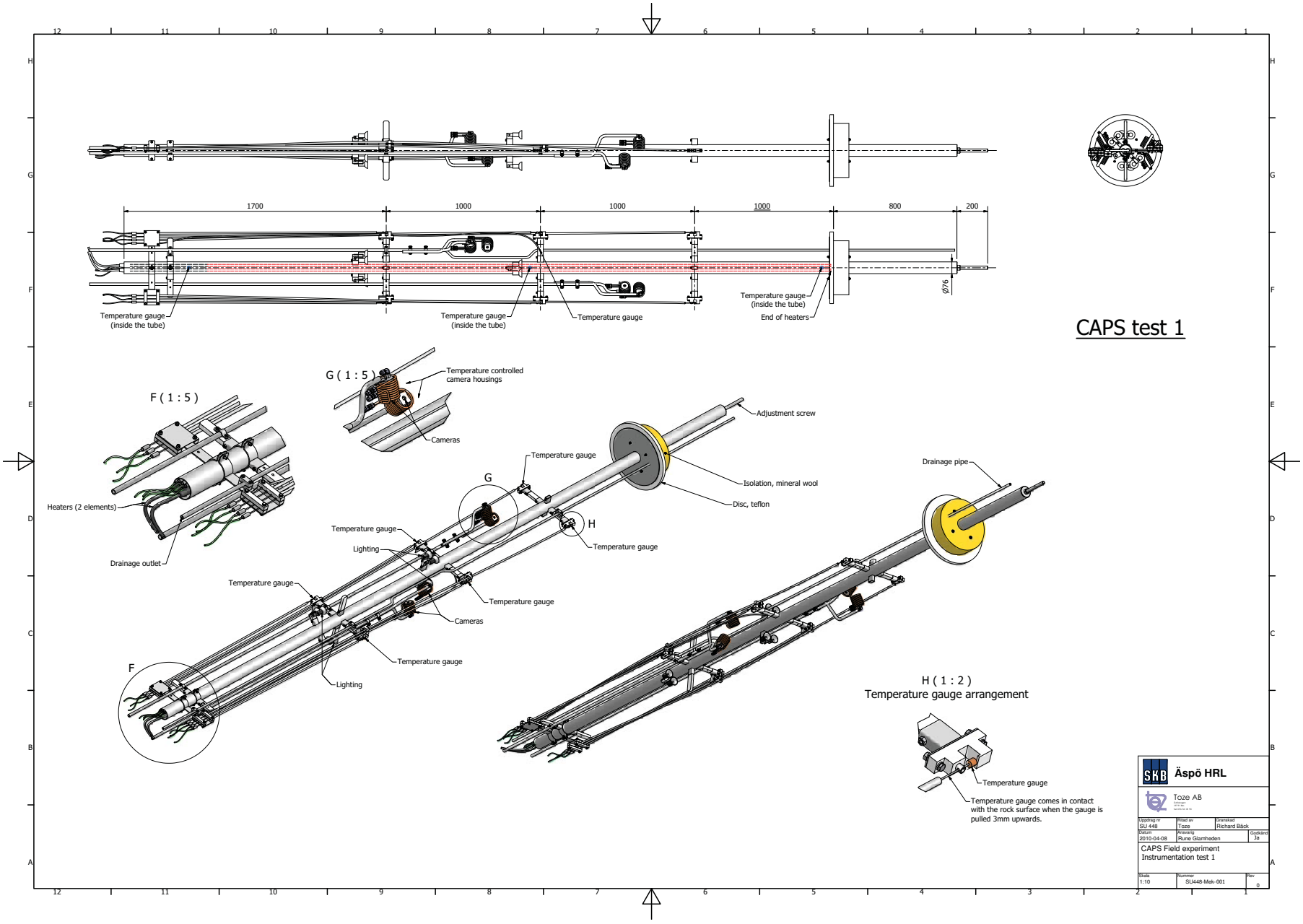
1700
1000
1000
1000
800
200
Ø76
Temperature gauge (inside the tube)
Temperature gauge (inside the tube)
Temperature gauge
Temperature gauge (inside the tube)
End of heaters
CAPS test 1
G (1 : 5)
Temperature controlled camera housings
Cameras
F (1 : 5)
Heaters (2 elements)
Drainage outlet
Adjustment screw
Temperature gauge
Isolation, mineral wool
Disc, teflon
Drainage pipe
Temperature gauge
Lighting
Temperature gauge
Temperature gauge
Temperature gauge
Cameras
Temperature gauge
Lighting
H (1 : 2)
Temperature gauge arrangement
Temperature gauge
Temperature gauge comes in contact with the rock surface when the gauge is pulled 3mm upwards.
SKB
Äspö HRL
Toze AB
Uppdrag nr SU 448
Ritad av Toze
Granskad Richard Bäck
Datum 2010-04-08
Ansvarig Rune Glamheden
Godkänd Ja
CAPS Field experiment
Instrumentation test 1
Skala 1:10
Nummer SU448-Mek-001
Rev 0

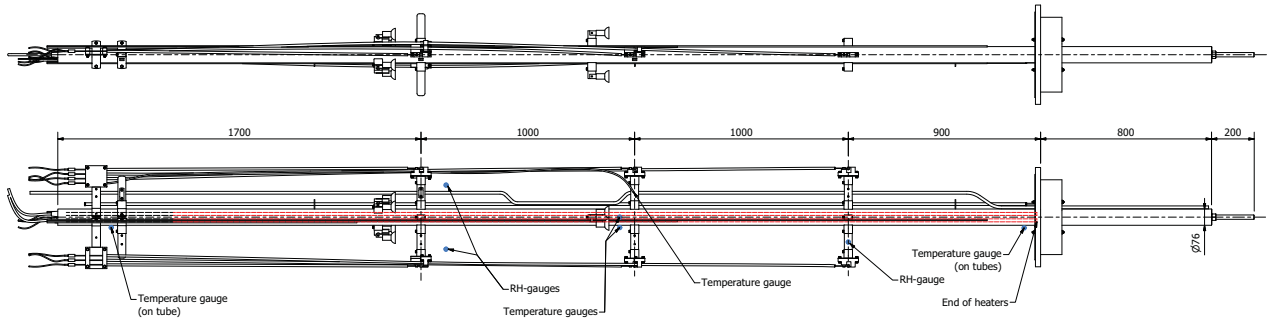

CAPS test 2

I (1 : 5)

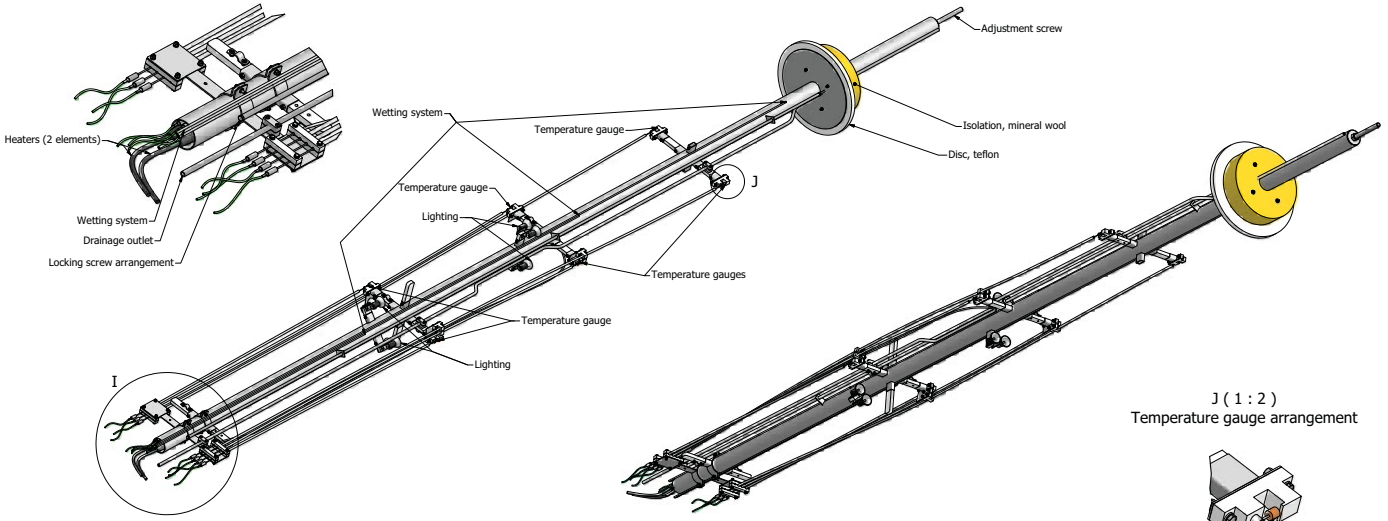

J (1 : 2)
Temperature gauge arrangement

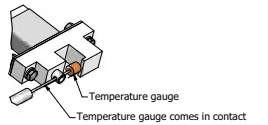

SKB Äspö HRL

Toze AB

Uppdrag nr	Ritad av	Granskad
SU 448	Toze	Richard Bäck
Datum	Ansvarig	Godkänd
2010-04-08	Rune Glamheden	Ja

CAPS Field experiment
Instrumentation test 2

Skala	Nummer	Rev
1:10	SU448-Mek-002	0

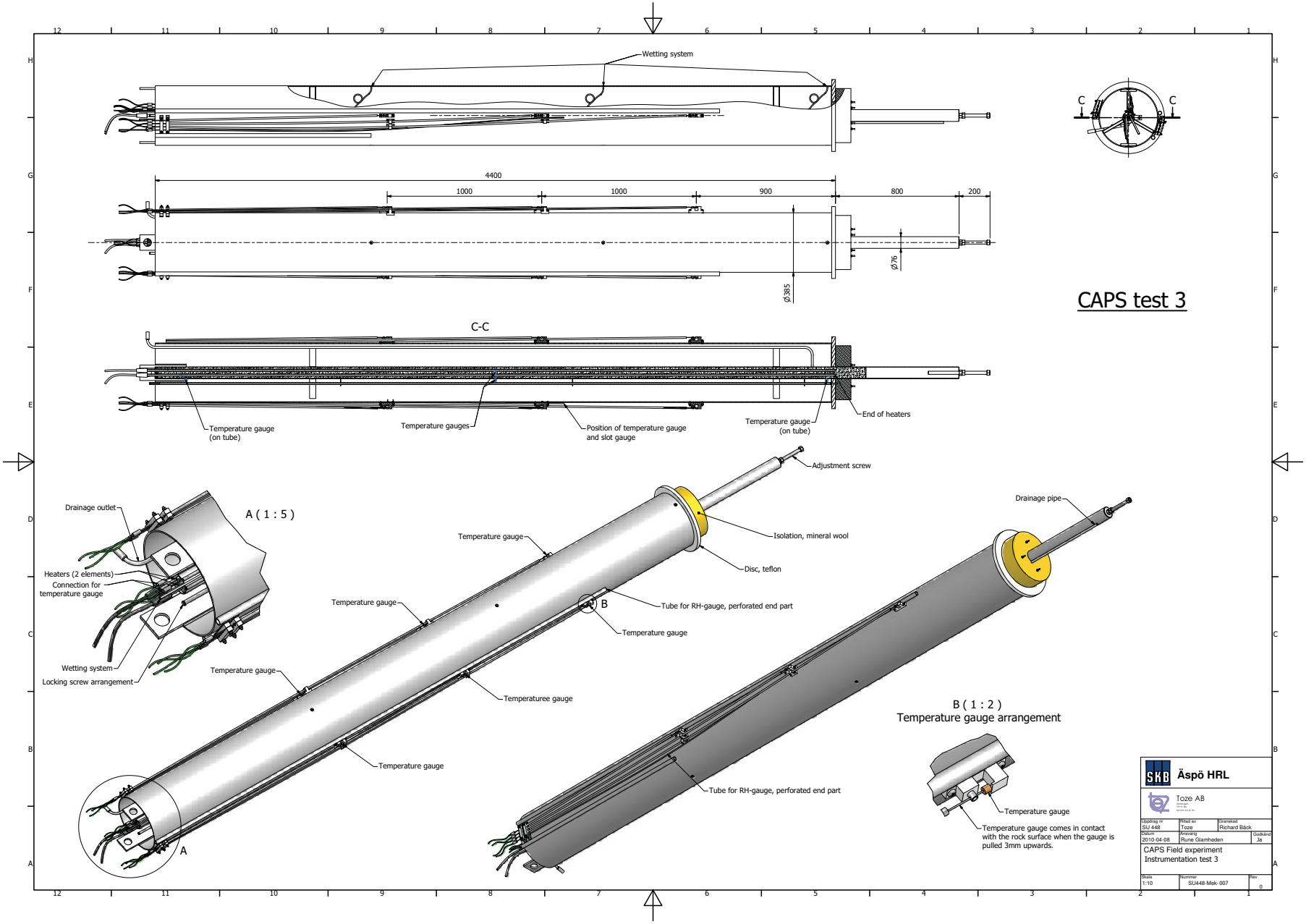
Wetting system
4400
1000
1000
900
800
200
Ø76
Ø385
C-C
C
C
Temperature gauge (on tube)
Temperature gauges
Position of temperature gauge and slot gauge
Temperature gauge (on tube)
End of heaters
CAPS test 3
Drainage outlet
A (1 : 5)
Heaters (2 elements)
Connection for temperature gauge
Wetting system
Locking screw arrangement
Adjustment screw
Temperature gauge
Isolation, mineral wool
Disc, teflon
Temperature gauge
B
Tube for RH-gauge, perforated end part
Temperature gauge
Temperature gauge
Temperaturee gauge
Temperature gauge
A
Drainage pipe
B (1 : 2)
Temperature gauge arrangement
Tube for RH-gauge, perforated end part
Temperature gauge
Temperature gauge comes in contact with the rock surface when the gauge is pulled 3mm upwards.
SKB Äspö HRL
Toze AB
Uppdrag nr SU 448
Ritad av Toze
Granskad Richard Bäck
Datum 2010-04-08
Ansvarig Rune Glamheden
Godkänd Ja
CAPS Field experiment
Instrumentation test 3
Skala 1:10
Nummer SU448-Mek- 007
Rev 0

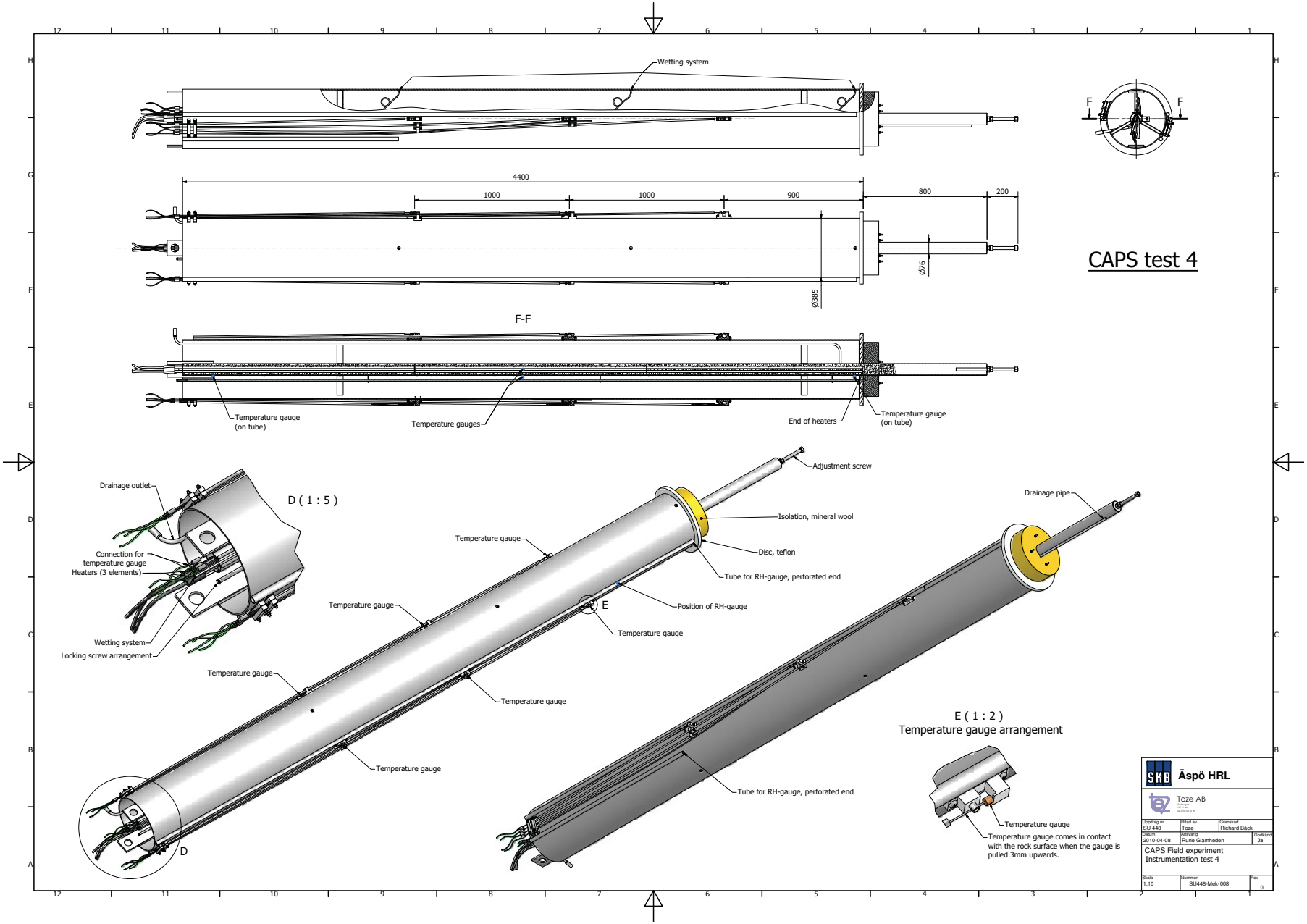
Wetting system
F
F
4400
1000
1000
900
800
200
Ø76
Ø385
F-F
Temperature gauge (on tube)
Temperature gauges
End of heaters
Temperature gauge (on tube)
CAPS test 4
Drainage outlet
D (1 : 5)
Connection for temperature gauge
Heaters (3 elements)
Wetting system
Locking screw arrangement
Adjustment screw
Isolation, mineral wool
Disc, teflon
Tube for RH-gauge, perforated end
Position of RH-gauge
Temperature gauge
E
Drainage pipe
Tube for RH-gauge, perforated end
E (1 : 2)
Temperature gauge arrangement
Temperature gauge
Temperature gauge comes in contact with the rock surface when the gauge is pulled 3mm upwards.
D
SKB
Äspö HRL
Toze AB
Uppdrag nr SU 448
Rittad av Toze
Granskad Richard Bäck
Datum 2010-04-08
Ändring Rune Glamheden
Godkänd Ja
CAPS Field experiment
Instrumentation test 4
Skala 1:10
Nummer SU448-Mek-008
Rev 0

Appendix H

Technical specifications of instruments and heater system

H1 Relative humidity gauges

H1.1 Technical specification

Table H-1. Specifications for Rotronics M120 transmitter.

	Humidity (%)	Temperature (°C)
Operation limits of the probe	–	–40–190
Operation limits of the electronics	0–99	–40–60
Measuring range	0–100	–30–150
Accuracy	± 1.5	± 0.3
Repeatability	±0.3	±0.1

Table H-2. Specifications for Comet T3111 transmitter.

	Humidity (%)	Temperature (°C)
Operation limits of the probe	–	–30–80
Operation limits of the electronics	–	–30–70
Measuring range	0–100	–30–105
Accuracy	±2.5	±0.4

Table H-3. Specifications for Kimo TH200 transmitter.

	Humidity (%)	Temperature (°C)
Operation limits of the probe	–	–40–180
Operation limits of the electronics	–	–10–70
Measuring range	0–100	–30–105
Resolution	0.1	0.1
Accuracy	±2.6	±0.3

H1.2 Calibration procedure

The instruments were calibrated before delivery by the manufacture according to methods and recommendations of national standards.

H2 Temperature gauges

H2.1 Technical specification

Table H-4. Specifications for Pentronic thermocouple Type K.

	Value	Unit
Measuring range	Max 1,200	°C
Resolution	Max 0.05	°C
Accuracy	±1.5	°C

H2.2 Calibration procedure

The instruments were calibrated before delivery by the manufacture according to methods and recommendations of national standards. Furthermore, the gauges were calibrated by SKB before and after the field experiment using a calibration bath of model Hart 7102 and a calibrated reference thermometer of model Hart 1521. The temperature levels used in the calibration were 20, 50 and 90°C. The gauges were stabilized for about 10 minutes on each temperature level.

H3 Heating system

H3.1 Technical specification

Table H-5. Specifications for Backer heater element.

	Value	Unit
Power supply	230	V
Output power	2,300	W
Length	4.2	m

Table H-6. Specifications for Jumbo Thyristor.

	Value	Unit
Fluctuations	Max 0.5	%
Permitted ambient temperature	0–45	°C
Permitted relative humidity	Max 75	%

H3.2 Calibration procedure

The thyristor units were calibrated with ABB DBB23000 electronic electricity meter.

The calibration of a thyristor unit is very difficult to make due to the noise made by the thyristor itself. The calibration was performed as follows:

The display on the DBB23000 was used to set a specific power output, when the thyristor internal electricity meter was set at the same value. This task was made at full power output (2,500 W) and also at 1,000 W. Estimated accuracy is about +/–5% of the measured output power.

H4 Technical specifications of monitoring cameras

Table H-7. Specifications for Eneo VK-134 digital video.

	Value	Unit
System	Black/white	
Picture elements	500(H) x 582(V)	Pixels
Sensitivity at F1.2	0.58	Lux
Lens type	Fixed focal length	
Lens	F2.0/3.6 mm	
Focal length	3.6	mm
Horizontal angle of view	69	deg
Iris control	no	
Temperature range	–10–50	°C

Table H-8. Specifications for Eneo VK-135 digital video.

	Value	Unit
System	Black/white	
Picture elements	500(H) x582(V)	Pixels
Sensitivity at F1.2	1.0	Lux
Rotation range	360	deg
Tilt range	±60	deg
Lens type	Fixed focal length	
Lens	F2.0/3.7 mm	
Focal length	3.7	mm
Horizontal angle of view	68	deg
Iris control	no	
Operating temperature range	–10–50	°C

Appendix I

Heating power in the field tests

Table I-1. Applied heating power per hole during the field tests. Recorded mean values for respective heating step.

	Test 1			Test 2			Test 3			Test 4		
	Time (Days)	G03 (W)	G04 (W)	Time (Days)	G04 (W)	G05 (W)	Time (Days)	G04 (W)	G05 (W)	Time (Days)	G03 (W)	G04 (W)
Total time	**28**			**16**			**31**			**57**		
	5	1,515	1,490	2	2,640	2,595	5	2,590	2,640	2	470	450
	2	1,800	1,770	1	3,245	3,200	0.5	2,045	2,645	4	1,015	1,010
	4	2,125	2,095	13	3,355	3,195	1.5	2,260	2,090	8	1,510	1,505
	7	2,675	2,660				24	2,590	2,090	4	2,015	1,950
	2	2,975	2,950							1	1,005	965
	8	3,785	3,715							3	2,015	2,145
										2	2,015	1,005
										1	2,010	2,010
										6	2,510	2,510
										7	3,005	3,000
										4	3,500	3,500
										2	3,010	3,010
										1	2,505	2,505
										2	2,005	2,005
										5	1,500	1,490
										2	1,005	1,000
										3	510	495

Note: The borehole label is shortened in the table due to limited space. The complete label included “KQ00” and borehole number. The times of the heating period have been round off to the closest day.

Test 1: 080829 11:08–080926 (G03) 18:28, (G04) 20:58
Test 2: 081106 14:51–081122 (G04) 16:19, (G05) 18:09
Test 3: 081128 13:06–091229 (G04) 14:33, (G05) 12:13
Test 4: 090213 10:51–090411 19:31

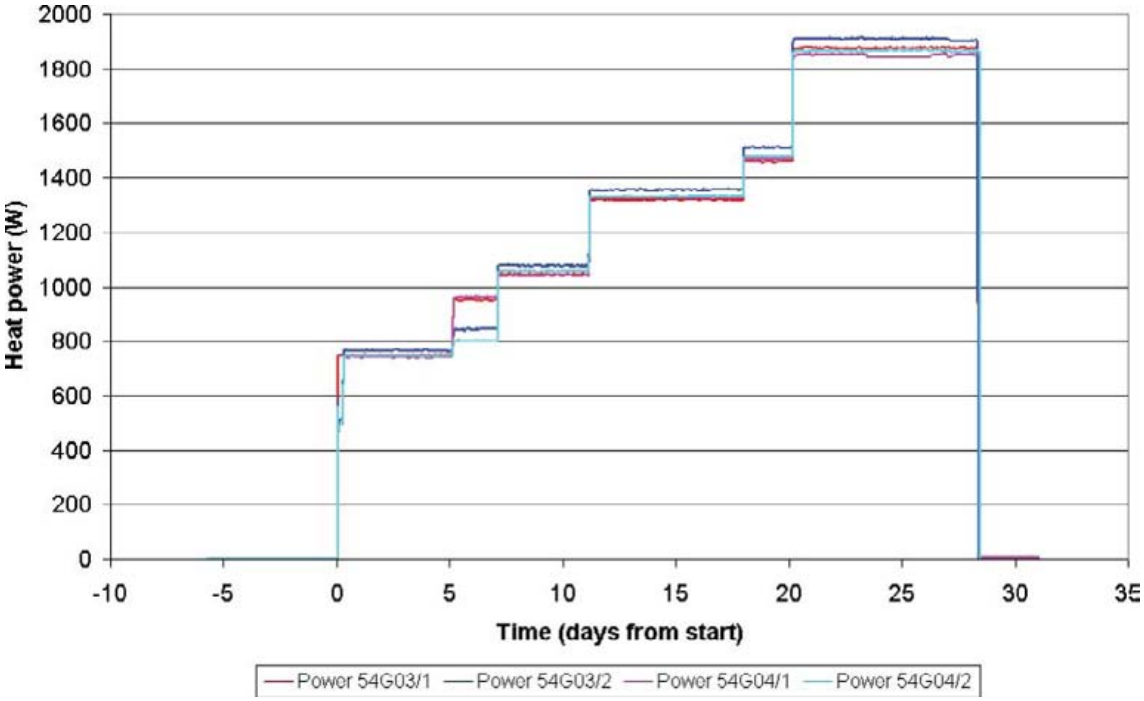

Figure I-1. *Applied heating power by each heating element during Field Test 1.*

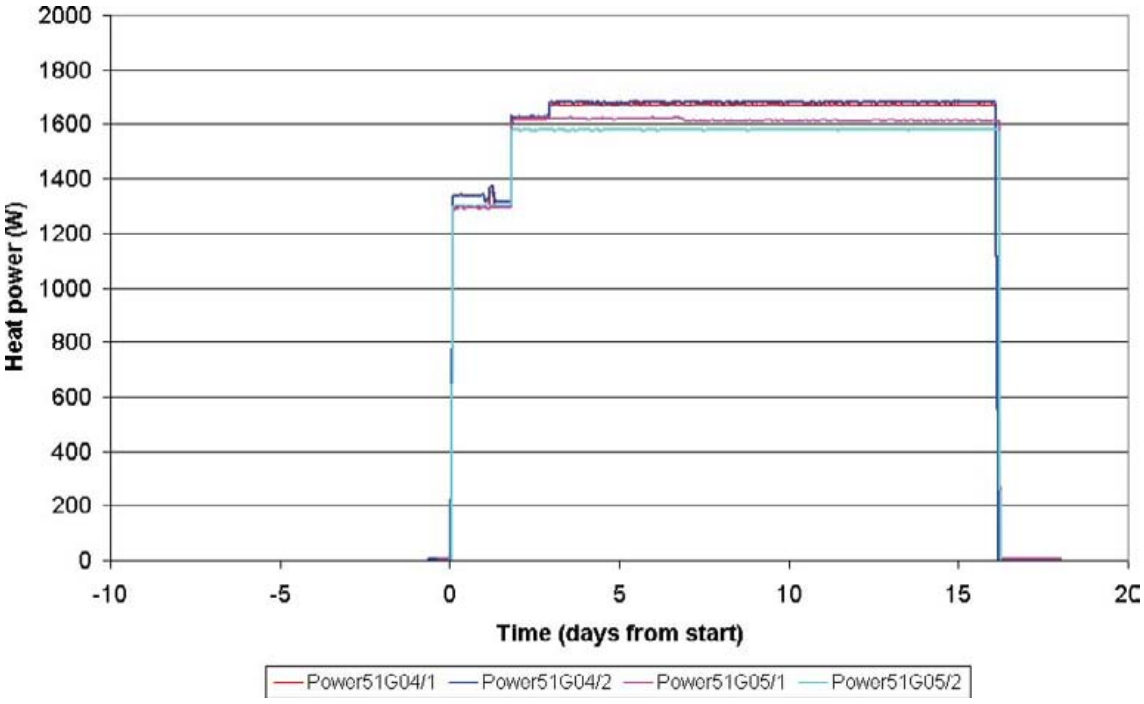

Figure I-2. *Applied heating power by each heating element during Field Test 2.*

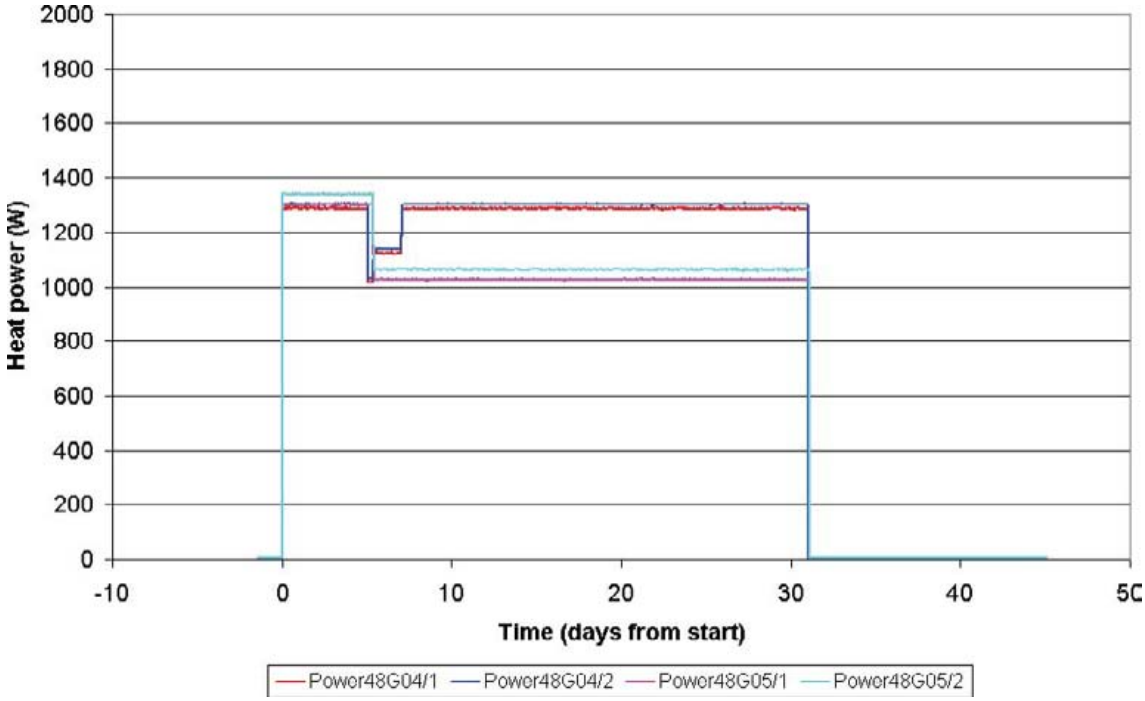

Figure I-3. *Applied heating power by each heating element during Field Test 3. The short interval in the change of power after five days was caused by an incorrect adjustment of the heating elements.*

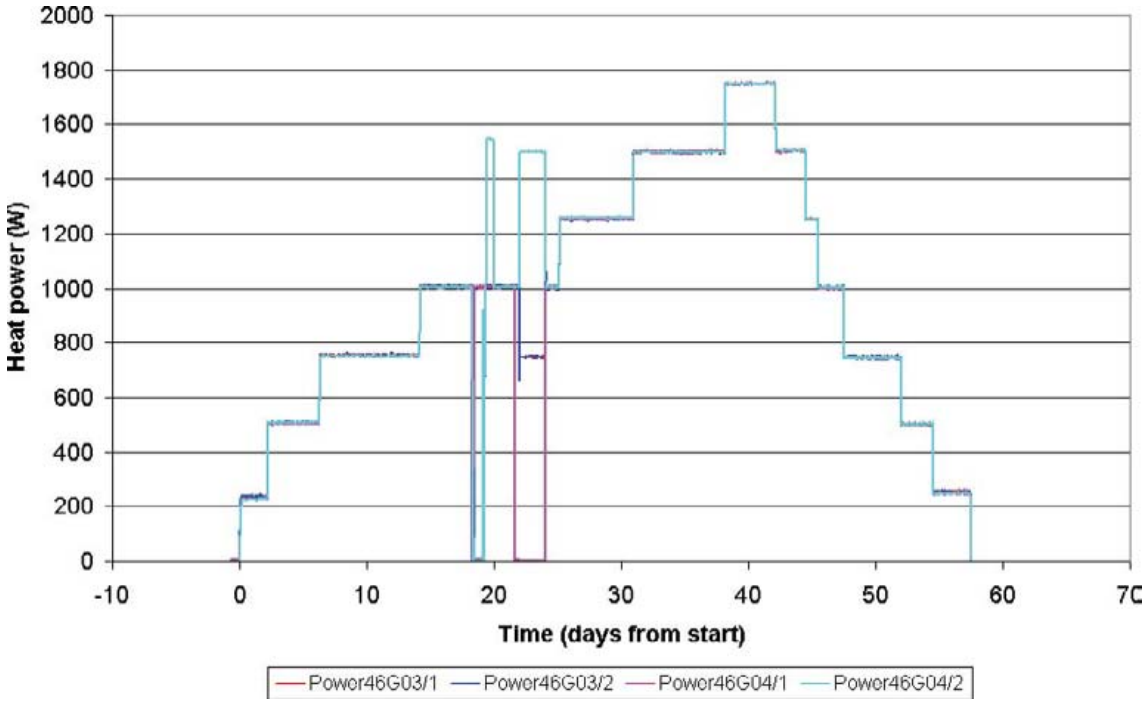

Figure I-4. *Applied heating power by each heating element during Field Test 4. The fluctuation in the power after approximately 18 and 22 days corresponds to replacements of faulty heating elements.*

Appendix J

Recorded relative humidity

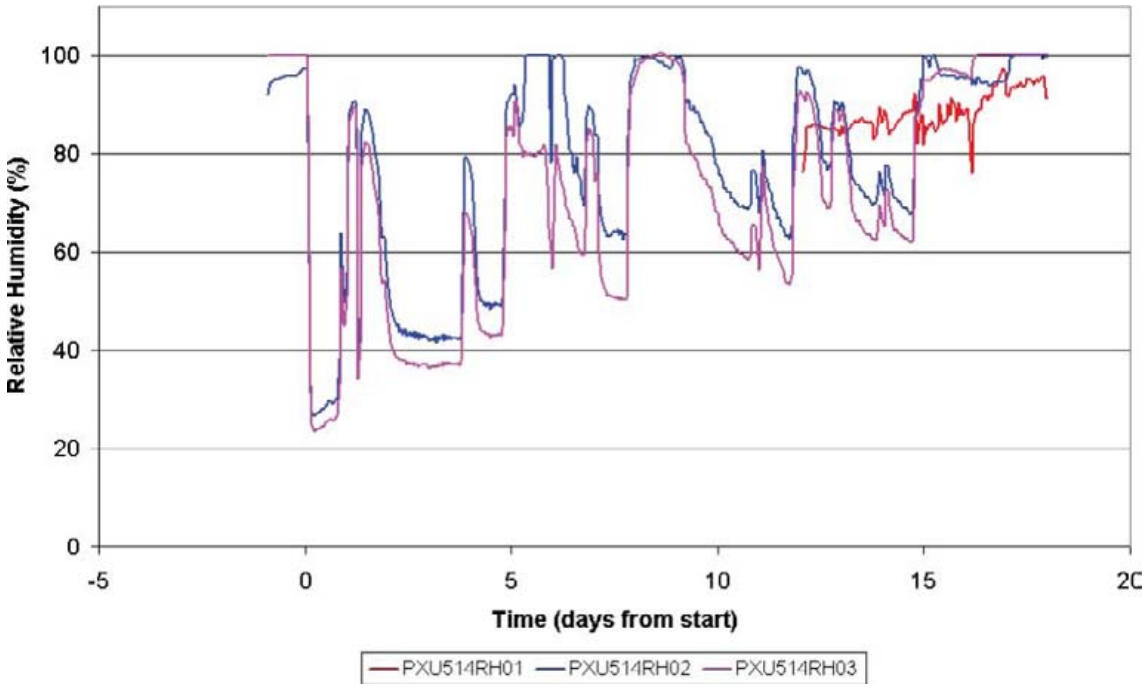

Figure J-1. *Recorded relative humidity in heating hole KQ0051G04 in Test 2.*

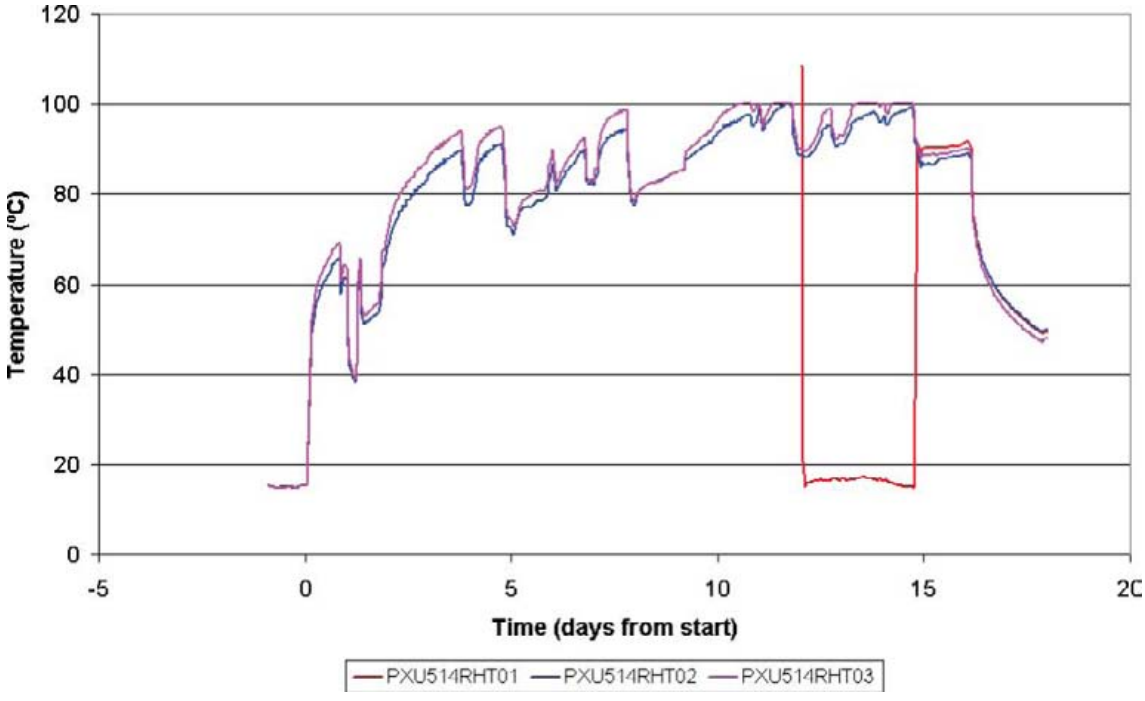

Figure J-2. *Recorded temperature by the RH-gauges in hole KQ0051G04 in Test 2.*

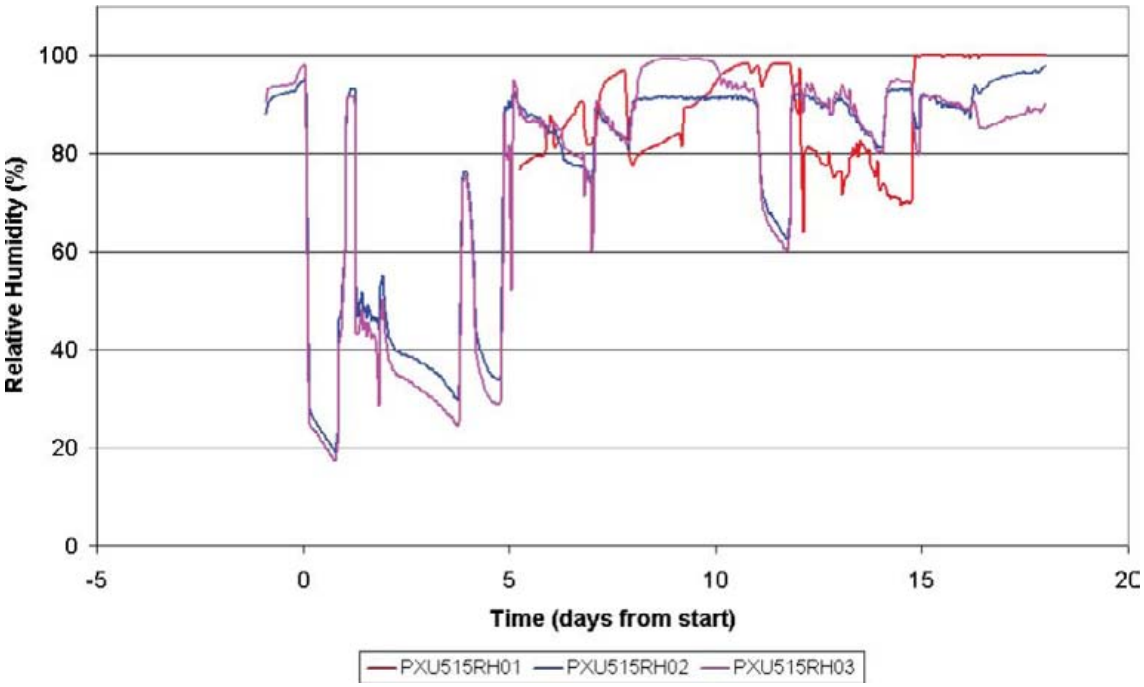

Figure J-3. *Recorded relative humidity in heating hole KQ0051G05 in Test 2.*

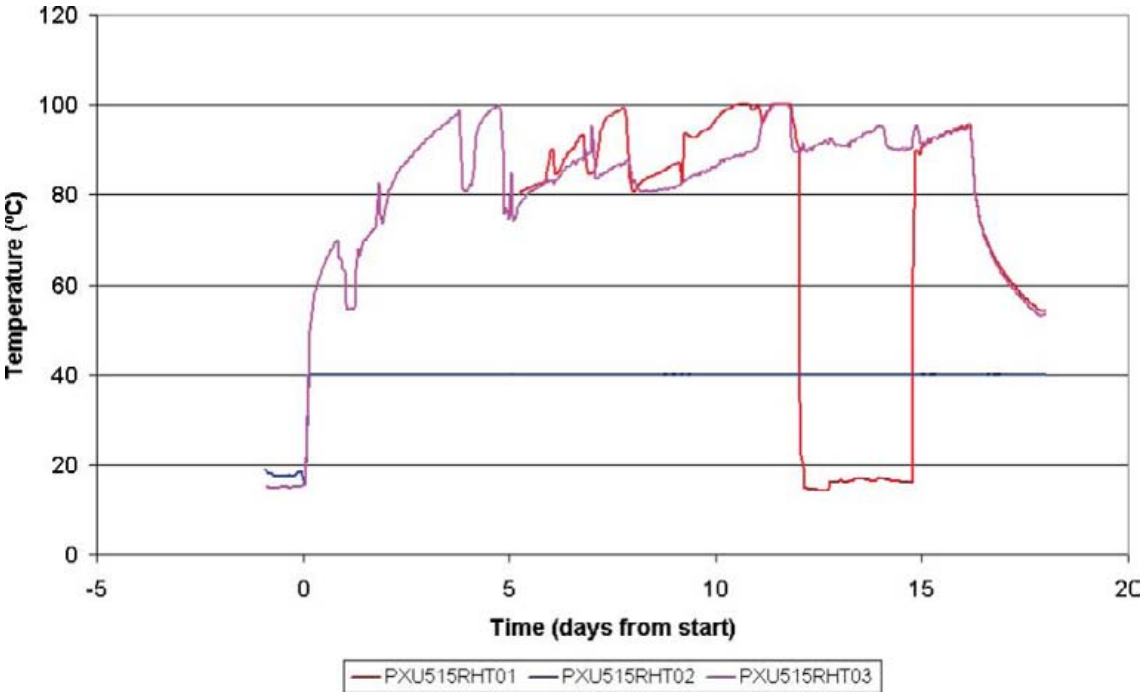

Figure J-4. *Recorded temperature by the RH-gauges in hole KQ0051G05 in Test 2.*

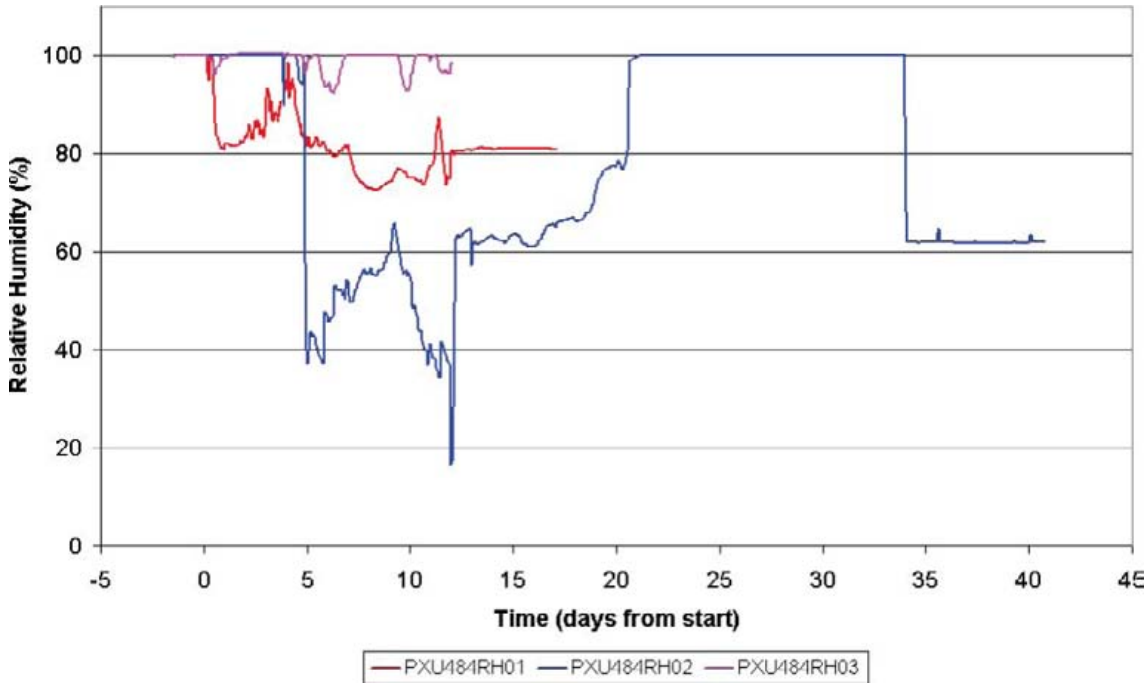

Figure J-5. *Recorded relative humidity in heating hole KQ0048G04 in Test 3.*

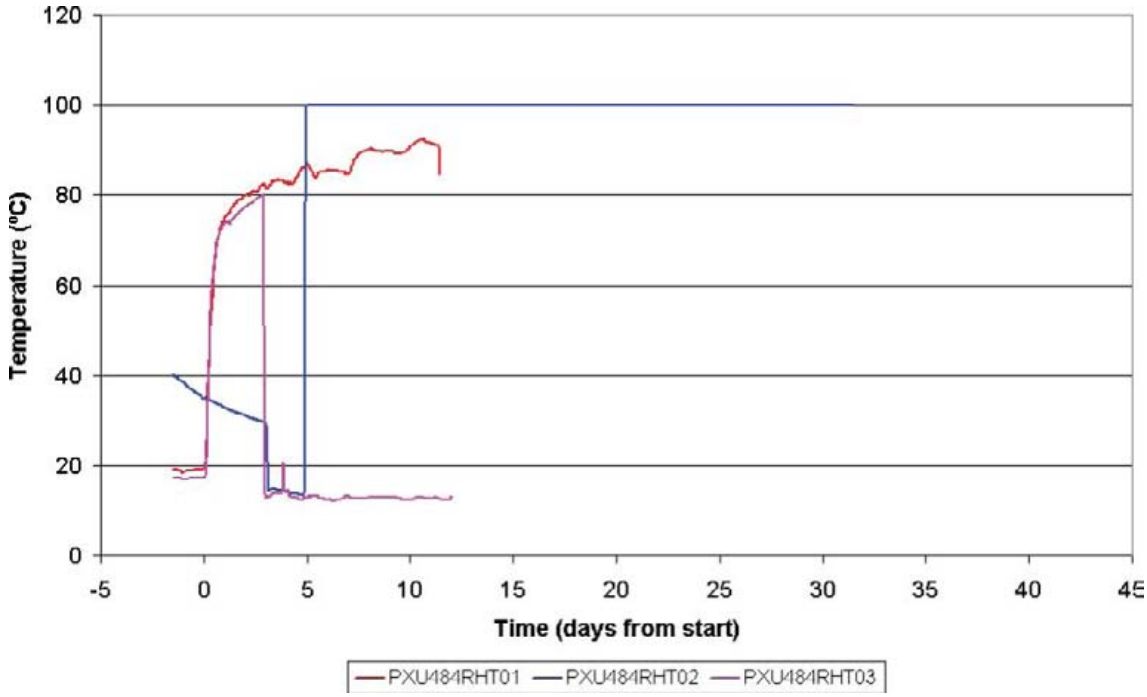

Figure J-6. *Recorded temperature by the RH-gauges in hole KQ0048G04 in Test 3.*

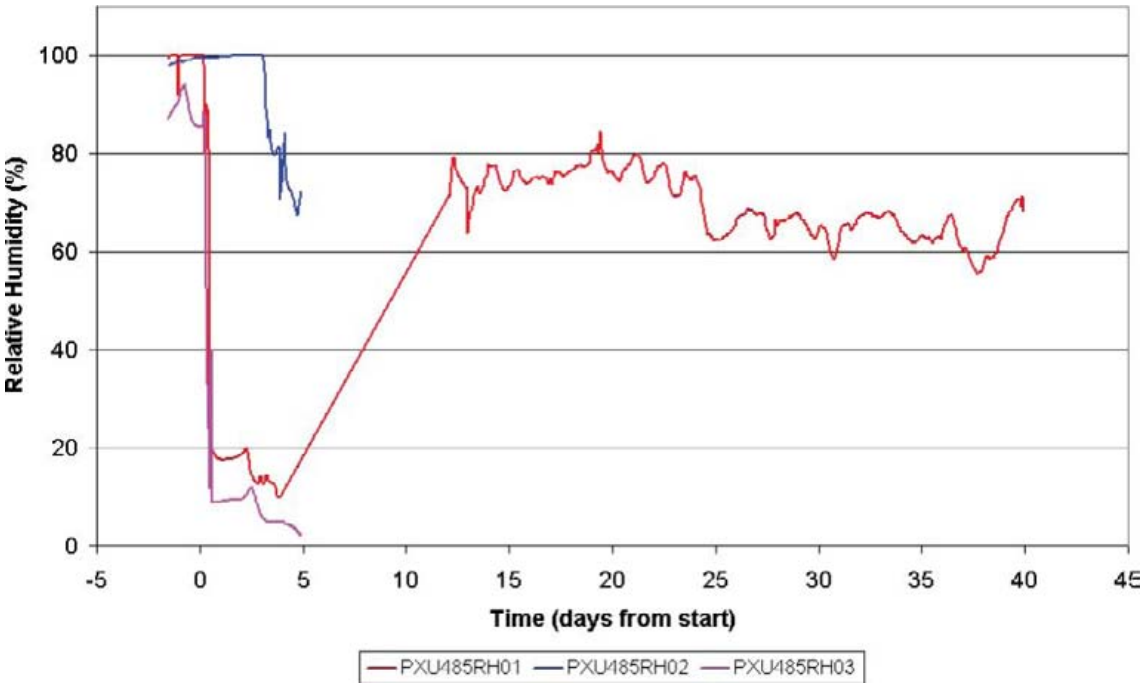

Figure J-7. *Recorded relative humidity in heating hole KQ0048G05 in Test 3.*

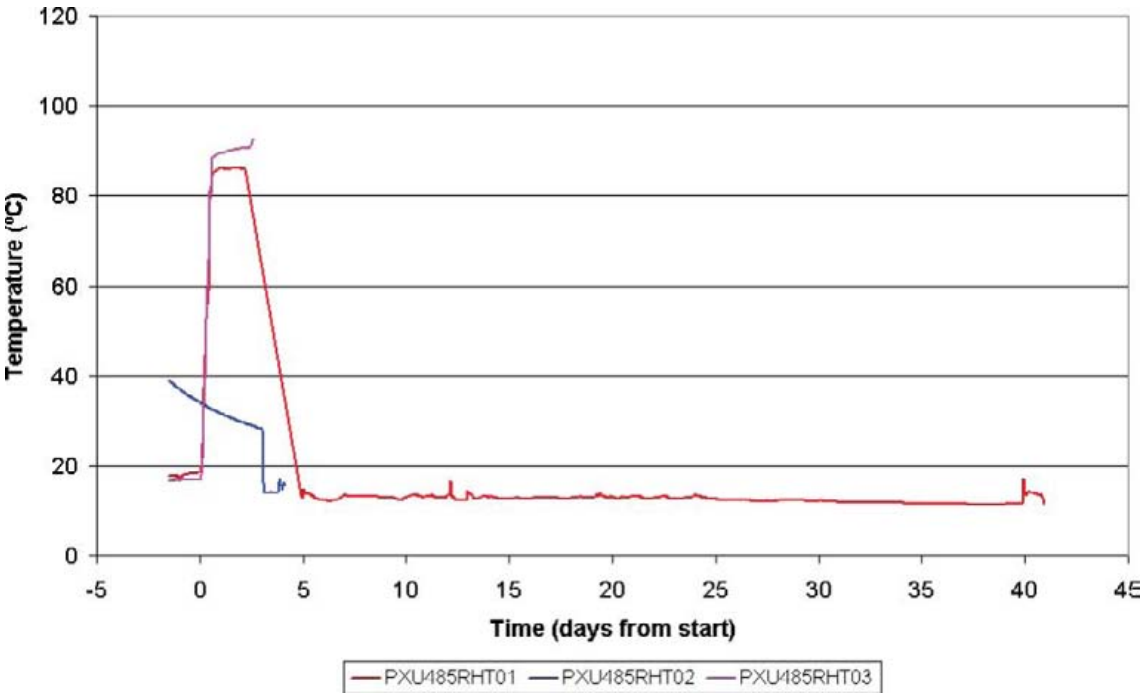

Figure J-8. *Recorded temperature by the RH-gauges in hole KQ0048G05 in Test 3.*

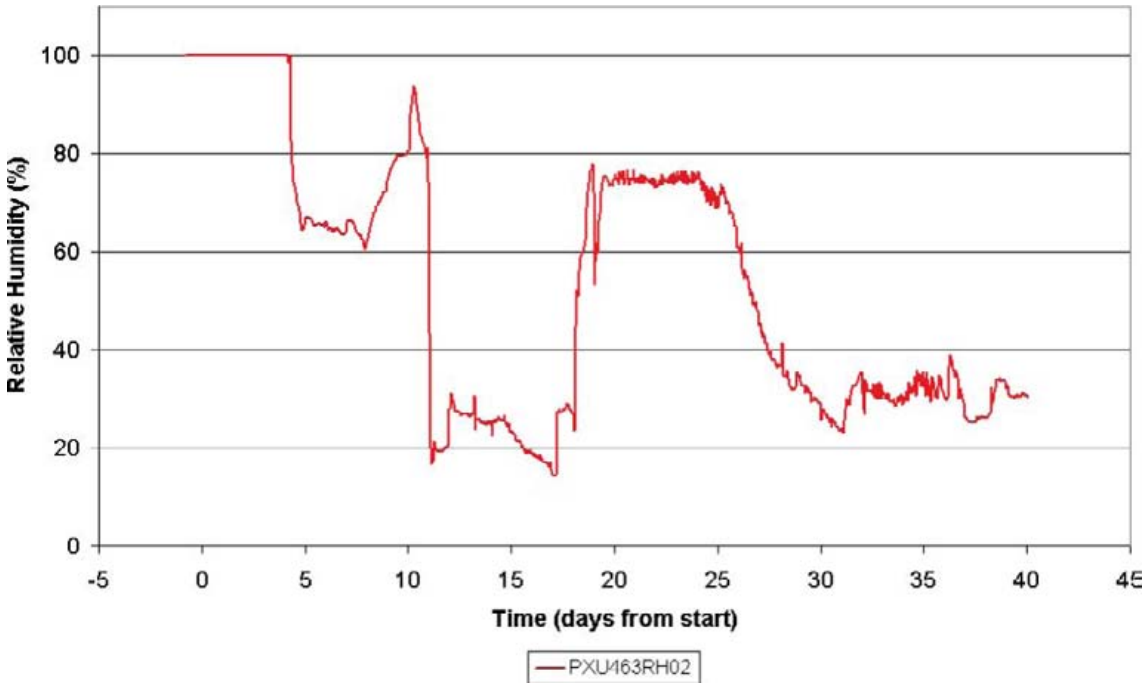

Figure J-9. *Recorded relative humidity in heating hole KQ0046G03 in Test 4.*

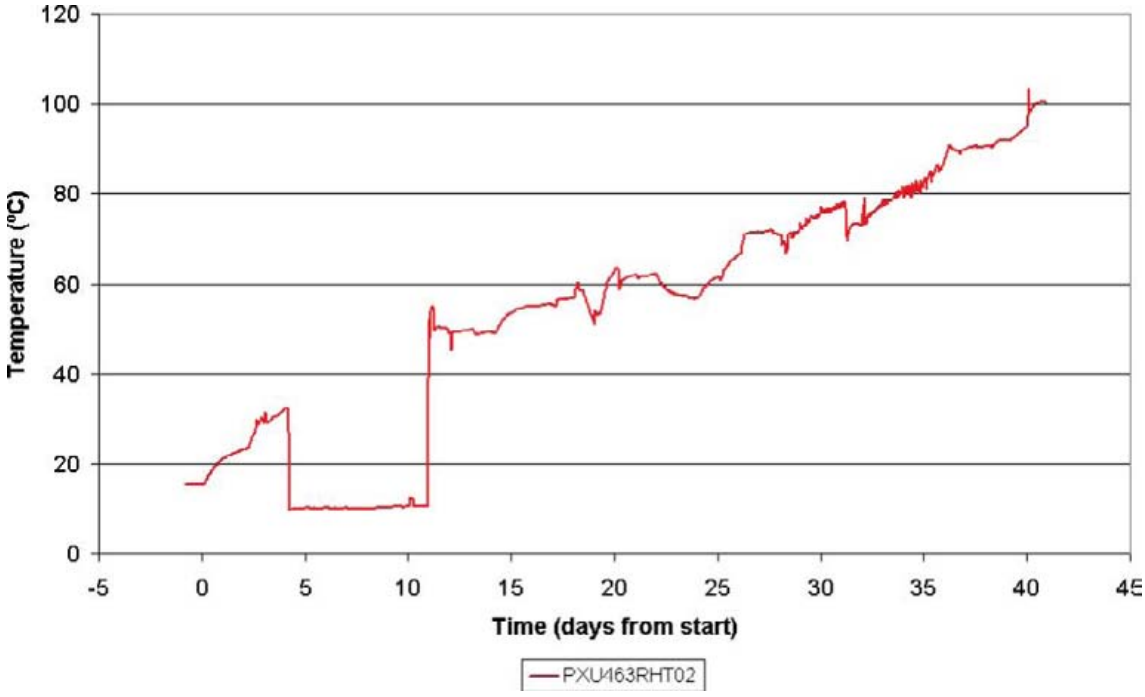

Figure J-10. *Recorded temperature by the RH-gauge in hole KQ0046G03 in Test 4.*

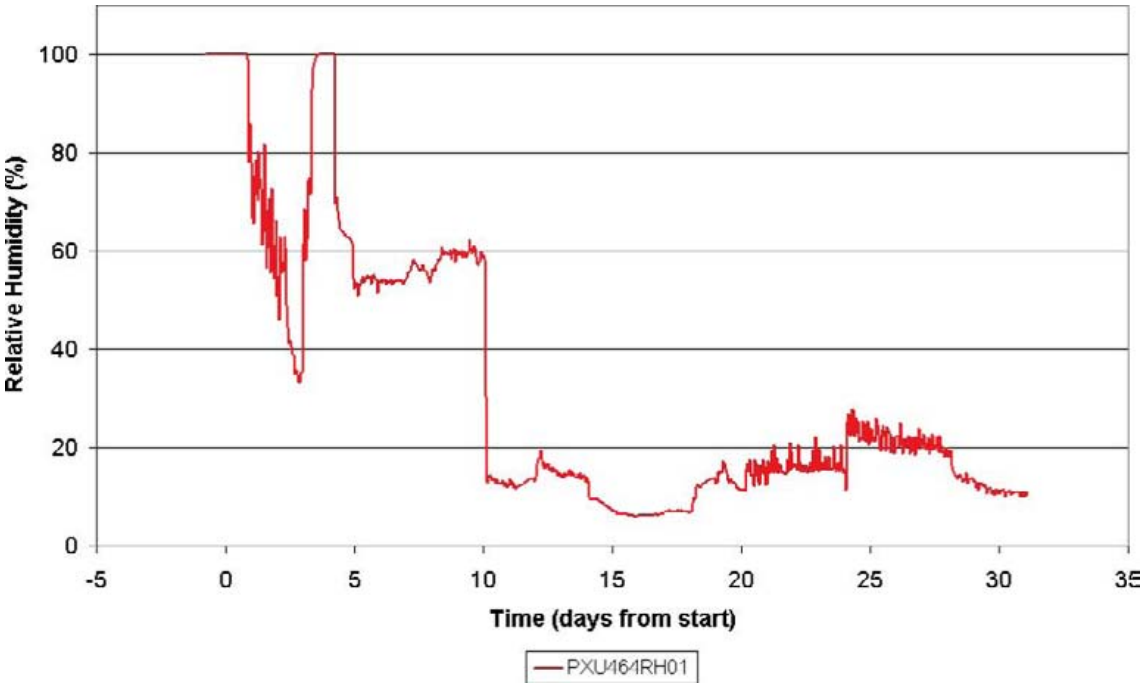

Figure J-11. *Recorded relative humidity in heating hole KQ0046G04 in Test 4.*

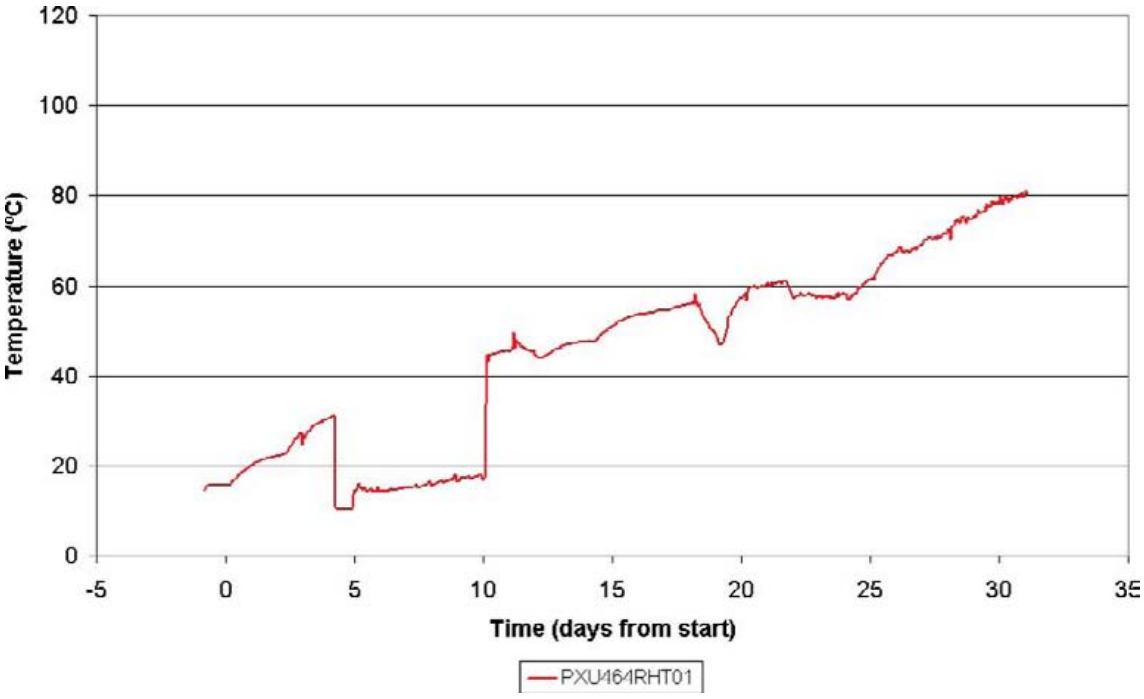

Figure J-12. *Recorded temperature by the RH-gauge in hole KQ0046G04 in Test 4.*

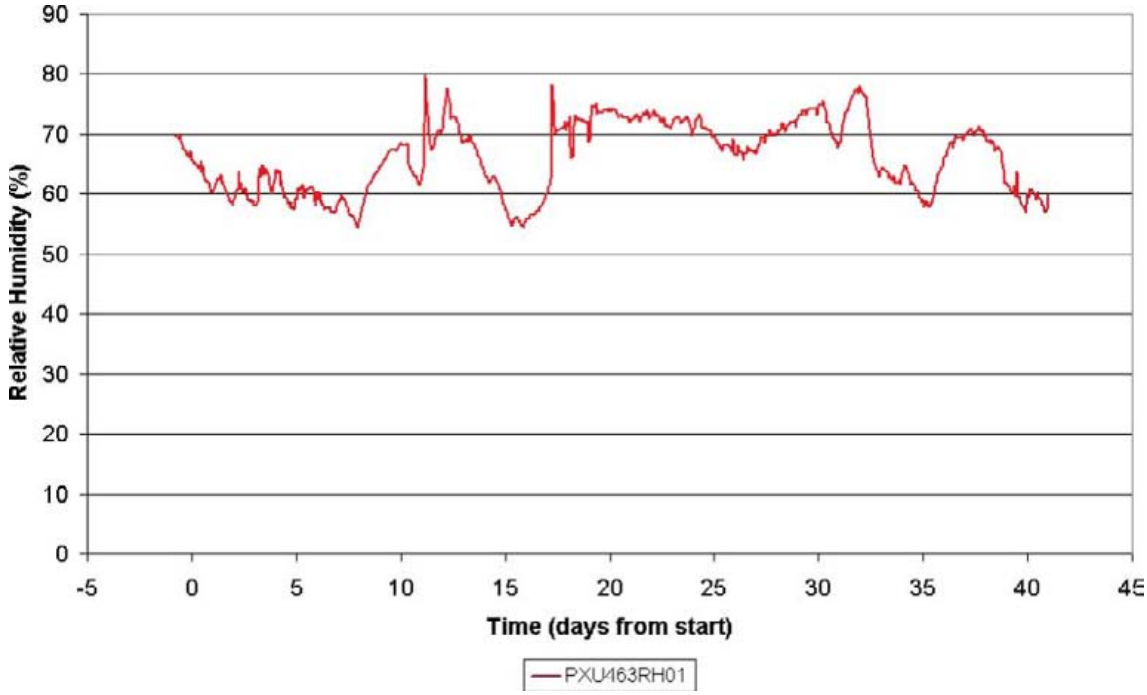

Figure J-13. *Recorded relative humidity in the TASQ-tunnel in Test 4.*

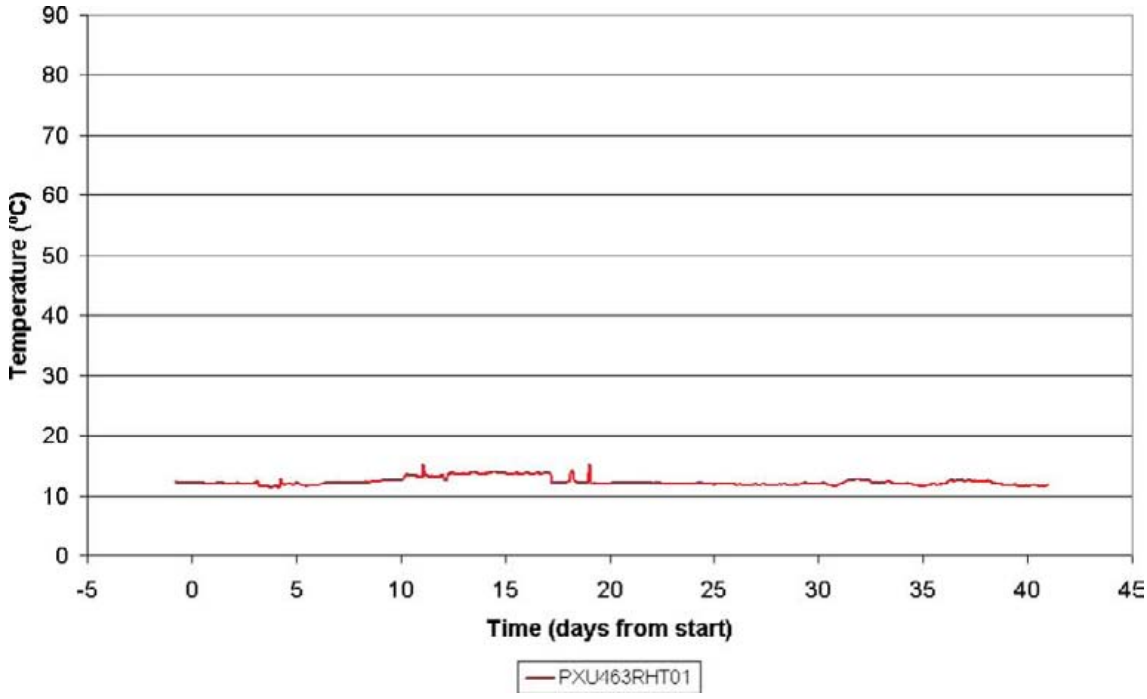

Figure J-14. *Recorded temperature by the RH-gauge in the TASQ-tunnel in Test 4.*

Recorded temperatures

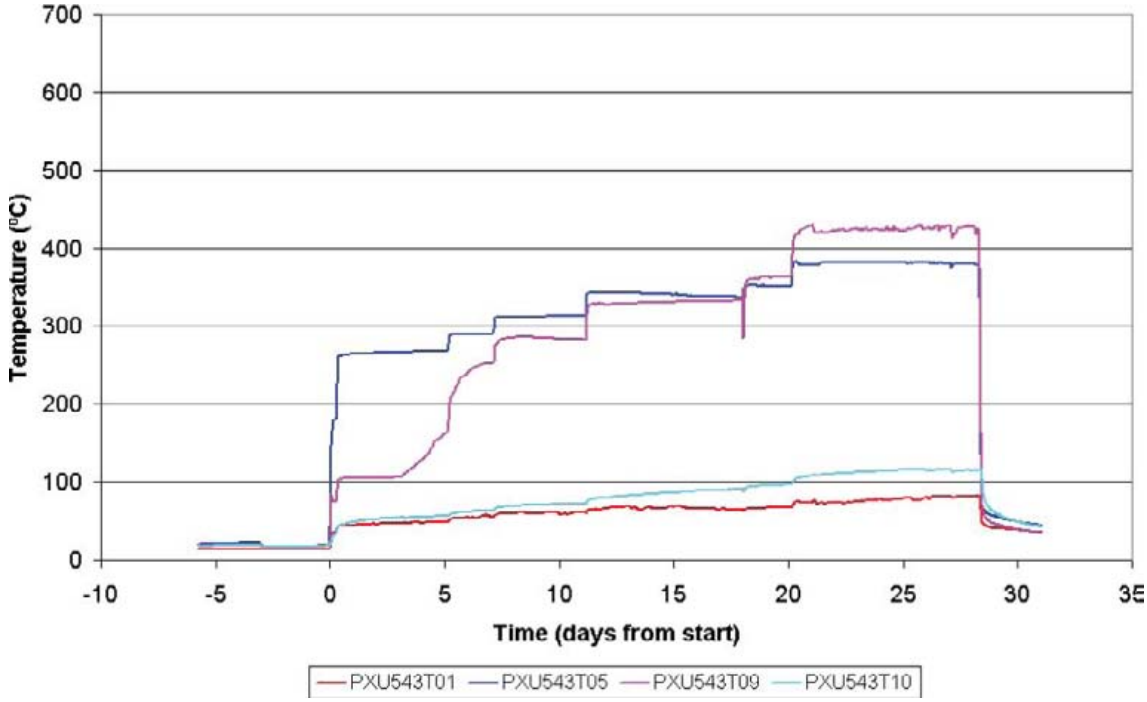

Figure K-1. *Test 1. Recorded temperature on the heater tube in heating hole KQ0054G03.*

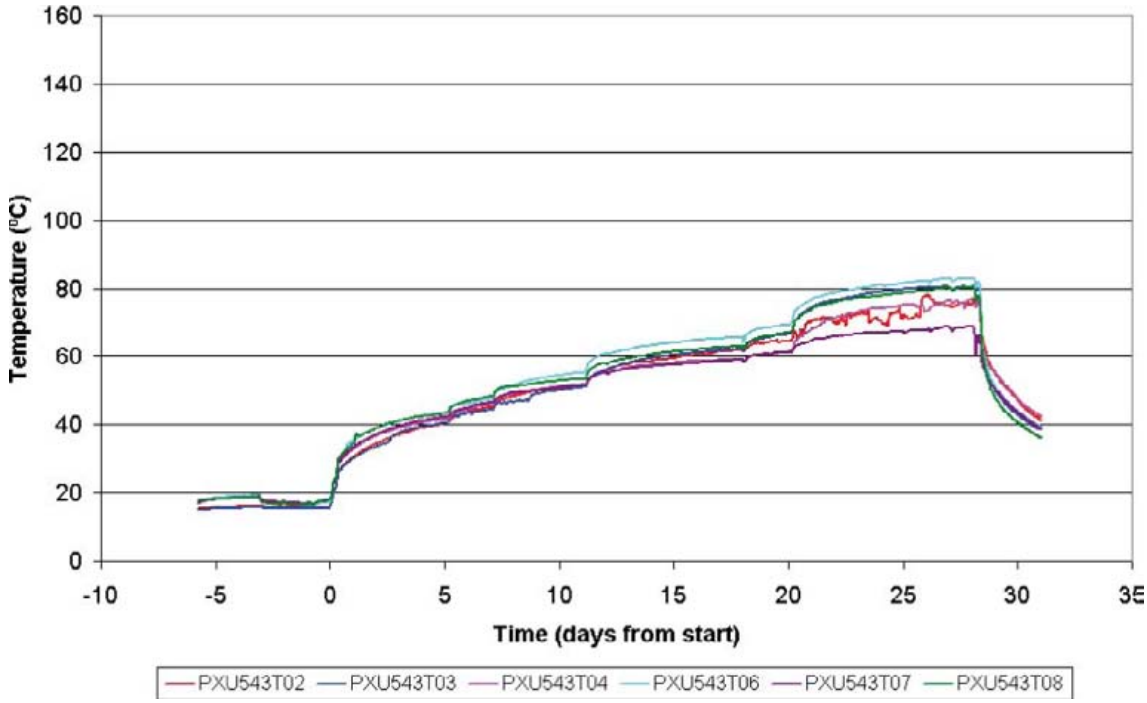

Figure K-2. *Test 1. Recorded temperature in heating hole KQ0054G03.*

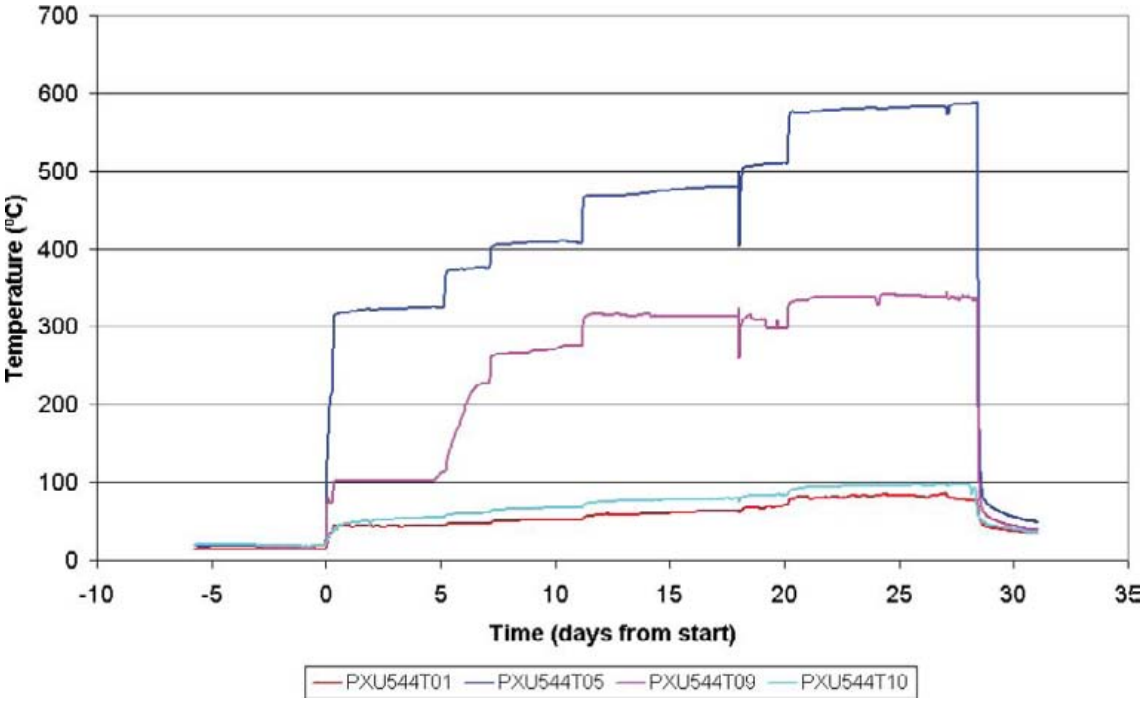

Figure K-3. *Test 1. Recorded temperature on the heater tube in heating hole KQ0054G04.*

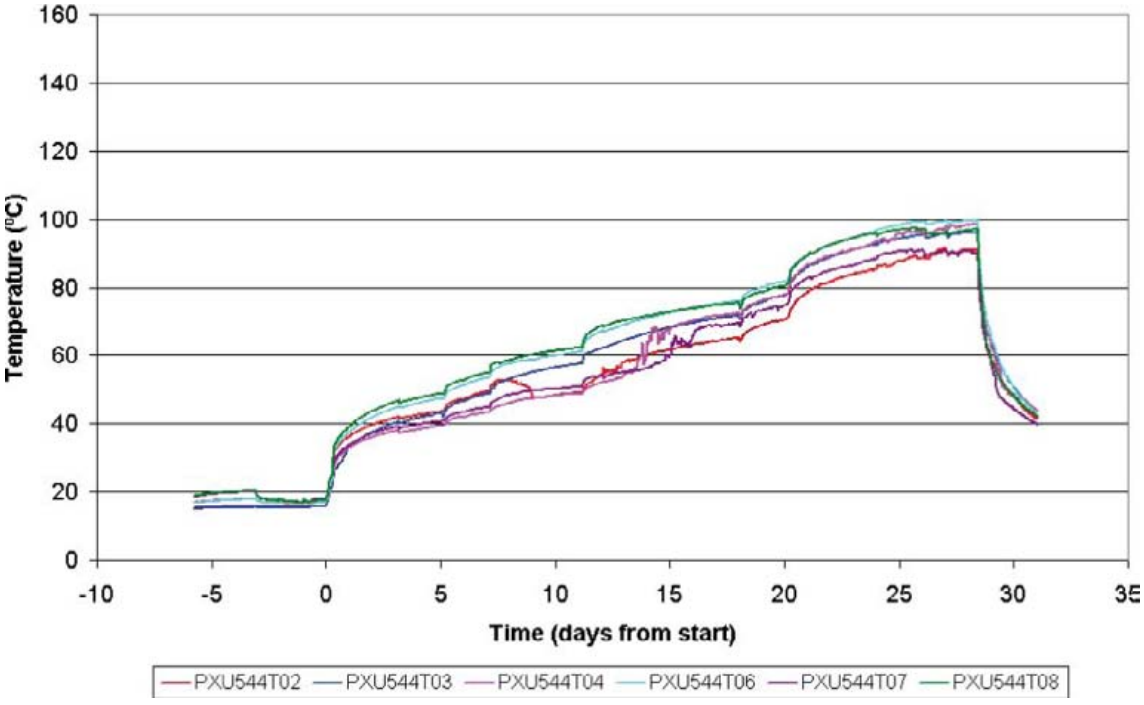

Figure K-4. *Test 1. Recorded temperature in heating hole KQ0054G04.*

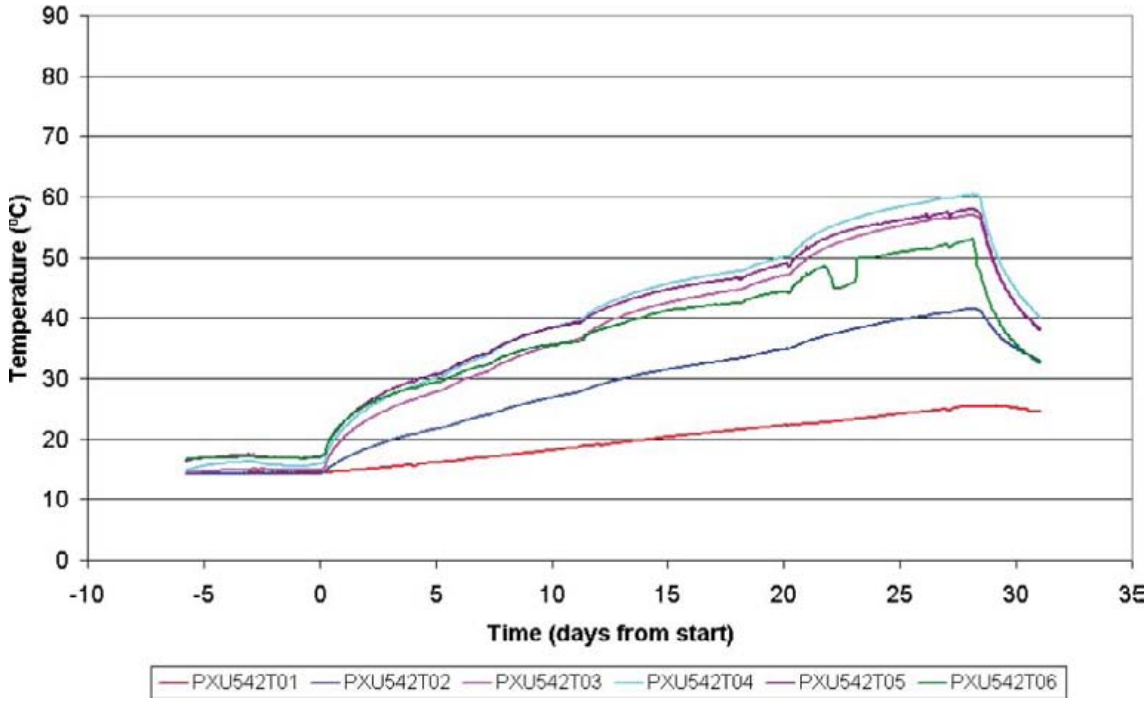

Figure K-5. *Test 1. Recorded temperature in borehole KQ0054G02.*

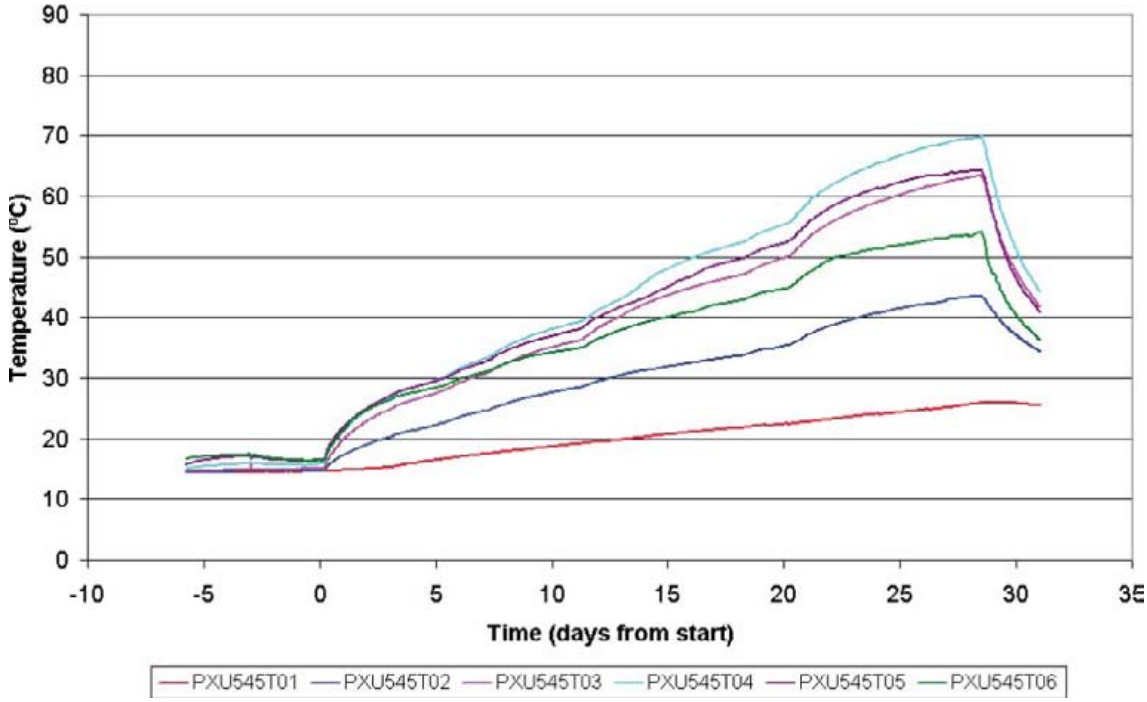

Figure K-6. *Test 1. Recorded temperature in borehole KQ0054G05.*

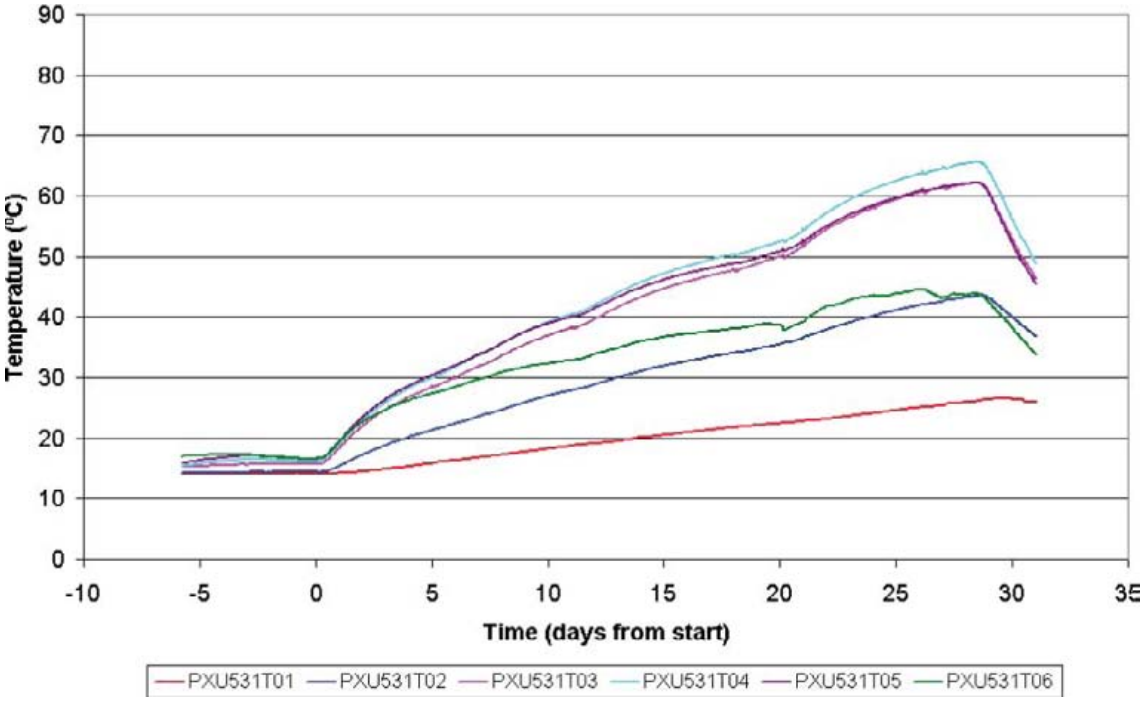

Figure K-7. *Test 1. Recorded temperature in borehole KQ0053G01.*

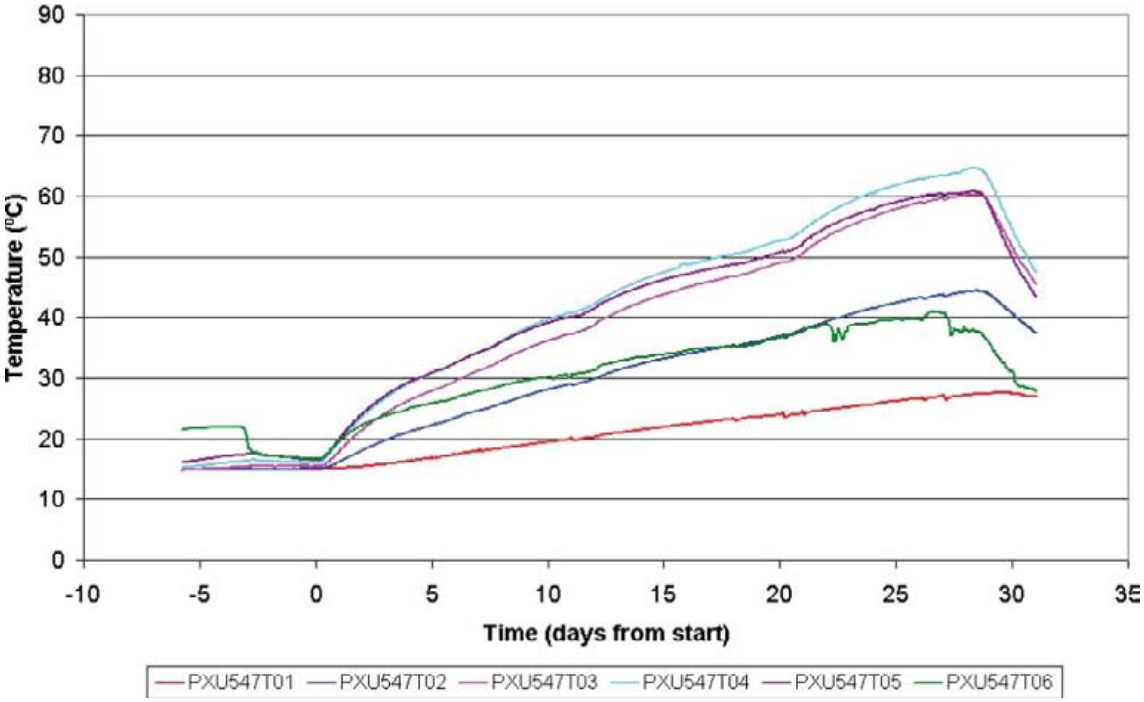

Figure K-8. *Test 1. Recorded temperature in borehole KQ0054G07.*

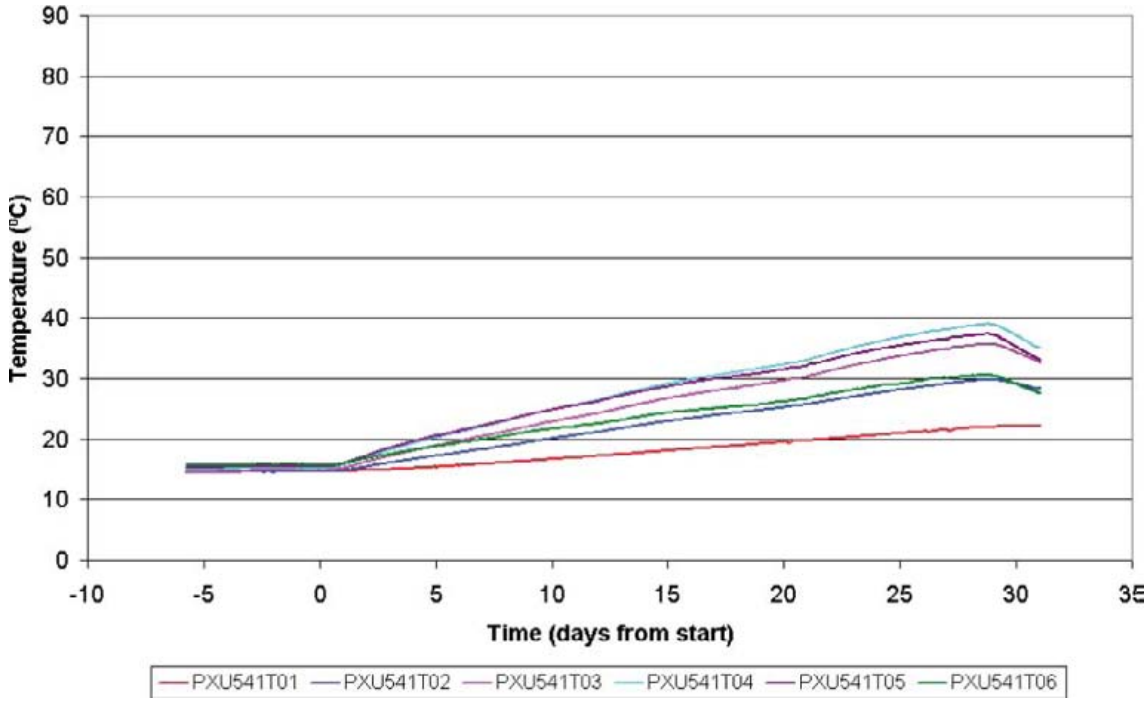

Figure K-9. *Test 1. Recorded temperature in borehole KQ0054G01.*

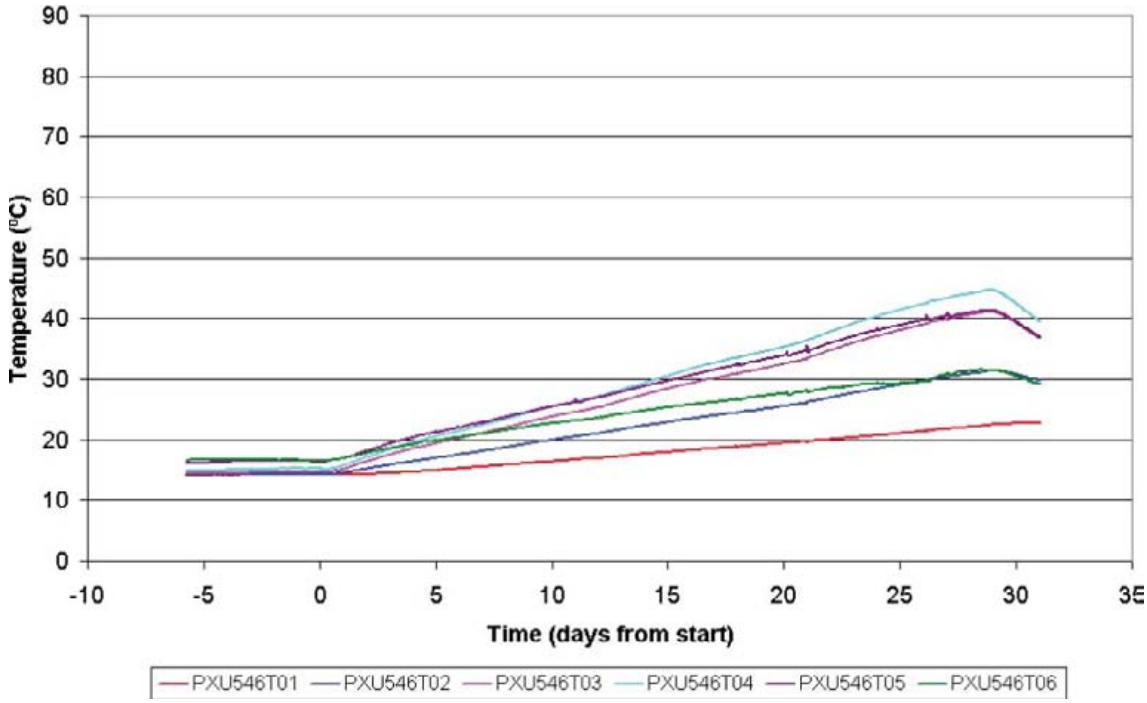

Figure K-10. *Test 1. Recorded temperature in borehole KQ0054G06.*

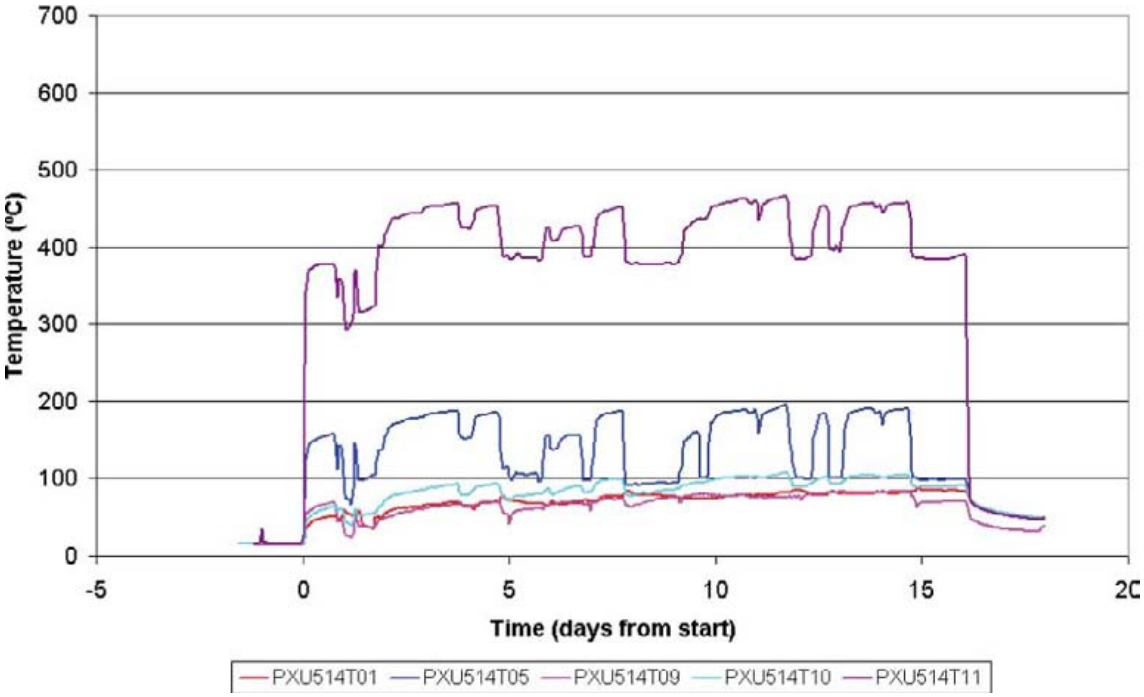

Figure K-11. *Test 2. Recorded temperature on the heater tube in heating hole KQ0051G04.*

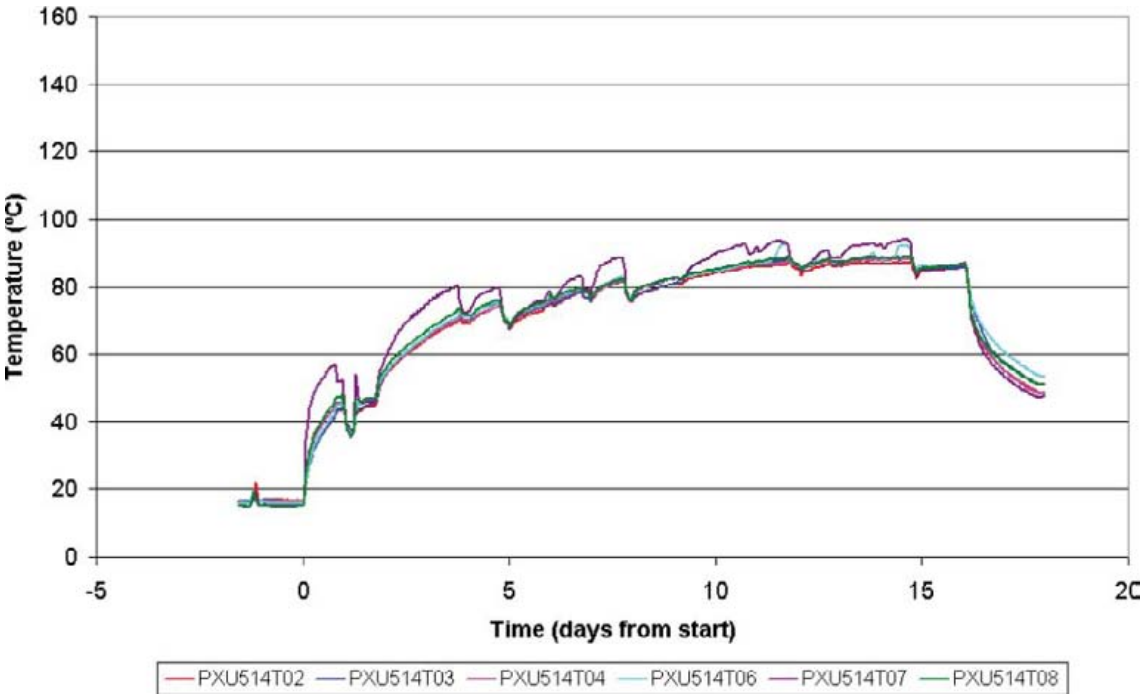

Figure K-12. *Test 2. Recorded temperature in heating hole KQ0051G04.*

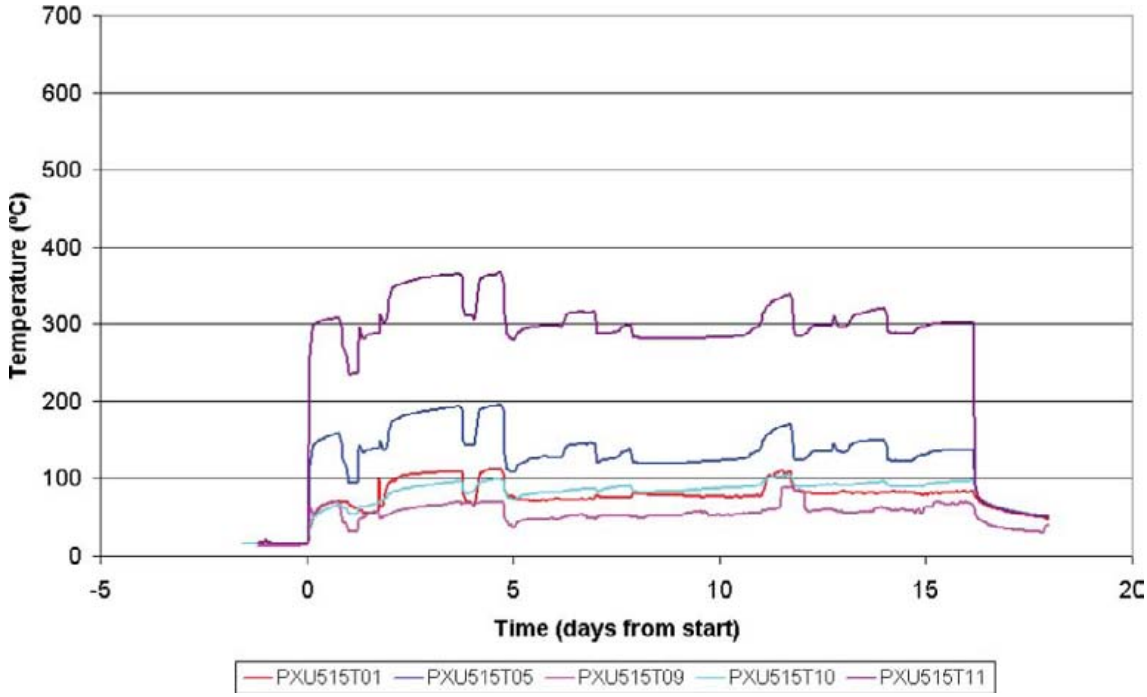

Figure K-13. *Test 2. Recorded temperature on the heater tube in heating hole KQ0051G05.*

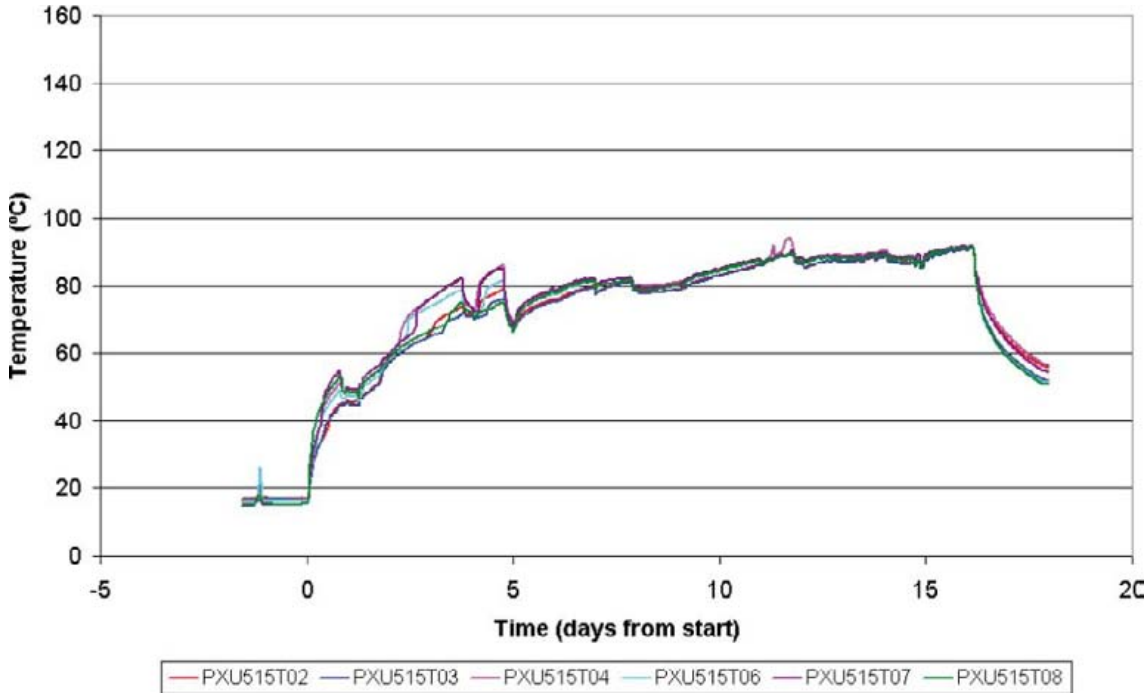

Figure K-14. *Test 2. Recorded temperature in heating hole KQ0051G05.*

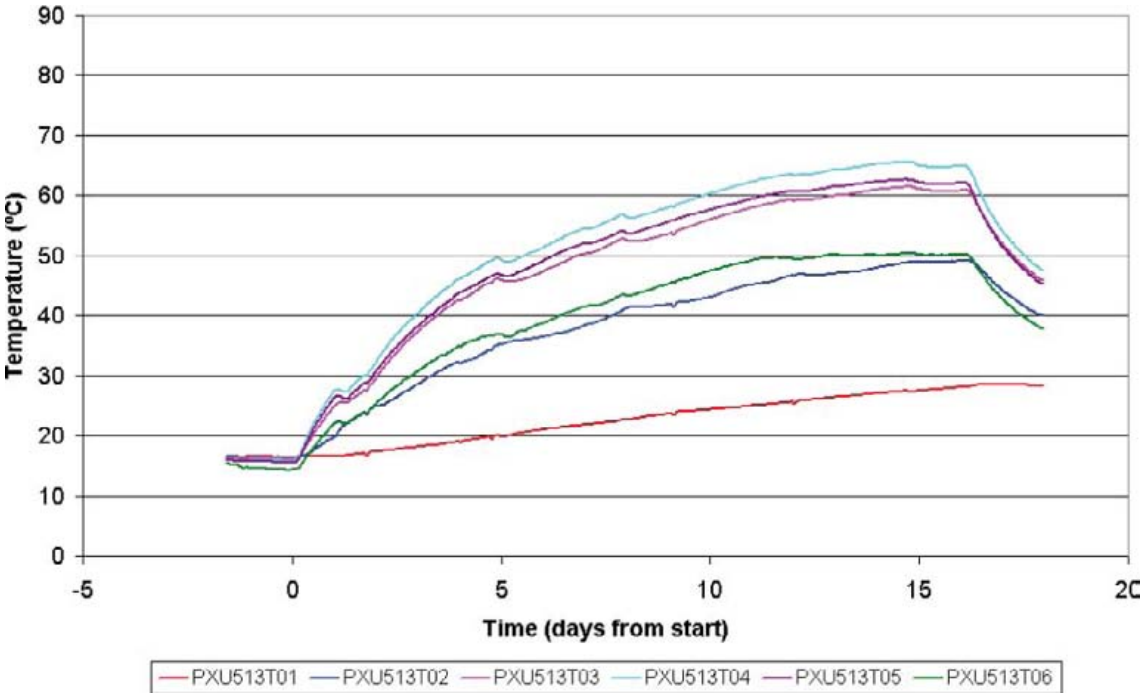

Figure K-15. *Test 2. Recorded temperature in borehole KQ0051G03.*

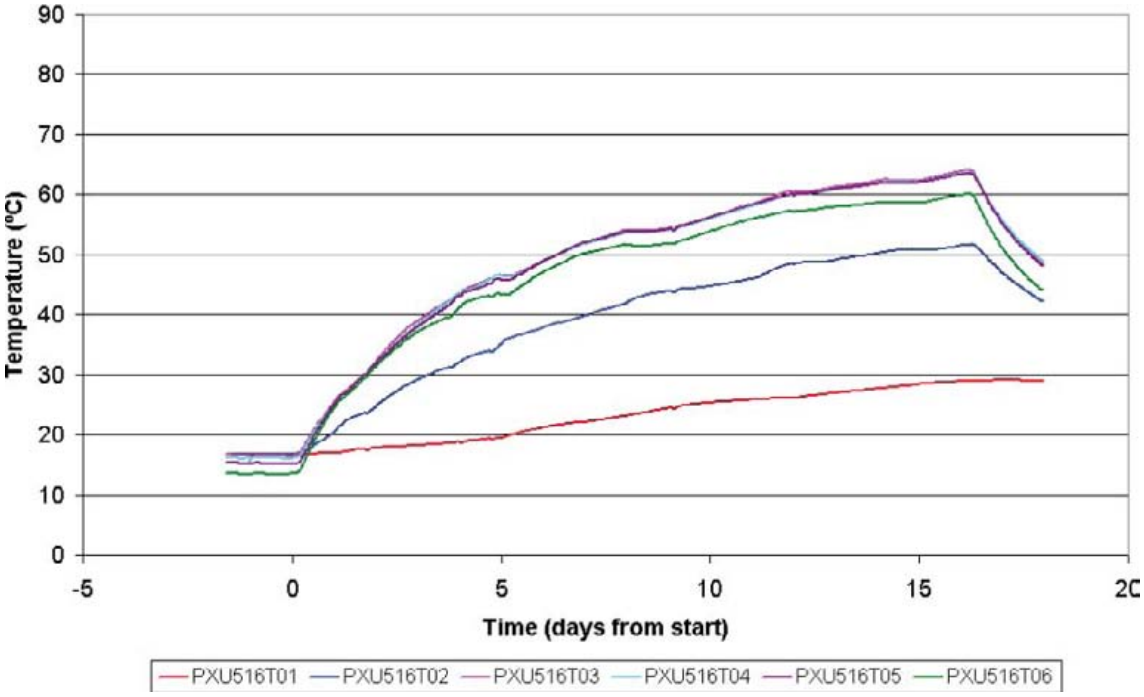

Figure K-16. *Test 2. Recorded temperature in borehole KQ0051G06.*

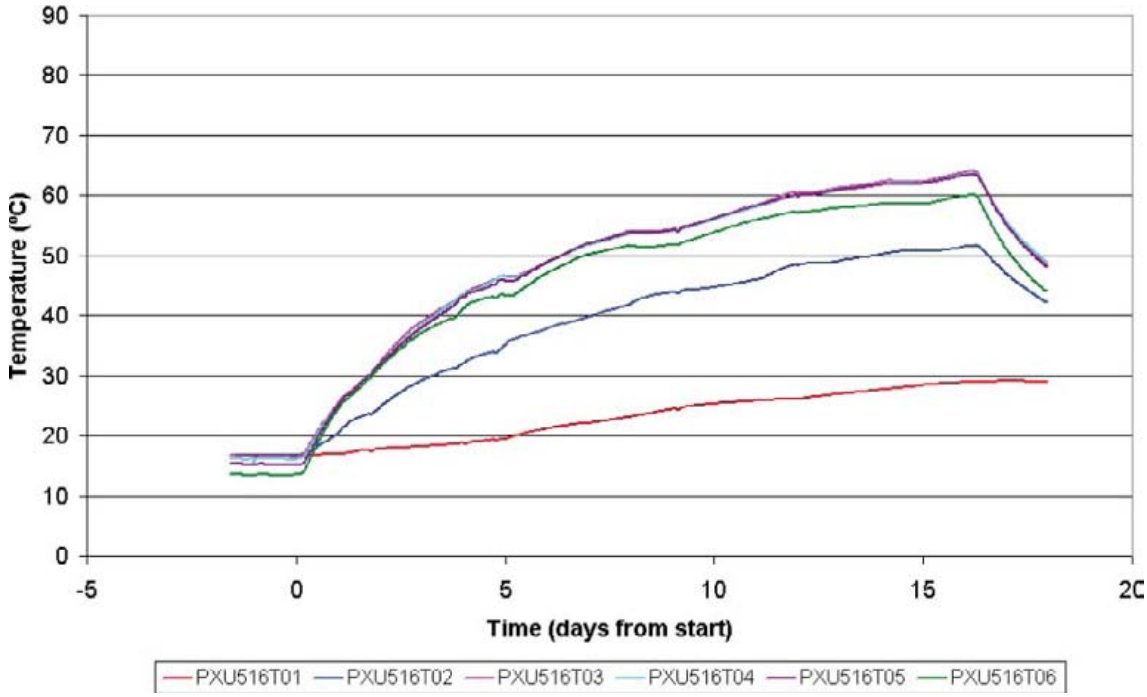

Figure K-17. *Test 2. Recorded temperature in borehole KQ0051G01.*

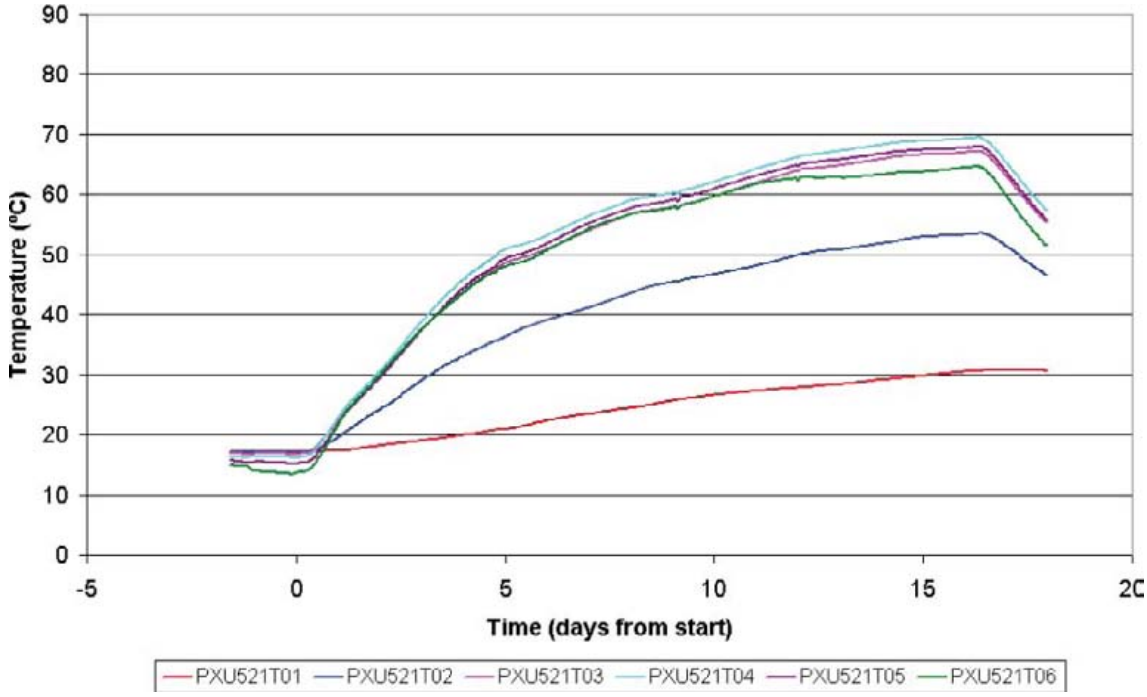

Figure K-18. *Test 2. Recorded temperature in borehole KQ0052G01.*

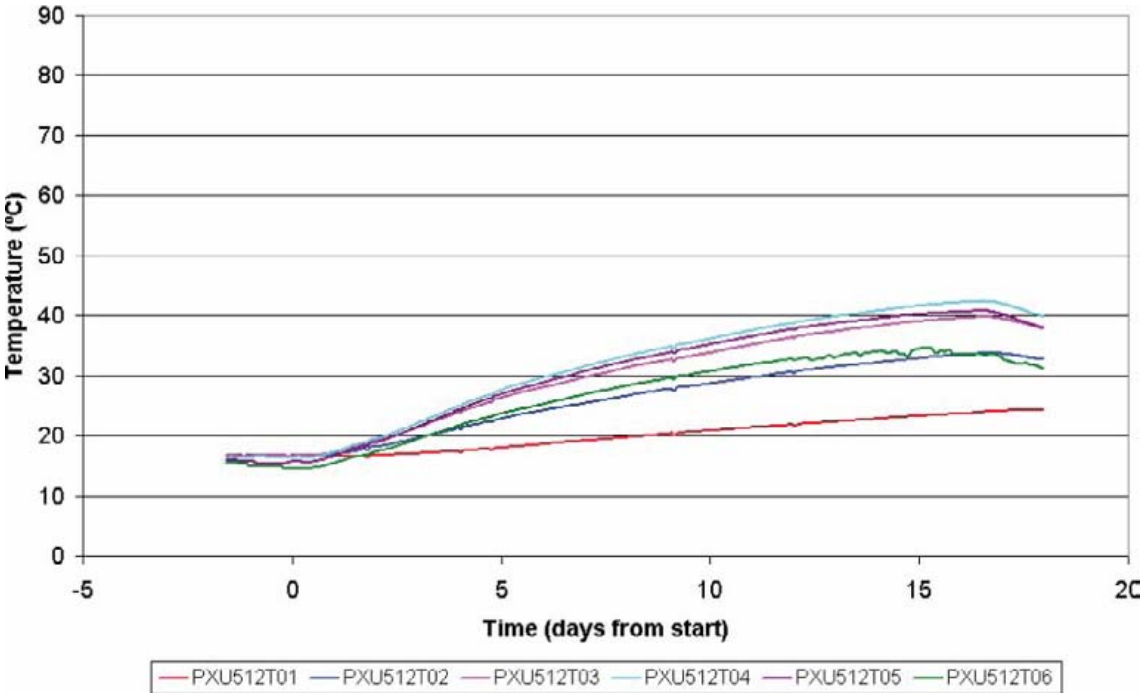

Figure K-19. *Test 2. Recorded temperature in borehole KQ0051G02.*

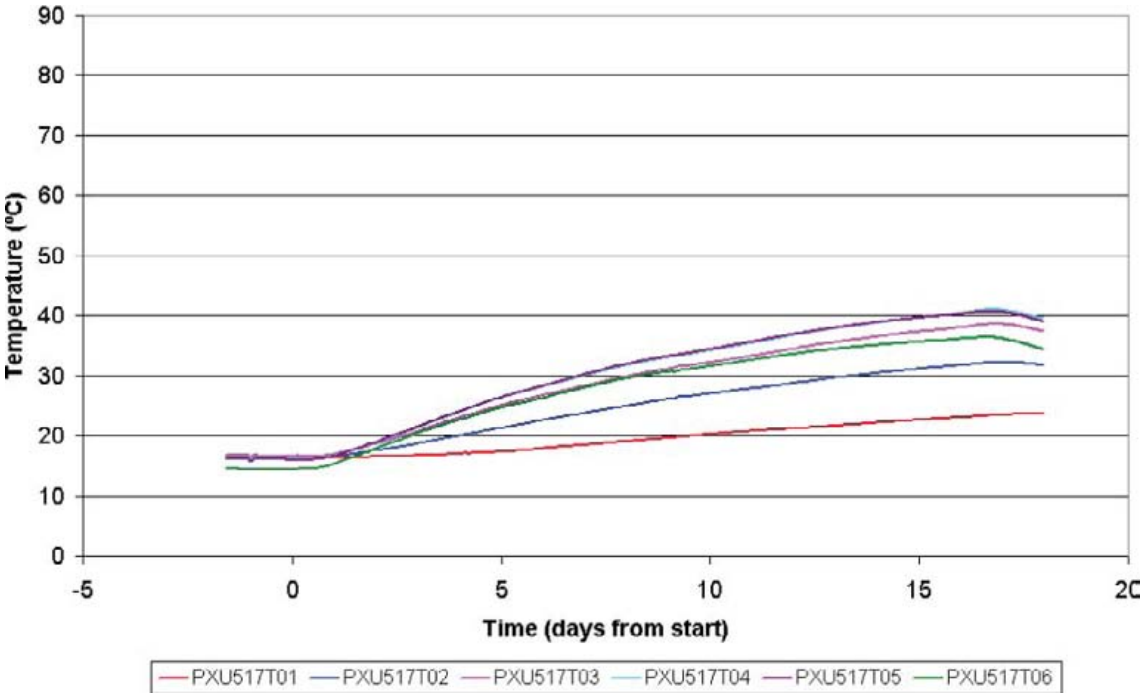

Figure K-20. *Test 2. Recorded temperature in borehole KQ0051G07.*

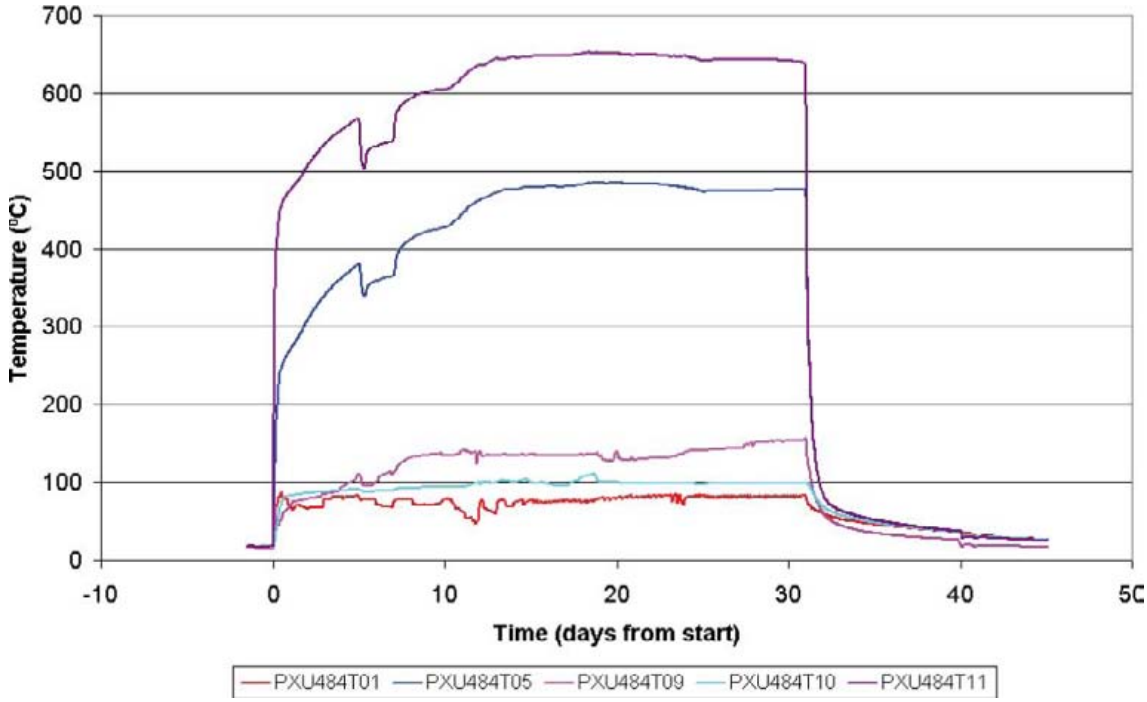

Figure K-21. *Test 3. Recorded temperature on the heater tube in heating hole KQ0048G04.*

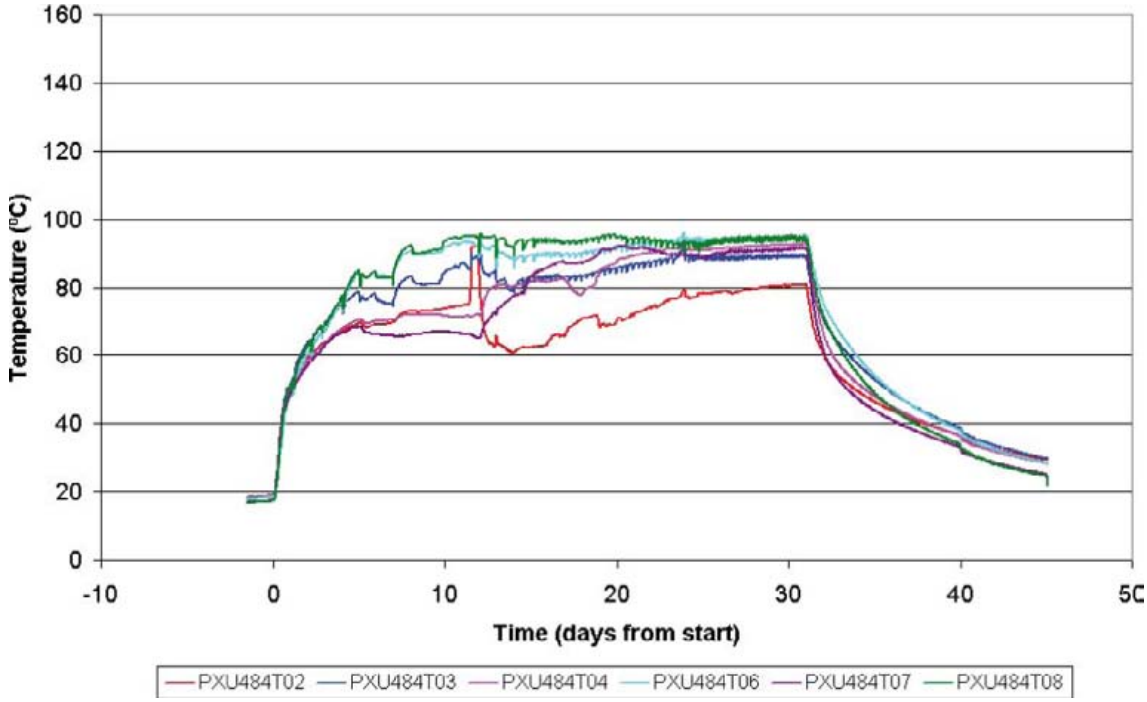

Figure K-22. *Test 3. Recorded temperature in heating hole KQ0048G04.*

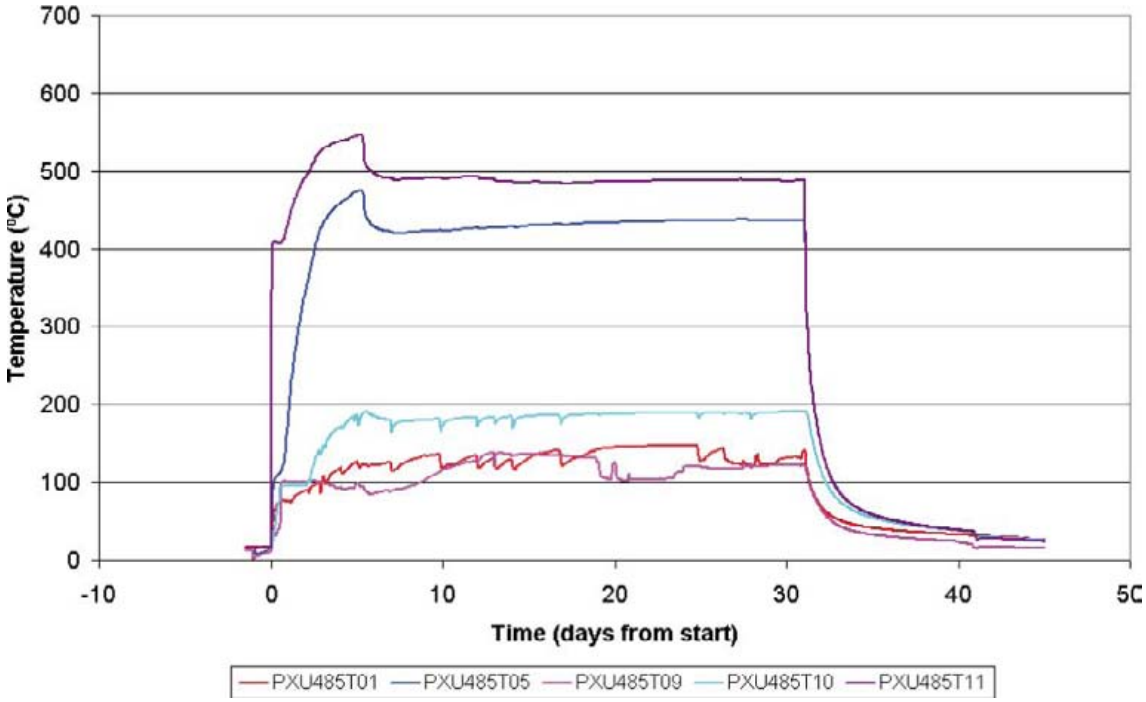

Figure K-23. *Test 3. Recorded temperature on the heater tube in heating hole KQ0048G05.*

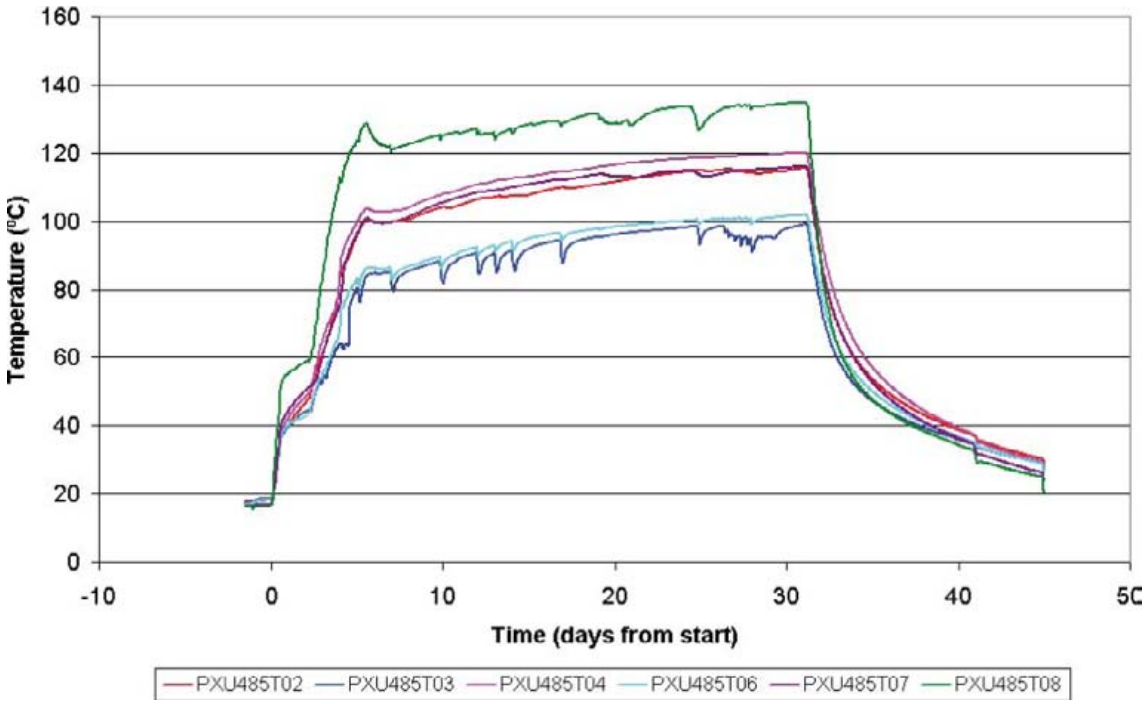

Figure K-24. *Test 3. Recorded temperature in heating hole KQ0048G05.*

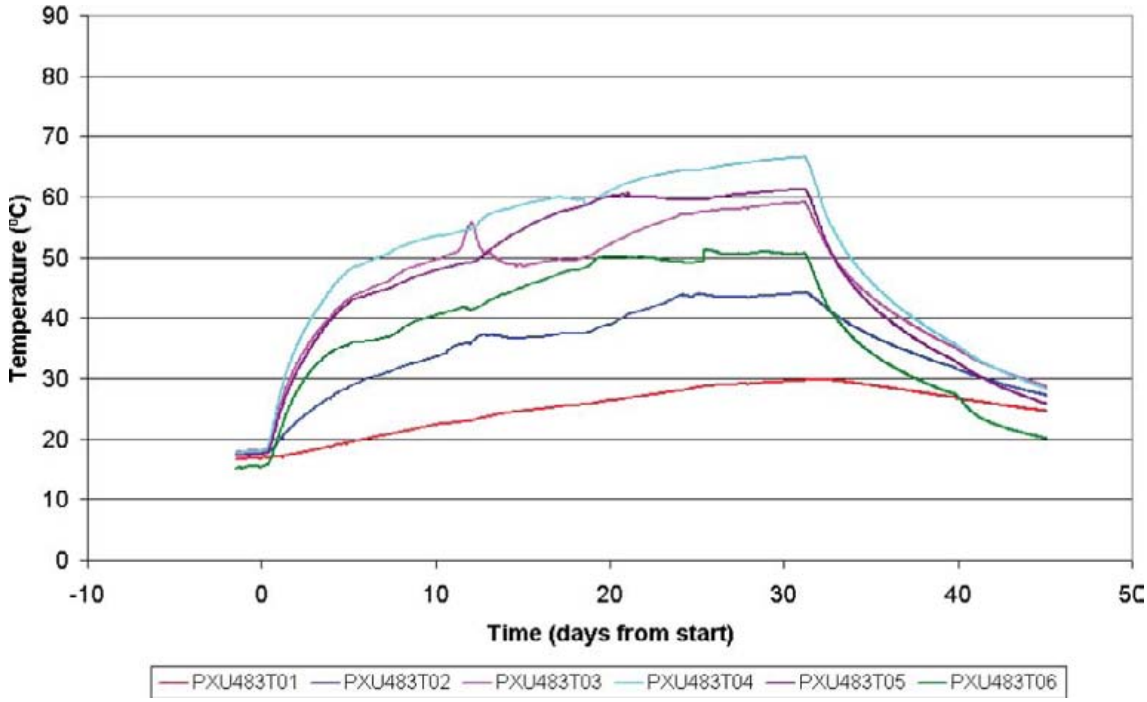

Figure K-25. *Test 3. Recorded temperature in borehole KQ0048G03.*

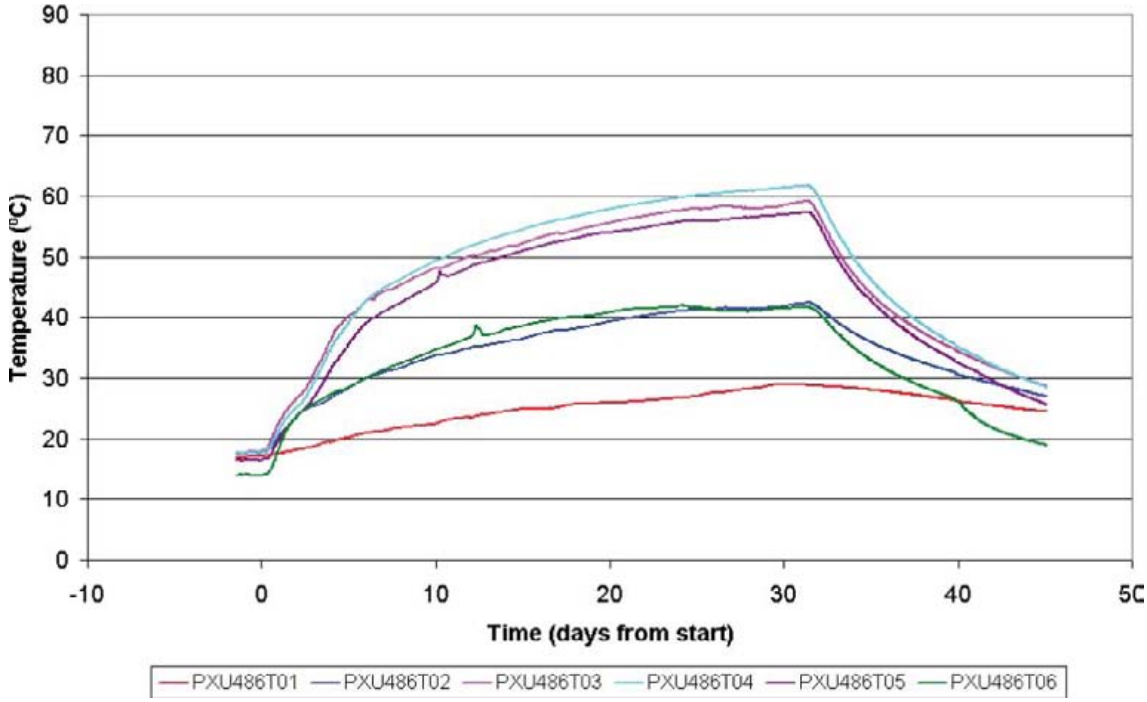

Figure K-26. *Test 3. Recorded temperature in borehole KQ0048G06.*

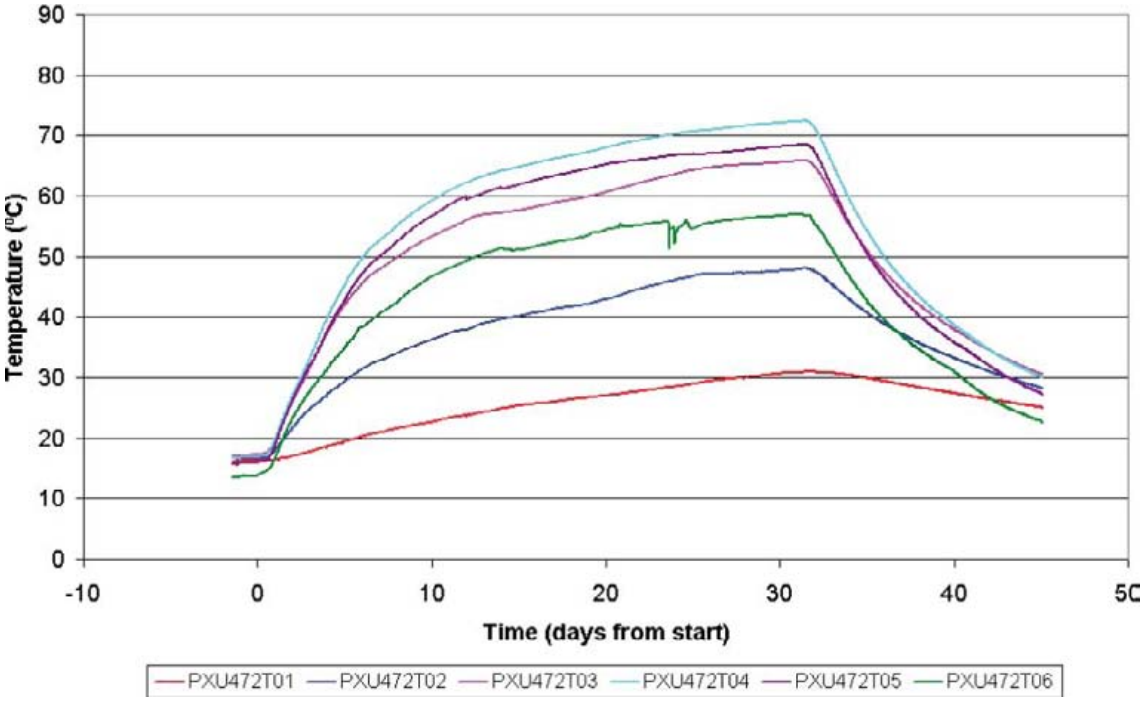

Figure K-27. *Test 3. Recorded temperature in borehole KQ0047G02.*

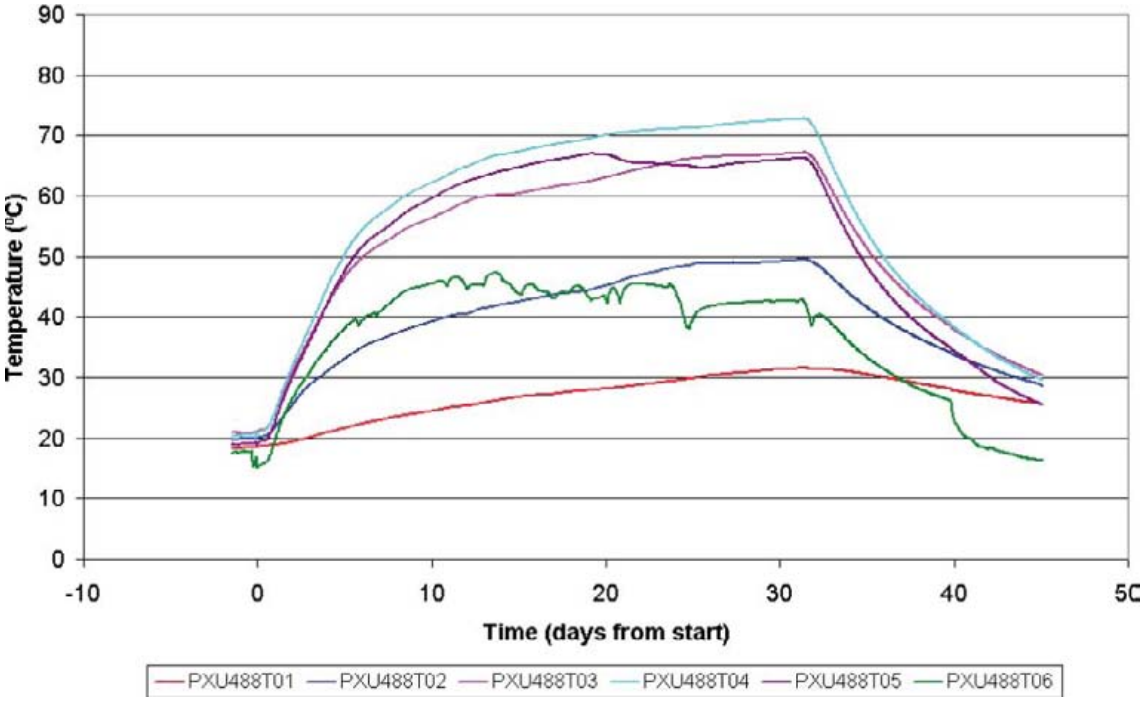

Figure K-28. *Test 3. Recorded temperature in borehole KQ0048G08.*

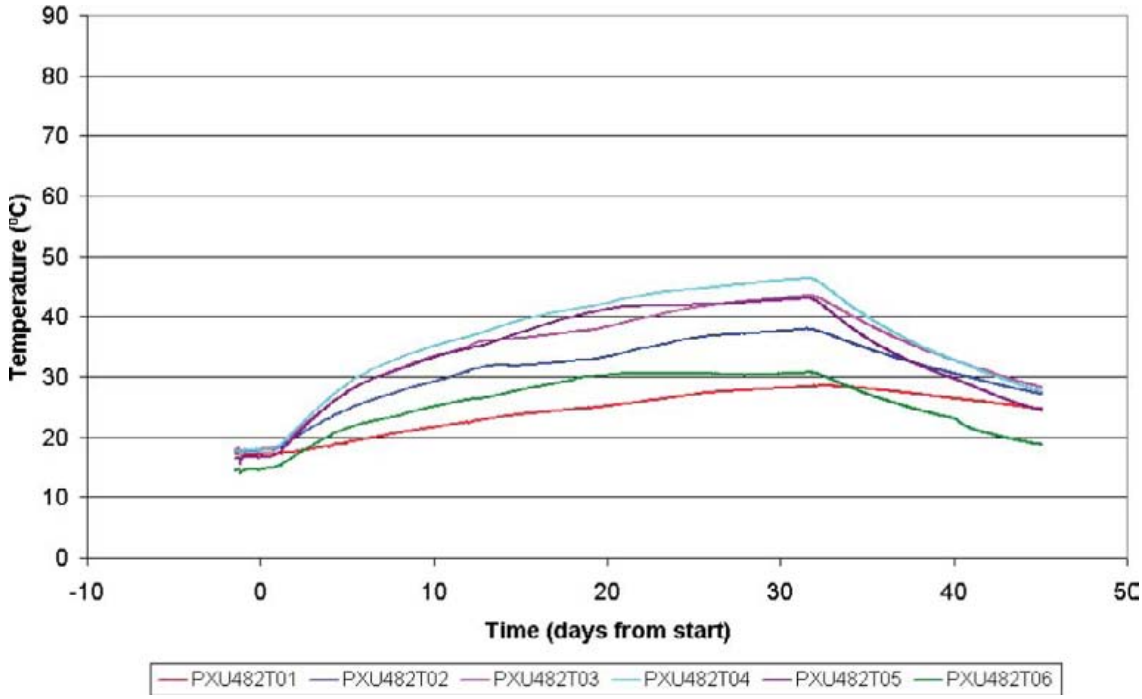

Figure K-29. *Test 3. Recorded temperature in borehole KQ0048G02.*

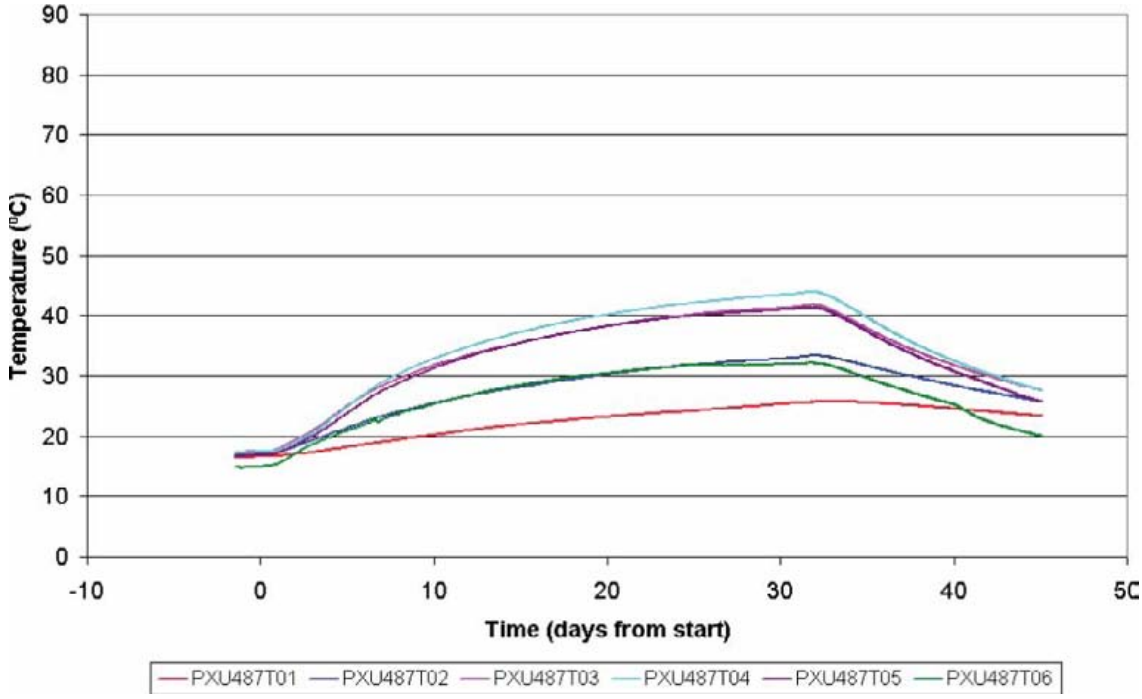

Figure K-30. *Test 3. Recorded temperature in borehole KQ0048G07.*

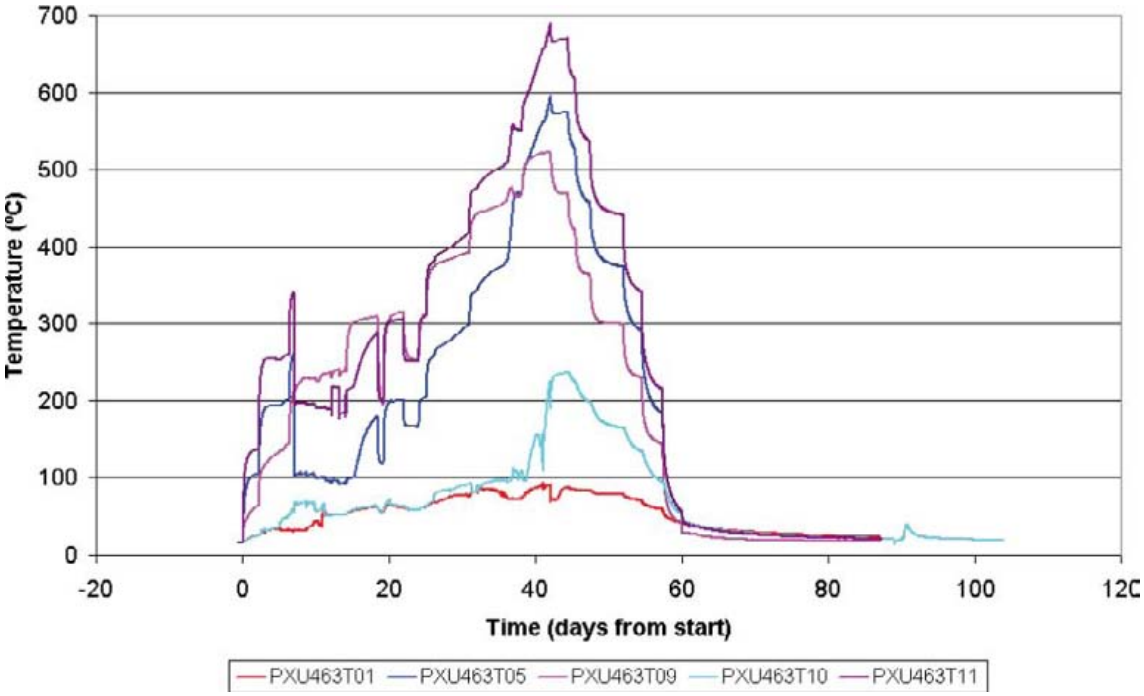

Figure K-31. *Test 4. Recorded temperature on the heater tube in heating hole KQ0046G03.*

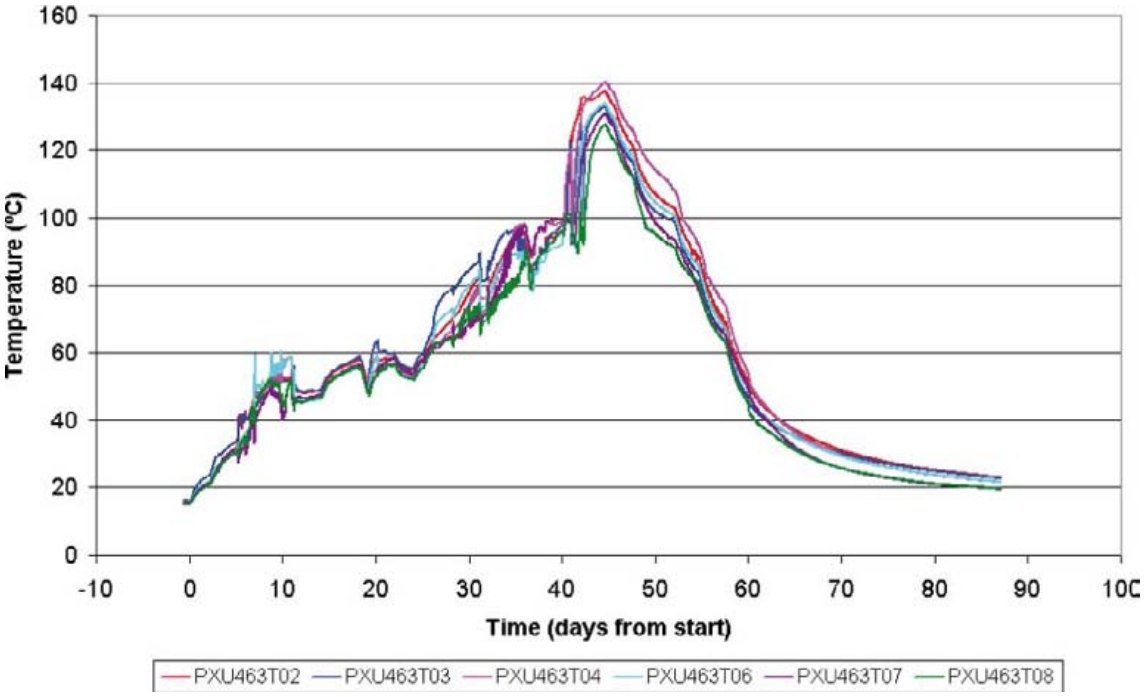

Figure K-32. *Test 4. Recorded temperature in heating hole KQ0046G03.*

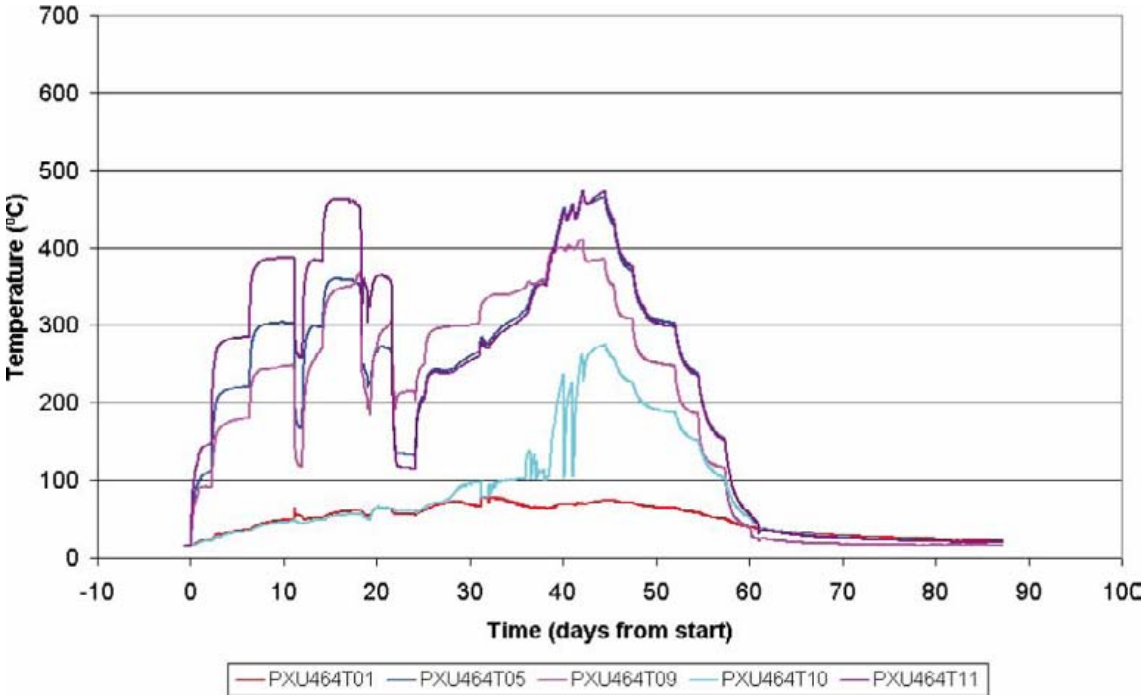

Figure K-33. *Test 4. Recorded temperature on the heater tube in heating hole KQ0046G04.*

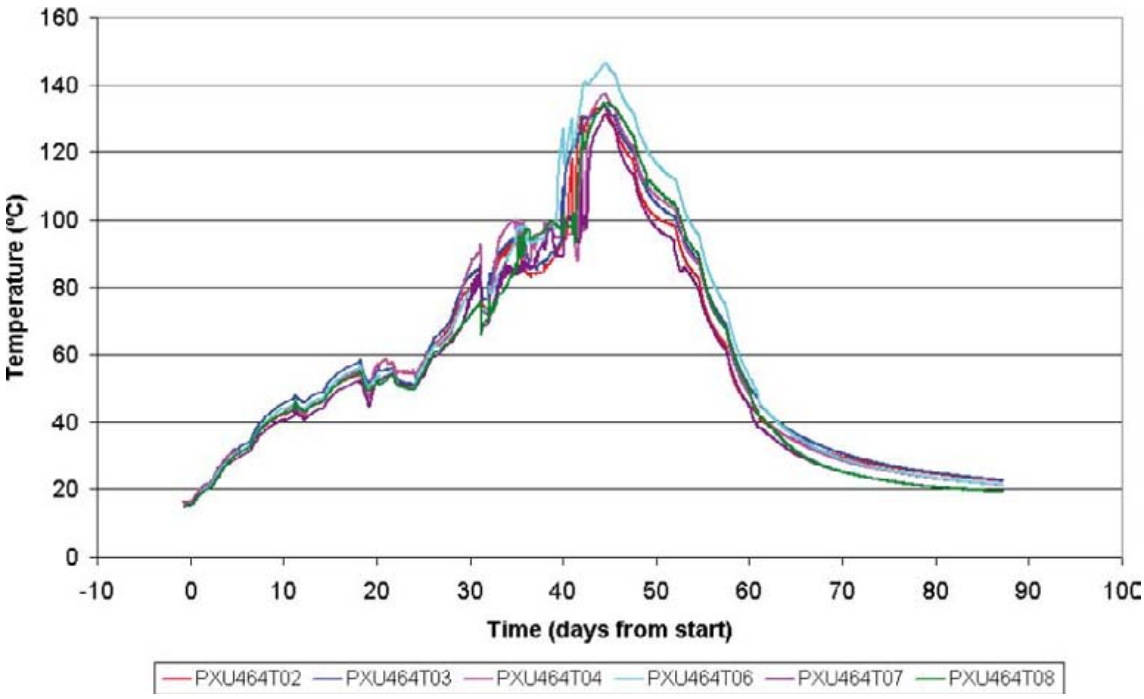

Figure K-34. *Test 4. Recorded temperature in heating hole KQ0046G04.*

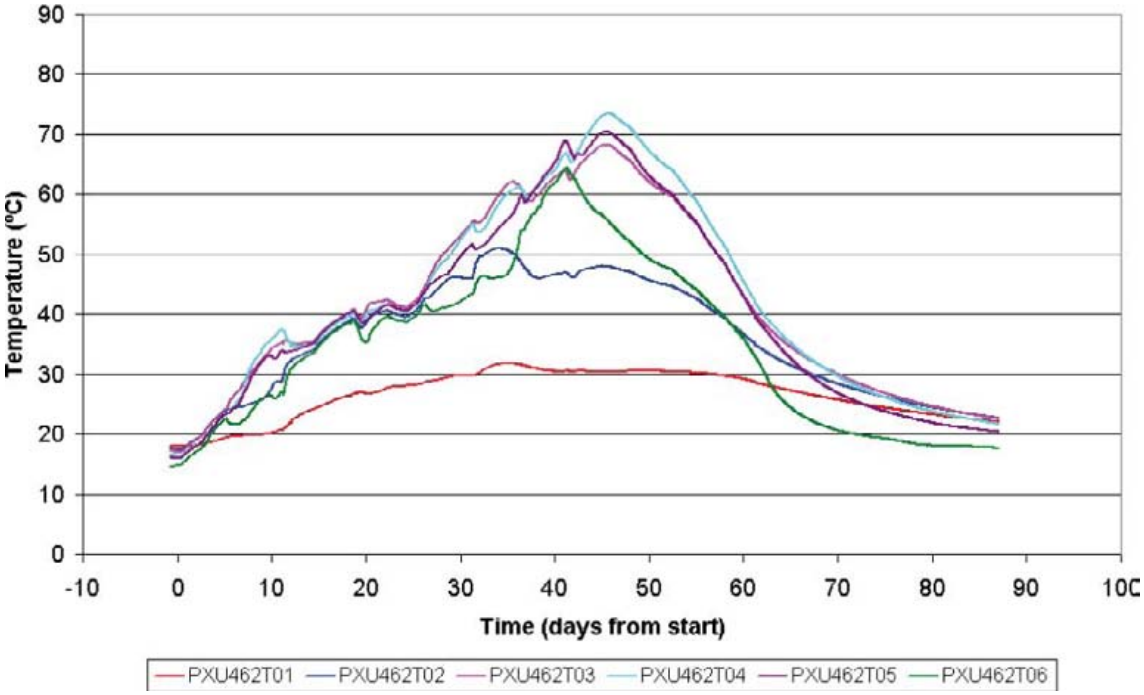

Figure K-35. *Test 4. Recorded temperature in borehole KQ0046G02.*

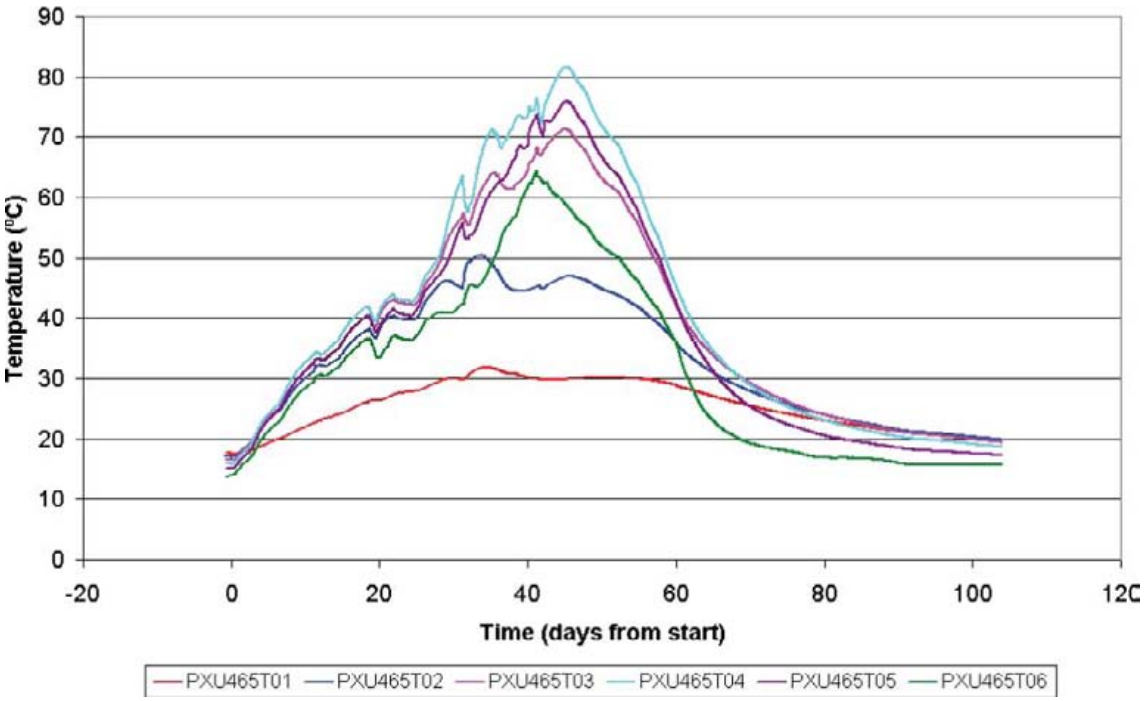

Figure K-36. *Test 4. Recorded temperature in borehole KQ0046G05.*

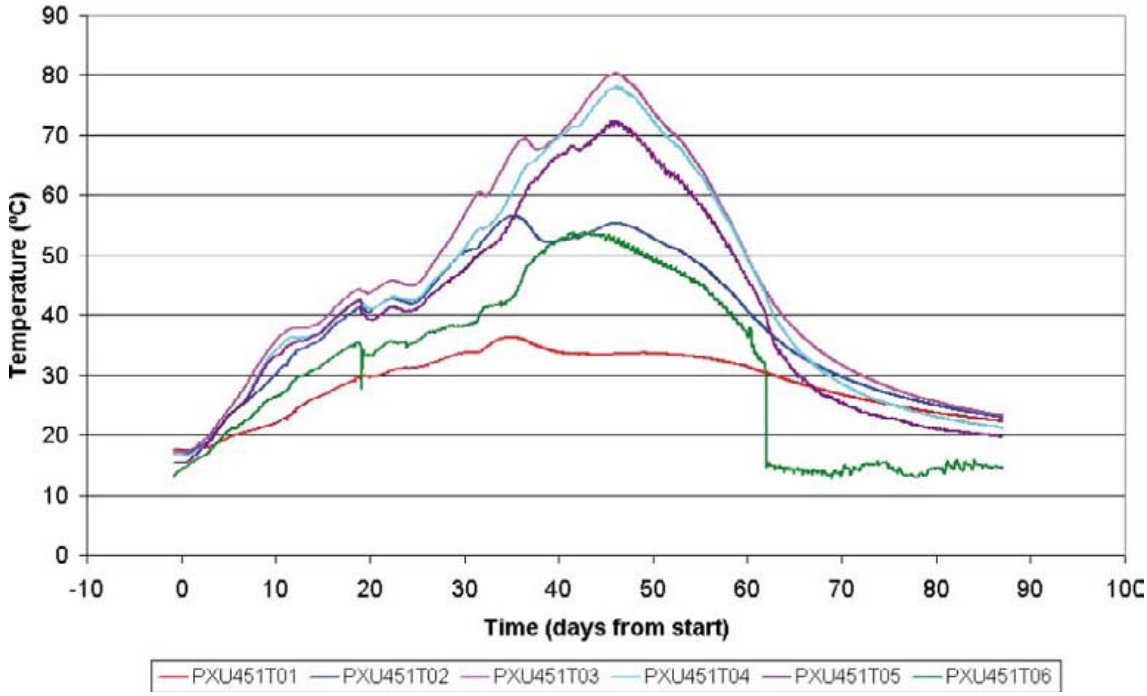

Figure K-37. *Test 4. Recorded temperature in borehole KQ0045G01.*

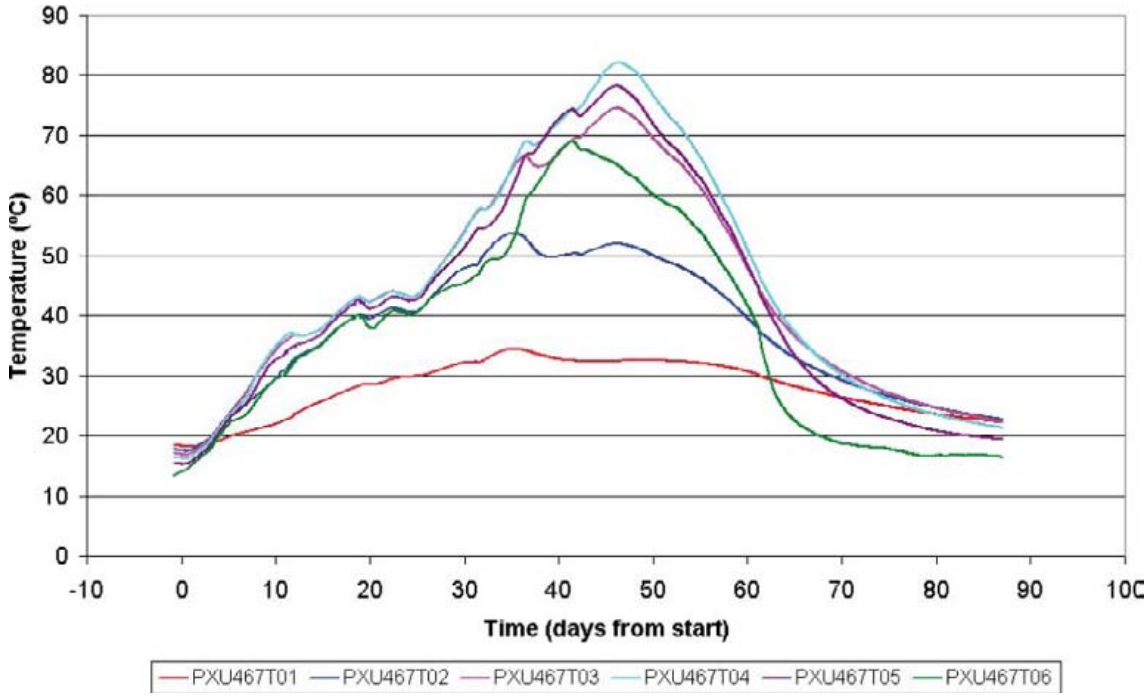

Figure K-38. *Test 4. Recorded temperature in borehole KQ0046G07.*

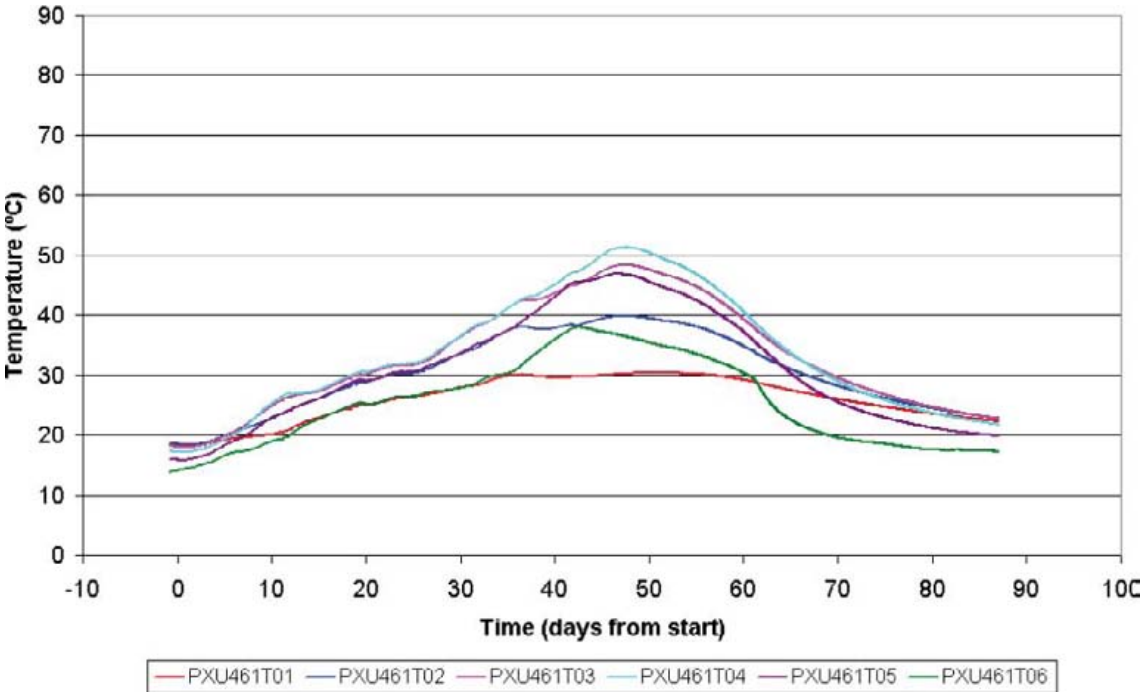

Figure K-39. *Test 4. Recorded temperature in borehole KQ0046G01.*

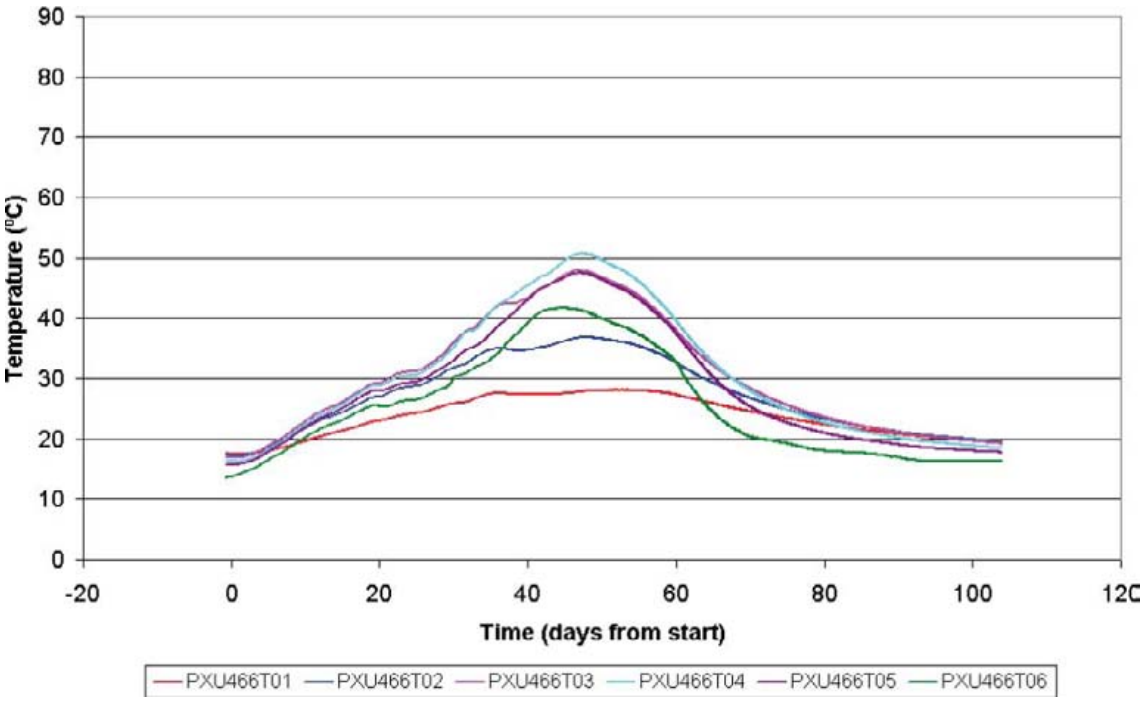

Figure K-40. *Test 4. Recorded temperature in borehole KQ0046G06.*

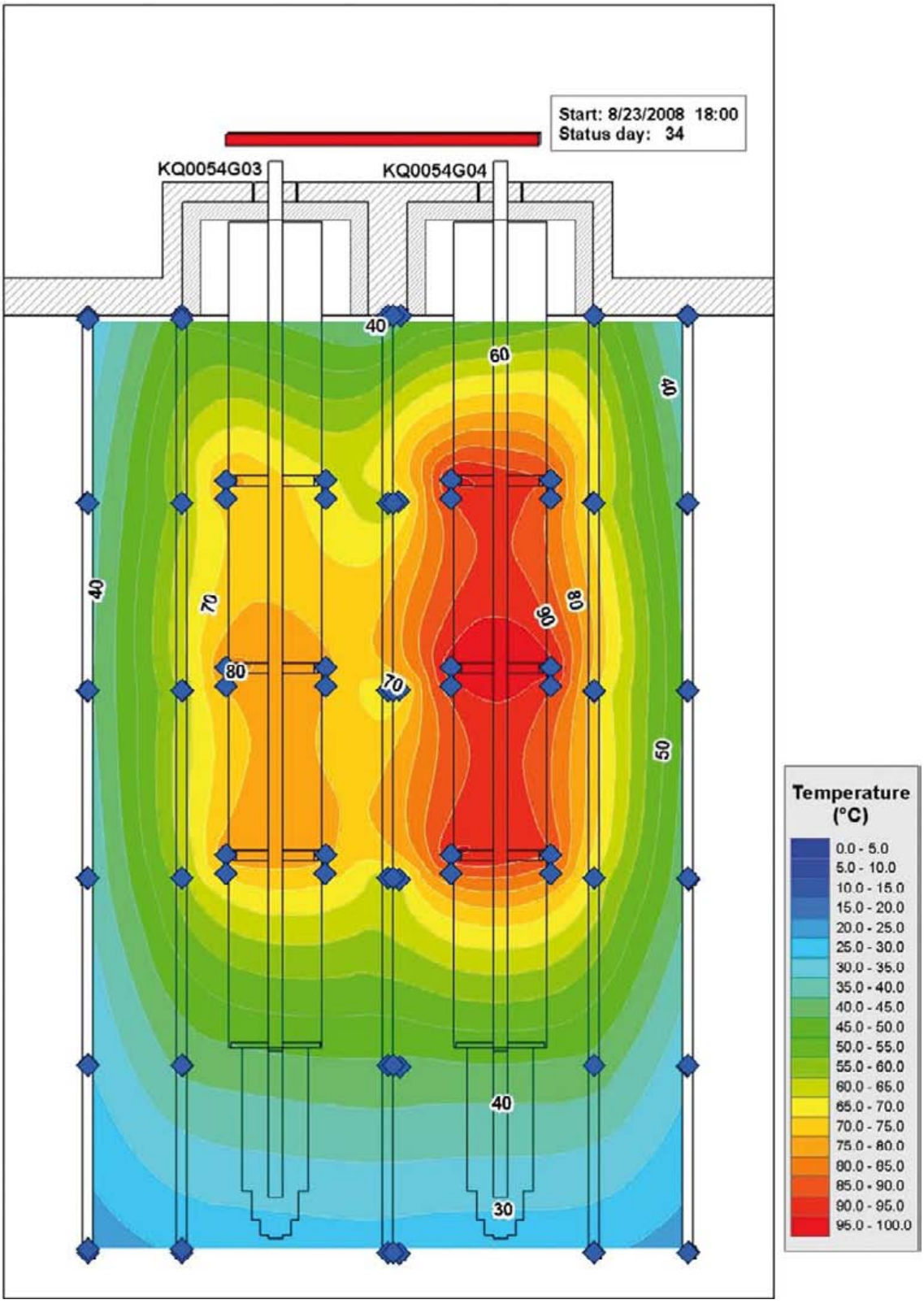

Figure K-41. *Recorded temperatures in Test 1 when the cooling phase is initiated. The squares in blue indicate the position of the temperature gauges.*

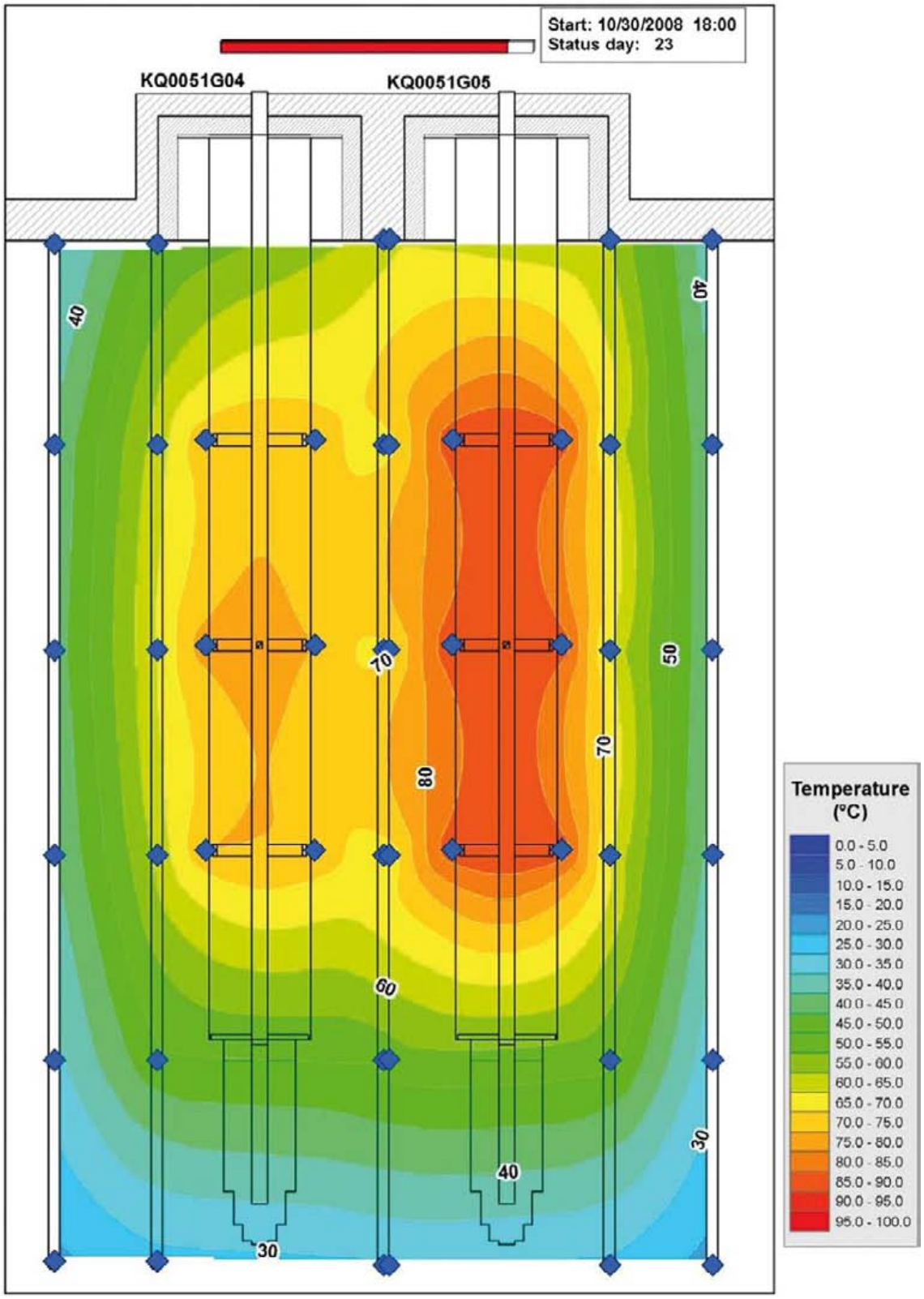

Figure K-42. *Recorded temperatures in Test 2 when the cooling phase is initiated. The squares in blue indicate the position of the temperature gauges.*

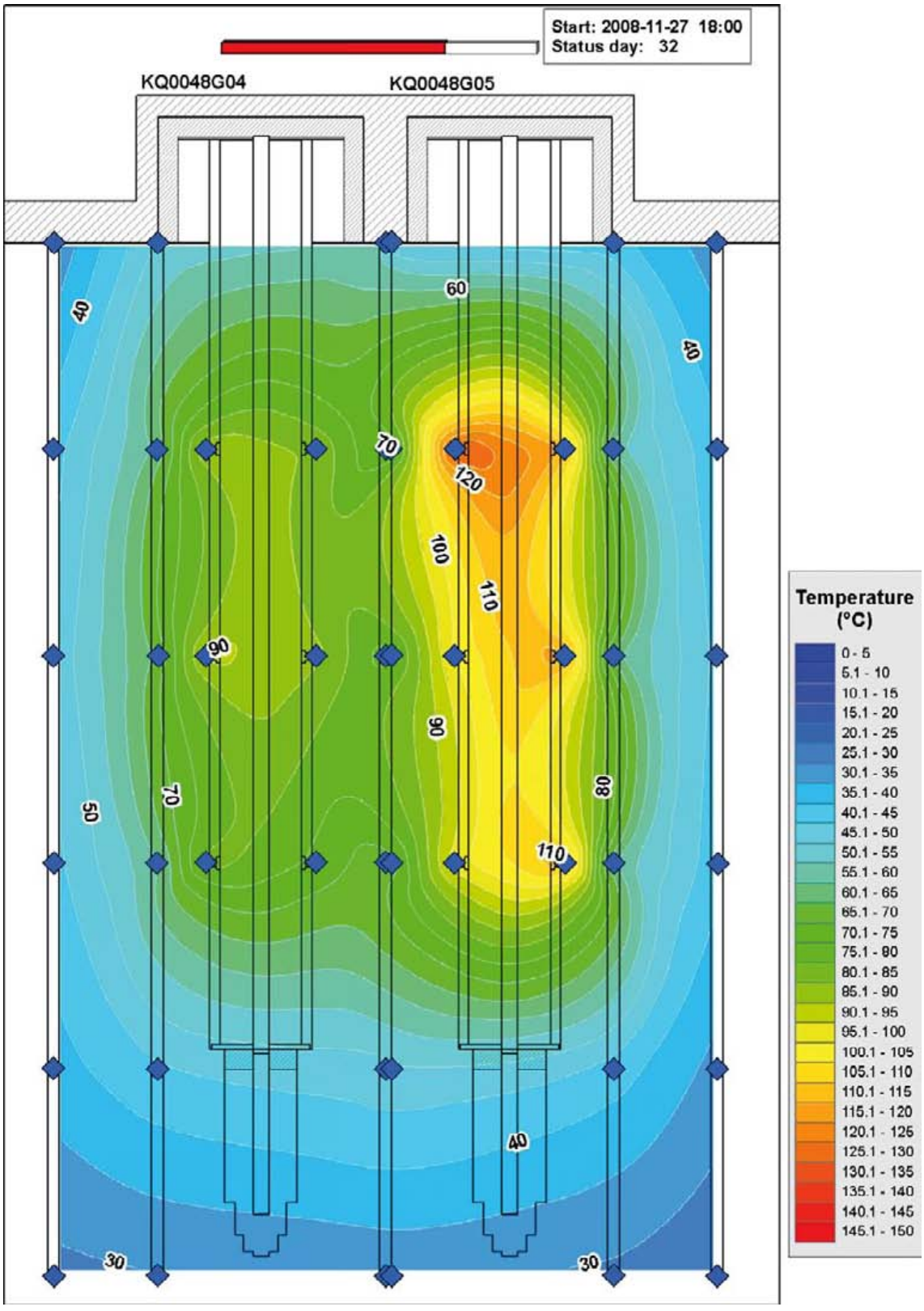

Figure K-43. *Recorded temperatures in Test 3 when the cooling phase is initiated. The squares in blue indicate the position of the temperature gauges.*

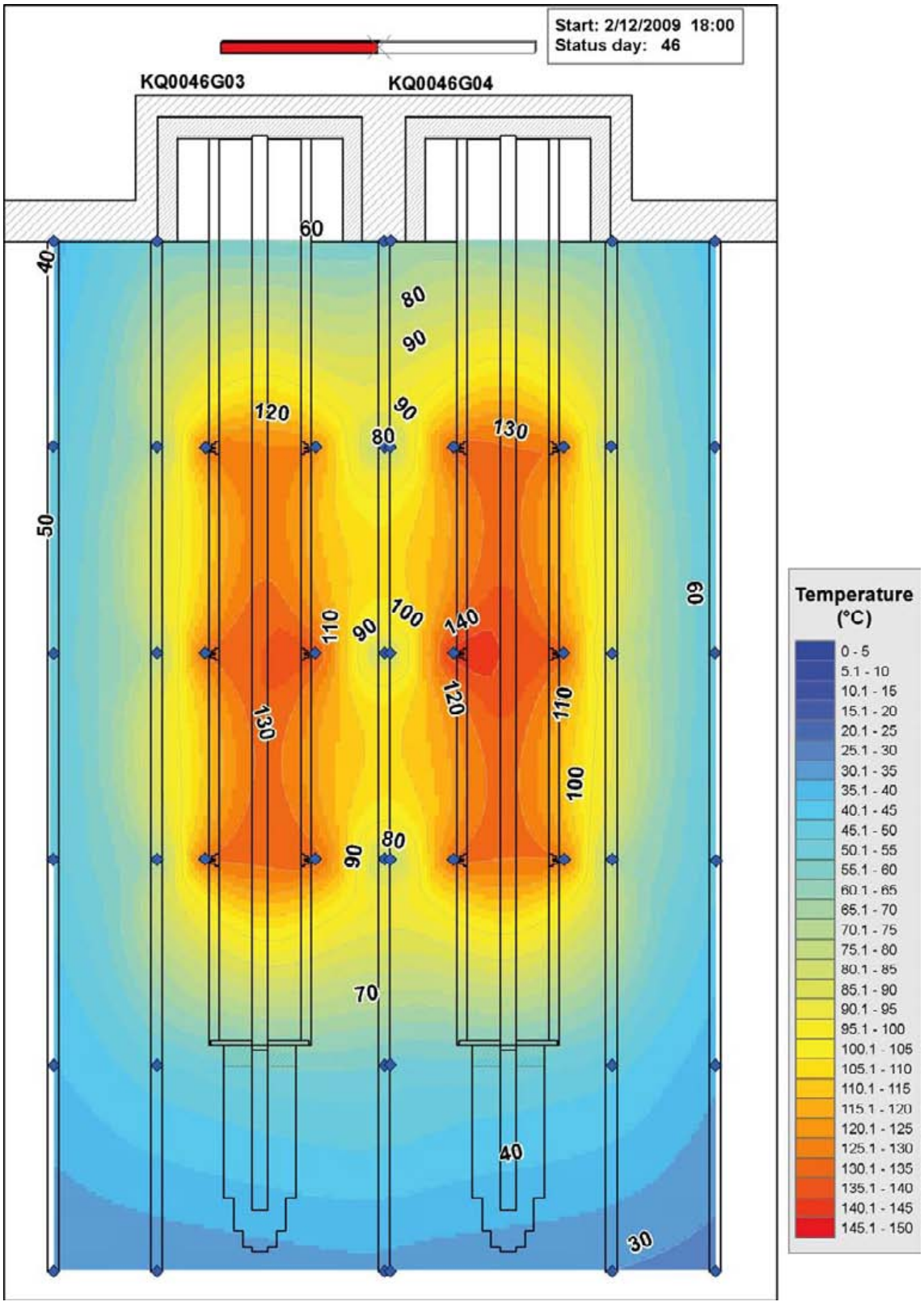

Figure K-44. *Recorded temperatures in Test 4 when the cooling phase is initiated. The squares in blue indicate the position of the temperature gauges.*

Appendix L

Investigation of rock fragments

Lars Bergkvist, Golder Associates AB
March 2010

Contents

L1 Introduction

The rock fragments collected in the heating holes of the CAPS field experiment were at first used merely to estimate the total volume of the spalled notches in the heating holes. Later on the fragments were also examined in a more extensive way regarding weight, dimensions and failure surfaces. The purpose of this latter study was to investigate possible differences in the geometry and size distribution of the fragments related to variations in counter pressure, moisture content and other geological conditions of the field experiment. The present PM describes the methods and results of this investigation. No fragments from the heating holes in Test 4 were included in the investigation since hole KQ0046G03 was grouted, and the number of collected fragments above the stipulated size was too few in KQ0046G04.

L2 Investigation procedure

L2.1 Scaling of borehole walls and collection of fragments

The rock slabs formed during the spalling process were removed from the heating holes by scaling. Using a scaling rod the borehole wall was cleaned from loose pieces until sound rock was exposed from the top to the bottom of the hole. Most fragments were hoisted up on a wooden plate during the scaling. Fragments that had dropped down to the borehole bottom were removed by a suction tube.

Spalling related to the drilling of the boreholes was only observed in three of the heating holes. In two of these holes, KQ0054G03 and KQ0054G04, the observed spalling was minor and consisted of only a couple of tiny rock slabs, whereas the size and number of spalled rock slabs in KQ0048G04 were more substantial and comprised an estimated volume of 1.0 litre. The rock fragments that had dropped down to the bottom during drilling of the hole were not removed until after the heating phase.

L2.2 Measurement of fragment dimensions

The investigation comprised measurement of the fragment geometry and examination of the failure surfaces and sealed fractures intersecting the fragments. The aim was to investigate all fragments with a length of 50 mm or more. The measurements comprised length, width, thickness and weight, along with an estimation of the volume. The length, width and thickness were measured in the centre of the fragments as illustrated in Figure L-1. A balance with an accuracy of 1 gram was used for the determination of the weight and a sliding calliper for determination of length, width and thickness. The measured dimensions of length and width were recorded to the nearest 1 mm and the thickness to 0.1 mm.

The volume was calculated from the weight based on a mean density of the rock of 2.75 g/cm^3 /Staub et al. 2004/. The shape of the fragments was very variable and therefore the percentage of a theoretical maximum volume according to the measured dimension was calculated for each fragment. This was done by taking the length, width and thickness and calculating the volume of a hypothetical parallelepiped (see Figure L-1). This volume was then compared to the calculated volume based on the measured weight. Finally, the calculated volume was divided by the hypothetical one to give a percentage value of how much of the fragments real volume would fit inside the hypothetical parallelepiped. A high value indicates that the fragment has a more rectangular shape with distinct sharp angles, i.e. it fits well inside the hypothetical parallelepiped. This value is termed percentage of the theoretical parallelepiped.

All fragments were documented by photographs. An example of the photographs is shown in Figure L-2. The other photographs are to be found in Appendix AL1 of the memo.

L2.3 Investigation of fragment geology

The procedure for the investigation of the fragment geology, which included the fragments failure surfaces and sealed fractures within the fragments, is described in this section.

All mineral coated fractures that were obvious in the fragments were noted and divided into the following two groups:

- sealed fractures that intersect a part or the whole fragment,
- coated fractures corresponding to the failure surfaces of the fragment.

The coated fractures were classified dependent on their position in relation to the A, B or C-side of the theoretical parallelepiped as seen in Figure L-3. For example, if a mineral coated fracture occurred on both C-sides it was recorded as C1 and C2. The same letters were used to describe both the failed and the sealed fractures.

In order to estimate how many of the fragments failure surfaces that had a natural mineral coating it was also recorded if the fragment had any surface that corresponded to the borehole wall.

Natural fractures without mineral coatings were not recorded since such fractures are difficult to distinguish from thermal induced fractures.

The petrology of the rock was almost the same for all fragments. When a fragment was dominated by any specific mineral or had any other uncommon feature it was noted. The mineral assembly on every coated fracture was also recorded. If the fractures included more than one mineral, all were recorded without consideration as to which of them that dominated.

The mineral coatings did not have to occur on the whole fragment surface to be noted, partial coatings of one fifth of the length were also recorded.

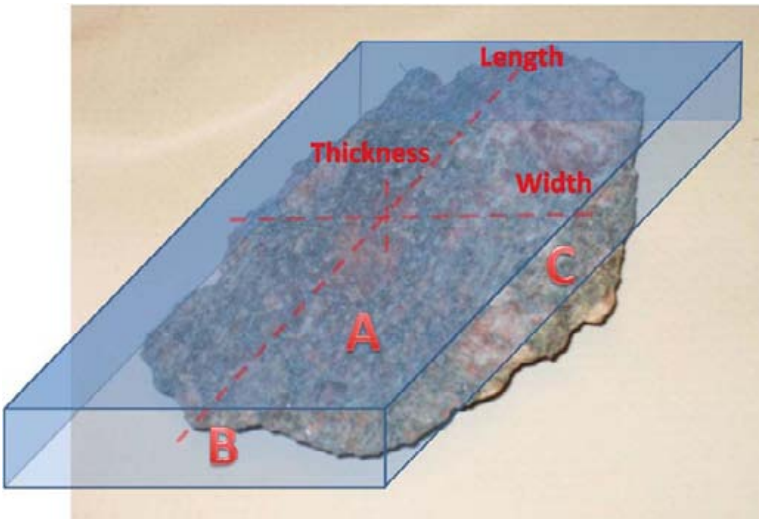

Figure L-1. *Schematic figure of a fragment inside a theoretical parallelepiped. The figure shows how the length, width and thickness were measured. A, B and C – are sides of the theoretical parallelepiped, relating to length, width and thickness.*

Figure L-2. *Photograph of fragments no. 38–89 from hole KQ0048G04. The scale bar is 10 cm.*

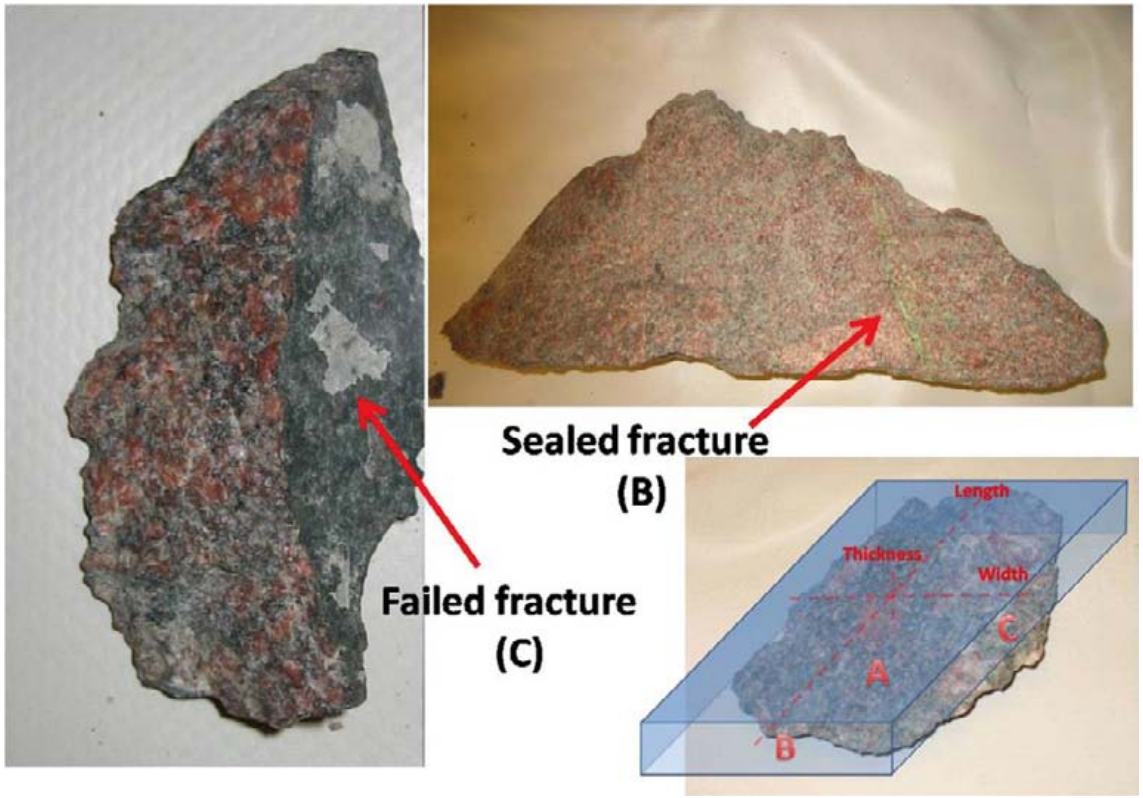

Figure L-3. *The theoretical parallelepiped from Figure L-1(lower right) shows how the fracture position on the fragment is described. An example of a failed fracture along the fragments C-side (left). A sealed fracture that if it had been broken would have been on the fragments B-side (top right).*

L3 Results of the investigation

L3.1 Weight and volume

After the heating experiments all rock fragments in the boreholes were collected. The total weight of all fragments was 83.1 kg. The total weight should however be reduced by 2.9 kg to exclude the fragments that dropped down before the heating in hole KQ0048G04. The total weight is therefore set to 80.2 kg. Table L-1 shows the total weight and estimated volume of all fragments per individual borehole and Table L-2 lists them grouped into the holes on each side of the tunnel. The rock fragments range in weight from less than 1 gram up to discs with a weight of 1.58 kg. The maximum recorded length was 300 mm.

The aim was to investigate all fragments with a length of 50 mm or more. An exception was made in the case of KQ0051G04 where the amount was too large and about half of the fragments of the stipulated size were excluded from the investigation. Statistical tests from the other holes showed that a random selection of about half the total amount of fragments is enough to ensure a statistically representative result.

The amount of fragments that had the stipulated size differs significantly between the holes. Figure L-4 shows that the percentage of fragments of the stipulated size was less in the heating holes in Test 3 than in Tests 1 and 2. This indicates that the spalling (or the scaling) in the heating holes of Test 3 in general has created smaller fragments. The difference is significant and according to the fragment investigation a possible explanation might be that the fragments from those two holes have a slightly different petrology. In those holes there seems to be more fragments that are fine grained and slightly epidotized than in the others holes.

Figure L-5 shows the mean values of weight, length, width and thickness of the investigated fragments in each hole. The mean values are almost equal for most of the holes. The deviating values are the mean length, width and weight in KQ0051G04 and the weight of KQ0048G04. Figures L-6 and L-7 illustrate the frequency of length and weight in selected intervals. These two figures clearly illustrate a higher amount of larger fragments as well as a lower amount of smaller fragments in KQ0051G04 compared to the other holes.

As the volume for each hole corresponding directly to the weight, Figure L-8 shows the differences between the fragment shapes in each hole according to what termed the theoretical parallelepiped (see explanation above). A borehole with a higher percentage indicates that the fragments have more obtuse angles and therefore are more rectangular in their shape. In other words, those fragments have a higher grade of breaks at a right angle which gives an obtuse shape. The high percentage in hole KQ0048G04 corresponds well to the higher mean fragment weight for this hole.

Table L-1. Total weight, number of investigated fragments and estimated volume[1] of all collected fragments from the field tests. The heaviest fragment in each borehole is also included. Hole KQ0046G04 is included in the table but not in the investigation since the number of fragments was too small.

Test number	Borehole	Weight of all collected fragments (kg)	Number of investigated fragments	Estimated total volume (litres)[1]	Heaviest fragment (kg)
3	KQ0048G04	18.7[2]	98	6.80	1.581
3	KQ0048G05	6.45	29	2.35	0.108
2	KQ0051G04	32.85	141	11.95	0.654
2	KQ0051G05	4.75	64	1.73	0.328
1	KQ0054G03	13.5	176	4.91	0.552
1	KQ0054G04	3.95	46	1.44	0.573
	Sum	80.2	564	29.16	
4	*KQ0046G04*	*0.9*	*9*	*0.33*	*0.072*
	Total	81.1	573	29.49	–

1) Based on a mean rock density of 2.75 g/cm^3.
2) Excludes 2.9 kg that came loose during the excavation.

Table L-2. Results from Table L-1 grouped into the heating holes on each side of the tunnel.

Boreholes	Weight of all collected fragments (kg)	Number of investigated fragments	Estimated total volume (litres)	Heaviest fragment (kg)
KQ0048G04 KQ0051G04 KQ0054G03	65.05	415	23.65	1.581
KQ0048G05 KQ0051G05 KQ0054G04	15.15	139	5.51	0.573
Total	80.2	554	29.16	–

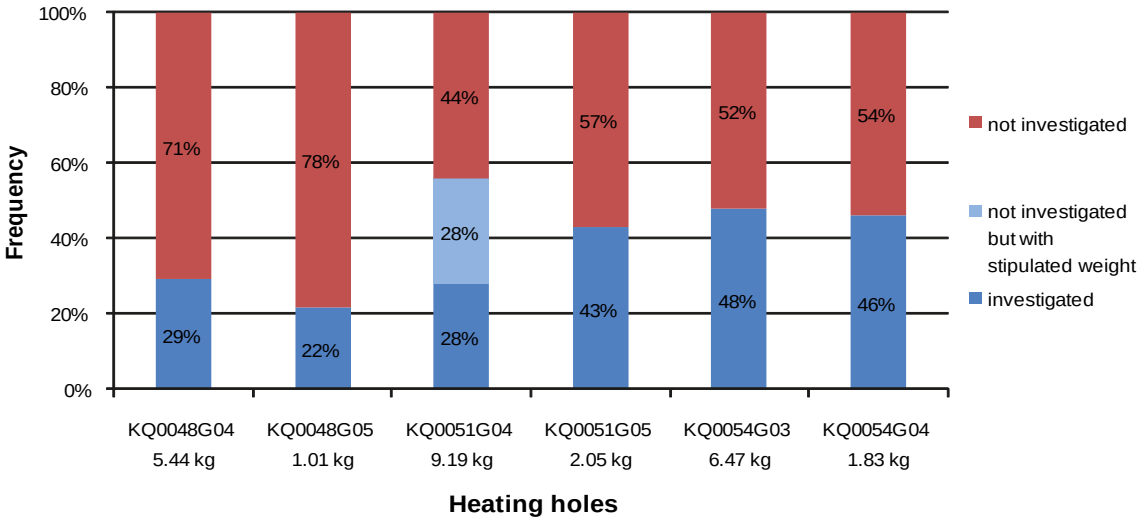

Figure L-4. *Frequency of fragments over the stipulated size included in the investigation. For five of the holes all of the fragments were investigated, however, for hole KQ0051G04 only about half were investigated. The total weight of investigated fragments is shown for each borehole.*

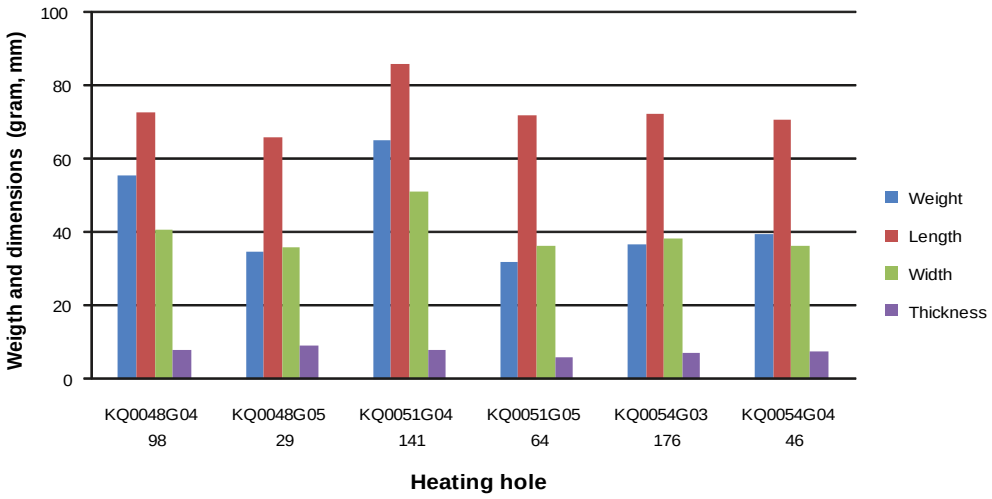

Figure L-5. *Mean fragment weight, length, width and thickness for each borehole.*

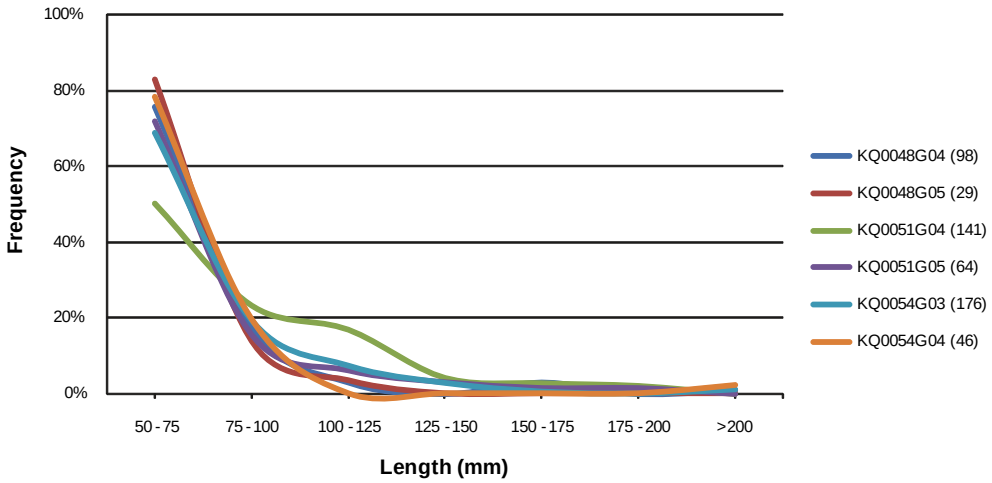

Figure L-6. *Length distribution of the investigated fragments. The minimum length was limited to 50 mm. the number of fragments included in the investigation is indicated in the legend.*

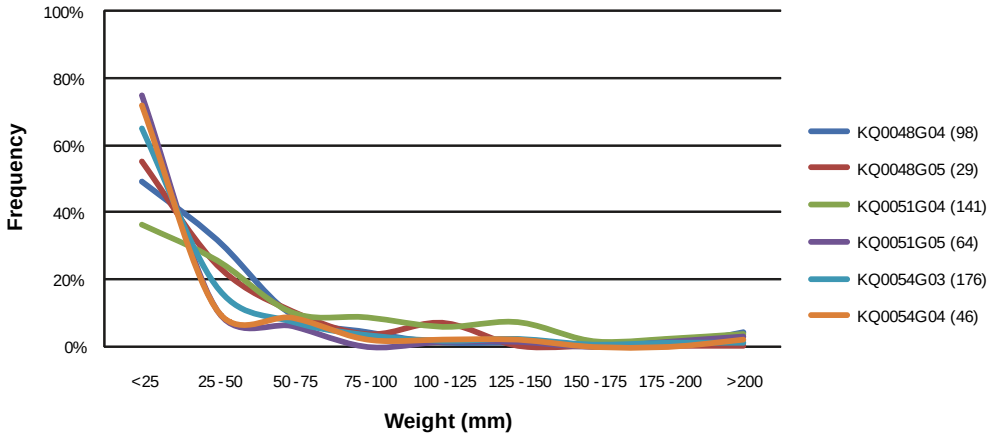

Figure L-7. *Distribution of the weight of the investigated fragments. The number of fragments included in the investigation is indicated in the legend.*

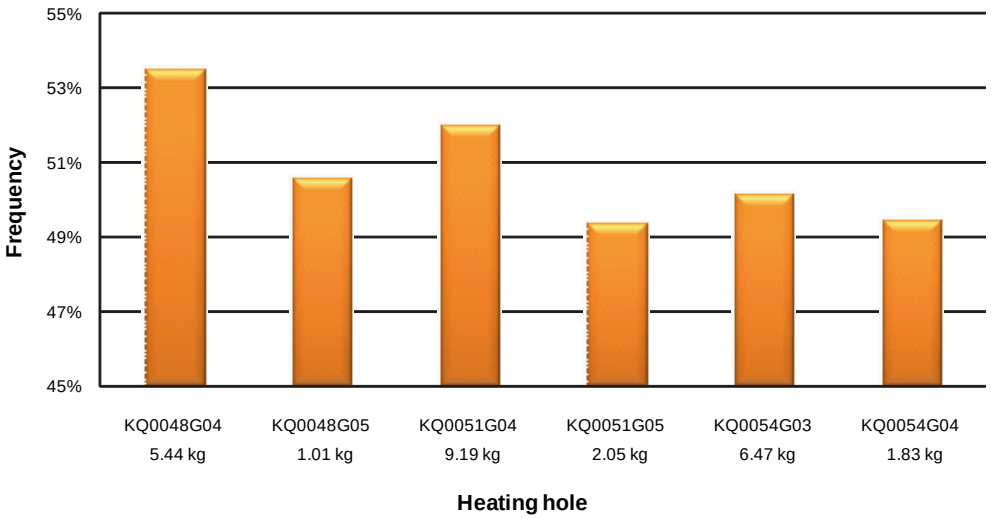

Figure L-8. *Mean percentage of the theoretical parallelepiped according to the measurements made at the centre of the fragment. The higher percentage the more rectangular the shape.*

L3.2 Fragment shape

The mean ratios for width vs. length, thickness vs. length and thickness vs. width were calculated for the fragments in each borehole and are illustrated in Figure L-9. According to the graph a few small anomalies can be commented upon:

- The T/L- and T/W-ratios for KQ0048G05 are higher than the ratios for fragments in the other holes. The fragments from this hole have, as is also seen from Figure L-5, the shortest length and therefore it can be concluded that they have a slightly different shape than fragments from the other holes. They are thicker compared to their length, but as observed in Figure L-8 they are not especially rectangular. The number of fragments is however quite small for this hole so it can be said that this feature has a high degree of uncertainty.
- The higher W/L-ratio of fragments from KQ0051G04 may be due to the fact that this hole had the largest amount of fragments and that the shapes of the fragments are generally shorter and more squared. Similarly the W/L-ratio for hole KQ0048G04 is the second highest and that this hole had the second highest number of fractures.
- Slightly lower T/L- and T/W-ratios of the fragments from Test 2 suggests that spalling produces slightly thinner fragments.

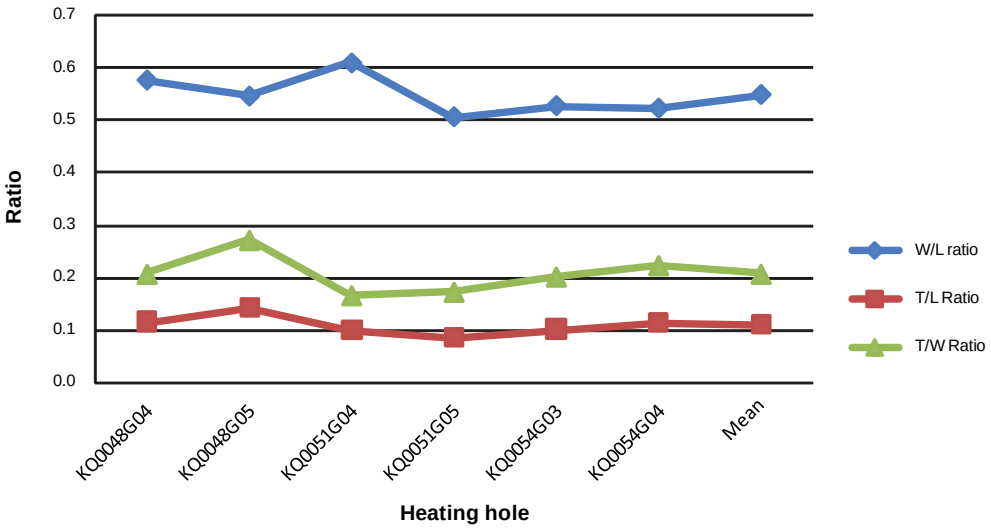

Figure L-9. *Mean ratios between width vs. length (W/L), thickness vs. length (H/L) and thickness vs. width (H/W) for the fragments in each borehole as well as the mean for all investigated fragments.*

Figures L-10 to L-12 show the distribution for the T/W-, T/L- and W/L ratios for all investigated fragments in each holes. The ratios for the fragments from the heating holes in Test 3 are the ones which are most evenly distributed in Figure L-10 and L-11 with the lowest peaks at any interval. This corresponds with the conclusion above that the fragment from hole KQ0048G05 have a different shape than the other. A conclusion that may be drawn from Figure L-10 is that the fragments from Test 2 in general have a more uniform shape as the distribution shows a rather high peak for booth holes at the ratio interval 0.11 to 0.20, something that confirm the conclusion above.

If we compare the determined ratios for fragments collected in the heating holes of different sides of the tunnel, we get a very evenly distribution between the two groups (Figure L-13 and L-14). The results indicate that the differences that exist in the geology due to the shear zone not influence the relative shape of the fragments.

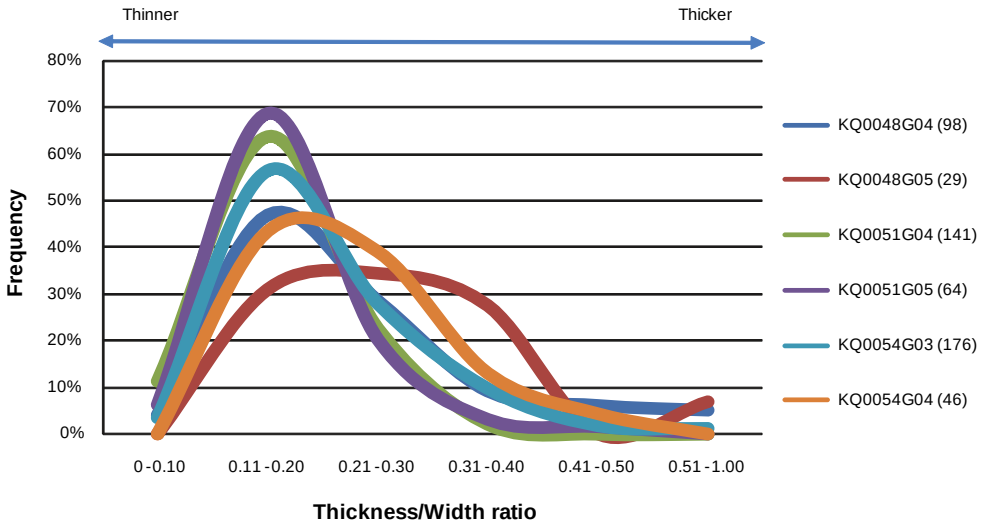

Figure L-10. *Thickness to width ratios of investigated fragments. The number of fragments included in the investigation is indicated in the legend. The selected interval is 0.10.*

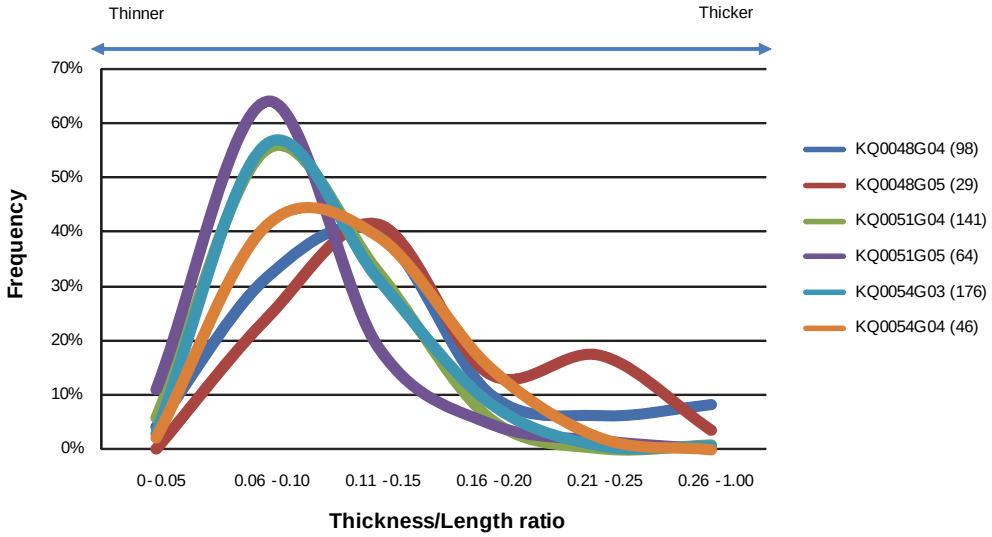

Figure L-11. *Thickness to length ratios of investigated fragments. The number of fragments included in the investigation is indicated in the legend. The selected interval is 0.05.*

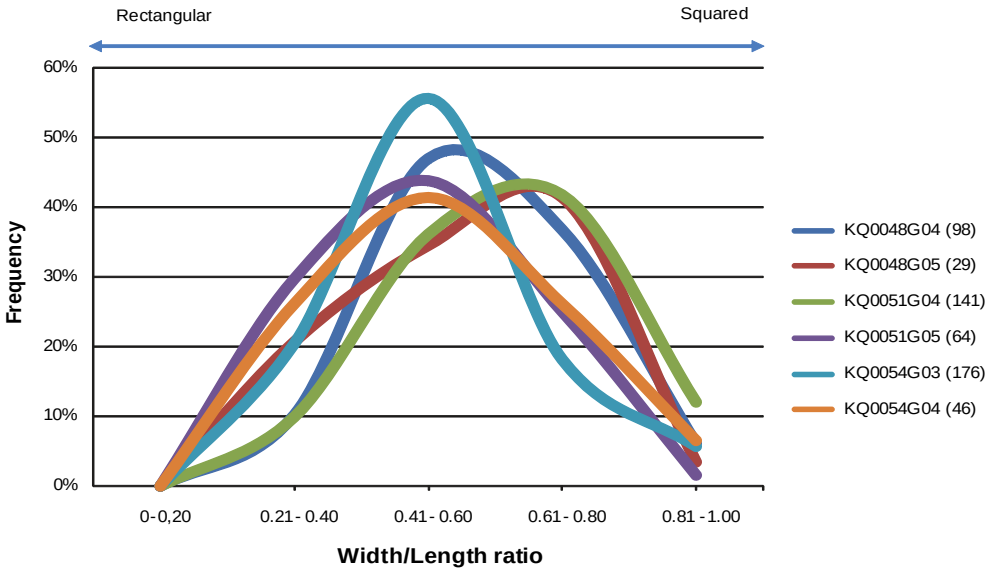

Figure L-12. *Width to length ratios of investigated fragments. The number of fragments included in the investigation is indicated in the legend. The selected interval is 0.20.*

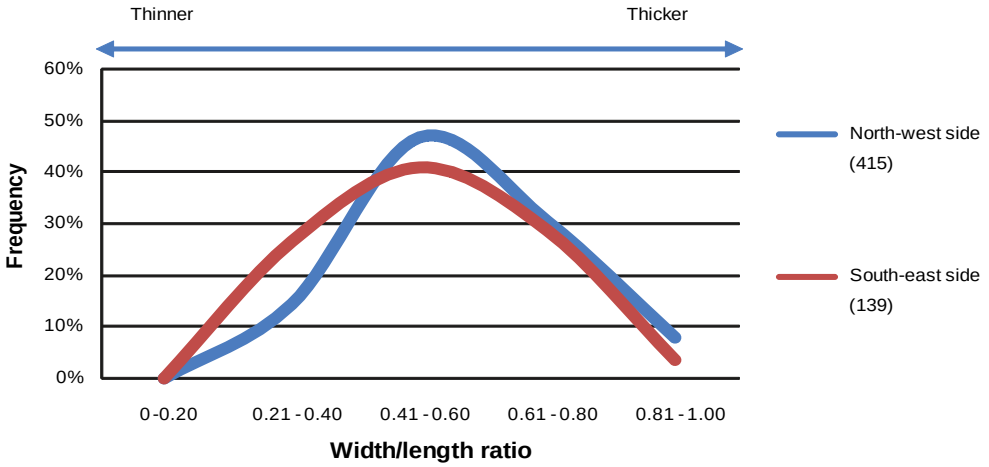

Figure L-13. *Width to length ratios of the investigated fragments in the holes of each side of the tunnel. The number of fragments included in the investigation is indicated in the legend.*

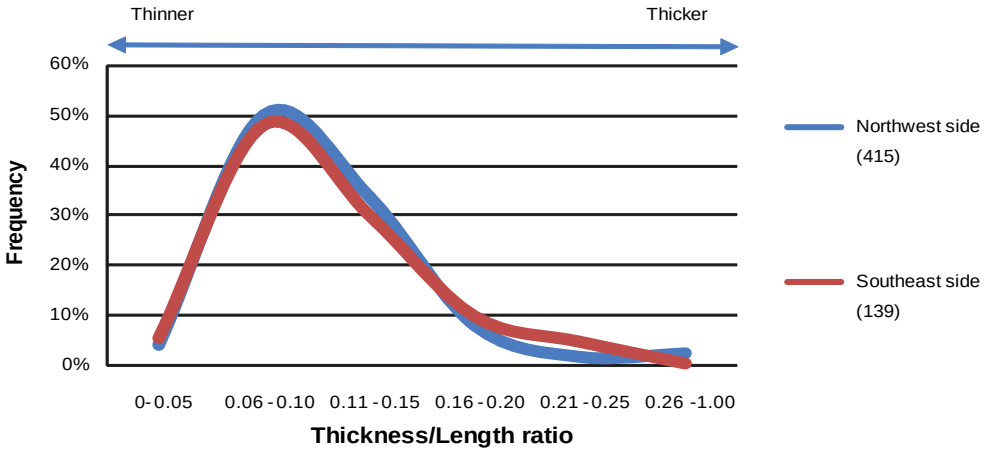

Figure 14. *Thickness to length ratios of the investigated fragments in the holes of each side of the tunnel. The number of fragments included in the investigation is indicated in the legend.*

L3.3 Fragment geology

The minerals that were found on failure surfaces and sealed fractures were mainly calcite, chlorite, epidote and lesser amounts of quartz, k-feldspar (adularia), biotite along with iron oxide coatings. In other geological investigations from the test area prehnite is often mentioned to be a common fracture mineral. However, in this study it is not specified since it was judged to be difficult to reliably identify by visual inspection.

In many fractures more than one mineral is present and the three most common minerals often occur together. When more than one mineral was observed no note was made as regards relative dominance.

The thickness of the mineral coating was not noted in a systematic way. However, in general the thickness ranged from 0.2 mm, covering only a few percentage of the surface, to a thickness of 3–4 mm on some fragments.

Figure L-15 shows what percentage of the fragments that could be categorized in a certain group dependent on the mineral coatings that were observed. The percentage of fragments that include any mineral coated fracture differs from 50 to nearly 90% between the holes.

In Figure L-16 the mean number of mineral coated fractures per fragment is illustrated for the different heating holes. The numbers show a great difference between the holes and in some of the holes it is common that the fragments have more than one mineral coated fracture in each fragment. Two of the holes, KQ0051G04 and KQ0054G04 have a mean of 1.5 mineral coated fractures per fragment while only a little more than half of the fragments from hole KQ0054G03 have any unbroken mineral coated fractures. If this difference is a product of how spalling has occurred or if it is because of a difference in petrography and the amount of mineral coated fractures in the holes is not clear.

The hole that has most mineral coated fractures is KQ0054G04 and this hole also has nearly the same amount of unbroken and failed mineral coated fractures. In the other holes the ratio between unbroken and failed is about one third to a half. A conclusion from this can be that the spalling has not broken up the rock along the former sealed fractures at the same rate in KQ0054G04 and KQ0051G04 as in the other holes.

The percentage of mineral coated fractures that remained unbroken during the tests is expressed as a percentage in Figure L-17. The highest percentage in Figure L-17 correlates with the highest ratios seen in Figure L-16. If this is compared to the shape of the fragments, see Figures L-9 to L-12, some correlation between the amounts of mineral coated fractures and the shape may be observed.

The main petrological difference in investigated fragments is the higher grade of epidotization of the fragments collected in the holes from Test 3. Epidote is seen in small thin bands. These fragments are considered to originate from a small structural deformed zone that intersects the heating holes of Test 3.

Figure L-18 shows the percentage of coated fractures that contained calcite, chlorite, epidote or some other mineral in each hole. It can be concluded that epidote coatings are by far the most common in the holes from Test 3 and that chlorite coatings are more common in Tests 1 and 2.

Figures L-19 and L-20 show the percentage of failed and unbroken sealed fractures that contains calcite, chlorite, epidote or some other mineral. A comparison of the two diagrams indicates that fractures containing chlorite fail easier than those containing calcite and epidote. This may be due to the fact that chlorite fractures often are situated in an already weakened deformed part of the rock whereas calcite more often intersects the more undeformed parts. The calcite fractures are also subdivided on failed and sealed fractures. This is however most probably dependent on the fact that the coating thickness also is variable. The thickness was not noted during the investigation in a systematic way but nevertheless it is a fact that thicker coatings are rather unusual for the sealed fractures. The epidote fractures that are sealed are often situated in areas where the surrounding rock has undergone metamorphic reactions and become epidotized.

The amount of epidote coated fractures is however interesting as the holes from Test 3 have the most of these fractures. As noted above these holes had more fragments that were partly epidotized. If these facts are then compared to the percentage of fragments with the stipulated size (see Figure L-4) it can be concluded that the epidotization produces smaller fragments during spalling. This is not considered to be due to the epidote coated fractures since they are often sealed as can be seen in Figure L-14. It is more probable that the epidotization, which has created a rock with smaller grains than the general rock in the area, breaks the rock in right angles.

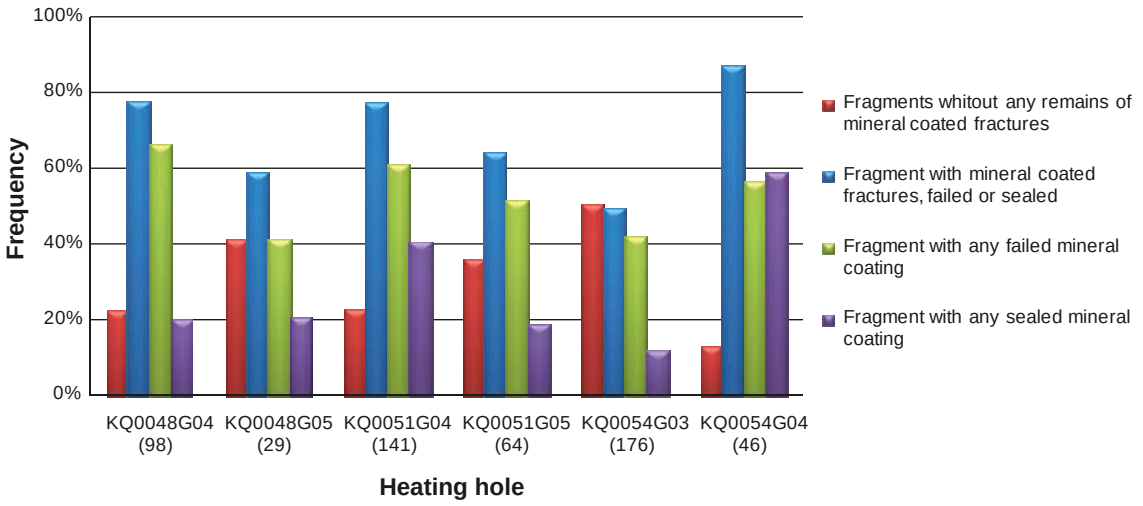

Figure L-15. *Percentage of fragments of different categories for each of the individual holes. The number of fragments included in the investigation is indicated below each hole-ID.*

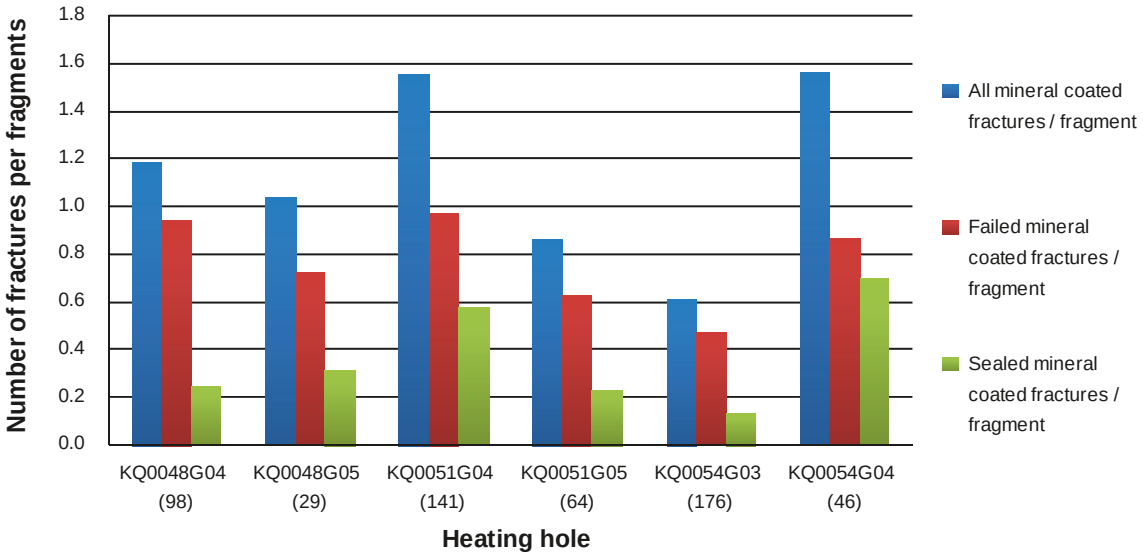

Figure L-16. *Number of fractures of different categories per fragments presented for each of the individual holes. The given numbers are mean values. The number of fragments included in the investigation is indicated below each hole-ID.*

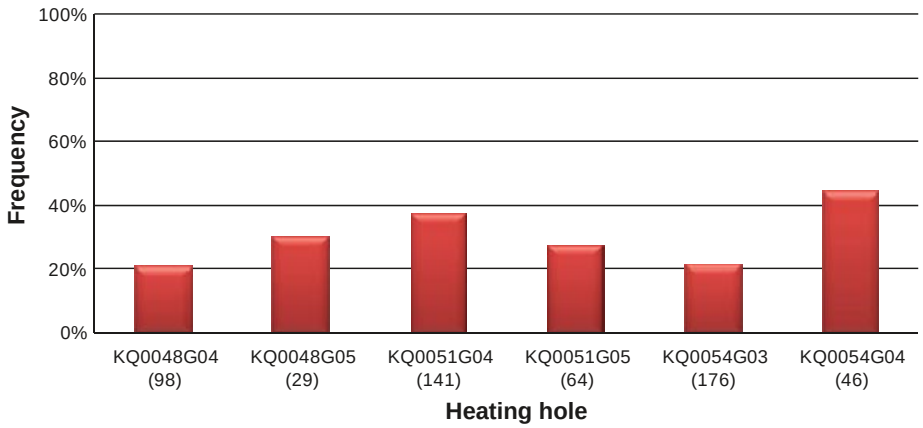

Figure L-17. *Proportions of mineral coated fractures that remained unbroken in the investigated fragment in each hole. The number of fragments included in the investigation is indicated below each hole-ID.*

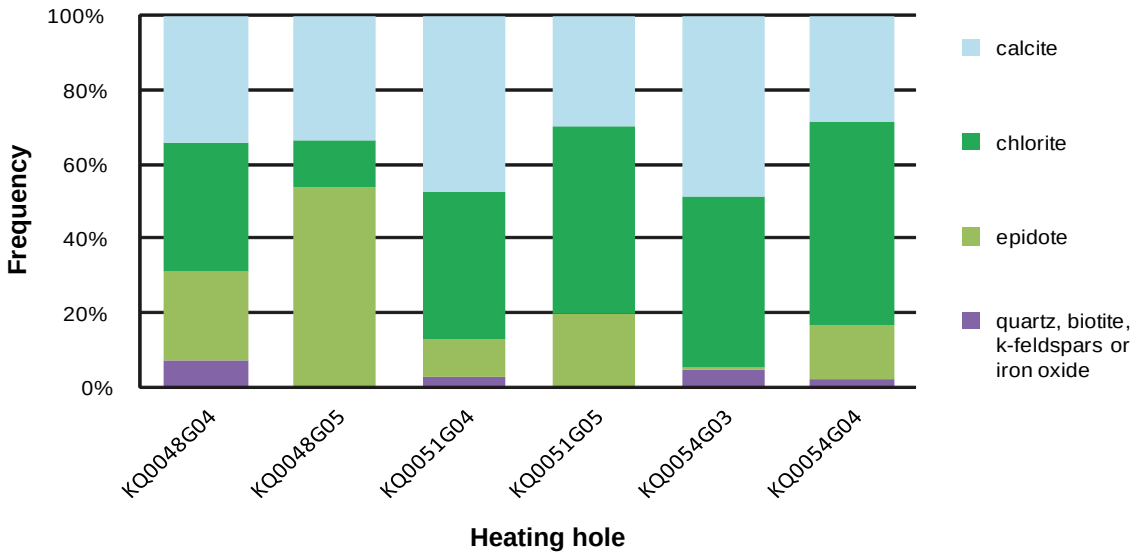

Figure L-18. *Distribution of the different mineral coatings (calculated on the basis that a specific fracture can have more than one mineral).*

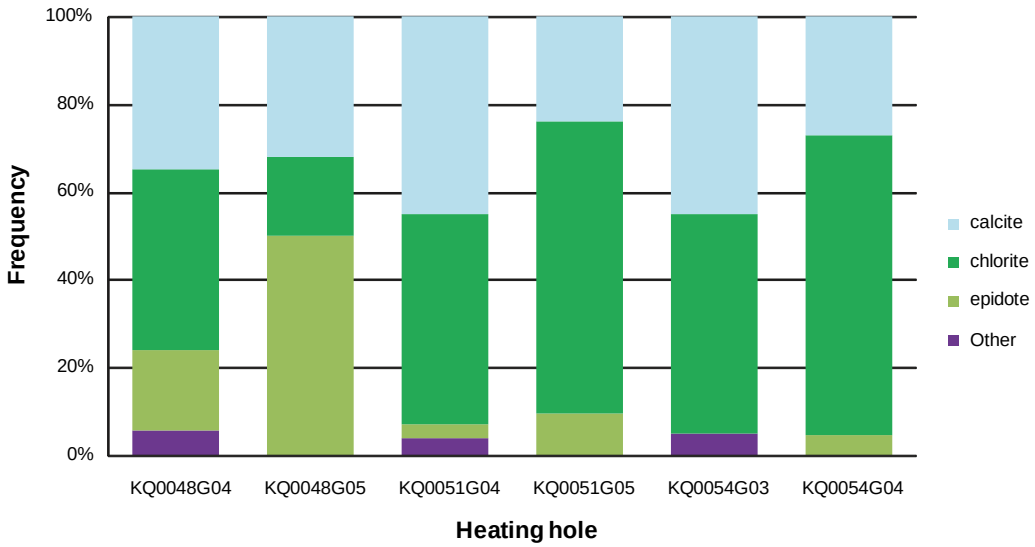

Figure L-19. *Proportions of different type of minerals on the failure surfaces of the investigated fragments.*

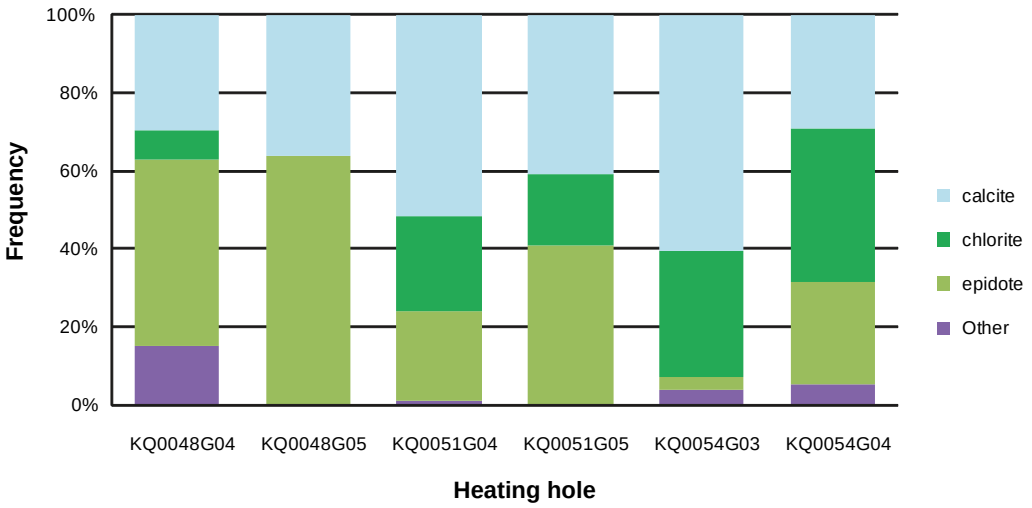

Figure L-20. *Proportions of different type of minerals of unbroken sealed included in the investigated fragments.*

L4 Conclusions

L4.1 Fragment shape

The spalling process in the heating holes in Test 3 seems to have produced thicker and shorter fragments with slightly sharpened edges compared to the other holes. The best proof for this is the low amount of fragments which had the stipulated size to be included in the investigation. Moreover, the higher mean weight in KQ0048G04 and the ratios for thicknesses vs. length and width in KQ0048G05 indicates that the fragments from Test 3 have a more compact shape and that the spalling has occurred in some ways that slightly differs from in the other holes.

The spalling seems to have occurred in a slightly different way in hole KQ0051G04. However, the larger mean values of length and weight and the peak in frequency of unusual large fragments can be a product of the large total amount of fragments that were generated in this hole.

The thinnest fragments and also those with the most uniform shape were collected in the heating holes of Test 2, which means that the spalling of the rock has occurred in a similar way in these holes.

The observed difference in shape of the fragments is too small to demonstrate any significant influence of the counter pressure of the spalling process. The difference in shape that was observed is probably a product of the different petrology of the bedrock.

L4.2 Fragment geology

The epidotized structural zone that occurs in the test area produces shorter and thicker fragments with a more obtuse shape. This seems to be mainly due to the smaller grain size of the rock that is the result of the epidotization.

Chlorite coated fractures seem to fail easier than calcite and epidote coated fractures, something that is thought to be related to the chlorite metamorphosed parts of the bedrock being generally weaker.

Thin calcite coated fractures that intersect the bedrock do not seem to influence the spalling while the thicker ones do.

L5 Reference

Staub I, Andersson J C, Magnor B, 2004. Äspö Pillar Stability Experiment, Geology and mechanical properties of the rock in TASQ. SKB R-04-01, Svensk Kärnbränslehantering AB.

Appendix AL1

Photographs of the investigated fragments

Figure AL1-1. *Investigated fragments in heating hole KQ0054G03 (Test 1), Group 1.*

Figure AL1-2. *Investigated fragments in heating hole KQ0054G03 (Test 1), Group 2.*

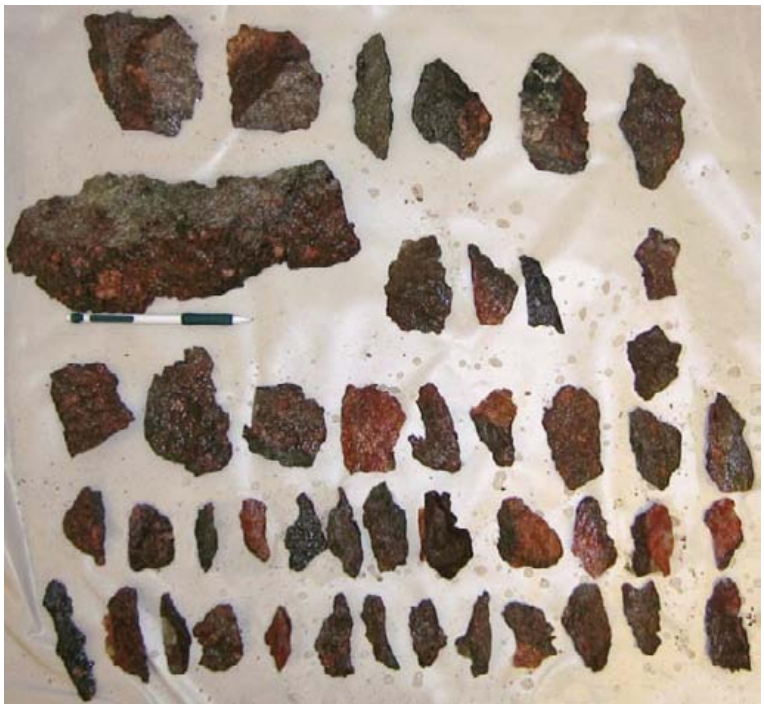

Figure AL1-3. *Investigated fragments in heating hole KQ0054G04 (Test 1).*

Figure AL1-4. *Investigated fragments in heating hole KQ0051G04 (Test 2), Group 1.*

Figure AL1-5. *Investigated fragments in heating hole KQ0051G04 (Test 2), Group 2.*

Figure AL1-6. *Investigated fragments in heating hole KQ0051G04 (Test 2), Group 3.*

Figure AL1-7. *Investigated fragments in heating hole KQ0051G05 (Test 2), Group 1.*

Figure AL1-8. *Investigated fragments in heating hole KQ0051G05 (Test 2), Group 2.*

Figure AL1-9. *Investigated fragments in heating hole KQ0048G04 (Test 3), Group 1. Fragments that were brought up with a suction pipe.*

Figure AL1-10. *Investigated fragments in heating hole KQ0048G04 (Test 3), Group 2.*

Figure AL1-11. *Investigated fragments in heating hole in KQ0048G04 (Test 3), Group 3.*

Figure AL1-12. *Investigated fragments in heating hole KQ0048G05 (Test 3), Group 1. Fragments that were brought up with a suction pipe.*

Figure AL1-13. *Investigated fragments in heating hole KQ0048G05 (Test 3), Group 2.*

Appendix AL2

Photographs of all fragments per heating hole

Figure AL2-1. *Collected fragments in heating hole KQ0054G03 in Test 1.*

Figure AL2-2. *Collected fragments in heating hole KQ0054G04 in Test 1.*

Figure AL2-3. *Collected fragments in heating hole KQ0051G04 in Test 2.*

Figure AL2-4. *Collected fragments in heating hole KQ0051G05 in Test 2.*

Figure AL2-5. *Collected fragments in heating hole KQ0048G04 in Test 3.*

Figure AL2-6. *Collected fragments from the bottom in heating hole KQ0048G04 by the suction pipe (Test 3).*

Figure AL2-7. *Collected fragments in heating hole KQ0048G05 in Test 3.*

Figure AL2-8. *Collected fragments in heating hole KQ0046G04 in Test 4.*

Appendix M

Characterization of the notch based on laser scanning

Crossections for KQ0054G03

40 crossections, 4mm wide, every 100mm, start at -446.122, end at -450.022

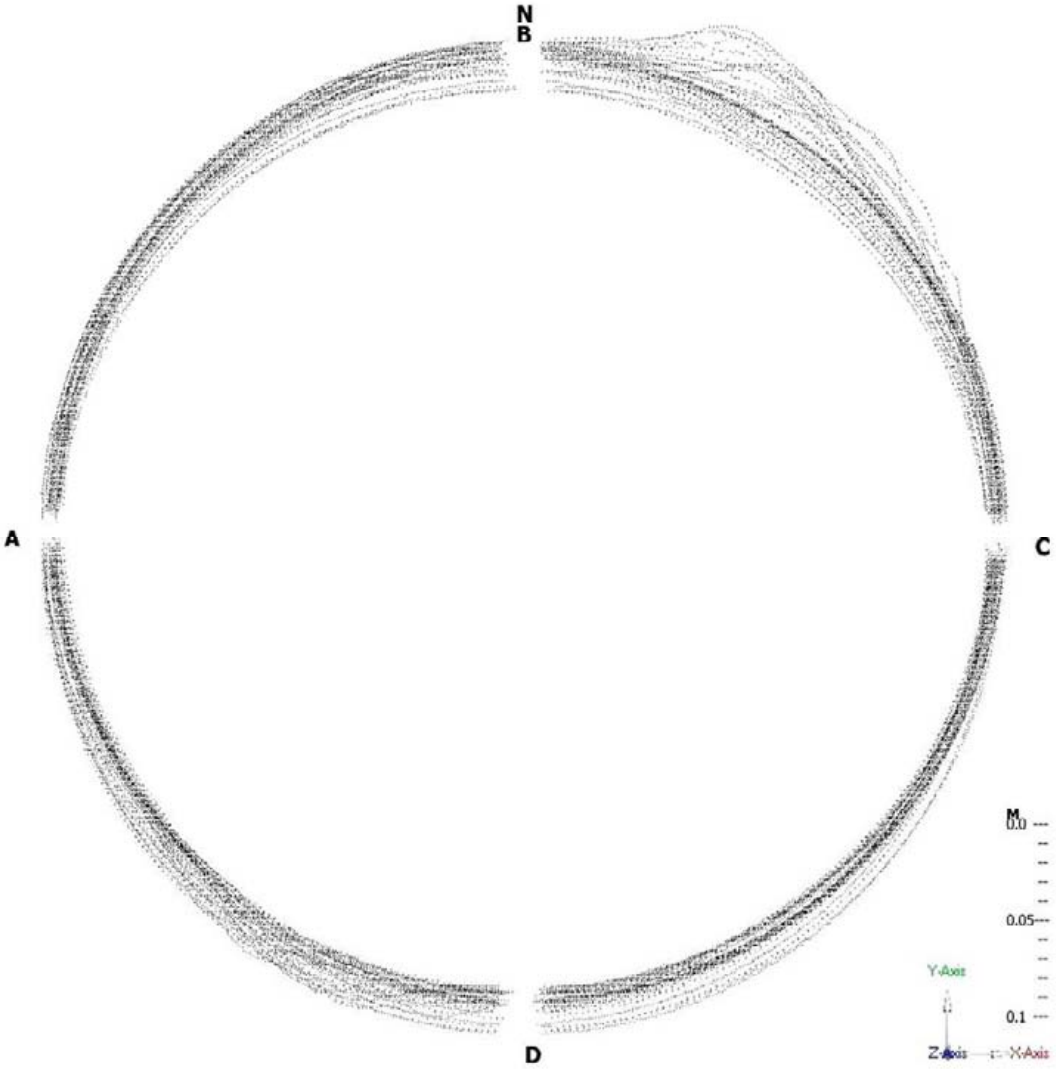

Max dimensions for KQ0054G03, sector BC NE-side

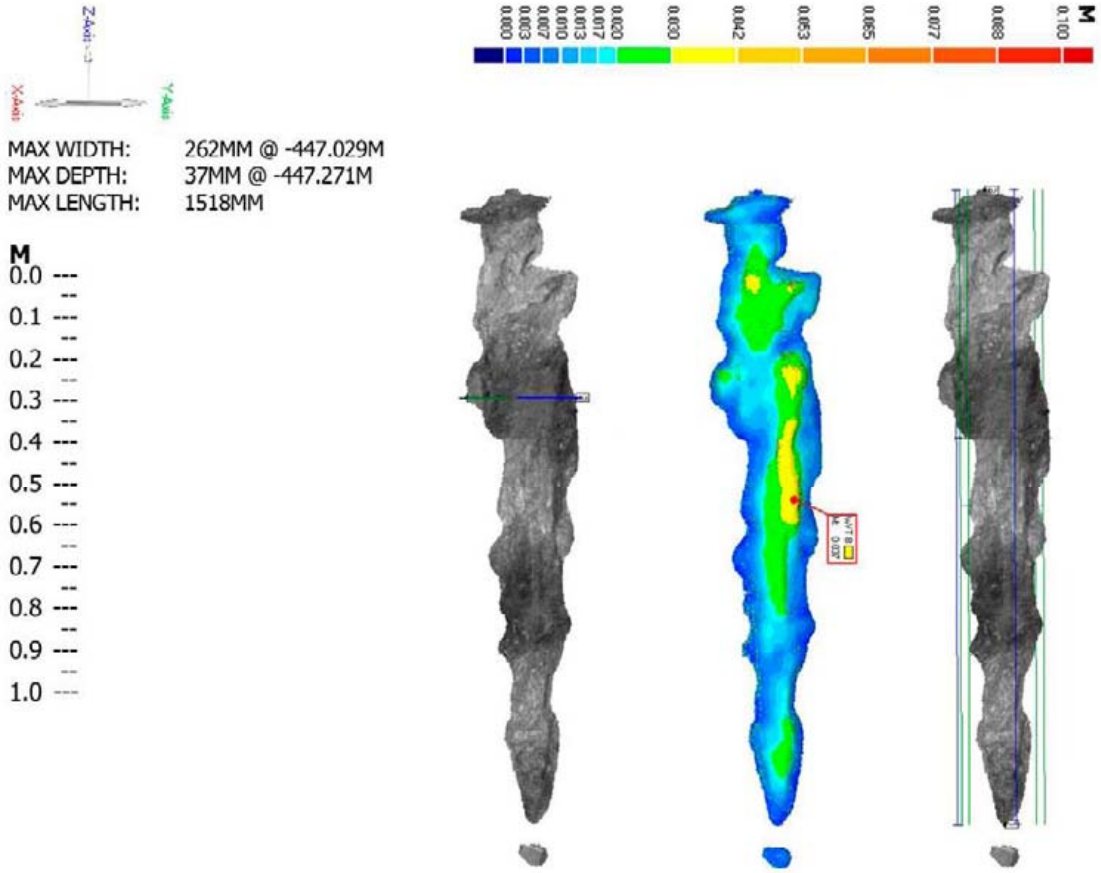

Max dimensions for KQ0054G03, sector AD SW-side

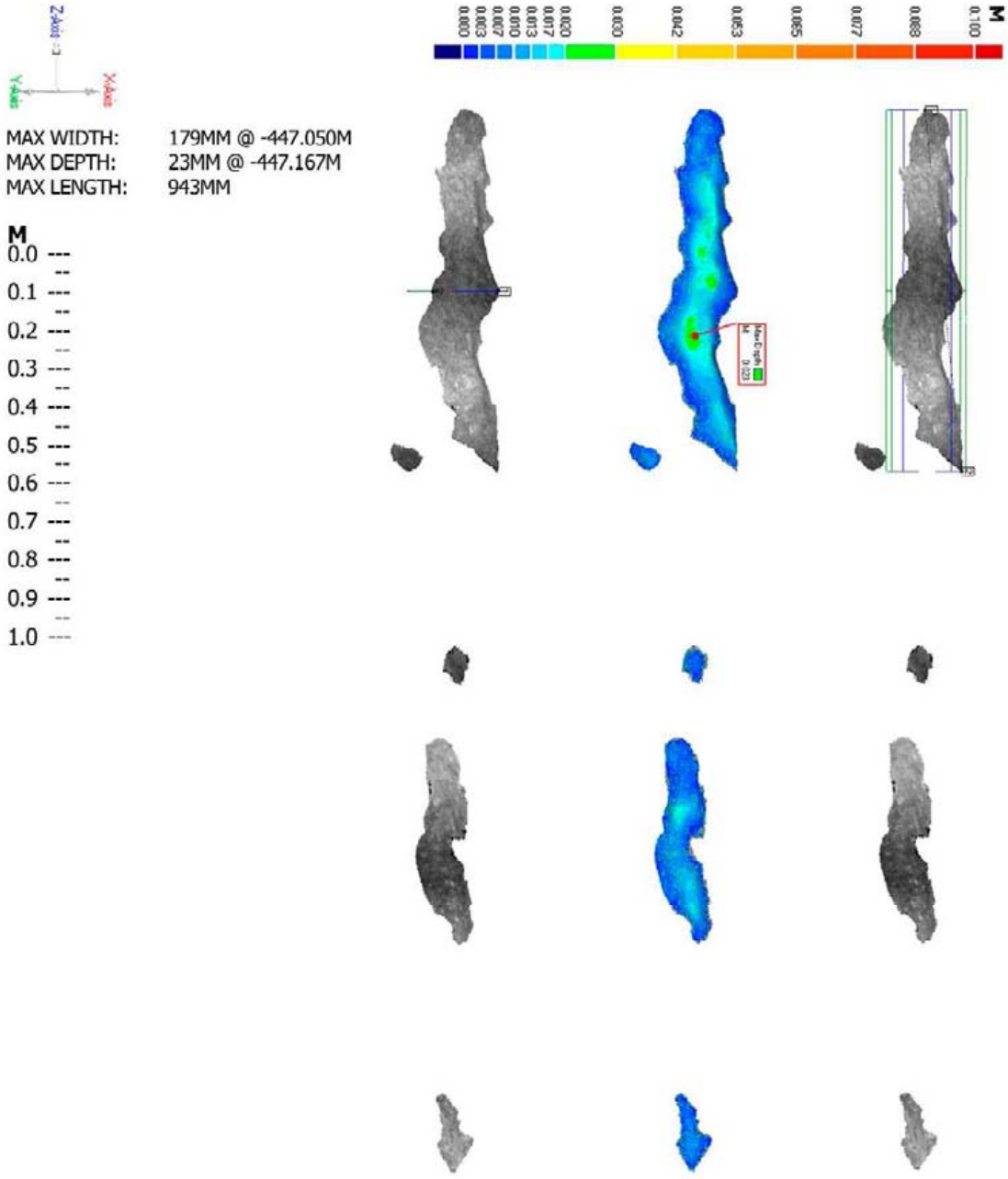

Volume determination for KQ0054G03, sector BC NE-side. Projection from outside.

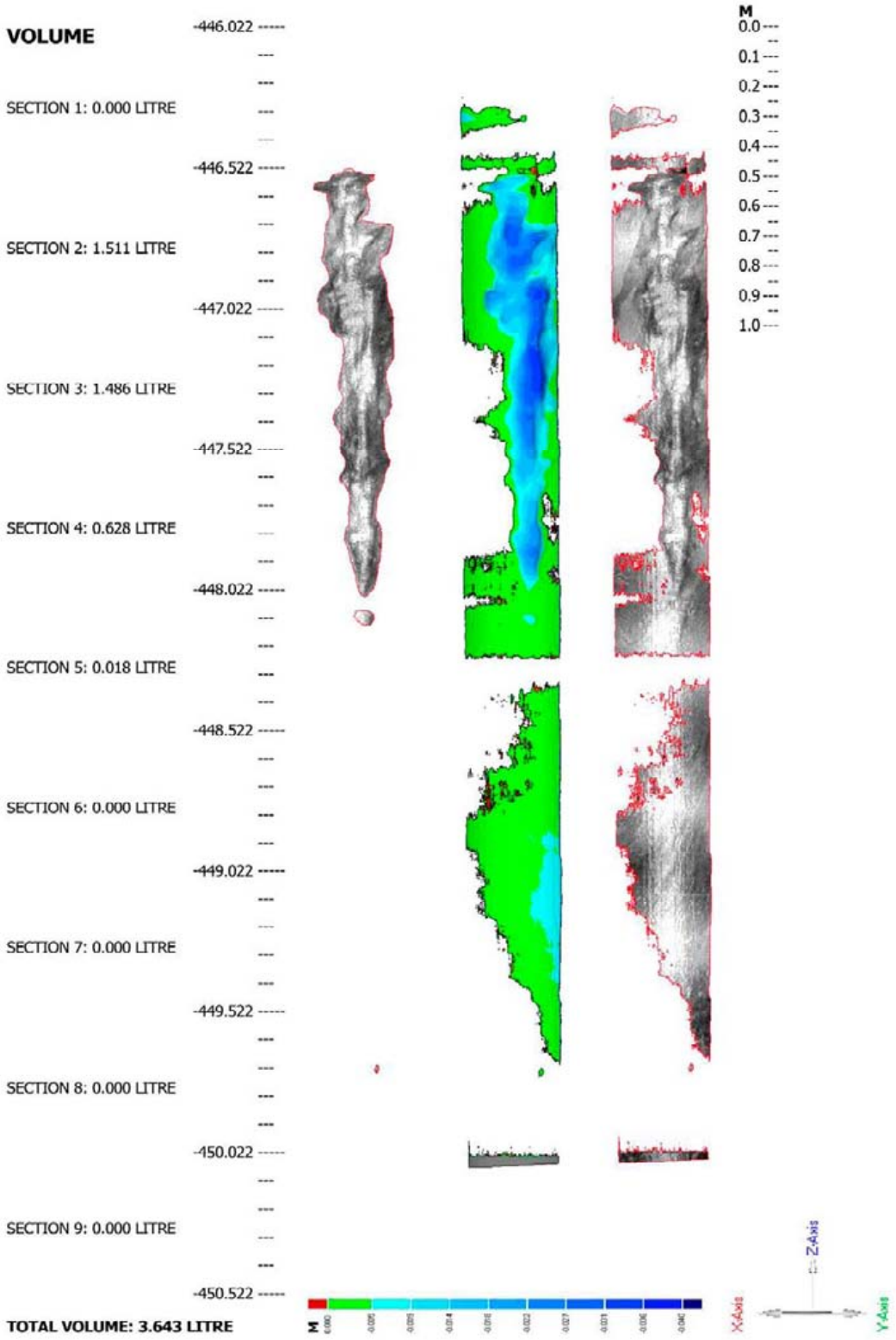

Volume determination for KQ0054G03, sector AD SW-side. Projection from outside.

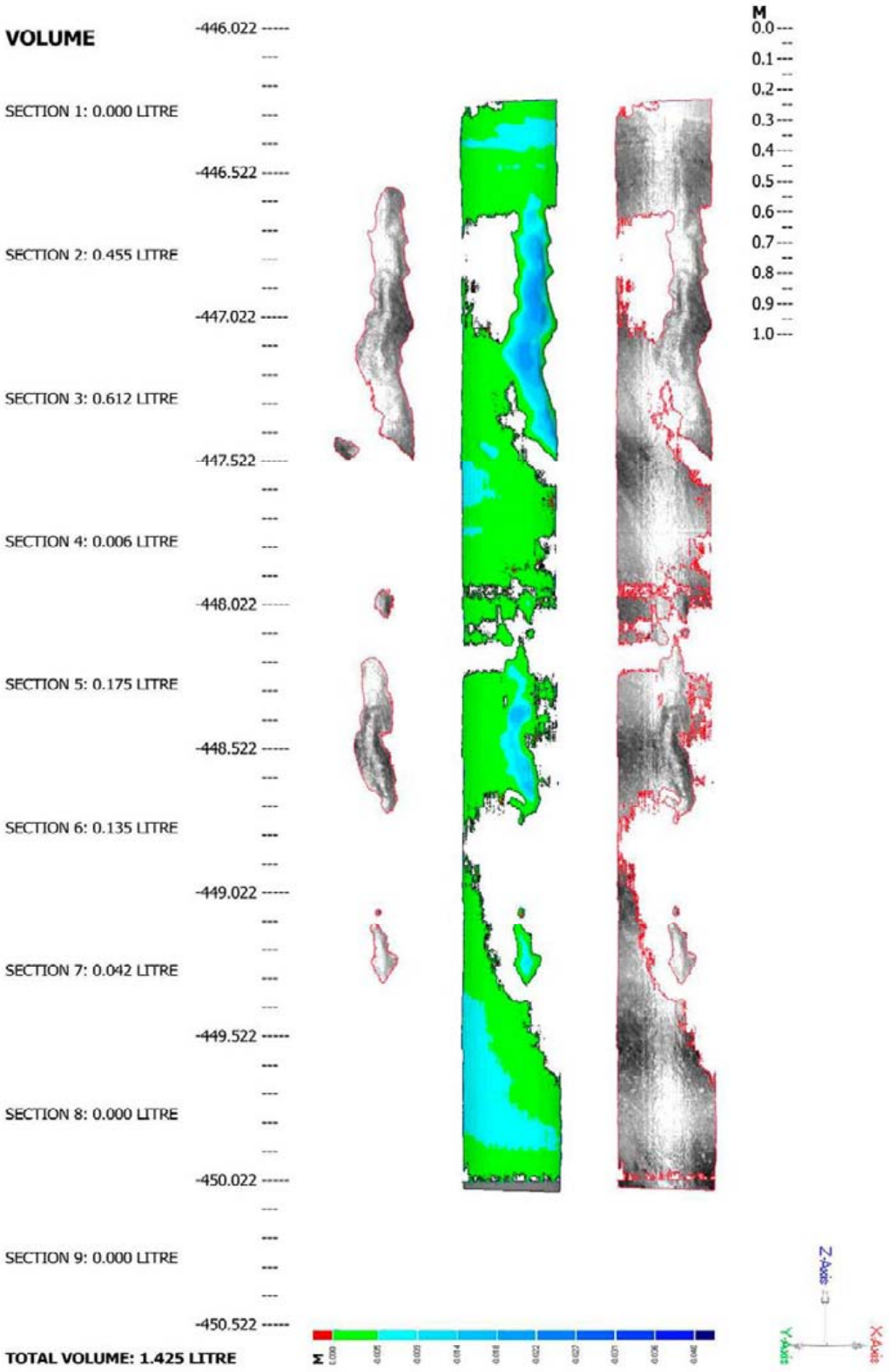

KQ0054G03

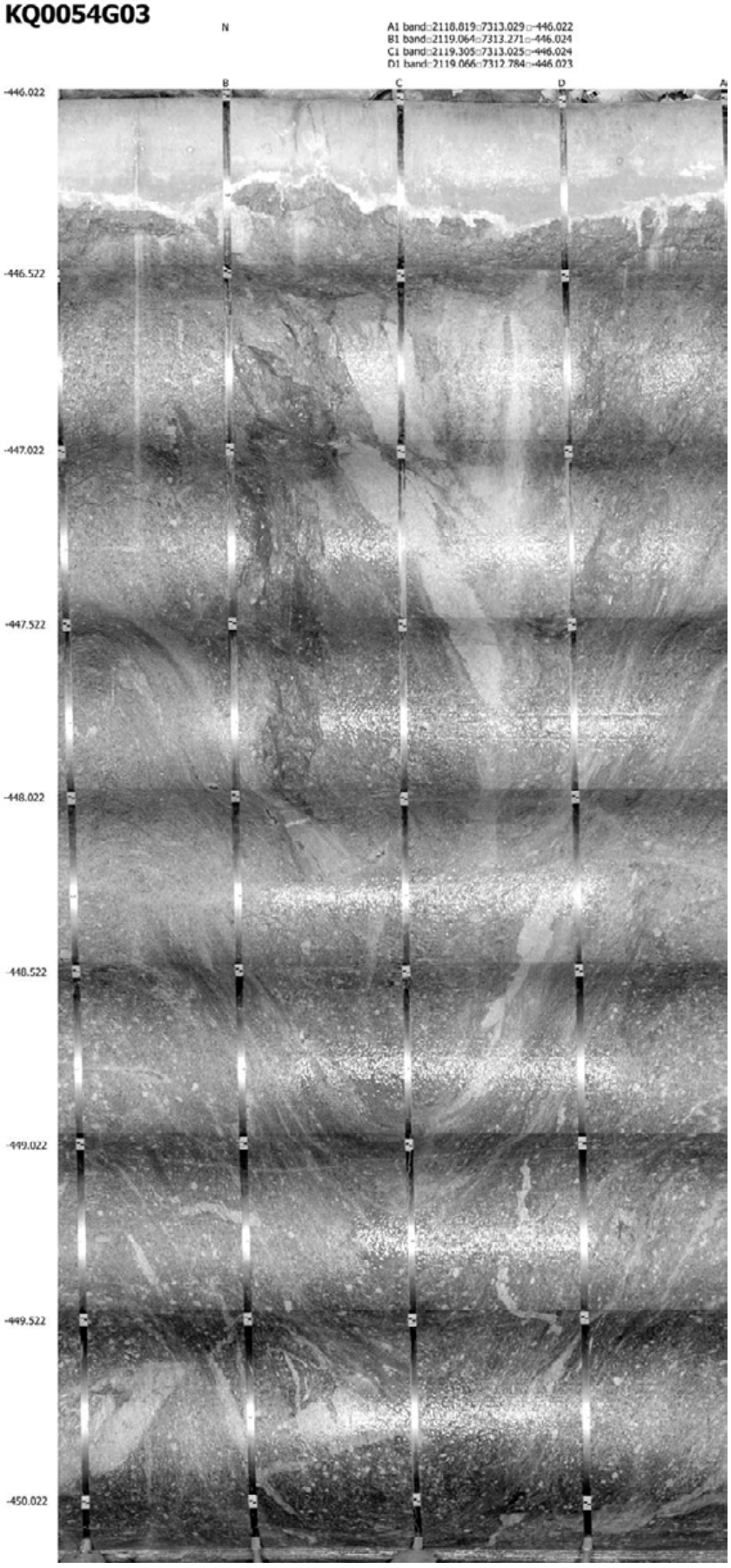
N
A1 band□2118.819□7313.029□-446.022
B1 band□2119.064□7313.271□-446.024
C1 band□2119.305□7313.025□-446.024
D1 band□2119.066□7312.784□-446.023
B
C
D
A
-446.022
-446.522
-447.022
-447.522
-448.022
-448.522
-449.022
-449.522
-450.022

Crossections for KQ0054G04

40 crossections, 4mm wide, every 100mm, start at -446.279, end at -450.179

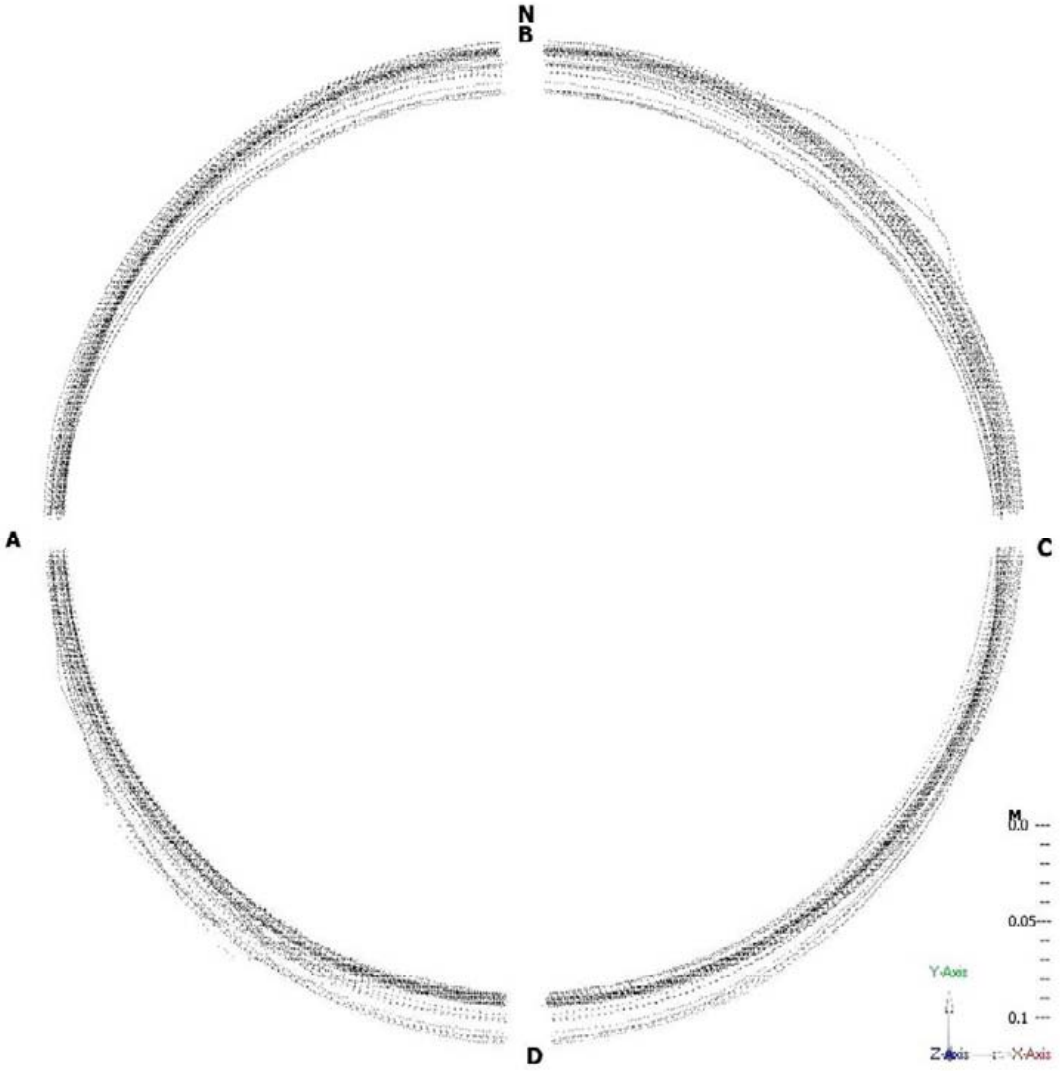

Max dimensions for KQ0054G04, sector BC NE-side

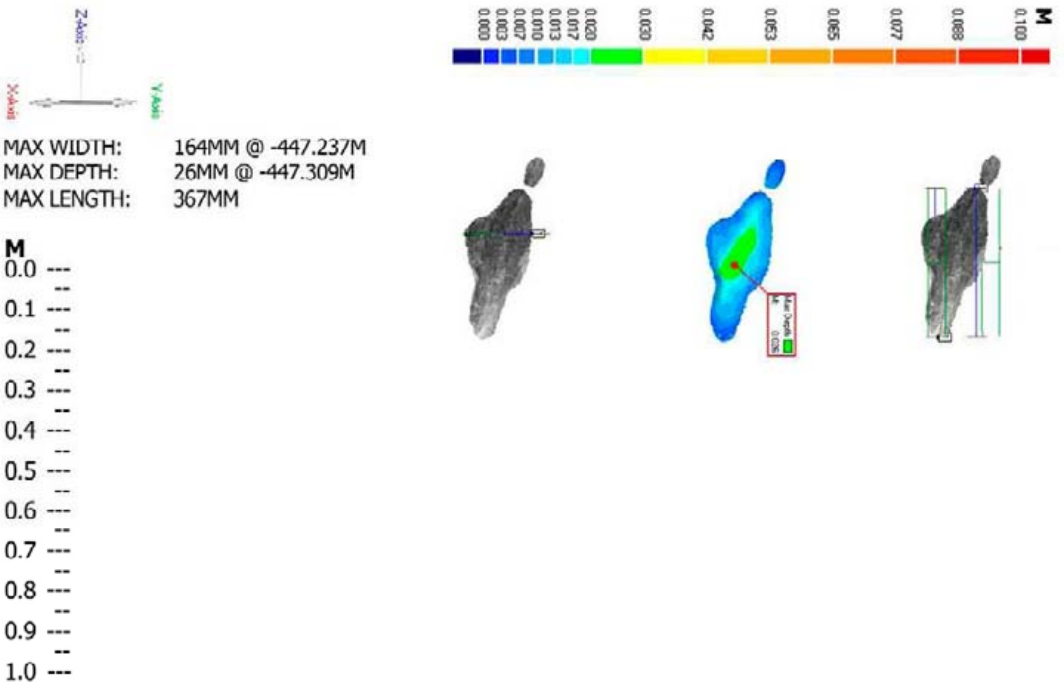

Max dimensions for KQ0054G04, sector AD SW-side

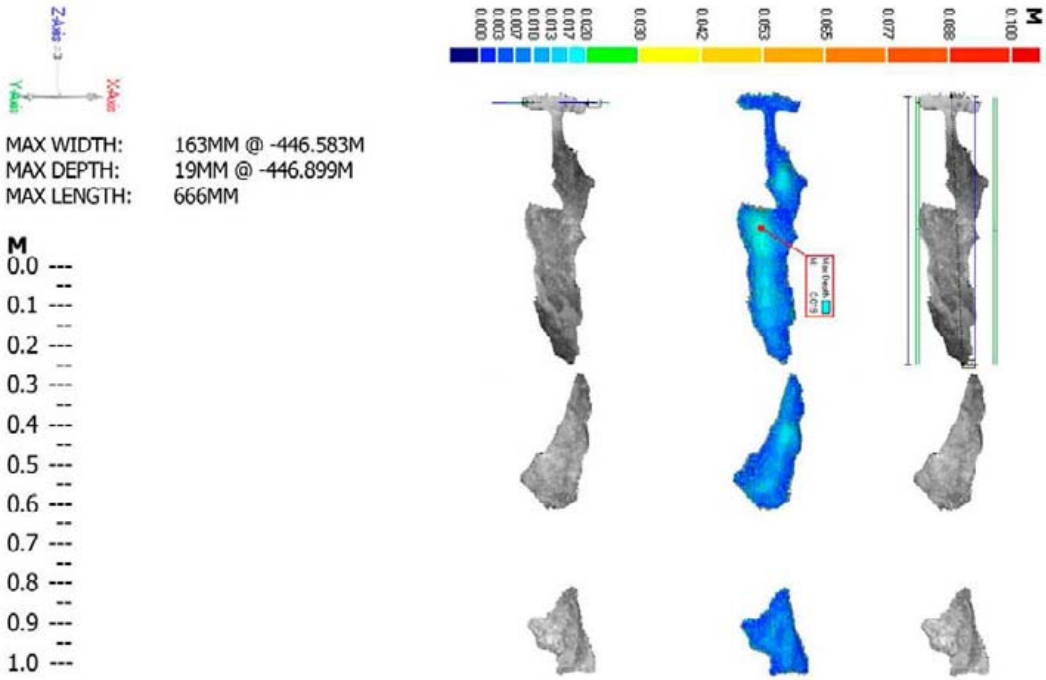

Volume determination for KQ0054G04, sector BC NE-side. Projection from outside.

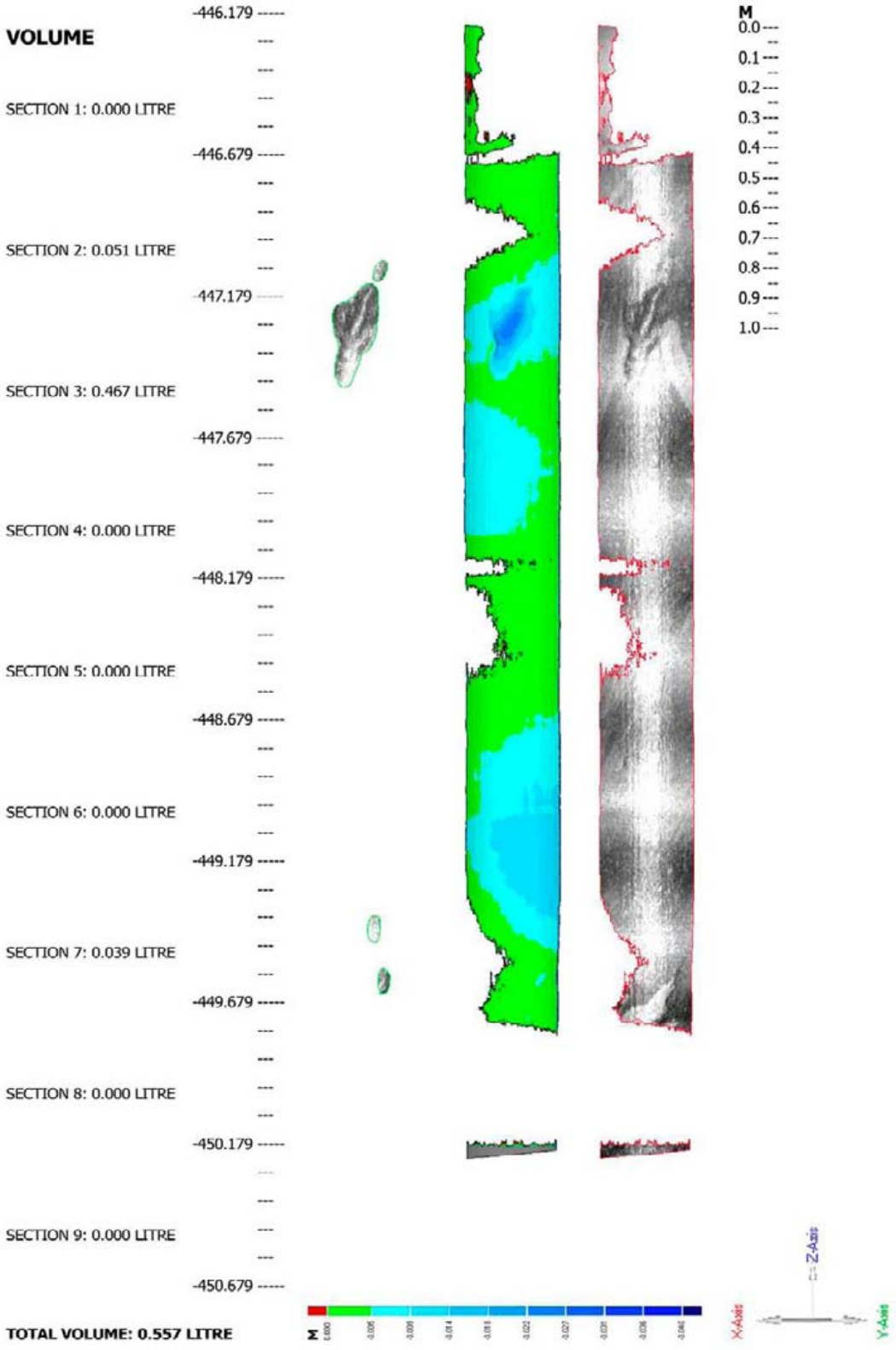

Volume determination for KQ0054G04, sector AD SW-side. Projection from outside.

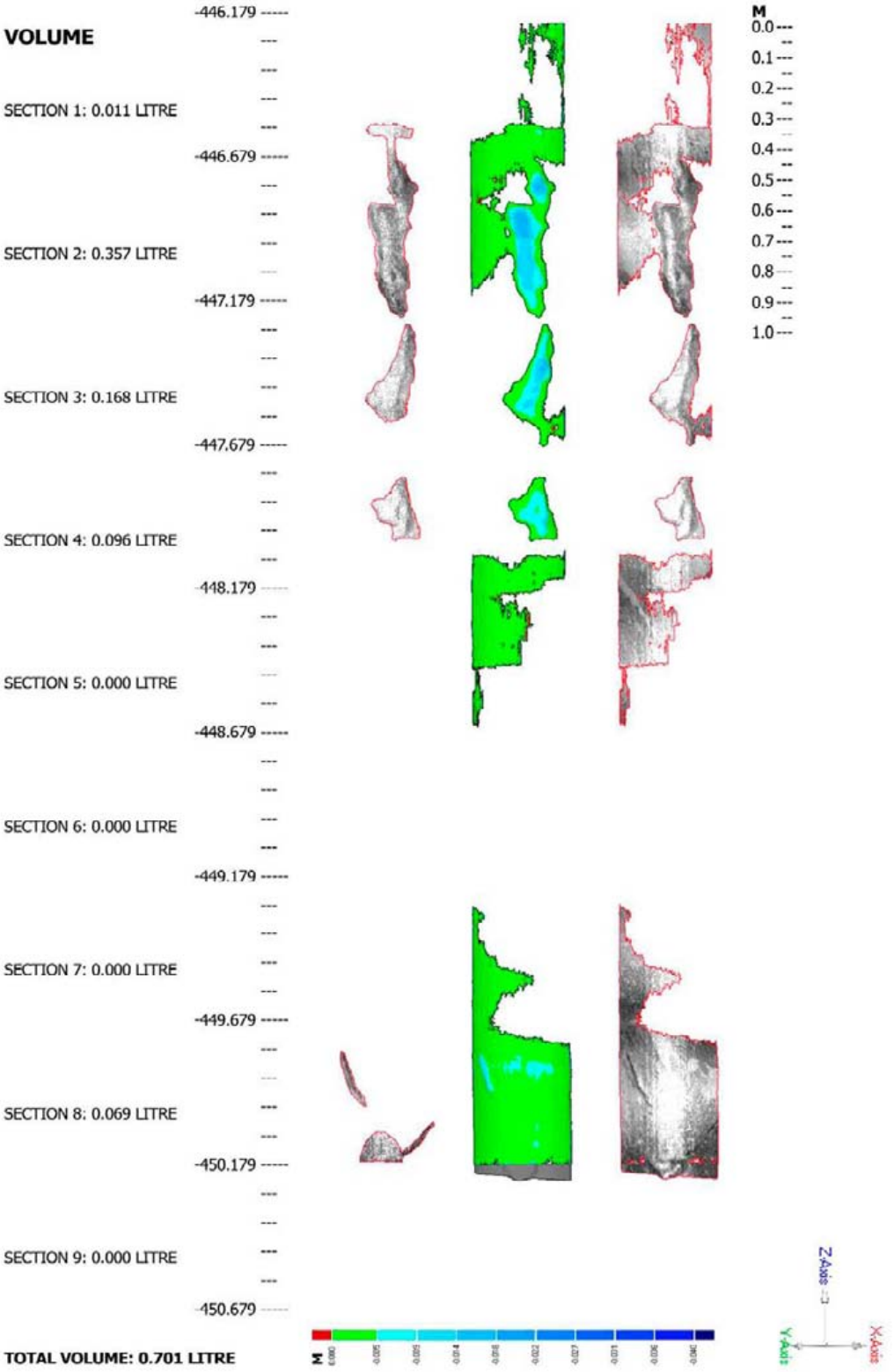

KQ0054G04

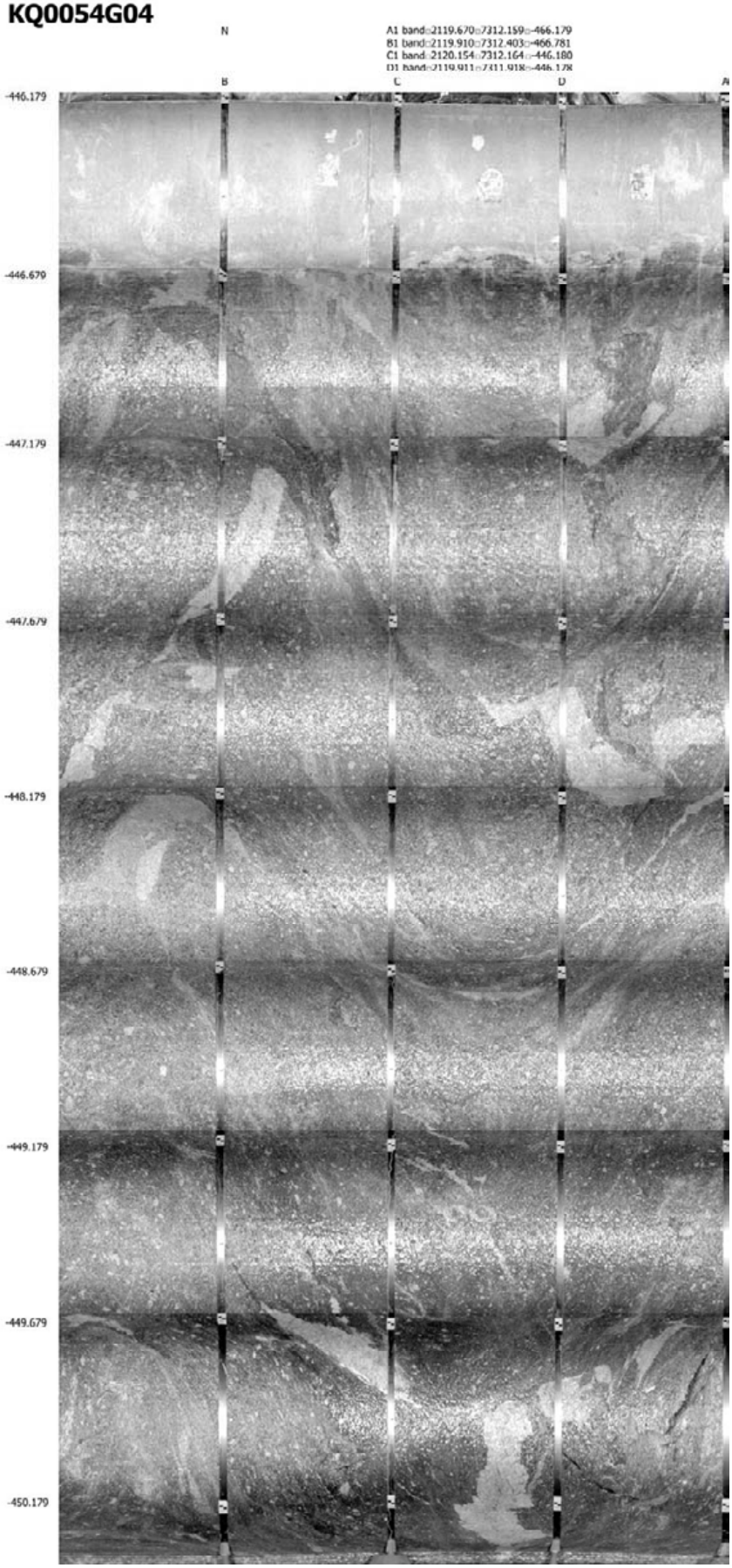
N
A1 band□2119.670□7312.159□-466.179
B1 band□2119.910□7312.403□-466.781
C1 band□2120.154□7312.164□-446.180
D1 band□2119.911□7311.918□-446.178
B
C
D
A
-446.179
-446.679
-447.179
-447.679
-448.179
-448.679
-449.179
-449.679
-450.179

Crossections for KQ0051G04

41 crossections, 4mm wide, every 100mm, start at -446.011, end at -450.011

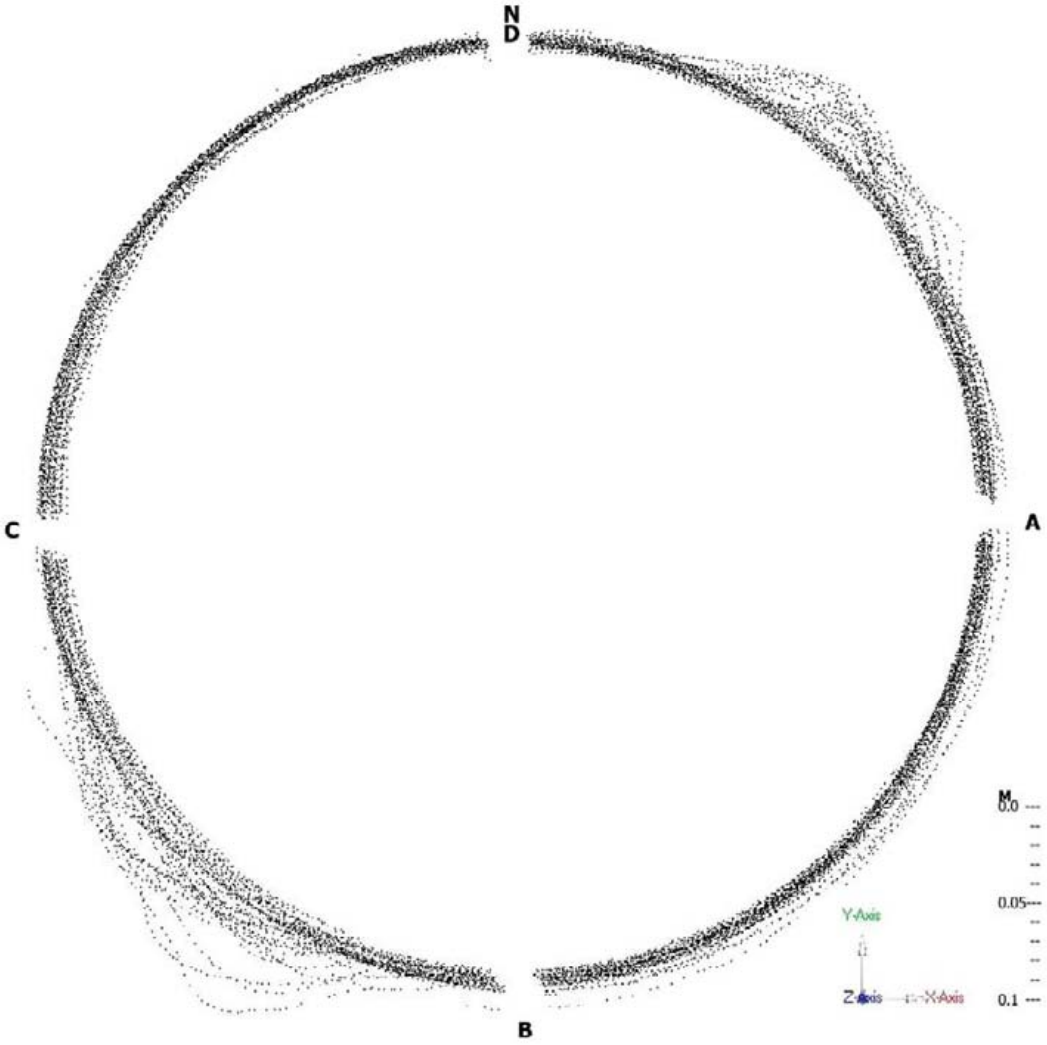

Max dimensions for KQ0051G04, sector AD NE-side

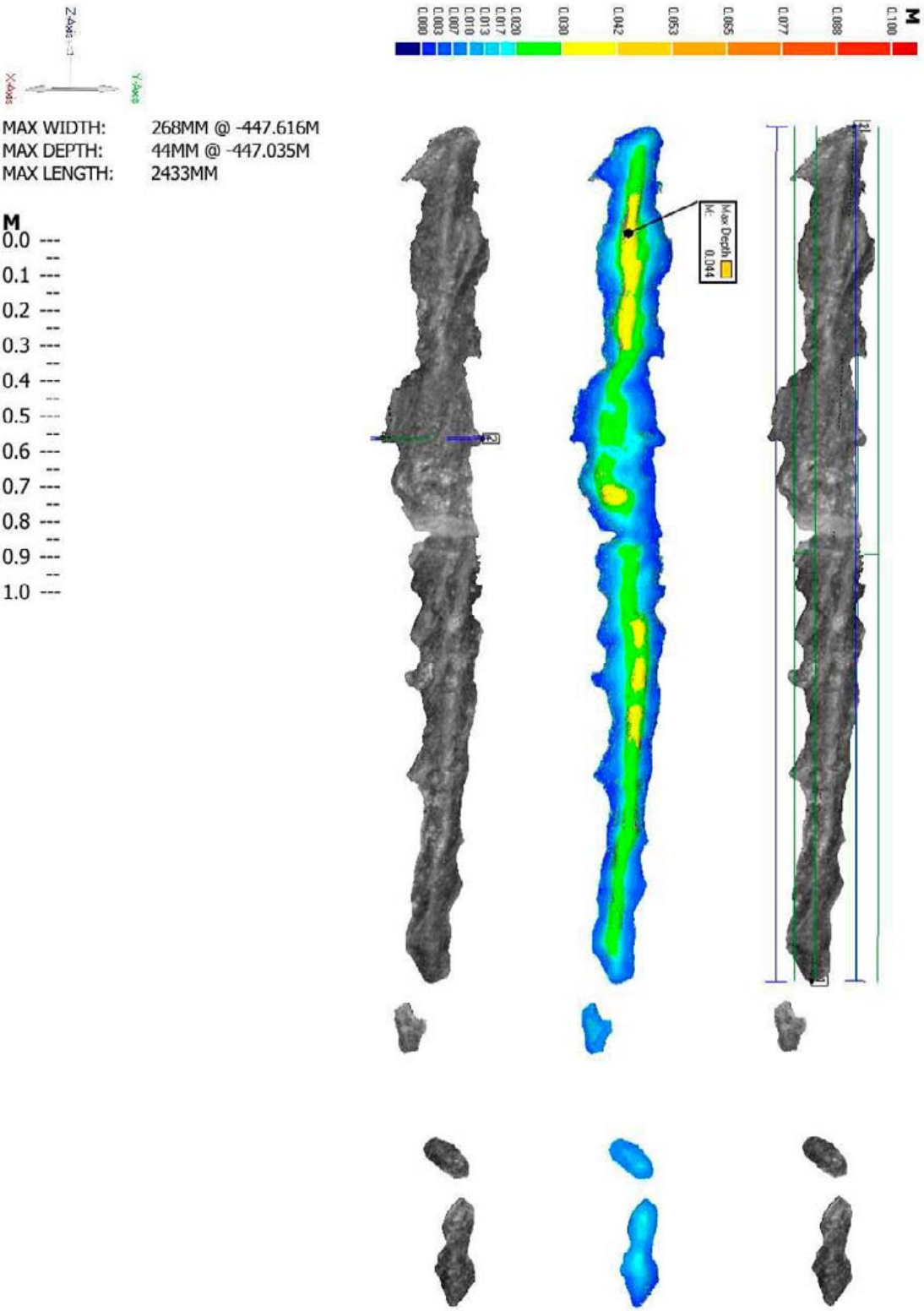

Max dimensions for KQ0051G04, sector BC SW-side

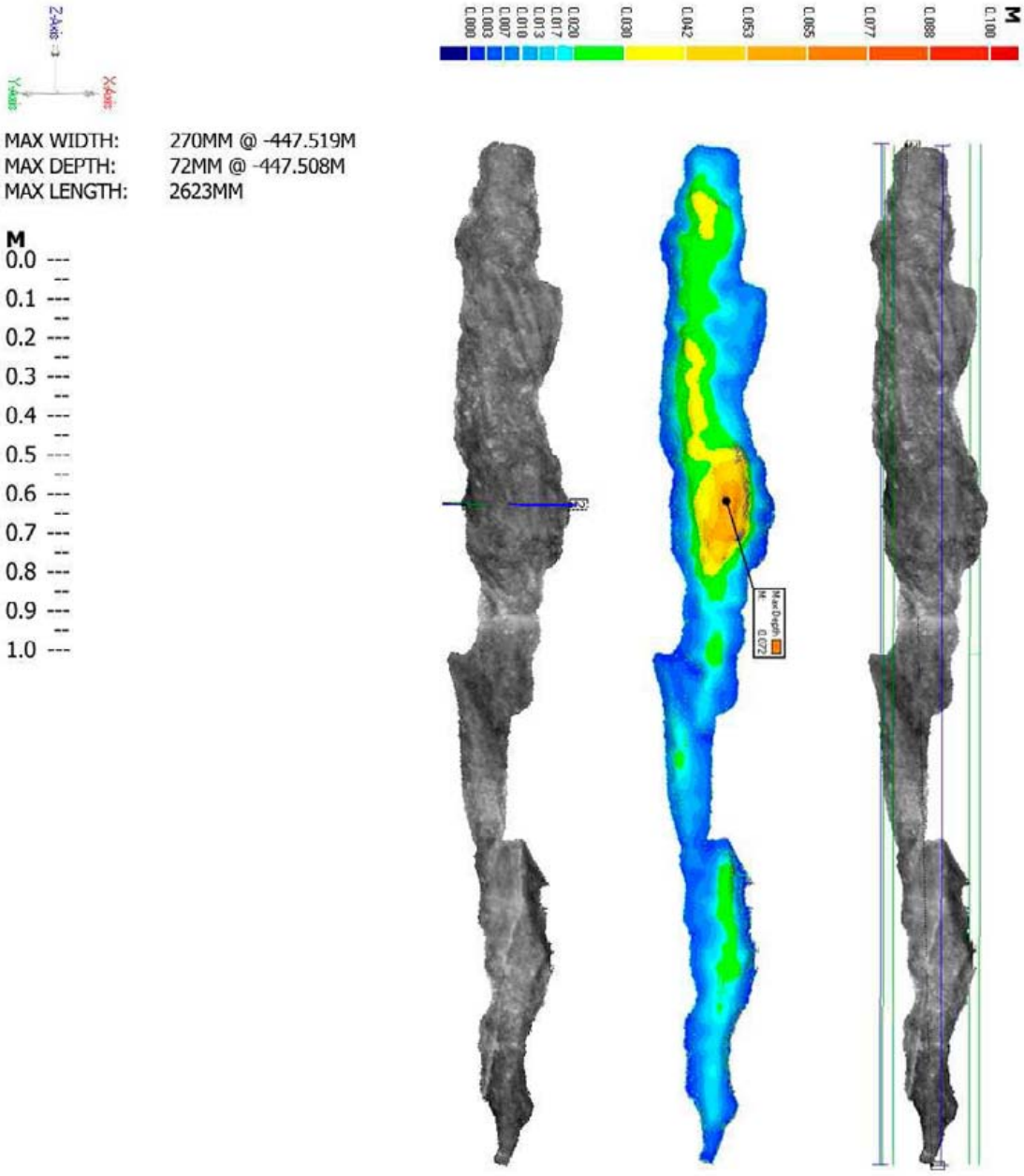

Volume determination for KQ0051G04, sector AD NE-side. Projection from outside.

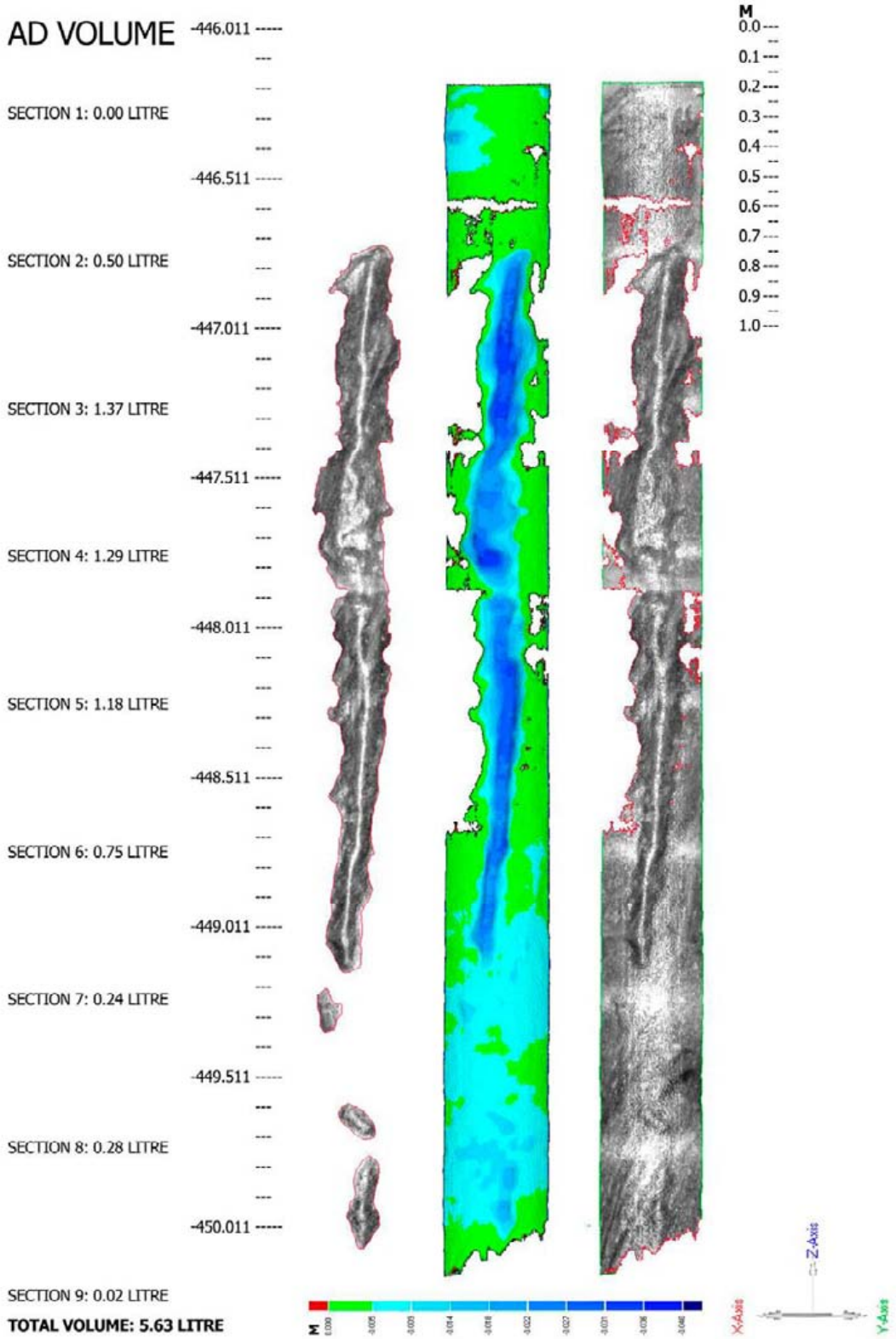

Volume determination for KQ0051G04, sector BC SW-side. Projection from outside.

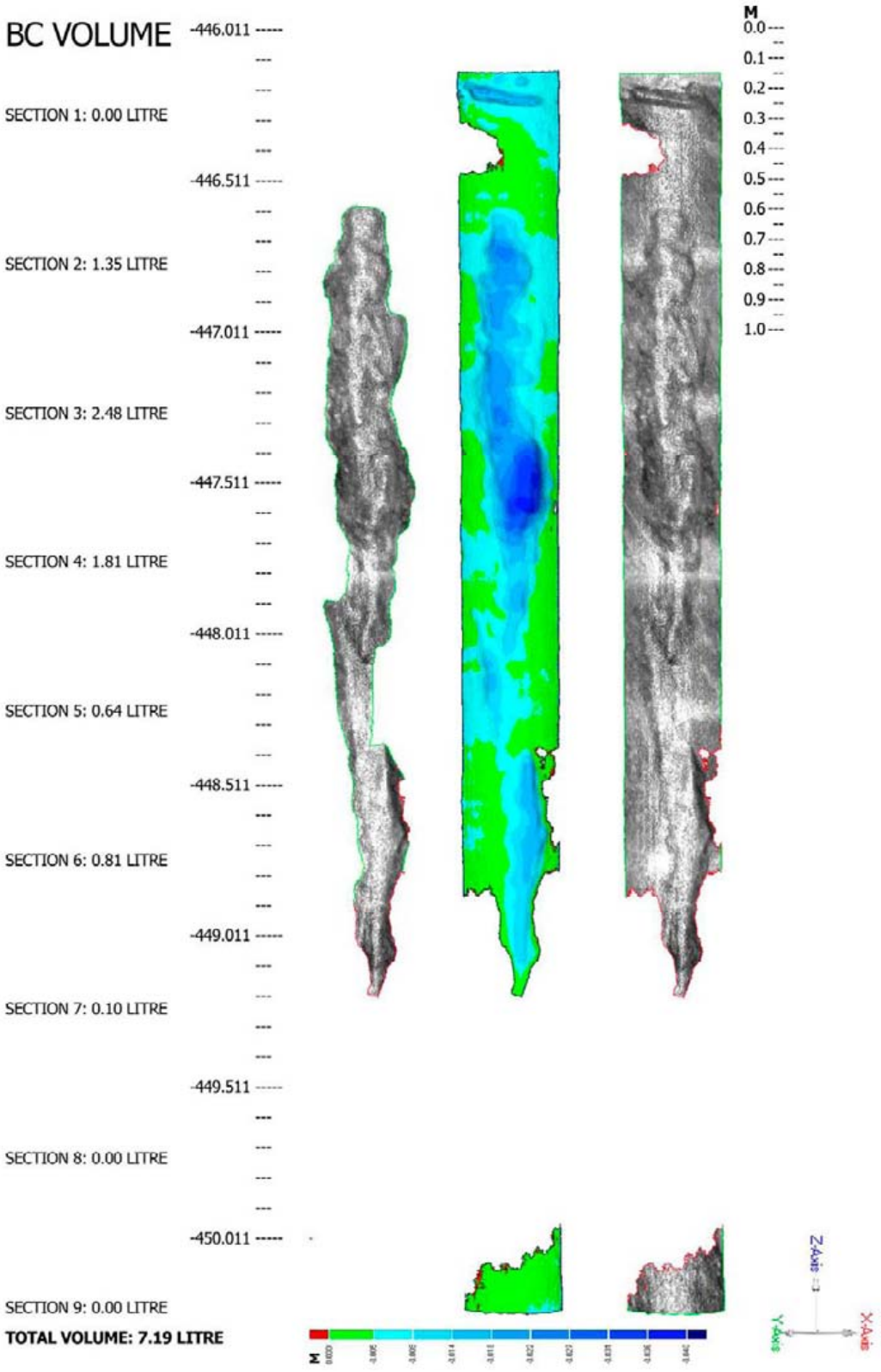

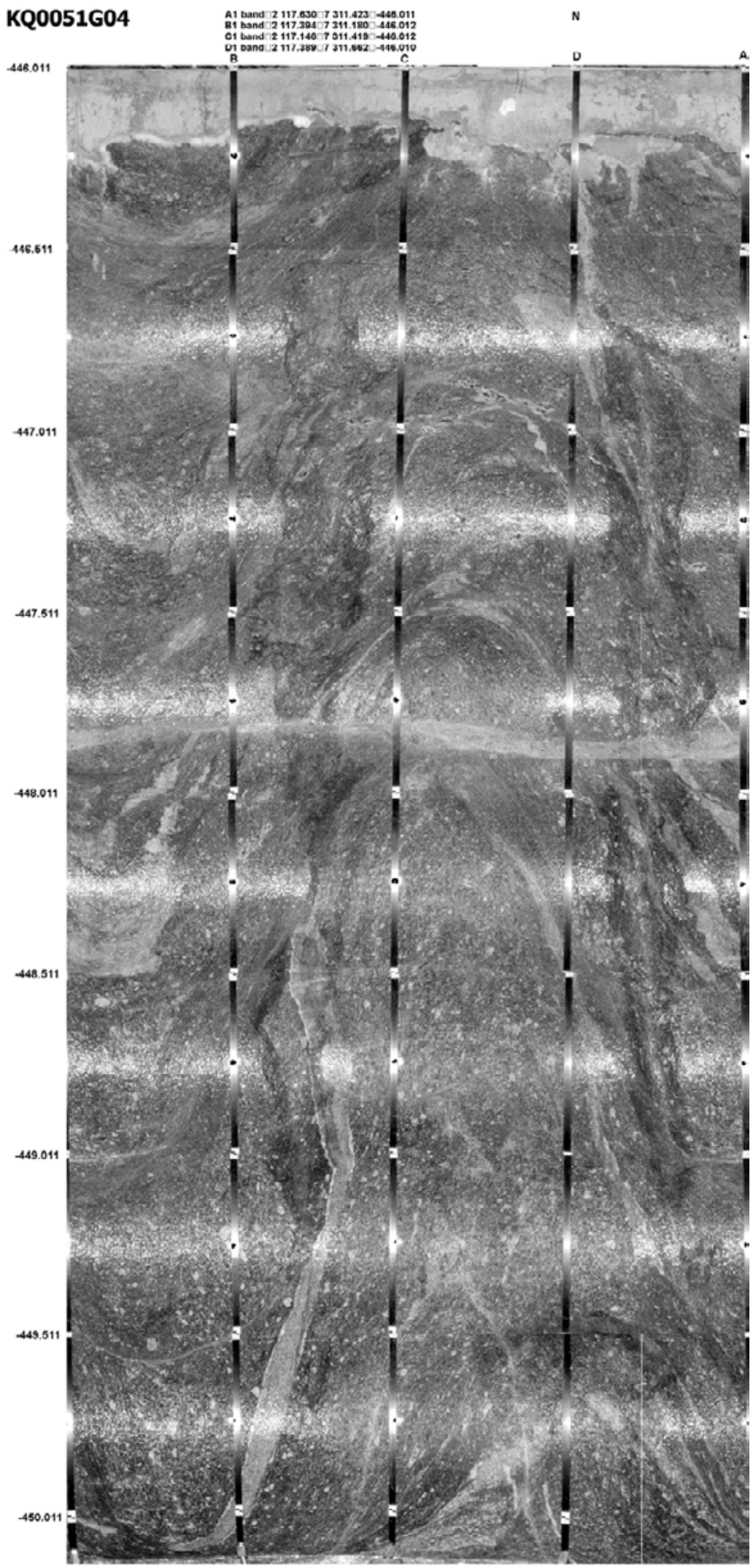
KQ0051G04
A1 band 2 117.630 7 311.423 -446.011
B1 band 2 117.394 7 311.180 -446.012
C1 band 2 117.146 7 311.419 -446.012
D1 band 2 117.389 7 311.662 -446.010
N
B
C
D
A
-446.011
-446.511
-447.011
-447.511
-448.011
-448.511
-449.011
-449.511
-450.011

Crossections for KQ0051G05

40 crossections, 4mm wide, every 100mm, start at -446.118, end at -450.018

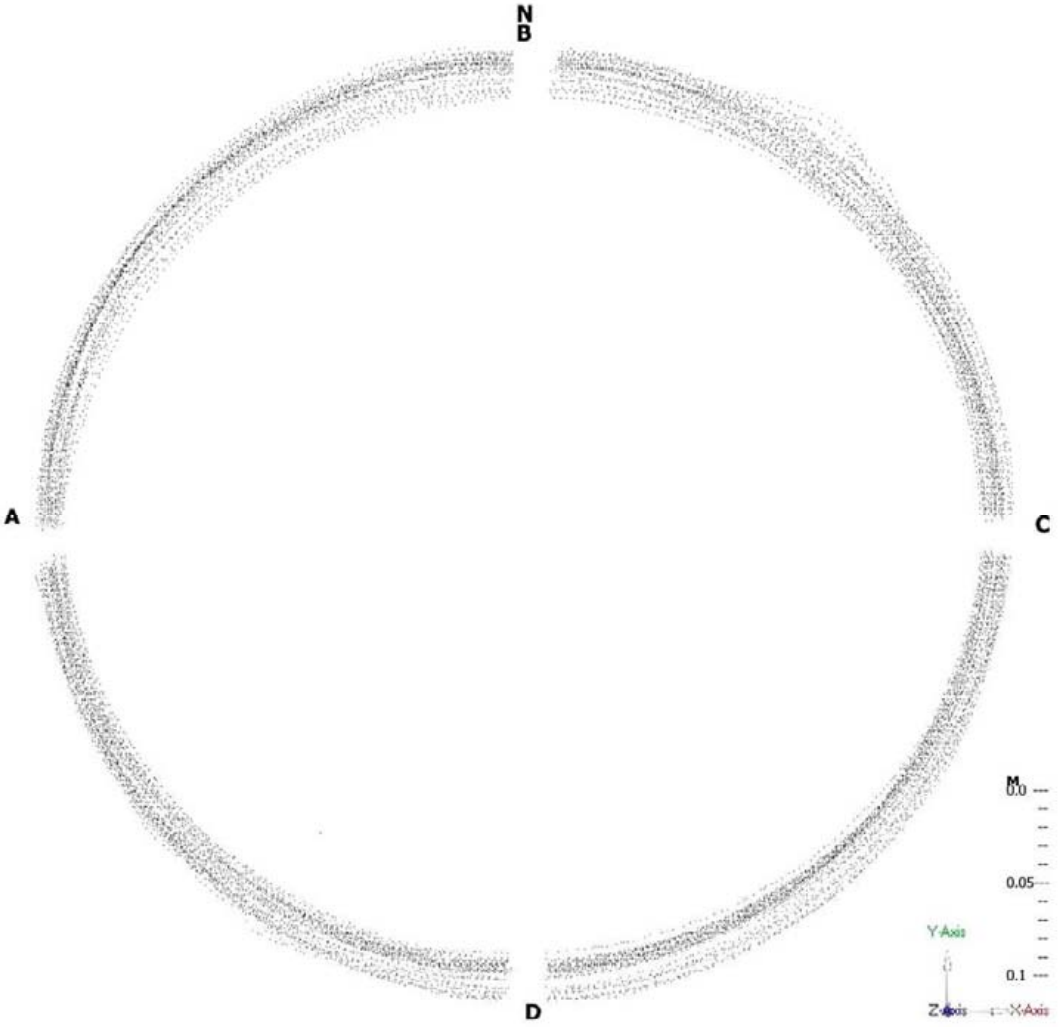

Max dimensions for KQ0051G05, sector BC NE-side

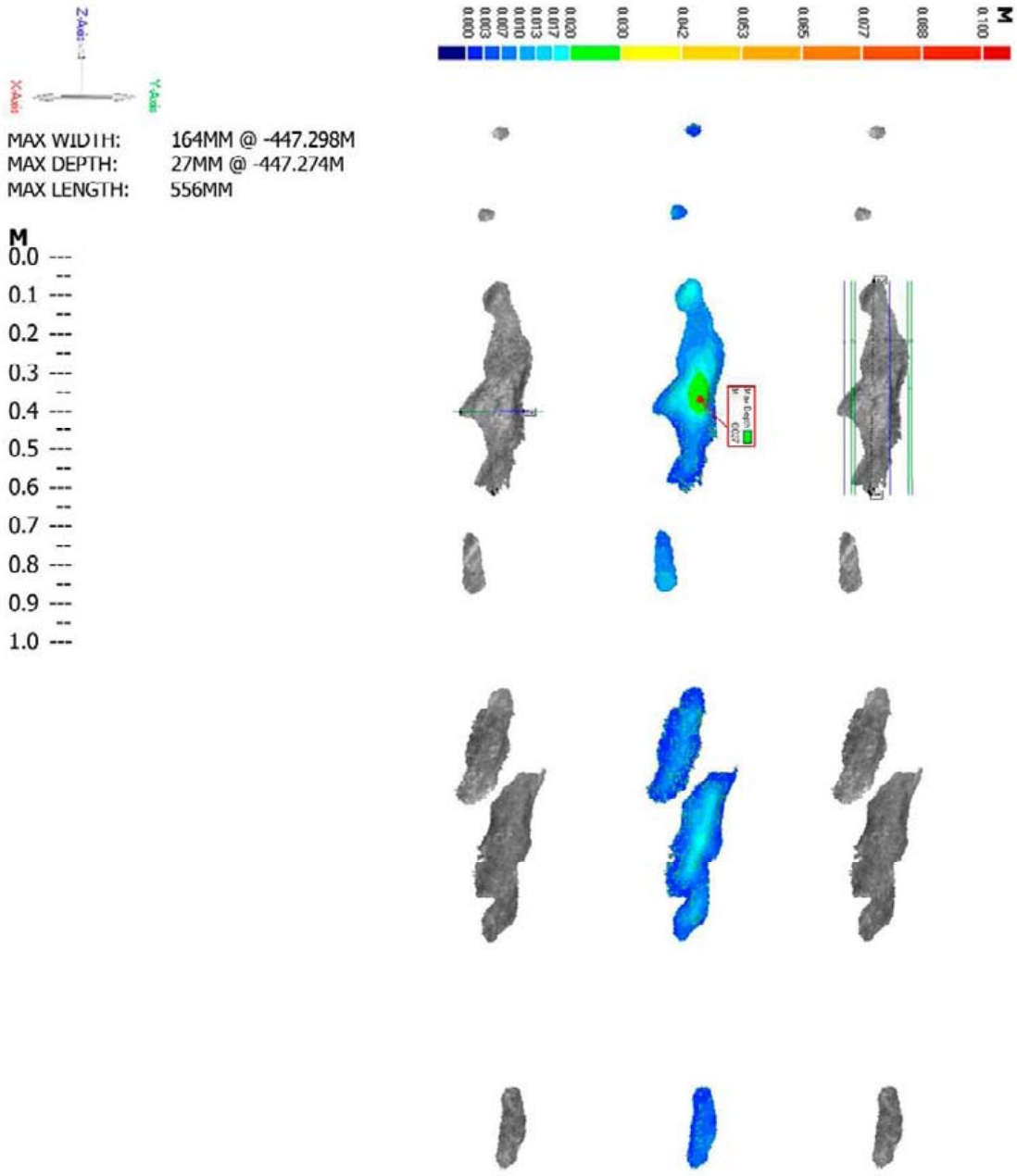

Max dimensions for KQ0051G05, sector AD SW-side

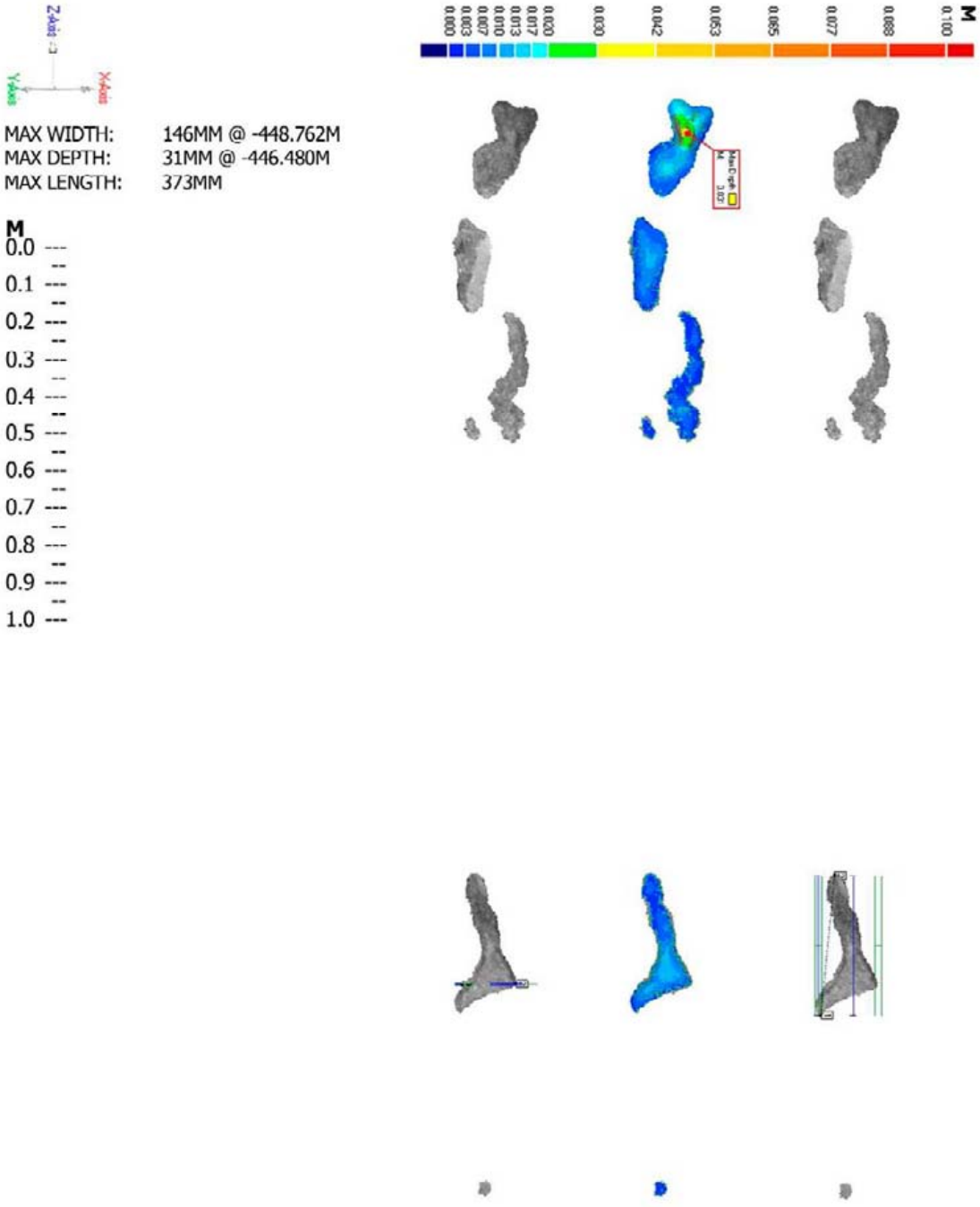

Volume determination for KQ0051G05, sector BC NE-side. Projection from outside.

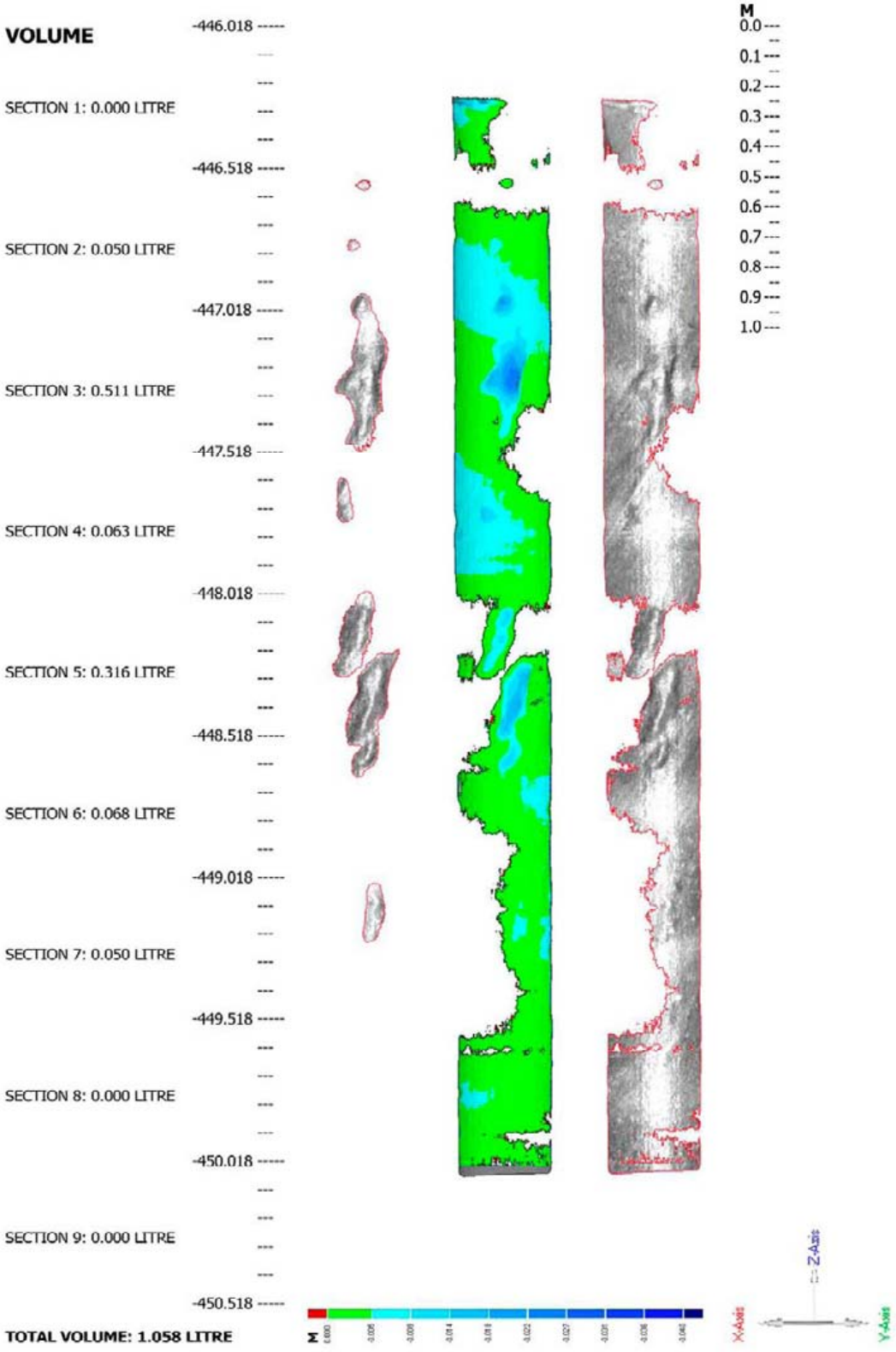

Volume determination for KQ0051G05, sector AD SW-side. Projection from outside.

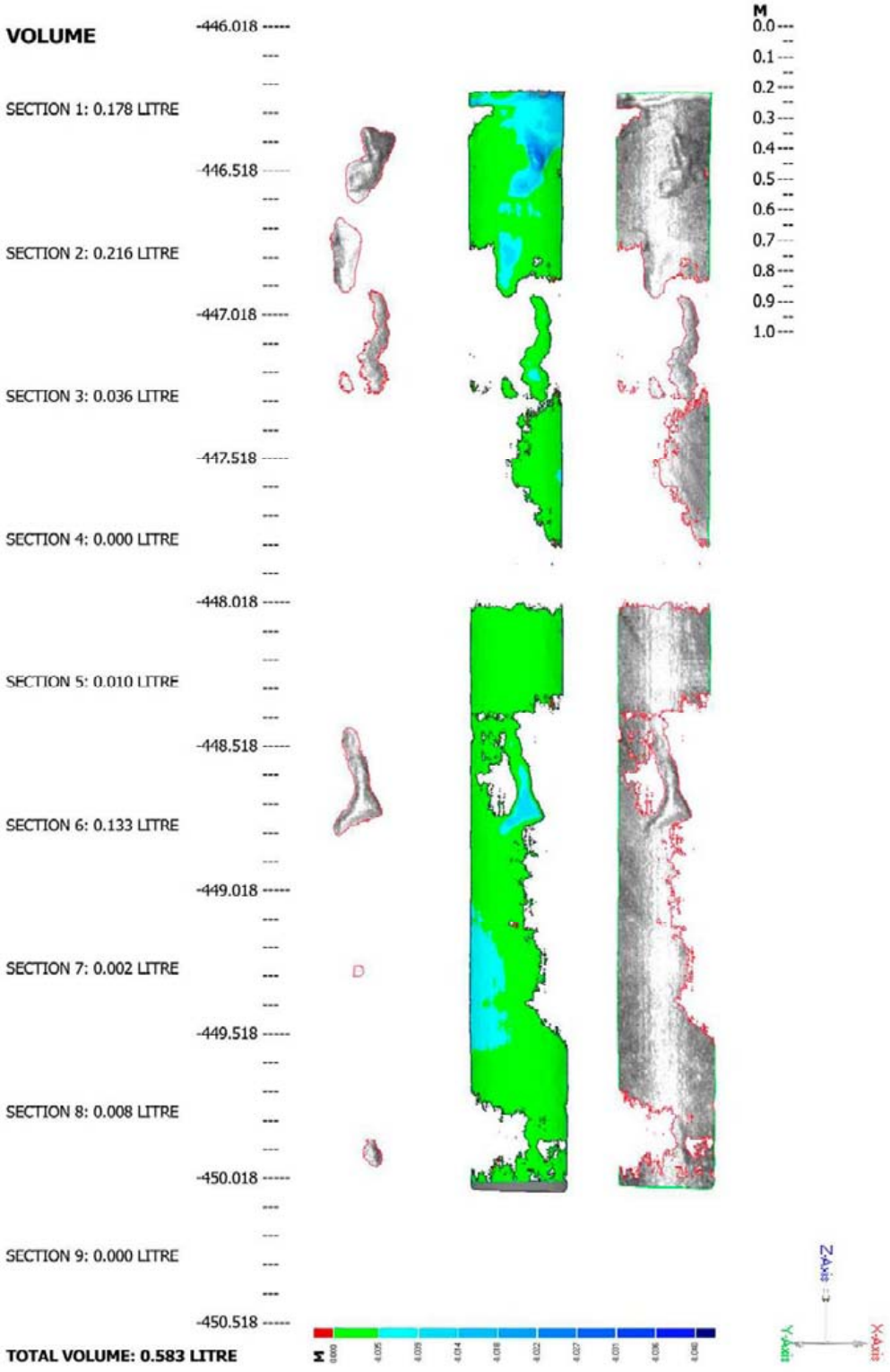

KQ0051G05

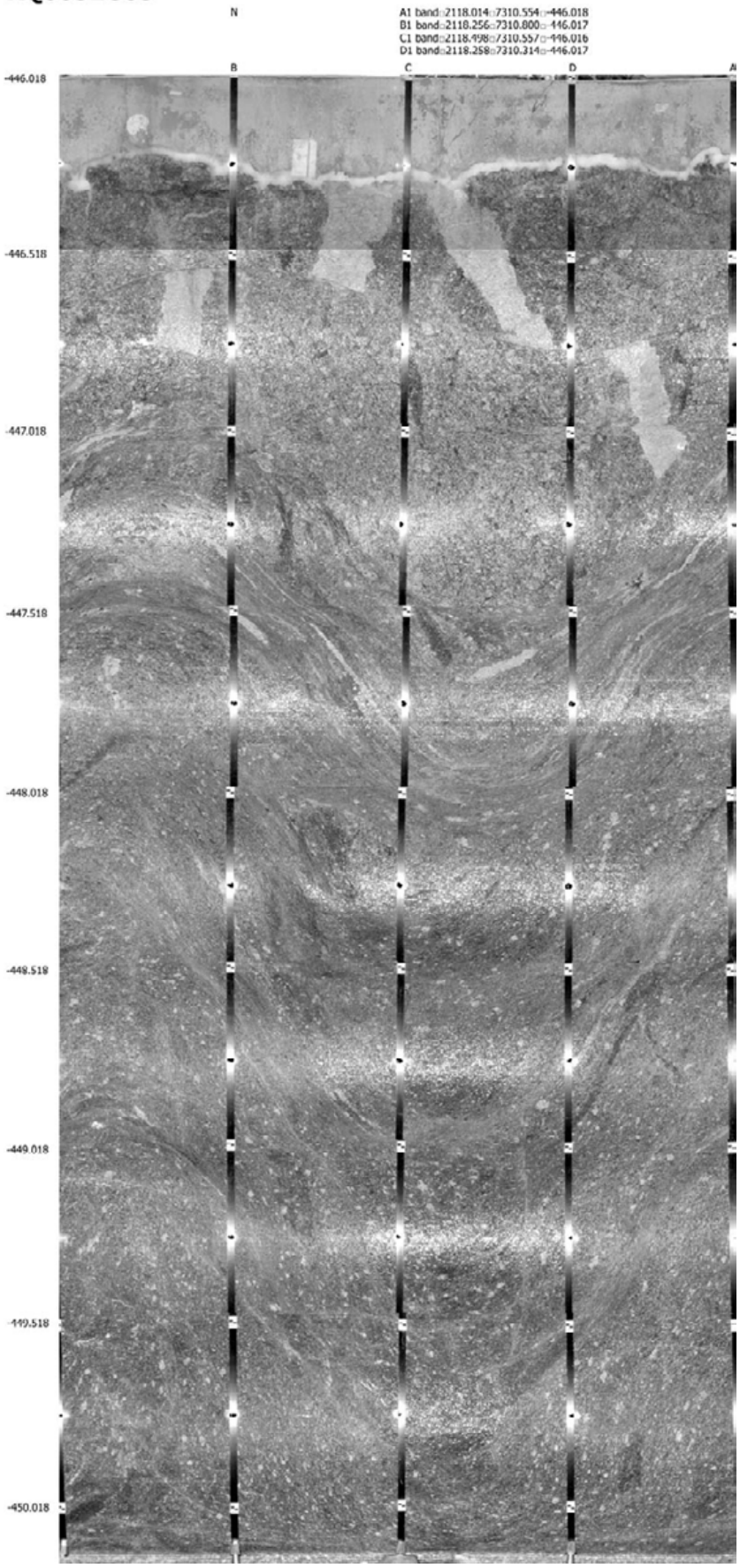
N
A1 band□2118.014□7310.554□-446.018
B1 band□2118.256□7310.800□-446.017
C1 band□2118.498□7310.557□-446.016
D1 band□2118.258□7310.314□-446.017
B
C
D
A
-446.018
-446.518
-447.018
-447.518
-448.018
-448.518
-449.018
-449.518
-450.018

Crossections for KQ0048G04

40 crossections, 4mm wide, every 100mm, start at -446.115, end at -450.015

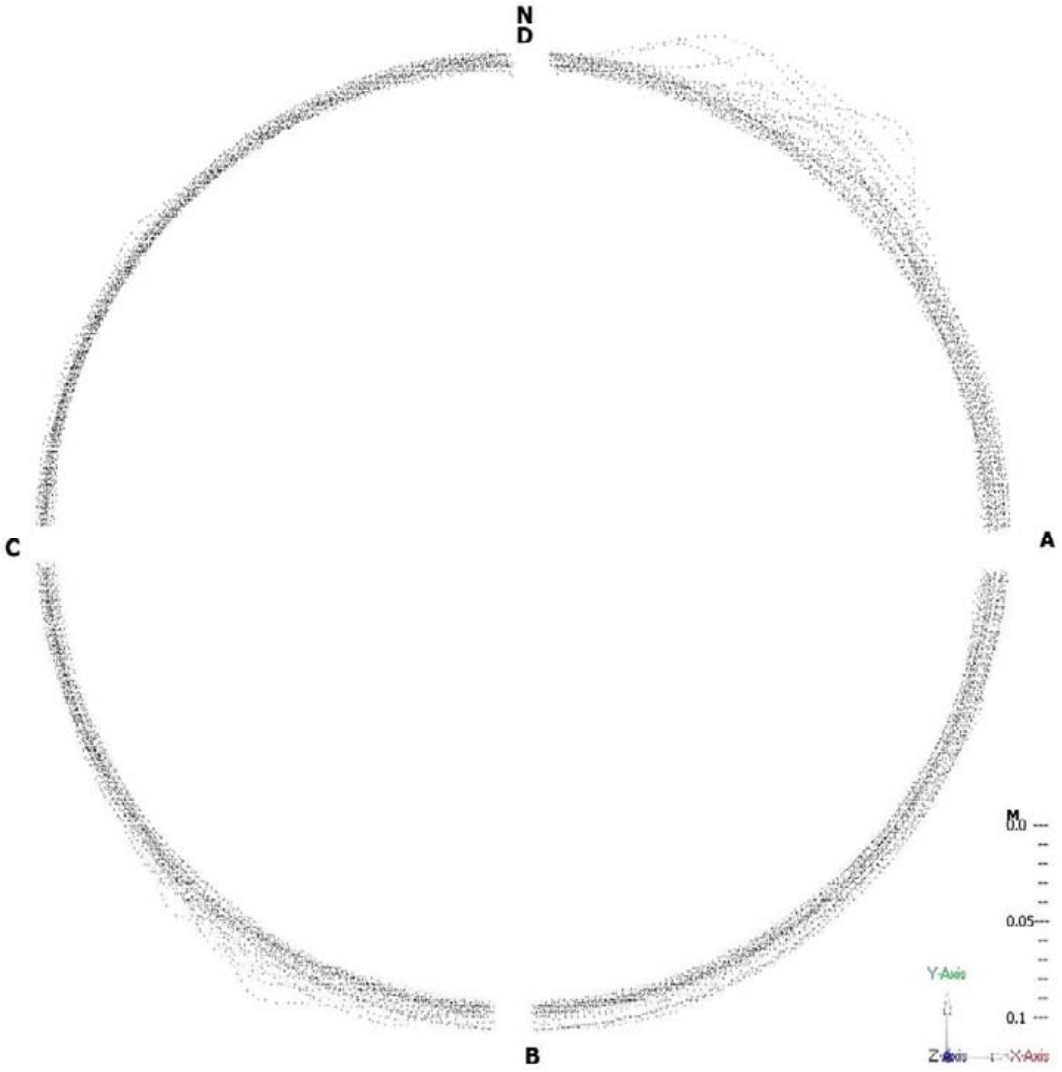

Max dimensions for KQ0048G04, sector AD NE-side

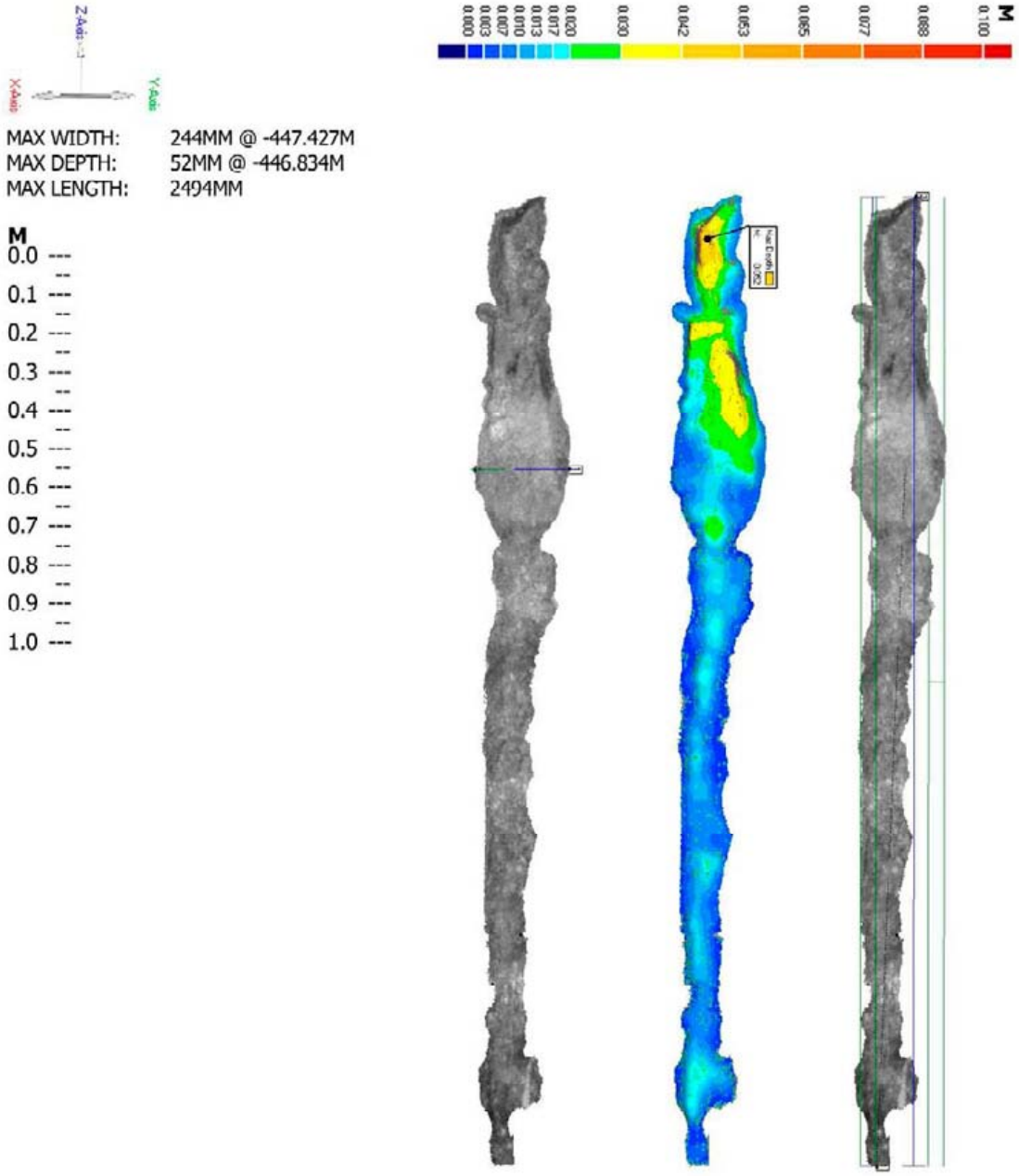

Max dimensions for KQ0048G04, sector BC SW-side

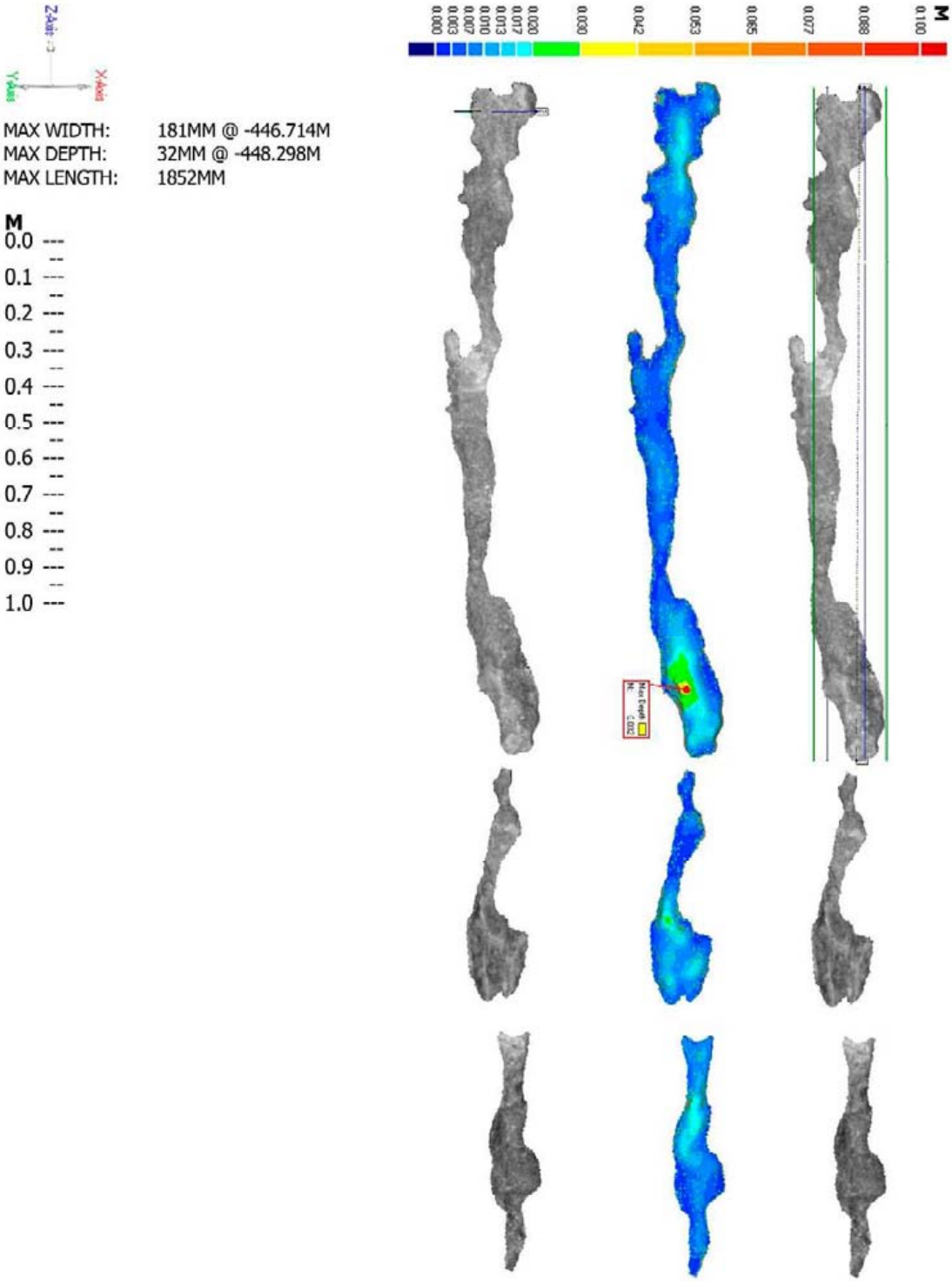

Volume determination for KQ0048G04, sector AD NE-side. Projection from outside

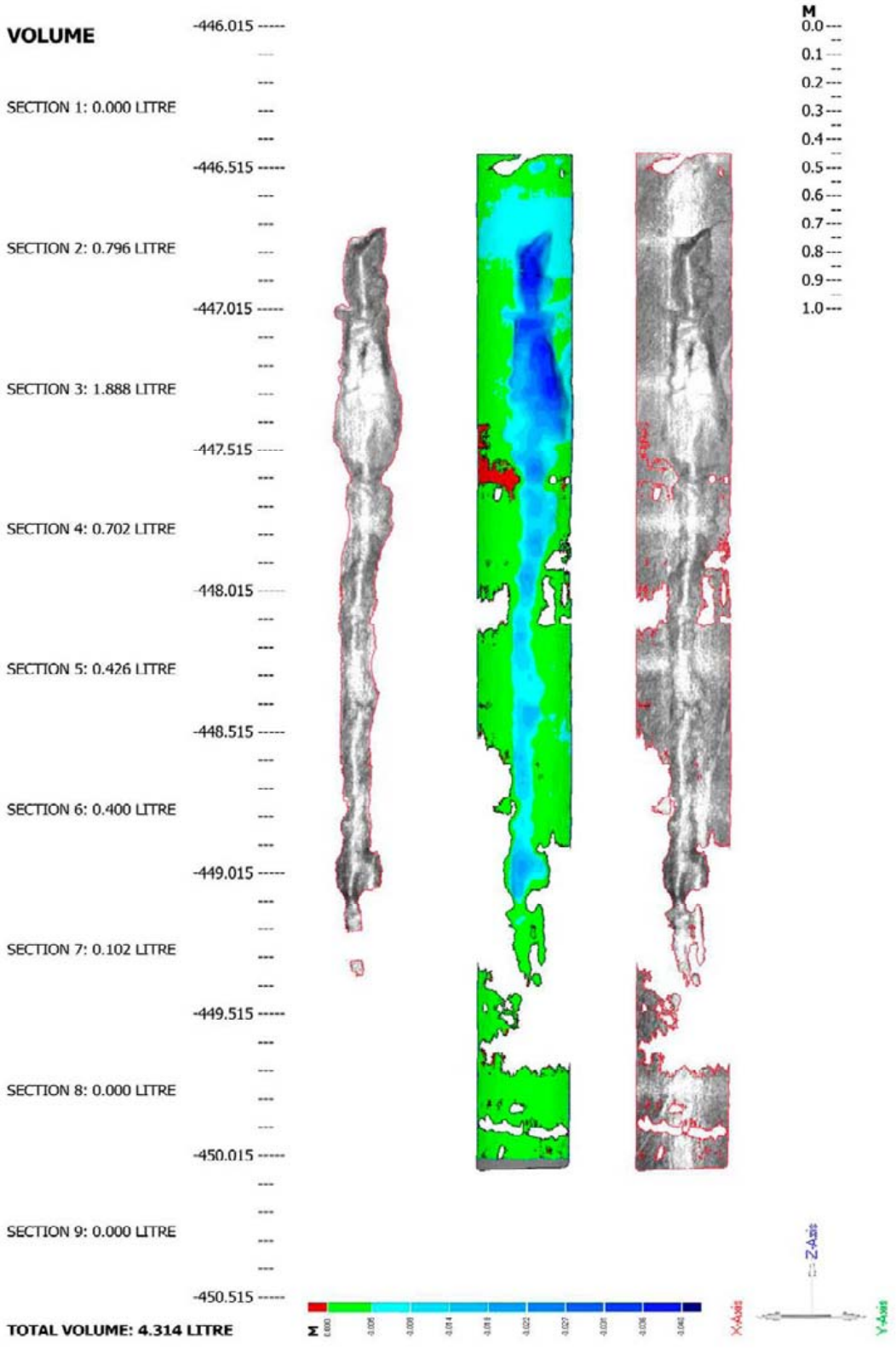

Volume determination for KQ0048G04, sector BC SW-side. Projection from outside

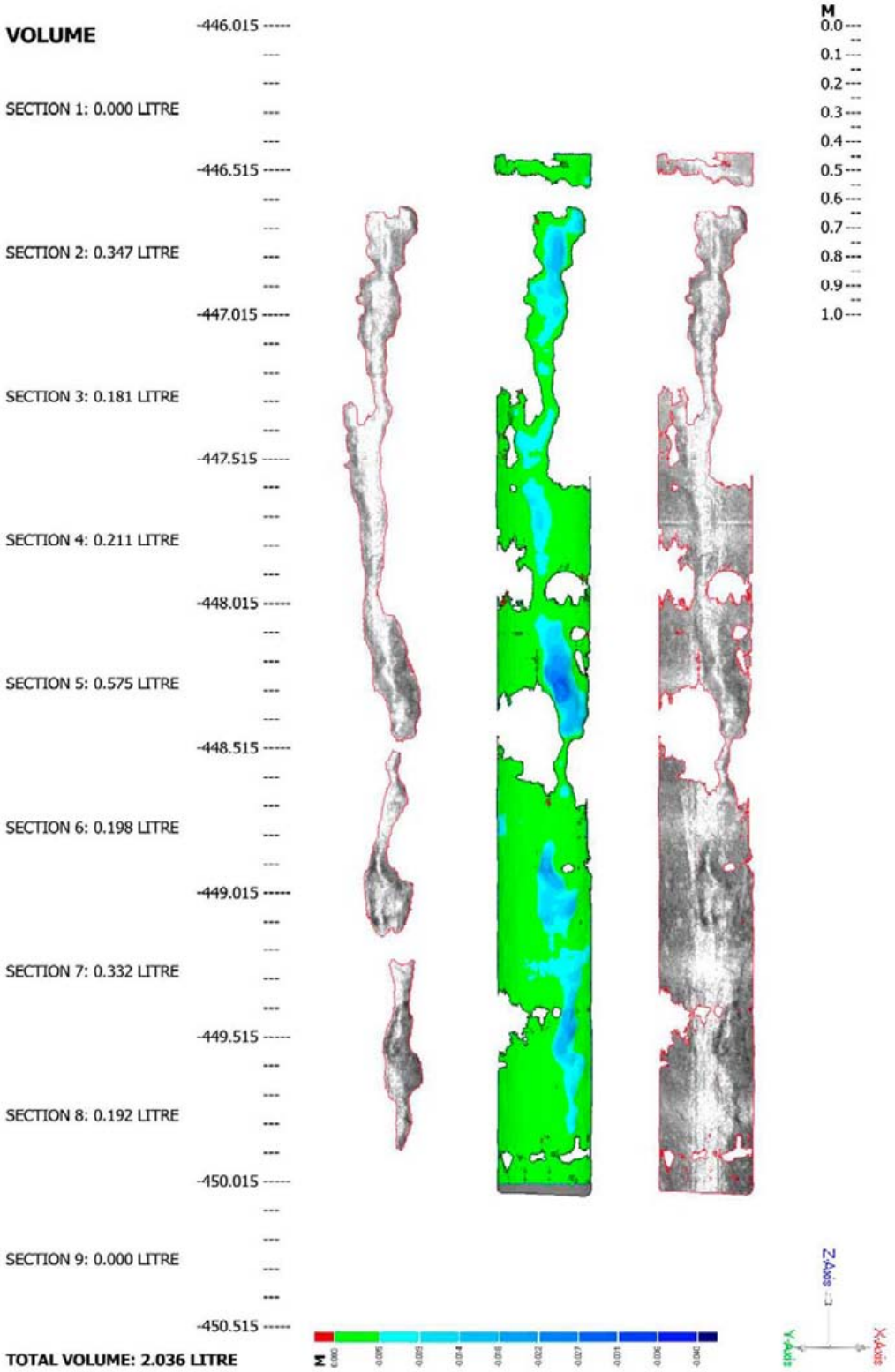

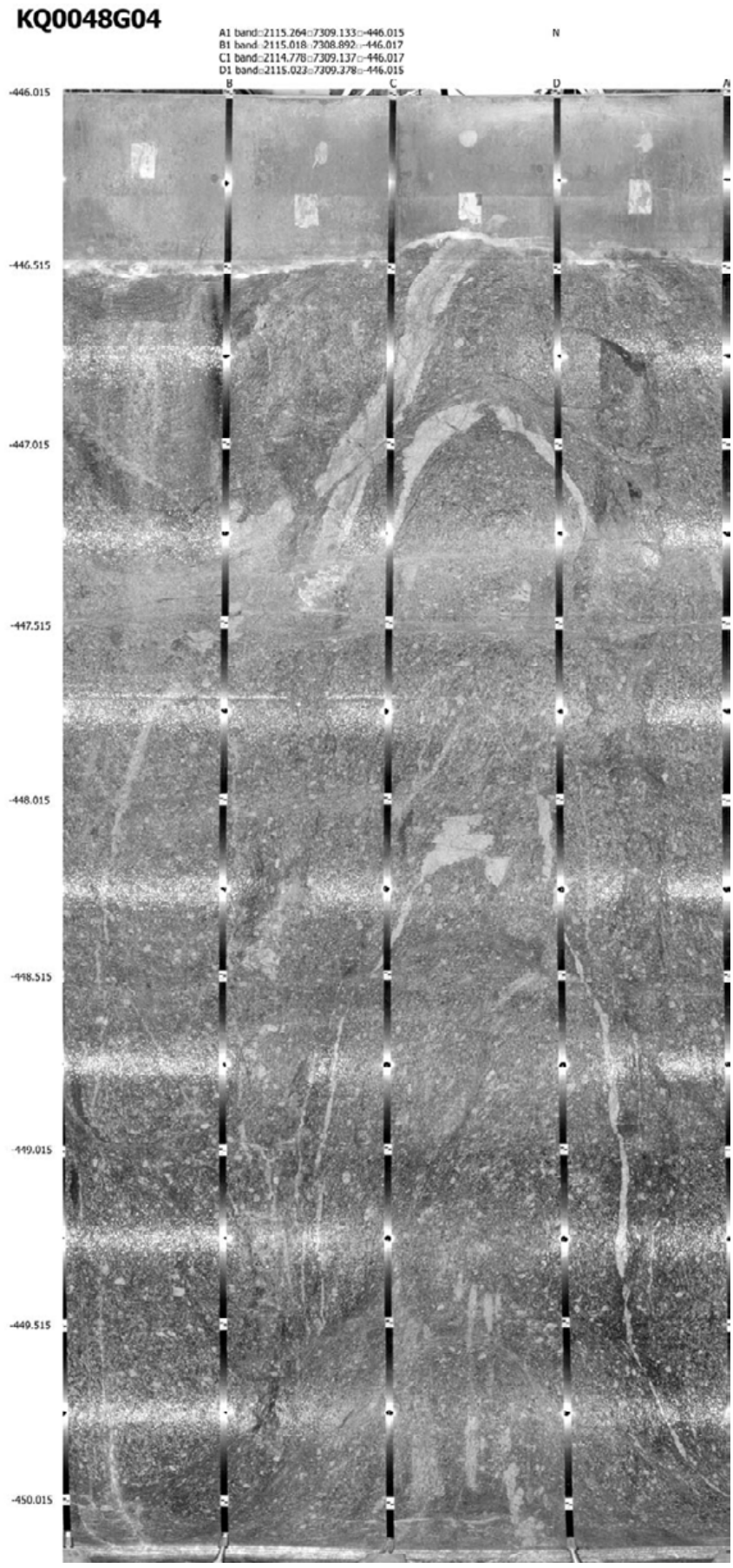
KQ0048G04
A1 band□2115.264□7309.133□-446.015
B1 band□2115.018□7308.892□-446.017
C1 band□2114.778□7309.137□-446.017
D1 band□2115.023□7309.378□-446.015
N
B
C
D
-446.015
-446.515
-447.015
-447.515
-448.015
-448.515
-449.015
-449.515
-450.015

Crossections for KQ0048G05

40 crossections, 4mm wide, every 100mm, start at -446.116, end at -450.016

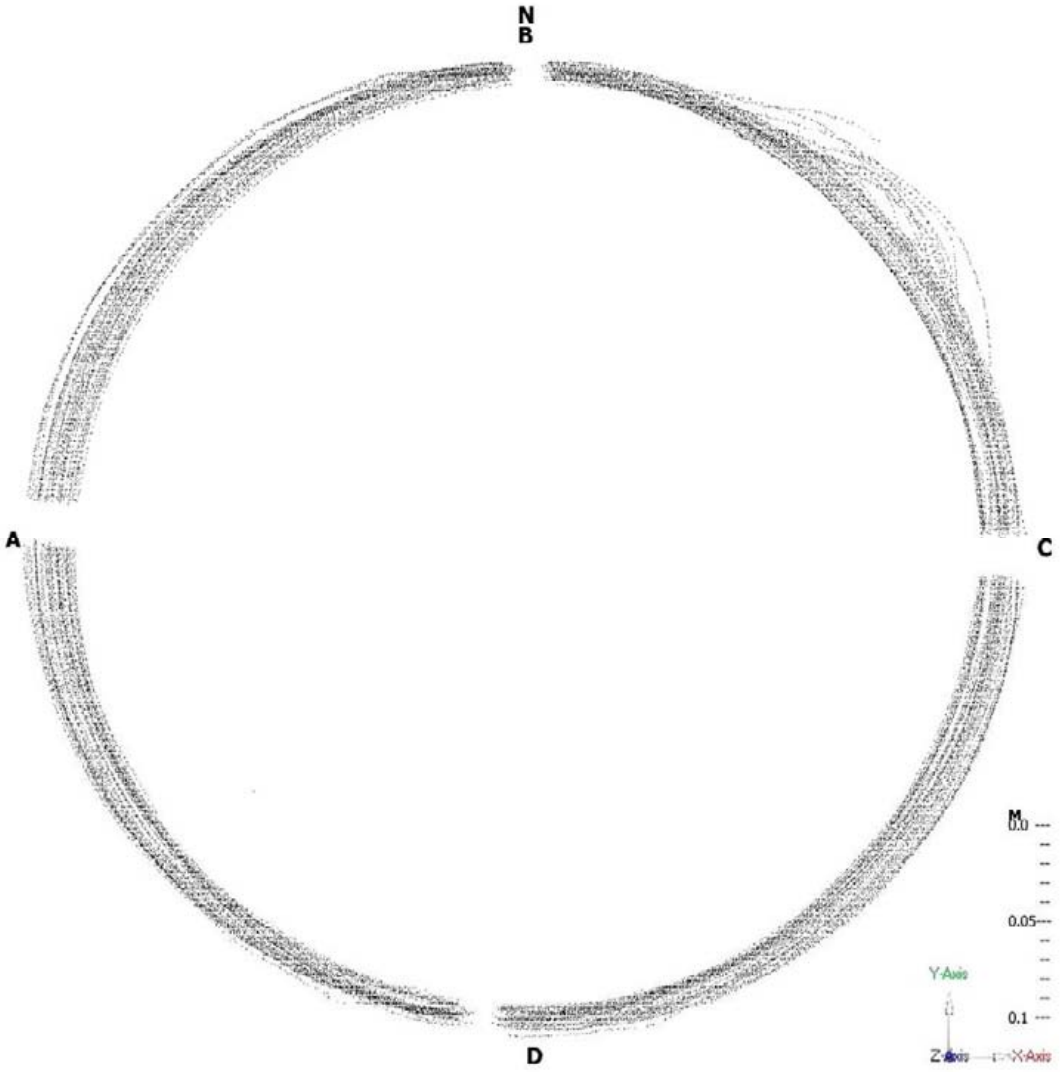

Max dimensions for KQ0048G05, sector BC NE-side

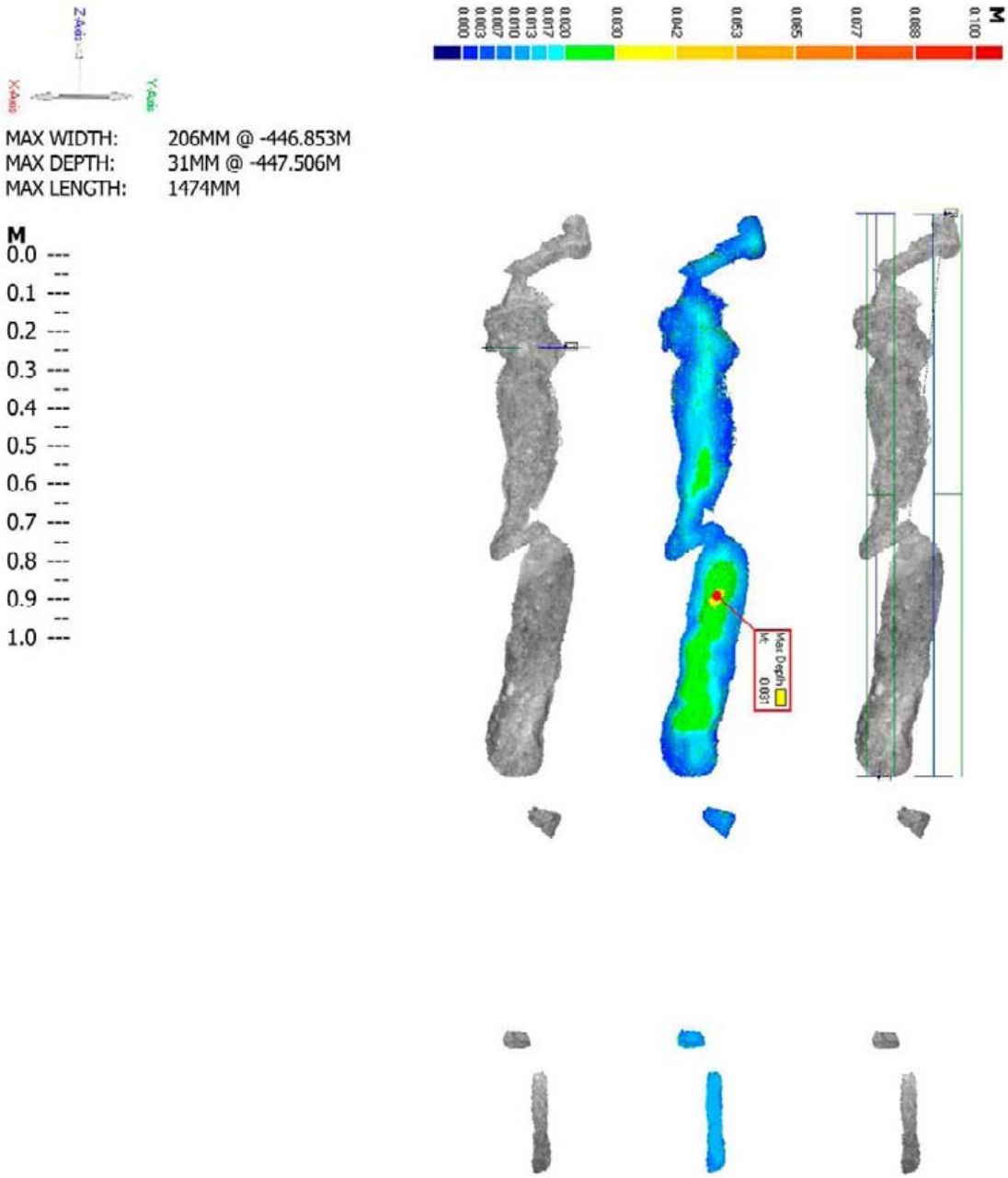

Max dimensions for KQ0048G05, sector AD SW-side

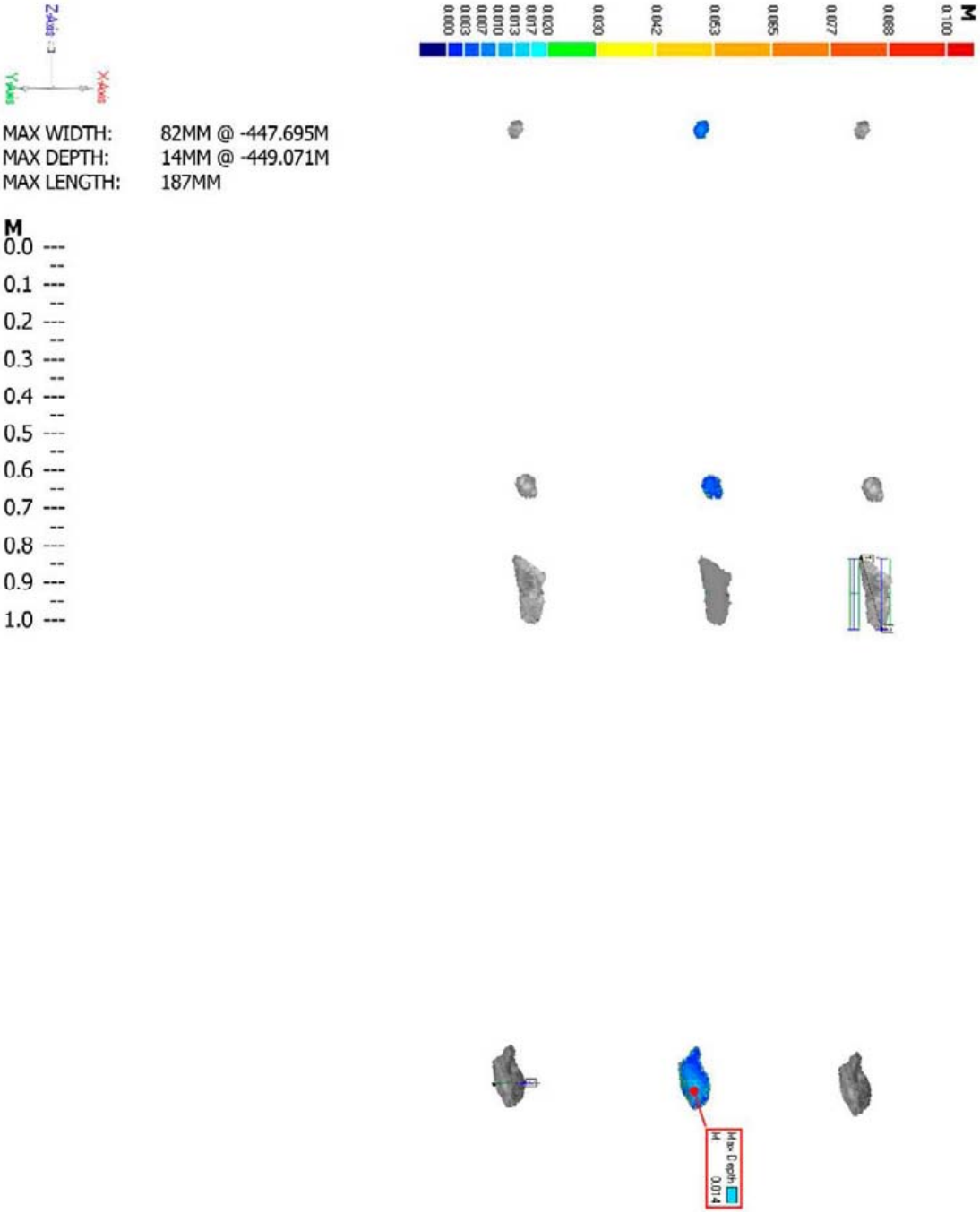

Volume determination for KQ0048G05, sector BC NE-side. Projection from outside.

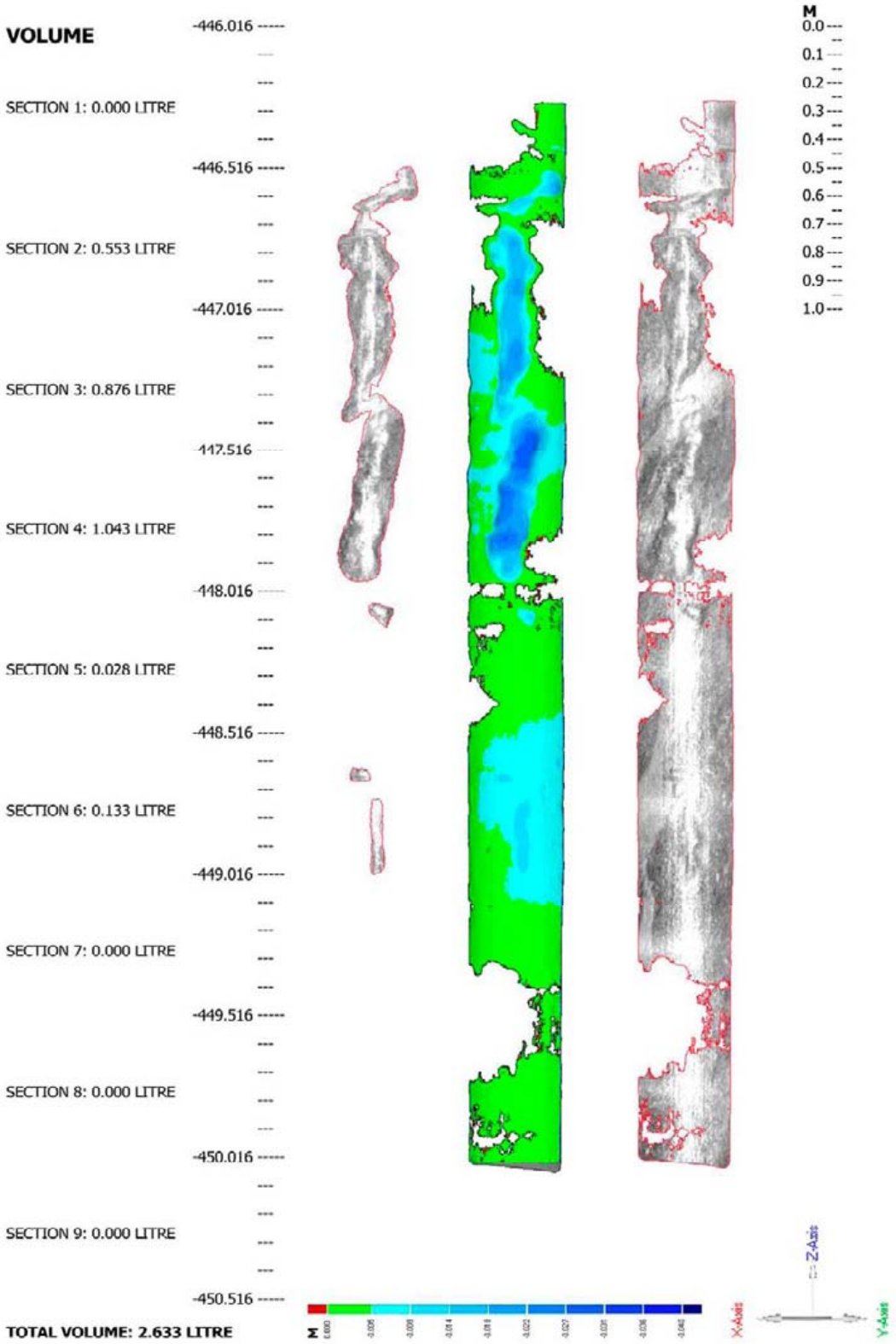

Volume determination for KQ0048G05, sector AD SW-side. Projection from outside.

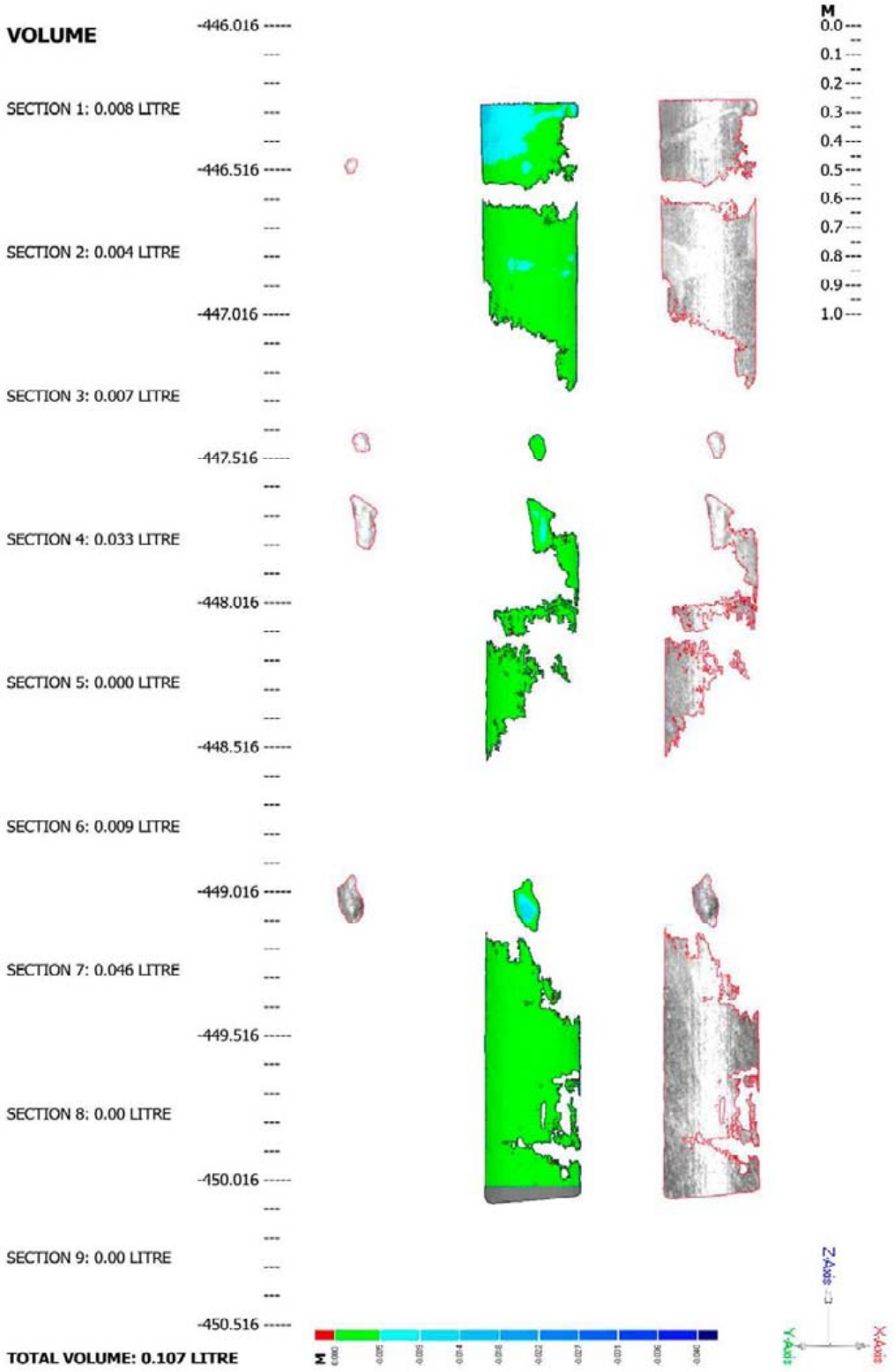

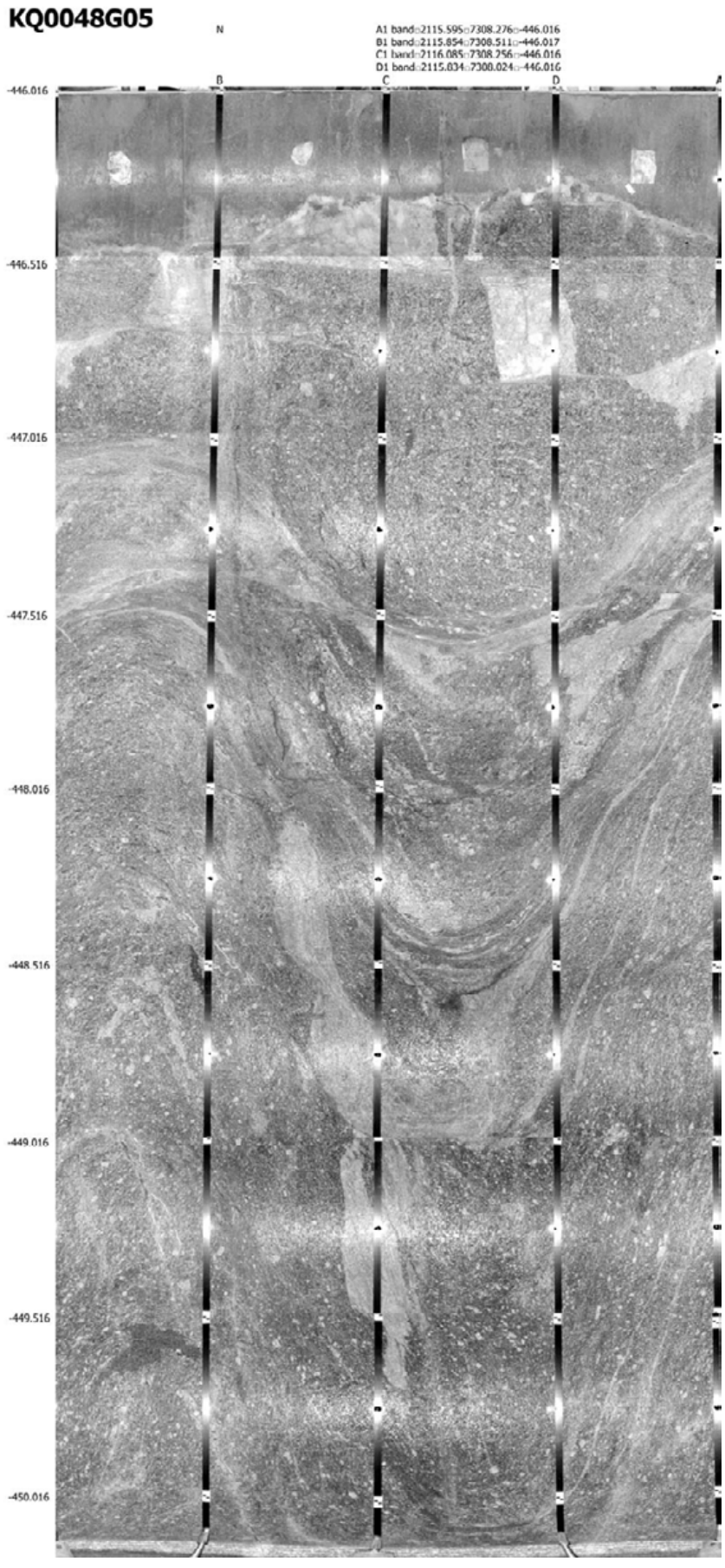
KQ0048G05
N
A1 band□2115.595□7308.276□-446.016
B1 band□2115.854□7308.511□-446.017
C1 band□2116.085□7308.256□-446.016
D1 band□2115.834□7308.024□-446.016
B
C
D
-446.016
-446.516
-447.016
-447.516
-448.016
-448.516
-449.016
-449.516
-450.016

Crossections for KQ0046G04

40 crossections, 4mm wide, every 100mm, start at -446.112, end at -450.012

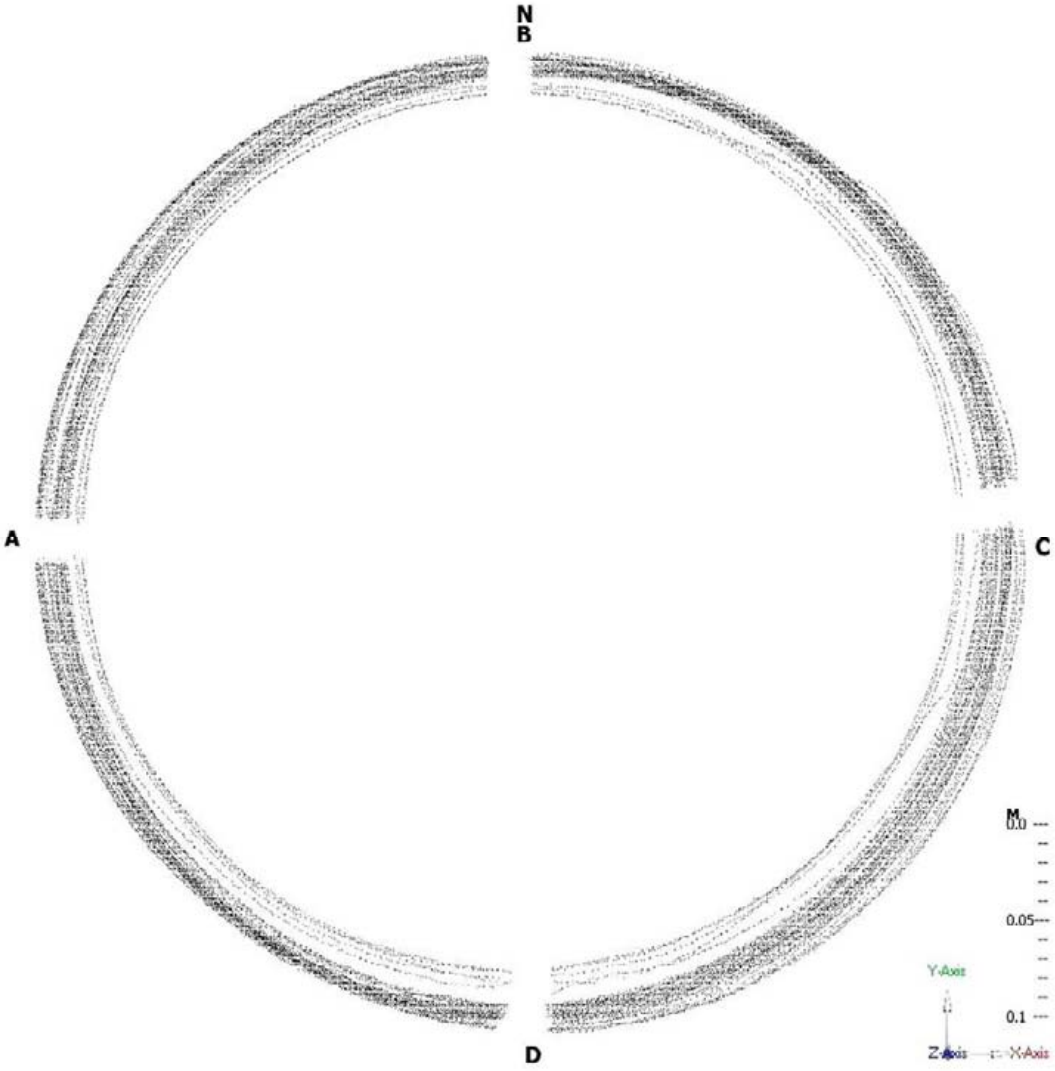

Max dimensions for KQ0046G04, sector BC NE-side

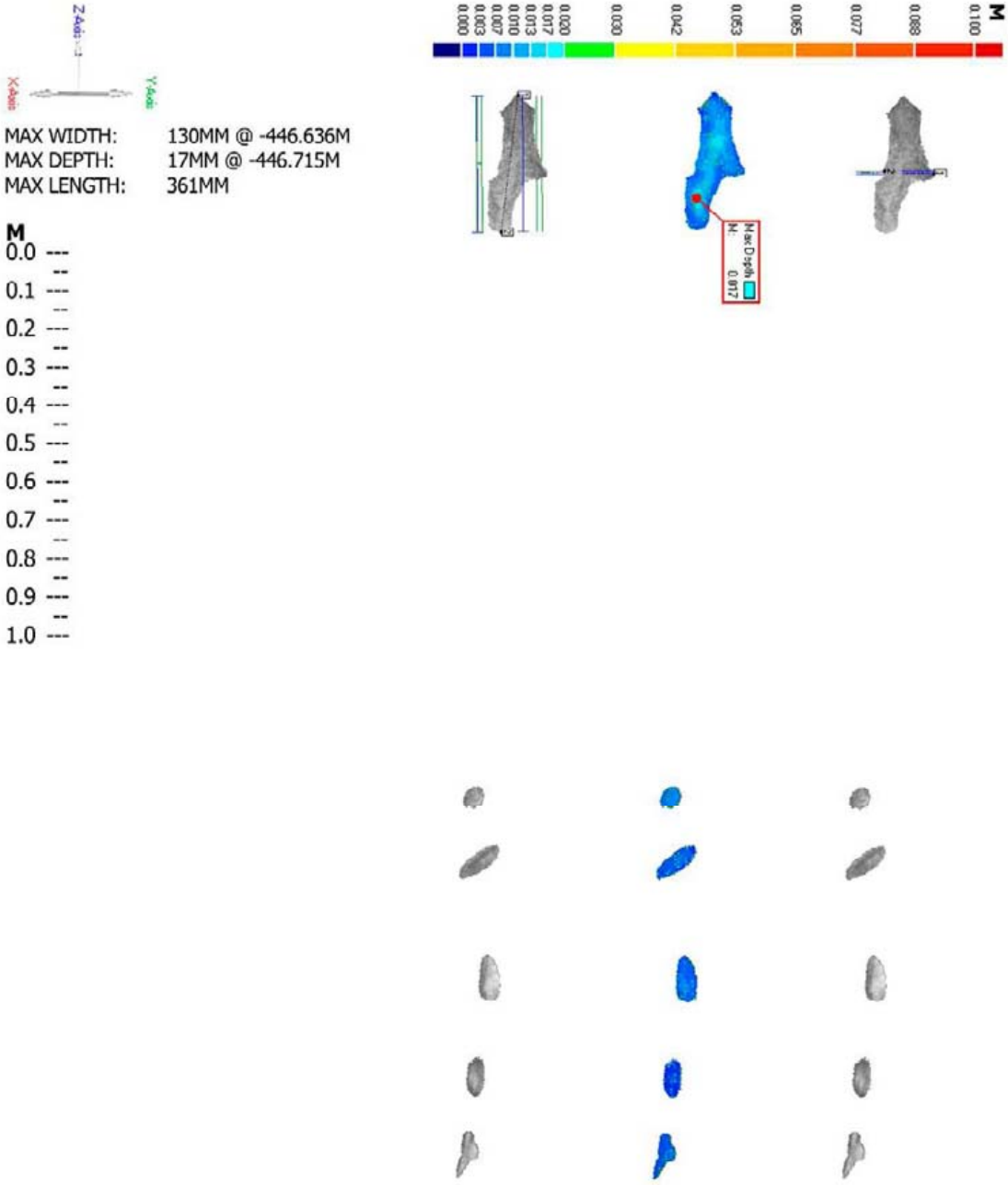

Max dimensions for KQ0046G04, sector AD SW-side

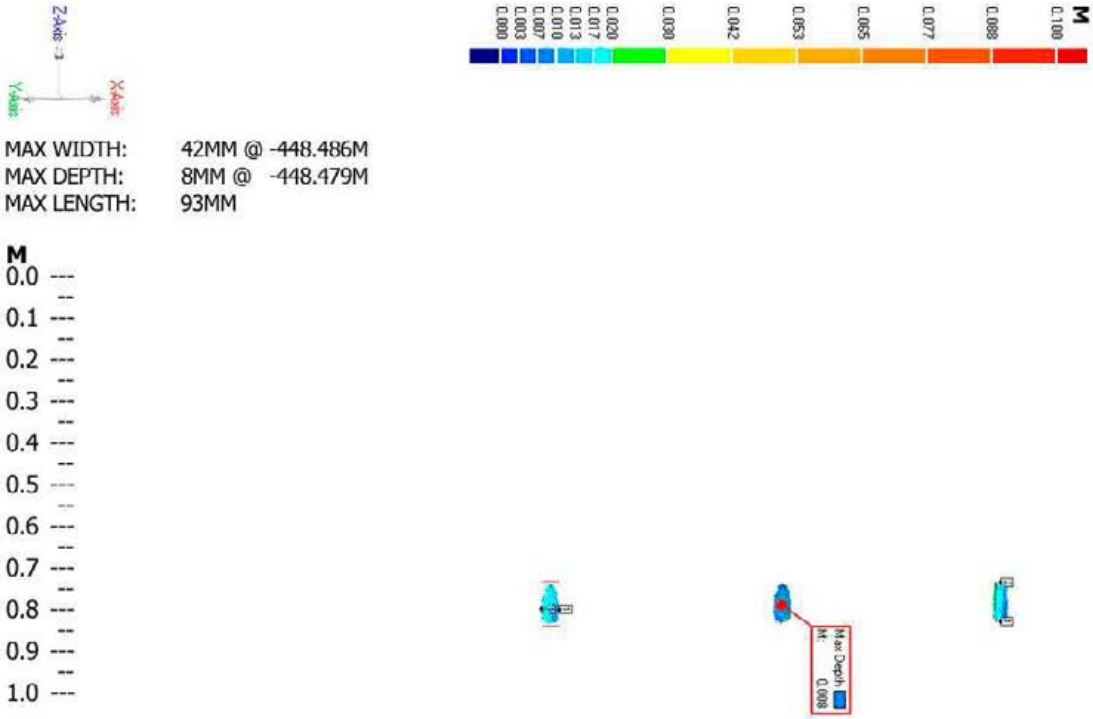

Volume determination for KQ0046G04, sector BC NE-side. Projection from outside.

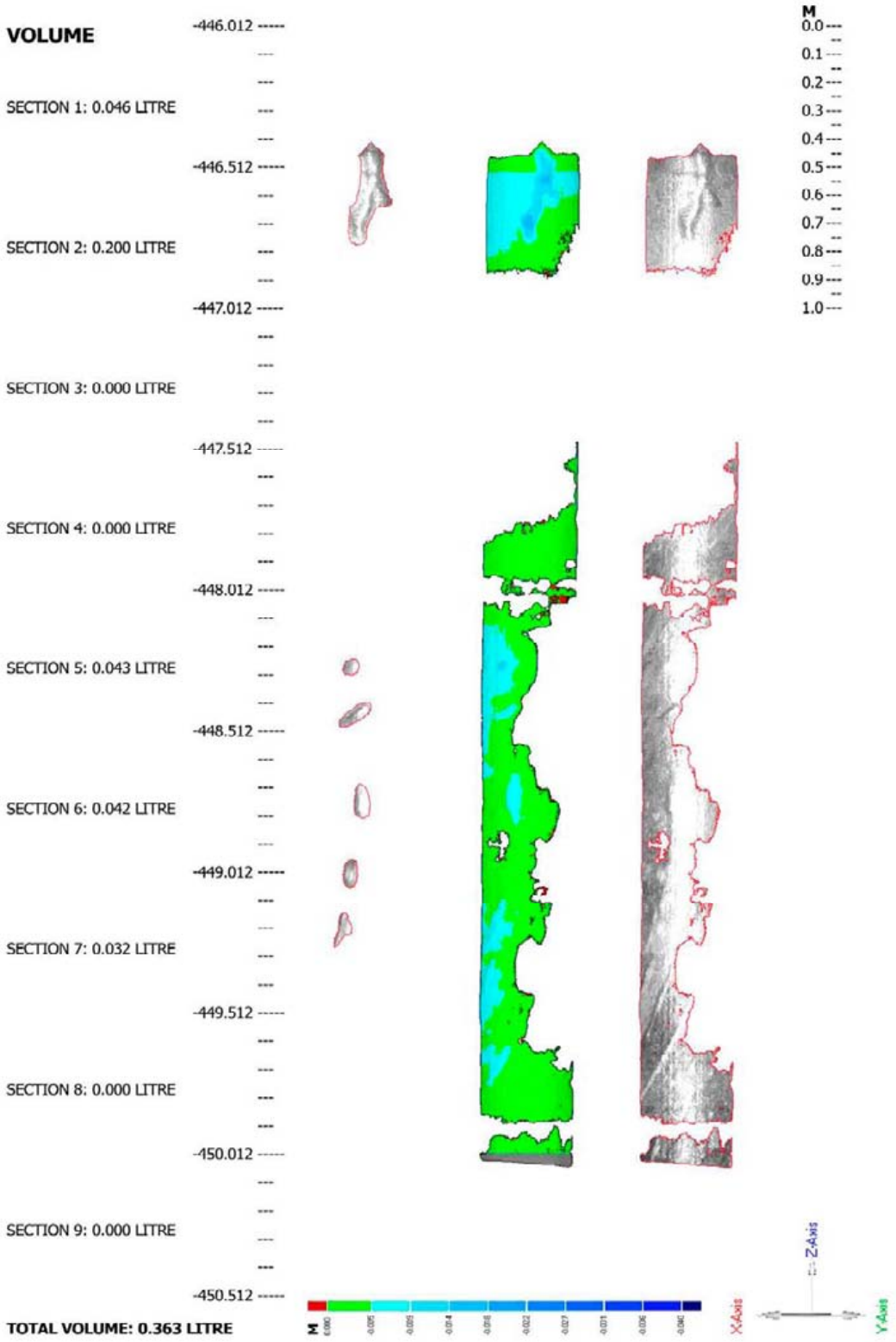

Volume determination for KQ0046G04, sector AD SW-side. Projection from outside.

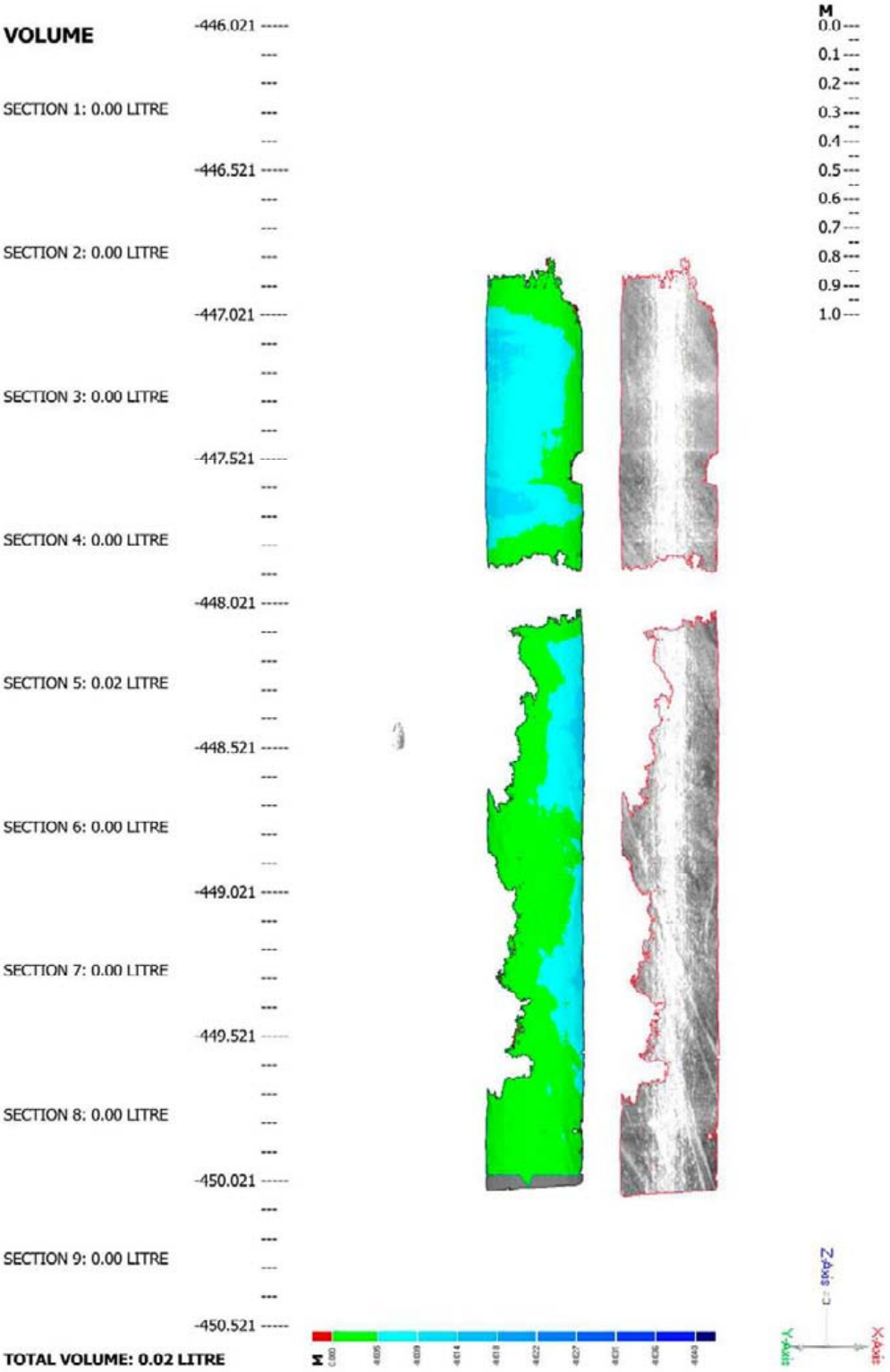

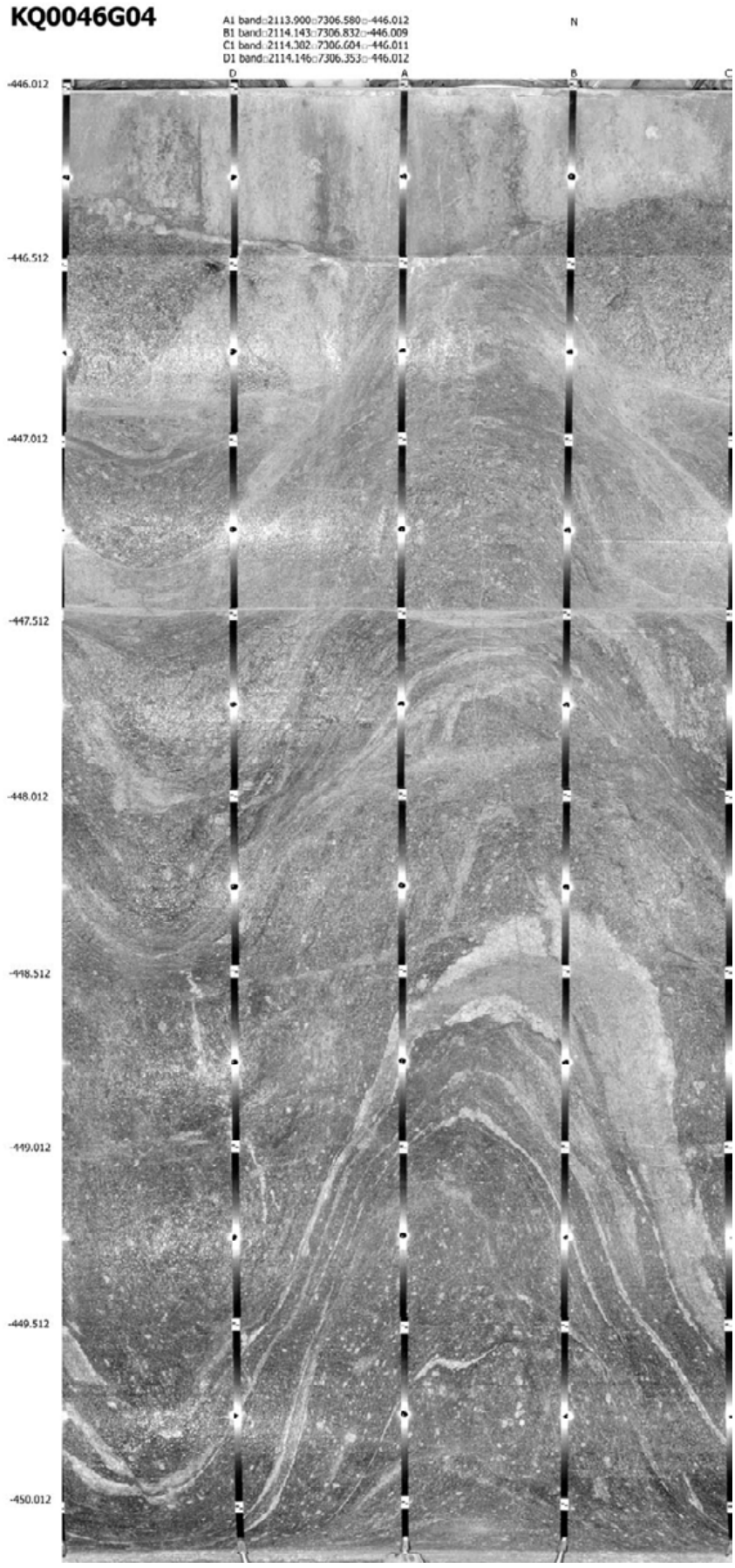
KQ0046G04
A1 band□2113.900□7306.580□-446.012
B1 band□2114.143□7306.832□-446.009
C1 band□2114.302□7306.604□-446.011
D1 band□2114.146□7306.353□-446.012
N
D
A
B
C
-446.012
-446.512
-447.012
-447.512
-448.012
-448.512
-449.012
-449.512
-450.012

Determined borehole deviation and variation in diameter of the heating holes based on ultra sonic measurements

Table N-1. Determined borehole deviation based on plumbing in four positions along the borehole wall of the heating holes.

Borehole	Parallel to the tunnel axis		Normal to the tunnel axis	
	NE-side (mm)	SW-side (mm)	NW-side (mm)	SE-side (mm)
KQ0046G03	0	5	7	0
KQ0046G04	10	8	35	43
KQ0048G04	0	5	9	5
KQ0048G05	15	15	4	17
KQ0051G04	23	22	6	31
KQ0051G05	5	5	5	3
KQ0054G03	8	14	0	2
KQ0054G04	34	30	36	30

Note: The deviation is evaluated between level -446.5 and -450.5 m.

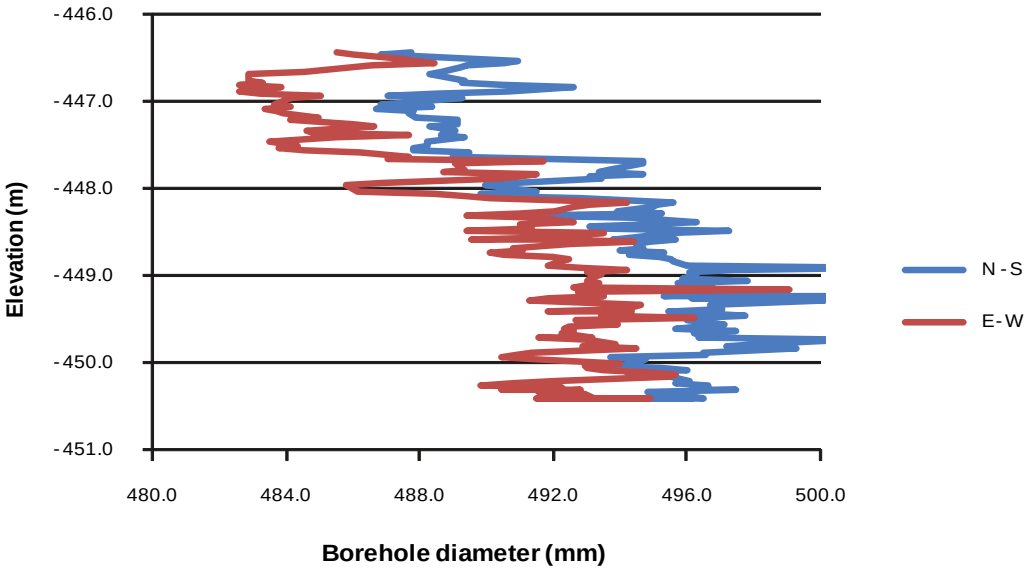

Figure N-1. *Determined variation in borehole diameter versus elevation in heating hole KQ0046G04.*

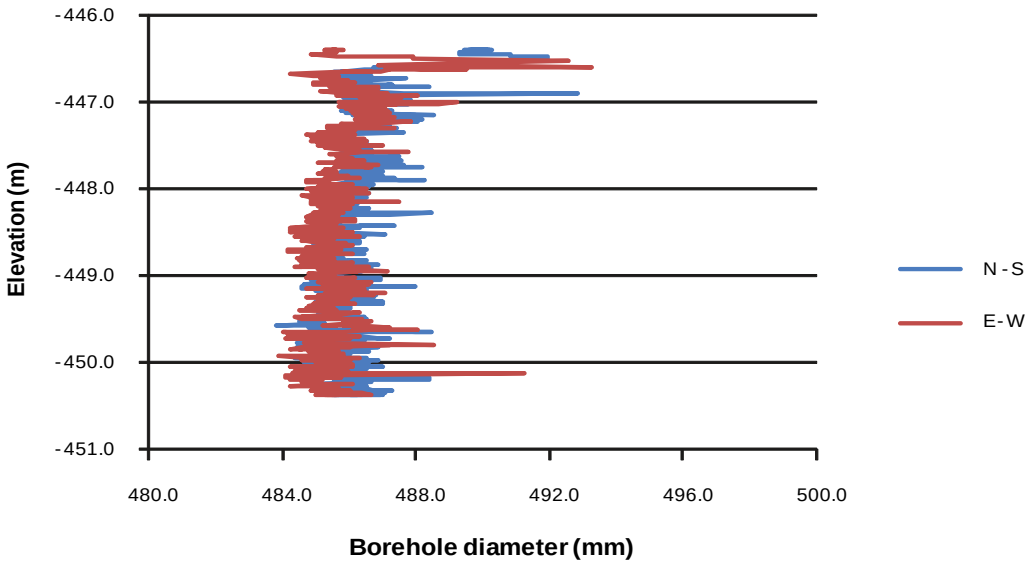

Figure N-2. *Determined variation in borehole diameter versus elevation in heating hole KQ0048G04.*

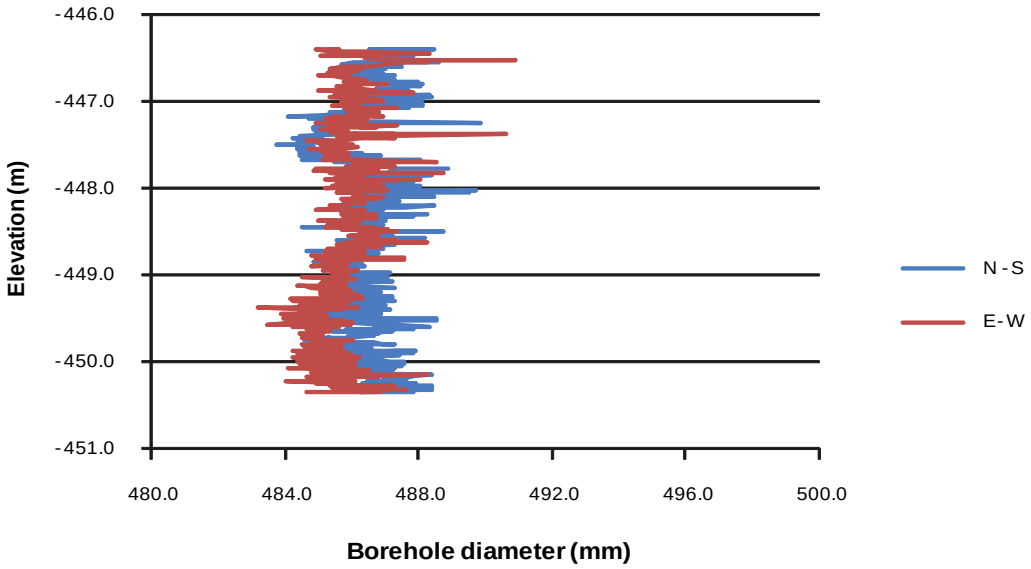

Figure N-3. *Determined variation in borehole diameter versus elevation in heating hole KQ0048G05.*

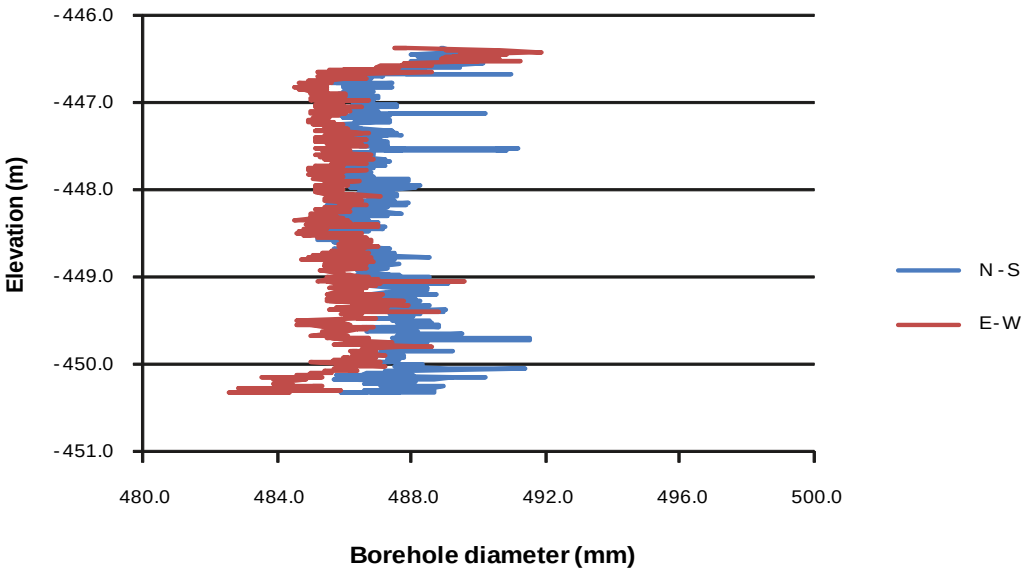

Figure N-4. *Determined variation in borehole diameter versus elevation in heating hole KQ0051G04.*

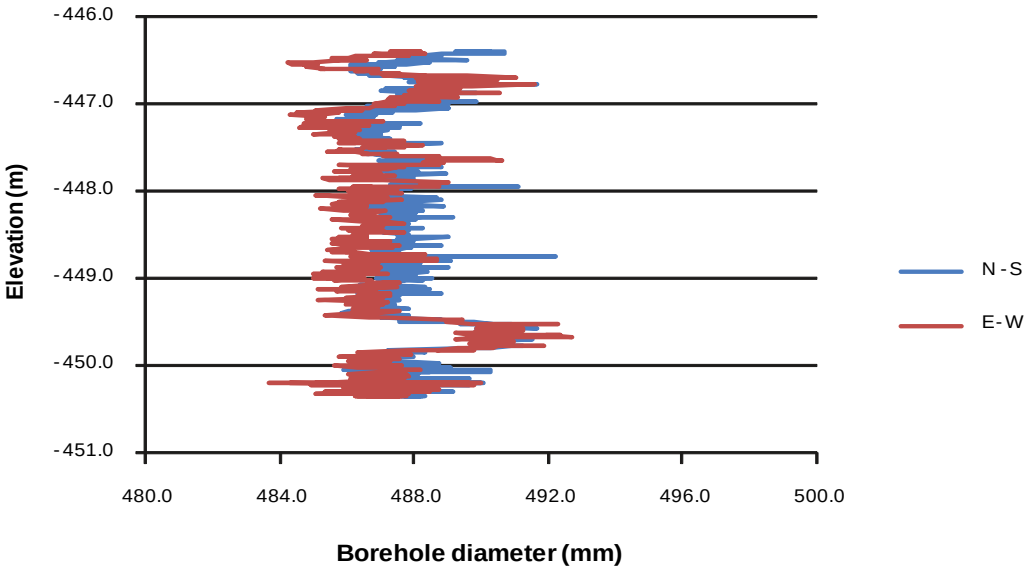

Figure N-5. *Determined variation in borehole diameter versus elevation in heating hole KQ0051G05.*

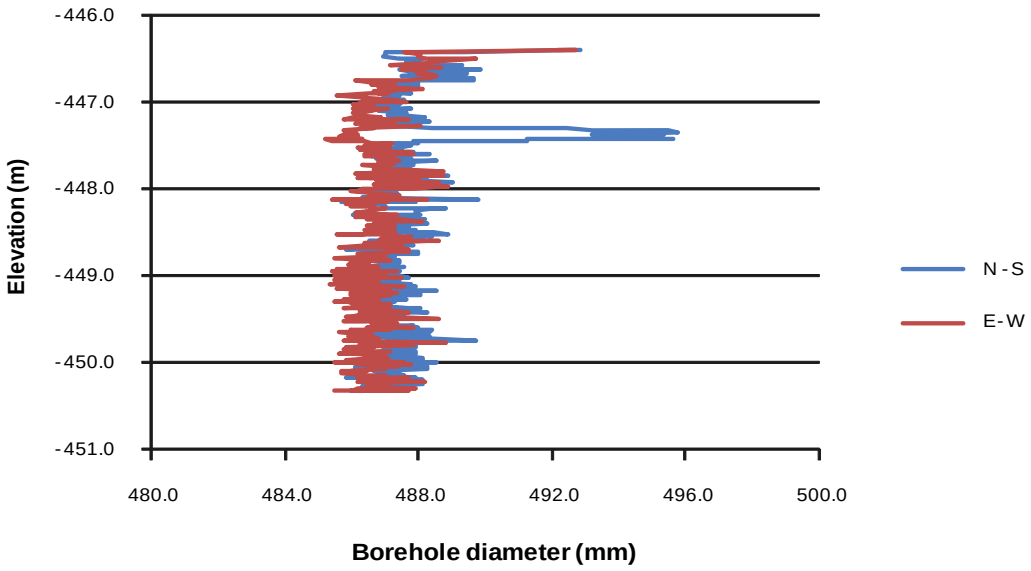

Figure N-6. *Determined variation in borehole diameter versus elevation in heating hole KQ0054G03*

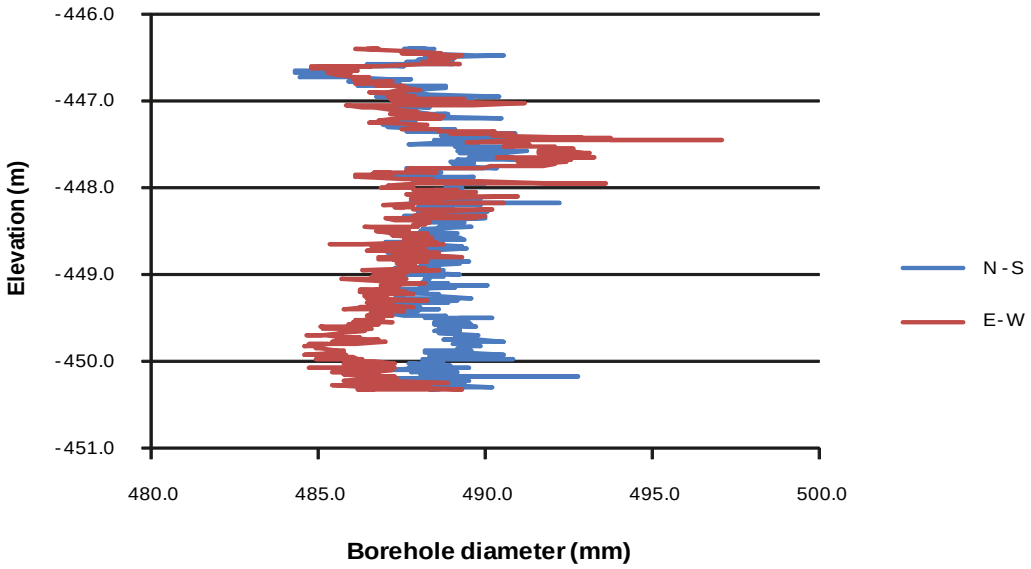

Figure N-7. *Determined variation in borehole diameter versus elevation in heating hole KQ0054G04*

Appendix O

Characterization of the notch based on photographs with thin lighted slot

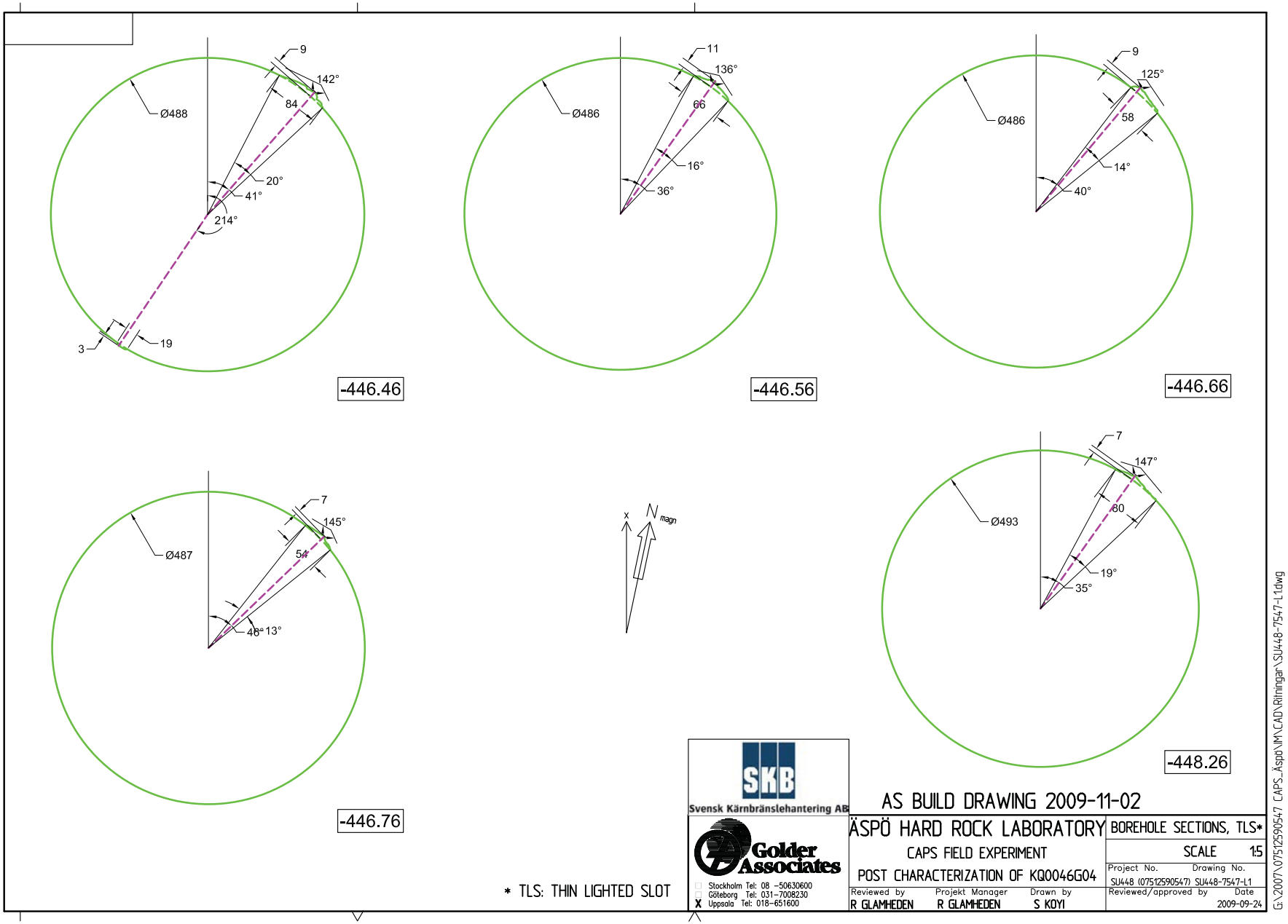

* TLS: THIN LIGHTED SLOT

Svensk Kärnbränslehantering AB

Golder Associates
Stockholm Tel: 08 -50630600
Göteborg Tel: 031-7008230
X Uppsala Tel: 018-651600

AS BUILD DRAWING 2009-11-02

ÄSPÖ HARD ROCK LABORATORY
CAPS FIELD EXPERIMENT
POST CHARACTERIZATION OF KQ0046G04

BOREHOLE SECTIONS, TLS*

SCALE 1:5

Project No. SU448 (07512590547)
Drawing No. SU448-7547-L1

Reviewed by	Projekt Manager	Drawn by
R GLAMHEDEN	R GLAMHEDEN	S KOYI

Reviewed/approved by
Date 2009-09-24

G:\2007\07512590547 CAPS_Äspö\MM\CAD\Ritningar\SU448-7547-L1.dwg

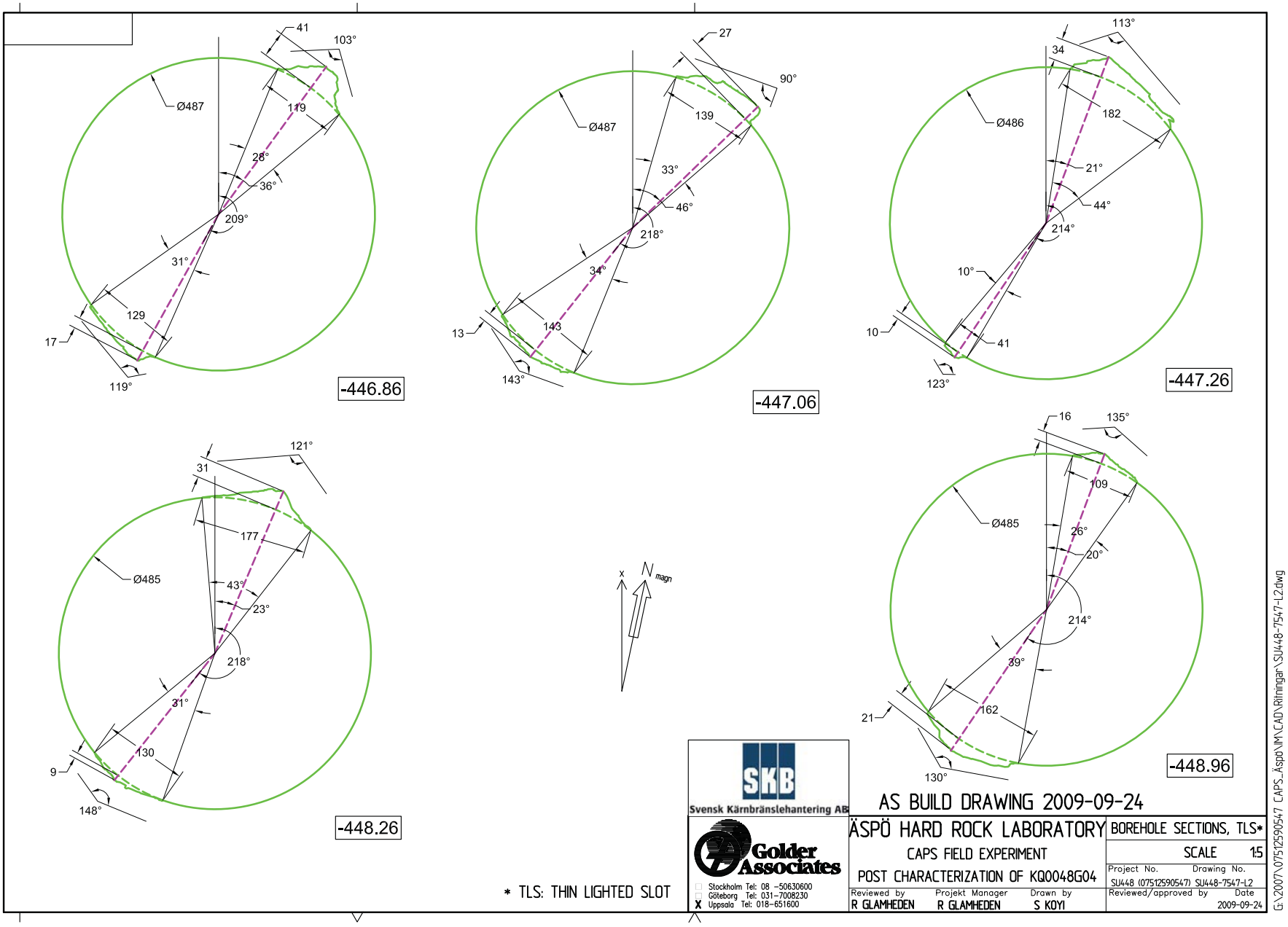
41
103°
Ø487
119
28°
36°
209°
31°
129
17
119°
-446.86
27
90°
Ø487
139
33°
46°
218°
34°
143
13
143°
-447.06
113°
34
Ø486
182
21°
44°
214°
10°
10
41
123°
-447.26
121°
31
177
Ø485
43°
23°
218°
31°
130
9
148°
-448.26
16
135°
109
Ø485
26°
20°
214°
39°
162
21
130°
-448.96
x
N magn
* TLS: THIN LIGHTED SLOT
SKB
Svensk Kärnbränslehantering AB
Golder Associates
Stockholm Tel: 08 -50630600
Göteborg Tel: 031-7008230
X Uppsala Tel: 018-651600
AS BUILD DRAWING 2009-09-24
ÄSPÖ HARD ROCK LABORATORY
CAPS FIELD EXPERIMENT
POST CHARACTERIZATION OF KQ0048G04
BOREHOLE SECTIONS, TLS*
SCALE 1:5
Project No. SU448 (07512590547)
Drawing No. SU448-7547-L2
Reviewed by R GLAMHEDEN
Projekt Manager R GLAMHEDEN
Drawn by S KOYI
Reviewed/approved by
Date 2009-09-24
G:\2007\07512590547 CAPS_Äspö\NM\CAD\Rlningar\SU448-7547-L2.dwg

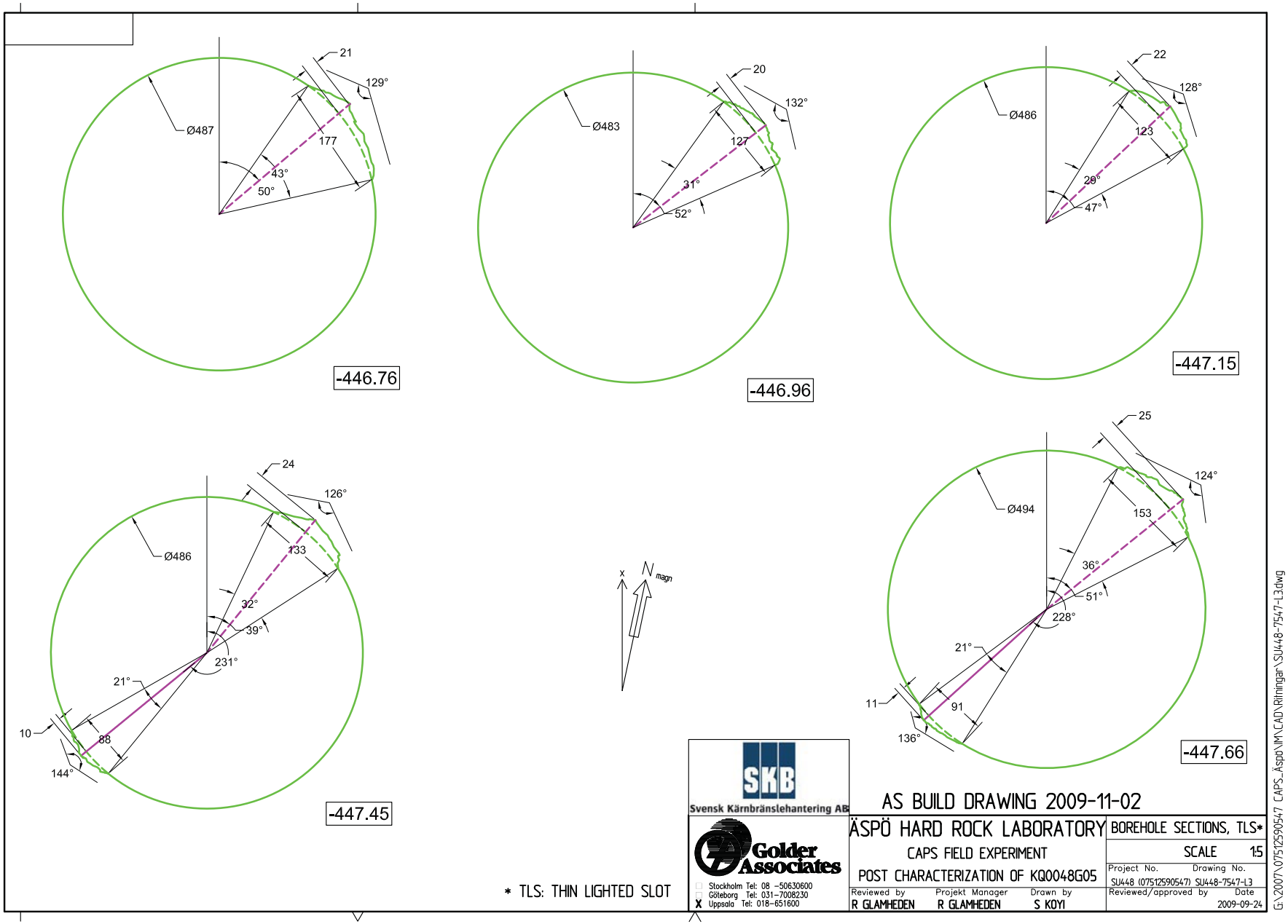

* TLS: THIN LIGHTED SLOT

SKB
Svensk Kärnbränslehantering AB

Golder Associates
Stockholm Tel: 08 -50630600
Göteborg Tel: 031-7008230
X Uppsala Tel: 018-651600

AS BUILD DRAWING 2009-11-02

ÄSPÖ HARD ROCK LABORATORY
CAPS FIELD EXPERIMENT
POST CHARACTERIZATION OF KQ0048G05

BOREHOLE SECTIONS, TLS*

SCALE 1:5

Project No. SU448 (07512590547)
Drawing No. SU448-7547-L3

Reviewed by	Projekt Manager	Drawn by
R GLAMHEDEN	R GLAMHEDEN	S KOYI

Reviewed/approved by R GLAMHEDEN
Date 2009-09-24

G:\2007\07512590547 CAPS_Äspö\VM\CAD\Ritningar\SU448-7547-L3.dwg

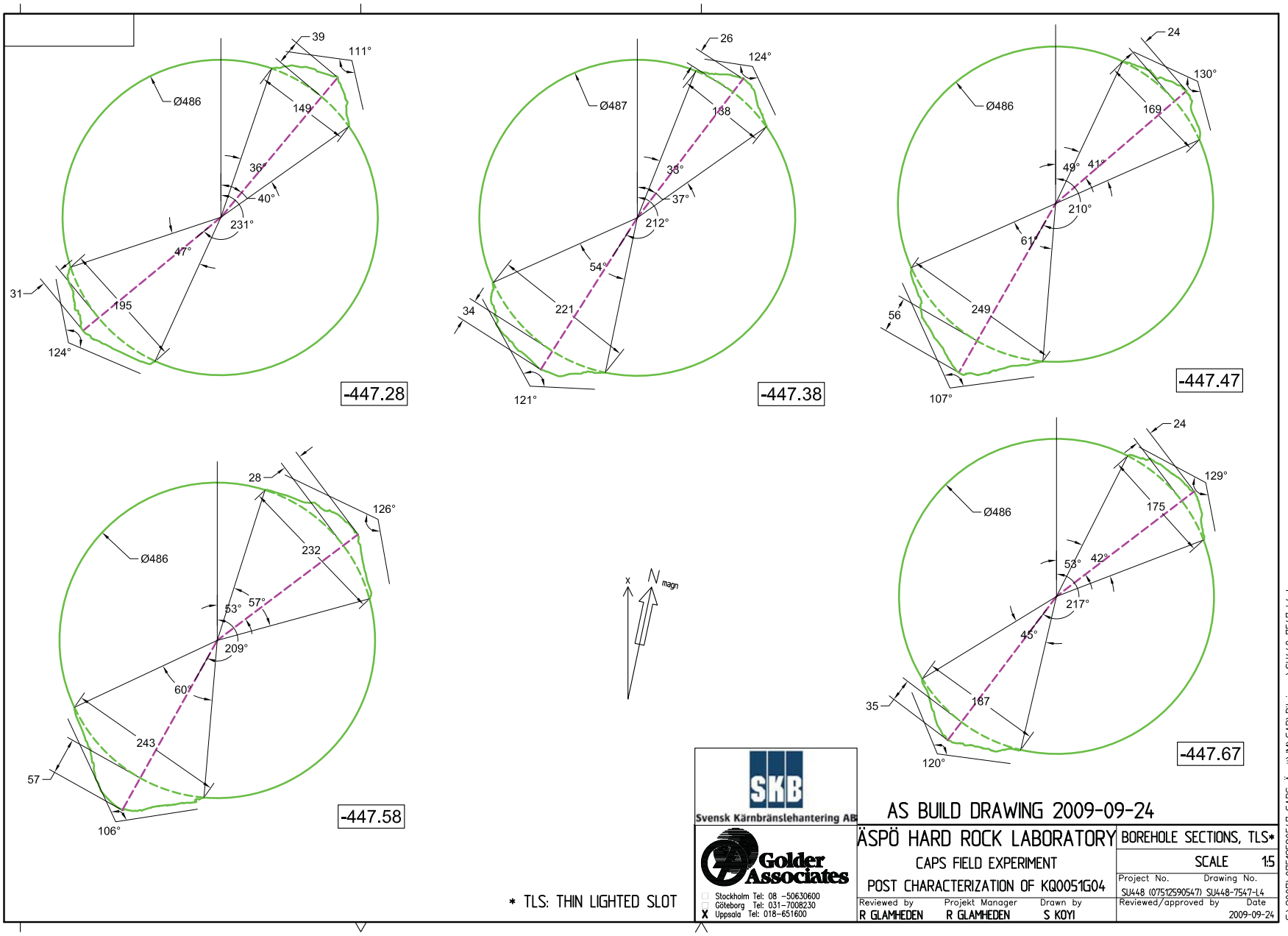
Ø486
39
111°
149
36°
40°
231°
47°
31
195
124°
-447.28
Ø487
26
124°
138
38°
37°
212°
54°
34
221
121°
-447.38
Ø486
24
130°
169
49°
41°
210°
61
56
249
107°
-447.47
Ø486
28
126°
232
53°
57°
209°
60°
243
57
106°
-447.58
x
N magn
Ø486
24
129°
175
53°
42°
217°
45°
35
187
120°
-447.67
* TLS: THIN LIGHTED SLOT
Svensk Kärnbränslehantering AB
Golder Associates
Stockholm Tel: 08 -50630600
Göteborg Tel: 031-7008230
X Uppsala Tel: 018-651600
AS BUILD DRAWING 2009-09-24
ÄSPÖ HARD ROCK LABORATORY
CAPS FIELD EXPERIMENT
POST CHARACTERIZATION OF KQ0051G04
BOREHOLE SECTIONS, TLS*
SCALE 1:5
Project No. SU448 (07512590547)
Drawing No. SU448-7547-L4
Reviewed by R GLAMHEDEN
Projekt Manager R GLAMHEDEN
Drawn by S KOYI
Reviewed/approved by
Date 2009-09-24
G:\2007\07512590547 CAPS_Äspö\MY\CAD\Ritningar\SU448-7547-L4.dwg

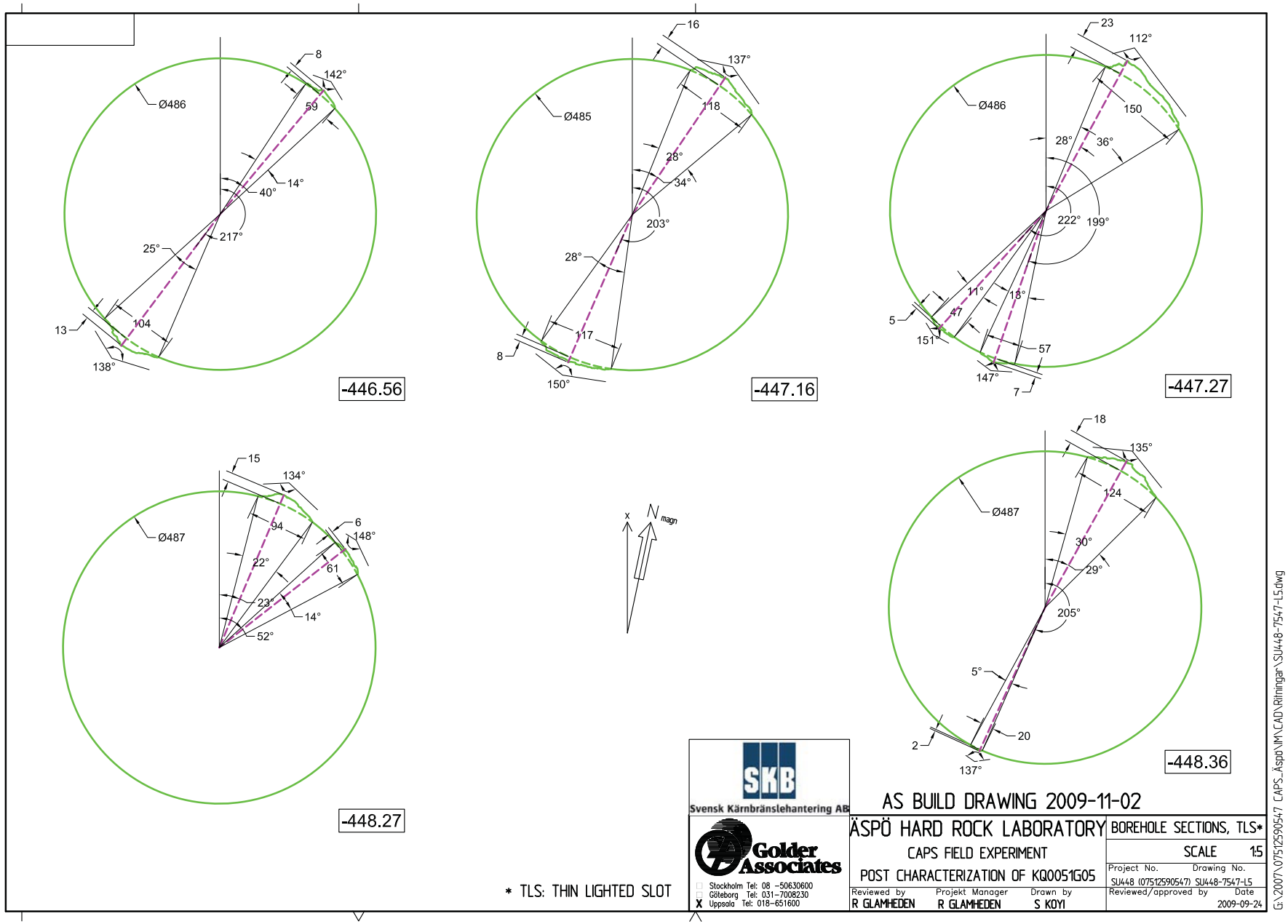
Ø486
8
142°
59
14°
40°
217°
25°
104
13
138°
-446.56
Ø485
16
137°
18
28°
34°
203°
28°
117
8
150°
-447.16
Ø486
23
112°
150
28°
36°
222°
199°
11°
18°
47
5
151
57
147°
7
-447.27
Ø487
15
134°
94
6
148°
22°
61
23°
14°
52°
-448.27
x
N magn
Ø487
18
135°
124
30°
29°
205°
5°
20
2
137°
-448.36
* TLS: THIN LIGHTED SLOT
SKB
Svensk Kärnbränslehantering AB
Golder Associates
Stockholm Tel: 08 -50630600
Göteborg Tel: 031-7008230
X Uppsala Tel: 018-651600
AS BUILD DRAWING 2009-11-02
ÄSPÖ HARD ROCK LABORATORY
CAPS FIELD EXPERIMENT
POST CHARACTERIZATION OF KQ0051G05
BOREHOLE SECTIONS, TLS*
SCALE 1:5
Project No. Drawing No.
SU448 (07512590547) SU448-7547-L5
Reviewed by R GLAMHEDEN
Projekt Manager R GLAMHEDEN
Drawn by S KOYI
Reviewed/approved by Date
2009-09-24
G:\2007\07512590547 CAPS_Äspö\MA\CAD\Ritningar\SU448-7547-L5.dwg

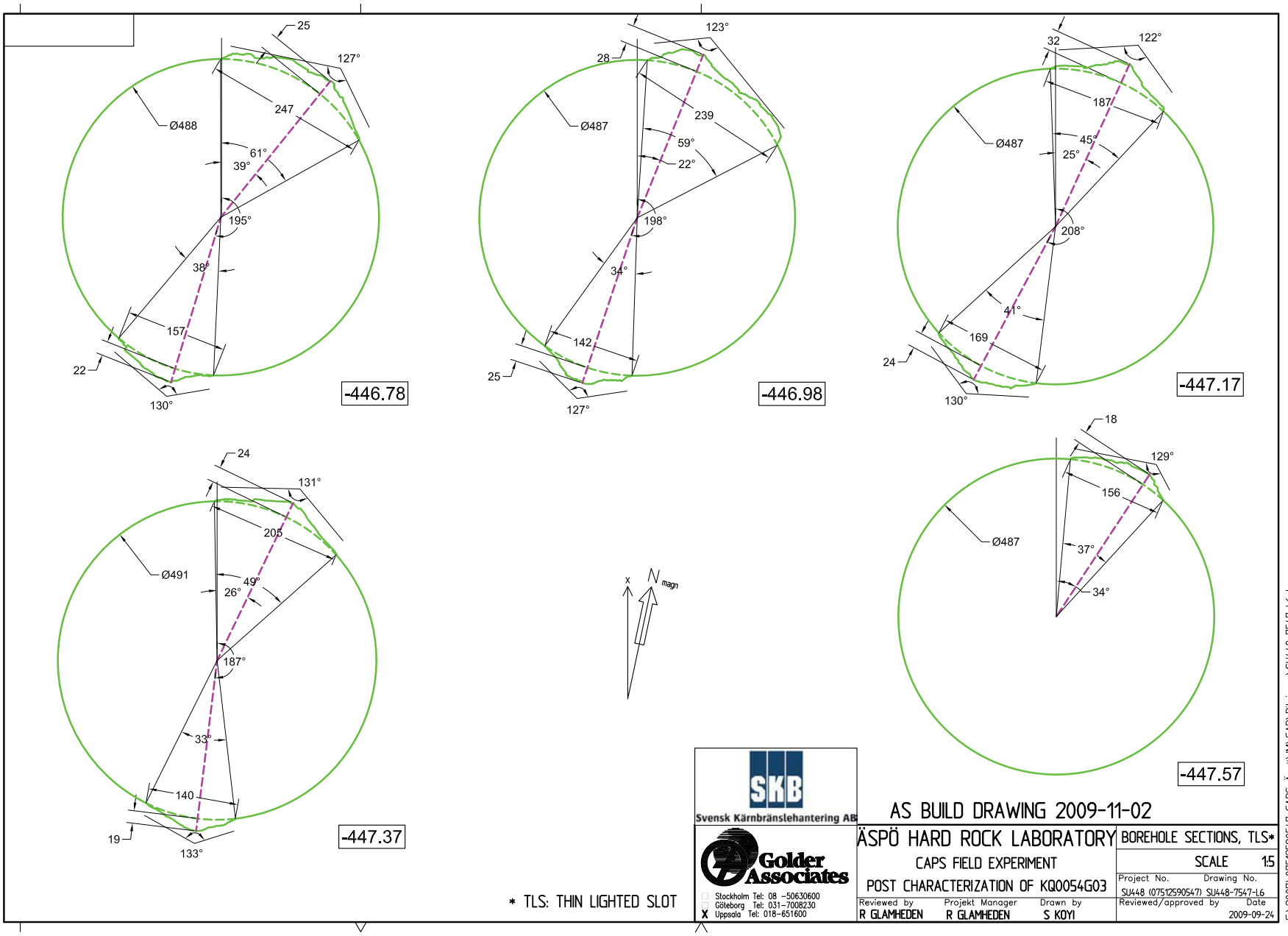
25
127°
Ø488
247
61°
39°
195°
38°
157
22
130°
-446.78
123°
28
Ø487
239
59°
22°
198°
34°
142
25
127°
-446.98
122°
32
187
Ø487
45°
25°
208°
41°
169
24
130°
-447.17
24
131°
205
Ø491
49°
26°
187°
33°
140
19
133°
-447.37
18
129°
156
Ø487
37°
34°
-447.57
N magn
X
* TLS: THIN LIGHTED SLOT
SKB
Svensk Kärnbränslehantering AB
Golder Associates
Stockholm Tel: 08 -50630600
Göteborg Tel: 031-7008230
X Uppsala Tel: 018-651600
AS BUILD DRAWING 2009-11-02
ÄSPÖ HARD ROCK LABORATORY
CAPS FIELD EXPERIMENT
POST CHARACTERIZATION OF KQ0054G03
BOREHOLE SECTIONS, TLS*
SCALE 1:5
Project No. SU448 (07512590547)
Drawing No. SU448-7547-L6
Reviewed by R GLAMHEDEN
Projekt Manager R GLAMHEDEN
Drawn by S KOYI
Reviewed/approved by
Date 2009-09-24
G:\2007\07512590547 CAPS_Äspö\IM\CAD\Ritningar\SU448-7547-L6.dwg

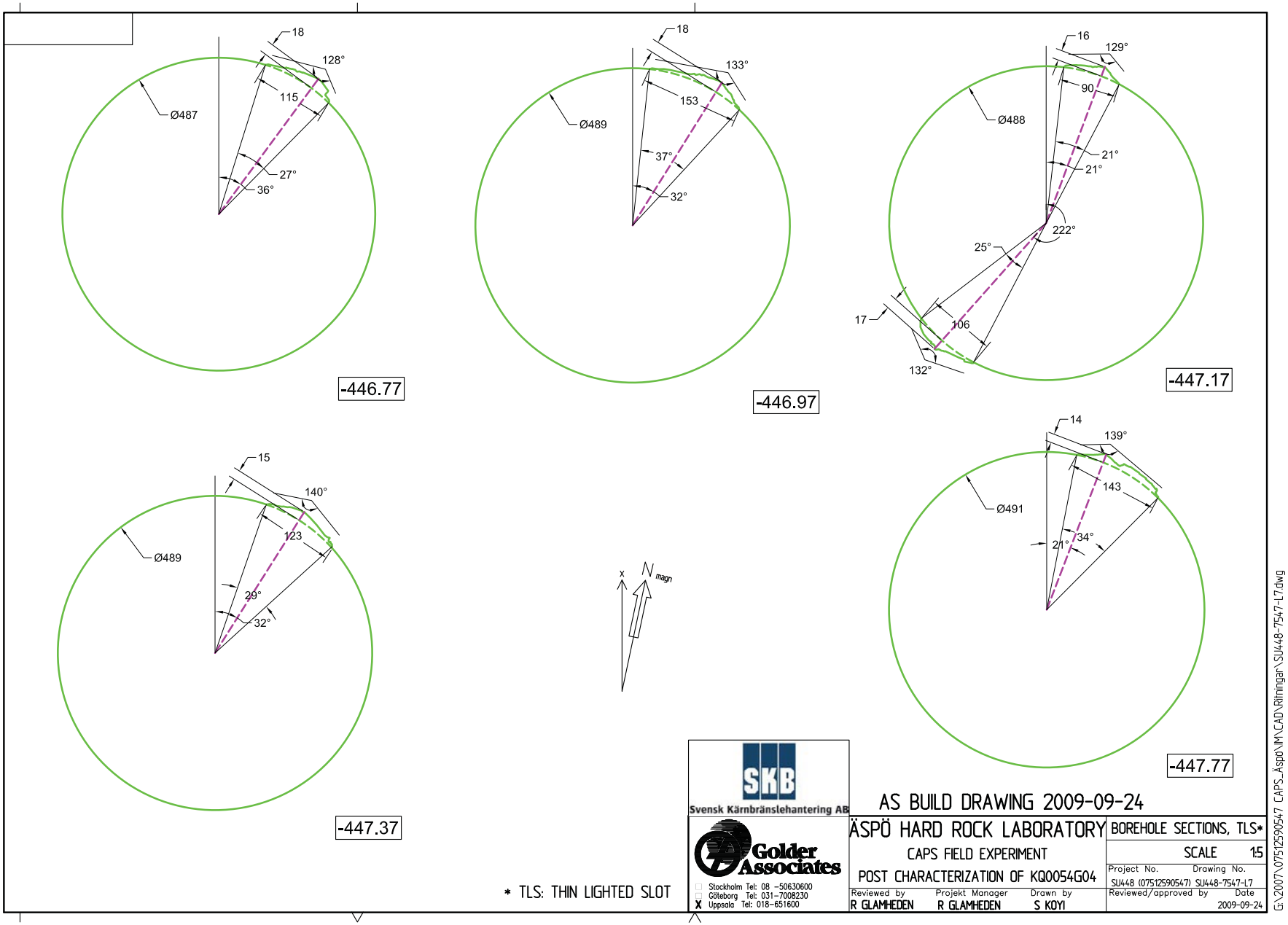
18
128°
115
Ø487
27°
36°
-446.77
18
133°
153
Ø489
37°
32°
-446.97
16
129°
90
Ø488
21°
21°
222°
25°
17
106
132°
-447.17
15
140°
123
Ø489
29°
32°
-447.37
x
N magn
14
139°
143
Ø491
21°
34°
-447.77
* TLS: THIN LIGHTED SLOT
SKB
Svensk Kärnbränslehantering AB
Golder Associates
Stockholm Tel: 08 -50630600
Göteborg Tel: 031-7008230
X Uppsala Tel: 018-651600
AS BUILD DRAWING 2009-09-24
ÄSPÖ HARD ROCK LABORATORY
CAPS FIELD EXPERIMENT
POST CHARACTERIZATION OF KQ0054G04
BOREHOLE SECTIONS, TLS*
SCALE 1:5
Project No. Drawing No.
SU448 (07512590547) SU448-7547-L7
Reviewed by Projekt Manager Drawn by
R GLAMHEDEN R GLAMHEDEN S KOYI
Reviewed/approved by Date
2009-09-24
G:\2007\07512590547 CAPS_Äspö\VM\CAD\Ritningar\SU448-7547-L7.dwg

Appendix P

Boreholes used for water injection tests of the damaged zone

Golder Associates	SKB	ÄSPÖ HARD ROCK LABORATORY CAPS FIELD EXPERIMENT POST CHARACTERIZATION OF KQ0046G03 DRILLINING FOR HYDRAULIC TESTING	Project No. SU448 (07512590547) As build drawing Date 2009-09-02	SU448-7547-H1:1 Rev:00

Project Manager: R GLAMHEDEN
Person responsible: R GLAMHEDEN
Drawn by: S KOYI
Source:

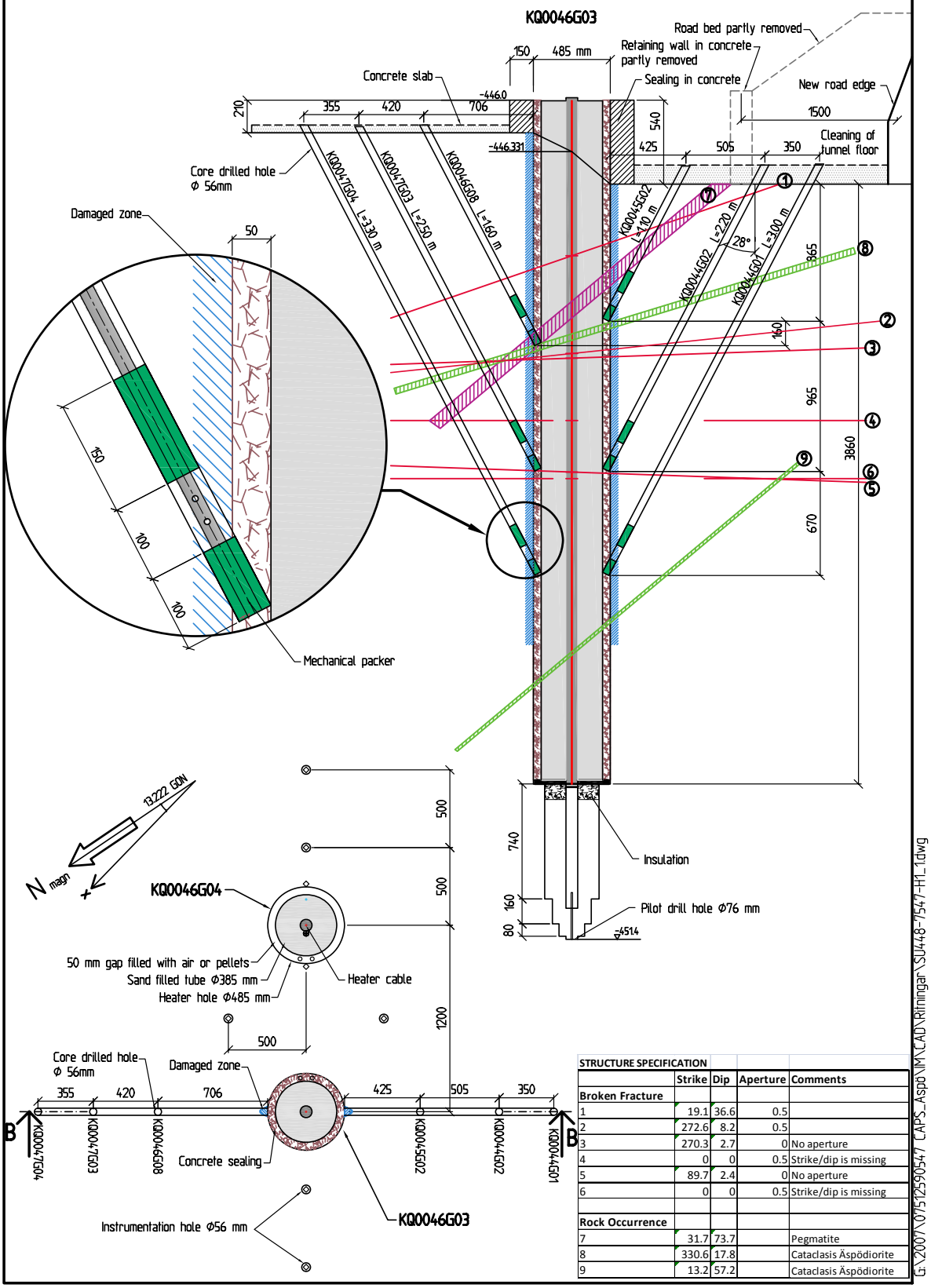

STRUCTURE SPECIFICATION				
	Strike	Dip	Aperture	Comments
Broken Fracture				
1	19.1	36.6	0.5	
2	272.6	8.2	0.5	
3	270.3	2.7	0	No aperture
4	0	0	0.5	Strike/dip is missing
5	89.7	2.4	0	No aperture
6	0	0	0.5	Strike/dip is missing
Rock Occurrence				
7	31.7	73.7		Pegmatite
8	330.6	17.8		Cataclasis Äspödiorite
9	13.2	57.2		Cataclasis Äspödiorite

G:\2007\07512590547 CAPS_Aspo\MCAD\Ritningar\SU448-7547-H1_1.dwg

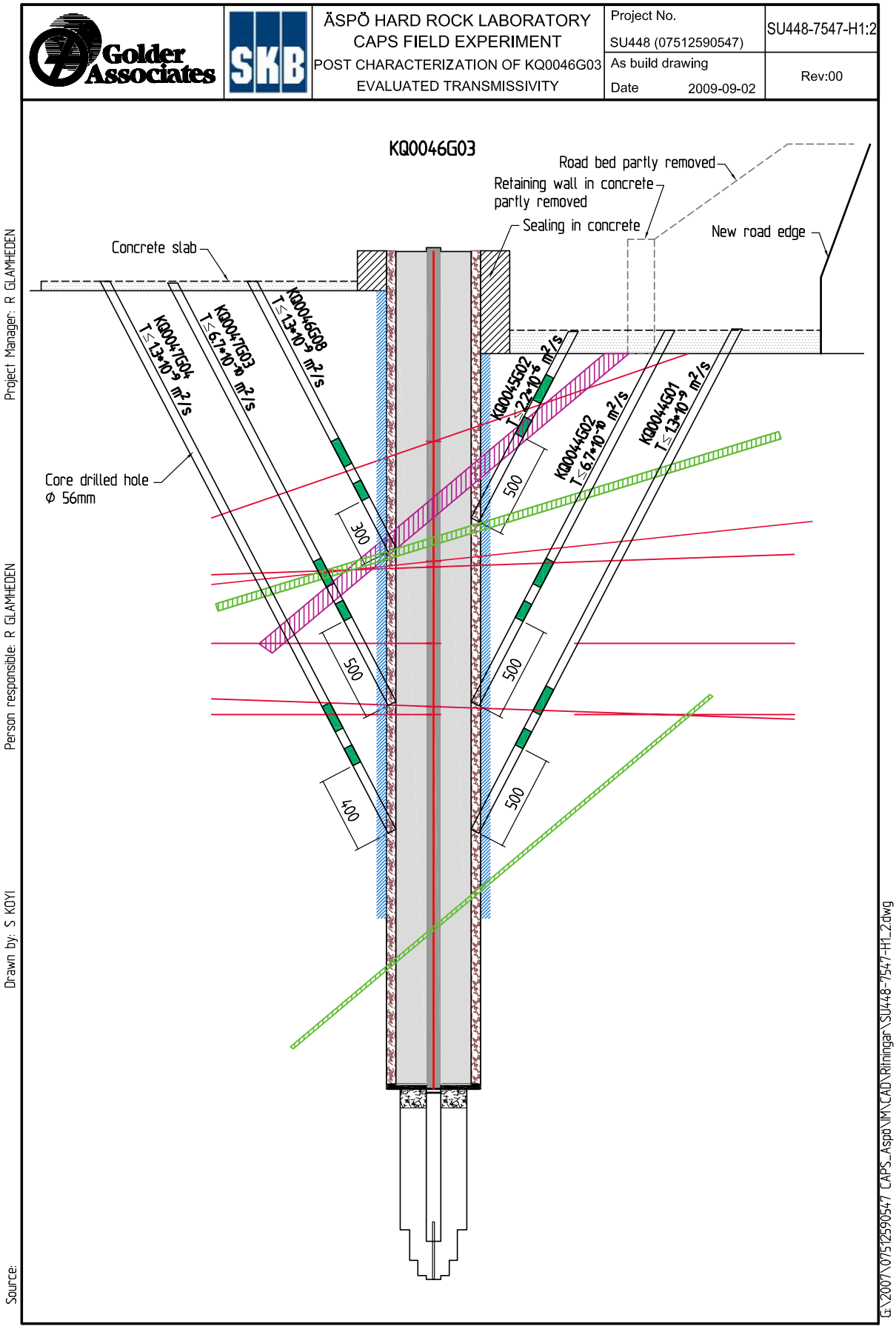
ÄSPÖ HARD ROCK LABORATORY
CAPS FIELD EXPERIMENT
POST CHARACTERIZATION OF KQ0046G03
EVALUATED TRANSMISSIVITY
Project No.
SU448 (07512590547)
As build drawing
Date 2009-09-02
SU448-7547-H1:2
Rev:00
KQ0046G03
Road bed partly removed
Retaining wall in concrete partly removed
Sealing in concrete
New road edge
Concrete slab
Core drilled hole
Φ 56mm
KQ0047G04 T≤1.3*10-9 m2/s
KQ0047G03 T≤6.7*10-8 m2/s
KQ0046G08 T≤1.3*10-9 m2/s
KQ0045G02 T≤2.2*10-6 m2/s
KQ0044G02 T≤6.7*10-10 m2/s
KQ0044G01 T≤1.3*10-9 m2/s
300
500
500
500
400
Project Manager: R GLAMHEDEN
Person responsible: R GLAMHEDEN
Drawn by: S KOYI
Source:
G:\2007\07512590547 CAPS_Aspo\IM\CAD\Ritningar\SU448-7547-H1_2.dwg

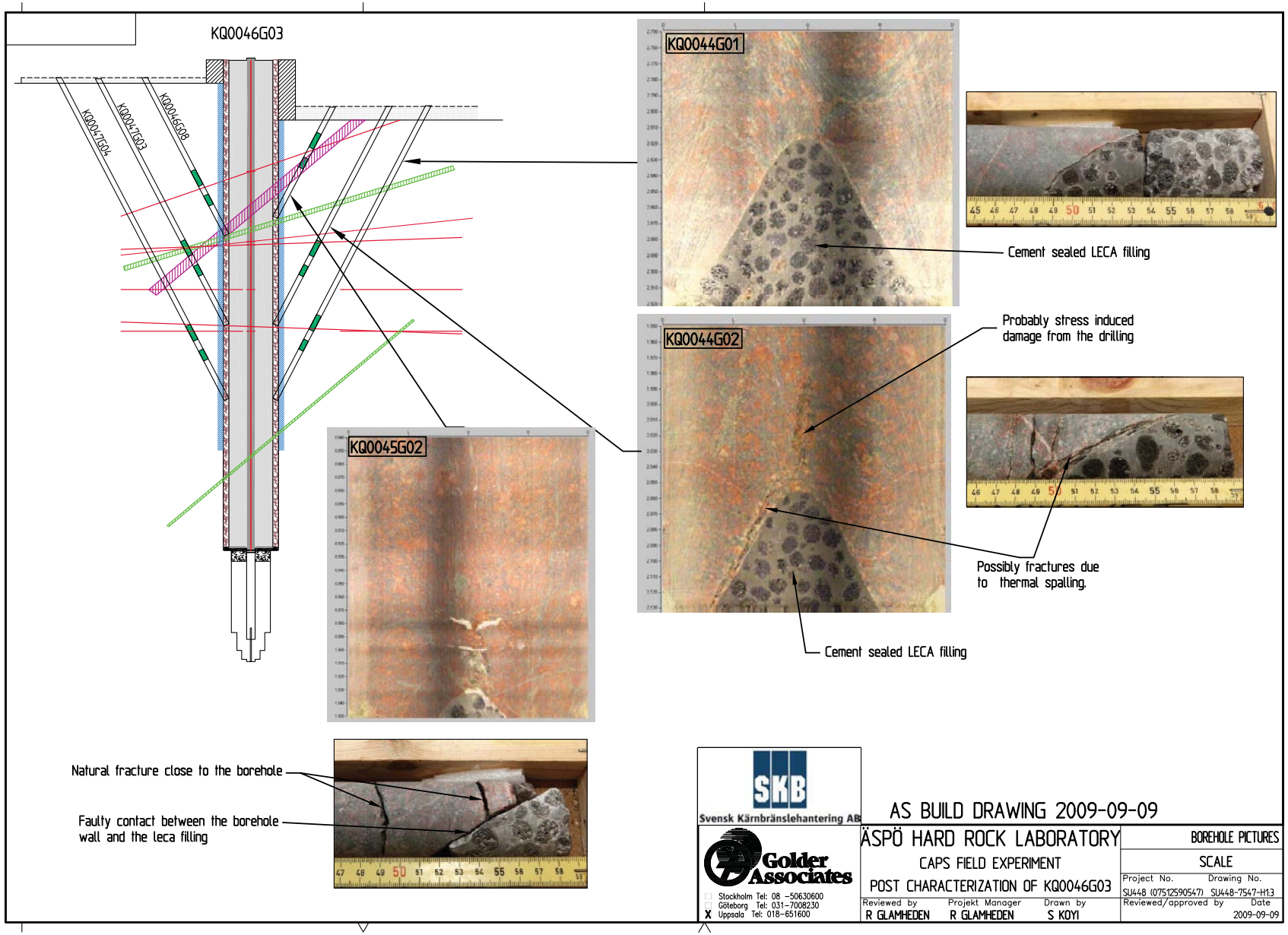

Svensk Kärnbränslehantering AB

Golder Associates
Stockholm Tel: 08 –50630600
Göteborg Tel: 031–7008230
X Uppsala Tel: 018–651600

AS BUILD DRAWING 2009-09-09

ÄSPÖ HARD ROCK LABORATORY
CAPS FIELD EXPERIMENT
POST CHARACTERIZATION OF KQ0046G03

BOREHOLE PICTURES
SCALE

Reviewed by	Projekt Manager	Drawn by
R GLAMHEDEN	R GLAMHEDEN	S KOYI

Project No. SU448 (07512590547) Drawing No. SU448-7547-H1:3
Reviewed/approved by R GLAMHEDEN Date 2009-09-09

G:\2007\07512590547 CAPS_Äspö\VM\CAD\Rhinngan\SU448-7547-H1_3.dwg

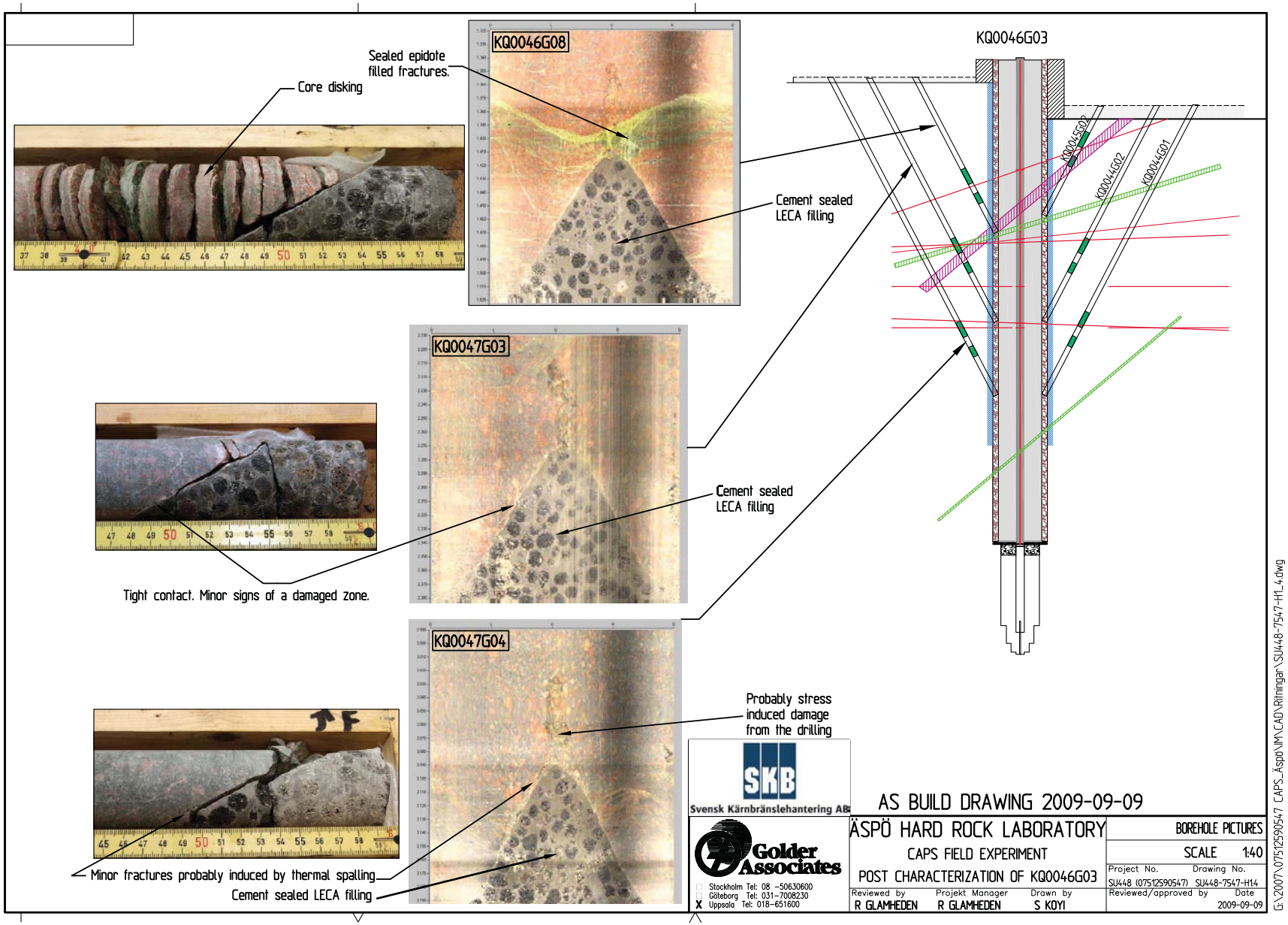

Svensk Kärnbränslehantering AB

AS BUILD DRAWING 2009-09-09

Golder Associates
Stockholm Tel: 08 -50630600
Göteborg Tel: 031-7008230
X Uppsala Tel: 018-651600

ÄSPÖ HARD ROCK LABORATORY
CAPS FIELD EXPERIMENT
POST CHARACTERIZATION OF KQ0046G03

BOREHOLE PICTURES
SCALE 1:40
Project No. SU448 (07512590547)
Drawing No. SU448-7547-H14
Reviewed/approved by Date 2009-09-09

Reviewed by R GLAMHEDEN
Projekt Manager R GLAMHEDEN
Drawn by S KOYI

G:\2007\07512590547 CAPS_Äspö\MY\CAD\Ritningar\SU448-7547-H1_4.dwg

Results from water injection test of the damage zone

Johan Harrström, Geosigma AB

March 2010

Injection tests in observation boreholes for the fractured skin-zone of heater borehole KQ0046G03

Johan Harrström, Geosigma AB

March 2010

Content

Q1 Background

The results from the third test in CAPS field experiment, the first test with a slot filled with LECA, indicated that dry pellets cannot prevent the borehole wall from cracking, whereas it might keep the slabs in place and by this preserving the geometry of the holes. The results have implied a focus on the hydraulic transmissivity of the spalled damaged zone and the intention with the measurements presented here has been to determine a value of this parameter in one of the holes of the final heating test. For details about interpreting transient evaluations see /Harrström et al. 2007/.

Q2 Test procedure

The heater borehole KQ0046G03 in the Q-tunnel has had the LECA filled slot grouted with cement to seal the borehole from the spalled damaged zone, further on called skin-zone, and surrounding rock. Into and through the skin-zone, six smaller observation boreholes with a diameter of 56 mm have been drilled at an angle of 28 degrees (Figure Q-1). The observation boreholes were sealed off with packers about 20 cm from the bottom and monitored with pressure transducers. Besides these observation boreholes, gauges were mounted for pressure monitoring in 12 other boreholes used as instrumentation holes in heating Test 3 and 4.

The aim of this project was to measure the possible fractures that have been evolved in the skin-zone as well as measure the overlying part of the boreholes. The tests were performed as injection tests with a pressure build-up of approximately 2 bars for 30 minutes. To seal off sections in the observation boreholes a special packer unit was manufactured with two sealing packer surfaces with a 10 centimetre section in between. The packer is constructed for injection to be made either in the 10 cm section or below the bottom packer without releasing the packers.

A total of 27 injection tests were made in the six boreholes, which are listed in Table Q-1 where the stationary values of the transmissivity for all tests also is calculated. The injection test was made as constant pressure tests with equipment designed by Geosigma called WIC (Water Injection Controller) where time, pressure and water flow is registered. During the injection tests the surrounding boreholes with transducers attached were monitored and logged to register any pressure changes indicating fractures in the spalled damaged zone. These pressures are plotted in Figure Q-2. The transducer in the measured borehole was disconnected during the tests. In Figure Q-2 the disconnection and connection of the transducers are seen as peaks and drops in the pressure. Each peak in the graph is correlated to disconnection of the transducer. To ensure that all pressure changes were registered in the bottom of the observation boreholes, the packers in the six observation boreholes were lifted about 20 cm from the bottom at about 3 p.m. of June 2, 2009.

No obvious responses from the hydraulic injections are seen in the observation boreholes, neither the ones with transducers nor the surrounding with gauges. During the tests below the packers in borehole KQ0045G02 the injected water did flow out of the heater borehole KQ0046G03 indicating an insufficient sealing of the LECA filled slot.

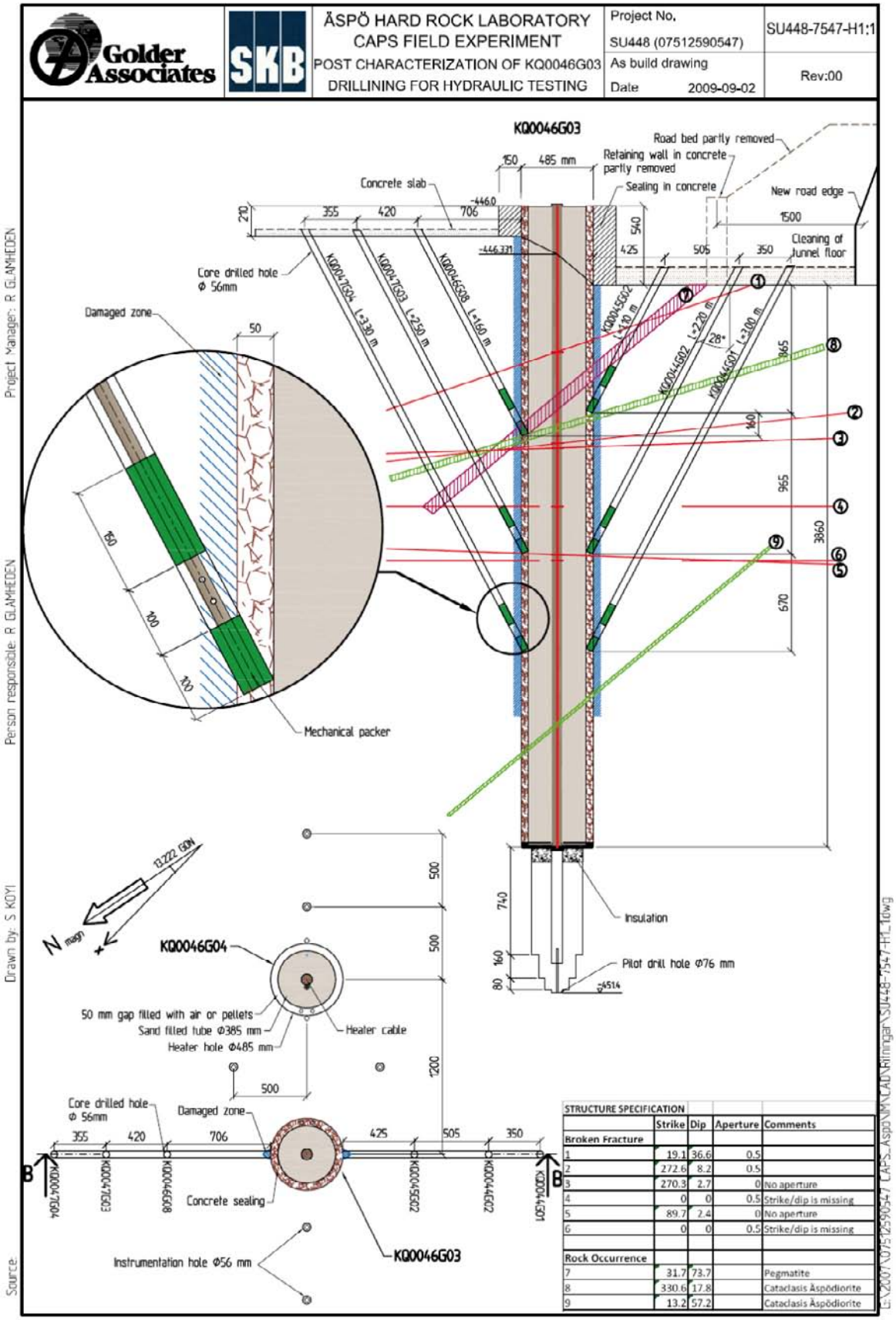

Figure Q-1. *Drawing of the heater borehole KQ0046G03 and the six observation boreholes drilled into it.*

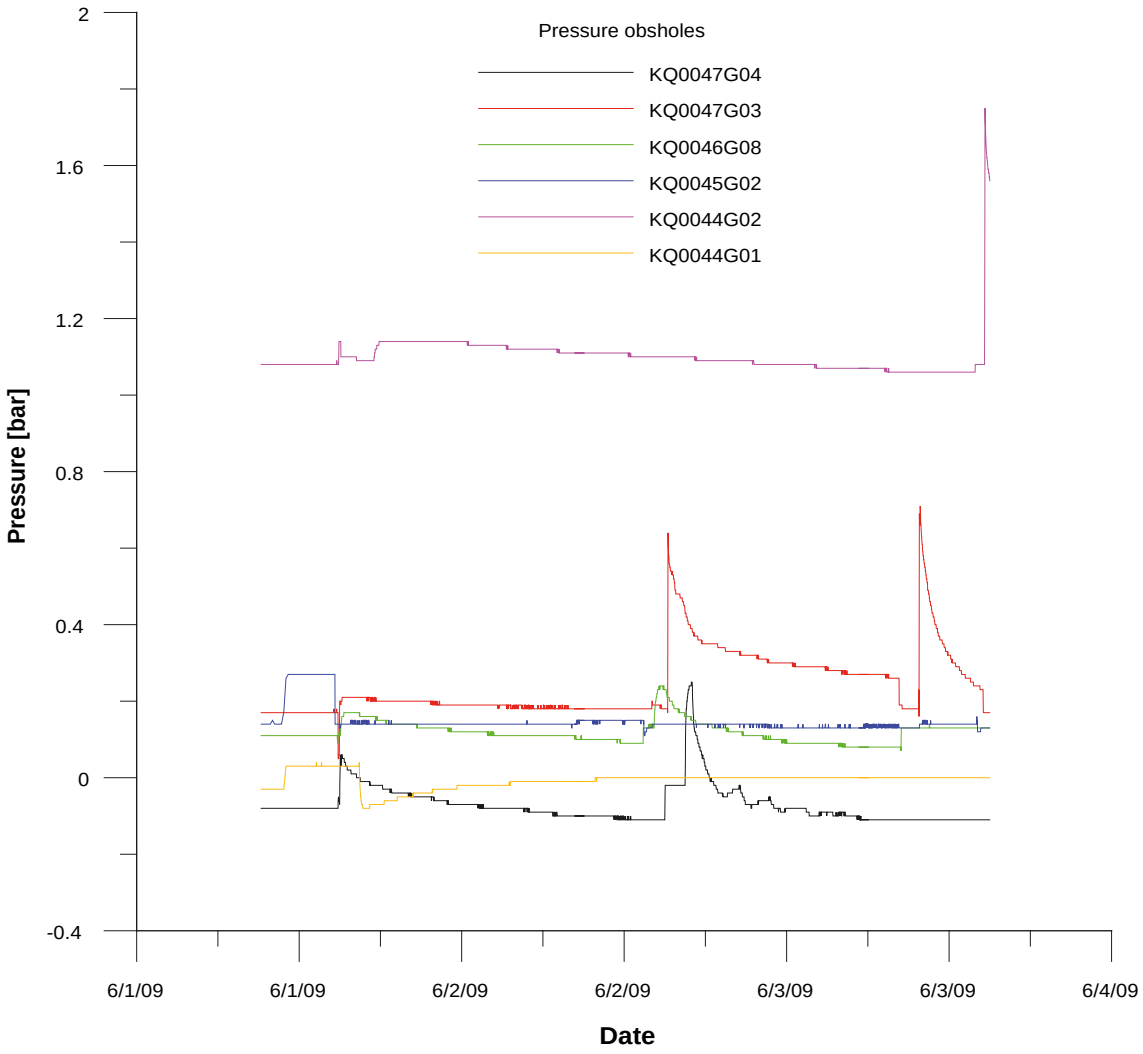

Figure Q-2. *Pressure registered by the transducers in the observation boreholes during the injection tests. The peaks seen in the pressure curves correlate with disconnection of the transducers prior and after injection tests.*

Q3 Results and evaluations

The stationary values were calculated for all tests in the sections using Thiems formula according to /Marsily 1986/ for a radius of 5 m and are seen in Table Q-1. Eight of the performed tests had a detectable flow rate and hence evaluated with transient methods in AQTESOLVE as well as stationary methods. For the remaining 19 tests the T-value is simply based on the lower measurement limit of the equipment which is 2 ml/min.

The transient evaluation of the transmissivity for these tests is made with the software AQTESOLVE where different flow regimes can be simulated.

The results from the transient evaluations of the eight tests are seen in Table Q-2 where the transmissivity (T_T), storativity (S), skin factor (S_W) and a leakage parameter (r/B) are presented. A skin factor is calculated when a radial flow model is used, in this case according to /Hurst et al. 1969/ and r/B is calculated when the Hantush model for spherical flow is used /Hantush 1955, 1959/. Overall the tests were rather straightforward to evaluate hence the results are considered as certain. Plots of the evaluations in AQTESOLVE are seen in Appendix AQ.

Table Q-1. Measured boreholes, flow- and pressure data and stationary values of the transmissivity. The position of the boreholes is indicated in Figure Q-1.

Borehole	Secup[1] [m]	Seclow[1] [m]	Test start	Flow final [m³/s]	Injected over-pressure [bar]	T[3] [m²/s]
KQ0044G01	2.50	3.00	2009-06-01 15:57	3.33E-08[2]	2.05	1.32E-09
KQ0044G01	2.70	2.80	2009-06-01 15:33	3.33E-08[2]	2.05	1.32E-09
KQ0044G01	2.80	2.90	2009-06-01 11:51	3.33E-08[2]	2.05	1.32E-09
KQ0044G01	2.90	3.00	2009-06-01 15:07	3.33E-08[2]	2.05	1.32E-09
KQ0044G01	2.98	3.00	2009-06-01 13:52	1.17E-07	2.05	4.61E-09
KQ0044G01	2.98	3.00	2009-06-01 14:20	3.33E-08[2]	2.05	1.32E-09
KQ0044G02	0.70	2.20	2009-06-01 17:08	3.33E-08[2]	2.05	1.32E-09
KQ0044G02	1.70	2.20	2009-06-01 16:37	3.33E-08[2]	2.05	1.32E-09
KQ0044G02	1.70	2.20	2009-06-03 14:08	3.33E-08[2]	4.05	6.67E-10
KQ0045G02	0.30	1.10	2009-06-03 11:02	8.67E-06	2.05	3.42E-07
KQ0045G02	0.30	1.10	2009-06-03 13:21	1.78E-05	4.05	3.57E-07
KQ0045G02	0.60	1.10	2009-06-02 08:41	5.48E-05	2.05	2.17E-06
KQ0045G02	0.77	0.87	2009-06-02 10:32	3.33E-08[2]	2.05	1.32E-09
KQ0045G02	0.80	1.10	2009-06-02 11:53	2.83E-06	2.05	1.12E-07
KQ0045G02	0.83	0.93	2009-06-02 11:25	3.33E-08[2]	2.05	1.32E-09
KQ0045G02	0.90	1.00	2009-06-02 09:15	3.33E-08[2]	2.05	1.32E-09
KQ0045G02	0.90	1.10	2009-06-03 10:12	6.67E-06	2.05	2.63E-07
KQ0045G02	0.97	1.10	2009-06-02 10:06	1.27E-05	2.05	5.00E-07
KQ0045G02	1.07	1.10	2009-06-02 09:42	6.67E-08	2.05	2.63E-09
KQ0046G08	1.30	1.60	2009-06-02 13:43	3.33E-08[2]	2.05	1.32E-09
KQ0047G03	0.50	2.50	2009-06-03 09:19	3.33E-08[2]	2.05	1.32E-09
KQ0047G03	2.00	2.50	2009-06-03 08:42	3.33E-08[2]	2.05	1.32E-09
KQ0047G03	2.00	2.50	2009-06-03 14:42	3.33E-08[2]	4.05	6.67E-10
KQ0047G03	2.10	2.20	2009-06-02 14:40	3.33E-08[2]	2.05	1.32E-09
KQ0047G03	2.30	2.50	2009-06-02 14:19	3.33E-08[2]	2.05	1.32E-09
KQ0047G04	1.30	3.30	2009-06-02 15:52	3.33E-08[2]	2.05	1.32E-09
KQ0047G04	2.90	3.30	2009-06-02 15:17	3.33E-08[2]	2.05	1.32E-09

1) Meter below top of casing, distance from surface of the tunnel.

2) Measurement limit for the WIC-equipment.

3) T calculated as Thiem with a 5 m radius.

Table Q-2. Boreholes with a detectable flow evaluated with transient methods in AQTESOLVE. Transient (T_T) and stationary (T_M) transmissivity, storativity, skin- and leakage factor.

Borehole	Secup [m]	Seclow [m]	Date	Time teststart	Flow [m³/s]	T_T [m²/s]	S [–]	S_W [–]	r/B [–]	T_M[2] [m²/s]
KQ0044G01	2.98	3.00	2009-06-01	13:52	1.17E-07	2.53E-09	3.52E-08	–3.66		1.70E-11
KQ0045G02	0.3	1.10	2009-06-03	11:02	8.67E-06	3.05E-07	3.87E-07		0.014	2.42E-07
KQ0045G02	0.3	1.10	2009-06-03	13:21	1.78E-05	1.57E-06[1]	8.31E-07		1.58E-05	2.52E-07
KQ0045G02	0.6	1.10	2009-06-02	08:41	5.48E-05	1.48E-06[1]	8.52E-07		0.039	1.33E-06
KQ0045G02	0.8	1.10	2009-06-02	11:53	2.83E-06	1.85E-08	9.52E-08	–6.57		5.78E-08
KQ0045G02	0.9	1.10	2009-06-03	10:12	6.67E-06	1.60E-07	2.80E-07		0.053	1.15E-07
KQ0045G02	0.97	1.10	2009-06-02	10:06	1.27E-05	1.19E-06	7.64E-07		7.59E-06	1.78E-07
KQ0045G02	1.07	1.10	2009-06-02	09:42	6.67E-08	3.82E-10	1.37E-08	–5.21		1.91E-10

1) Evaluation not unambiguous hence not representative.

2) T-Moye.

Seven of the eight tests with a detectable flow were made in KQ0045G02. They were conducted below the lower packer in different positions. The leakage through the LECA zone described earlier probably increases the transmissivity in KQ0045G02. The transmissivity of these tests vary a lot and one of the tests between 0.97 and 1.10 m changes flow very rapidly about 40 seconds into the tests as seen in Figure AQ1–AQ4 in Appendix AQ. The most probable reason for this change of flow is that some fractures have been altered during the injection. The skin factors in all three tests evaluated with a radial model are rather low indicating a fractured skin zone in the boreholes.

In two of the tests, section 0.6–1.1 m and 0.3–1.1 m in KQ0045G02, no unambiguous evaluation was possible in AQTESOLVE. For these tests T-Moye is considered as representative. For more details about interpreting transient evaluations see /Harrström et al. 2007/.

No interference could be detected between any of the observation boreholes surrounding the heater borehole KG0046G03. This indicates that no continuous zone in the walls of the heater borehole has occurred. No fracture zones connecting any of the six observation boreholes with the surrounding rock could be detected as well. The sealing of the LECA filled slot seems to be good except in the bottom of borehole KQ0045G02 where there seems to be a probable leakage.

The test in KQ0044G01 displaying a detectable flow gives a very low transmissivity and since no pressure response is seen in the surrounding observation holes this zone might be of limited extent. The steady-state value (T_M) for transmissivity in KQ0044G01 differs from the transient (T_T) indicating that a stationary flow not has been reached during the test. The flow and also transmissivity during the seven tests in KQ0045G02 vary a lot in between, making it impossible to say anything about any fracture zones or anomalies in this borehole. Most of the flow probably passes through the leaking LECA filled slot into the heater borehole somewhere. There might be a fractured zone in the wall of the heater borehole but since the flow dropped after the initial tests the characteristics of the fracture zone must have been altered and therefore impossible to characterize.

References

Hantush M S, 1955. Nonsteady radial flow in an infinite leaky aquifer. Am. Geophys. Union Trans., v. 36, no 1, pp 95–100.

Hantush M S, 1959. Nonsteady flow to flowing wells in leaky aquifer. Jour. Geophys. Research, v. 64, no 8, pp 1043–1052.

Harrström J, Svensson T, Ludvigsson JE, 2007. Forsmark site investigation, Single-hole hydraulic tests in borehole KFM11A. SKB P-07-177, Svensk Kärnbränslehantering AB.

Hurst W, Clark J D, Brauer E B, 1969. The skin effect in producing wells. J. Pet. Tech., Nov. 1969, pp.1483–1489.

Marsily G M, 1986. Quantitative Hydrogeology. Academic Press, Inc.

Plots of the transient evaluations using AQTESOLVE

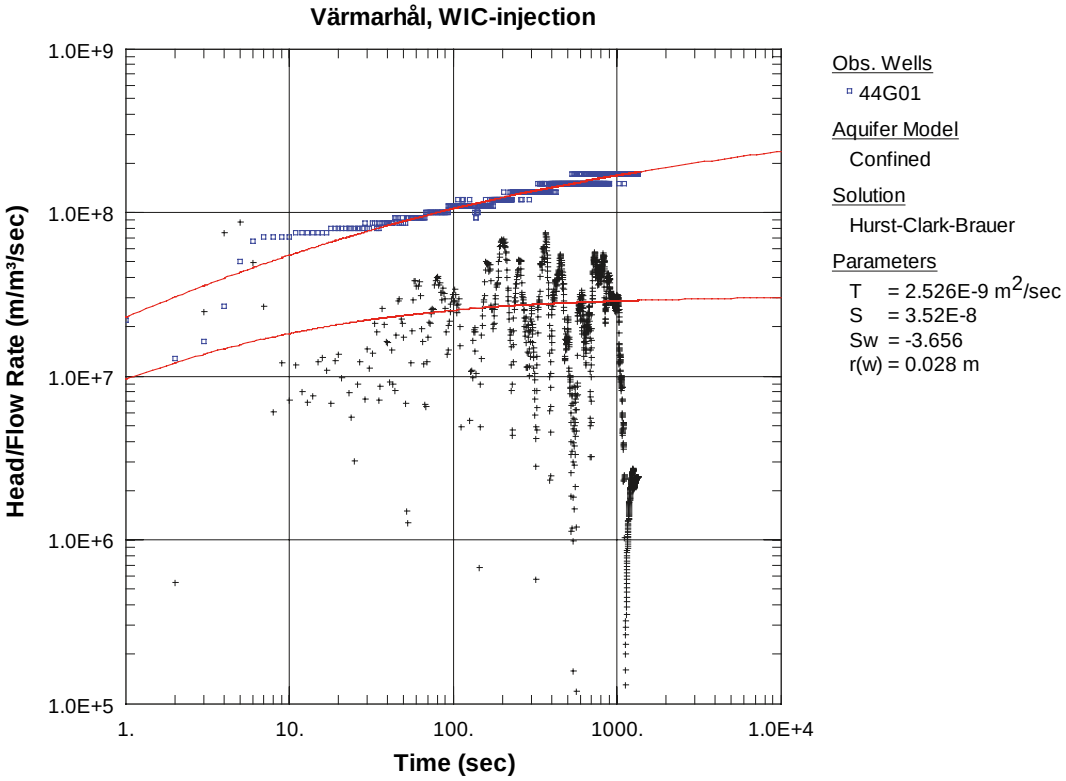

Figure AQ-1. *Log-log plot of drawdown (▫) and derivative, (+), versus equivalent time in KQ0044G01, section 2.98–3.0 m.*

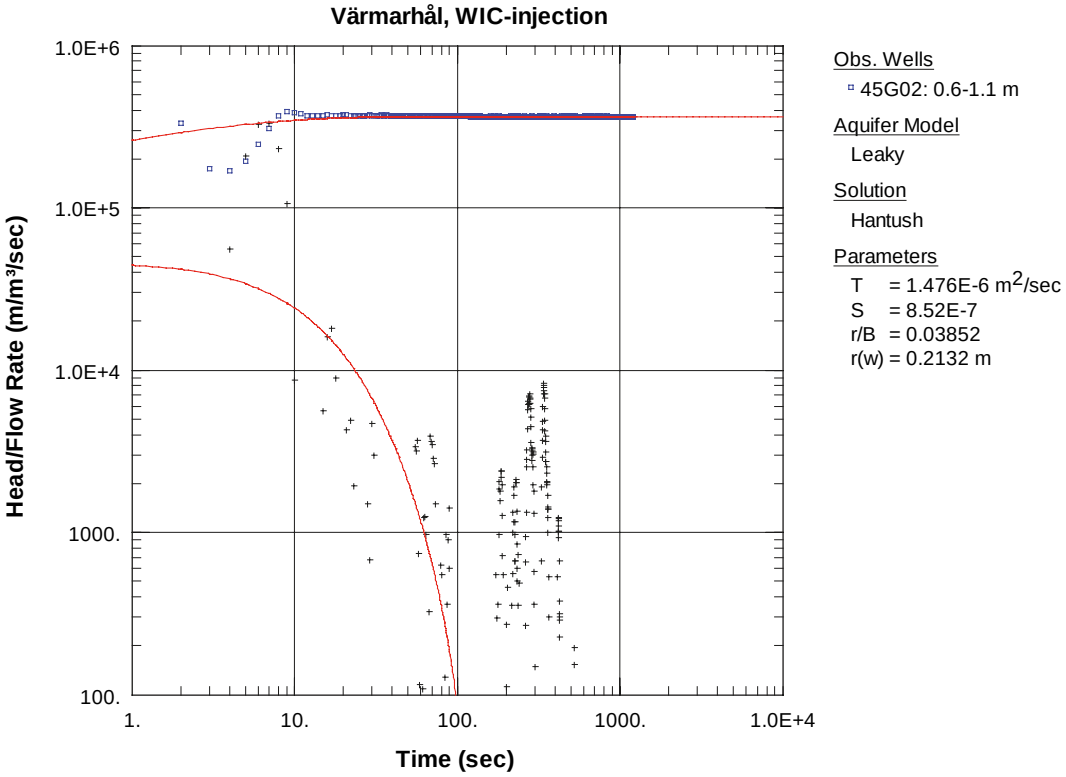

Figure AQ-2. *Log-log plot of drawdown (▫) and derivative, (+), versus equivalent time in KQ0045G02, section 0.6–1.1 m. This evaluation is not unambiguous hence not representative.*

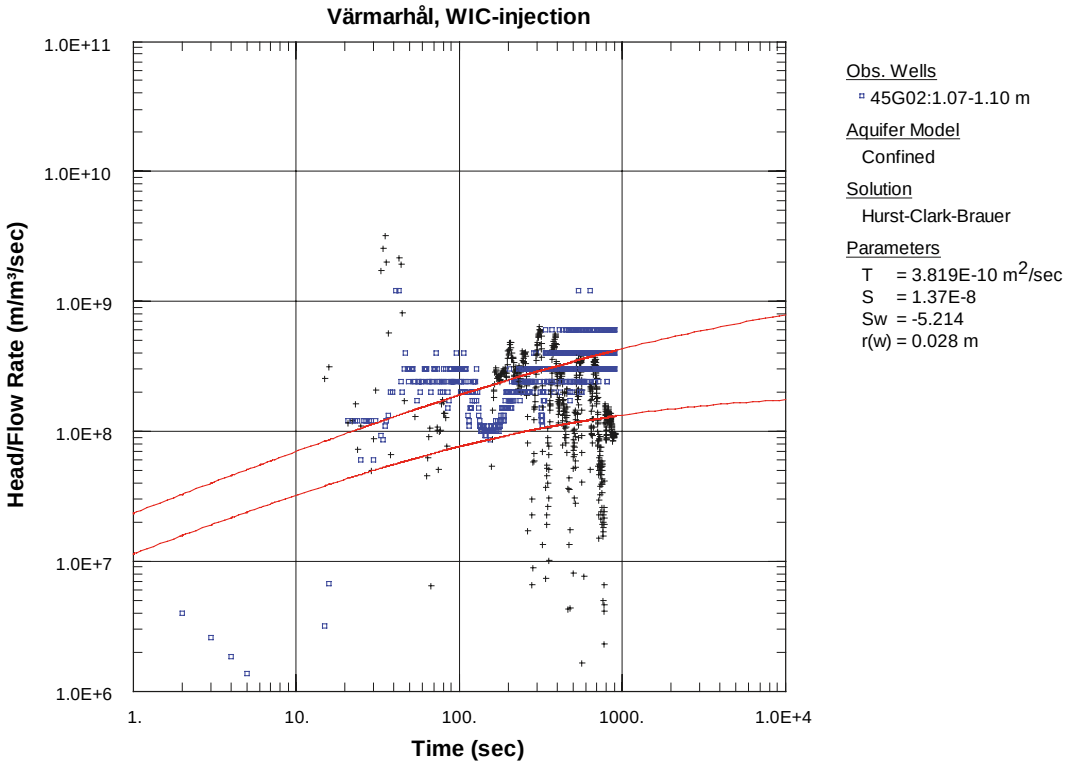

Figure AQ-3. *Log-log plot of drawdown (▫) and derivative, (+), versus equivalent time in KQ0045G02, section 1.07–1.10 m.*

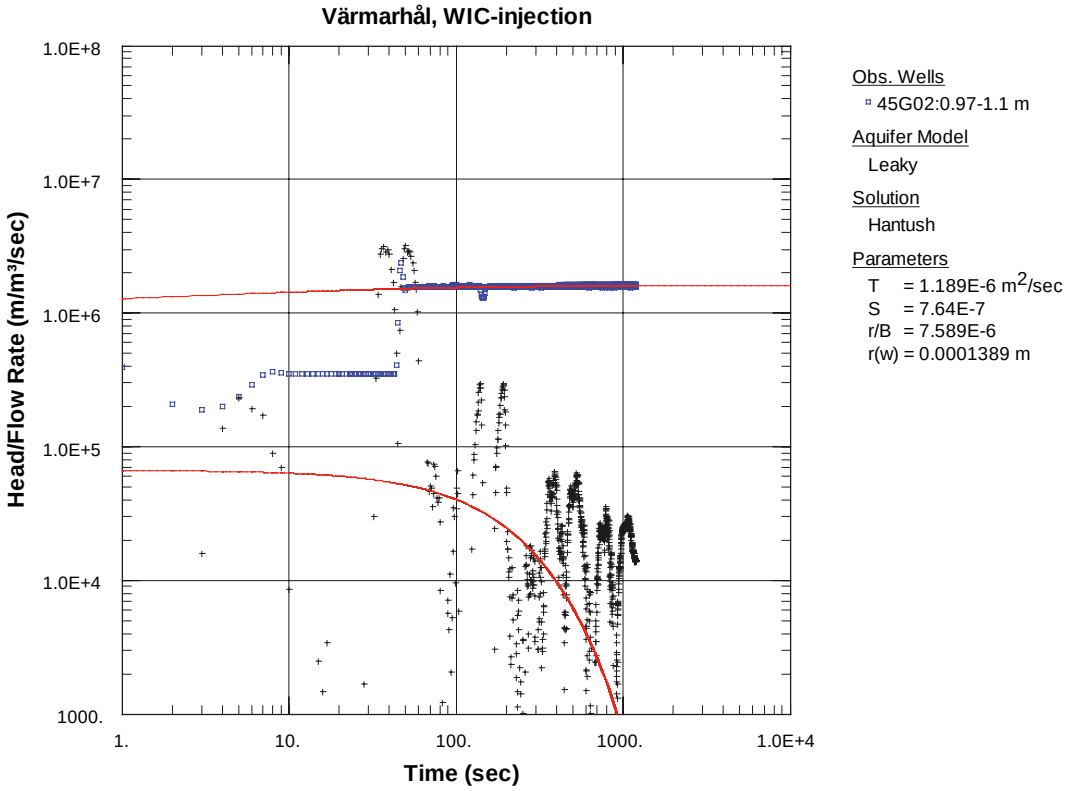

Figure AQ-4. *Log-log plot of drawdown (▫) and derivative, (+), versus equivalent time in KQ0045G02, section 0.97–1.10 m.*

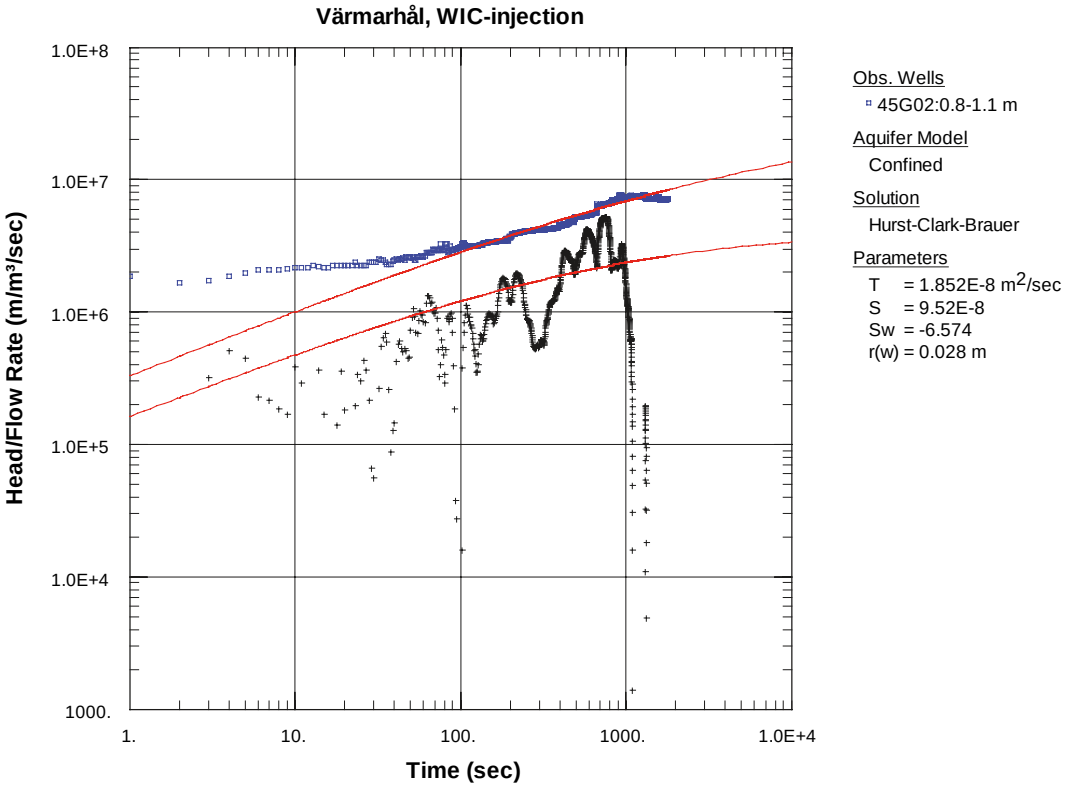

Figure AQ-5. *Log-log plot of drawdown (▫) and derivative, (+), versus equivalent time in KQ0045G02, section 0.8–1.1 m.*

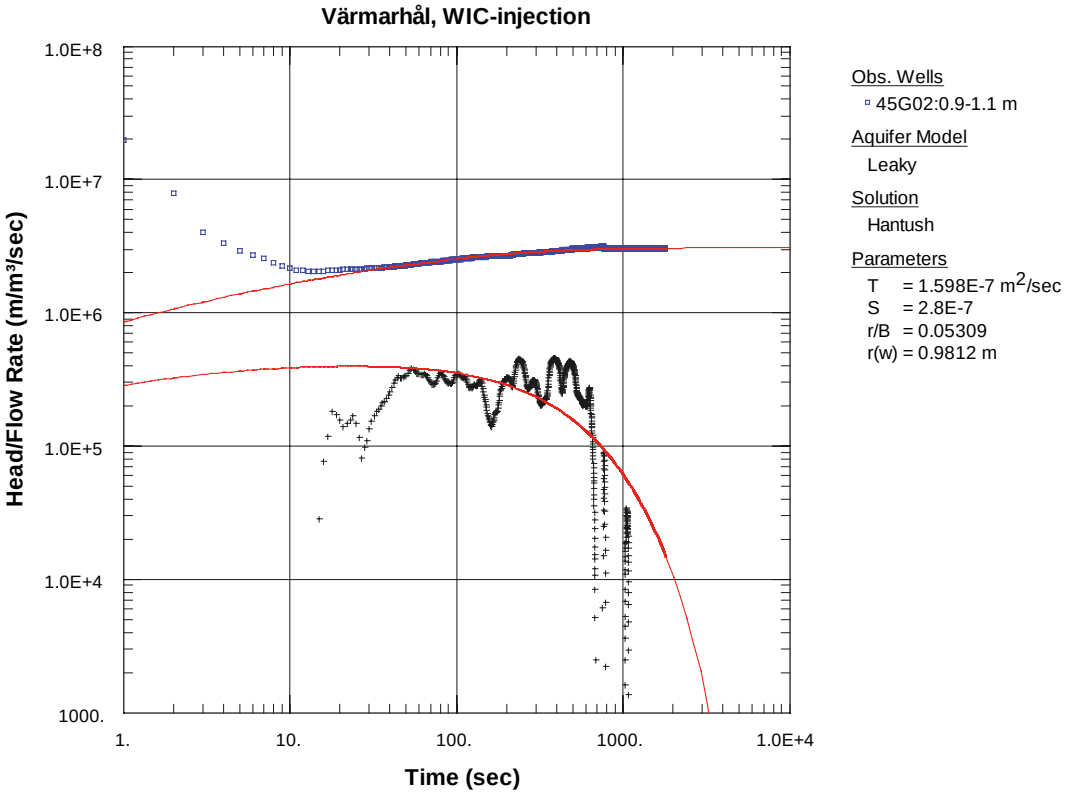

Figure AQ-6. *Log-log plot of drawdown (▫) and derivative, (+), versus equivalent time in KQ0045G02, section 0.9–1.1 m.*

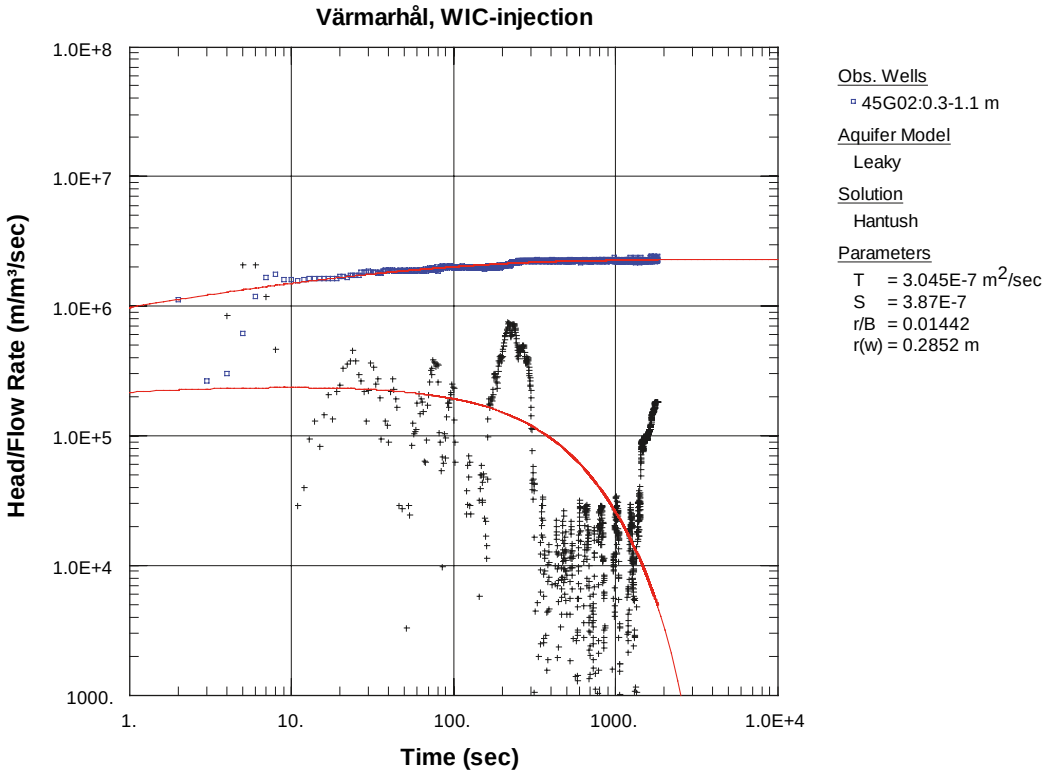

Figure AQ-7. *Log-log plot of drawdown (▫) and derivative, (+), versus equivalent time in KQ0045G02, section 0.3–1.1 m.*

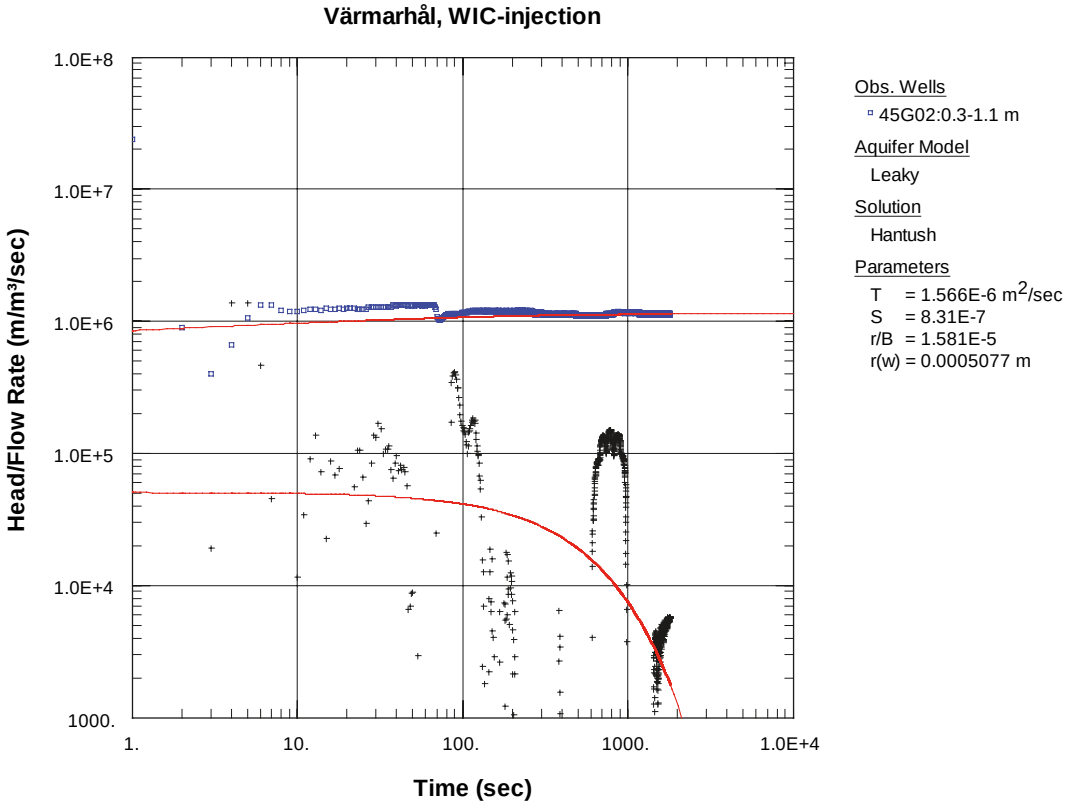

Figure AQ-8. *Log-log plot of drawdown (▫) and derivative, (+), versus equivalent time in KQ0045G02, section 0.3–1.1 m. This test was made in the same position as the previous but with twice the injection pressure. The transient evaluation is not unambiguous hence not representative for the section.*

Appendix R

Results from back-calculation of temperatures and stresses

Billy Fälth, ClayTechnology AB

February 2010

Contents

R1 Model description

R1.1 General

Estimates of the stress development in the heating hole walls are done by numerical modelling. The finite element program Code_Bright, version 3 is used to analyse four thermo-mechanical models, each representing one test. The modelling approach comprises two steps:

1. A thermal model is calibrated in order to capture the temperature development at points which correspond to the instrument locations in the tests. The possible heat losses in the real tests are not accounted for explicitly in the model. Instead, the heat loads are adjusted in order to get a good temperature fit.
2. The calibrated heat loads are applied in a thermo-mechanical model which calculates the stresses after excavation of heating holes and simulates the stress evolution during the following heating phase.

R1.2 Geometry

Figure R-1 shows the outlines and main dimensions of the models and Figure R-2 shows a detailed view of the heating holes. The diameter of the heating holes is 0.485 m down to 4 m depth. The total depth including the concrete foundation and the bottom parts of the holes is 5.4 m. The regions denoted “Slot 1” and “Slot 2” are assumed to be air-filled when Test 1 and Test 2 are simulated. When Test 3 and Test 4 are simulated, “Slot 1” is assumed to be filled with LECA pellets and “Slot 2” represents the sand-filled 385 mm diameter tube.

R1.3 Material properties

In /Andersson 2007/ the geology of the APSE tunnel, as well as the *in situ* stress state and the means used to determine, is quite extensively described. The property parameter values for the rock and for the other materials in the models are summarized in Table R-1. All materials are assumed to be linear elastic. Linear heat conduction is assumed for all materials.

Values in brackets are fictitious material properties used when the excavation of the heating holes is simulated. The values are applied to materials in the interior of the openings in order to reduce irrelevant influence on the stresses around the holes.

It is assumed that the bond between the concrete foundation and the rock is not strong enough to withstand the shear stresses resulting from the difference in thermal expansion between rock and concrete. In order not to induce irrelevant effects on the calculated rock stresses, the thermal expansion coefficient of the concrete is set equal to that of the rock.

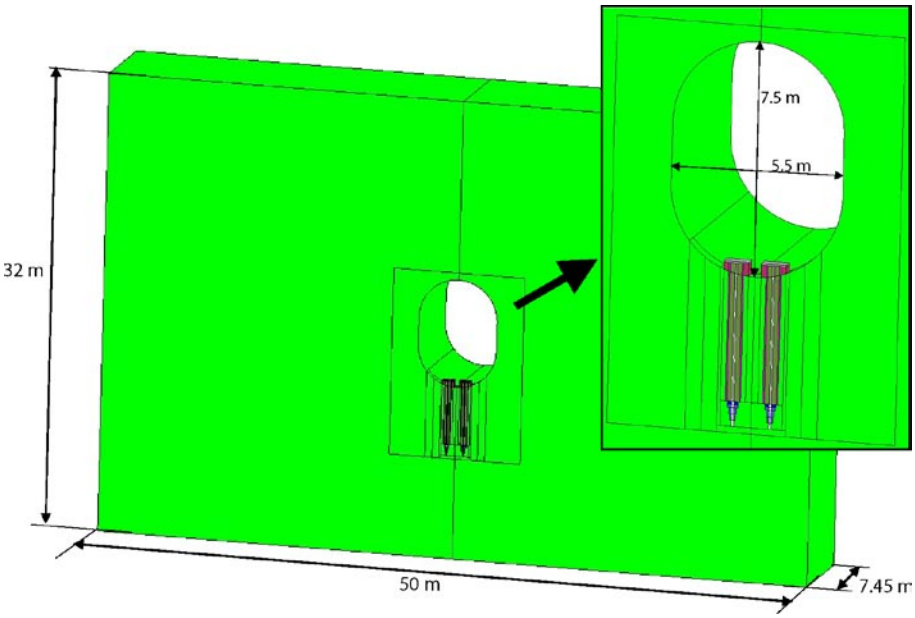

Figure R-1. *Geometric outlines of the models.*

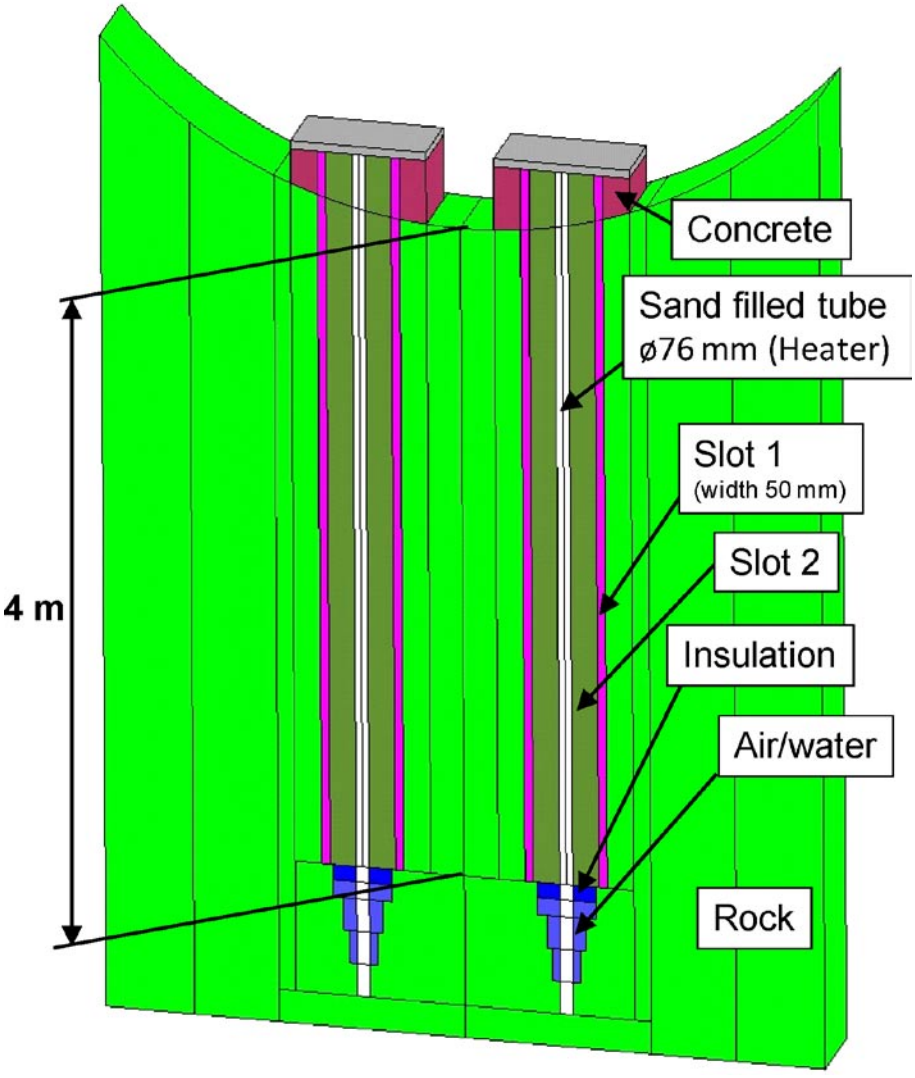

Figure R-2. *Detailed view of heating holes.*

Table R-1. Material property parameter values. Values in brackets are fictitious material properties used during the excavation phase to minimize the influence on the stresses around the heating hole.

	ρ [kg/m³]	C [J/(kg·K)]	λ [W/(m·K)]	E [GPa]	ν [–]	α [1/K]
Rock	2,730	770	3.2	55	0.25	$7 \cdot 10^{-6}$
Concrete	2,000	900	1.7	30 (0.030)	0.25	$7 \cdot 10^{-6}$ *)
Insulation	20	5,000	0.04	0.001	0.25	0
Heater tube	7,500	500	8.3	0.05	0.25	$1 \cdot 10^{-5}$
Leca pellets	300	1,000	0.15	0.005 (0.001)	0.25	$7 \cdot 10^{-6}$
Air	1.3	1,000	1.5	0.001	0.25	0
Air/water	1.3	1,000	0.1	0.001	0.25	0
Sand filled steel tube	1,700	800	0.7	0.05	0.25	$7 \cdot 10^{-6}$

*) Value set equal to that of the rock in order to simulate slip between concrete and rock during heating.

R1.4 Initial conditions, boundary conditions and heat loads

The *in situ* stresses applied in the model are presented in Table R-2. The values are back-calculated and best-estimate stress state for the APSE site /Andersson 2007/. The S_{yy} stress is the largest and is perpendicular to the tunnel axis. The smallest stress, S_{xx}, is parallel to the tunnel and the intermediate stress, S_{zz}, is the vertical component. These stress components are principal stresses.

The model initial temperatures (Table R-3) are based on the temperature data from the tests. Since the four tests were run in sequence the rock mass temperature was slightly increased after each test. For presentation purpose, different initial temperatures were set for each test (see Section R2.1, below). Note that the model initial temperature has no importance for the calculated thermal stresses since these are based on temperature increments only. The results from one model were used to control that it is an appropriate approximation to ignore the possible stress effects of the pre-heating (cf Section R2.2.4).

The thermal boundary conditions in the tunnel are illustrated in Figure R-3. The values of the convection heat transfer coefficient, γ, set at different parts are shown. The value is set at 0.5 W/(m^{2}K) above the experiment holes in order to simulate coverage by insulation. At the remaining parts of the tunnel the value is set at 10 W/(m^{2}K). The temperature in the tunnel is assumed to be 15°C. It shall be noted that there may be differences between the model and the field tests regarding the exact extent and heat transfer coefficients of the thermal boundary conditions.

All outer boundaries of the model are adiabatic and locked for normal displacements (roller boundaries).

The heat loads in the models are adjusted in order to fit the temperatures recorded during the tests. The heat loads applied in the models are presented in Figure R-4 along with the heat loads in the tests. The heat loads in the models are in general significantly lower than the real heat loads. The difference between experiment and model is due to heat losses in the experiment which not are explicitly accounted for in the models. In Test 1 the heat losses were caused primarily by the camera cooling system. In Test 2 and Test 4 it was caused by the wetting system. In Test 2 water was evaporated at the heater tube and in Test 4 water was circulated in the LECA-filled slot.

Table R-2. In situ stresses.

S_{xx}	S_{yy}	S_{zz}
10 MPa	30 MPa	15 MPa

Table R-3. Initial temperatures.

Test 1	Test 2	Test 3	Test 4
15°C	16°C	17.5°C	16°C

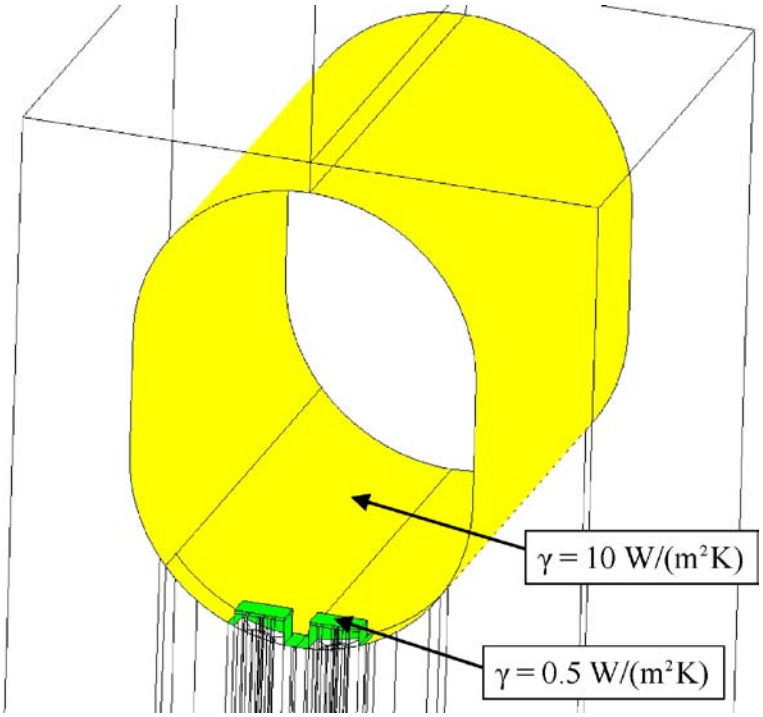

Figure R-3. *Thermal boundary conditions. The γ-factor is a convection heat transfer coefficient. The temperature in the tunnel is assumed to be 15°C.*

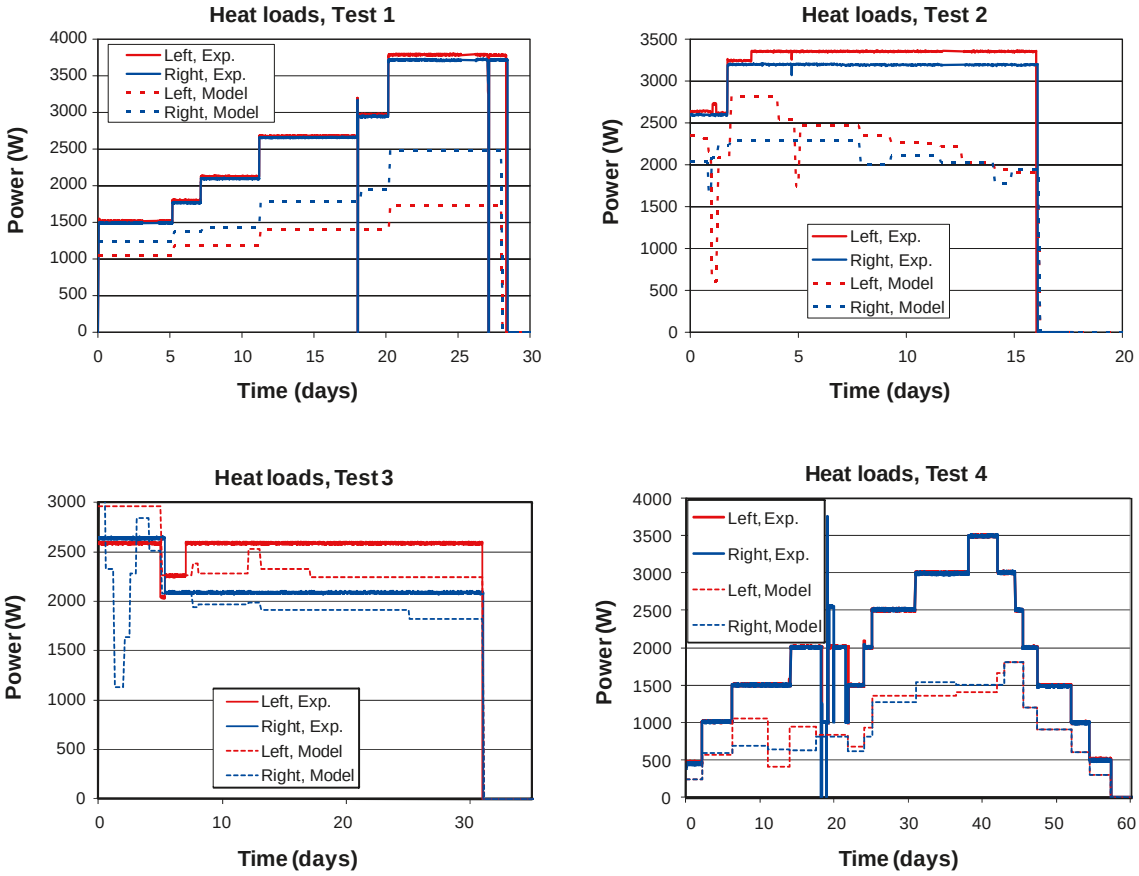

Figure R-4. *The diagrams show the temporal development of heat loads applied in the models plotted along with the heat loads in the corresponding field tests.*

R2 Results

R2.1 Temperatures

In this section the temperature results are presented. The results are divided into four sections; one for each test. In order to show the fit between the temperatures measured in the tests and the temperatures recorded in the models, the temperature diagrams show both calculated and measured temperatures. The figure above each pair of diagram shows the location of the measurement points relative to the heating holes. The legends in the diagrams indicate the depth below the upper surface of the concrete foundations.

In order to achieve a relevant heating power input, the power calibration was primarily focused on capturing the temperature development in the outer instrument holes and at locations at some depth from the tunnel floor. At these locations, the thermal development is less sensitive to details in the heat source geometry, to local water movements around and inside the heating holes, details in the floor insulation and to small scale variations of the rock heat diffusivity.

It can be observed in the diagrams that a reasonably good temperature fit is achieved at most locations whereas the agreement between model and experiment is less good at some other. A good fit is particularly difficult to achieve inside the heating holes in Test 3 and Test 4 (Figure R-18, Figure R-19, Figure R-23 and Figure R-24) whereas the fit in the heating holes of Test 1 and Test 2 is better (Figure R-8, Figure R-9, Figure R-13 and Figure R-14). In Test 1 and Test 2 the thermocouples inside the heating holes monitor a temperature that depends both on the rock wall temperature and the air temperature inside the hole. The monitored temperature may vary depending on the contact pressure achieved between the thermocouple and the rock wall. In Test 3 and Test 4 the annular space between the sand-filled 385 mm diameter tube and the rock wall was filled with LECA pellets. It can’t be excluded that the filling with LECA have caused some contact loss between some temperature gauges and the rock wall, meaning that it is the LECA temperature rather than the rock wall temperature that is monitored. In addition, the thermal conductivity of the LECA filling may vary depending on its moisture content (see e.g. Figure R-19). This may also have some influence on the monitored temperatures.

At the shallow measurement points (0.5 m) the monitored temperatures may be strongly influenced by the properties of the floor isolation (thickness, tightness etc.) and by local water movements inside and around the instrumentation holes. This is reflected by the results at this depth; the temperature fit at 0.5 m depth is poor in many cases.

R2.1.1 Test 1

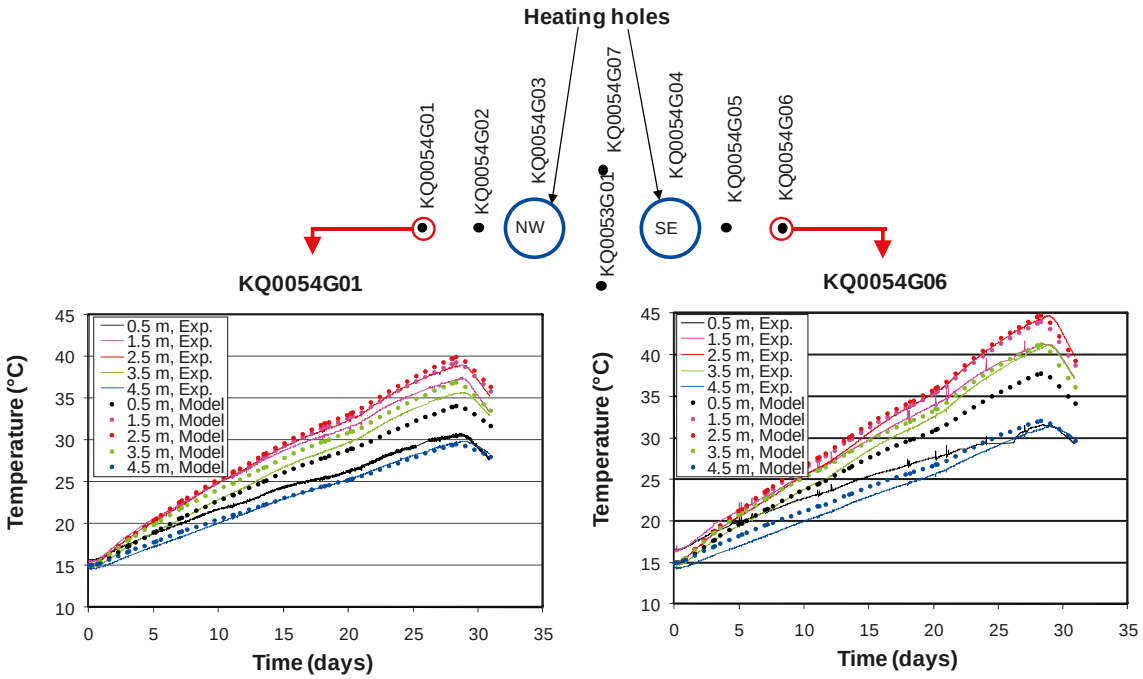

Figure R-5. *Comparison between temperatures recorded in instrumentation holes KQ0054G01 and KQ0054G06 during Test 1 and corresponding calculated temperatures.*

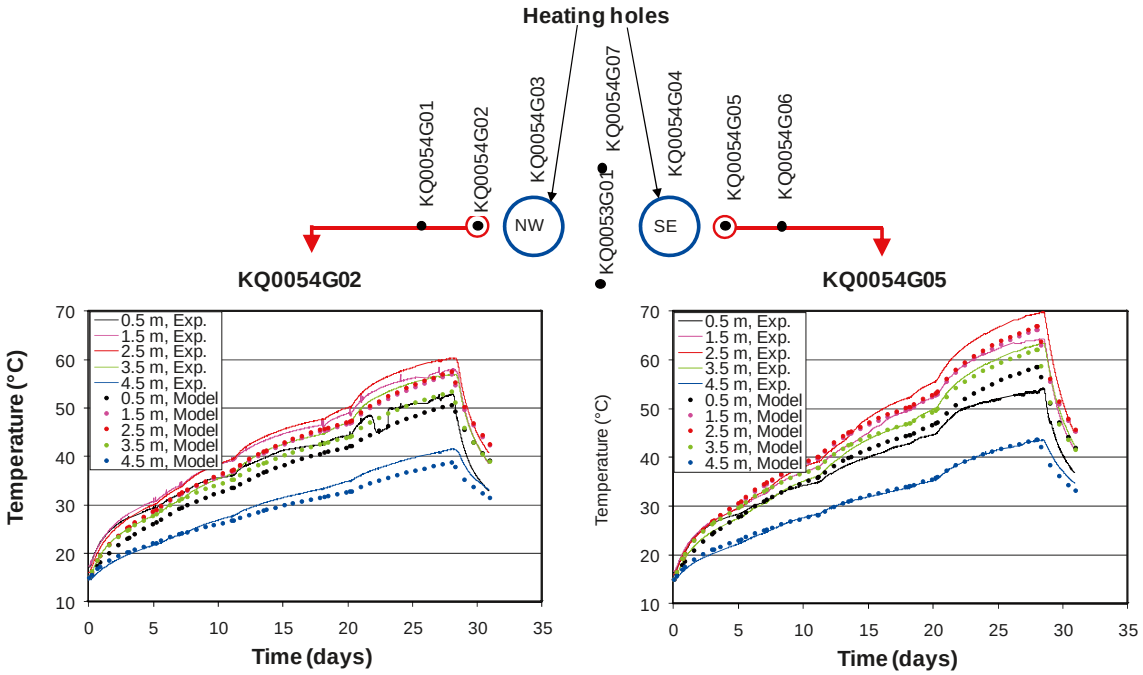

Figure R-6. *Comparison between temperatures recorded in instrumentation holes KQ0054G02 and KQ0054G05 during Test 1 and corresponding calculated temperatures.*

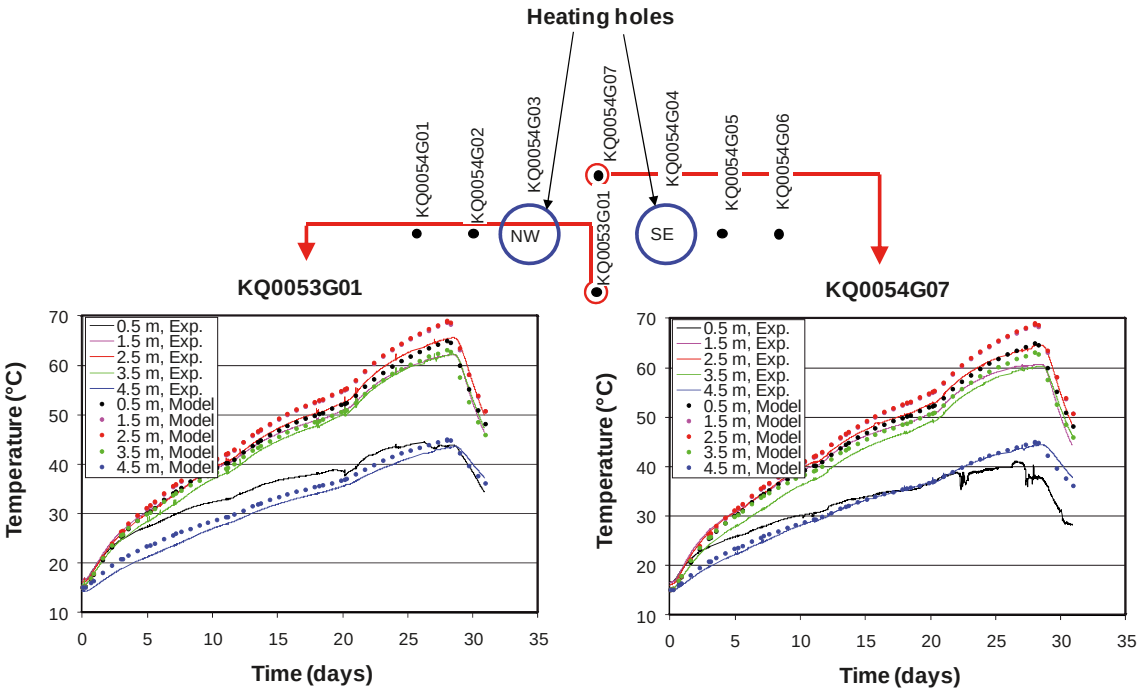

Figure R-7. *Comparison between temperatures recorded in instrumentation holes KQ0053G01 and KQ0054G07 during Test 1 and corresponding calculated temperatures.*

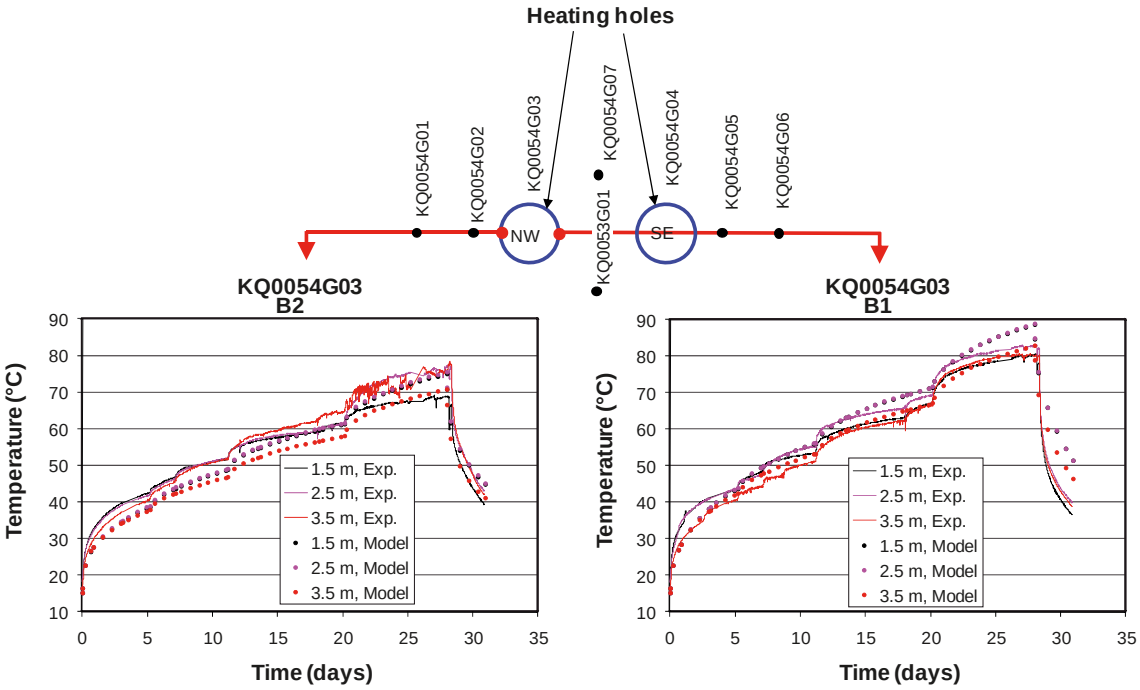

Figure R-8. *Comparison between temperatures recorded at borehole wall in KQ0054G03 during Test 1 and corresponding calculated temperatures.*

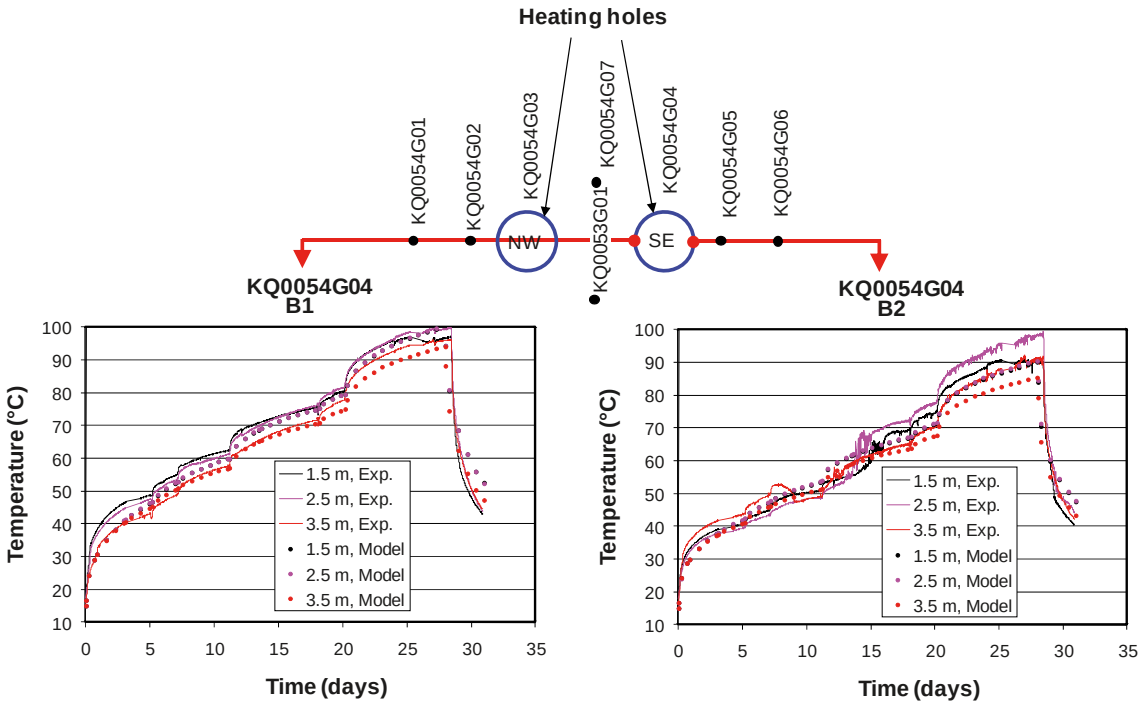

Figure R-9. *Comparison between temperatures recorded at borehole wall in KQ0054G04 during Test 1 and corresponding calculated temperatures.*

R2.1.2 Test 2

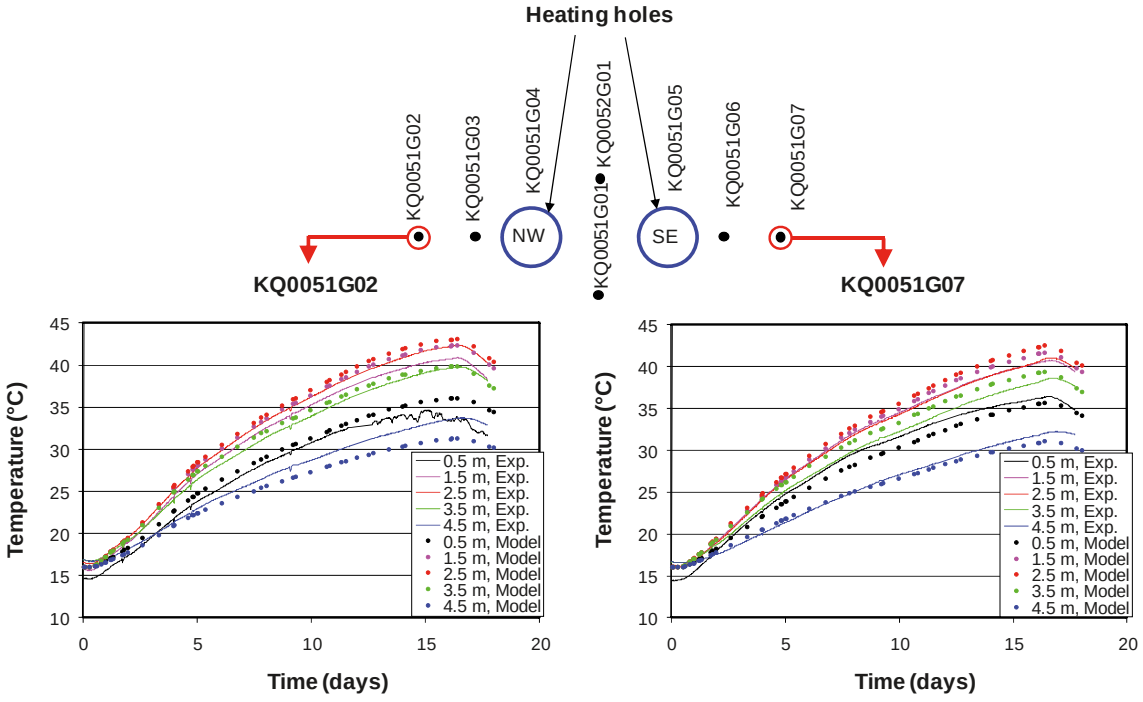

Figure R-10. *Comparison between temperatures recorded in instrumentation holes KQ0051G02 and KQ0051G07 during Test 2 and corresponding calculated temperatures.*

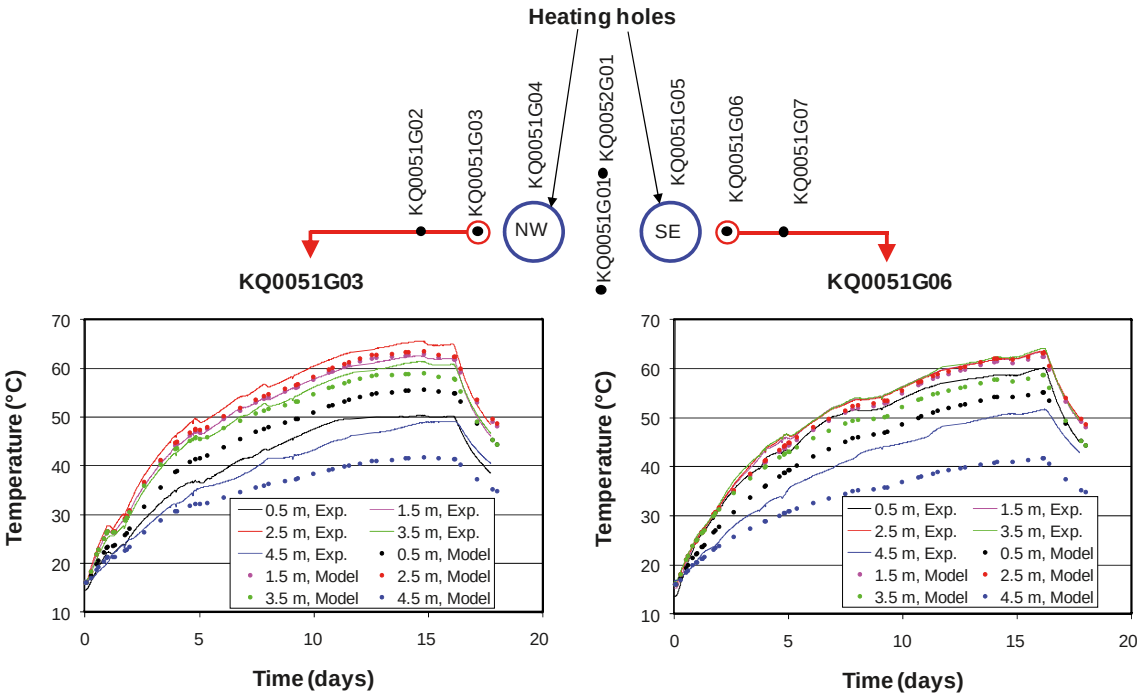

Figure R-11. *Comparison between temperatures recorded in instrumentation holes KQ0051G03 and KQ0051G06 during Test 2 and corresponding calculated temperatures.*

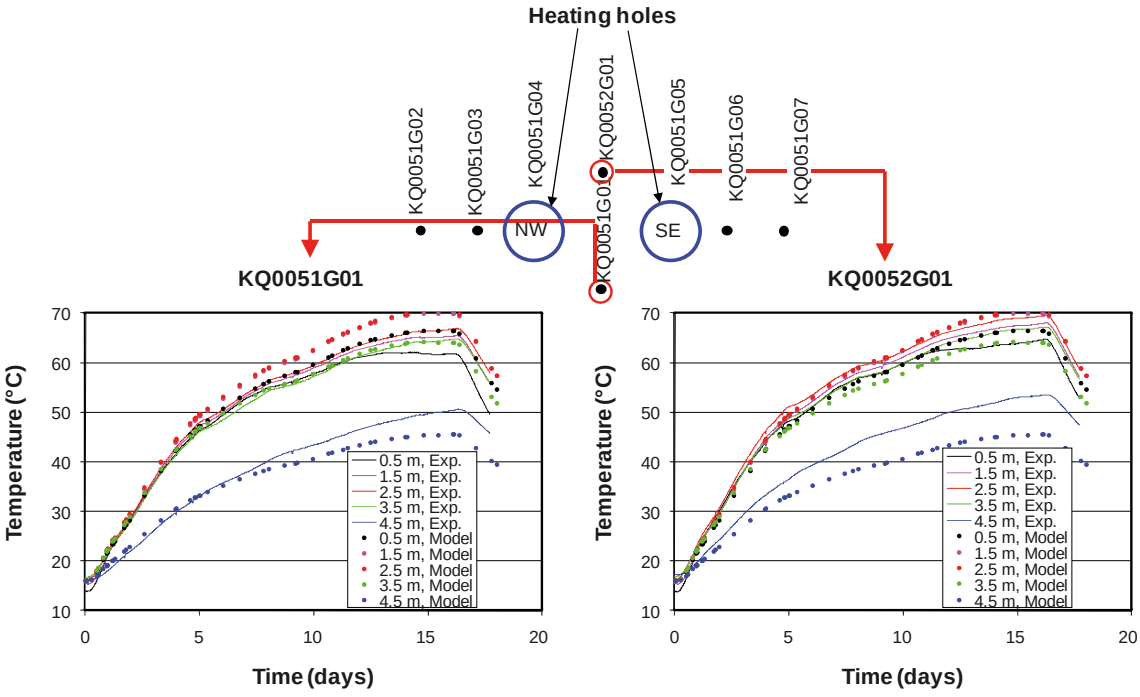

Figure R-12. *Comparison between temperatures recorded in instrumentation holes KQ0051G01 and KQ0052G01 during Test 2 and corresponding calculated temperatures.*

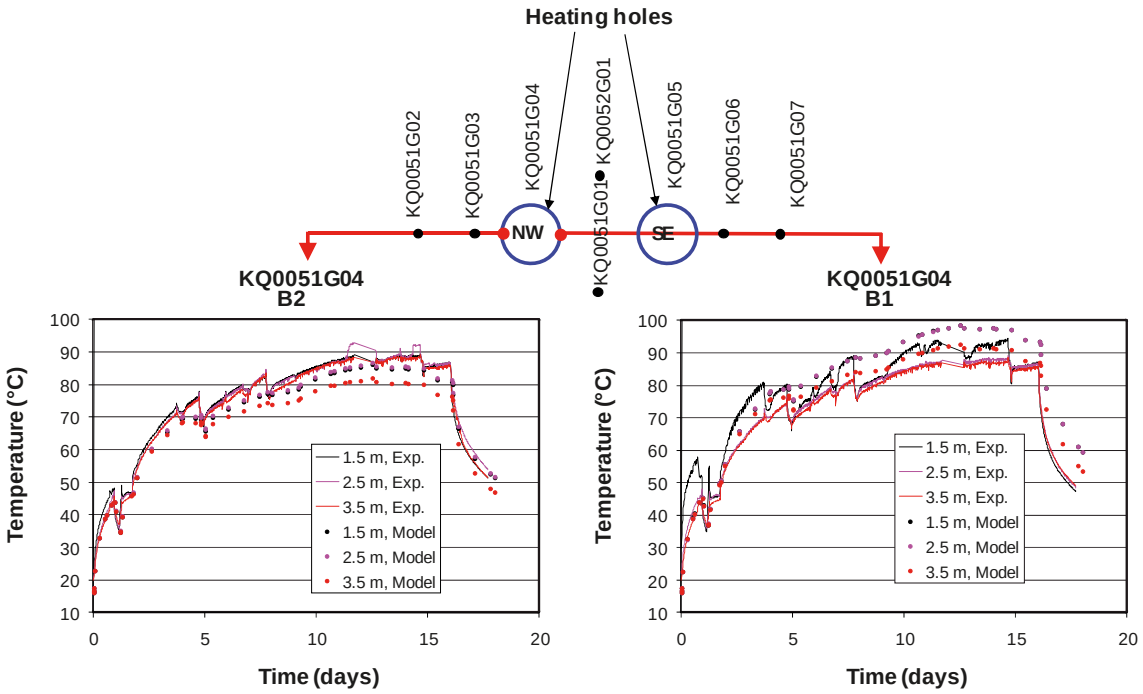

Figure R-13. *Comparison between temperatures recorded at borehole wall in KQ0051G04 during Test 2 and corresponding calculated temperatures.*

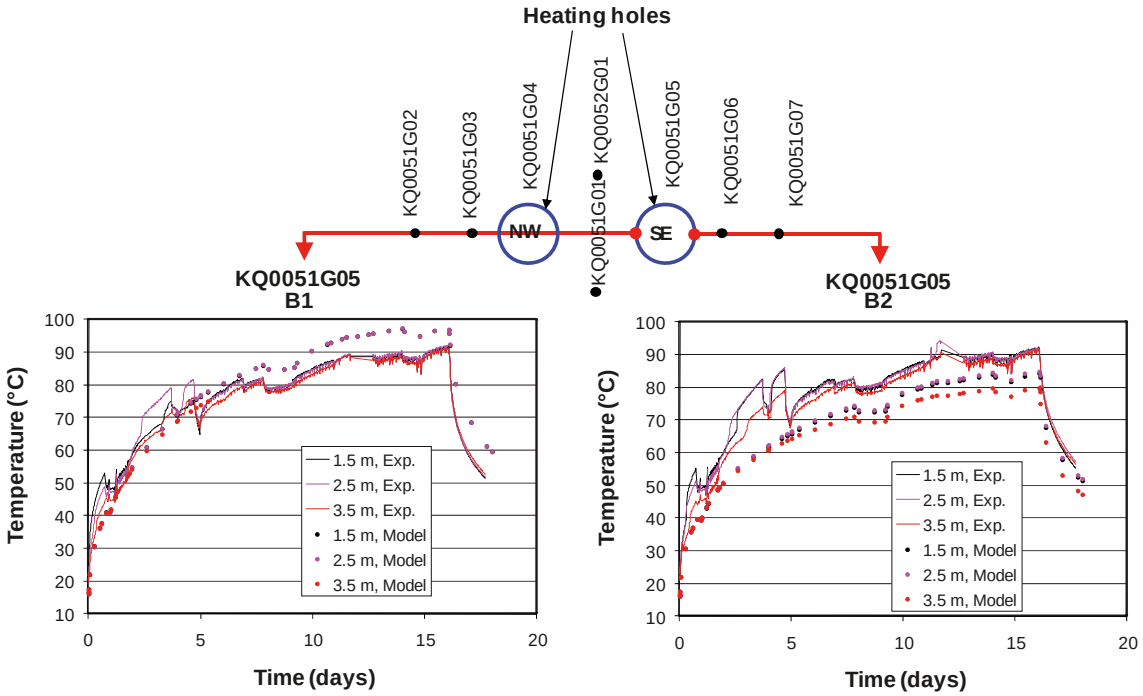

Figure R-14. *Comparison between temperatures recorded at borehole wall in KQ0051G05 during Test 2 and corresponding calculated temperatures.*

R2.1.3 Test 3

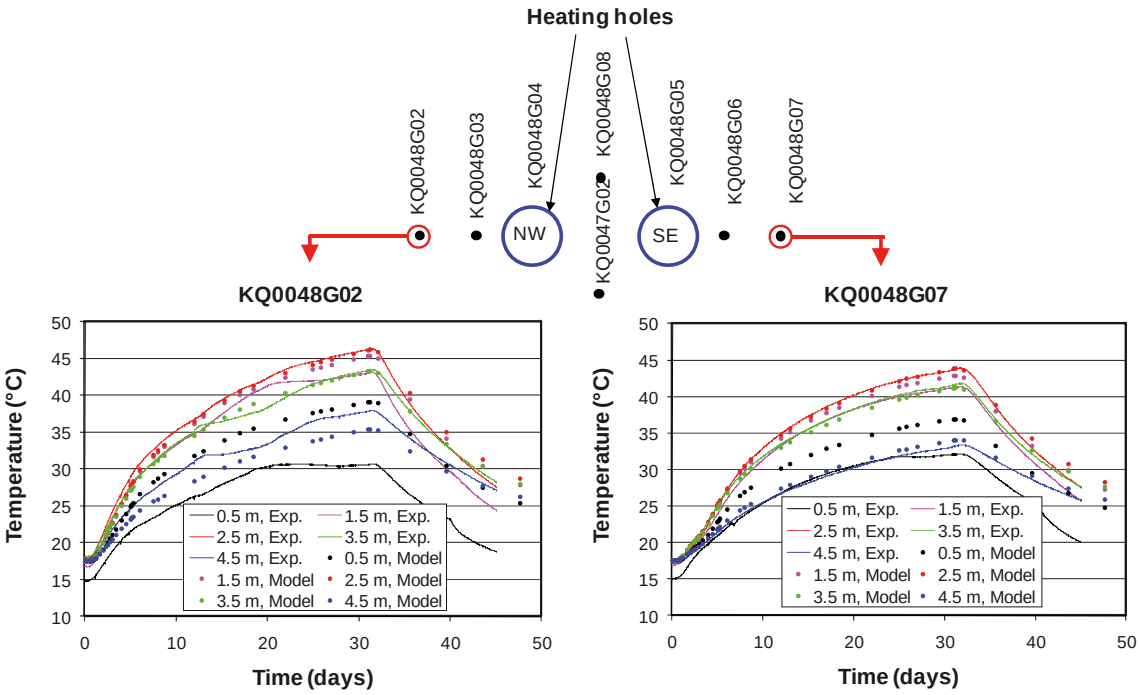

Figure R-15. *Comparison between temperatures recorded in instrumentation holes KQ0048G02 and KQ0048G07 during Test 3 and corresponding calculated temperatures.*

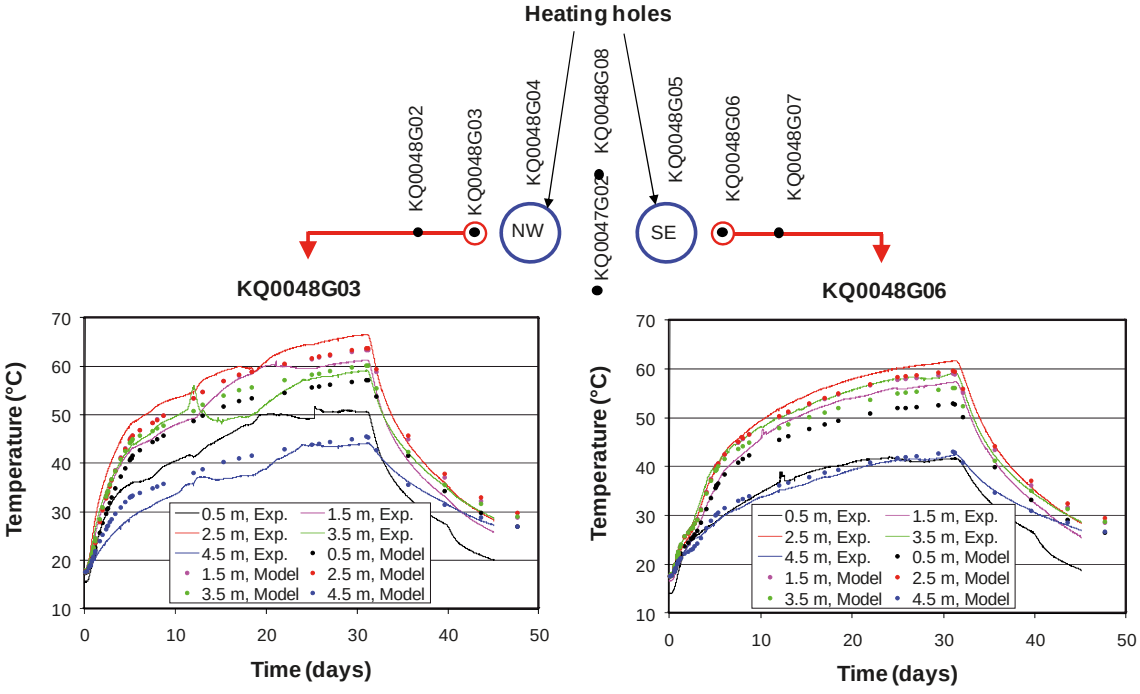

Figure R-16. *Comparison between temperatures recorded in instrumentation holes KQ0048G03 and KQ0048G06 during Test 3 and corresponding calculated temperatures.*

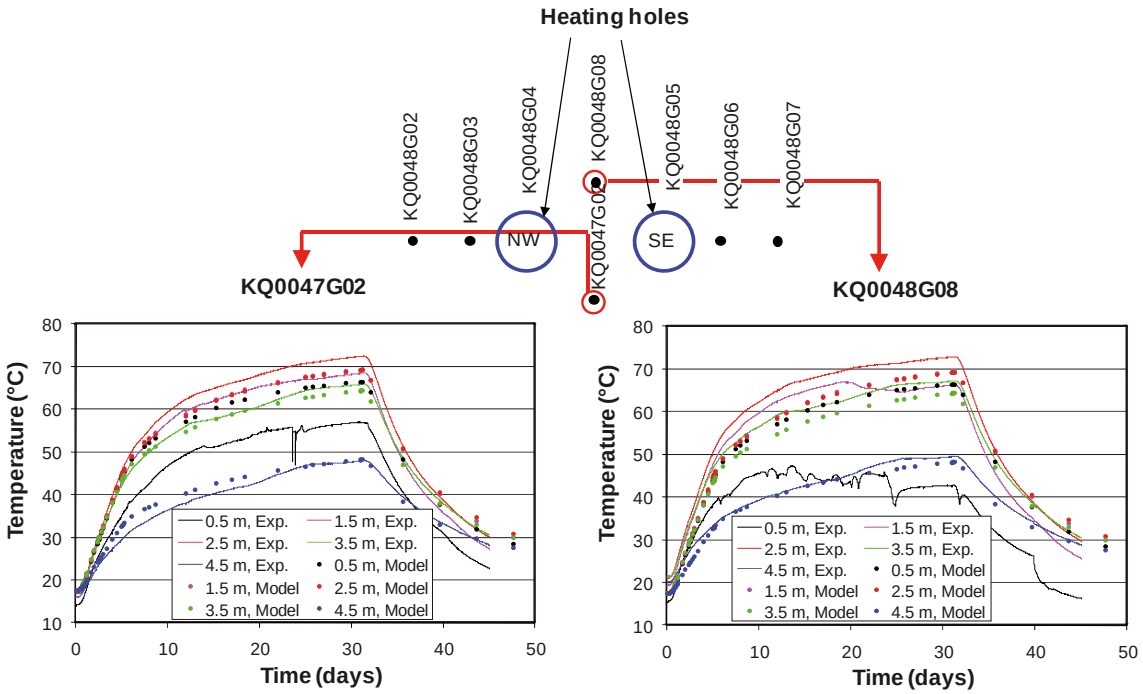

Figure R-17. *Comparison between temperatures recorded in instrumentation holes KQ0047G02 and KQ0048G08 during Test 3 and corresponding calculated temperatures.*

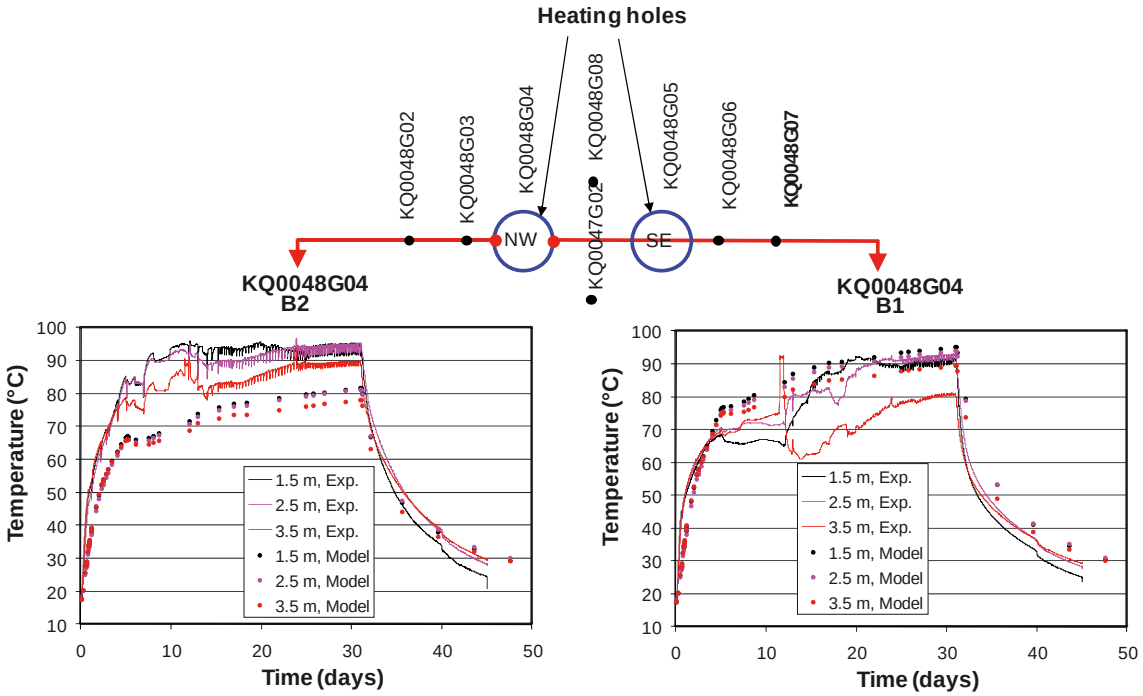

Figure R-18. *Comparison between temperatures recorded at borehole wall in KQ0048G04 during Test 3 and corresponding calculated temperatures.*

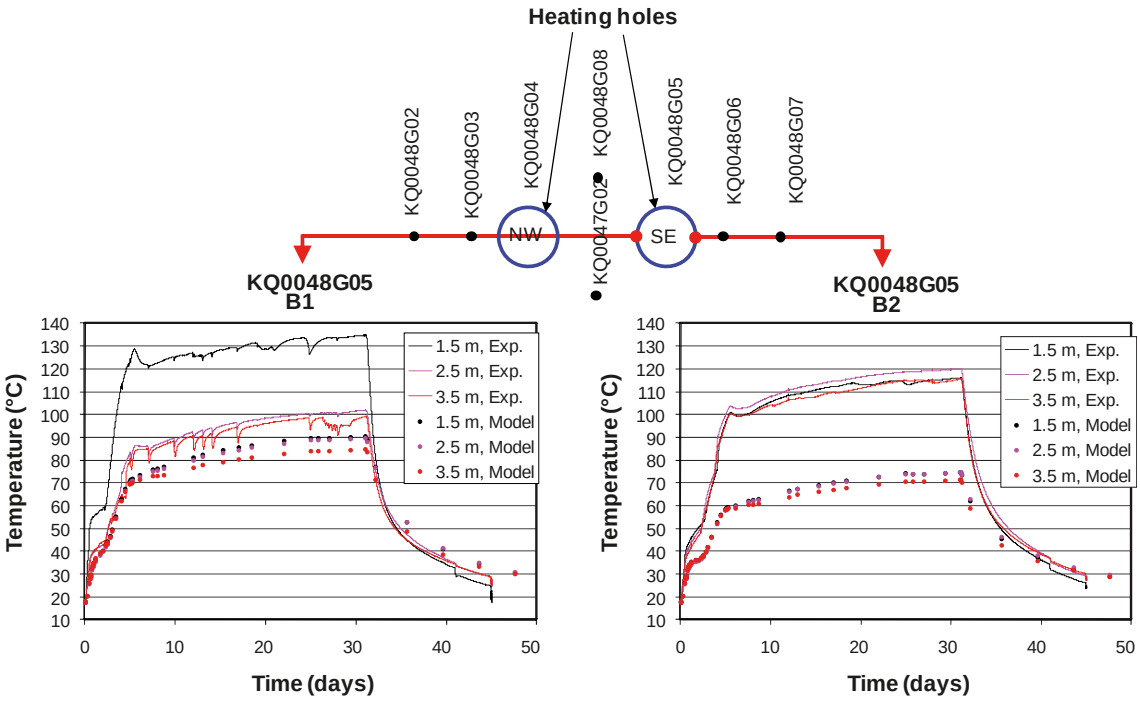

Figure R-19. *Comparison between temperatures recorded at borehole wall in KQ0048G05 during Test 3 and corresponding calculated temperatures.*

R2.1.4 Test 4

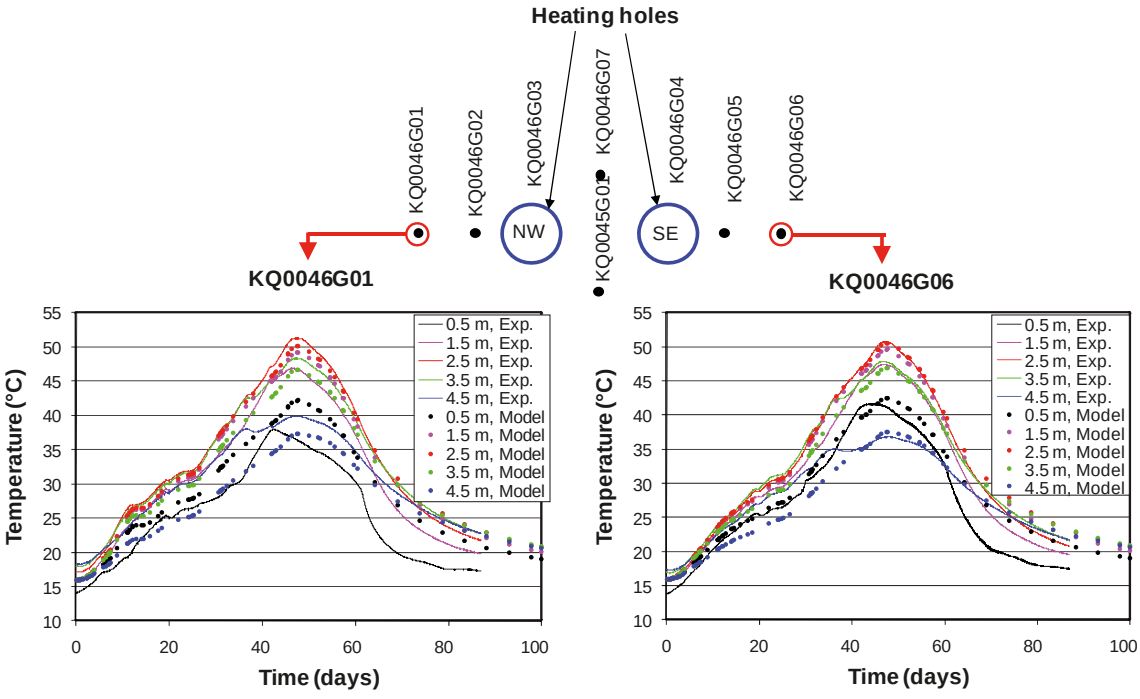

Figure R-20. *Comparison between temperatures recorded in instrumentation holes KQ0046G01 and KQ0046G06 during Test 4 and corresponding calculated temperatures.*

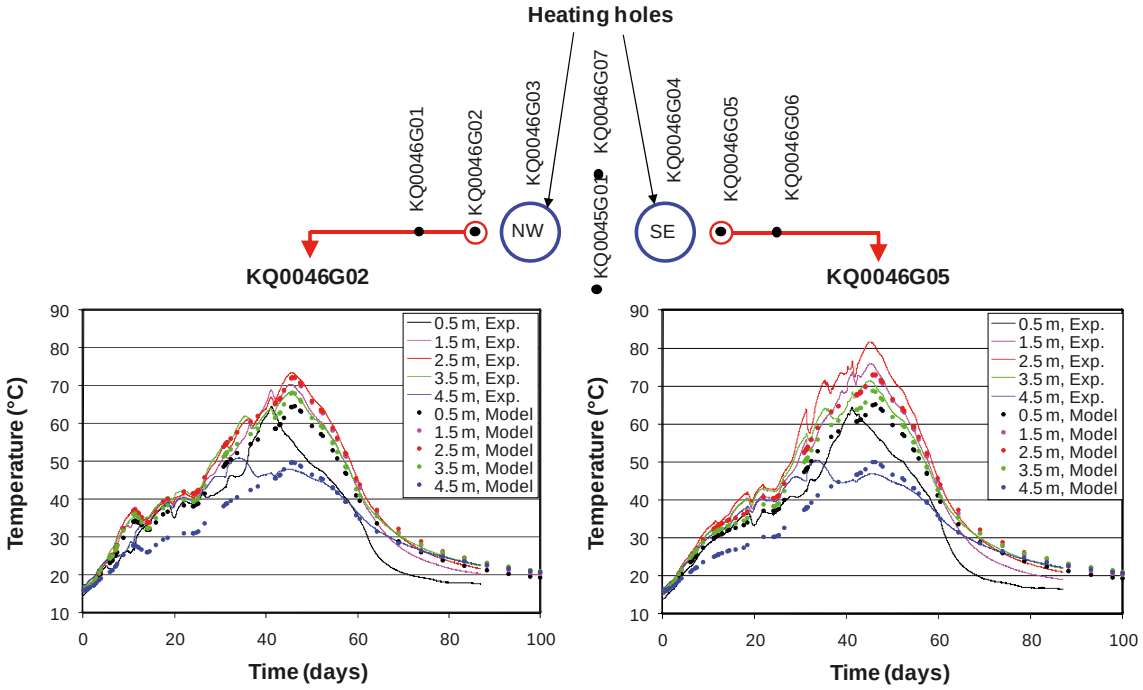

Figure R-21. *Comparison between temperatures recorded in instrumentation holes KQ0046G02 and KQ0046G05 during Test 4 and corresponding calculated temperatures.*

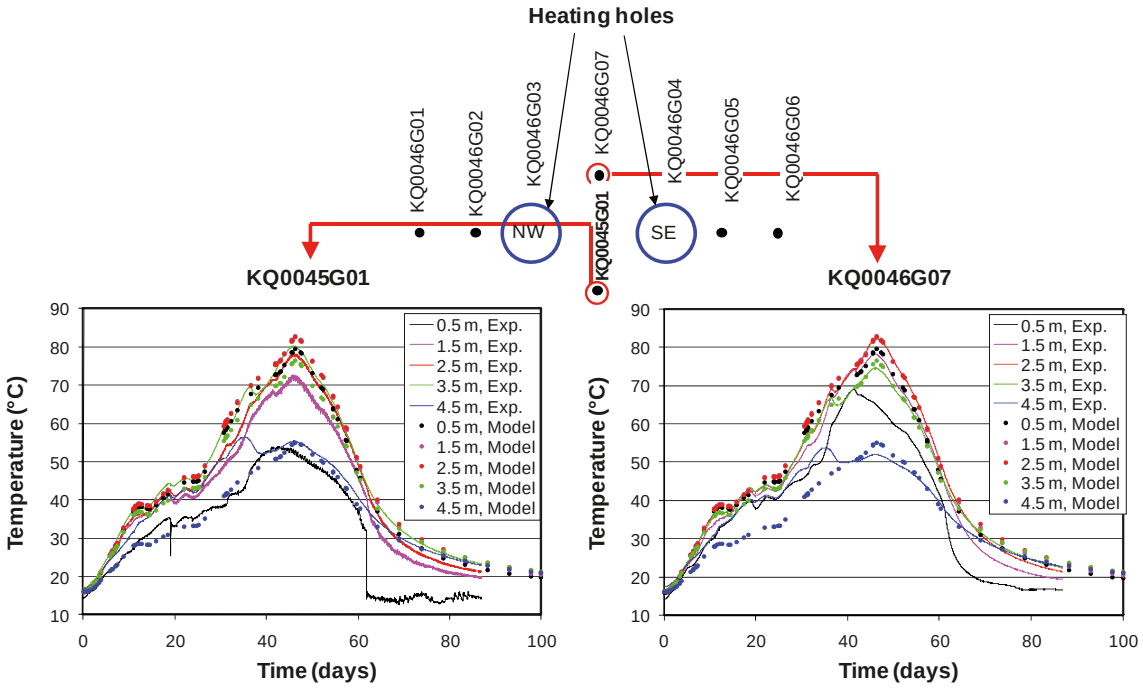

Figure R-22. *Comparison between temperatures recorded in instrumentation holes KQ0045G01 and KQ0046G07 during Test 4 and corresponding calculated temperatures.*

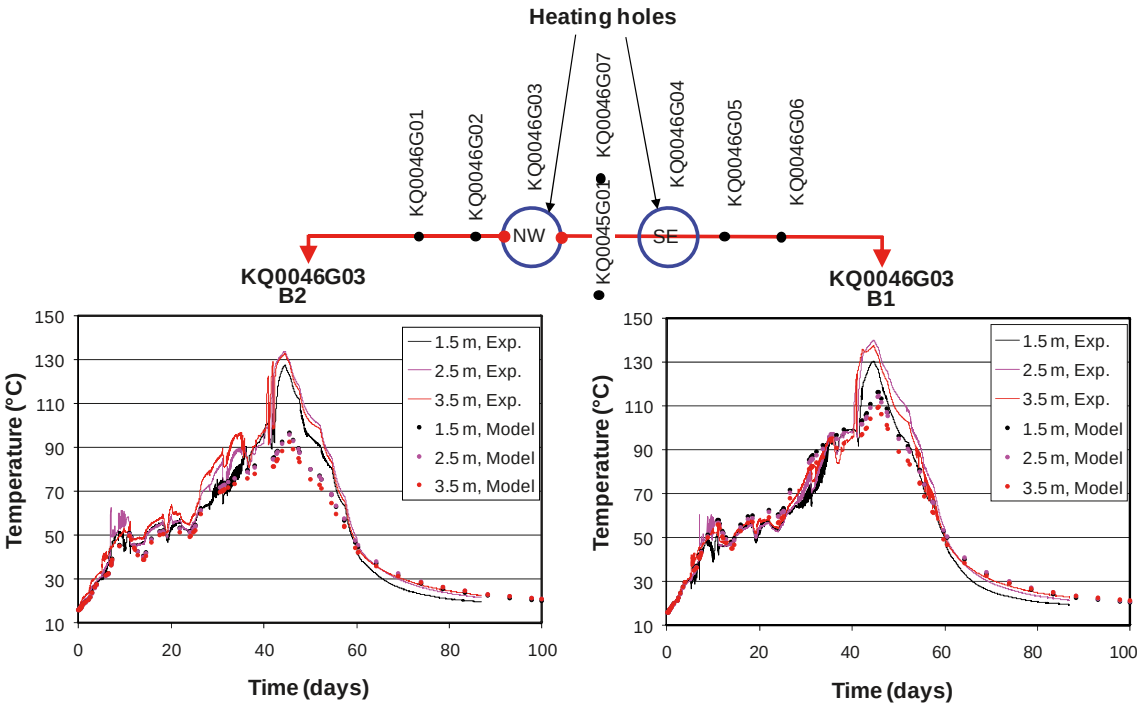

Figure R-23. *Comparison between temperatures recorded at borehole wall in KQ0046G03 during Test 4 and corresponding calculated temperatures.*

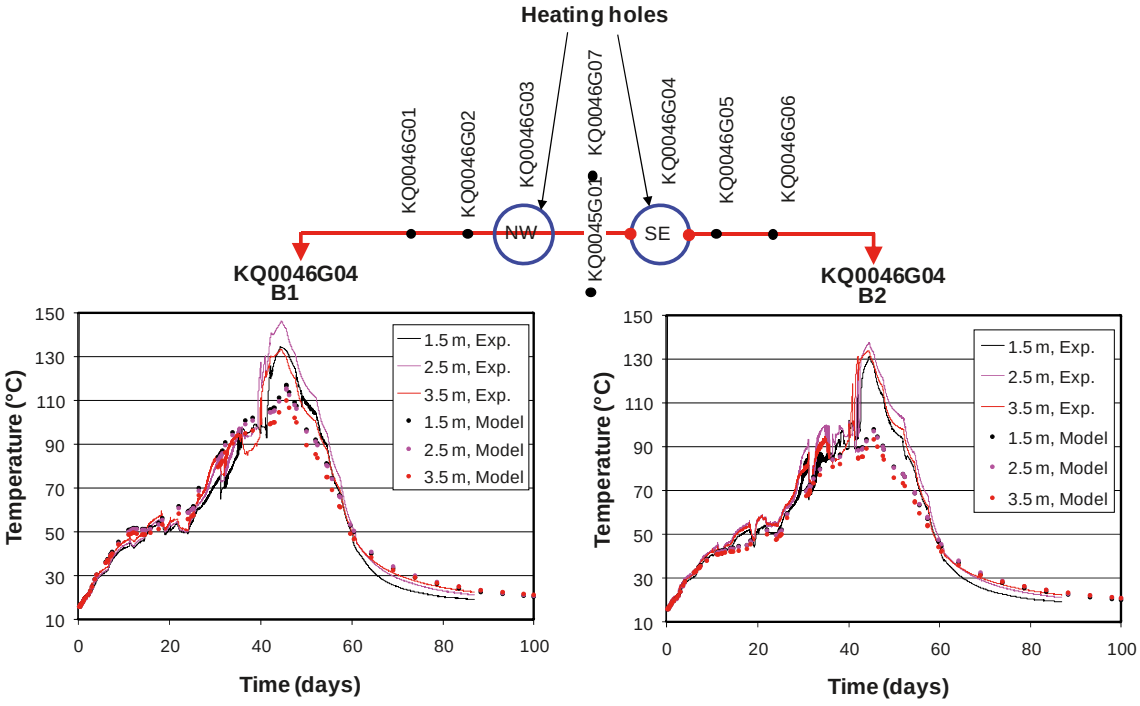

Figure R-24. *Comparison between temperatures recorded at borehole wall in KQ0046G04 during Test 4 and corresponding calculated temperatures.*

R2.2 Stresses

R2.2.1 Stresses at borehole walls

The calculated tangential stresses along vertical scan-lines at the heating hole walls are presented in Figure R-25 through Figure R-28. Results are showed after excavation and at some different time instances during the heating phase. The spalling initiation stress for Äspö diorite as estimated by /Andersson 2007/ is indicated in the diagrams. The following observations can be made:

- The spalling threshold is exceeded down to about 1.3 m depth after excavation. The threshold is exceeded down to a depth of 3.7–4 m in Test 1–Test 3 due to the heating. In Test 4 the spalling stress is exceeded down to about 4.3 m at a maximum.
- The highest tangential stress is found close to the tunnel floor (0.5 m depth). The maximum stress amounts at 185–190 MPa in Test 1, Test 2 and Test 3. In Test 4, where the peak temperatures are higher, the maximum stress exceeds 200 MPa.
- There are significant differences in stress increase rate between the tests. The stress at 1 m depth exceeds 155 MPa after about 12 days in Test 1 and Test 4. In Test 2 and Test 3 the stress at the same depth is about 165 MPa already after 5 days.
- The stress development is similar in the NW and SE experiment holes in all tests. The largest observed difference between the NW and SE holes is about 5%.

In the models presented here the rock was represented by a linear elastic continuum with uniform properties. The presence of an excavation-damage zone (EDZ) close to the openings was not taken into account. However, /Olsson et al. 2004/ report that there are indications that possible induced fractures can be found down to a maximum depth of 0.3 m below the tunnel floor in the TASQ tunnel. /Staub et al. 2004/ report results from *in situ* p-wave measurements from the APSE site which indicate that the Young's modulus is reduced down to a depth of about 0.05 m below the floor. The presence of an EDZ may cause some stress reduction in this upper region. The amount of stress reduction is difficult to quantify but the observations in the CAPS heating holes indicate however that the stresses may still exceed the spalling threshold close to the tunnel floor. In three of the CAPS holes, spalling was observed at the tunnel floor level and in four holes there was spalling 0.1 m below the floor.

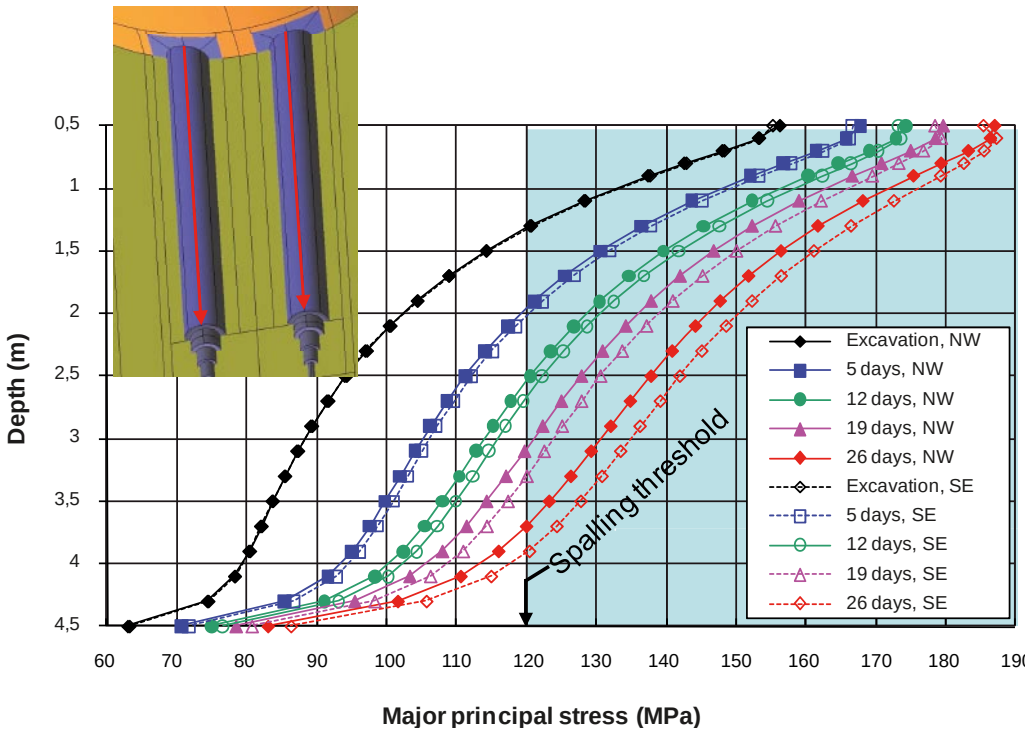

Figure R-25. *Calculated tangential stresses along the heating hole walls in Test 1. The y-axis indicates the depth below the concrete's upper edge. The inset shows the location of the scan-lines.*

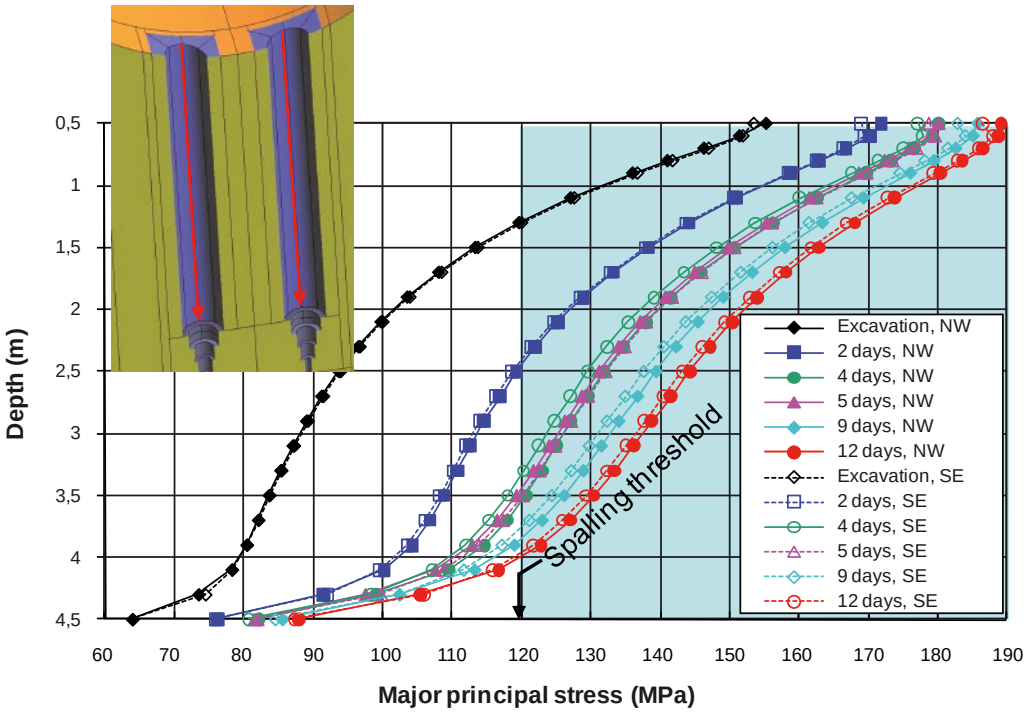

Figure R-26. *Calculated tangential stresses along the heating hole walls in Test 2. The y-axis indicates the depth below the concrete's upper edge. The inset shows the location of the scan-lines.*

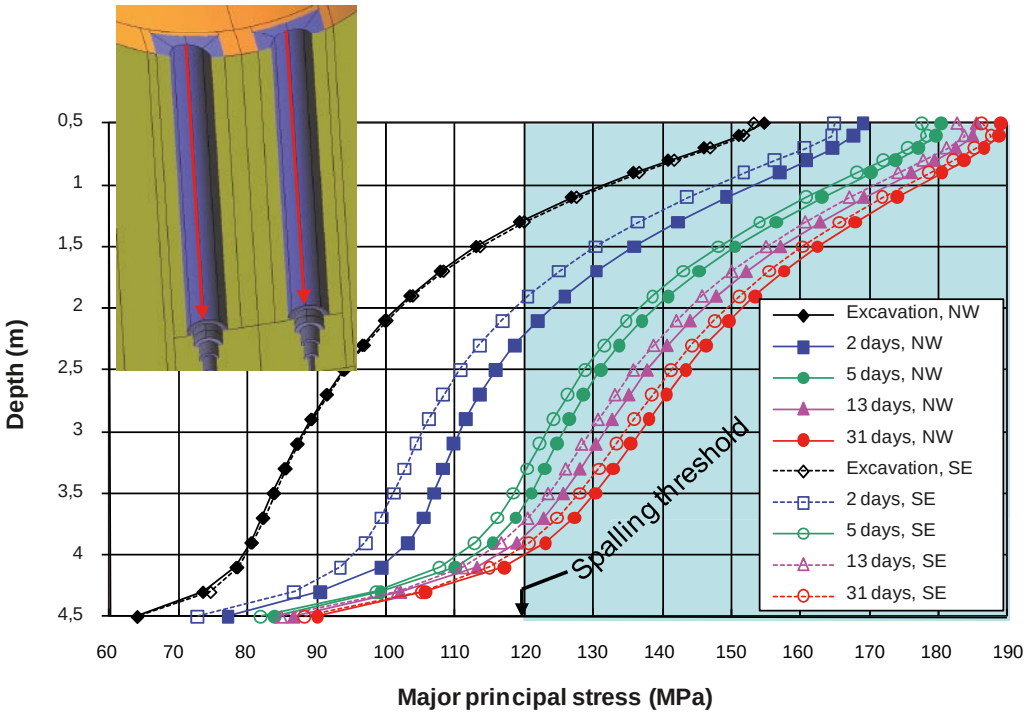

Figure R-27. *Calculated tangential stresses along the heating hole walls in Test 3. The y-axis indicates the depth below the concrete's upper edge. The inset shows the location of the scan-lines.*

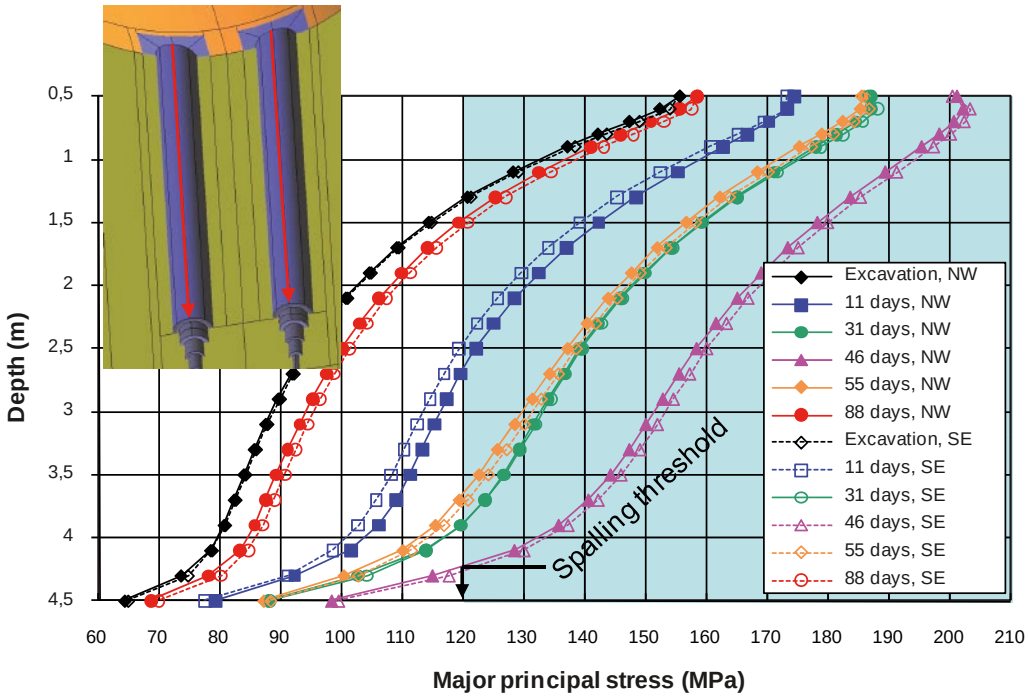

Figure R-28. *Calculated tangential stresses along the heating hole walls in Test 4. The y-axis indicates the depth below the concrete's upper edge. The inset shows the location of the scan-lines.*

R2.2.2 Stress- and temperature gradients

The two diagrams in Figure R-29 show S_{yy}-stresses and temperatures along a scan-line at 1.5 m depth close to the NW heating hole. Results at two time instances for each of the four models are shown. The curves with filled plot symbols represent the times with maximum stress. The shaded area in the upper diagram indicates stresses that exceed the spalling threshold. The sketch at the bottom shows the location of the scan-line.

During the first days there are significant differences in heating rate between the tests. After about 5 days of heating the temperature increase in Test 2 and Test 3 is more than twice as high as in Test 1 and Test 4. The diagrams also show that higher temperatures result in higher temperature gradients, higher stress levels and higher stress gradients.

The temporal developments of stress gradients at 1.5 m depth in all models are shown in Figure R-30. The gradient is calculated based on the stress difference between a point at the heating hole wall and a point located 0.16 m from the wall (see inset). The highest stress gradients are achieved in Test 4 where the stress levels are higher than in the other tests. Correspondingly, the lowest gradients are found in Test 1 where the stress levels are lower than in Test 2 and Test 3 (cf Figure R-29). Thus, the modelling results indicate that there were differences in stress gradient between the tests. However, the potential impact of this on the spalling process is not known.

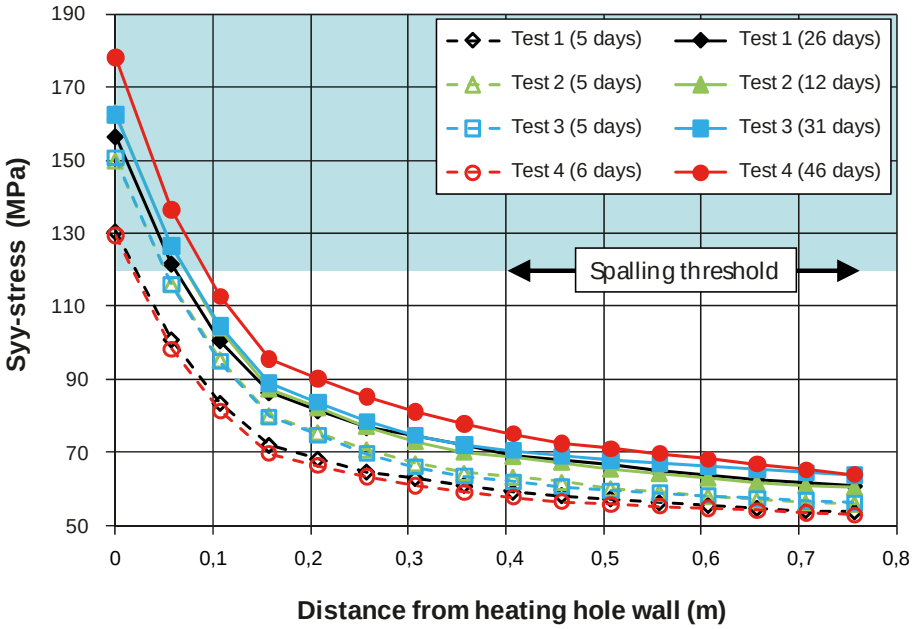

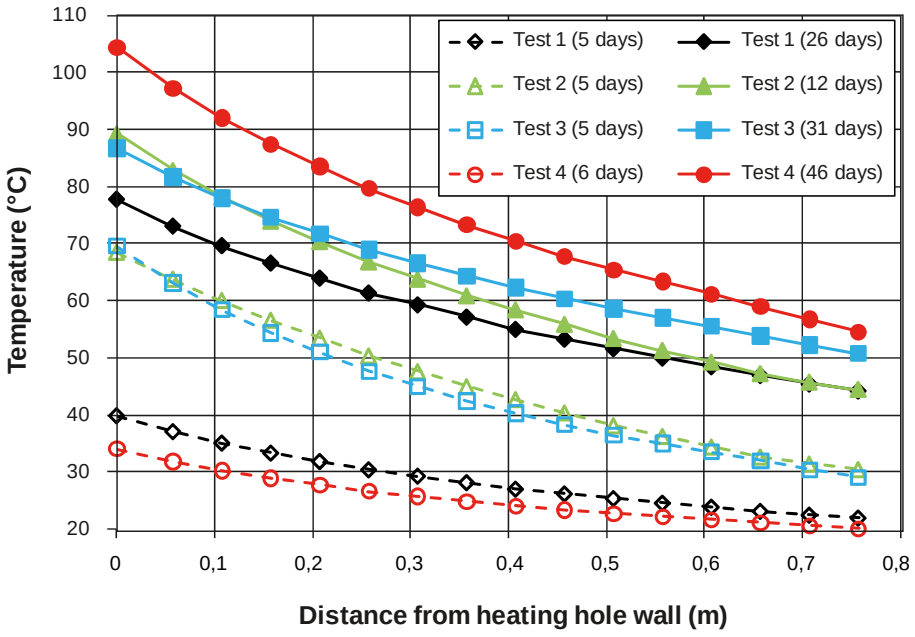

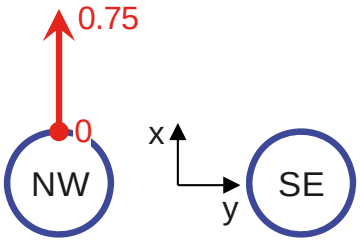

Figure R-29. *Upper: Syy-stresses at two time instances along scan-line at 1.5 m depth close to NW heating hole. Middle: Temperatures at two time instances along scan-line at 1.5 m depth close to NW heating hole. Bottom: Location of scan-line.*

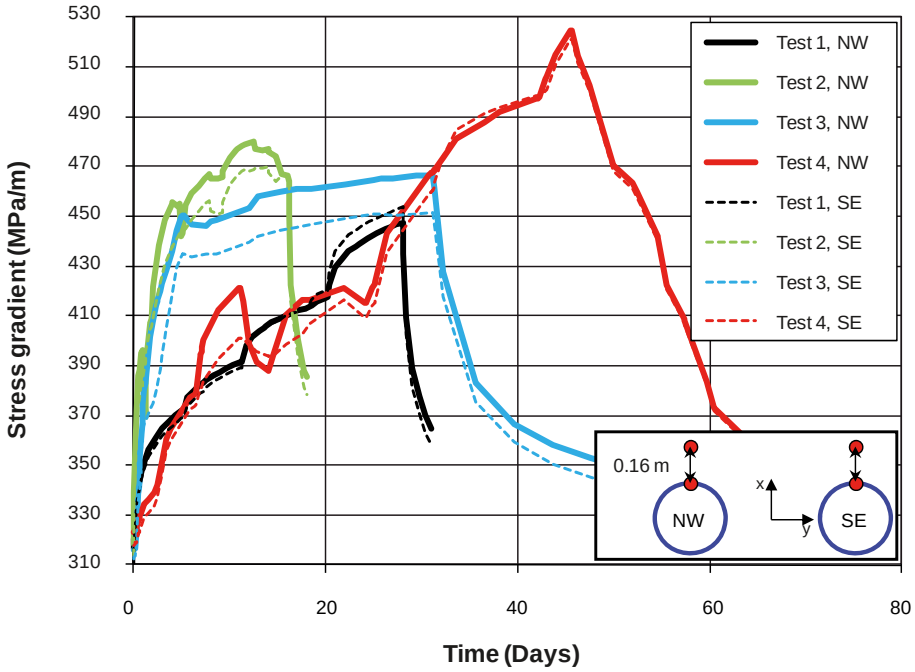

Figure R-30. *Temporal development of stress gradients at 1.5 m depth in all models. The gradients are based on the stress difference between the points indicated by the inset.*

R2.2.3 Stress versus temperature

Figure R-31 shows the tangential stress at heating hole wall plotted versus temperature at 1.5 m, 2.5 m and 3.5 m depth. The locations of the recording points for stress and temperature are shown by the sketch at the bottom. The temperature recording points are the same as the monitoring points in the real test. The phases of temperature increase and temperature decrease are indicated with solid lines and dotted lines, respectively.

The stress developments in the tests follow approximately the same trend. The curves suggest that a 20 degree temperature change results in a tangential stress change of about 12 MPa. This trend holds at all three depths and both during temperature increase and temperature decrease.

It shall be noted that these stress-temperature correlations are unique for this particular experiment setup (i.e. geometry, *in situ* stress assumption, heating scheme, rock thermo-mechanical properties) and do not imply any temperature dependence.

R2.2.4 Influence of pre-heating

The four tests were run in sequence. This means that the heat from one test resulted in some pre-heating of the rock surrounding the heating holes in the subsequent tests. The amount of pre-heating obtained from a preceding test depends on the heating power, the duration of the test and of the time lag between the tests. The average initial temperatures in the tests were in the range 15–18°C (cf Table R-3) and the undisturbed bedrock temperature at the test site is about 15°C. Thus, the average temperature increase due to pre-heating was about 3°C at a maximum.

The effect of pre-heating is not included in the models here, but results from the Test 3 model are used here to make an estimate of its effect on the stresses. Figure R-32 shows the stress increase plotted versus temperature increase at 2.5 m depth at 2.5 m distance from the experiment holes in the Test 3 model. The curves suggest that if the remaining temperature increase is 3°C (corresponding to an initial temperature of 18°C in the following test), the remaining S_{xx} and S_{yy} stress increase in the continuum would be about 1.5 MPa and 0.75 MPa, respectively. According to the Kirsch solution /Brady and Brown 1993/ this would correspond to a tangential stress increase at the heating hole walls (S_{yy}-direction) in the following test of about 0.75 MPa.

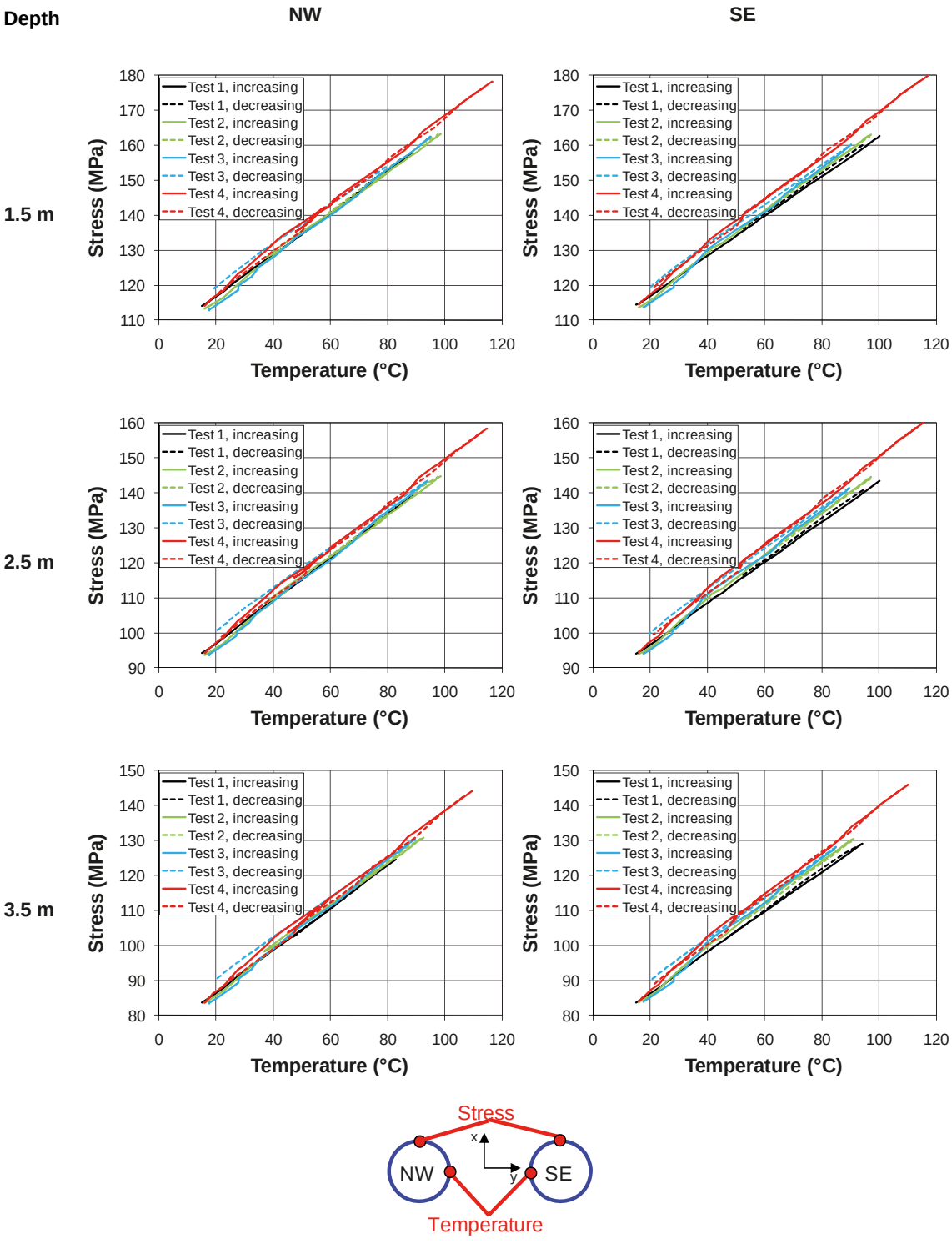

Figure R-31. *Tangential stress at heating hole wall plotted versus temperature for three depths. The locations of the recording points are indicated by the bottom inset.*

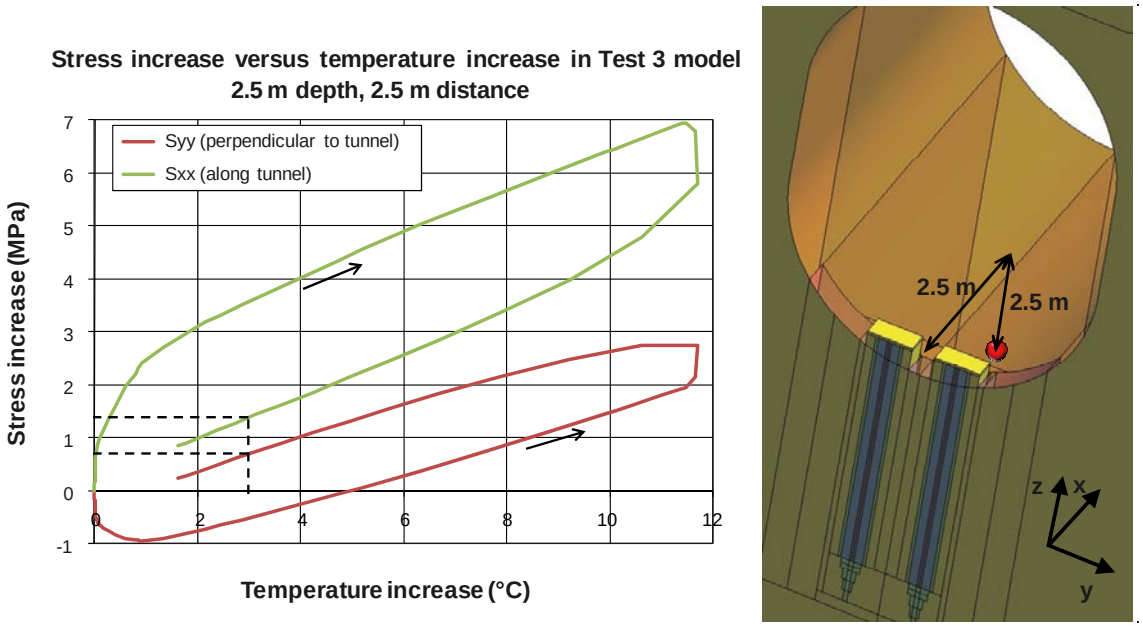

Figure R-32. *Stress increase plotted versus temperature increase at 2.5 m depth, 2.5 m from the heating holes in the Test 3 model.*

R2.2.5 Influence of boundary

The model dimension in the tunnel direction is relatively small. Thus, there may be a concern that this has an undesired impact on the stress results. The temporal development of S_{xx}-stresses at the boundary (x = –7.45 m) at given depths below the tunnel floor in the Test 3 model are shown in Figure R-33. The stress increase due to the heating amounts at about 2 MPa at a maximum. Since the boundary is locked for displacements the normal direction, this is an upper bound estimate of the stress increase at this location. If it is conservatively assumed that the S_{xx}-stresses are overestimated by 2 MPa and that there is no impact of the boundary on the S_{yy}-stresses, the tangential stresses (perpendicular to the tunnel axis) in the test holes would be underestimated by about 2 MPa (Kirsch solution /Brady and Brown 1993/). This corresponds to about 1% of the maximum tangential stresses.

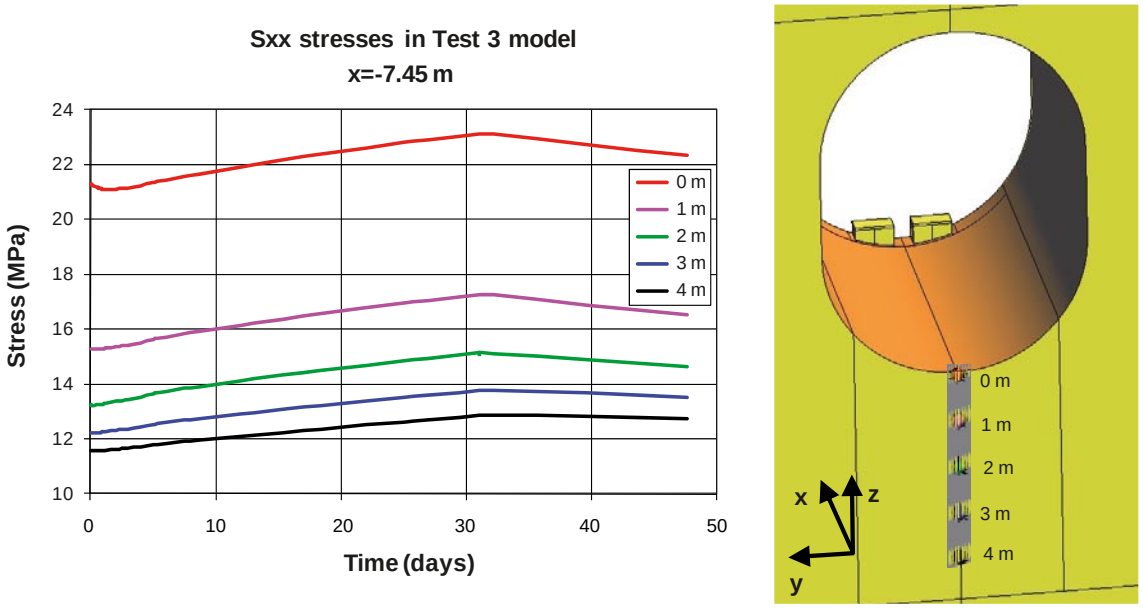

Figure R-33. *Temporal development of Sxx-stress at the boundary (x = –7.45 m) at given depths below the tunnel floor in the Test 3 model. The stress increase amounts at about 2 MPa at a maximum.*

R2.3 Conclusions

The finite element code Code_Bright has been used to analyse four thermo-mechanical models simulating the excavation and heating phases of the four CAPS tests. Thermal and mechanical properties relevant for the bedrock at the test site were used in the models. All materials were assumed to be linear elastic with uniform properties. The heat loads in the models were calibrated in order to fit the temporal development of temperatures in the models to the temperatures recorded during the tests. The focus was at obtaining a good temperature fit to the temperature gauges located in the outer instrumentation holes and at depths below 1 m. At these locations, the thermal development is less sensitive to details in the heat source geometry, local water movements around and inside the heating holes, details in the floor insulation and to small scale variations of the rock heat diffusivity.

Regarding the estimated tangential stresses at the experiment hole walls the following can be concluded:

- After excavation the spalling stress threshold for Äspö diorite (120 MPa) is exceeded down to a depth of about 1.3 m below the concrete's upper edge. During the heating phase the threshold is exceeded down to between 3.7 and 4.3 m depth below the same reference level.
- The highest stresses are obtained close to the tunnel floor and amount at 185–190 MPa in Test 1–Test 3. In Test 4, in which the highest temperatures were reached, the maximum stress exceeds 200 MPa. No EDZ was accounted for in the models. Thus, it is likely that the stresses in a region down to about 0.3 m below the tunnel floor are over estimated. The amount of over estimation is however difficult to quantify.
- The stress gradients close to the experiment holes are correlated to the stress levels. The highest stress gradients are found in Test 4 where the temperatures and the stress levels are highest.
- The stress changes scale linearly to temperature changes. The dependence seems to be similar at all depths and both during temperature increase and temperature decrease.

Since the tests were run in sequence, the heating of one test caused some pre-heating of the bedrock around the following tests. The effect of this on the stresses was not explicitly accounted for in the models. However, the tangential stress increase due to pre-heating was estimated here to be of the order of 1 MPa, i.e. about 0.5% of the maximum calculated stresses.

The underestimation of the tangential stresses in the test holes caused by the relatively small model dimension in the tunnel direction is estimated to be less than 1%.

References

Andersson J C, 2007. Rock Mass Response to Coupled Mechanical and Thermal Loading. Äspö Pillar Stability Experiment, Sweden. Doctoral Thesis. Division of Soil and Rock Mechanics. Department of Civil and Architectural Engineering. Royal Institute of Technology, Stockholm.

Brady B H G, Brown E T, 1993. Rock mechanichs for underground mining. Second edition. Chapman & Hall, London.

Olsson M, Niklasson B, Wilson L, Andersson J C, Christiansson R, 2004. Äspö HRL. Experiences of blasting of the TASQ tunnel. SKB R-04-73, Svensk Kärnbränslehantering AB.

Staub I, Andersson J C, Magnor B, 2004. Äspö Pillar Stability Experiment. Geology and mechanical properties of the rock in TASQ. SKB R-04-01, Svensk Kärnbränslehantering AB.

Appendix S

Correlation between spalling and geology

Johan Berglund, Vattenfall Power Consultant AB
November 2009

Comments on the geometric relations between the occurrence of spalling and geology in seven boreholes studied in the CAPS project

Contents

S1 Introduction

The following text is a compilation and evaluation of the extent of spalling in the boreholes KQ0046G04, KQ0048G04, KQ0048G05, KQ0051G04, KQ0051G05, KQ0054G03, KQ0054G04, and its relation to geology. The evaluation is based on the mesh produced from laserscanning (ATS AB), orthographic photos taken in the boreholes, the BIPS images and the Boremap loggings.

Through the CAPS investigation volume in the TASQ tunnel at Äspö runs a brittle-ductile shear zone, in a southwest – northeast direction and with a dip of about 50–60 degrees to the southeast. Much of the geology in the boreholes is affected by this fact. Not only does the intensity of brittle and ductile structures increase distinctly in the shear zone, but also the intensity of oxidation is related to brittle structures (sealed networks included) and hence indirectly to the brittle-ductile shear zone.

All boreholes that have gone through thermal heating in the CAPS project are drilled through at least some part of this zone. The boreholes on the southeast side of the tunnel; KQ0046G04, KQ0048G05, KQ0051G05 are drilled through the full width of the shear zone, whereas the other boreholes only penetrate part of the zone. The top of the shear zone can not be seen in these boreholes. In the inner part of the studied volume of rock the shear zone become more complex below the tunnel floor, it splays up in two–three separate shear zones. This is already indicated in borehole KQ0048G05.

S2 Evaluations of the spalling occurrence

S2.1 Heating hole KQ0046G04

Only restricted spalling has been identified in this borehole. It can be seen both in the mesh from the laser scanning (Figure S-1) and in photographic image (Figure S-2).

The spalling ends just above the cataclastic structure. Below this level spalling is virtually absent. The rock above the shear zone is the normal “Äspö diorite” of the area, which here is very weakly deformed and with a weak alteration. Some sharp edges that bound the spalling, particularly in the top, show that sealed fractures has played some role as a guide. The spalling ends a few cm above a cataclastic structure filled with phrenite and epidote (Figure S-2). In this cataclastically deformed rock and further down, the rock has been much more deformed both by brittle and ductile processes, as evidences by sealed networks, breccias and brittle-ductile shear zones.

Figure S-1. *Laser scanned mesh of heating hole KQ0046G04. Spalling can be seen as a vertical trace along the mesh, at a location between ca –446.3 and –446.75 m.*

Figure S-2. *Observed spalling in heating hole KQ0046G04 on the same side as in Figure S-1. The top of the shear zone to the left cuts through the borehole down to the southeast. An epidote/phrenite filled cataclastic structure runs sub horizontally across the borehole. The latter is cut by the shear zone.*

S2.2 Heating hole KQ0048G04

On both sides of the borehole (sectors BC and DA) spalling is observed along a major part of the borehole (see Figure S-3). To a large extent it seems to be unaffected by geology. However, there are indications of a geological connection in a few places, such as the start of spalling in sector DA which apparently runs along a sealed fracture and the ending of the spalling in the lowermost part in sector DA is slightly stretched along the foliation in the weak shear zone below, see Figure S-4.

S2.3 Heating hole KQ0048G05

Restricted spalling seems to have occurred along the borehole. In sector DA hardly any spalling can be seen. In sector BC, between –447.2 and –447.9 the spalling is most pronounced and the orientation seem to be guided by the surrounding, partly strong, foliation, see Figure S-5. Shear zones occur both above and below the spalling The spalling itself do, however, seem to be more pronounced in the less deformed rock just next to the shear zones, between the two splays of the shear zone.

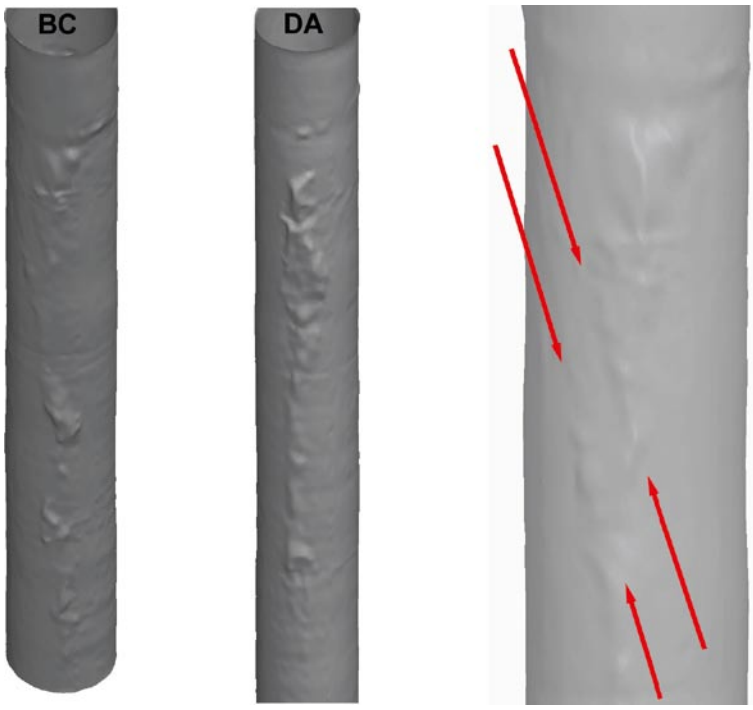

Figure S-3. *Mesh from the laser scanning in heating hole KQ0048G04. To the left both sides of the full scan, between –446 and –450 m. Spalling on both sides of the borehole can be seen (left figure). There is a tendency at around –447.5 m in sector BC (close-up to the right) that the spalling runs from upper left to lower right as indicated by the red arrows. This may be caused by the local, narrow fine grained granitic dykes in the area, which runs in this direction.*

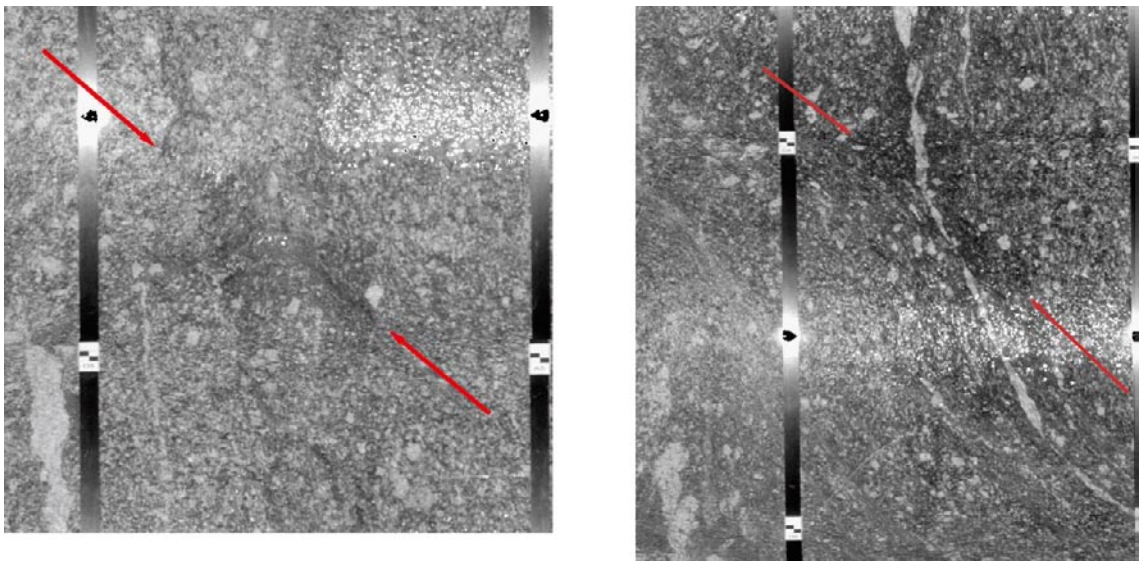

Figure S-4. *Sector DA of heating hole KQ0048G04. Left figure; at –447.7 to –447.8 a local, minor sealed fracture guides the boundary between spalling and surrounding rock. To the right, at –449.4 to –450 m in sector DA, the lower boundary which appears to be slightly guided by the weak ductile shearing below.*

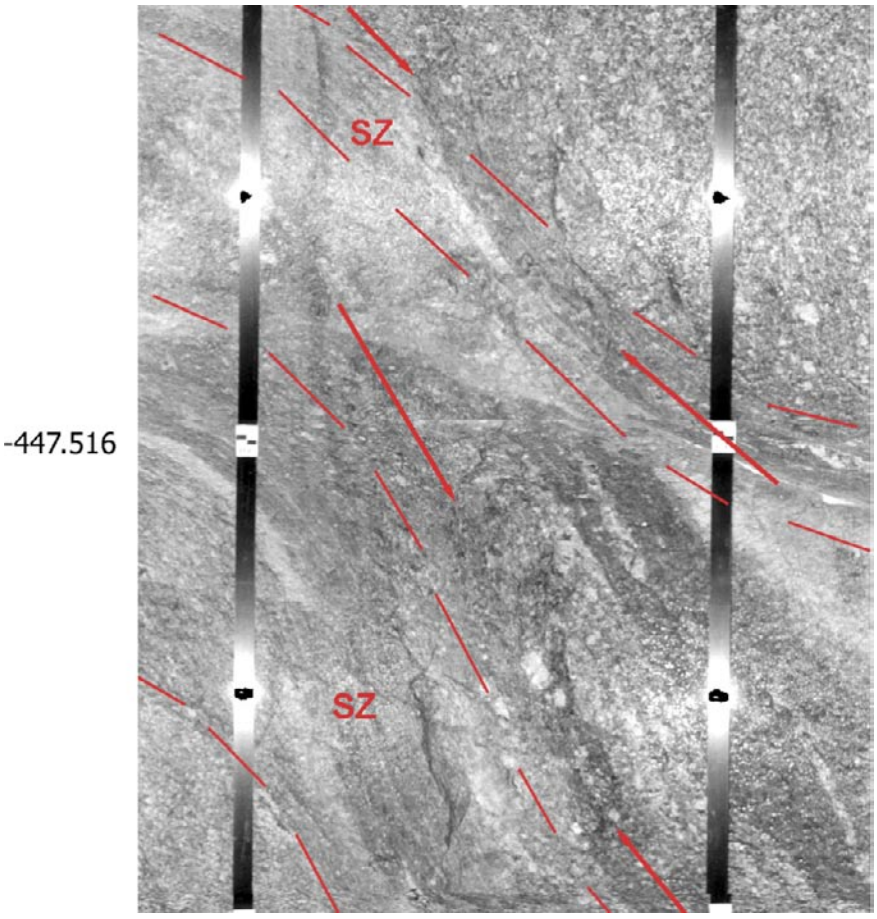

Figure S-5. *Sector BC of heating hole KQ0048G05. More pronounced spalling is marked with red arrows pointing in the direction corresponding to the elongation of the spalling. SZ means Shear Zone, and these (two) are delineated by narrow red lines.*

S2.4 Heating hole KQ0051G04

Spalling appear at –446.6 m and starts guided by a sub-horizontal fracture in sector BC (Figure S-6). It then occurs continuously as an almost vertical "channel", down to –449.7. The occurrence of spalling is apparently unaffected by the geology (Figure S-7), but the boundary towards adjoining areas are guided by the geological structures as exemplified in Figures S-8 and S-9.

The foliation which generally dips towards the lower left side in sector BC, is opposite on the other side of the core (dips towards the lower right), in sector DA and thus guide the boundaries in the opposite direction here, see Figure S-9.

S2.5 Heating hole KQ0051G05

The spalling in this borehole is rather discontinuous and not very pronounced, as can be seen in Figure S-10 below. The first appearance of spalling occur between –447.1 and –447.4 m in sector BC (Figure S-11). It appears in two small separated areas just above the major shear zone that runs across the investigation area sub-parallel to the tunnel. In fact the spalling is less pronounced within sheared part of the rock (see especially sector AD in Figure S-10).

The two lower occurrences of spalling in sector BC (red arrows in Figure S-12 below) in fact parallels the adjoining foliation, which seem to be weak apart from the lower shear zone where a strong foliation is developed. The spalling ends towards this high strain zone and no or very minor spalling appears within the zone. In fact between –448.0 and –448.6 it appears as if spalling is located primarily in lower strain areas and once again guided by the foliation.

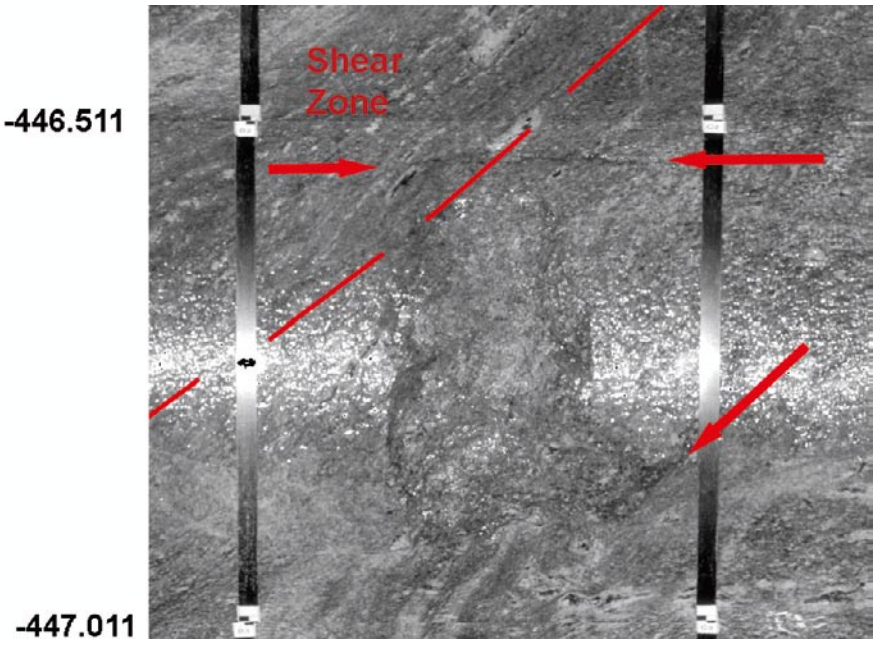

Figure S-6. *Sector BC of heating hole KQ0051G04. Start of spalling along fracture (upper two arrows), whereas the spalling do not appear in the shear zone above. The lower right arrow point at a part of the boundary guided by adjoining foliation.*

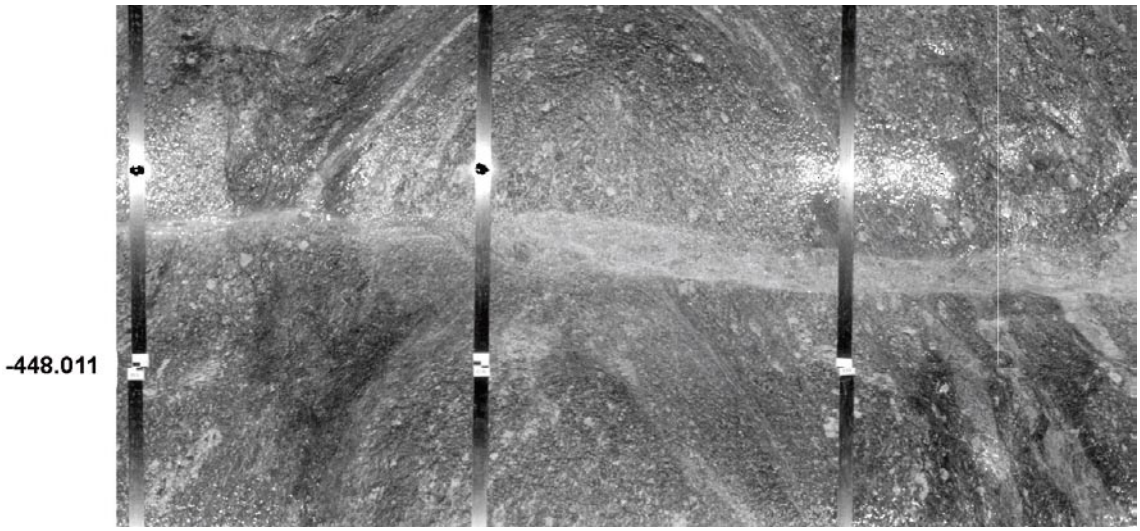

Figure S-7. *Sector BC, CD and DA of heating hole KQ0051G04. Sub-horizontal, narrow breccia, probably sealed with epidote and prehnite. The structure does not appear to affect the occurrence or shape of the spalling.*

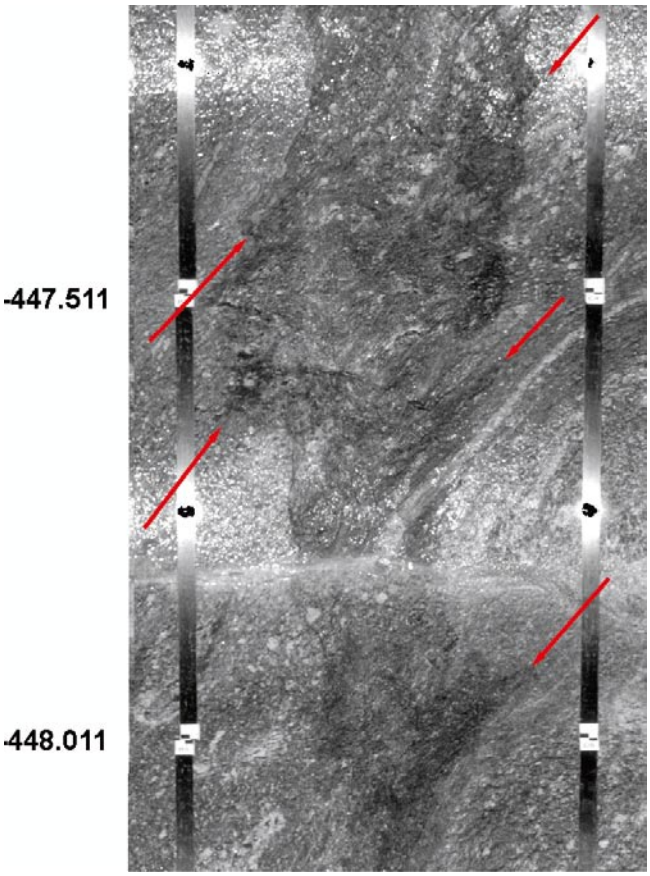

Figure S-8. *Sector BC of heating hole KQ0051G04. Arrows pointing at examples of boundaries guided by the local foliation in sector BC.*

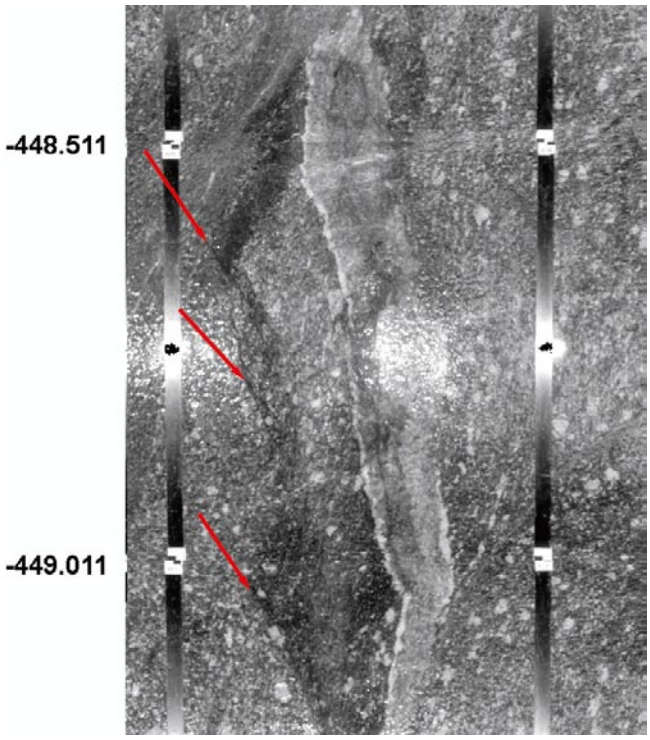

Figure S-9. *Sector BC of heating hole KQ0051G04. Example where minor fracturing (in en echelon shape) guide the left boundary of spalling, whereas the narrow fine-grained granite (light grey) not appear to have any impact on the spalling.*

Figure S-10. *Mesh from the laser scanning in KQ0051G05 showing the spalling and the shear zone in the hole. Discs mark the upper and lower boundary of the zone and the internal foliation. The spalling is not very pronounced in the borehole and is mostly absent within the strongly sheared parts of the shear zone.*

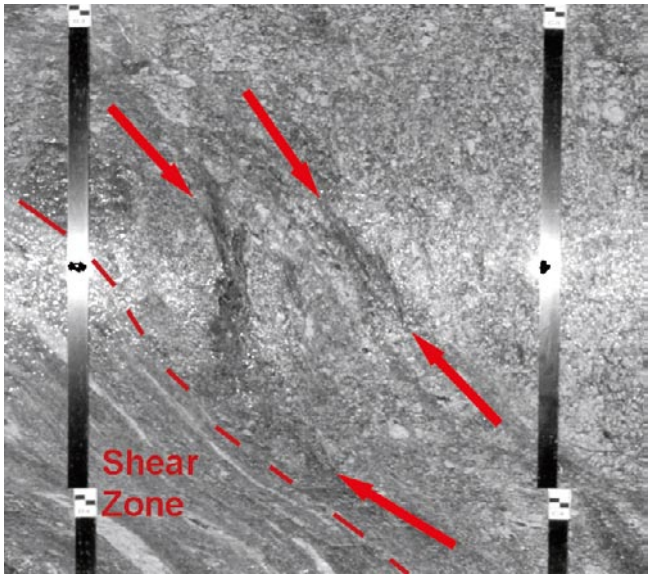

Figure S-11. *Sector BC of heating hole KQ0051G05. The first appearance of spalling at –447.1 and –447.4 m and its relation to the shear zone.*

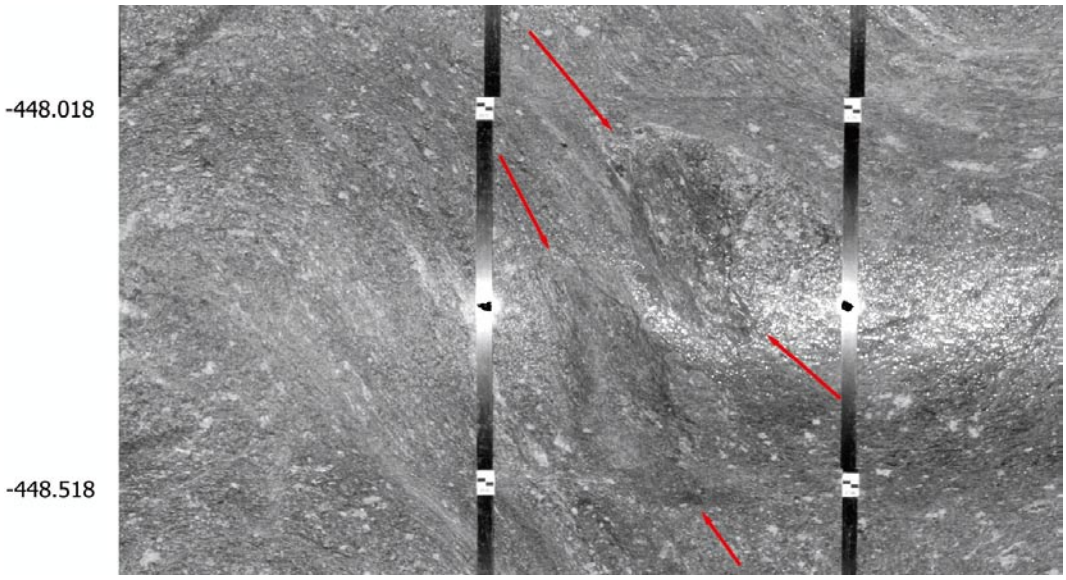

Figure S-12. *The lower spalling in sector BC in heating hole KQ0051G05 seen in Figure S-10, occurs within slightly less sheared part in the shear zone and aligns with the local foliation.*

S2.6 Heating hole KQ0054G03

Spalling has occurred along a large part of the borehole, but is particularly pronounced in sector BC between –446.5 and –448.0 m, see Figure S-13. The spalling do not seem to be affected by geological characteristics in any evident way, except for the boundaries to unaffected rock that seem to be somewhat guided by the orientation of the local foliation and felsic rock layers. This is especially obvious in the lowermost part of the spalling where it ends towards, and is extended along the boundary to a ductile shear zone (see Figure S-13).

S2.7 Heating hole KQ0054G04

Not very pronounced spalling has occurred in this borehole. All spalling has occurred above the shear zone, in the upper 1.6–1.7 m depth as can be seen in Figure S-14.

S3 Summary

The spalling occurs in all boreholes, but to a significantly variable extent. It is more pronounced below the shear zone that runs through the investigated volume of rock. It also appears as if it is less developed in sheared sections in the boreholes.

Alterations and the intensity of alteration do not seam to affect the spalling in any systematic way. There could be a relation between more extensive (stronger) oxidation and larger outfall, but this has to be studied in greater detail in order to reach conclusive results. No difference in alteration intensity was apparently found during mapping since all alterations are logged as weak intensity, and hence the logging may have been too generalized for the purpose of such study. Epidotization has occurred along all sections of all seven boreholes, except for very short sections in KQ0046G04 and all intensities are logged as weak. No consideration can thus be made regarding the possible effect from epidotization on spalling.

Sealed fractures and Sealed Networks are, to a large extent, related to oxidation and epidotization, and the same conclusion can be made regarding brittle structures of this kind on the basis on the existing seven boreholes, that no obvious relation to spalling occurs. When it comes to some individual fractures, however, they often guide the form of the outfall boundaries towards areas unaffected by spalling.

The rock volume in the studied area has a variable foliation. It ranges from almost massive to strongly foliated shear zones. The boundaries between less and more deformed sections are often sharp and frequently coincides with the boundary to outfalls, where the outfall exist in the less foliated or massive rock. In sections where outfall occurs in foliated rock, the foliation seems to guide the outfall boundary.

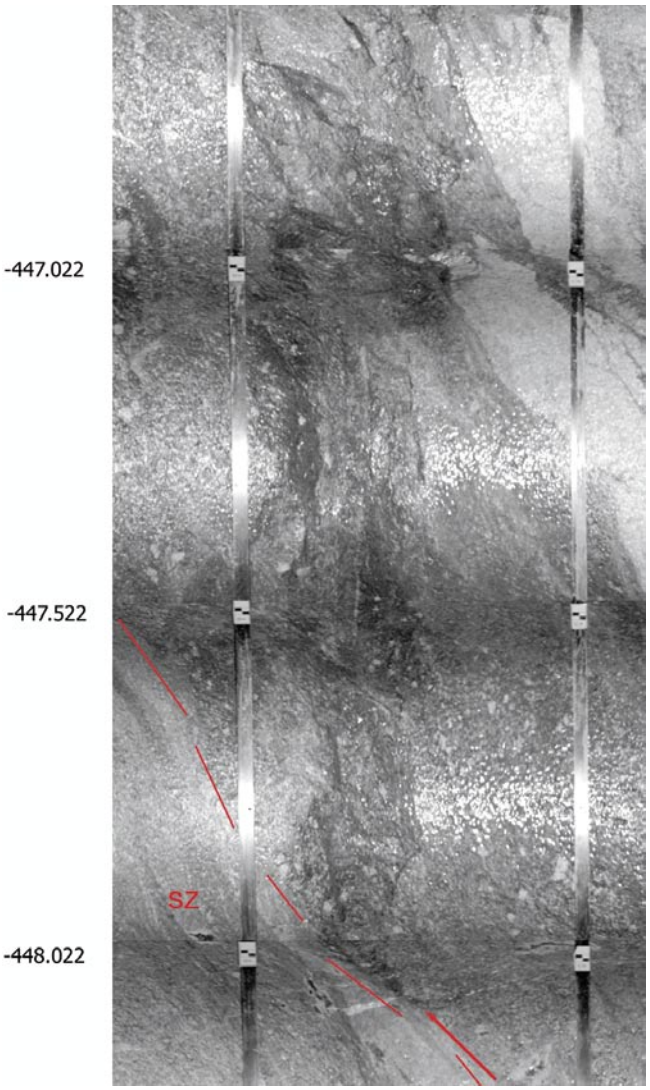

Figure S-13. *Sector BC of heating hole KQ0054G03. Lower shear zone delineated and the spalling seen as a central darker are. Note the boundary of the somewhat asymmetric shape of the boundaries between the spalling to the surrounding rock and how it is slightly stretched sub-parallel with the orientation of foliation and lithology.*

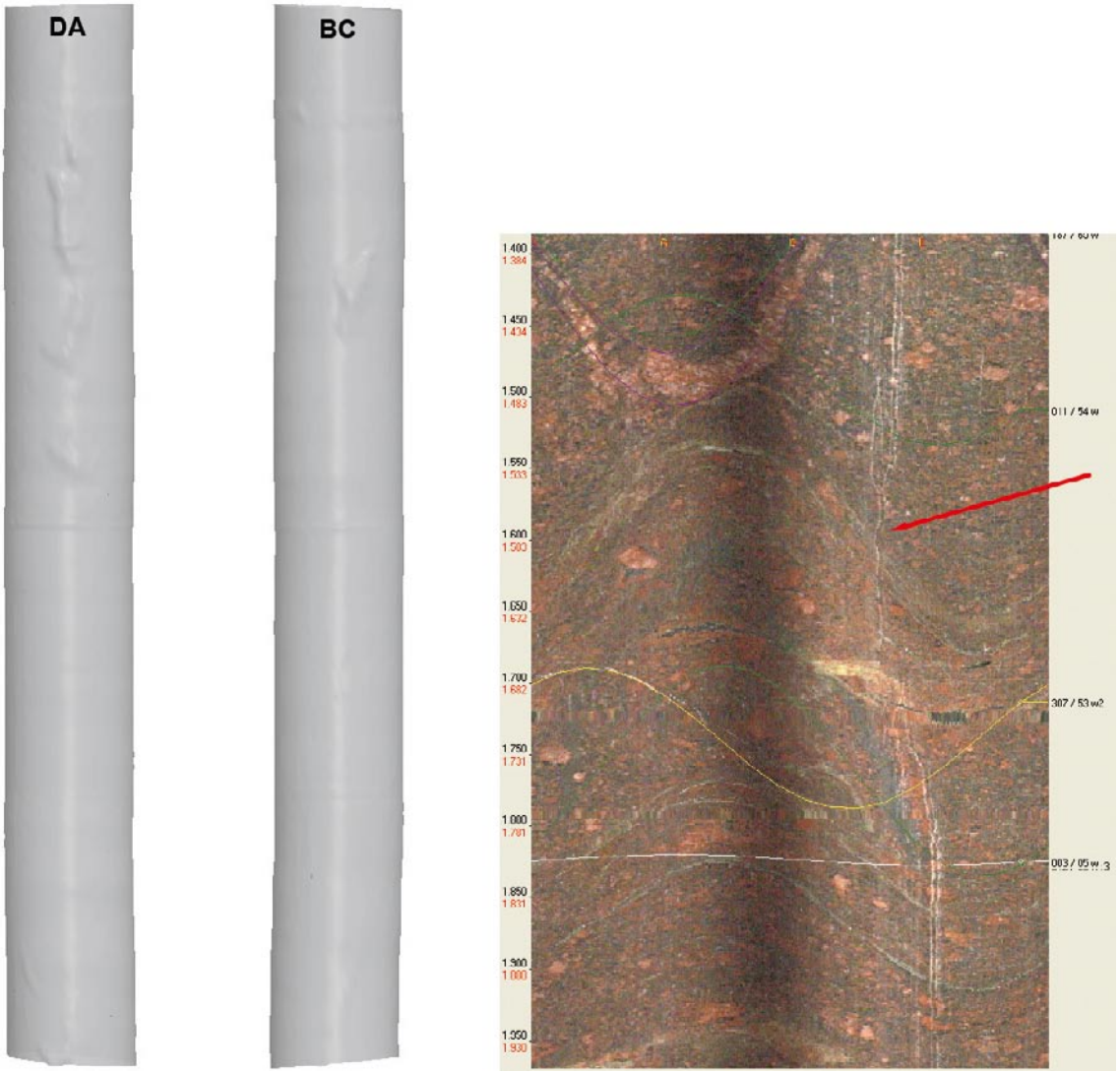

Figure S-14. *Mesh from laser scanning and BIPS image in KQ0054G04. To the left both sides of the full mesh (–446 to –450 m). Minor spalling can be seen in the upper part of sector DA (left). This is located above the shear zone seen to the right, an image from the BIPS taken in the central 76 mm borehole between ca 1.3 and 2 metres depth. The start of the shear zone is pointed at by the red arrow.*

Appendix T

Photographs of the heating holes

Figure T-1. *Photograph of borehole KQ0054G03 in Field Test 1 before initiating the heating phase.*

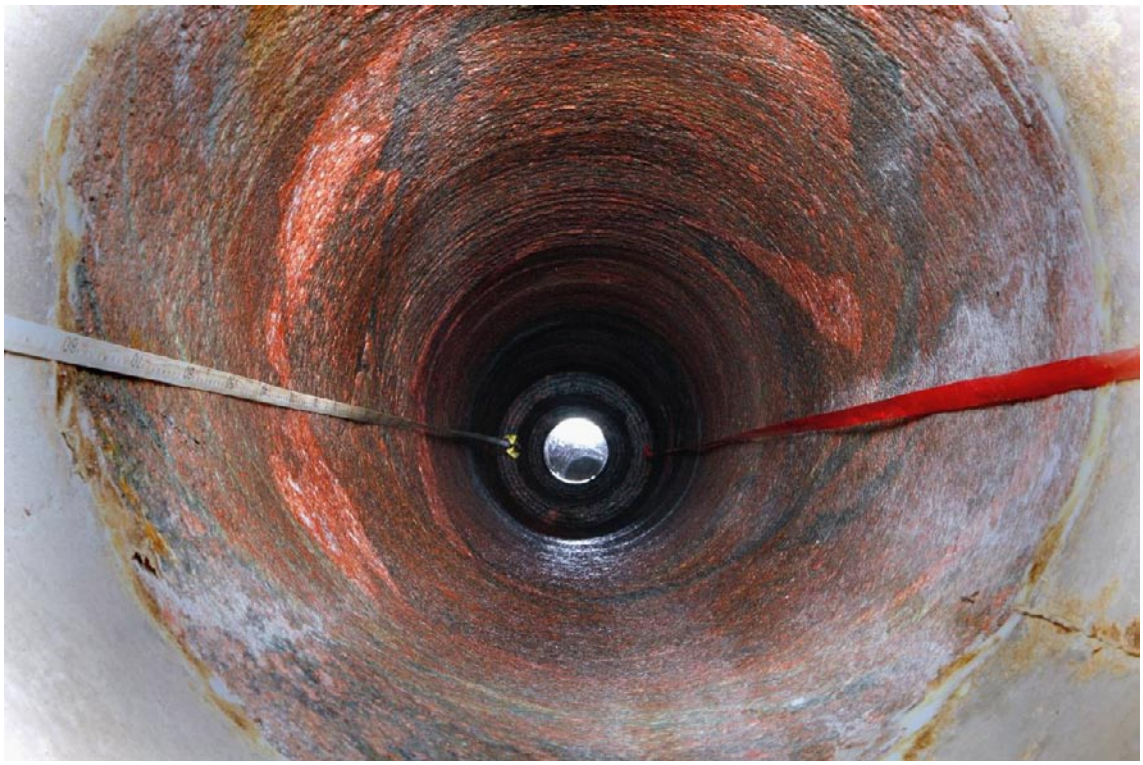

Figure T-2. *Photograph of borehole KQ0054G04 in Field Test 1 before initiating the heating phase.*

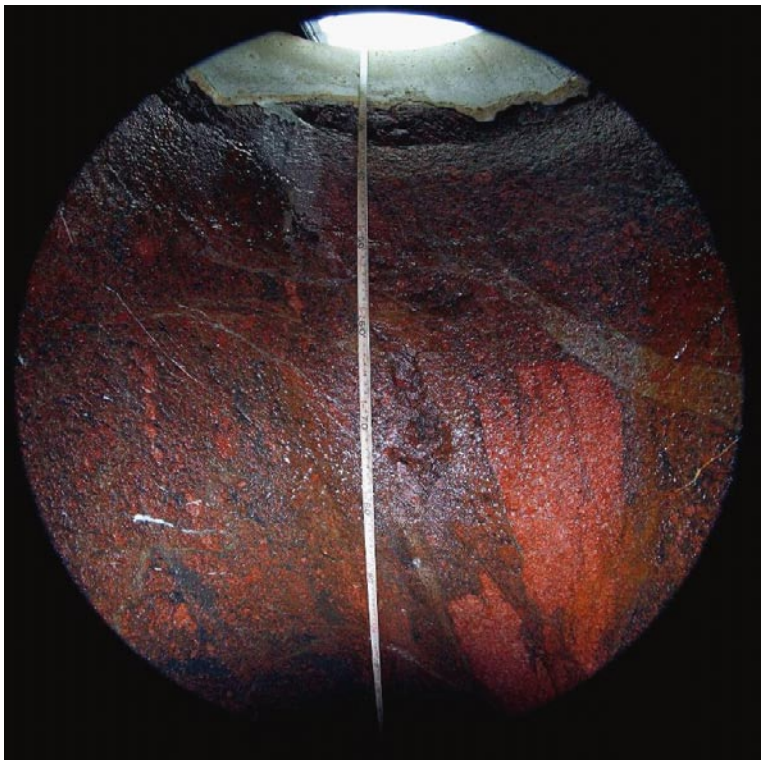

Figure T-3. *Fish-eye photograph of NE-side in borehole KQ0054G03 in Field Test 1 before initiating the heating phase.*

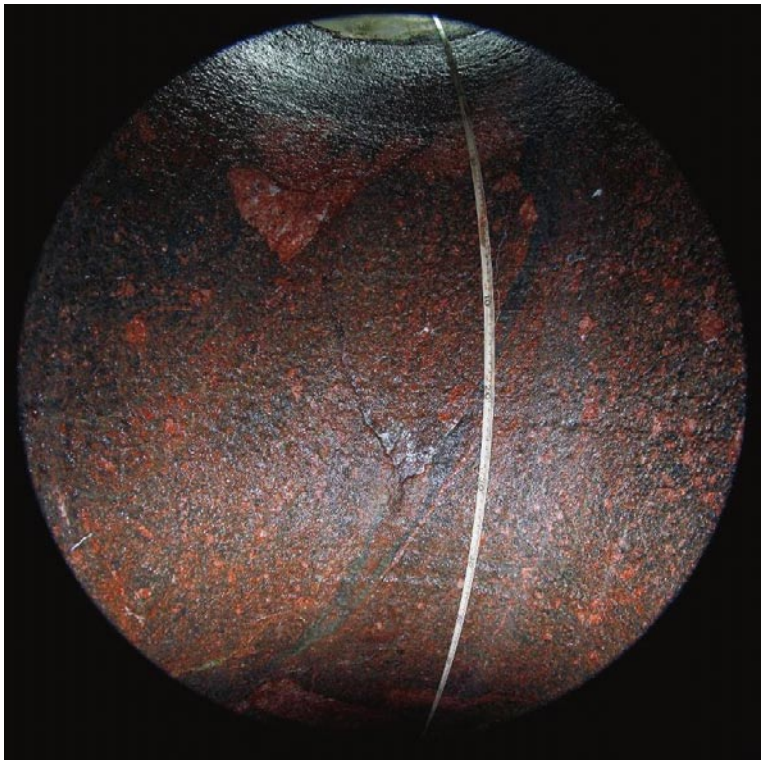

Figure T-4. *Fish-eye photograph of SW-side in borehole KQ0054G04 in Field Test 1 before initiating the heating phase.*

Figure T-5. *Photograph of borehole KQ0051G04 in Field Test 2 before initiating the heating phase.*

Figure T-6. *Photograph of borehole KQ0051G05 in Field Test 2 before initiating the heating phase.*

Figure T-7. *Photograph of borehole KQ0048G04 in Field Test 3 before initiating the heating phase.*

Figure T-8. *Photograph of borehole KQ0048G05 in Field Test 3 before initiating the heating phase.*

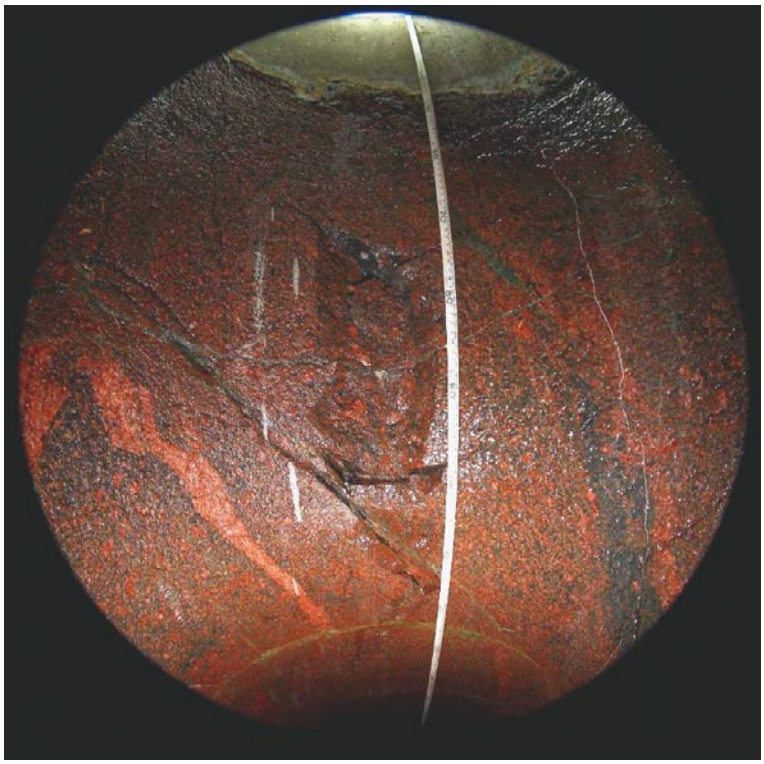

Figure T-9. *Fish-eye photograph of NE-side in borehole KQ0048G04 in Field Test 3 before initiating the heating phase.*

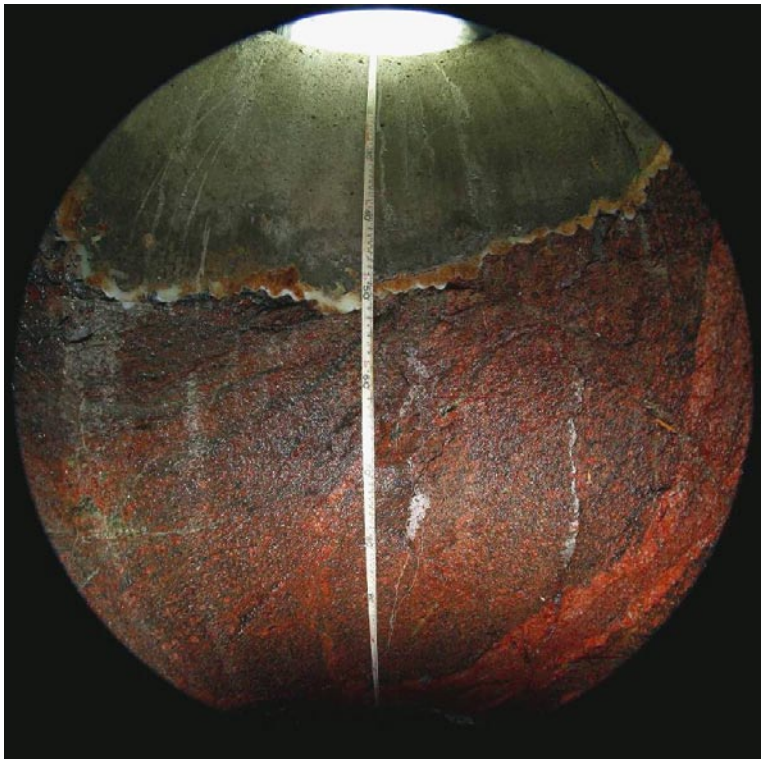

Figure T-10. *Fish-eye photograph of SW-side in borehole KQ0048G04 in Field Test 3 before initiating the heating phase.*

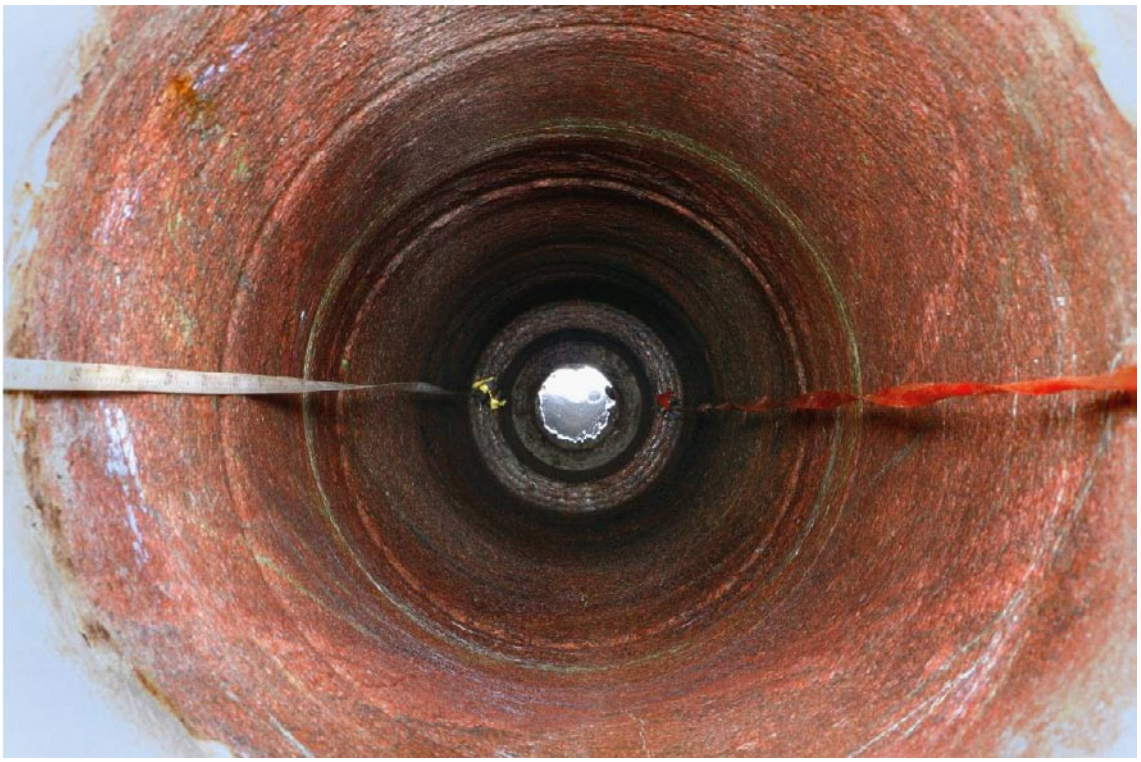

Figure T-11. *Photograph of borehole KQ0046G03 in Field Test 4 before initiating the heating phase.*

NE-side ***SW-side***

Figure T-12. *Photograph of borehole KQ0046G03 in Field Test 4 before initiating the heating phase.*

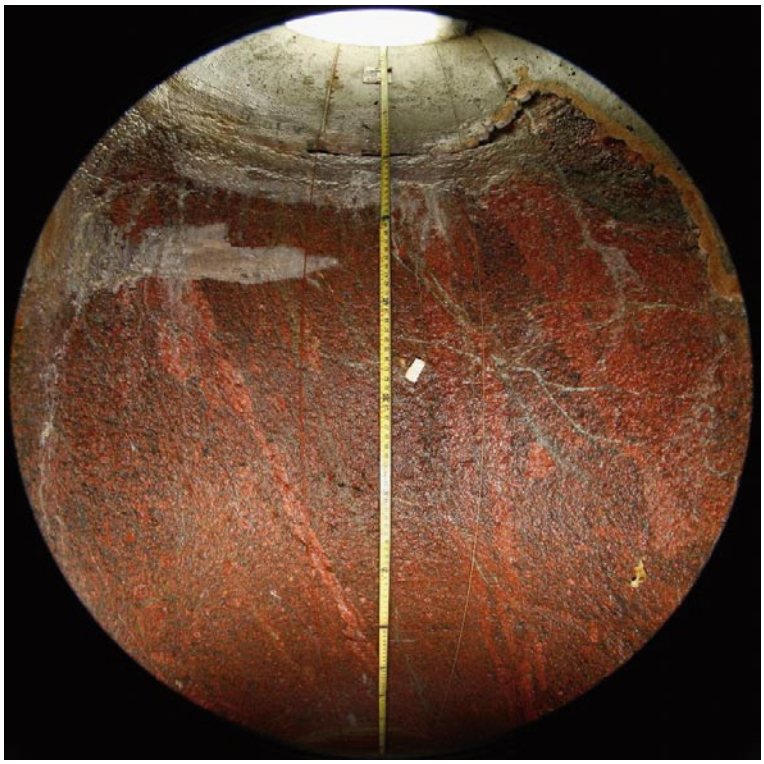

Figure T-13. *Fish-eye photograph of borehole KQ0046G03 NE-side in Field Test 4 before initiating the heating phase.*

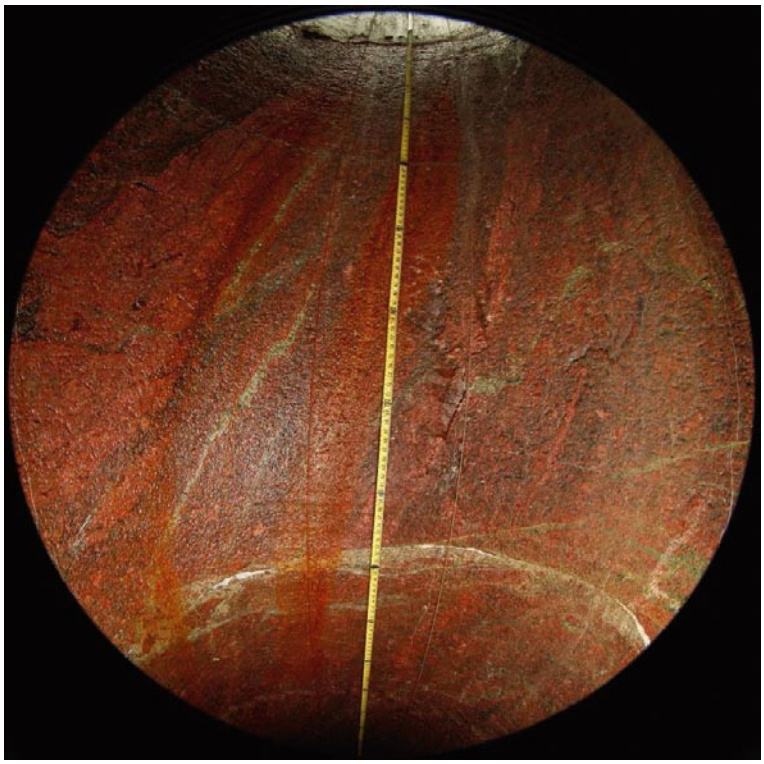

Figure T-14. *Fish-eye photograph of borehole KQ0046G03 SW-side in Field Test 4 before initiating the heating phase.*

Figure T-15. *Photograph of borehole KQ0046G04 in Field Test 4 before initiating the heating phase.*

NE-side ***SW-side***

Figure T-16. *Photograph of borehole KQ0046G04 in Field Test 4 before initiating the heating phase.*

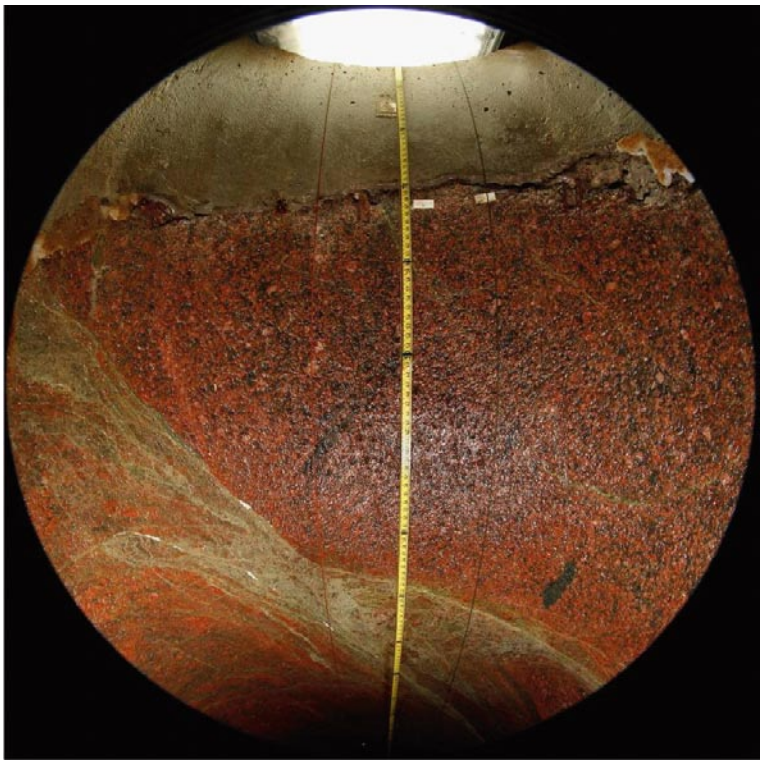

Figure T-17. *Fish-eye photograph of borehole KQ0046G04 NE-side in Field Test 4 before initiating the heating phase.*

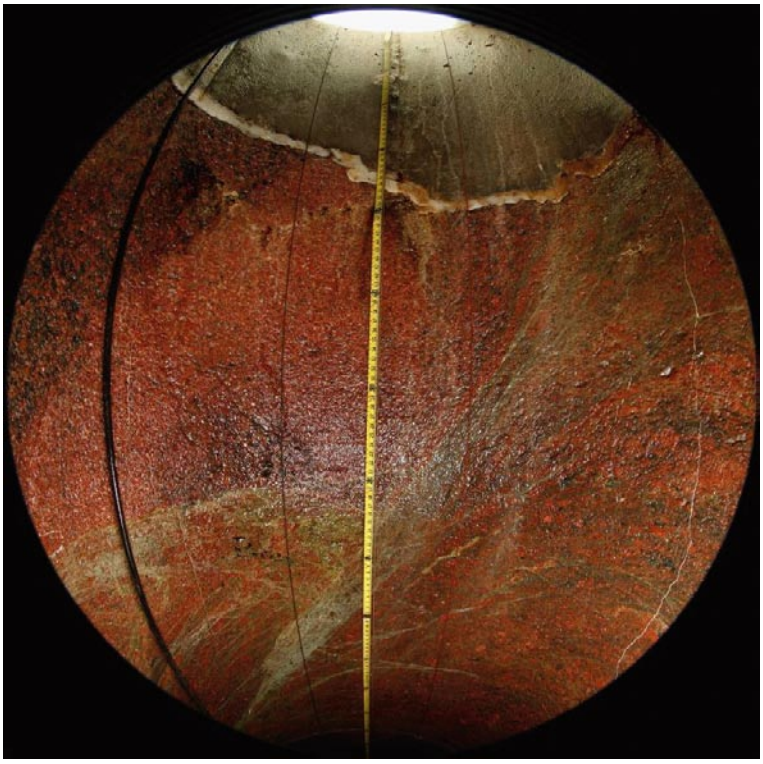

Figure T-18. *Fish-eye photograph of borehole KQ0046G04 SW-side in Field Test 4 before initiating the heating phase.*

Before scaling

NE-side ***SW-side***

Figure T-19. *Photographs of the borehole wall in heating hole KQ0054G03 after finished the cooling phase, before scaling of the wall. Field Test 1 was performed without confinement.*

NE-side ***SW-side***

Figure T-20. *Photographs of the borehole wall in heating hole KQ0054G04 after finished the cooling phase, before scaling of the wall. Field Test 1 was performed without confinement.*

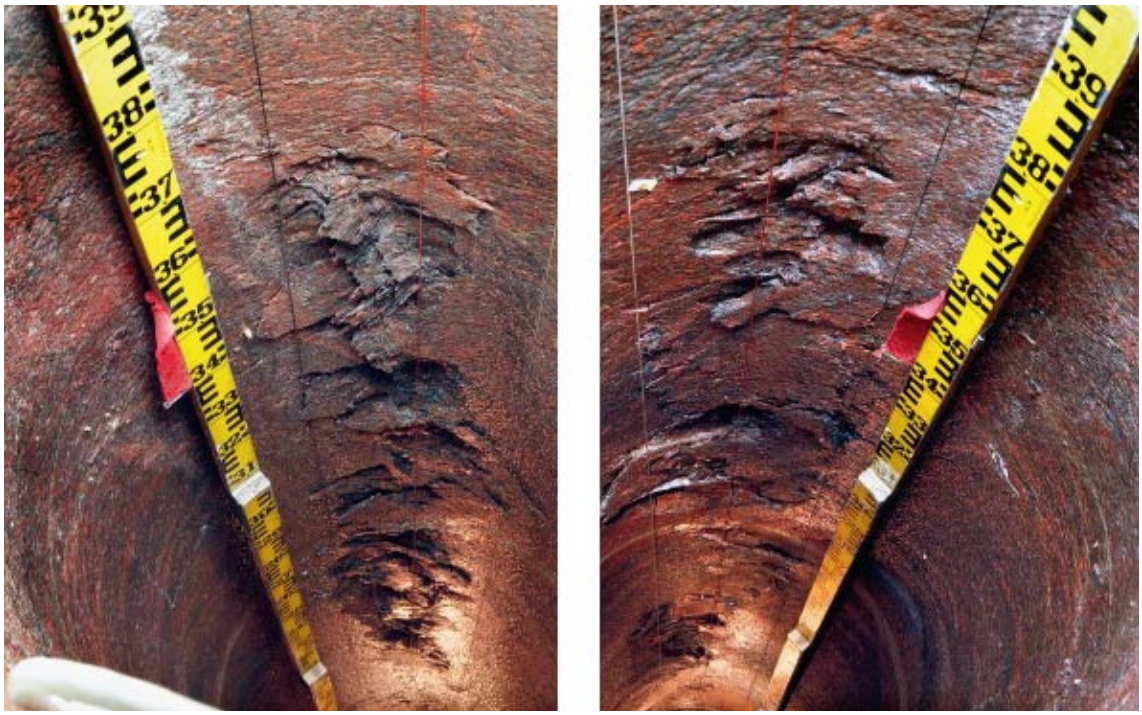

NE-side ***SW-side***

Figure T-21. *Photographs of the borehole wall in heating hole KQ0051G04 after finished the cooling phase, before scaling of the wall. Field Test 2 was performed without confinement.*

NE-side ***SW-side***

Figure T-22. *Photographs of the borehole wall in heating hole KQ0051G05 after finished the cooling phase, before scaling of the wall. Field Test 2 was performed without confinement.*

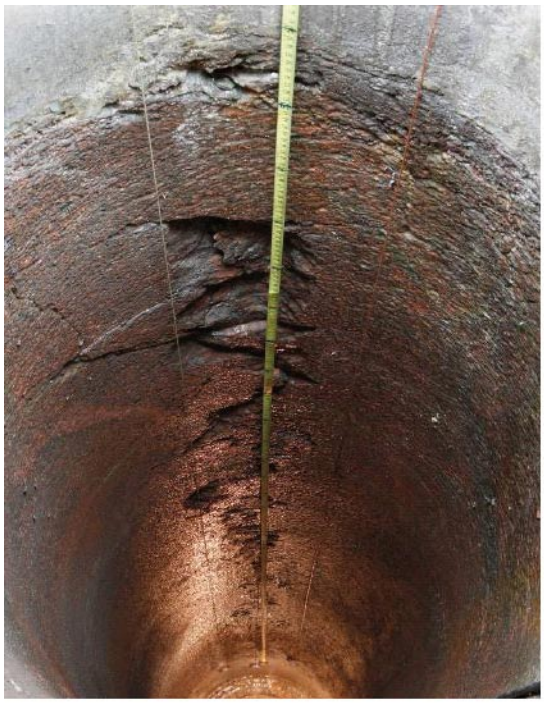

NE-side ***SW-side***

Figure T-23. *Photographs of the borehole wall in heating hole KQ0048G04 after finished the cooling phase, before scaling of the wall. Field Test 3 was performed with confinement.*

NE-side ***SW-side***

Figure T-24. *Photographs of the borehole wall in heating hole KQ0048G05 after finished the cooling phase, before scaling of the wall. Field Test 3 was performed with confinement.*

NE-side ***SW-side***

Figure T-25. *Photographs of the borehole wall in heating hole KQ0046G04 after finished the cooling phase, before scaling of the wall. Field Test 4 was performed with confinement.*

After scaling

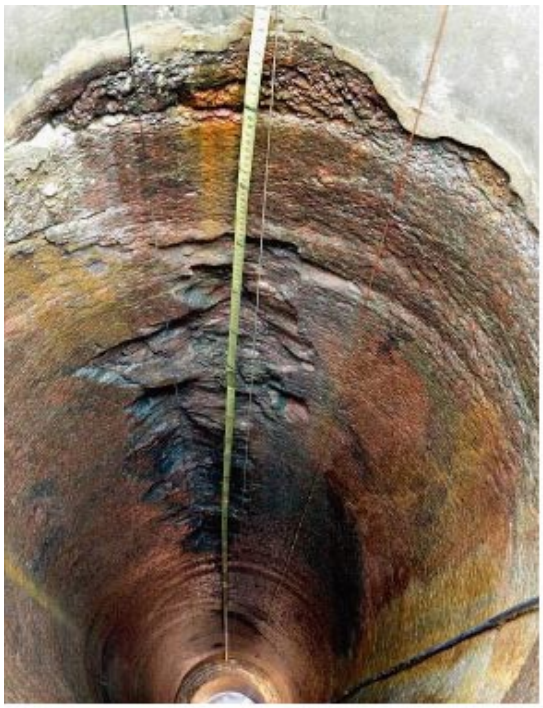

NE-side

SW-side

Figure T-26. *Photographs of the borehole wall in heating hole KQ0054G03 after scaling the wall from loose rock fragments. Field Test 1 was performed without confinement.*

NE-side

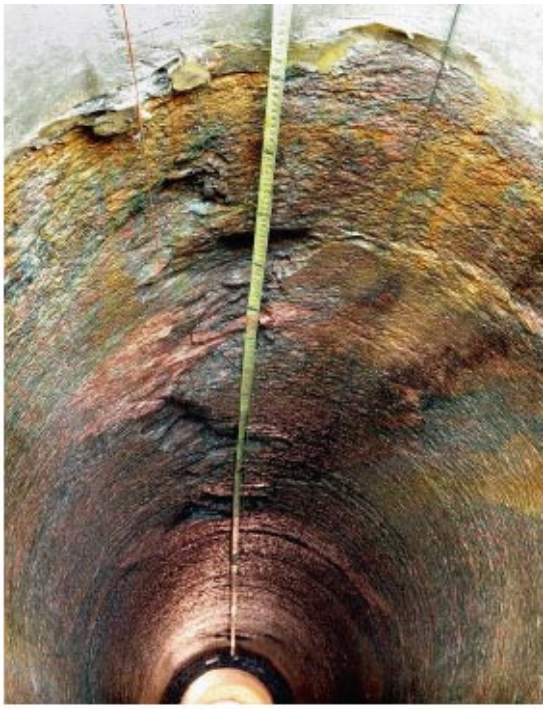

SW-side

Figure T-27. *Photographs of the borehole wall in heating hole KQ0054G04 after scaling the wall from loose rock fragments. Field Test 1 was performed without confinement.*

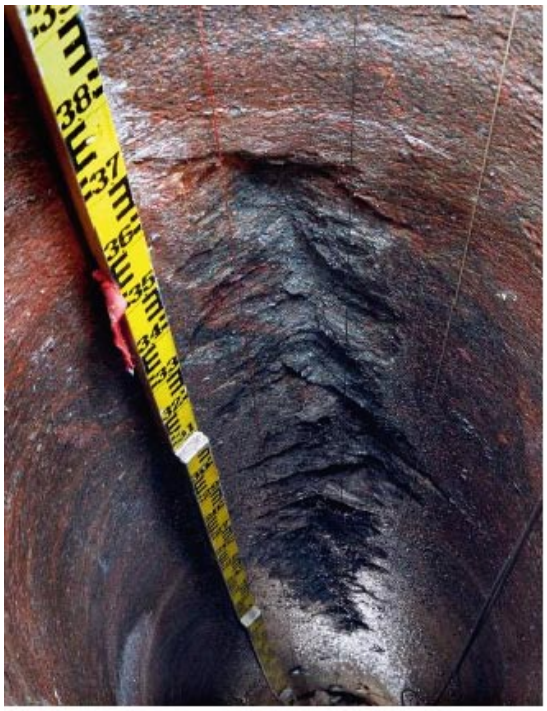

NE-side ***SW-side***

Figure T-28. *Photographs of the borehole wall in heating hole KQ0051G04 after scaling the wall from loose rock fragments. Field Test 2 was performed without confinement.*

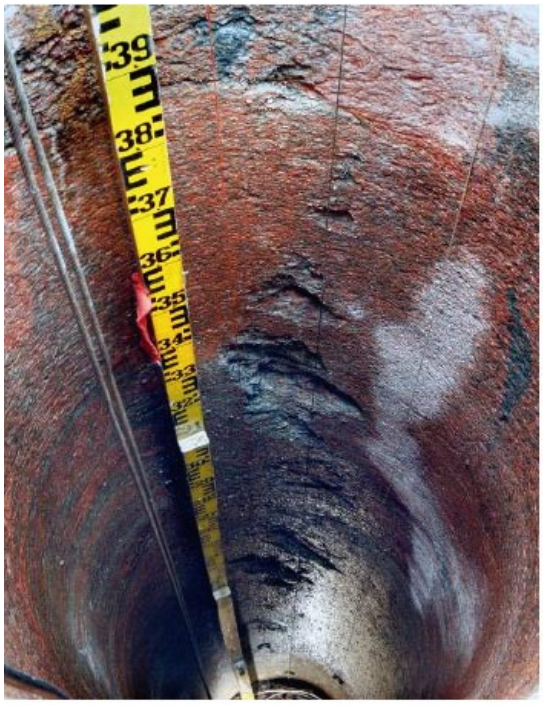

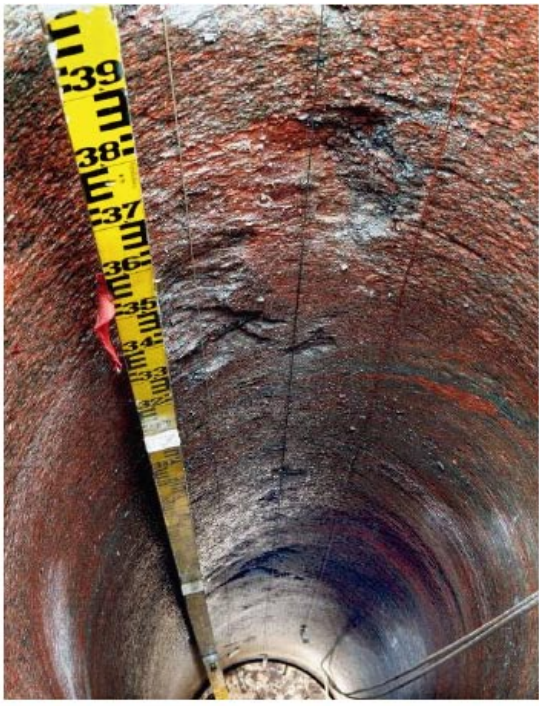

NE-side ***SW-side***

Figure T-29. *Photographs of the borehole wall in heating hole KQ0051G05 after scaling the wall from loose rock fragments. Field Test 2 was performed without confinement.*

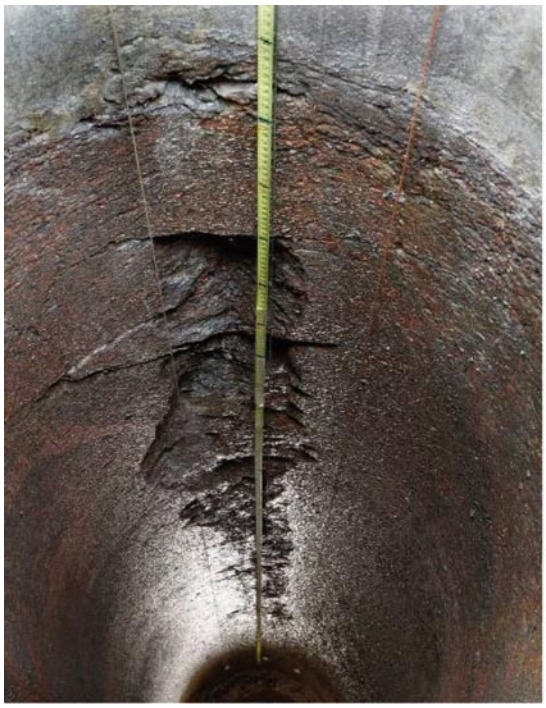

NE-side ***SW-side***

Figure T-30. *Photographs of the borehole wall in heating hole KQ0048G04 after scaling the wall from loose rock fragments. Field Test 3 was performed with confinement.*

NE-side ***SW-side***

Figure T-31. *Photographs of the borehole wall in heating hole KQ0048G05 after scaling the wall from loose rock fragments. Field Test 3 was performed with confinement.*

NE-side

Figure T-32. *Photographs of the borehole wall in heating hole KQ0046G04 after scaling the wall from loose rock fragments. Field Test 4 was performed with confinement.*

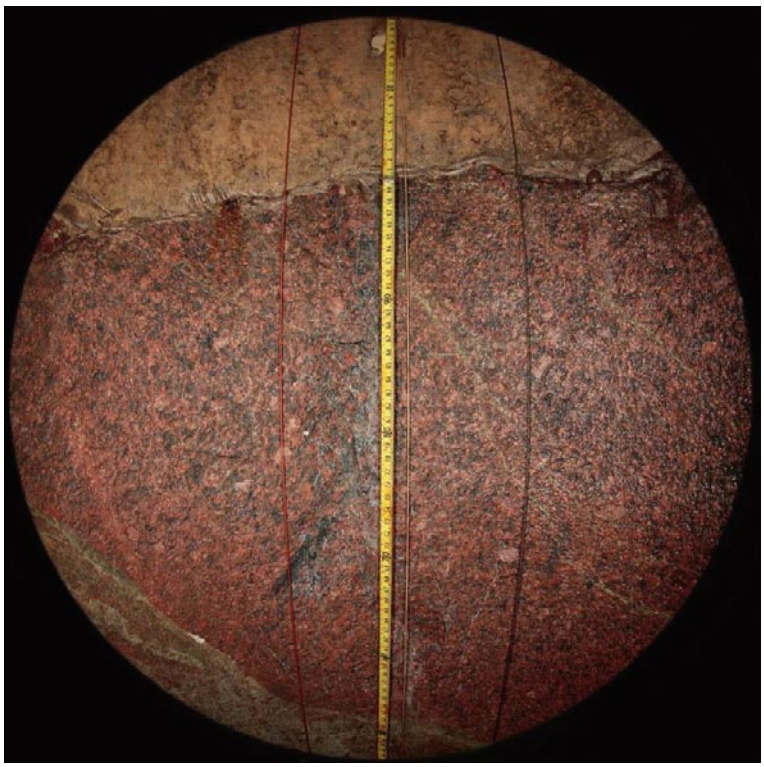

Figure T-33. *Fish-eye photograph of the NE-side of the borehole wall in heating hole KQ0046G04 after scaling the wall from loose rock fragments. Field Test 4 was performed with confinement.*

Appendix U

Photographs of the instrumentation

Figure U-1. *Shows the instrument holder installed in Field Test 1.*

Figure U-2. *Shows the instrument holder installed in Field Test 2.*

Figure U-3. *Shows the instrument holder installed in Field Test 3.*

Figure U-4. *Shows close-up view of the bottom disc and the level guard of the holder installed in Field Test 2.*

Figure U-5. *Shows a close-up view of the spacers in clinker used in Field Test 2.*

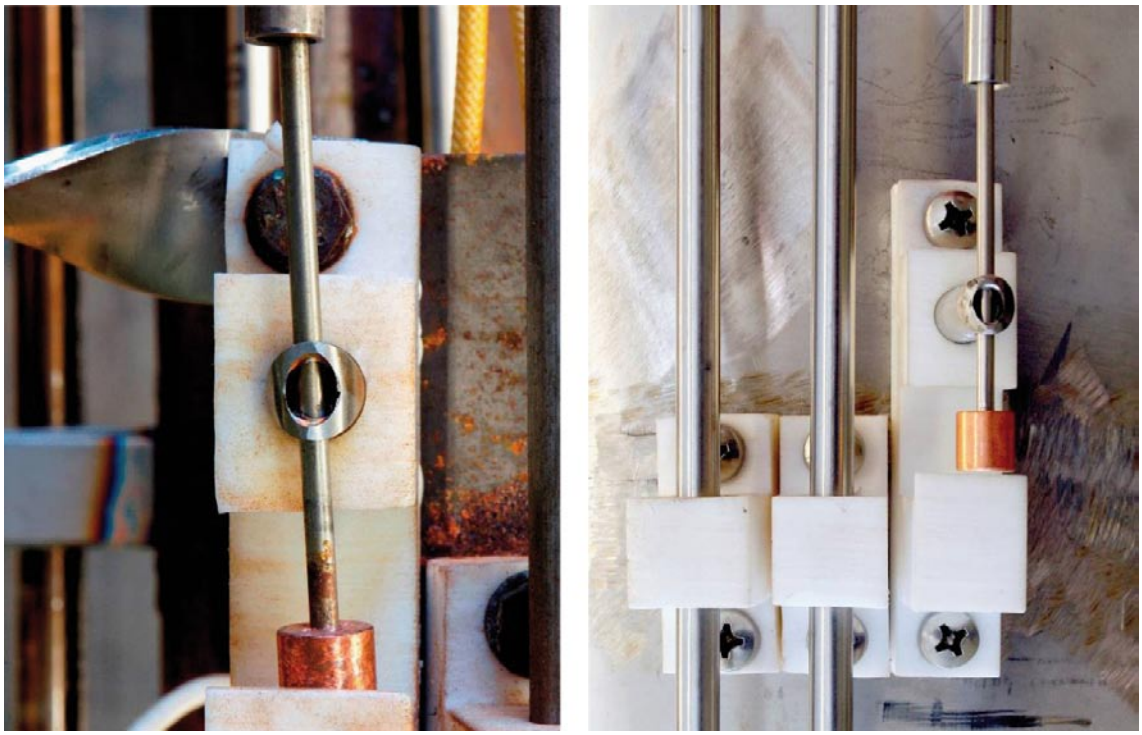

Figure U-6. *Shows a close-up view of the spring loaded mechanism after modification before Field Test 2. The edge of the guide bushing has been chamfered.*

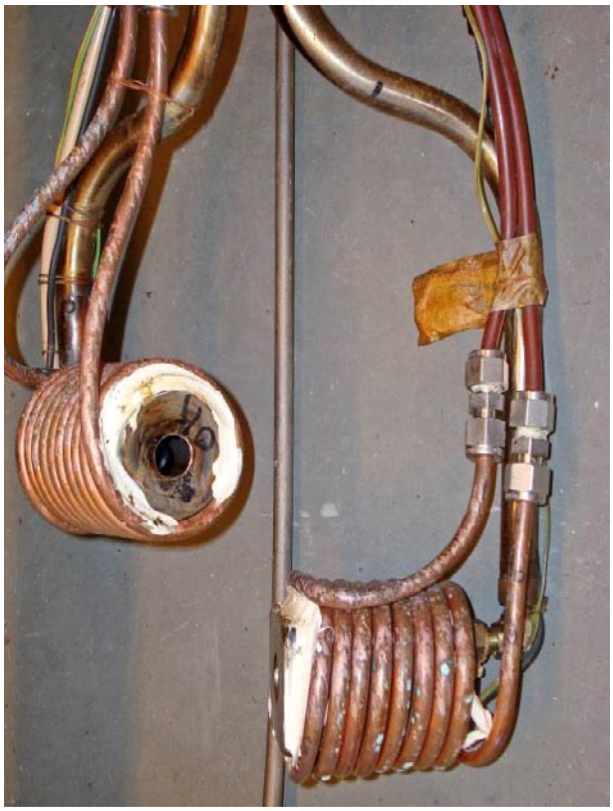

Figure U-7. *Shows the state of the monitoring camera after completion of Field Test 1.*

Figure U-8. *Shows the state of the holder after completion of Field Test 2.*

Figure U-9. *Shows a close-up view of one of the drip holes in the wetting system after completion of Field Test 2.*

Appendix V

Photographs from the accomplishment of the field test

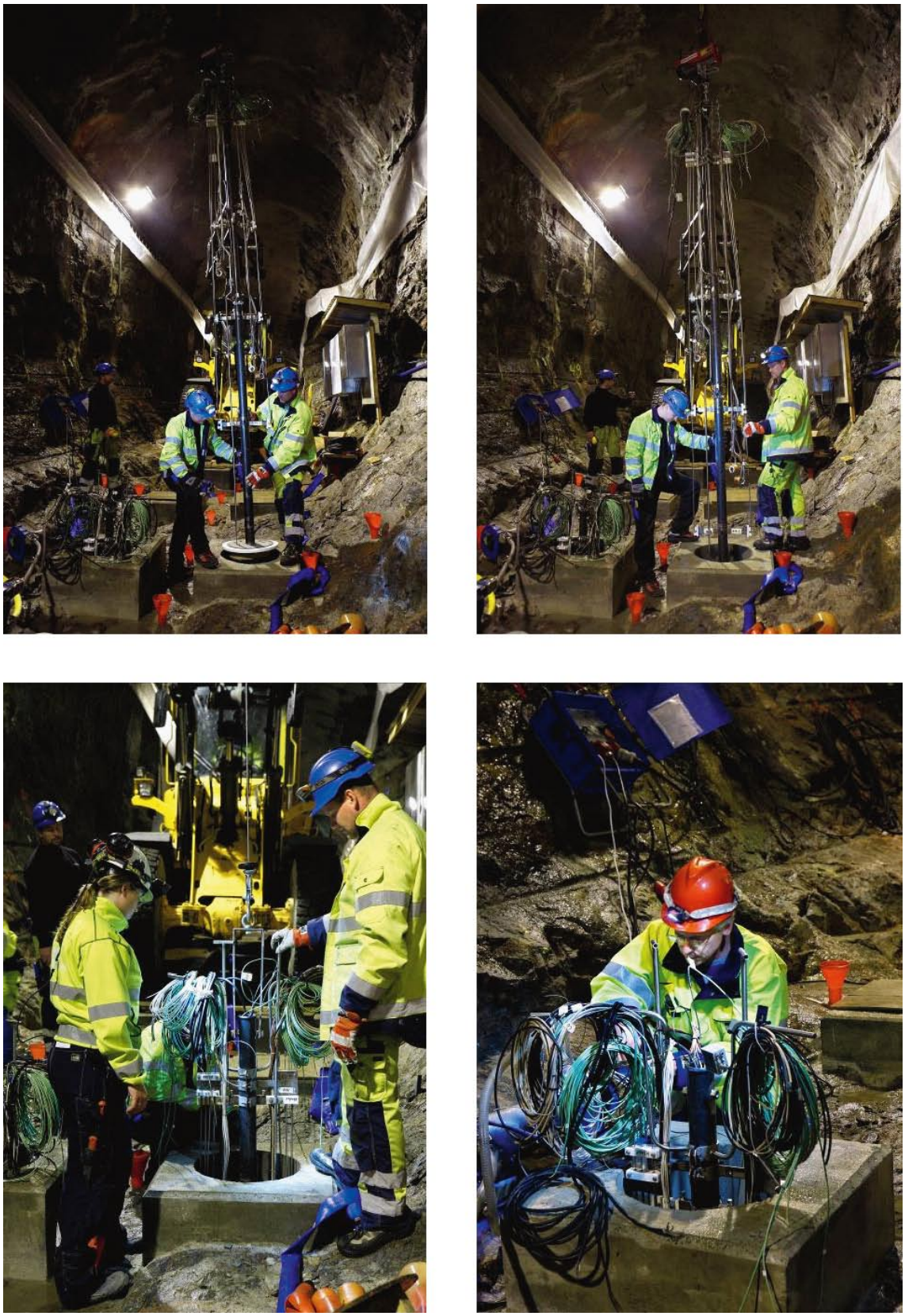

Figure V-1. *Shows a sequence of photographs from the installation of the test equipment in Field Test 1.*

Figure V-2. *Shows the test equipment in place in Field Test 1.*

Figure V-3. *Shows the test equipment in place Field Test 2.*

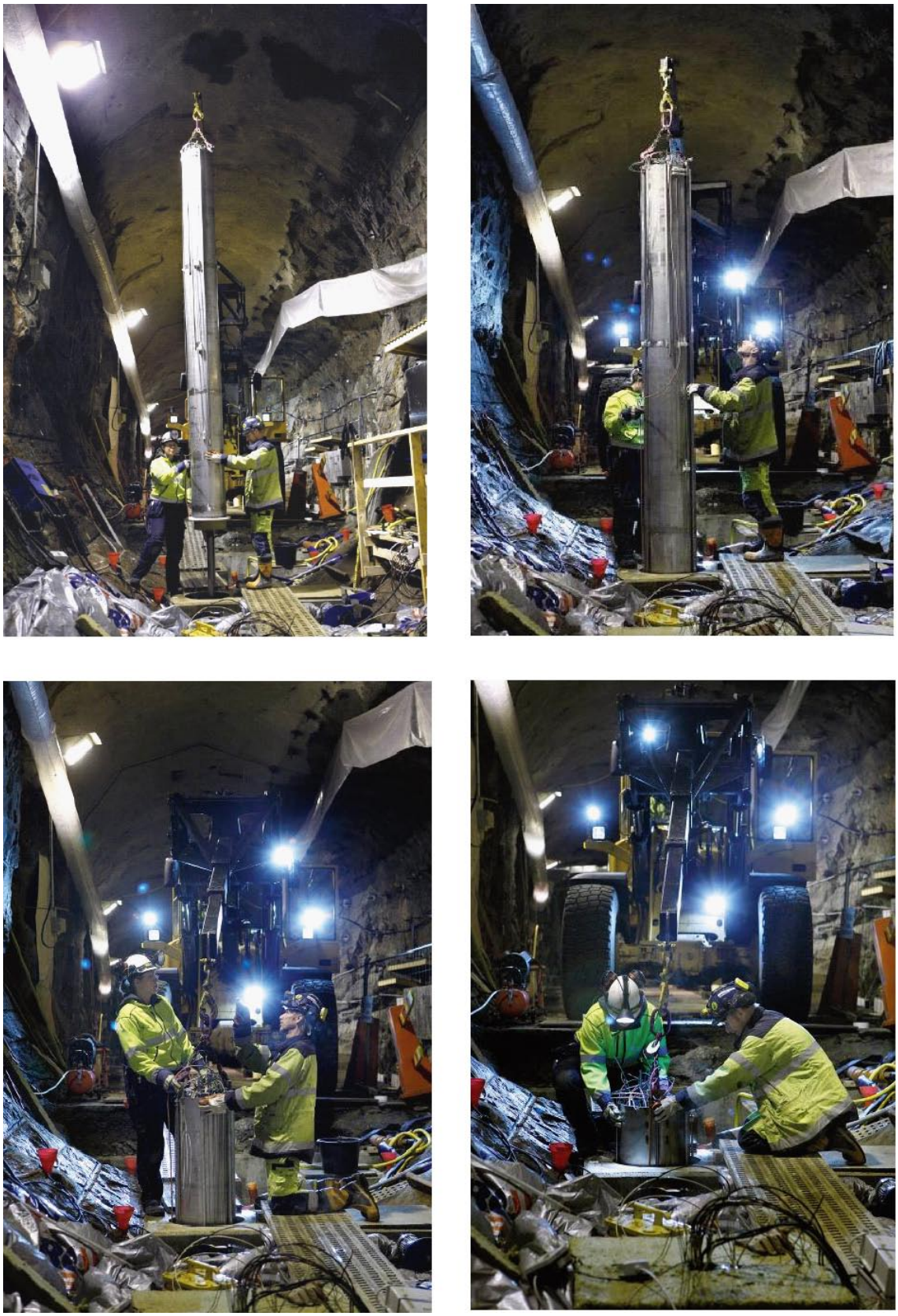

Figure V-4. *Shows a sequence of photographs from the installation of the test equipment in KQ0048G05 in Field Test 3.*

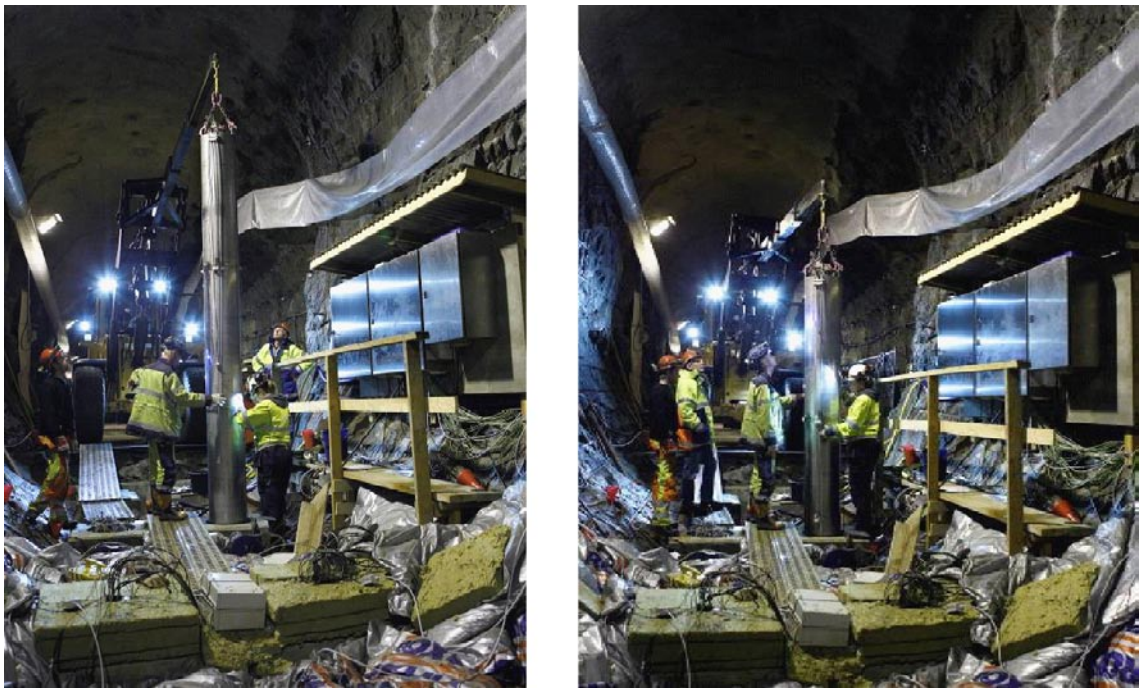

Figure V-5. *Shows the installation of the test equipment in borehole KQ0048G04 in Field Test 3.*

Figure V-6. *Shows the test equipment in place before and after sand filling of the larger tube during preparation for Field Test 3.*

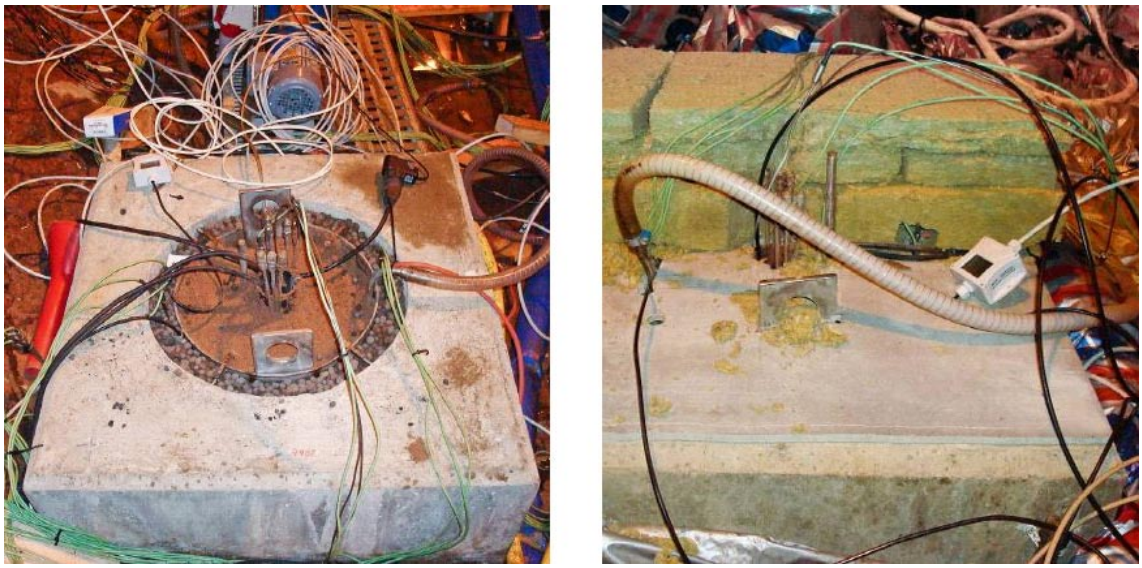

Figure V-7. *Shows the test site just before starting Field Test 3.*

Figure V-8. *Shows the test site during the Field Test 3.*

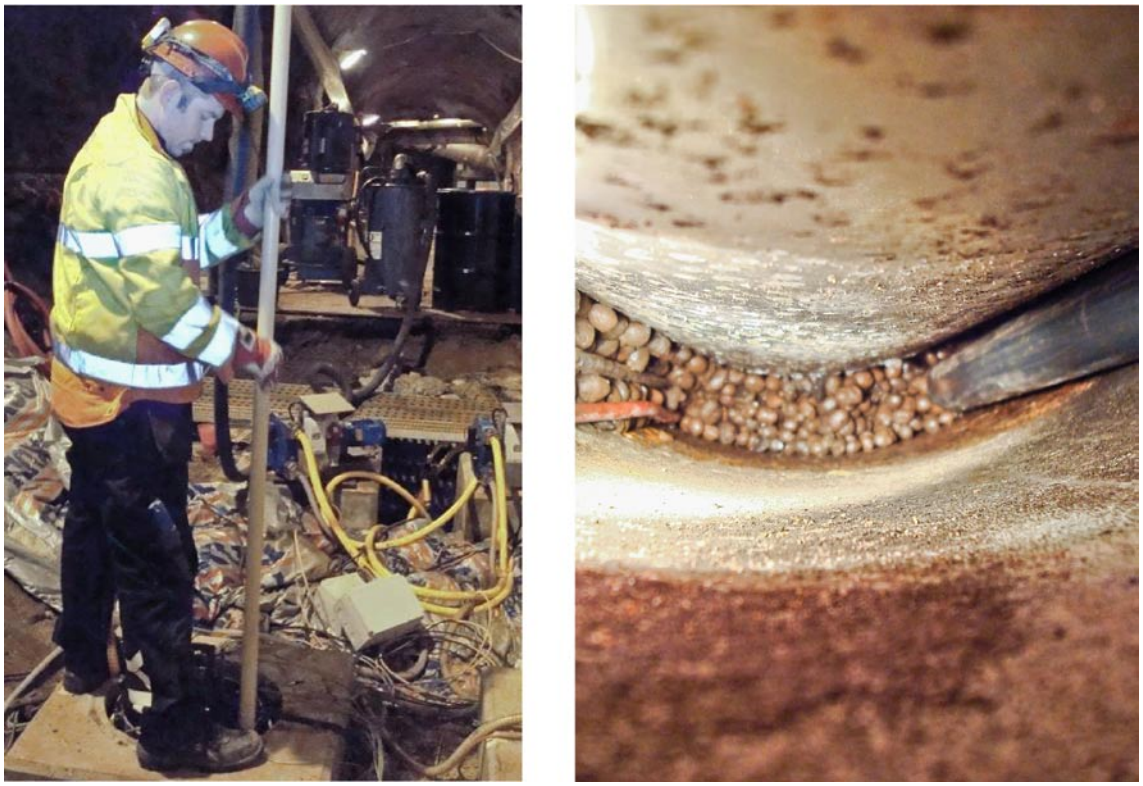

Figure V-9. *Shows the emptying of the pellet filled slot after the completion of Test 3.*

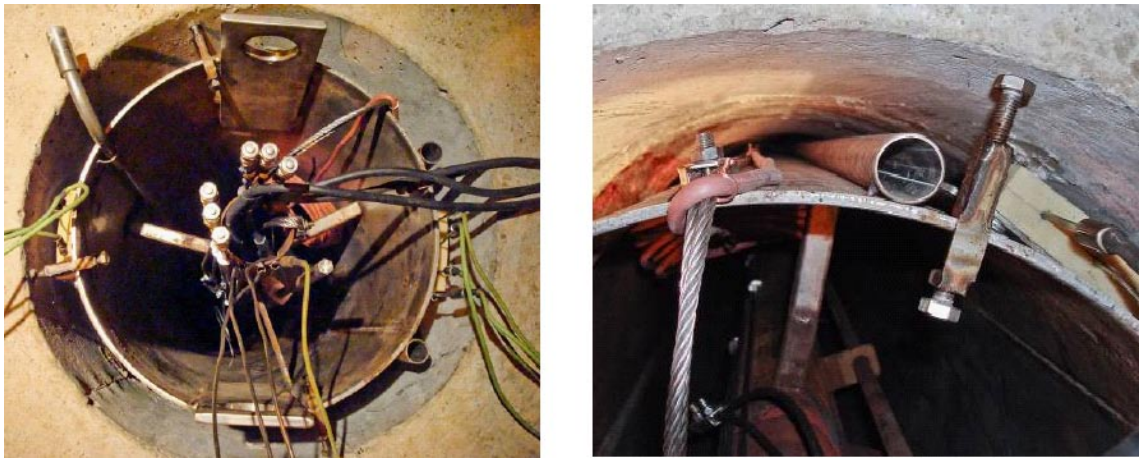

Figure V-10. *Shows the test equipment in place in filed Test 4 with a close-up view of the slot in the position of the RH-tube.*

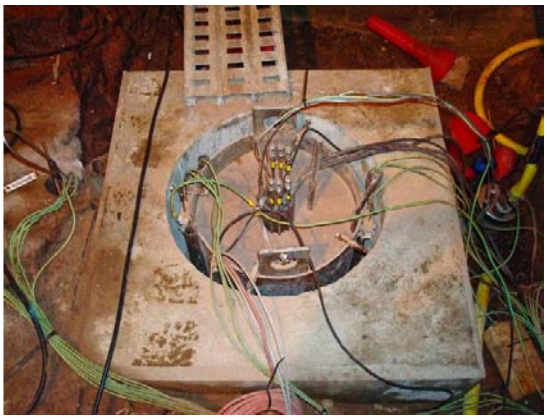

Figure V-11. *Shows the sand filling of the larger tube during the preparation for Test 4.*

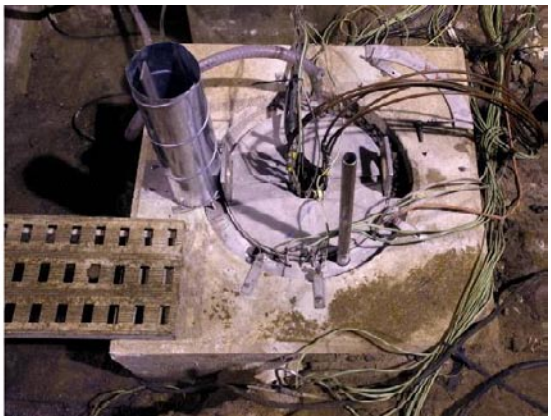

Figure V-12. *Shows the test equipment in place after filling the slot with pellets in the preparation for Field Test 4.*

Figure V-13. *Shows KQ0046G04 after replacement of a heater element in Field Test 4.*

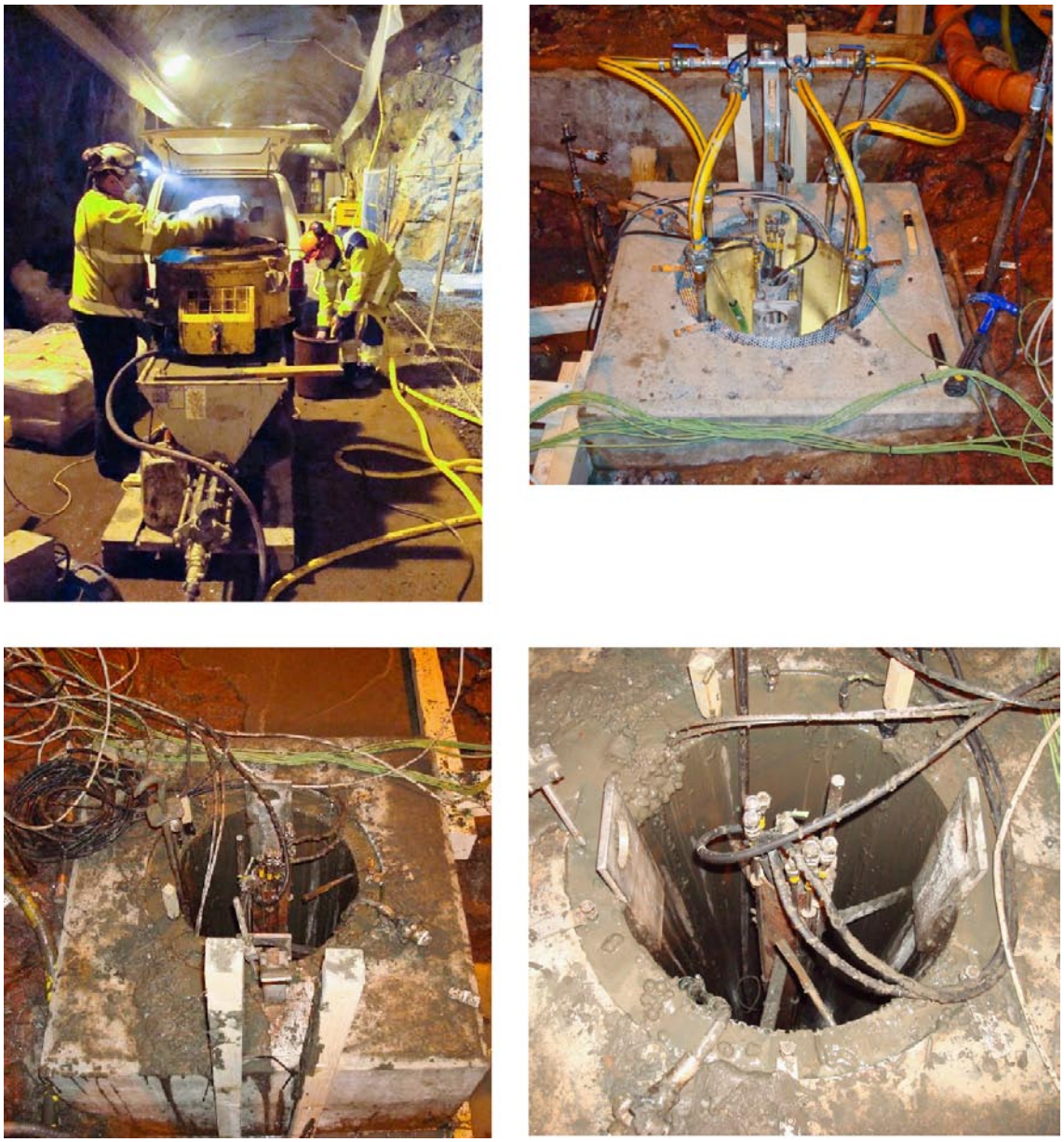

Figure V-14. *Shows the equipment and the pellet filled slot before en after the grouting of the pellet filled slot in KQ0046G03.*

Figure V-15. *Shows the core drilling of the water injection holes used in the post characterization damage zone in KQ0046G03.*

Figure V-16. *Shows the equipment utilized for the water injection tests of the damage zone in KQ0046G03.*

Figure V-17. *Shows the injection holes with installed packers during the hydraulic testing of the damaged zone in KQ0046G03.*